Contribution to Characterization Techniques for Practical Metamaterials and Microwave Applications

THÈSE N^{O} 4407 (2009)

PRÉSENTÉE LE 19 JUIN 2009

À LA FACULTÉ SCIENCES ET TECHNIQUES DE L'INGÉNIEUR
LABORATOIRE D'ÉLECTROMAGNÉTISME ET ACOUSTIQUE
SECTION DE GÉNIE ÉLECTRIQUE ET ÉLECTRONIQUE

ÉCOLE POLYTECHNIQUE FÉDÉRALE DE LAUSANNE

POUR L'OBTENTION DU GRADE DE DOCTEUR ÈS SCIENCES

PAR

Frédéric BONGARD

acceptée sur proposition du jury:

Prof. H. Bourlard, président du jury
Prof. J. R. Mosig, directeur de thèse
Prof. F. Rachidi-Haeri, rapporteur
Prof. S. Tretyakov, rapporteur
Dr M. van der Vorst, rapporteur

ÉCOLE POLYTECHNIQUE
FÉDÉRALE DE LAUSANNE

Suisse
2009

Abstract

Metamaterials (MTMs) are broadly defined as artificial composite materials specifically engineered to produce desired unusual electromagnetic properties not readily available in nature. The most interesting unusual property achievable with MTMs is probably negative refraction, which is achieved when both the permittivity and the permeability of a medium are negative. Such structures are also referred to as *left-handed media* (LHM). From the first evidences in the early 2000's showing that materials with a negative refractive index were indeed physically realizable, numerous entirely new devices or improvements of existing devices have been reported in the microwave and antenna fields.

In this context, the objective of this thesis is to contribute to the development of new characterization techniques for practical implementations of MTMs, aiming at determining a set of relevant equivalent medium parameters describing the structure from a macroscopic point of view. For this purpose, analysis techniques were developed based on the theory of wave propagation in periodic structures, and tested on selected existing or entirely new MTM structures of the two main reported categories: arrays of resonant particles and loaded transmission lines.

In the first part of the work, an improved retrieval procedure which allows the determination of equivalent dyadic permittivity and permeability of MTMs from reflection and transmission coefficients obtained for several incidences was developed and tested, thereby extending current techniques which only dealt with normal incidence. The main achievement obtained with this technique is the ability to evaluate to which extent a given MTM slab can be considered as an equivalent homogeneous medium obeying some specific constitutive relations. This technique was tested on various structures, including a novel highly isotropic artificial magnetic material which was shown to exhibit a negative permeability in the three dimensions.

In a second step, MTMs based on the transmission line approach have been investigated. In this context, the theory of the so-called composite right/left-handed transmission line (CRLH TL) has been revisited, and several planar implementations of this structure in various technologies were designed and realized. Subsequently, a volumetric LHM obtained by layering several planar artificial TLs of the CRLH type was proposed and fully characterized. This volumetric structure was shown to support left-handed propagation over a quite large bandwidth, compared to other resonant LHM made of split-ring resonators and wires. We provided an extensive experimental assessment of potential applications of this structure as an exotic substrate for microstrip patch antennas. An important contribution here consisted in the assessment of the ability of such a volumetric structure based on the TL approach to behave as a material filling in this type of configurations.

The next part presents an enhanced analysis technique for periodic structures which allows accurately characterizing MTMs exhibiting higher order coupling phenomena between successive cells. This technique also allows an accurate and complete description of more elaborated structures such as periodically loaded multiconductor TLs. The main idea of this technique is to model the periodic structure with an equivalent multiconductor TL, a model which pro-

vides all the parameters needed to describe the phase response (dispersion) and terminations (excitation and matching) of finite size periodic structures.

In the last part, we introduced and analyzed a novel unit cell topology for the CRLH TL which employs a lattice network in place of the conventional ladder-type topology. This new CRLH TL was shown to exhibit a more wideband behaviour than its conventional counterpart, both in terms of impedance and phase. These performances were numerically and experimentally demonstrated on several practical implementations. The possibilities of using this unit cell to reduce the beam squinting in leaky-wave antennas and in series-fed arrays were highlighted. It is foreseen that this new CRLH TL can be potentially used to improve the performances of many of the well-known CRLH TL applications.

Keywords: *Electromagnetics, Microwaves, Antennas, Metamaterials, Negative refraction, Left-handed media, Periodic structures, Artificial transmission lines, Dispersion engineering, Homogenization.*

Résumé

Les métamatériaux sont des matériaux composites artificiels spécifiquement conçu pour présenter des propriétés électromagnétiques qu'on ne retrouve pas aisément dans la nature. Une des propriétés les plus intéressantes réalisables avec les métamatériaux est la *réfraction négative*, qui est obtenue lorsque la permittivité et la perméabilité d'un milieu sont toutes deux négatives. De tels milieux sont aussi appelés *matériaux main gauche, ou "left-handed medium" (LHM)*. Depuis les premières validations expérimentales des métamatériaux à indice de réfraction négatif au début des années 2000, de nombreux dispositifs entièrement nouveaux ou des améliorations de dispositifs existant ont été proposés dans le domaine des hyperfréquences et des antennes.

Dans ce contexte, l'objectif de cette thèse est de contribuer au développement de nouvelles techniques de caractérisation s'appliquant aux réalisations pratiques de métamatériaux. Ces techniques ont pour but de déterminer un ensemble de paramètres équivalents, ou effectifs, décrivant la structure d'un point de vue macroscopique. Dans ce but, des techniques d'analyse ont été développées, essentiellement sur la base de la théorie de la propagation des ondes dans les structures périodiques, et testées sur des métamatériaux existants ou complètement nouveaux appartenant aux deux principales catégories reportées à ce jour: les matrices d'inclusions résonantes et les lignes de transmission chargées périodiquement.

Dans la première partie du travail, une méthode permettant d'extraire les tenseurs de permittivité électrique et de perméabilité magnétique à partir des coefficients de réflexion et de transmission obtenus pour diverses incidences a été développée et testée, élargissant ainsi les techniques existantes qui ne considèrent que l'incidence normale. Cette technique permet entre autres d'évaluer dans quelle mesure un métamatériau donné peut être considéré comme un milieu homogène équivalent satisfaisant des relations constitutives prédéterminées. Cette technique a été testée sur diverses structures, dont un nouveau métamatériau magnétique artificiel hautement isotrope, pour lequel la méthode révèle une perméabilité négative dans les trois dimensions.

Dans un deuxième temps, les métamatériaux basés sur l'approche ligne de transmission ont été étudiés. Dans ce contexte, la théorie de la ligne composite main droite/main gauche [*composite right/left-handed transmission line (CRLH TL)*] a été revisitée, et plusieurs implémentations planaires de cette structure ont été conçues et réalisées dans diverses technologies. Par la suite, un LHM volumétrique obtenu par superposition de lignes de transmission artificielles planaires de type CRLH a été proposé et entièrement caractérisé. L'analyse révèle que cette structure présente un indice de réfraction négatif sur une bande de fréquence relativement large, comparé à d'autres LHM résonants basés sur les résonateurs en anneau fendu et les réseaux de tiges. Une étude expérimentale approfondie des applications potentielles de cette structure comme substrat exotique pour des antennes patch microruban a été effectuée. Une contribution importante résultant de cette étude consiste en l'évaluation de la faculté d'une telle structure, basée sur des lignes de transmission, de se comporter comme un matériau au sens habituel du terme dans ce type de configurations.

La partie suivante présente une nouvelle méthode d'analyse de structures périodiques permettant de caractériser de façon précise des métamatériaux présentant des phénomènes de couplages entre cellules successives. Cette technique permet également une description précise et complète de structures plus élaborées, telles que des lignes de transmission multiconducteur chargées périodiquement. L'idée principale de cette technique est de modéliser la structure périodique par une ligne de transmission multiconducteur, un modèle qui fournit tous les paramètres nécessaires pour décrire la réponse en phase (dispersion) et les terminaisons (excitation et adaptation) de structures périodiques de taille finie.

Dans la dernière partie, nous avons proposé et étudié une nouvelle topologie pour la cellule de base de la ligne CRLH, basée sur un biporte en treillis en lieu et place de la topologie conventionnelle en échelle. Cette nouvelle ligne CRLH présente un comportement plus large bande comparé à la version conventionnelle, à la fois en termes d'impédance et de phase. Ces performances ont été démontrées numériquement et expérimentalement sur plusieurs réalisations pratiques, puis les possibilités d'utiliser cette cellule pour minimiser la déviation du lobe principal avec la fréquence dans les antennes à ondes de fuite et les réseaux d'antennes alimentés en série ont été mises en évidence. Cette nouvelle ligne CRLH peut être en principe utilisée pour améliorer les performances de la plupart des applications de ces structures.

Mots clés: *Electromagnétisme, Hyperfréquences, Antennes, Métamatériaux, Réfraction négative, Milieux main gauche, Structures périodiques, Lignes de transmission artificielles, Ingénierie de dispersion, Homogénéisation.*

Acknowledgements

First and foremost, I would like to deeply thank my thesis supervisor, Prof. Juan Mosig, for supporting this research, for his advice and encouragement, and especially for his trust all along this thesis. Thanks also to him for providing an excellent working environment and maintaining a great atmosphere in the laboratory.

I would also like to acknowledge the members of my thesis jury, Prof. Sergei Tretyakov from Helsinki University of Technology, Dr. Maarten van der Vorst from European Space Agency, and Prof. Farhad Rachidi from EPFL, for having accepted to examine this work and for their valuable comments and insights. Thanks also to Prof. Hervé Bourlard for chairing this jury.

I will take some lines here to deeply acknowledge Sir Julien Perruisseau-Carrier, my friend and former colleague, for all the fruitful exchanges and technical discussions we had on many parts of this thesis, and for reviewing parts of this report and most of the papers I have written. Thanks also for all the memorable moments we shared in conferences and outside work.

A special thank goes to Jean-François Zürcher, for his assistance in the realization and measurement of the meta-devices presented in this work, and for transmitting me some of his secret tricks of the Engineering Art. Thanks also to the members of the ACI and AEM workshops for the technical support. My appreciation also goes to Prof. Olivier Martin of NAM-EPFL, with who we collaborated on the first part of this work, for some nice ideas he brought to this thesis. Also thanks to the senior scientists Ivica Stevanovic, Michael Mattes, Pedro Crespo Valero and Prof. Anja Skrivervik for having shared their time for stimulating talks.

A special hug to my roomy for most of these years, Gabriela Quintero, for transmitting me part of her natural enthusiasm. My warmest thanks also go to all the actual and former members of the Laboratory of Electromagnetics and Acoustics (LEMA) that I had the chance to meet during this stay. Thank you all for the unforgettable time that we spent together. I also express my sincere gratitude to the LEMA permanent members, our secretary Mrs. Eulalia Durussel and our system managers Sébastien Halouze-Lamy and David Desscan, for their dedicated help and availability.

I am also grateful to Prof. Mario Rossi for hiring me for my first job as an assistant at LEMA-acoustics, and who gave me the opportunity to concretize my Master Project. Thanks also to the acoustics members for the exchanges we had at that time.

Finally, thanks to my old friends, Didier and Inch, for their friendship throughout the years, and last but not least, I wish to deeply thank my parents and sister, for the unconditional support you have given me in these years. — To all of you I dedicate this thesis.

Contents

1 General Introduction

1.1 Basic concepts on metamaterials

1.1.1 Terminology and definitions

The concept of emergence

In recent years, there has been rapidly growing interest in engineered materials commonly called "metamaterials". Although a universally accepted definition of the term "metamaterial" does not exist, a general description of this concept as it is considered within the framework of the present thesis is provided in this section. Metamaterials (MTMs) are broadly defined as artificial composite materials specifically engineered to produce desired unusual electromagnetic properties not readily available in nature. The prefix "meta", which means "beyond" or "after" in Greek, suggests that MTMs exhibit *emergent* electromagnetic properties, that is, properties that the constituent elements do not exhibit when they are considered separately [1]. The prefix "meta" also suggests that the resulting properties transcend those available in nature, or at least that they cannot be readily available in nature.

The effective medium concept

The aforementioned emergent properties are related to the fact that the inclusions interact with electromagnetic waves in a subtle manner. Indeed, waves are not sensitive to each detail of the structure, but they "see" an equivalent homogeneous medium, for which it is possible to define equivalent medium parameters like the permittivity and the permeability: this is the *effective medium* approach. This approach relies on homogenization procedures, which consist in defining equivalent macroscopic parameters from a microscopic description of the medium. As a matter of fact, such an approach is not new. Indeed, for conventional materials the permittivity and permeability are already macroscopic parameters describing the average response of the material to electromagnetic phenomena, whereas microscopic models describe these interactions by taking into account the molecular and atomic structure of the material. From that point of view, one may consider that there is no fundamental difference between MTMs and conventional materials, since the engineered particles in MTMs play the role of the atoms and molecules in conventional materials, but at a different length scale. Furthermore, the aforementioned emergence of properties may also occur for conventional materials, since their overall response may represent something completely different from that of a single atom. A difference between MTMs and conventional materials yet exists at a structural level. Indeed, a MTM is made of its elements, which are themselves made of conventional material, thus of atoms and molecules. Accordingly, MTMs represent the next level of structural organization [2],

thereby justifying the use of the prefix "meta". This point of view mostly relies on a *structural* definition of MTMs, based on their composite nature, whereas the considerations of the first paragraph where mainly concerned with the capability to provide *unusual responses*, thus corresponding to a more *phenomenological* definition.

It results from the discussion above that the distinction between MTMs and conventional materials is not obvious, and even asks for metaphysical reasonings, which is not the main concern of this work. Further considerations on the concept of MTM and on the circumstances under which such a term is appropriate can be found in [1,2]. From now on, we concentrate on a more pragmatic description of this concept, as usually understood in the scientific community.

The scope of the term metamaterial

Practical implementations of MTMs are often found under the form of periodic structures. However, this is by no means a necessary restriction, but rather a choice of convenience for the analysis. Indeed, MTMs can also be implemented as random composite structures, although this approach is less common in the physical and engineering communities. Nowadays, there is also considerable interest in another type of periodic structures: the photonic band gap (PBG) structures (or electromagnetic band gap (EBG) structures). A key difference between the concept of MTM, as considered in this work, and PBG/EBG structures is the electrical size of the unit cell:

- The electromagnetic properties of PBG/EBG rely on the periodicity, which is on the order of half a wavelength or more. In that case, the electromagnetic behaviour of the structure is essentially governed by Bragg reflection and diffraction phenomena, in which the lattice topology plays a crucial role.

- The properties of MTMs can be deduced from the electromagnetic properties of their elementary constituents through an appropriate homogenization procedure. In such a case, the lattice topology itself has limited effect, and can even be random. To make possible this effective medium approach, the electrical size of the unit cell should be much smaller than the wavelength in the equivalent medium.

It can be inferred from this distinction that a given periodic structure can be used as both PBG/EBG and MTM, depending on the operating frequency.

As already mentioned, the definition of MTM adopted in this work relies on the effective medium approach. In other words, MTMs should satisfy the *effective-homogeneity* condition [3], which requires that the structural average cell size is much smaller than the guided wavelength. Although a well defined limit does not exist, a value of one tenth of a wavelength is often considered as a favorable value for potentially applying effective medium concepts. A less restrictive limit of a quarter of a wavelength has also been proposed in [3], by analogy with the condition commonly used by microwave engineers for lumped components. This condition should "*ensure that refractive phenomena will dominate over scattering/difraction phenomena when a wave propagates inside the medium*" [3]. On the other hand, other authors do not impose a limit on the unit cell size, and thus extend the definition of MTMs to structures such as PBG/EBG [4, 5]. Even further, a wider definition of MTMs also comprises other types of

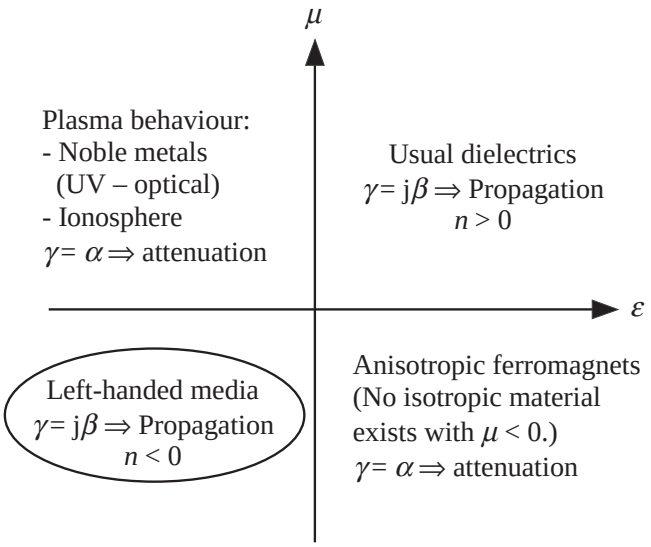

Figure 1.1: Simplified ε - μ diagram. $\gamma = \alpha + j\beta$ is the propagation constant and n is the refractive index (see Section 2.1 for the corresponding definitions).

periodic structures based on different working principles, such as artificial magnetic conductors (AMC), high impedance surfaces (HIS) or frequency selective surfaces (FSS). In this work, it has been decided to renounce to these last structures (PBG, EBG, AMC, HIS, FSS) with well demonstrated usefulness, and to stick to the restricted definition of MTM based on *effective homogeneity*. In general, it is also agreed upon that the MTM concept is not only restricted to volumetric 3D structures, as the word "material" could suggest, but is also commonly extended to 2D planar or even 1D guiding or radiating structures.

Metamaterial responses, negative refraction among others

Among all the unusual properties MTMs can exhibit, the one targeted from the very beginning of this work is negative refraction, because it was the most surprising and promising phenomenon reported at that time. A negative refractive index is achieved when both the permittivity and the permeability of a medium are negative. Such structures were referred to as *left-handed media* (LHM) by Veselago in 1968 [6]. He also predicted that LHM would have quite interesting and unusual electromagnetic properties, like reversed Doppler effect and reversed Cherenkov-like radiation. In the literature, various terms have been subsequently proposed for LHM, such as negative refractive index medium, negative phase velocity medium, backward wave medium or double negative medium. The correspondence between these terms is discussed in more detail in Section 2.1.8.

Figure 1.1 illustrates the type of media of interest in terms of the sign of the permittivity ε and the permeability μ. It is a simplified representation since only real values of ε and μ are considered. Whereas media with negative ε or negative μ can be found in nature, there is still no occurrence of a medium for which both ε and μ are negative. While progressing in this work, the door has been kept open to MTMs exhibiting other types of potentially interesting

responses, such as epsilon negative (ENG) materials, mu negative (MNG) materials, combinations of complementary materials, zero index materials or materials exhibiting both usable negative index (or left-handed, LH) and positive index (or right-handed, RH) bands, with possible seamless transition between them, like the so-called (balanced) composite right/left-handed transmission line (CRLH TL) [3]. It is also worth mentioning that, although the definition of MTMs involves *composite* materials, thereby denoting the physical implementation of MTMs, the term MTM is also commonly extended to idealized homogeneous (i.e. continuous) media exhibiting the targeted unusual properties. For instance, in a theoretical analysis, we may also call a MTM an idealized homogeneous medium with negative refractive index, although this is only its practical implementation which consists of a composite material.

The two main approaches of metamaterials

From the very early investigations, there has been two rather different ways of considering and realizing MTMs:

- Periodic arrays of dielectric and/or metallic inclusions in a host dielectric.
- Periodically loaded transmission line (TL) networks.

The first approach, referred to here as the *inclusion-based* approach, was the first originally proposed in the pioneer works on MTMs (see the historic in Section 1.1.2), and has mainly been investigated by the physical community. The second approach, referred to here as the *TL-based* approach, appeared slightly after. It is based on circuital representations and has mainly been investigated by the engineering community. In the early developments of MTMs, the TL-based approach was mainly restricted to planar 1D or 2D structures, whereas the inclusion-based approach already applied to volumetric 3D structures. This is only in the latest years that the TL-based approach has been extended to volumetric structures, essentially obtained by stacking planar TL-based MTMs. One of the main differences between these two classes of structures comes from the fact that TL-based MTMs always rely on a host TL network, which complicates the extension to 3D structures and, more importantly, prevents an efficient and straightforward coupling by an external field, such as a wave incident from free-space. As a result, the ability of TL-based MTMs to be really considered as material filling is still questionable. Therefore the pertinent question arises, whether TL-based MTMs can be considered as *materials*, or if they only "*model specific features of MTMs on the phenomenological level*" [2]. Answering this question is by no means an easy task. Nevertheless, TL-based MTMs clearly deserve attention since they are at the basis of most of the well demonstrated applications of MTMs. In the present work, both approaches of MTMs have been considered.

1.1.2 History of metamaterials

This section summarizes the pioneer works on MTMs, more particularly of LHM, from the first theoretical speculations to recent experimental results which confirm the physical existence of negative refraction and LHM.

1968: Russian physicist Victor Veselago studied the electromagnetic properties of an hypothetical medium in which both the permittivity and the permeability were simultaneously

negative [6]. In such a medium, the three vectors **E**, **H** and **k** do not follow the usual "right-hand" rule as in conventional media, but they rather follow a "left-hand" rule. In other words, the wave vector **k** is antiparallel to the right-handed cross product of **E** and **H** (Poynting's vector). For this reason, Veselago referred to such a medium as *left-handed medium* (LHM). He also predicted that LHM would have quite interesting and unusual electromagnetic properties, like a negative refractive index, reversed Doppler effect and Reversed Cherenkov-like radiation.

1996-1999: John Pendry, a theoretical physicist at Imperial College in London, published his investigations on two types of periodic arrays of metallic elements, both of them working in the microwave range:

- Arrays of thin parallel conducting wires: These composite structures act as equivalent media exhibiting a plasma-like permittivity, with possible negative values below the plasma frequency [7, 8].
- Arrays of metallic rings called *split-ring resonators* (SRRs): These composite structures act as equivalent media exhibiting a resonant permeability, with possible negative values just above the resonant frequency [9].

May 2000: Inspired by the work of Pendry, Physicist David Smith at San Diego's University of California (UCSD) proposed to combine parallel wires and SRRs to obtain a composite material which simultaneously exhibits negative permittivity and permeability over a finite frequency band [10]. They have created the first LHM ! This first prototype only exhibited a left-handed behaviour for one direction of propagation (1D LHM) and for one polarization of the fields. An improved 2D isotropic version of this structure was subsequently proposed in [11].

October 2000: Pendry made the most provocative suggestion about negative refraction and LHM: he found that, in addition to refocusing the far-field propagating components by negative refraction, a LHM-lens could also refocus the near-field evanescent components [12]. With a conventional lens these components, which carry information on details smaller than about a wavelength, disappear almost completely at a distance of about two wavelengths. Pendry predicted that these evanescent waves will grow within a flat LHM-lens, thereby allowing a perfect image reconstruction, that is, without any resolution limit. He invented the term *superlens* for such lenses able to refocus waves far beyond the well-known diffraction limit (or *perfect lens* in the ideal lossless case where the image reconstruction is perfect).

April 2001: The group of David Smith demonstrated for the first time the phenomenon of negative refraction [13]. They used a 2D isotropic composite LHM working at microwave frequencies similar to that presented in [11]. These experimental results were consistent with Snell's law if a negative refractive index is taken for the LHM.

May-June 2002: Two groups of scientists published their disagreement with Pendry's and Smith's articles about negative refraction and perfect lenses, beginning then a controversial debate about the subject:

- First, Prashant Valanju and colleagues at the University of Texas at Austin claimed that causality and finite signal speed preclude negative refraction for real non-monochromatic

waves [14]. They also stated that the inherent dispersion in LHM implies that group fronts refract positively even when phase fronts refract negatively, therefore a wideband signal will bend and travel in the usual direction (see also Pendry's comment [15] and Valanju's reply [16]). In an article published in October 2002 [17], Smith and Pendry explained in detail the error made by Valanju in [14]. It concerned a confusion between the normal of the modulation interference front of a wideband signal and the direction of the group velocity. The use of a finite-width beam incident on an interface instead of a plane wave greatly helped to understand this issue. Similar theoretical results have been reported by J. Pacheco and co-workers at the Research Laboratory of Electronics at MIT, who calculated the time average of the Poynting's vector to show that negative refraction was also possible for wideband signals [18].

- Second, Nicolas Garcia and Manuel Nieto-Vesperinas, of the National Research Council of Spain in Madrid, claimed that losses and dispersion in a real LHM would prevent restoration of evanescent waves and perfect focusing [19] (see also Garcia's erratum [20], Pendry's comment [21] and Garcia's reply [22]). Furthermore, they also criticized in [23] the experimental results obtained by Smith in [13], arguing that high losses present in LHM and the geometry used can mimic negative refraction. According to them, the intensity was not recorded far enough to be considered as far field components. Considering the measurement results in [13] as highly ambiguous, they concluded that neat experimental verification of negative refraction remained undone.

June 2002: In parallel to the investigations on SRR-wire LHM, three groups proposed almost at the same time a novel kind of MTMs based on a circuit approach: the group of Christophe Caloz and Tatsuo Itoh at University of California in Los Angeles (UCLA) [24], the group of George V. Eleftheriades at University of Toronto [25] and the group of Arthur A. Oliner [26]. The main idea consisted in realizing a TL with a capacitive element in the series branch and an inductive element in the shunt branch, i.e. the dual topology of a conventional TL. Concretely, these novel MTMs were obtained by periodically loading a TL (for the 1D case) or a grid of TLs (for the 2D case) with lumped L-C elements.

December 2002: G. V. Eleftheriades presented clear experimental evidence confirming negative refraction and went even further to demonstrate for the first time focusing of electromagnetic waves from a left-handed lens [27]. The structure used was a 2D periodically L-C loaded TL network (dual TL medium).

March-April 2003: Good news for LHM: Several groups carried out experiments and simulations which confirmed the existence of negative refraction, and that LHM do not violate basic physical laws like causality:

- In March 2003, Claudio G. Parazzoli at Boeing Phantom Works at Seattle carried out an experiment similar to that made by Smith in [13]. Using a free-space measurement setup, they detected negatively refracted waves at a remarkably long distance from the LHM sample [28], thereby dispelling any doubt concerning the far field nature of these waves. These results, which fully supported the theoretical results of [17, 18], clearly confirmed the existence of negative refraction.

- In April 2003, Andrew A. Houck at MIT Media Laboratory at Cambridge reported measurement results demonstrating that refraction through a 2D LHM obeys Snell's law with a negative index of refraction [29]. He also presented preliminary evidence that a flat rectangular slab of this material could focus power from a point source, as predicted by Pendry in [12].

March 2003: The group of G. V. Eleftheriades presented simulation results showing subwavelength focusing capability of a LHM lens [30]. They used a 2D dual TL medium sandwiched between two 2D conventional TL media (right-handed media). Evidence of growing evanescent waves within the dual TL medium was shown for both infinite and finite length structures. In December 2003, they published further analytical and simulation results on subwavelength focusing. In particular, they discussed the required criteria for perfect focusing, as well as the restrictions imposed on the resolution by the periodicity of the LHM used.

March 2004: G. V. Eleftheriades presented for the first time experimental results showing subwavelength focusing with a planar TL-based left-handed lens [31]. At a frequency of 1.057 GHz, the resolution was three times better than the one imposed by the diffraction limit. This resolution enhancement was quite small because of the mismatch at the lens interfaces and the losses in the left-handed lens.

2006: More recent research on MTMs focuses on the new exciting topic of invisibility, also referred to as cloaking [32, 33], which consists in hiding objects by bending the light around them with MTM cloaks. These applications do not directly involve LHM, but rather MTMs with refractive indices varying between 0 and 1.

From 2006 to present: Since the pioneer works mentioned above, many groups worldwide have investigated metamaterials and the number of related papers published has been continuously increasing. A selection of the most significant contributions regarding microwave engineering is provided in the state-of-the-art of Chapter 2. In parallel to these developments, some serious concerns have emerged, concerning the pertinence of considering MTMs as a real *new* field of research, or whether these findings can be fully explained in the frame of more traditional areas of research, such as filter theory. These issues are currently being debated (see for instance [34]).

In this section, we have reported the most significant milestones in the emergence of MTMs, more particularly of LHM. However, as is often the case with such a fundamental new field of research as MTMs, there exist former works which are to some extent related to these modern concepts. Reference [35] reports some of these "germs" of negative refractive index MTMs (see also Section 1.10 of [3]). We can also mention the works on artificial dielectrics, a field of research sharing many similarities with the modern concept of MTM. Nevertheless, the contributions reported in this section were indeed the starting point of the systematic study of the physical properties, possible implementations and applications of MTMs.

1.1.3 Overview of microwave applications of metamaterials

The first evidences showing that materials with negative parameter values were indeed physically realizable opened the door to a systematic study of potential applications of MTMs. In this context, common microwave and optical devices have been revisited in the light of an improvement of their performances or an extension of their functionality by the use of MTMs with exotic parameters in place of conventional dielectrics. It results from these investigations a variety of novel applications and devices, some of which being well demonstrated while others remain at a conceptual level. Historically, the first foreseen application of MTMs was the flat negative refractive index lens initially suggested by Veselago [6], and subsequently analyzed by Pendry [12] under the name of "perfect lens". This subwavelength focusing device has been further investigated by many groups, thereby opening new fields of research on manipulation of light and imaging. The resulting optical applications are however out of scope of the present work and are therefore not further discussed here.

Most of the well demonstrated applications of MTMs are however to be found in the microwave field, where MTMs have offered many interesting possibilities to enhance the performances of existing guided-wave and antenna devices. The most significant improvements rely on the particular phase responses (dispersion) MTMs can exhibit, in particular on the possibilities to achieve negative or zero refractive index. To that respect, the resulting new field of applications has recently been referred to as *dispersion engineering*, as opposed to *magnitude engineering*, which is mainly concerned with filters and has now become very mature. In this context, most of the well demonstrated applications of MTMs rely on the TL approach, which mostly results in 1D or 2D planar structures which can be conveniently analyzed, realized and measured. On the other hand, 3D volumetric MTMs applications mostly remain at a conceptual level. Indeed, promising applications have been foreseen by considering idealized homogeneous and often isotropic media, but their implementation with realistic 3D inclusion-based or TL-based MTMs remains to be demonstrated, mainly because of their high level of complexity in terms of analysis (theoretical and numerical) and fabrication.

Since their apparition, TL-based MTMs have quickly led to a plethora of microwave applications. Indeed, any microwave device including TLs can be potentially improved by replacing these with TL-based MTMs. This principle has been applied to phase shifters, couplers, power dividers or baluns, to name a few. Typical enhancements which have been achieved are size reduction, bandwidth enhancement, dual/multi band behaviour and novel functionalities. A selection of guided-wave applications of MTMs is presented in Section 2.4.1. MTMs have also produced interesting concepts in the antenna field. The richness of their dispersion has been exploited for leaky-wave antennas with forward/backward scanning capabilities, miniaturization of resonant antennas, directivity enhancement and multi-band behaviour. As for guided-wave applications, most of these concepts have been demonstrated with TL-based MTMs, although their implementation with inclusion-based MTMs is also possible. A selection of antenna applications of MTMs is presented in Section 2.4.2. It is foreseeable that MTMs are going to be more and more often integrated in guiding and radiating systems in order to increase their degrees of freedom or to enhance their performances.

Applications of MTMs in general are widely covered in recent books devoted to the subject [3–5, 36]. The present research work is mainly concerned with guided-wave and antenna applications of LHM, which are further detailed in Section 2.4

1.2 Objectives and organization of the thesis

1.2.1 Context of the work: research projects

An important part of the work carried out in this thesis has been accomplished in the frame of the project for the European Space Agency (ESA-ESTEC): "Metamaterials for antenna (sub)systems", ESTEC Contract Number 18545/04/NL/LvH, extending from October 2004 to December 2007. The main objective of this project was to *prove by analysis, breadboarding and testing that novel compact Metamaterials, possessing a negative refractive index in 3D dimensions, can be suitable materials for challenging antenna applications*. This project was thus oriented toward the two following objectives:

- Development of 3D isotropic LHM.
- Antenna applications of the developed LHM.

An important point of this research work was the choice made at the very beginning to focus on volumetric (or 3D) LHM structures that can be considered as material filling and that would interact with an antenna as a conventional material does, and thus to go beyond the well demonstrated antenna applications of planar 1D and 2D LHM, which essentially consist of guiding and radiating structures.

The first part of this project was oriented toward the development of 3D isotropic LHM, which had never been experimentally demonstrated at that time. This required the development of novel analysis techniques for the evaluation of the isotropy of the investigated structures. During the project, it was agreed upon that a perfectly isotropic LHM structure would be very difficult to realize, and that for the considered antenna applications the structure should only exhibit the desired "meta-properties" in the directions required by the electromagnetic fields.

The second part of this project was dedicated to the analysis of LHM based on the TL approach, which were preferred to the initially considered inclusion-based LHM since they exhibit a much wider bandwidth of operation and lower losses. At that time, TL-based LHM were mainly restricted to planar guiding or radiating structures, but very few studies on volumetric realizations of these structures had been reported. To that respect, a possible implementation of such a volumetric TL-based LHM was proposed, analyzed and fully characterized in the light of the targeted antenna applications. In particular, this structure was tested as a substrate for a classical patch antenna in order to enhance its radiation performances. To this aim, specific characterization techniques had to be developed for the characterization of the selected structure.

Several other aspects of the work presented in this thesis have been carried out in the context of the Network of Excellence METAMORPHOSE in the 6th Framework Program of the European Union, in which our laboratory LEMA-EPFL was able to participate, thanks to the direct financial support of the Swiss Government. METAMORPHOSE provided both an excellent forum for our research and the possibility of mutual exchanges and cross-fertilizing with leading European groups working in the area. With a four years duration (2004−2008), METAMORPHOSE allowed the author of this thesis not only to complete several aspects of the researches initiated in the ESA project, but also to initiate some fruitful parallel investigations. In this respect, the last part of this thesis (Chapters 6 and 7) must be ascribed to this activity.

1.2.2 Motivations and objectives of the thesis

The main research directions taken in this thesis were strongly motivated and driven by the two projects mentioned in Section 1.2.1, as well as by additional objectives identified all along the work from intermediate conclusions.

Following the pioneer works on MTMs, there has been considerable interest in the theoretical behavior of various systems including ideally homogeneous and isotropic MTMs, such as lenses and novel microwave and antenna concepts. However, practical realizations of these MTMs were mainly limited to arrays of highly resonant and lossy particles (SRR and wires), or loaded TLs restricted to planar 1D or 2D topologies. Moreover, very few works showed a clear evidence that volumetric MTMs can be advantageously used to improve the performances of microwave devices and antennas, since the realized practical MTMs were often rather different from their idealized homogeneous and isotropic models.

In this context, the objective of this thesis is to contribute to the development of characterization techniques suitable for practical MTM structures. The purpose of these techniques is to determine a set of relevant parameters describing a MTM from a macroscopic point of view. Those can be equivalent medium parameters such as the permittivity and the permeability, or equivalent propagation constants and characteristic impedances.

Many published works describe new composite structures able to provide a negative refractive index, but these are often characterized using incomplete approaches, such as the extraction of parameters from scattering parameters. Indeed, the reported investigations using this technique only characterize the MTM samples under normal incidence, which is clearly too restrictive for the investigation of their degree of isotropy, as required in the ESA project. To this end, one of the first goal was to develop and test an improved retrieval procedure dealing with normal and oblique incidences for the extraction of dyadic medium parameters. A common problem encountered with this type of retrieval procedures is the alteration of the extracted parameters by complex coupling phenomena occurring between adjacent cells, which makes the resulting parameters dependent on the size and shape of the considered MTM sample. To that respect, improved modeling techniques which can account for these coupling phenomena have also been investigated.

The modeling of TL-based MTMs has also been addressed in detail in this work. In

this context, enhanced techniques are sought after for the characterization of more elaborated MTMs consisting of periodically loaded multiconductor TLs. An example of such a structure is the volumetric TL-based LHM selected in the ESA project for challenging antenna applications. In this context, an important goal was to assess the ability of such a structure to behave as a material filling in an antenna system.

In parallel with the development of characterization techniques, the objective was also to perform a comprehensive analysis of the structures selected in the projects mentioned in Section 1.2.1, and to potentially develop new MTMs on the basis of the results obtained for the initial structures. In particular, an important goal was to fully characterize a novel topology of CRLH TL introduced in this thesis.

1.2.3 Organization of the thesis and original contributions

In this section, we describe the organization of the thesis and provide some comments on the original contributions linked with each chapter.

Chapter 2: Basic physics of LHM and state-of-the-art

This chapter provides a comprehensive state-of-the-art on MTMs with special emphasis on LHM structures. It covers various aspects, from the continuous medium theory of LHM to microwave applications of the reported LHM implementations. An original contribution is the particular effort made to categorize the reported LHM structures, characterization techniques, and microwave applications of LHM according to the physical mechanism involved.

Chapter 3: Dyadic medium parameters retrieval procedure from scattering parameters

This chapter describes the development and application of an improved retrieval procedure which allows the determination of equivalent dyadic permittivity and permeability of MTMs from reflection and transmission coefficients obtained for several incidence directions and polarizations. This novel technique is an extension of the commonly used retrieval procedure for normal incidence, and is aimed at investigating the isotropy of 3D MTMs. An additional original contribution is the investigation of the isotropy of a novel type of highly symmetrical magnetic resonator referred to as crossed split-ring resonator (CSRR).

Chapter 4: TL-based MTMs

This chapter consists of a collection of technical considerations pertinent to the analysis design and realization of 1D planar MTMs based on the TL approach, such as the CRLH TL. Although based on studies available in the literature, this chapter brings new contributions to the various topics addressed, such as (i) the evaluation of the effect of the reference planes position on the Bloch parameters (Section 4.2.6), (ii) a symmetrization technique for some classes of periodic structures (Section 4.2.8), (iii) a comparison between the various models used for the CRLH TL (Section 4.3), (iv) the investigation of the duality principle between coplanar waveguide (CPW) and coplanar stripline (CPS) circuits (Section 4.4.5), (v) a special design technique for CRLH TL based on a given

type of layout elements (Section 4.5.3), and (vi) the realization of CRLH TLs in a CPS host TL (Section 4.6).

Chapter 5: Volumetric layered TL-based MTMs

This chapter presents a detailed analysis of a particular type of volumetric layered MTM based on the TL approach. This structure is obtained by layering several 1D planar CRLH TLs implemented in a CPS host TL. Very few studies on this type of structures have been reported in the literature, and therefore this chapter consists in a significant contribution to this area. In particular, this is the first time that such a structure is used as a substrate for a microstrip patch antenna. An important contribution is also the analysis of the ability of such a volumetric structure to behave as material fillings in such configuration.

Chapter 6: Enhanced periodic structure analysis based on a multiconductor TL model

This chapter presents a novel general technique for the characterization of periodic structures based on a multimodal representation of their unit cell. This enhanced Bloch wave analysis consists in modeling an arbitrary 1D periodic structure with an equivalent multiconductor TL (MTL). This technique represents an important contribution to the characterization of periodic structures in general, since it allows an accurate representation of the dispersion properties, as well as the terminations (excitation and matching) of finite size periodic structures. When applied to MTMs, it allows accounting for complex inter-cell coupling phenomena occurring in arrays of resonant inclusions such as SRR-wire media, as well as characterizing more elaborated MTMs consisting of periodically loaded MTLs.

Chapter 7: CRLH TLs based on a lattice network unit cell

In this chapter, we introduce a novel unit cell topology for the CRLH TL based on a lattice network. In a first step, its superior performances in terms of bandwidth are theoretically demonstrated. Then, practical implementations are proposed, realized and experimentally characterized. Finally, potential applications to antenna systems are discussed.

Chapter 8: Conclusions and perspectives

We conclude with a summary and general assessment of the work achieved in this thesis, and outline possible future research directions for the characterization and microwave applications of MTMs.

The four main contributions of the thesis are Chapters 3, 5, 6, and 7. The two remaining chapters — the state-of-the-art of Chapter 2 and the material for TL-based MTMs in Chapter 4 — comprise detailed information supporting the main contributions. It is noticeable that these chapters have been written in a comprehensive way in order to give to this document a textbook value for possible future work performed at LEMA-EPFL on MTMs.

2 Basic physics of LHM and state-of-the-art

This chapter presents a general state-of-the-art on LHM covering various aspects from theory to applications. In particular, this review focuses on (i) the fundamental properties of wave propagation in idealized continuous LHM (Section 2.1), (ii) the reported LHM structures (Section 2.2), (iii) characterization techniques and homogenization procedures for the analysis of real composite LHM (Section 2.3), and (iv) microwave applications of LHM (Section 2.4).

2.1 Continuous medium theory of LHM

Fundamental theoretical investigations on the physics of wave propagation in continuous LHM are revisited in this section, with special emphasis on the very meaning of various terms associated with negative refraction (left-handedness, backward wave,...). An in-depth analysis of the correspondence between these concepts first requires a rigorous definition of the involved physical quantities, which is the purpose of Sections 2.1.1 to 2.1.7. In all these developments, the effective medium approach is adopted, which means that the LHM is considered as an equivalent homogeneous (or continuous) medium characterized by macroscopic parameters.

2.1.1 Time harmonic dependence

An harmonic time dependence of the electromagnetic fields is assumed (time dependence in $e^{+j\omega t}$). In a source-free medium, the corresponding time-harmonic Maxwell's equations are:

$$\boldsymbol{\nabla} \times \mathbf{E} = -j\omega\mathbf{B} \tag{2.1a}$$

$$\boldsymbol{\nabla} \times \mathbf{H} = j\omega\mathbf{D} \tag{2.1b}$$

$$\boldsymbol{\nabla} \cdot \mathbf{D} = 0 \tag{2.1c}$$

$$\boldsymbol{\nabla} \cdot \mathbf{B} = 0 \tag{2.1d}$$

where $\mathbf{E}$, $\mathbf{D}$, $\mathbf{H}$ and $\mathbf{B}$ are complex vectors representing the electromagnetic field. To recover the real time dependent corresponding fields, the following transformation is used:

$$\boldsymbol{\mathcal{E}}(\mathbf{r}, t) = \sqrt{2}\ \mathrm{Re}\big[\mathbf{E}(\mathbf{r})e^{+j\omega t}\big] \tag{2.2}$$

and similarly for the other fields. Using the convention with the factor $\sqrt{2}$ in (2.2) implies that the modulus of the complex fields represents the root mean square (RMS) value, and not the peak value.

2.1.2 Constitutive relations

Interactions between matter and electromagnetic fields are described by constitutive relations. If we assume that these interactions can be essentially represented by dipole moments, a linear material can be described by second order tensors (higher order multipoles are neglected). In this case, the constitutive relations take the general form corresponding to a bianisotropic medium, that is, in the Tellegen form [37]

$$\mathbf{D} = \bar{\bar{\varepsilon}} \cdot \mathbf{E} + \bar{\bar{\xi}} \cdot \mathbf{H} \tag{2.3a}$$

$$\mathbf{B} = \bar{\bar{\zeta}} \cdot \mathbf{E} + \bar{\bar{\mu}} \cdot \mathbf{H} \tag{2.3b}$$

The tensors $\bar{\bar{\xi}}$ and $\bar{\bar{\zeta}}$ in (2.3) represent magneto-electric coupling. The media considered here are assumed to be homogeneous, thus the medium parameters do not depend on the position $\mathbf{r}$. We do not consider here spatial dispersion, which means that the four tensors $\bar{\bar{\varepsilon}}$, $\bar{\bar{\mu}}$, $\bar{\bar{\xi}}$ and $\bar{\bar{\zeta}}$ do not contain any spatial differential operators. The material is thus characterized by 36 parameters (complex in general), which are not all independent from each other if reciprocity is assumed [37, 38] (see also the Post's constraint [37, 39]).

Most of the following developments assume that the medium is isotropic and does not present any magneto-electric coupling. In such a case, the medium is completely characterized by the scalar permittivity ε and permeability μ, and the constitutive relations reduce to

$$\mathbf{D} = \varepsilon \mathbf{E} \tag{2.4a}$$

$$\mathbf{B} = \mu \mathbf{H} \tag{2.4b}$$

A medium characterized by the constitutive relations (2.4) will be referred to here as a *simple medium*. The permittivity ε and the permeability μ are complex functions of the frequency, whose real and imaginary parts are separated as follows:

$$\varepsilon = \varepsilon' - j\varepsilon'' \tag{2.5a}$$

$$\mu = \mu' - j\mu'' \tag{2.5b}$$

Relative values of permittivity and permeability are defined as follows:

$$\varepsilon_r = \frac{\varepsilon}{\varepsilon_0} \tag{2.6a}$$

$$\mu_r = \frac{\mu}{\mu_0} \tag{2.6b}$$

The real and imaginary parts of ε_r and μ_r (ε_r', ε_r'', μ_r' and μ_r'') are defined in a similar way as in (2.5). In the following developments, a clear distinction is made between results applying to general bianisotropic media, and those only applying to simple media.

2.1.3 Power considerations

We first recall that the Poynting's vector $\mathbf{S}$ is defined by

$$\mathbf{S} = \mathbf{E} \times \mathbf{H}^* \tag{2.7}$$

In any medium, the following relation can be deduced from Maxwell's equations (in the source-free case):

$$\oint_A \mathbf{S} \cdot d\mathbf{A} = -\int_V j\omega(\mathbf{H}^* \cdot \mathbf{B} - \mathbf{E} \cdot \mathbf{D}^*)\, dV \tag{2.8}$$

where A represents any closed surface and V is the corresponding interior. This is the well known Poynting's theorem [40–42], which expresses the conservation of energy. In a simple medium, this relation becomes

$$\oint_A \mathbf{S} \cdot d\mathbf{A} = -\int_V \omega\left(\mu''|\mathbf{H}|^2 + \varepsilon''|\mathbf{E}|^2\right) + j\omega\left(\mu'|\mathbf{H}|^2 - \varepsilon'|\mathbf{E}|^2\right)\, dV \tag{2.9}$$

The time average over one period of the power flowing outside the surface A is given by

$$P_a = \mathrm{Re}\left[\oint_A \mathbf{S} \cdot d\mathbf{A}\right] = \oint_A \mathbf{S}_a \cdot d\mathbf{A} = -\int_V \omega\left(\mu''|\mathbf{H}|^2 + \varepsilon''|\mathbf{E}|^2\right)\, dV \tag{2.10}$$

where we have introduced $\mathbf{S}_a = \mathrm{Re}[\mathbf{S}]$, which represents the time-averaged power density[1]. For a passive medium, P_a must be negative or zero, otherwise the medium provides power. Therefore, a sufficient condition for a passive medium is

$$\varepsilon'' \geq 0 \tag{2.11a}$$

$$\mu'' \geq 0 \tag{2.11b}$$

The limit case where $\varepsilon'' = 0$ and $\mu'' = 0$ corresponds to a lossless medium. Otherwise, the medium is lossy. In fact, the condition (2.11) is also necessary, since the condition $P_a \leq 0$ must be true for *any* type of field. Indeed, if we consider a configuration in which the electric field is high and the magnetic field is very low (negligible), like between the plates of a big capacitor, or in which the magnetic field is high and the electric field is very low (negligible), like inside a big coil inductor, we arrive at the conclusion that both μ'' and ε'' must be positive or zero.

2.1.4 Energy densities in simple media

We summarize here the main considerations regarding the electromagnetic energy density stored in passive continuous simple media, and the impact of these considerations on media with negative parameters.

Let us first recall that the time-averaged energy density w (in [J/m^3]) stored in the electric and magnetic fields in a lossless non-dispersive simple medium is given by [41, 42]

$$w = w_e + w_m = \frac{1}{2}\varepsilon|\mathbf{E}|^2 + \frac{1}{2}\mu|\mathbf{H}|^2 \tag{2.12}$$

As a result, a medium with negative values of ε and/or μ cannot be non-dispersive [as assumed in (2.12)], since both the electric and magnetic energy densities w_e and w_m must be positive in a passive medium. Therefore, a passive medium with negative parameters is necessarily dispersive.

[1] The subscript "a" refers to "active" power, by comparison to "reactive" power.

It is known that defining an electromagnetic energy density as a thermodynamical quantity in terms of the macroscopic medium parameters is only possible in the absence of losses [43,44]. Strictly speaking, this means that such a definition of energy density is not possible in dispersive media, since dispersion usually implies dissipation of energy (by causality). However, if losses are small and can be neglected, the energy density can still be defined and formulated in terms of the macroscopic medium parameters. Considering fields with narrow spectrum (compared to the dispersion at the considered frequencies) around a carrier frequency ω, the time-averaged energy density stored in a dispersive medium with negligible losses can be expressed as [40, 42, 43, 45]

$$w = w_e + w_m = \frac{1}{2}\frac{d(\omega\varepsilon)}{d\omega}|\mathbf{E}|^2 + \frac{1}{2}\frac{d(\omega\mu)}{d\omega}|\mathbf{H}|^2 \tag{2.13}$$

Both the electric and magnetic energy densities w_e and w_m must be positive for a passive medium, which implies that the permittivity and permeability functions must satisfy the following conditions, also called *entropy conditions* [3]:

$$\frac{d(\omega\varepsilon)}{d\omega} \geq 0 \qquad \text{and} \qquad \frac{d(\omega\mu)}{d\omega} \geq 0 \tag{2.14}$$

Furthermore, by combining causality requirement and the entropy conditions, it can be shown that the following relations must also be satisfied [43]:

$$\begin{aligned} &\frac{d\varepsilon_r}{d\omega} \geq 0 && \frac{d(\omega\varepsilon_r)}{d\omega} \geq \varepsilon_r && \\ &\frac{d\varepsilon_r}{d\omega} \geq \frac{2(1-\varepsilon_r)}{\omega} && \frac{d(\omega\varepsilon_r)}{d\omega} \geq 2-\varepsilon_r && \frac{d(\omega\varepsilon_r)}{d\omega} \geq 1 \end{aligned} \tag{2.15}$$

and similarly for the relative permeability μ_r. As a result, the requirement for positive energy density does not preclude the possibility that ε and/or μ be negative, provided that the medium is dispersive and satisfy the conditions (2.14) and (2.15).

For materials with considerable losses near the frequency of interest, like near a resonance for instance, it is not possible to define the stored energy in terms of the material permittivity and permeability. Nevertheless, it is explained in [44, 45] that such a quantity can still be defined and calculated from the microstructure of the medium, i.e., from the type of mechanism which is the source of its macroscopic properties. Following this idea, several groups have proposed approaches to determine the energy density in lossy dispersive media by considering the microscopic detail of the material [44, 46, 47]. In particular, they showed that material responses usually used to provide negative values of ε and/or μ (such as Drude or Lorentz models) always lead to a positive stored energy density, even in the presence of losses and near resonances. Although these methods are general, it is worth mentioning that a specific derivation of the energy density must be carried out for each considered material.

2.1.5 Plane waves and associated parameters

The fields of a plane wave are given by

$$\begin{aligned} \mathbf{E}(\mathbf{r}) &= \mathbf{E}_0\, e^{-\boldsymbol{\gamma}\cdot\mathbf{r}} & \mathbf{D}(\mathbf{r}) &= \mathbf{D}_0\, e^{-\boldsymbol{\gamma}\cdot\mathbf{r}} \\ \mathbf{H}(\mathbf{r}) &= \mathbf{H}_0\, e^{-\boldsymbol{\gamma}\cdot\mathbf{r}} & \mathbf{B}(\mathbf{r}) &= \mathbf{B}_0\, e^{-\boldsymbol{\gamma}\cdot\mathbf{r}} \end{aligned} \tag{2.16}$$

The complex vector $\boldsymbol{\gamma}$ is the propagation vector[2], whose real and imaginary parts are separated as follows:

$$\boldsymbol{\gamma} = \boldsymbol{\alpha} + j\boldsymbol{\beta} \tag{2.17}$$

The fields expressed in (2.16) satisfy Maxwell's equations if the following relations are satisfied:

$$\begin{aligned} \boldsymbol{\gamma} \times \mathbf{E} &= j\omega\mathbf{B} & \qquad \boldsymbol{\gamma} \cdot \mathbf{D} &= 0 \\ \boldsymbol{\gamma} \times \mathbf{H} &= -j\omega\mathbf{D} & \qquad \boldsymbol{\gamma} \cdot \mathbf{B} &= 0 \end{aligned} \tag{2.18}$$

Using the constitutive relations of the medium, a relation can be found between the possible values of $\boldsymbol{\gamma}$ satisfying (2.18) and the medium parameters. This relation is called the *dispersion relation*. We also use the term *dispersion diagram* for the graphical representation of the possible values of $\boldsymbol{\gamma}$ in function of the frequency. In a general bianisotropic medium characterized by (2.3), the dispersion relation can be found by solving an eigenvalue problem, as described in [48].

Now we introduce some parameters and properties of plane wave propagation in a general bianisotropic medium, without any particular assumption concerning the orientation of the two vectors $\boldsymbol{\alpha}$ and $\boldsymbol{\beta}$ (i.e., they are not necessarily collinear, as is the case for a *uniform* plane wave).

a. Phase and group velocities

In the present general context, the phase and group velocities $\mathbf{v}_p$ and $\mathbf{v}_g$ are vectorial quantities defined by [17, 49]

$$\mathbf{v}_p = \frac{\omega}{|\boldsymbol{\beta}|} \cdot \frac{\boldsymbol{\beta}}{|\boldsymbol{\beta}|} \tag{2.19}$$

$$\mathbf{v}_g = \boldsymbol{\nabla}_{\boldsymbol{\beta}} \big[\omega(\boldsymbol{\beta})\big] = \frac{\partial\omega}{\partial\beta_x}\hat{\mathbf{x}} + \frac{\partial\omega}{\partial\beta_y}\hat{\mathbf{y}} + \frac{\partial\omega}{\partial\beta_z}\hat{\mathbf{z}} \tag{2.20}$$

where $(\hat{\mathbf{x}}, \hat{\mathbf{y}}, \hat{\mathbf{z}})$ is the orthonormal basis associated to the Cartesian coordinate system. In this definition of the group velocity, we consider that ω is a function of the vectorial variable $\boldsymbol{\beta}$.

b. Wave impedance

The concept of wave impedance expresses the relation between the $\mathbf{E}$ and $\mathbf{H}$ fields of the plane wave. This relation can be expressed in a general form using a dyadic wave impedance $\bar{\bar{\eta}}$:

$$\mathbf{E} = \bar{\bar{\eta}} \cdot \mathbf{H} \tag{2.21}$$

It is only in some specific cases that a scalar wave impedance can be defined [as in (2.34) or (2.35)].

[2] The complex wave vector $\mathbf{k}$ is sometimes used instead of $\boldsymbol{\gamma}$. The relation between these two quantities is simply $\boldsymbol{\gamma} = j\mathbf{k}$.

c. Poynting's theorem and passivity

Assuming the fields dependence of (2.16), the Poynting's vector (2.7) writes

$$\mathbf{S} = (\mathbf{E}_0 \times \mathbf{H}_0^*)\, e^{-2\boldsymbol{\alpha}\cdot\mathbf{r}} \tag{2.22}$$

and the Poynting's theorem (2.8) becomes

$$\oint_A \mathbf{S} \cdot d\mathbf{A} = -j\omega(\mathbf{H}_0^* \cdot \mathbf{B}_0 - \mathbf{E}_0 \cdot \mathbf{D}_0^*) \int_V e^{-2\boldsymbol{\alpha}\cdot\mathbf{r}}\, dV \tag{2.23}$$

It can further be demonstrated that the passivity condition $P_a \leq 0$ mentioned in Section 2.1.3 is strictly equivalent to impose that the time-averaged power density $\mathbf{S}_a$ forms an acute angle with the direction of the exponential decay $\boldsymbol{\alpha}$. In other words, for a passive medium we have the following equivalence:

$$P_a = \mathrm{Re}\left[\oint_A \mathbf{S} \cdot d\mathbf{A}\right] \leq 0 \qquad \Leftrightarrow \qquad \boldsymbol{\alpha} \cdot \mathbf{S}_a = \boldsymbol{\alpha} \cdot \mathrm{Re}[\mathbf{S}] \geq 0 \tag{2.24}$$

Finally, it is worth mentioning that the analysis of problems involving non-uniform plane waves may become rather complex, since in general the vectors $\boldsymbol{\alpha}$, $\boldsymbol{\beta}$, $\mathbf{v}_g$ and $\mathbf{S}_a$ may all be oriented in different directions.

2.1.6 Uniform plane waves

The simplest type of electromagnetic waves are *uniform* plane waves. A plane wave is called uniform when the two vectors $\boldsymbol{\alpha}$ and $\boldsymbol{\beta}$ are in the same direction, for instance given by the unit vector $\hat{\mathbf{u}}$. In such as case, we can write

$$\begin{cases} \boldsymbol{\gamma} = \gamma\, \hat{\mathbf{u}} \\ \boldsymbol{\alpha} = \alpha\, \hat{\mathbf{u}} \\ \boldsymbol{\beta} = \beta\, \hat{\mathbf{u}} \end{cases} \qquad \Rightarrow \qquad \gamma = \alpha + j\beta \tag{2.25}$$

where γ, α and β are the propagation constant, the attenuation constant and the phase constant, respectively. The assumption of uniformity implies that the fields have no dependence on the directions transverse to the propagation direction $\hat{\mathbf{u}}$. As a result, the Poynting's vector, the phase velocity and the group velocity are also oriented along $\hat{\mathbf{u}}$, which allows defining the corresponding scalar quantities as follows:

$$\mathbf{S} = S\, \hat{\mathbf{u}} \tag{2.26a}$$

$$\mathbf{v}_p = v_p\, \hat{\mathbf{u}} \qquad \text{with} \qquad v_p = \frac{\omega}{\beta} \tag{2.26b}$$

$$\mathbf{v}_g = v_g\, \hat{\mathbf{u}} \qquad \text{with} \qquad v_g = \frac{d\omega}{d\beta} \text{ or } \left(\frac{d\beta}{d\omega}\right)^{-1} \tag{2.26c}$$

Both formulations of v_g in (2.26c) are possible, depending on whether ω is considered as a function of β, or the opposite. Furthermore, the assumption of uniformity allows defining a scalar refractive index n as

$$n = \frac{\gamma}{jk_0} \qquad \text{with} \qquad k_0 = \frac{\omega}{c_0} = \omega\sqrt{\mu_0\varepsilon_0} \tag{2.27}$$

where k_0 and c_0 are the free-space wave number and velocity of light, respectively. With this definition, n is in general a complex quantity, whose real and imaginary parts are separated as follows:

$$n = n' - jn'' \tag{2.28}$$

As a result, it follows from (2.25), (2.27) and (2.28) that

$$\alpha = k_0 n'' \tag{2.29a}$$
$$\beta = k_0 n' \tag{2.29b}$$

2.1.7 Uniform plane waves in simple media

In simple media characterized by (2.4), Maxwell's equations are satisfied for a plane wave if

$$\begin{aligned} \boldsymbol{\gamma} \times \mathbf{E} &= j\omega\mu\mathbf{H} & \boldsymbol{\gamma} \cdot \mathbf{E} &= 0 \\ \boldsymbol{\gamma} \times \mathbf{H} &= -j\omega\varepsilon\mathbf{E} & \boldsymbol{\gamma} \cdot \mathbf{H} &= 0 \end{aligned} \tag{2.30}$$

and the dispersion relation is found to be

$$\boldsymbol{\gamma} \cdot \boldsymbol{\gamma} = -\omega^2\mu\varepsilon \tag{2.31}$$

This is the general dispersion relation for a plane wave in a simple medium. It can noted that (2.31) is also valid for non-uniform plane waves. For the rest of this section, we restrict the discussion to uniform plane waves whose propagation direction is given by the unit vector $\hat{\mathbf{u}}$. In such a case, the dispersion relation reduces to

$$\gamma^2 = -\omega^2\mu\varepsilon \tag{2.32}$$

Using the definition of the refractive index n in (2.27), equation (2.32) can be written

$$n^2 = \mu_r\varepsilon_r \tag{2.33}$$

Furthermore, a scalar wave impedance η can be now defined. Indeed, using the second equation with the vectorial product in (2.30), the relation between $\mathbf{E}$ and $\mathbf{H}$ can be written

$$\mathbf{E} = \eta(\mathbf{H} \times \hat{\mathbf{u}}) \qquad \text{with} \qquad \eta = \frac{\gamma}{j\omega\varepsilon} \tag{2.34}$$

In terms of the dyadic wave impedance introduced in (2.21), we have (if $\hat{\mathbf{u}} = \hat{\mathbf{z}}$)

$$\bar{\bar{\eta}} = \frac{\gamma}{j\omega\varepsilon}(\hat{\mathbf{x}}\hat{\mathbf{y}} - \hat{\mathbf{y}}\hat{\mathbf{x}}) = \eta(\hat{\mathbf{x}}\hat{\mathbf{y}} - \hat{\mathbf{y}}\hat{\mathbf{x}}) \tag{2.35}$$

By definition, the quantity η also corresponds to the characteristic impedance of the medium, since it is the wave impedance of a uniform plane wave propagating in that medium. A normalized wave impedance z can also be defined as follows:

$$z = \frac{\eta}{\eta_0} = \frac{\gamma}{j\omega\varepsilon\eta_0} \qquad \text{with} \qquad \eta_0 = \sqrt{\frac{\mu_0}{\varepsilon_0}} \tag{2.36}$$

where η_0 is the free-space characteristic impedance. The real and imaginary parts of z are separated as follows:

$$z = z' - jz'' \tag{2.37}$$

Using the definition of the refractive index n in (2.27) and the expression of z in (2.36), it can be found that

$$z = \frac{n}{\varepsilon_r} \tag{2.38}$$

The information contained in (2.33) and (2.38) can be summarized as follows:

$$\begin{cases} n^2 = \mu_r \varepsilon_r \\ z^2 = \dfrac{\mu_r}{\varepsilon_r} \end{cases} \quad \text{and} \quad \begin{cases} \mu_r = nz \\ \varepsilon_r = \dfrac{n}{z} \end{cases} \tag{2.39}$$

The two parameters n and z are referred to here as the *wave parameters*, and ε_r and μ_r to the *medium parameters*. The relations (2.39) reveal several important points:

- If we consider that the medium parameters ε_r and μ_r are known, there are two possible solutions for each n and z, which correspond to the two possible directions of propagation.
- The choices of a particular root for n and z are not independent, since these two quantities are related through (2.38). It is also useful to recall that n and γ are also unambiguously linked by (2.27).
- If we consider that n and z are known, the medium parameters ε_r and μ_r can be determined unambiguously.

For uniform plane waves in simple media, the Poynting's vector (2.7) becomes

$$\mathbf{S} = -\frac{\boldsymbol{\gamma}^*}{jw\mu^*}|\mathbf{E}|^2 = \frac{\boldsymbol{\gamma}}{jw\varepsilon}|\mathbf{H}|^2 = \frac{1}{\eta^*}|\mathbf{E}|^2\hat{\mathbf{u}} = \eta|\mathbf{H}|^2\hat{\mathbf{u}} = \eta|\mathbf{H}_0|^2 e^{-2\boldsymbol{\alpha}\cdot\mathbf{r}}\hat{\mathbf{u}} \tag{2.40}$$

and the Poynting's theorem (2.8) can be written

$$\oint_A \mathbf{S}\cdot d\mathbf{A} = -\omega|\mu|\left[\left(\frac{\mu''}{|\mu|} + \frac{\varepsilon''}{|\varepsilon|}\right) + j\left(\frac{\mu'}{|\mu|} - \frac{\varepsilon'}{|\varepsilon|}\right)\right]\int_V |\mathbf{H}|^2\, dV \tag{2.41}$$

In this case, the passivity requirement $P_a \leq 0$ implies that

$$\frac{\mu''}{|\mu|} + \frac{\varepsilon''}{|\varepsilon|} \geq 0 \tag{2.42}$$

Compared to the conditions in (2.11), the condition above is necessary and sufficient, but it is limited to the case of uniform plane waves. Now we consider the time average (over one period) of the power density, which is given by the real part of the Poynting's vector. From (2.40), we find

$$\mathbf{S}_a = \mathrm{Re}[\mathbf{S}] = S_a\hat{\mathbf{u}} \quad \text{with} \quad S_a = \mathrm{Re}[\eta]|\mathbf{H}_0|^2 e^{-2\boldsymbol{\alpha}\cdot\mathbf{r}} = \eta_0 z'|\mathbf{H}_0|^2 e^{-2n''k_0(\hat{\mathbf{u}}\cdot\mathbf{r})} \tag{2.43}$$

As already explained in Section 2.1.5.c., imposing the passivity with (2.42) is strictly equivalent to impose that the power flow is in the same direction as the exponential decay. In other words, we have the following equivalences for the passivity condition:

$$P_a \leq 0 \quad \Leftrightarrow \quad \alpha\, S_a \geq 0 \quad \Leftrightarrow \quad z'n'' \geq 0 \quad \Leftrightarrow \quad \frac{\mu''}{|\mu|} + \frac{\varepsilon''}{|\varepsilon|} \geq 0 \tag{2.44}$$

Interestingly, the condition (2.44) is independent from the choice of a particular root for n and z. Indeed, if we replace n by $-n$, z also changes its sign according to (2.38), and the condition (2.44) remains the same. If we specify that the source is placed in the $-\hat{\mathbf{u}}$ direction, the active power must flow in the $+\hat{\mathbf{u}}$ direction, that is, $S_a > 0$. As a result, we have $\alpha > 0$, hence $n'' > 0$ [see (2.29a)], and thus $z' > 0$.

2.1.8 Reverse propagation in metamaterials

The developments of Sections 2.1.1 to 2.1.7 are now used to clarify various concepts associated with abnormal, or "reverse" properties of metamaterials (MTMs). In particular, we describe and compare the following terms introduced in the literature for MTMs which enable the unusual phenomenon of negative refraction:

- Double negative medium
- Left-handed medium
- Negative phase velocity medium
- Backward-wave medium
- Negative refractive index medium

These definitions are known to be almost equivalent, but they are all based on different physical quantities. For this reason, it is not obvious under which conditions an equivalence can be established. Furthermore, some definitions are based on the properties of the medium itself, whereas others are based on the properties of a given plane wave propagating in it. To that respect, it is worth discussing the scope of applicability of each of these definitions.

a. Double negative medium

A *double negative medium* (DNG medium, or DNM) is a simple medium characterized by simultaneous negative values for the real part of the permittivity and permeability, as expressed in (2.45a). This terminology was first introduced in [50]. We also recall in (2.45) the corresponding definitions for a *double positive medium* (DPS medium, or DPM), an *epsilon negative medium* (ENG medium) and a *mu negative medium* (MNG medium). Moreover, the denomination *single negative medium* (SNG medium) includes both ENG and MNG media.

$$\varepsilon' < 0 \quad \text{and} \quad \mu' < 0 \quad \equiv \quad \text{DNG medium} \tag{2.45a}$$
$$\varepsilon' > 0 \quad \text{and} \quad \mu' > 0 \quad \equiv \quad \text{DPS medium} \tag{2.45b}$$
$$\varepsilon' < 0 \quad \text{and} \quad \mu' > 0 \quad \equiv \quad \text{ENG medium} \tag{2.45c}$$
$$\varepsilon' > 0 \quad \text{and} \quad \mu' < 0 \quad \equiv \quad \text{MNG medium} \tag{2.45d}$$

These definitions do not rely on any particular type of waves, but they only apply to simple media.

b. Left-handed medium

The term *left-handed medium* (LHM) has been coined by Veselago in 1968 [6]. The terms *left-handed* (LH) and *right-handed* (RH) themselves do not directly refer to a medium, but rather to a certain type of plane wave propagation, more precisely to the orientation of the triplet formed by the vectors $\mathbf{E}$, $\mathbf{H}^*$ and $\boldsymbol{\beta}$ [51]. As the vectors $\mathbf{E}$, $\mathbf{H}^*$ and $\mathbf{S}$ always form a right-handed triplet [see (2.7)], the LH or RH nature of the wave can be determined by comparing the directions of $\mathbf{S}$ and $\boldsymbol{\beta}$. More specifically, we compare the direction of the time-averaged power density $\mathbf{S}_a = \mathrm{Re}[\mathbf{S}]$ with that of the phase variation of the wave, which is given by the vector $\boldsymbol{\beta}$. This leads to the following definitions for LH and RH propagations:

$$\boldsymbol{\beta} \cdot \mathbf{S}_a < 0 \quad \equiv \quad \text{LH propagation} \tag{2.46a}$$

$$\boldsymbol{\beta} \cdot \mathbf{S}_a \geq 0 \quad \equiv \quad \text{RH propagation} \tag{2.46b}$$

A *left-handed medium* (LHM) is then defined as a medium capable of supporting LH propagation. The opposite is a *right-handed medium* (RHM). It is worth mentioning that the conditions (2.46) can be applied both to uniform and non-uniform plane waves, and that no particular assumption has been made on the nature of the corresponding medium (i.e. they also apply to a general bianisotropic medium). When applied to a uniform plane wave in a simple medium, it can be shown that the condition for LH propagation can be expressed in terms of the wave parameters n and z and medium parameters ε_r and μ_r as follows:

$$\boldsymbol{\beta} \cdot \mathbf{S}_a < 0 \quad \Leftrightarrow \quad \beta\, S_a < 0 \quad \Leftrightarrow \quad z'n' < 0 \quad \Leftrightarrow \quad \frac{\mu'}{|\mu|} + \frac{\varepsilon'}{|\varepsilon|} < 0 \tag{2.47}$$

Comments

- An important point is the fact that the condition (2.47) has been derived without addressing the problematic of the choice of a particular root for the refractive index n and wave impedance z. As a matter of fact, the LH condition is completely independent from this problematic. Indeed, if we replace n by $-n$, z also changes its sign according to (2.38), and the condition remains the same.
- It can be seen in (2.47) that the DNG medium condition (2.45a) is a sufficient but not necessary condition to obtain a LH propagation. However, for a lossless medium ($\varepsilon'' = 0$ and $\mu'' = 0$), the DNG medium condition is equivalent to the LH condition.
- To avoid confusions, let us emphasize that the terminology *right-handed* and *left-handed* has nothing to do with chirality.
- The term *Veselago medium* is sometimes used for a LHM.
- Similar developments have been reported in [52], where they used the term *backward wave* for what we have called left-handedness in (2.46a).

Several alternative LH conditions formulated in terms of the medium parameters have been proposed in [53]:

$$(|\varepsilon| - \varepsilon')(|\mu| - \mu') > \varepsilon''\mu'' \tag{2.48a}$$

$$\varepsilon'|\mu| + \mu'|\varepsilon| < 0 \tag{2.48b}$$

$$\varepsilon'\mu'' + \mu'\varepsilon'' < 0 \tag{2.48c}$$

According to [53], these three conditions are equivalent, and the condition (2.48b) is obviously the same as (2.47). Nevertheless, it is worth clarifying the following points about these relations:

- The condition (2.48a) was originally derived in [54] under the assumption that the medium is passive ($\varepsilon'' \geq 0$ and $\mu'' \geq 0$), and is therefore only valid in this case. The condition (2.47) is more general since it is independent from the the sign of ε'' and μ''.
- The same observation also applies to the condition (2.48c), with in addition the restriction that it cannot be applied to lossless media. Indeed, it is clear that this condition is not equivalent to the other ones when $\varepsilon'' = 0$ and $\mu'' = 0$ (lossless case).
- The applicability of these conditions for active media has been further discussed and clarified in a recent paper [55], where it comes out that (2.47), or equivalently (2.48b), is the most general formulation regarding the passive or active nature of the medium.

c. Negative phase velocity medium

The term *negative phase velocity medium* (or NPV medium) has been proposed in [56] as an alternative for LHM, because of the possible confusion with the structural handedness in chiral media. This terminology concerns the orientation of the phase velocity with respect to that of the power flow, which leads to the following definitions for *negative phase velocity* (NPV) and *positive phase velocity* (PPV) propagations:

$$\mathbf{v}_p \cdot \mathbf{S}_a < 0 \quad \equiv \quad \text{NPV propagation} \tag{2.49a}$$

$$\mathbf{v}_p \cdot \mathbf{S}_a \geq 0 \quad \equiv \quad \text{PPV propagation} \tag{2.49b}$$

By definition, the phase velocity $\mathbf{v}_p$ and the vector $\boldsymbol{\beta}$ are always collinear [see (2.19)], which implies that the definition of NPV (PPV) medium is exactly equivalent to LHM (RHM).

d. Backward-wave medium

We call a *backward wave* (BW) a wave in which phase velocity and group velocity have opposite signs [57]. In the general case in which the vectorial phase and group velocities $\mathbf{v}_p$ and $\mathbf{v}_g$ are not collinear [see definitions (2.19) and (2.20)], the backward wave condition is given by (2.50a), and the opposite *forward wave* (FW) condition by (2.50b).

$$\mathbf{v}_p \cdot \mathbf{v}_g < 0 \quad \equiv \quad \text{BW propagation} \tag{2.50a}$$

$$\mathbf{v}_p \cdot \mathbf{v}_g \geq 0 \quad \equiv \quad \text{FW propagation} \tag{2.50b}$$

As for the LH and RH concepts, the terms BW and FW themselves do not directly refer to a medium, but to a certain type of propagation. A *backward-wave medium* (BWM) is then defined as a medium capable of supporting BW waves. The opposite is a *forward-wave medium* (FWM). It can be noted that the term *backward-wave medium* when associated with MTMs has been first proposed in 2001 in [52], but they used the term BWM for what we have called a LHM in Section 2.1.8.b..

It is worth mentioning that the BW and FW conditions (2.50) are very general in the sense that they only rely on the knowledge of the dispersion relation, i.e the relation $\omega(\boldsymbol{\beta})$. As a result, they can be applied to characterize any type of plane waves (uniform or non-uniform) in any type of continuous media, as well as waves in periodic structures, provided that the dispersion relation is known.

When applied to a uniform plane wave in a simple medium, the condition for BW propagation can be expressed using the corresponding scalar quantities as follows:

$$v_p v_g < 0 \quad \Leftrightarrow \quad \frac{\omega}{\beta}\left(\frac{d\beta}{d\omega}\right)^{-1} < 0 \quad \text{or} \quad \frac{\omega}{\beta}\left(\frac{d\omega}{d\beta}\right) < 0 \tag{2.51}$$

Both formulations of v_g in (2.51) are possible, depending on whether ω is considered as a function of β, or the opposite.

An important conceptual difference between the BW and LH conditions is that the LH condition (2.47) at a given frequency can be expressed in terms of the medium parameters at the same frequency, which is not possible with the BW condition (2.51) since it also depends on the frequency variation of the parameters at the considered frequency. Nevertheless, considering a dispersive medium with negligible losses, a relation between left-handedness and backward wave can be obtained. Neglecting losses means that ε, μ, n and z are taken to be real quantities and $\gamma = j\beta$. In this case, the dispersion relation (2.32) writes $\beta^2 = \omega^2\mu\varepsilon$. Taking the derivative of both sides of this relation with respect to ω and identifying the phase and group velocities, one finds

$$(v_p v_g)^{-1} = \frac{1}{2}\left[\mu\frac{d(\omega\varepsilon)}{d\omega} + \varepsilon\frac{d(\omega\mu)}{d\omega}\right] = \frac{nz}{2c_0^2}\left[\frac{d(\omega\varepsilon_r)}{d\omega} + \frac{1}{z^2}\frac{d(\omega\mu_r)}{d\omega}\right] \tag{2.52}$$

As the quantities $\frac{d(\omega\varepsilon_r)}{d\omega}$ and $\frac{d(\omega\mu_r)}{d\omega}$ are always positive in a passive medium with negligible losses (see Section 2.1.4), the product $v_p v_g$ has the same sign as the product nz, and thus the BW condition (2.51) is equivalent to the LH condition (2.47). This equivalence is only valid in frequency bands in which the definition of the energy density w in (2.13) and the entropy conditions (2.14) are valid, that is, for small (negligible) losses and outside abnormal dispersion bands like near resonances. This equivalence is further confirmed by the fact that in such bands the group velocity corresponds to the energy velocity given by $v_e = S_a/w$ [43, 45, 58]. In other words, if the phase velocity is opposite to the group (or energy) velocity (BW condition), it is also opposite to the the time-averaged power density S_a (LH condition).

e. Negative refractive index medium

The term *negative refractive index* (NRI) refers to the real part of the complex refractive index n (i.e. n'). The corresponding definitions for *negative refractive index medium* (NRI medium, or NIM) and *positive refractive index medium* (PRI medium, or PIM) are:

$$n' < 0 \quad \equiv \quad \text{NRI medium} \tag{2.53a}$$

$$n' \geq 0 \quad \equiv \quad \text{PRI medium} \tag{2.53b}$$

However, it has already been observed in Section 2.1.7 in the case of simple media that the determination of n from the medium parameters [equation (2.33)] is subject to a sign ambiguity. As a result, the sign of n' is linked to the choice of a particular root for n. To resolve this ambiguity, one should first consider the question of the nature of n: is n a parameter characterizing the medium or the wave propagating in it ? When dealing with conventional (PRI) materials, it is usually accepted that n is a parameter characterizing the medium. However, considering the example of the simple medium, only the square of n is unambiguously linked to the medium parameters through the relation $n^2 = \mu_r \varepsilon_r$ (2.33), but the sign of n is dependent on the convention used to define the direction of propagation $\hat{\mathbf{u}}$ [see (2.25)]. In fact, the two possible signs for n correspond to the two possible opposite propagation directions. Moreover, according to the definition (2.27), n is fundamentally a parameter characterizing the plane wave, not the medium itself. Therefore, in determining the sign of n, one should refer to the direction of another physical quantity like the time-averaged power density S_a or the group velocity v_g. More precisely, if we decide that $\hat{\mathbf{u}}$ is the unit vector in the direction of S_a (or v_g), it appears that the NRI condition $n' < 0$ is equivalent to the LH (or BW) condition.

Let us further consider in detail the *phenomenon of negative refraction* occurring at an interface between two semi-infinite media. Negative refraction means that the transmitted wave is directed on the same side of the normal to the interface as the incident wave. It is known that this problem is governed by Snell's law, which usually writes $n_1 \sin\theta_1 = n_2 \sin\theta_2$. There is common understanding in the field of MTMs that Snell's law *implies* that a negative refractive index ($n_2 < 0$) corresponds to a negatively refracted wave ($\theta_2 < 0$), or, equivalently, that the signs of both n_2 and θ_2 have to be changed simultaneously to satisfy Snell's law. This reasoning has been criticized in [52], where it is explained that in Snell's law there is usually no well defined convention concerning the definition of the angles θ_1 and θ_2. For instance, we can replace θ_2 by $\pi + \theta_2$ and thus the sign of n_2 must be changed in order to verify Snell's law again. This problematic is further discussed and clarified in the rest of this section. The resulting conclusions fully support the point of view of [52].

Let us consider in detail the simplest case of an interface between two lossless simple media, as shown in Figure 2.1. The incident plane wave in medium 1 and the transmitted wave in medium 2 have wave vectors $\boldsymbol{\beta}_1$ and $\boldsymbol{\beta}_2$, respectively, and the corresponding Poynting's vectors are $\mathbf{S}_1$ and $\mathbf{S}_2$. The interface is the xy plane and the incidence plane is the xz plane. The angles of incidence θ_1 and transmission θ_2 are defined in such a way that the corresponding wave vectors write

$$\boldsymbol{\beta}_i = |\boldsymbol{\beta}_i|(\sin\theta_i\,\hat{\mathbf{x}} + \cos\theta_i\,\hat{\mathbf{z}})\,, \quad i = 1, 2 \tag{2.54}$$

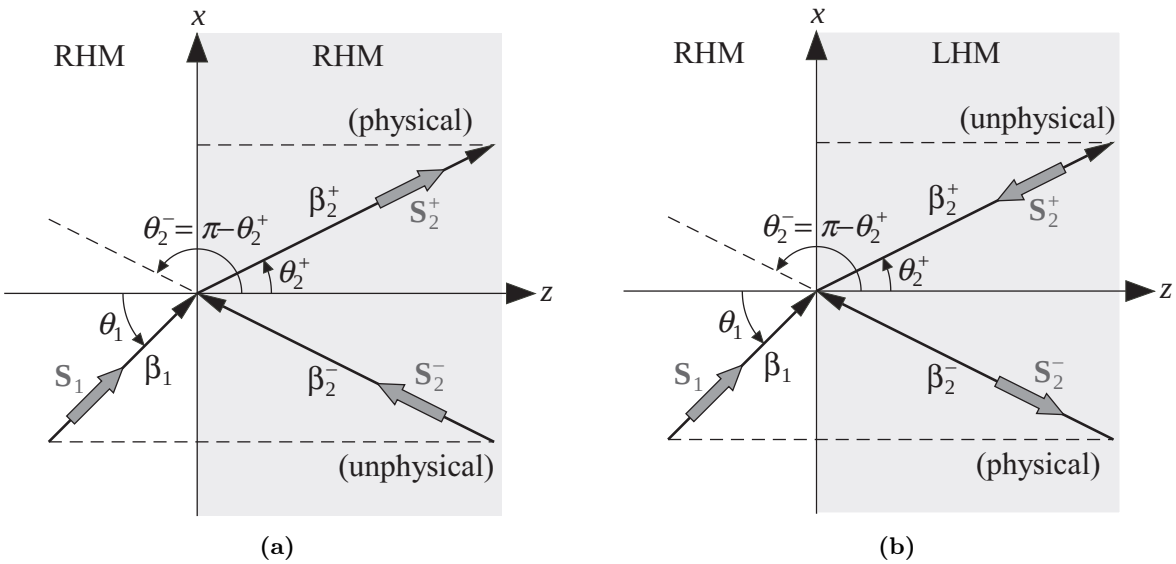

Figure 2.1: Positive and negative refraction at an interface between two semi-infinite lossless simple media (the reflected wave is not shown). The thin black arrows represent the wave vectors $\boldsymbol{\beta}$ and the thick grey arrows represent the Poynting's vectors $\mathbf{S}$. (a) RHM-RHM interface, (b) RHM-LHM interface.

In order to satisfy the continuity of the tangential fields at the interface, the tangential wave vectors must also be continuous. In the present case, this means that the x components of the incident and transmitted wave vectors are the same, that is

$$|\boldsymbol{\beta}_1| \sin\theta_1 = |\boldsymbol{\beta}_2| \sin\theta_2 \tag{2.55}$$

Using the definition of the refractive index (2.27) in (2.55) yields the well-known Snell's law:

$$|n_1| \sin\theta_1 = |n_2| \sin\theta_2 \tag{2.56}$$

where n_1 and n_2 are real quantities since the medium is lossless. It can be noted that (2.56) is only valid if $|n_2| \geq |n_1| \sin\theta_1$. Otherwise, we are in the total reflection regime. Two important properties can be inferred from (2.56):

- The signs of n_1 and n_2 have no impact on Snell's law (2.56) since only their absolute value is involved. As a matter of fact, Snell's law does not feel the sign of the refractive index [52].
- There are *always* two possible values of the angle θ_2 satisfying Snell's law (θ_2^+ and $\theta_2^- = \pi - \theta_2^+$) [27,52]. In both configurations of Figure 2.1, the two possible refracted waves are shown, where the superscript $^+$ ($^-$) refers to the positively (negatively) refracted wave.

The actual direction of the refracted wave cannot be determined without referring to passivity requirements. Indeed, the solution is only physically acceptable if the time-averaged power flow (i.e. the Poynting's vector $\mathbf{S}$) is outgoing from the interface, that is, if its z component is positive. As a result, for the RHM-LHM interface shown in Figure 2.1(b), the solution

satisfying the passivity condition is the negatively refracted wave, since the wave vector and the Poynting's vector are antiparallel in a LHM [see (2.46a)]. Similar considerations can be formulated to show that a wave is positively refracted at a RHM-RHM interface, as in Figure 2.1(a) [27]. In conclusion, there are always two possible refracted waves verifying the continuity of the tangential wave vectors (Snell's law), but Snell's law itself does not tell us which one is the actual physical solution.

The interface problem involving lossy simple media is more complex since the transmitted plane wave is in general non-uniform, which means that wave vector $\boldsymbol{\beta}$ and the Poynting's vector $\mathbf{S}$ are in general not collinear. As a result, to determine the direction of the refracted wave, one should first decide if this direction is given by $\boldsymbol{\beta}$ or $\mathbf{S}$.

Let us finally note that the phenomenon of negative refraction may also occur at an interface involving more complex media, such as uniaxial media [52], general anisotropic media [59, 60] or chiral media [61]. It is explained in these references how various combinations of the signs of the medium parameters may lead to a wide range of possible effects related to negative refraction. Finally, negative refraction can also be observed even if macroscopic medium parameters cannot be defined through an appropriate homogenization procedure, like in photonic crystals, for instance [62, 63].

f. Summary and conclusions

In this section, we have described five terms related to media exhibiting unusual properties (DNG, LH, NPV, BW and NRI media). It has been shown that, although fundamentally different, those terms in general imply the same type of phenomenon related to negative refraction. The subtle differences between these concepts and their scope of applicability are briefly recalled and discussed in the following lines.

It has been shown that a NPV medium is strictly equivalent to a LHM, and that a DNG medium (for simple media) and a BW medium correspond in general to a LHM, provided that losses are negligible (i.e. not near resonances). A NRI medium can be considered as equivalent to either a LHM or a BW medium, depending on the convention used for the definition of the propagation direction.

Concerning the scope of applicability of these concepts, the DNG medium condition is different from the others in the sense that it is directly formulated in terms of the medium parameters ε and μ, and thus only applies to simple media. Evaluating the DNG condition also requires that macroscopic permittivity and permeability can be properly defined, which is not obvious for many physical composite implementations of MTMs.

Unlike the DNG condition which does not assume any particular type of wave, the other conditions (LH, NPV and BW) are formulated in terms of the parameters of a plane wave propagating in the medium. It is worth mentioning that these concepts can also apply to a Bloch-Floquet mode in a periodic structure. Let us also note that the LH, NPV and BW concepts are not limited to simple media, but can also be applied to a general bianisotropic medium.

A special case is the NRI medium condition. Indeed, this concept is subject to an ambiguity concerning the fundamental nature of the refractive index, depending on whether it is considered as a medium parameter or a wave parameter. In fact, the term NRI was not found to be appropriate for characterizing a medium, because the choice of the sign of n' is dependent on the definition of the propagation direction $\hat{\mathbf{u}}$. Furthermore, the term NRI suggests the wrong idea that Snell's law implies a negatively refracted wave for a negative refractive index, whereas it was shown that Snell's law in fact does not feel the sign of the refractive index. As a result, Snell's law itself does not imply any choice for the sign of n' or for the positive/negative nature of the refraction. The NRI condition is also more restrictive than the LH, NPV and BW conditions, since it requires that a scalar refractive index can be defined, which is in general not possible when complex media or non-uniform plane waves are involved.

The criterion having the largest scope of applicability is the BW condition, because it is only based on the knowledge of the dispersion diagram. As a consequence, it can be conveniently applied to the characterization of any type of periodic structures, whatever they can be homogenized or not.

In conclusion, for simple media with small losses and outside abnormal dispersion bands like near resonances, the five concepts DNG, LH, NPV, BW and NRI media are equivalent. Generally speaking, these five terms are equivalently used to characterize the "reverse" or "unusual" properties of MTMs. In this work, the term which has been mostly used is LHM, since it was the most commonly used at the beginning of the work in 2004. This is also consistent with the terminology introduced in [3] for a structure which has been extensively investigated in this thesis: the composite right/left-handed transmission line (CRLH TL), which is basically an artificial TL exhibiting BW and FW bands.

2.1.9 Further unusual phenomena associated with LHM

Beside the phenomenon of negative refraction of a monochromatic plane wave discussed in Section 2.1.8, a plethora of unusual effects involving continuous LHM have been reported in the literature since the pioneer works on the topic. Describing all of them is out of scope of the present report, but we rather provide here a list of the most important effects, along with some references of related works:

- Negative refraction of modulated waves in space and time (Gaussian beams, wave packets,...) [17, 18, 64, 65].
- Reversal of Doppler effect [3, 6].
- Reversal of Cherenkov radiation [3, 4, 6, 66].
- Reversal of Goos-Hänchen shift [3].
- Subwavelength focusing and perfect lenses [12, 67, 68].
- Superluminal group velocity and negative group velocity [4, 69].
- Guided-waves with DNG and SNG layers [4, 5, 70, 71].
- Propagation in near zero index media [5, 72].
- Causality with LHM [73, 74].

It is worth recalling that the studies reported above involve idealized homogeneous LHM, and therefore do not discuss the physical implementations of such MTMs. Further information on these phenomena can also be found in recent books on MTMs [3–5].

2.2 Reported LHM structures

The present state-of-the-art on LHM implementations mainly focuses on the works reported until the beginning of this thesis, in end 2004. However, more recent contributions are also sometimes referenced for some structures which have been considered in more detail in this work. As a result, this is not an exhaustive catalog containing all the most recent contributions. A special effort has been made to classify the reported LHM implementations according to there working principles. The following four categories have been identified:

- Arrays of metallic inclusions, such as the SRR-wire medium.
- Arrays of dielectric inclusions, or purely dielectric LHM.
- LHM based on loaded waveguides below cutoff.
- Transmission line based LHM.

Parameters that usually come into consideration for the evaluation of LHM performances are the LH bandwidth, losses, isotropy, magneto-electric coupling, effective homogeneity, ease of fabrication, scalability to higher frequencies, and its capability to be coupled from free-space, to name a few.

2.2.1 Arrays of metallic inclusions

a. SRR-wire media

As already mentioned in the historic (Section 1.1.2), the first reported LHM structure consisted of a combination of an array of magnetic resonators called *split-ring resonators* (SRRs) and a *wire medium*, which provide negative values of the permeability and the permittivity, respectively [10]. We first briefly describe these two subsystems:

- **The wire medium** consists of an array of thin parallel conducting wires. When excited with an external electric field parallel to the wires, it acts as an equivalent medium exhibiting a plasma-like permittivity, thereby providing negative values below the plasma frequency [7,8,75]. The wire medium may also be implemented with discontinuous wires, in which case it exhibits a resonant Lorentz-type permittivity, with possible negative values just above the resonant frequency. Generalization of the wire medium obtained by loading the wires with lumped elements has also been investigated in [76]. Further detailed analysis revealed that the wire medium exhibits strong spatial dispersion [77].
- **The split-ring resonator (SRR)**, which was first proposed in [9], is basically a sub-wavelength magnetic resonator made of inductive metallic rings loaded with capacitive gaps, as shown in Figure 2.2(a). An impressed magnetic field along the ring axis induces

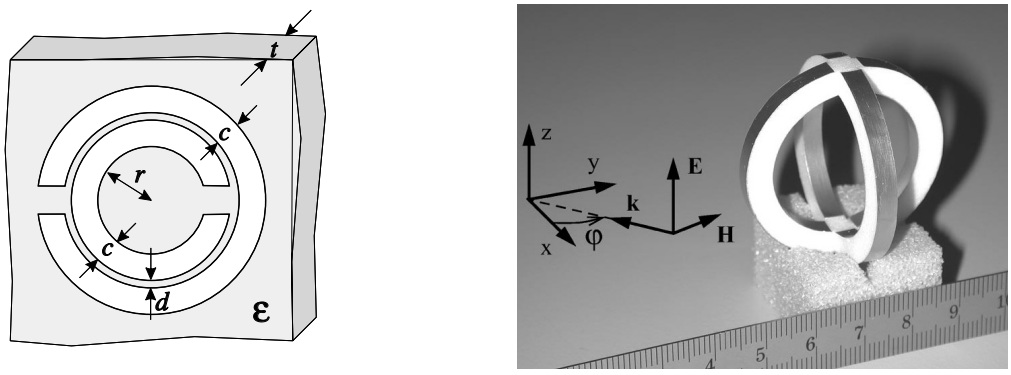

(a) (b)

Figure 2.2: Examples of SRRs. (a) Basic planar "edge-coupled" SRR (taken from [78]), (b) crossed split-ring resonator (CSRR) (taken from [79]).

circulating currents in the rings, which in turn give rise to a magnetic dipole moment. As a consequence, an array of SRRs acts as an equivalent medium exhibiting a Lorentz-like permeability, with possible negative values just above the resonant frequency. This structure therefore provides a magnetic response without containing any magnetic material. The SRR is a complex structure which deserved a lot of attention in the literature. In particular, coupling effects between SRRs in an array have been investigated in [80], and magneto-electric couplings (bianisotropy) occurring in these structures have been highlighted and described in [81, 82]. Many variants of SRRs have been subsequently reported in the literature. For instance, spiral resonators have been proposed in [83] to lower the resonant frequency, thus decreasing the electrical size of the cells at resonance. Moreover, the "broadside-coupled" SRR (BC-SRR) reported in [84] was shown to exhibit lower magneto-electric coupling compared to the initial "edge-coupled" SRR (EC-SRR) shown in Figure 2.2(a). Furthermore, an extension of the SRR to volumetric structures suitable for MTMs with higher level of isotropy has been proposed in [79]. An example of such a structure, which has been called *crossed split-ring resonator* (CSRR), is shown in Figure 2.2(b). This structure was shown to be perfectly isotropic in the xy plane.

The first reported LHM obtained by combining these two subsystems is shown in Figure 2.3(a) [10]. This structure only exhibits a LH behaviour for one direction of propagation (1D LHM) and for one polarization of the fields. Figure 2.3(b) shows an improved 2D isotropic version of this LHM [11], which allowed the first experimental verification of negative refraction [13]. Since these first investigations, SRR-wire media have been extensively investigated and many variants have been reported. The additional effect of the electrical response of the SRRs on the effective permittivity has been highlighted in [85, 86], and further investigations also revealed the importance of the interactions between the wires and the SRRs [87]. Recently, simulation results on a 3D isotropic version of the SRR-wire LHM have been reported [88], but this structure has not been fabricated yet.

(a) 1D LHM **(b)** 2D LHM (taken from [13])

Figure 2.3: Examples of SRR-wire LHM.

b. LHM based on Ω-like metallic patterns

A new kind of LHM based on Ω-like metallic patterns has been proposed in [89]. The unit cell consists of a cube with a Ω pattern printed on each face, as suggested in Figure 2.4(a). The Ω is a combined electric-magnetic resonator. Indeed, an electric field parallel to the branches of the Ω gives rise to an electric resonance, whereas a magnetic field along the axis of the round part, which represents some kind of SRR, induces a magnetic resonance. By adjusting the two resonant frequencies, simultaneous negative permittivity and permeability can be achieved. To avoid bianisotropic effects, pairs of opposite Ω patterns are used, as shown in Figure 2.4(a). The final structure is obtained by printing, with appropriate orientation, three pairs of Ω patterns on the three pairs of opposite faces of a cube, as shown in Figure 2.4(b). The resulting LHM is expected to be fully isotropic according to the analytical study performed in [89]. Experimental confirmation of LH behaviour in 1D arrays of Ω patterns has been subsequently reported by another group in [90, 91].

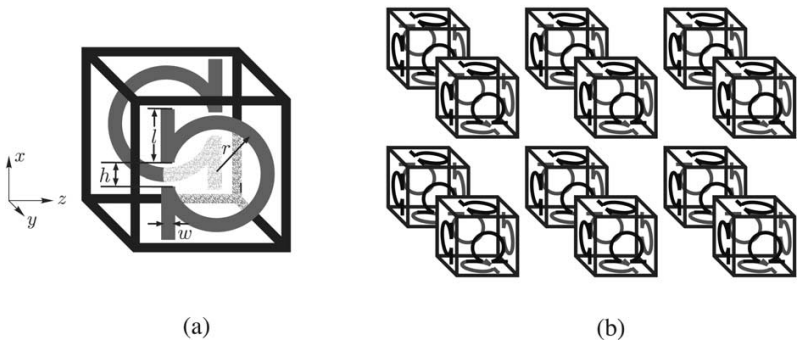

Figure 2.4: 3D isotropic LHM based on Ω patterns (taken from [89]). (a) Unit cell (only one of the three pairs of Ω patterns is shown), (b) rectangular lattice of such unit cells.

c. LHM based on S-shaped resonators

An alternative LHM implementation using S-shaped resonators has been proposed in [92]. The unit cell consists of two metallic S-patterns, one on each face of the substrate. It is known that classical SRRs also exhibit a frequency band of negative permittivity (due to an electric resonance) occurring at higher frequency than the negative permeability band. As these two bands do not overlap in general, the idea was to deform a classical SRR in order to shift the negative permittivity band to lower frequencies, allowing then the two negative bands to overlap. Simulation and experimental results on S-shaped LHM have been reported in [92], and detailed analytical studies in [93].

d. LHM based on the fishnet structure

More recent works concern the investigation of simplified structures initially derived from the SRR-wire medium. For instance, in [94] a new LHM is obtained by replacing the SRRs by short wire pairs, which still provide a resonant magnetic response analogous to that of the SRRs, resulting from strong antiparallel currents in the two wires of the pairs. This structure has been further modified by enlarging the short wires and merging them with the continuous wires. The resulting structure and its variations have been called *fishnet* structures [95]. The main advantage of these simplified structures resides in their planar topology, which facilitates their fabrication with conventional microfabrication techniques. Due to its planar topology, the fishnet structure is well suited for 1D or 2D LHM, but its extension to 3D isotropic structures is not straightforward.

2.2.2 Purely dielectric LHM

LHM based on metallic patterns are well suited for microwave frequencies, but they become prohibitively lossy as the frequency is increased towards millimeter and submillimeter waves. To that respect, purely dielectric LHM represent an interesting alternative. Several groups have proposed various implementations of LHM consisting of arrays of dielectric inclusions, some of which are briefly described here:

- A LHM based on the combination of two lattices of high permittivity dielectric spherical particles has been proposed in [96]. The dielectric spheres support TE/TM resonant modes, from which it results equivalent magnetic/electric dipole moments. When the lattice constant is small compared to the wavelength, an homogenization procedure is possible, which leads to the definition of resonant equivalent permittivity and permeability, with possible negative values just above the resonant frequency. The idea is to combine two lattices of dielectric spherical particles with different diameters, in such a way that both magnetic and electric resonances can be achieved at the same frequency, thereby leading to a narrow band with simultaneous negative permeability and permittivity.
- A very similar structure had been reported before in [97], where they used a single lattice

of magnetodielectric spherical particles instead of a bilattice of purely dielectric ones. The main drawback of this structure is the requirement for a magnetodielectric material.

- A LHM made of clustered dielectric cubes was further proposed in [98]. Interactions between the closely spaced dielectric cubes in the unit cell result in plasmonic artificial magnetic and electric dipole moments, which may lead to simultaneous negative permeability and permittivity. Such cubic inclusions are expected to be easier to fabricate than spheres.

An advantage of these purely dielectric LHM over their metallic counterparts is that an isotropic response is achieved in a straightforward manner, due to the isotropy of the particles themselves. On the other hand, obtaining isotropy with metallic LHM appears to be a more challenging task. Although the purely dielectric LHM are expected to exhibit lower losses than the metallic ones, they remain rather narrowband since still relying on resonance phenomena. The aforementioned works showed proofs of concept through analytical and numerical investigations, but experimental validations remain to be done.

2.2.3 LHM based on loaded waveguides below cutoff

Considering that a waveguide (WG) operated below the cutoff frequency of the first TE mode can be seen as a guiding structure exhibiting a negative permittivity, LH propagation can be achieved by loading such a WG with artificial mu-negative medium (MNG), such as an array of SRRs for instance. This principle of LHM was first suggested in [78], where a cutoff rectangular WG periodically loaded with SRRs was proposed. This first prototype being clearly limited to 1D propagation, a 2D isotropic version of this LHM was subsequently proposed in [99], where a parallel plate WG operated below the cutoff frequency of the first TE mode was used. This structure had the advantage of being fully planar. Further investigations on related structures have been reported in [100], where analytical and experimental studies showed that a rectangular WG filled with an anisotropic uniaxial MTM with transversal negative effective permeability supports LH propagation.

The underlying theory of the equivalence between evanescent WG modes and artificial plasmas has been carefully investigated in [101], from which it comes out that magnetic plasma responses can also be simulated in a WG by means of evanescent TM modes. As a result, It is also possible to obtain a LHM by periodically loading a cutoff WG with an epsilon negative medium (ENG), such as the wire medium. The resulting structure is therefore the dual of the SRR loaded cutoff WG mentioned above. Importantly, it has been emphasized in [101] that the analogy between evanescent WG modes and artificial plasmas requires that the filling material be anisotropic.

In summary, LH propagation can be achieved in WGs operated below cutoff when they are filled with an anisotropic uniaxial single negative (SNG) MTM (i.e. a material for which the transversal permeability or permittivity is negative), such as an array of SRRs or a 1D or 2D wire medium. This second approach is expect to provide low loss structures compared to the SRR based approach, since ENG wire media do not rely on resonances. Experimental

investigations on ENG loaded cutoff WGs have also been reported in [102]. Despite some suggestions given in [78, 99] for stacking these loaded WGs to form volumetric MTMs, these structures have been mainly restricted to 1D, possibly 2D, guiding structures. No chance seems to exist for extending these structures to 3D isotropic LHM.

Recently, another variant of a 2D LHM belonging to the present category has been proposed in [103]. It consists of a parallel plate WG operated below the cutoff of TE modes and loaded with cylindrical dielectric resonators. Negative permeability is provided by a collective effect of the dielectric resonators under their fundamental TE resonance.

2.2.4 Transmission line based LHM

As already mentioned in the historic (Section 1.1.2), LHM based on a transmission line (TL) approach have been proposed almost at the same time by three groups [24–26]. The basic idea behind TL-based LHM consists in implementing a TL with a capacitive element in the series branch and an inductive element in the shunt branch, i.e. the dual topology of a conventional TL. Such an ideal continuous dual TL exhibits a LH behavior at all frequencies. As fully distributed dual TLs cannot be realized, practical implementations of TL-based LHM consist of a host TL periodically loaded with lumped series capacitances and shunt inductances. A LH response is achieved at frequencies where the loading L-C elements dominate the overall response. At higher frequencies, the response is mainly governed by the natural (right-handed, RH) propagation along the host TL sections. For applications where both the LH and RH bands are exploited, the general term *composite right/left-handed* (CRLH) TL has been introduced [3, 104]. An interesting property of the CRLH TL is the possibility to obtain a seamless transition between the LH and RH bands by a proper choice of the design parameters, in which case the structure is called a *balanced* CRLH TL. It can be noted that a (balanced) CRLH response can also be achieved with the other types of LHM previously presented, but this concept is introduced here because it has mainly been considered in the frame of TL-based LHM and related applications. In contrary to the other types of LHM, TL-based LHM do not rely on any resonance phenomena, thereby leading to low loss and wideband behavior compared to their resonant counterparts. In that context, a TL analysis of the SRR-wire medium showed that the SRR resonance was not necessary to obtain an effective negative permeability [105].

A plethora of implementations of TL-based LHM have been reported in the literature, based on different host TLs (microstrip, coplanar waveguide, coplanar stripline...), using different types of lumped L-C elements (SMT elements or printed elements) and with different physical dimensionality (1D, 2D or 3D). TL-based LHM have been widely covered in two books specifically dedicated to the subject [3, 4]. We only provide here a couple of representative examples of implementation. The first example in Figure 2.5(a) shows the unit cell of a 1D CRLH TL implemented in microstrip technology [106, 107]. The series capacitance is implemented by an interdigital capacitor, and a shorted stub is used for the shunt inductance. The second example in Figure 2.5(b) shows a 2D isotropic microstrip CRLH TL based on the mushroom structure, which was first reported in [108] in the frame of artificial magnetic conductors (AMC). In this structure, the vertical connections provide the shunt inductances, and the se-

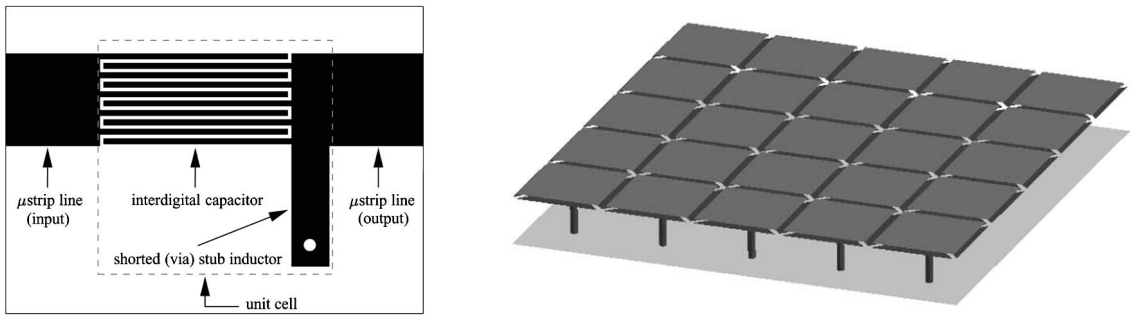

(a) **(b)**

Figure 2.5: Examples of TL-based LHM in microstrip technology. (a) Unit cell of a 1D LHM (taken from [107]), (b) 2D LHM based on the mushroom structure (taken from [109]).

ries capacitances are implemented by parallel plate capacitors [109]. Similar structures using lumped SMT elements for the L-C loadings have also been reported (see for instance [27,110]). It can be noted that the later structures are usually limited to a few GHz frequencies, due to the parasitic self-resonance of the chip components.

The first investigations on TL-based LHM were mainly concerned with planar 1D or 2D structures, but recently some possible extensions towards volumetric 3D LHM have been proposed. In particular, various topologies of 3D isotropic TL-based LHM have been analytically investigated in [111–114], and experimentally tested in [115] for a single unit cell and in [116] for a full 3D LHM. Due to their complex topology, these 3D isotropic structures require complex manufacturing processes. This has motivated the developments of alternative non-isotropic, but still volumetric, TL-based LHM obtained by stacking planar 2D TL-based LHM, as suggested in [117]. This type of structures, which exhibit 2D isotropy and work for a given polarization of the excitation field, have been called *volumetric layered TL-based LHM*, or also 2.5D TL-based LHM. As already mentioned in the introduction (Section 1.1.1), coupling of external incident waves into these volumetric TL structures is not straightforward. In some cases, special techniques based on transition layers have been resorted to for efficient coupling from free-space, as in [118] for instance.

Finally we can note that, although the initially proposed TL-based LHM do not rely on resonances, there also exist a category of TL-based LHM consisting of periodically loaded TLs with resonant particles like SRRs. One of the first proposed structures in this category consisted of a coplanar waveguide (CPW) loaded with SRRs printed on the other face of the substrate [36, 119]. This approach has been further extended to TLs periodically loaded with complementary SRRs (CSRRs[3]), which are the dual of SRRs etched in the ground plane. Various possibilities of CPW or microstrip TLs loaded with SRRs or CSRRs to realize 1D LHM have been reported in the literature (see for instance [120]). These structures are in general narrow band compared to

[3]It should be noted that the same acronym CSRR is used for "complementary SRR" and "crossed SRR" (see Section 2.2.1.a.).

their non-resonant counterparts. Targeted applications mainly concern miniaturized microwave components and filters.

2.2.5 Discussion

In the present state-of-the-art, the various reported LHM have classified into four categories. We conclude this section by making a link with the conceptual distinction performed in the introduction (Section 1.1.1) between the two main approaches for considering and realizing MTMs: the *inclusion-based approach* and the *TL-based approach*. On the one hand, the LHM of the first and second categories of this state-of-the-art (arrays of metallic or dielectric inclusions) obviously belong to the main class of *inclusion-based* MTMs. These structures can be implemented in free-space (or in a host dielectric), can be extended to volumetric (3D) possibly isotropic structures in a straightforward manner, and can be in principle efficiently coupled from an external field, such as an incoming wave from free-space. On the other hand, the LHM of the third and fourth categories (LHM based on loaded waveguides below cutoff and TL-based LHM) belong to the other main class of MTMs based on the *TL approach*. In the latter denomination, the term "TL" should be considered with its very general meaning of a host guiding structure, which can be a physical TL or a waveguide. Indeed, the LHM of both the third and fourth categories rely on a host guiding structure to achieve the LH response, and therefore cannot be directly implemented "in free-space". This results in structures for which an extension to 3D possibly isotropic structures is less straightforward than for inclusion-based MTMs. Moreover, when this is possible, the coupling of power from an external source (excitation of the LH modes) may appear as a challenging task, as observed for the volumetric TL LHM investigated in Chapter 5. Further considerations on this problematic are reported in Section 5.7.2, in the conclusions of the related chapter.

2.3 Characterization techniques and homogenization procedures

This section provides an overview on analysis techniques commonly used for the characterization of MTMs. The purpose of these techniques is to determine a set of relevant parameters which characterize a MTM from a macroscopic point of view. Those can be equivalent medium parameters such as the permittivity and the permeability, the refractive index, bianisotropic medium parameters, or an equivalent propagation constant and a characteristic impedance, the latter approach being essentially used for TL-based MTMs.

2.3.1 Bloch wave analysis

A common way of analyzing MTMs implemented as periodic structures consists in performing an eigenmode analysis usually referred to as the *Bloch wave analysis*, or more generally *Bloch theory*. This technique, which is based on the Floquet's Theorem [40, 121], consists in determining the eigen solutions which can exist in the infinite periodic structure in the absence of

excitation. Each of these solutions is usually referred to as a *Bloch wave*, or also *Floquet mode*. The properties of these waves are usually obtained by solving an eigenvalue problem. The resulting eigenvalues represent the possible *Bloch propagation constants* γ_B, while the associated fields solutions can be regarded as the eigenvectors. The possible values of γ_B in function of the frequency is the dispersion relation, or band structure, and its graphical representation is the dispersion diagram, or Brillouin diagram. Although the information contained in the dispersion relation is sufficient to assess the LH or RH nature of the considered mode, it does not provide a complete picture of the MTM properties. Accordingly, the information contained in the eigenvectors can be further exploited, and possibly combined with the dispersion relation, in order to derive additional macroscopic parameters such as the Bloch impedance, or equivalent medium parameters like the permittivity and the permeability, as described thereafter. Practically, a single unit cell is considered and periodic boundary conditions (PBC) with variable phase shifts between them are applied to its boundaries. Applying Floquet's Theorem to this system results in an eigenvalue problem which can be solved analytically or numerically, depending on the complexity of the problem.

a. Circuital representation

The simplest implementation of the Bloch wave analysis, suitable for 1D periodic structures, is based on a two-port circuital representation of the unit cell. The Floquet's Theorem allows a direct determination of the dispersion relation $\gamma_B(\omega)$, provided that the transmission matrix of the unit cell is known, either from a simplified circuit model, or from full-wave S parameters numerical calculation. A Bloch impedance Z_B associated to each Bloch wave can be deduced from the corresponding eigenvectors, which are now expressed in terms of voltages and currents. Basic foundations of this technique can be found in [40, 122–124], and its application to the analysis of the CRLH TL have been reported in [3, 4, 125, 126], for instance. This technique can also be extended to 2D or 3D periodic structures in a straightforward manner. Detailed analysis for the 2D case can be found in [127], or again in [3, 4]. Due to its circuital based formulation, this technique has mainly been used for TL-based MTMs, for which the couple of parameters (γ_B, Z_B) represents the most relevant information in view of practical microwave applications. It should be noted that this approach is accurate provided that the interaction between cells can be accurately described by a single mode of the host guiding structure. Otherwise, a multimode description of the unit cell has to be resorted to, an approach that has been developed in this work and which is reported in Chapter 6.

b. Full-wave approach

In a more general formulation, i.e. not based on a circuital representation, the eigen solutions are usually found through some specific numerical computations performed by an "eigenmode solver". Such codes are included in several commercial softwares, such as Ansoft HFSS or CST Microwave Studio. Although the dispersion diagram $\gamma_B(\omega)$ is directly provided, this is not sufficient for a complete description of the MTM properties. To that purpose, several techniques

have been proposed to derive macroscopic parameters from the eigen fields and currents in the unit cell (eigenvectors). These techniques are based on various kinds of averaging procedures, such as those described in Section 2.3.2 [128, 129].

2.3.2 Averaging procedures

In the context of homogenization of artificial dielectrics, the averaging strategy commonly used consists in performing volume-averages of the fields over a unit cell, and in defining the equivalent medium parameters as those which satisfy the constitutive relations for the macroscopic (or averaged) fields. A well known result obtained with this approach is the Maxwell-Garnett mixing formula [130]. This approach, which has been developed for dielectric inclusions in the static regime, is not easily adapted for the case of metallic inclusions (which can be infinitely thin, like strips) and for the high frequency regime, which is why other averaging strategies have been proposed in the MTM literature.

In particular, an averaging scheme directly inspired from the topology of Maxwell's equations (in integral form) has been proposed in [129]. The fields $\mathbf{B}$ and $\mathbf{D}$ are averaged over the faces of the unit cell, as they are related to flux densities, whereas $\mathbf{E}$ and $\mathbf{H}$ are averaged over the edges of the cell, since related to circulations (integration on a path). This averaging scheme is sometimes referred to as the surface/line averaging technique, by comparison to the aforementioned volume/volume approach commonly used for artificial dielectrics. The equivalent medium parameters are those which satisfy the constitutive relations for the macroscopic fields. This technique has been applied in [129] to arrays of SRRs and SRR-wire media, where the averaging was performed on the fields calculated through a numerical eigenmode analysis, as described in Section 2.3.1.b.. It should be noted that a similar approach had already been used in the pioneer works on SRRs and SRR-wire media reported in [9, 128]. Some variants of this technique involving the calculation of the wave impedance z from the averaged field quantities, or the calculation of the averaged polarization $\mathbf{P}$ and magnetization $\mathbf{M}$ from the currents distribution in the unit cell, have also been suggested in [128].

Another field averaging procedure, also referred to as the field summation method, has been reported in [131], applied to arrays of SRRs and compared to other approaches in [132], and further applied to SRR-wire media in [133]. This technique involves a volume/surface averaging scheme applied to the fields numerically calculated for a finite thickness slab under plane wave incidence (scattering parameters analysis). Extension of this technique to the retrieval the bianisotropic parameters of SRRs has also been proposed in [133].

2.3.3 Retrieval procedures from scattering parameters

Among the various homogenization procedures used to determine equivalent medium parameters for composite structures, one of the most common in the field of MTM consists in the extraction of these parameters from reflection and transmission coefficients (scattering parameters, or Fresnel coefficients) of a slab of finite thickness under plane wave incidence [134–136].

This technique consists in determining the medium parameters (usually the permittivity ε and the permeability μ) of a homogeneous slab exhibiting the same scattering parameters as the real composite periodic structure under study. The refractive index n and the normalized wave impedance z are first determined from the scattering parameters, and ε and μ are subsequently determined from n and z (as done in Section 2.1.7). As is often the case with such inverse problems, ambiguities are encountered in the determination of n and z. A robust retrieval procedure has been proposed in [137] in order to resolve these ambiguities.

It has been observed that the parameters extracted with this method often exhibit anomalous behaviours, incompatible with fundamental physical principles such as causality and passivity [see relations (2.15)]. In particular, when one of the extracted parameters experiences a resonance, the other exhibits an "antiresonant" behaviour, which is also accompanied with a "wrong" sign of the imaginary part of ε or μ. This problem has been addressed in [138] in the frame of the analysis of arrays of SRRs, where this unexpected frequency behaviour has been attributed to the periodic nature of the structure, more precisely to the finite (non zero) size of the unit cell. Moreover, the extracted parameters are sometimes function of the thickness of the MTM slab, i.e. of the number of cells in the propagation direction, which is a consequence of coupling phenomena occurring between adjacent cells. This issue has challenged the validity of this method since material parameters are expected to be independent from the sample size and shape. These issues are still subject to controversy in the recent literature ; they will be further discussed in Chapter 3.

To the best of the author's knowledge, the retrieval procedure from scattering parameters has only been developed for normal incidence. As a result, it only provides the equivalent medium parameters associated to this specific direction of propagation, which is not sufficient to assess the degree of isotropy of 3D complex MTM unit cells. Furthermore, it is often assumed that the material is only described by a permittivity and a permeability, whereas other parameters related to magneto-electric coupling (bianisotropy) cannot be easily extracted with this basic approach. To that respect, an improved retrieval procedure also allowing the retrieval of the bianisotropic parameters of MTMs composed of SRRs has been reported in [139]. This technique also involves normal plane wave incidence, but several orientations of the unit cell are considered in order to obtain enough equations to deduce all the medium parameters. To avoid the aforementioned anomalies observed on the extracted parameters, ref. [140] proposes an alternative approach which consists in considering the MTM as a periodic effective medium, instead of a homogeneous effective medium. In this method, the MTM is modeled as a succession of homogeneous slabs of unknown parameters ε and μ (to be determined with the method), with layers of vacuum placed in-between. Such an approach allows to distinguish the resonant behaviour of the parameters from periodicity effects. This approach has also been addressed by the same group in [141].

Finally, it should be noted that the retrieval procedure from scattering parameters is equivalent to the Bloch wave analysis based on a monomode circuital representation mentioned in Section 2.3.1.a., since the latter also involves a description of the unit cell obtained from scattering parameters. As a result, the expressions obtained for n ($= \gamma_B/(jk_0)$) and z (=

Z_B/η_0) are exactly the same.

2.3.4 Quasi-static approaches

For MTMs with lattice constant much smaller than the wavelength, effective material parameters can also be derived from a quasi-static analysis. These techniques, such as the quasi-static Lorentz theory or the Maxwell Garnett model, for instance, were initially developed for the characterization of conventional and artificial dielectrics [40, 130, 142]. Most of these quasi-static approaches rely on a dipolar representation of the particles forming the (meta)material. More specifically, it is assumed that the response of the particles to an impressed field can be accurately represented by electric and magnetic dipole moments (higher order multipoles are neglected). Those dipole moments are further averaged over the volume of the unit cell, resulting in averaged polarization and magnetization in the material, from which effective material parameters can be derived.

An example of such a technique is the quasi-static Lorentz theory [40], which has also been formulated in a general way in [143] for the characterization of MTMs. It comes out from this technique that effective material parameters can be obtained provided that the polarizabilities of the particles are known. These polarizabilities often have to be determined numerically, by calculating the dipole moments from the currents or fields distribution under a specific excitation. For instance, it is proposed in [143] to excite the particles by pairs of opposite plane waves, thereby approximating a constant electric or magnetic field excitation over the unit cell, consistently with the quasi-static assumption on which the method is based. This allows treating the problem with high frequency codes such as those usually used in microwave engineering. This technique has been applied in [143] to MTMs made of arrays of metallic inclusions such as SRRs, and to arrays of CSRRs (crossed SRR) in [144]. It should be pointed out that the quasi-static Lorentz theory is applicable provided that not only the unit cell is small compared to the wavelength, but also the spacing between inclusions, so that the interaction between them can be accurately described by dipole moments.

Several variants of quasi-static analyses based on simplified models for the inclusions have been applied to specific MTM structures and reported in the literature. In particular, examples of quasi-static approaches applied to the wire-medium can be found in [75], and to SRRs in [81, 84, 145]. Furthermore, the analysis of the Ω-like periodic array proposed in [89] revealed that the Maxwell Garnett model did not provide reliable results for the effective permittivity and permeability in the resonant bands. The limit of the quasi-static approach has also been discussed in [87] in the case of the SRR-wire medium.

2.3.5 Discussion

The four previous sections were devoted to the description of various aspects associated with the characterization of MTMs. It is noticeable that a given technique aimed at deriving equivalent material parameters may combine aspects which were presented in different sections. For

instance, the fields in the MTM can be first calculated considering either an infinite periodic structure supporting the fundamental Floquet mode (Section 2.3.1.b.), or a finite sample under plane wave incidence (like in Section 2.3.3), and a particular averaging procedure (as those described in Section 2.3.2) can be subsequently applied to derive equivalent medium parameters.

From a general point of view, these techniques can be conceptually separated into two categories. The first category concerns homogenization procedures oriented toward the determination of effective parameters which are consistent with their physical definition, which involve induced dipole moments or averaged macroscopic fields (Sections 2.3.2 and 2.3.4), thereby providing significant physical insight into the nature of the MTM. The techniques of the second category provide *formal* parameters, like the parameters of the Floquet modes (Section 2.3.1), or parameters which result from the equivalence between a given problem involving the actual composite MTM and the corresponding problem with a homogeneous material in place of the MTM (Section 2.3.3). The techniques of the second category are also referred to as *retrieval procedures*.

The retrieval procedure from scattering parameters has the advantage of being the most straightforward to implement, and this is the only one which can be directly applied to simple measurement results of a real piece of LHM (S parameters). On the other hand, elaborated techniques such as averaging procedures and quasi-static analysis provide an additional physical insight into the electromagnetic behaviour of the structure, which cannot be easily obtained from the rather "blind" retrieval procedures. For instance, they allow the identification of eventual magneto-electric coupling effects, along with the calculation of the associated bianisotropic parameters, whereas retrieval procedures from scattering parameters are mainly limited to the extraction of simple media parameters (i.e. ε and μ). The Bloch wave analysis has the advantage of directly providing the dispersion relation, which allows a straightforward identification of pass bands and stop bands, from which the location (in the frequency spectrum) of the LH bands can be deduced. From a numerical point of view, full-wave Bloch wave analyses require rather extensive numerical computations to obtain a reasonable number of points in the dispersion diagram, whereas retrieval procedures from scattering parameters can rely on efficient and fast frequency sweep algorithms.

It is also noticeable that applying different characterization techniques to a given MTM often results in some discrepancies in the extracted parameters, especially around resonances. This is so because the lattice constant a in most of the reported MTMs, although smaller than the wavelength λ, is not negligible compared to it (typically, $0.01 < a/\lambda < 0.25$). To that respect, it cannot be guarantied a priori that these structures can be homogenized in an ambiguous way, as is the case for conventional dielectrics, for which $a/\lambda \ll 0.01$. In particular, several authors agree upon that the very foundation of homogenization may not hold in some frequency bands near resonances, essentially because the unit cell in not small enough compared to the wavelength in the equivalent medium.

2.4 Microwave applications of LHM

This section presents a selection of the microwave applications of MTMs already discussed in a general context in Section 1.1.3. These applications have been classified into two main categories: guided-wave and radiated-wave (or antenna) applications. Although the focus is put on applications of LHM, or more generally MTMs exhibiting both usable RH and LH bands (CRLH MTMs), some examples of applications involving other types of MTM responses are also reported, such as SNG MTMs or combinations of complementary materials.

2.4.1 Guided-wave applications

MTMs have led to a variety of novel guided-wave applications and devices, some of which are reviewed in this section. It is noticeable that among the four categories of LHM reported in Section 2.2, most of the well demonstrated applications use 1D TL-based LHM (fourth category), more specifically the CRLH TL. The main reason is that the considered applications consist of microwave circuits already involving TLs, hence a more straightforward implementation than with inclusion-based LHM. Moreover, the non-resonant nature of TL-based LHM results in a more wideband behaviour and lower losses compared to their resonant counterparts. Applications of TL-based LHM are widely covered in two books devoted to the subject [3, 4], which is why they are recalled here in a concise manner.

a. Typical improvements achievable with the CRLH TL

Most of the LHM applications rely on the particular phase responses LHM can exhibit, which are given by their dispersion relation. The term *dispersion engineering* has been recently proposed for the study and development of *phase-engineered* devices [146], such as those based on the CRLH TL, by opposition to the field of *magnitude engineering*, which is mainly concerned with filters. In this dispersion engineering context, typical improvements achievable with CRLH TLs are size reduction, bandwidth enhancement and dual/multi band behaviour. To that respect, the most interesting structure is probably the *balanced* CRLH TL (see Section 2.2.4), for which a typical dispersion diagram is shown in Figure 2.6. As can be seen in the figure, this structure exhibits both LH and RH bands with a seamless transition between them at the so-called transition frequency f_0. It is noticeable that at f_0, the structure exhibits a zero phase shift with a non-zero group velocity. This particular point in the dispersion diagram has been exploited in many guided-wave and antenna applications, as will be shown thereafter. For applications requiring a given value of $|\beta| = \beta_1$, the CRLH TL provides two frequencies f_1 and f_2 corresponding to $-\beta_1$ and $+\beta_1$, respectively, hence a dual band behaviour [147]. Furthermore, if a given phase shift in absolute value $|\phi| = |\beta L|$ is required at a frequency f_1, the CRLH TL presents a larger value of $|\beta|$ than the corresponding unloaded TL (dielectric line), which allows using a shorter length L for a given phase shift $|\phi|$, hence a miniaturization. Broadband enhancement is also possible for applications such as TL phase shifters by combining CRLH and conventional RH TLs, as explained in [3]. It is noticeable that while

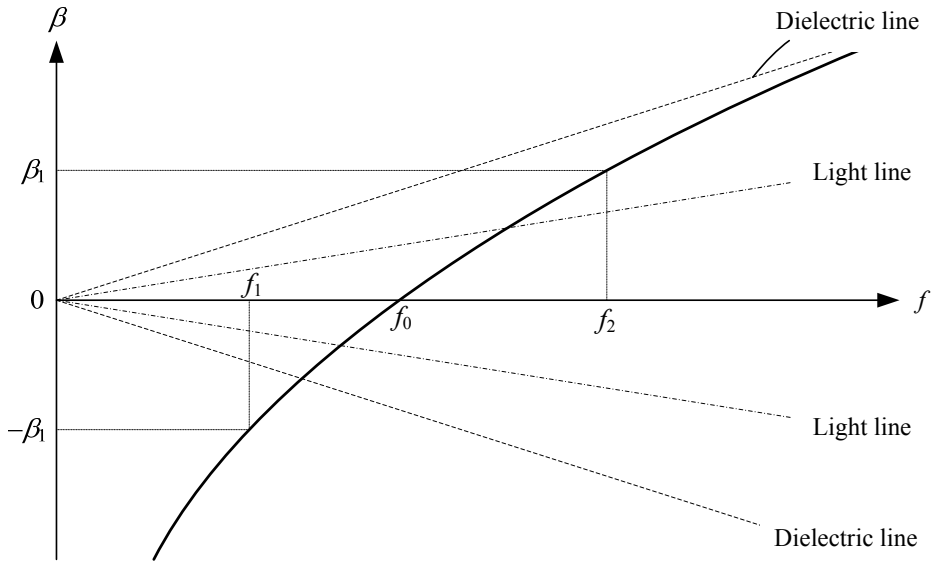

Figure 2.6: Typical dispersion diagram for a balanced CRLH TL. The light lines correspond to the dispersion relation in free-space and the dielectric lines to the dispersion in an unloaded TL.

the dispersion relation is the main particularity of the CRLH TL, its equivalent characteristic impedance can be made smoothly varying with frequency, hence a wideband matching for the considered applications.

b. Dispersion engineering applications

The most straightforward dispersion-engineered device which can be improved by using the CRLH TL is probably the phase shifter. To that respect, compact phase shifters with possible positive/zero/negative phase shifts have been reported in [110, 126, 148]. These devices, which consist of one or several cells of the CRLH TL, are more compact than their conventional TL counterpart and may exhibit lower group delay, which is desirable for applications requiring broadband operation. Interesting phase responses have also been obtained by phase compensation between a CRLH TL operated in the LH band and a conventional RH TL [149]. Several other microwave devices involving phase-shifting lines have been improved by using CRLH TLs in place of conventional TLs:

- Broadband baluns using $+90°$ and $-90°$ phase shifting CRLH TLs [150].
- Branch-line couplers with reduced size and enhanced bandwidth [151, 152].
- Series power dividers using the transition frequency f_0, with possible extension to an arbitrary number of output ports [153, 154].
- Distributed amplifiers and mixers with enhanced functionalities [155].
- Various delay systems for UWB pulses manipulations [146, 156, 157].

Various concepts of coupled-line couplers exploiting the unusual backward/foreward coupling phenomena occurring between two closely spaced CRLH TLs, or between a CRLH TL and a conventional RH TL, have also been reported in [158–161]. The complex modes phenomenon involved in some of these couplers is further discussed in [162], while further phenomenological explanations on the physical coupling mechanism involved in these couplers have been recently reported in [163]. The main improvements achieved by these novel MTM-based couplers over their conventional counterparts are broad bandwidth, arbitrary coupling levels and compactness.

The phase compensation phenomenon occurring between a LHM and a RHM has also been used to achieve subwavelength cavities. Indeed, by partially filling a cavity with a LHM slab and the rest with a RHM slab, one can obtain a cavity resonator whose dispersion relation may not depend on the overall size of the resonator, but rather on the ratio of the slabs thicknesses [164]. In other words, cavity resonators with total thickness far less than the conventional $\lambda/2$ size can be achieved.

c. Other guided-wave applications and related topics

The CRLH TL has also been used in other types of microwave applications. In particular, the CRLH TLs of the resonant type mentioned at the end of Section 2.2.4 have led to various interesting filter concepts, most of them being reported in a recent book on the subject [36]. One can also note the possibilities offered by the CRLH TL to achieve extreme high/low characteristic impedance values [165, 166], or impedance transformers for matching purpose [167, 168]. Micromachined MMIC CRLH TLs have also been reported in [126, 169], while silicon-integrated CRLH TLs with MEMS tuning capabilities for Ku-band operation have been reported in [170,171]. Resonant MTMs with negative permeability only, such as arrays of SRRs, may also be applied to microwave absorbers in order to miniaturize their dimensions [172], as well as to waveguide miniaturization [100].

2.4.2 Antenna applications

The unique features of LHM, or more generally CRLH MTMs, have recently produced interesting antenna concepts, some of which are reviewed in this section. Achieved improvements over conventional antennas are size reduction, dual/multi-band behaviour, enhanced directivity and novel functionalities. As for guided-wave applications, most of the well demonstrated antenna applications are based on the CRLH TL, because of its more wideband behaviour and lower level of complexity in terms of physical realization (fully planar structures) compared to the other types of MTMs reported in Section 2.2.

a. Leaky-wave antennas

It is known that Leaky-wave (LW) radiation occurs when the phase velocity of a wave propagating along an open structure exceeds the velocity of light (fast-wave propagation), as suggested

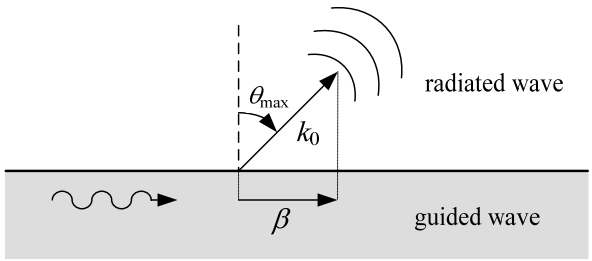

Figure 2.7: Schematic representation of a leaky wave.

in Figure 2.7. This effect is analogous to Cherenkov radiation of a charged particle which exceeds the speed of light in a medium. The direction of radiation is approximately given by $\sin\theta_{\max} = \beta/k_0$, where β is the phase constant of the guided wave and k_0 the free-space wave number. As a can be seen on the dispersion diagram of Figure 2.6, the CRLH TL exhibits a fast-wave region around the transition frequency f_0, where β remains between the two light lines. As a result, a simple open CRLH TL can be used as a leaky-wave antenna (LWA) in this frequency range, as initially proposed in [173,174] and further described in the two books [3,4]. The most interesting particularity of these antennas is that they can radiate in the forward (RH band; $f > f_0$) and backward (LH band; $f < f_0$) directions with continuous scanning through broadside (at f_0). In contrast, conventional LWAs can radiate forward *or* backward, depending on the mode used, but they do not allow broadside radiation. Moreover, it is noticeable that CRLH TL LWAs radiate in their dominant mode, thereby not requiring any special feeding system as is the case for conventional LWAs using higher order radiating modes.

Improved versions of these antennas have been subsequently proposed. For instance, varactors have been included in each cell of the CRLH TL to achieve beam-scanning and tunable beamwidth at a fixed frequency [175, 176], and gain enhancement has been achieved by periodically inserting amplifiers in the structure [177]. Many other implementations of CRLH TL LWAs in various technologies (microstrip, CPW,...) have been proposed and can be found in the literature. As conventional LWAs, these new structures allow for high gain and wideband matching, and their direction of maximum radiation varies with frequency, which is often considered as a drawback.

The 1D CRLH TL LWAs discussed so far usually produce a fan beam radiation pattern due to their long and thin topology, but they can be combined in arrays if high directivity is required in both planes. The concept of CRLH TL LWA has been further extended to the 2D case, by using 2D CRLH TLs similar to the mushroom structure shown in Figure 2.5(b) [178, 179]. When fed in their center, these antennas produce conical beam radiation. Recent research concerns alternative excitations to achieve other types of radiation patterns [180, 181].

It is worth mentioning that some LHM based on loaded waveguides below cutoff (Section 2.2.3) have also been investigated as LWAs, such as the structure presented in [103] and the waveguide filled with a wire medium reported in [182].

b. Resonant antennas

The richness of the dispersion diagram of the CRLH TL also offers several possibilities of application to resonant antennas. The most relevant concepts are synthetically reported thereafter:

- Miniaturized resonant antennas can be obtained by making use of the large negative phase constant β that can be achieved at low frequency. This leads to a small guided wavelength $\lambda_g = 2\pi/|\beta|$ which allows obtaining a $\lambda_g/2$ field distribution over a physically small distance [183–185]. An example of such a structure is shown in Figure 2.8(a). A similar principle as also been applied to dipole antennas in [186].

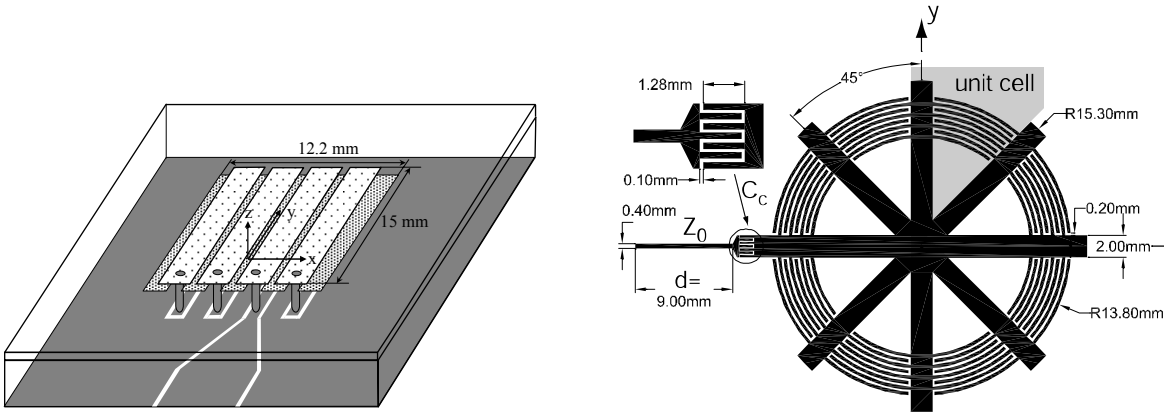

(a) **(b)**

Figure 2.8: Examples of resonant antennas based on the CRLH TL. (a) Small resonant microstrip antenna (taken from [184]), (b) dual-band ring antenna (taken from [187]).

- The CRLH TL also allows obtaining low values of $|\beta|$ (positive or negative), hence large values of λ_g, which can be used for the design of enlarged half-wavelength resonant antennas with enhanced gain due to larger radiation aperture [188].
- A CRLH TL at the transition frequency f_0 (infinite wavelength) acts a zero order resonator, whose resonant frequency does not depend on its total size. Using this principle, zero order resonant antennas have been proposed [104]. These structures can be made much smaller than conventional $\lambda/2$ patch antennas.
- Ring antennas obtained by wrapping around the two ends of a CRLH TL have been proposed. The miniaturized square ring antenna of [189] uses the $\beta = 0$ point, whereas the circular ring antenna shown in Figure 2.8(b) [187] is operated in the two first RH/LH resonant modes (perimeter = λ). This antenna can be fed at different points to achieve circular polarization.
- Finally, using several resonant operating points in the dispersion diagram allows implementing dual-mode [190] or dual-frequency [187] CRLH TL based antennas by combining several of the principles described above.

c. Other antenna concepts with LHM and MTMs

We report here some interesting antenna concepts that do not fit into the two main categories above. Some of them use other types of MTMs, while others are still at a conceptual level.

- Possibilities of reducing the size of resonant antennas using pairs of complementary materials have been discussed. Whereas the first investigations were based on the phase compensation effect between a LHM and a RHM [191, 192], further investigations revealed that subwavelength resonant cavities can also be achieved by combining single negative (SNG) media with conventional RHM. In this context, a circular patch antenna including a MNG medium has been reported in [193] and further studied in [194], where a particular implementation with SRRs has been investigated.
- MTMs with low positive or negative refractive index can be used to achieve high directivity antennas. Indeed, considering a simple ray optics approach, it can be observed that all the rays coming from a source placed inside such a material will leave the interface between the slab and air with an angle very close to the normal of the interface, hence a very high directivity. This principle has been first suggested in [195], where a high directivity antenna using a wire medium as a low positive index material has been experimentally demonstrated. Further analysis on this type of structures can be found in [196], and more general properties of wave propagation in zero index media in [72].
- Theoretical investigations showed that the power radiated by electrically small antennas such as small electric or magnetic dipoles can be enhanced by using spherical shells of materials with negative permittivity and/or permeability. The MTM shell was shown to act a natural matching circuit for the small antenna. This principle has been first proposed in [197], and further simulation results have been reported in [198, 199]. To the best of out knowledge, the predicted enhancements, which were based on idealized homogeneous isotropic MTMs, have not been experimentally demonstrated with real practical MTMs.
- Miniaturization of resonant patch antennas using artificial magnetics (MTMs with $\mu > 1$) is also a recent subject of interest. It is known that using a non-dispersive magnetic material in place of a conventional dielectric substrate allows size reduction without significantly affecting the bandwidth. To that respect, many antenna prototypes including artificial magnetic materials, such as arrays of SRR-like particles, have been proposed in the literature. However, theoretical investigations reveal that artificial magnetics do not offer any advantage in terms of bandwidth over conventional dielectric substrates, because of their inherent frequency dispersion [200]. It should be noted that this question is still subject to controversy (see [201] with comments in [202] and reply in [203], and references inside).
- Combination of slabs with complementary material parameters may lead to low profile leaky-wave antennas with very high directivity, as suggested in [204]. These structures have not been experimentally demonstrated yet.
- CRLH phase shifting lines can also be advantageously used in series-fed antenna arrays.

They allow for size reduction of the feed network and reduction of the beam squinting with frequency, as explained in [149, 205].

3 Dyadic medium parameters retrieval procedure from scattering parameters

3.1 General Considerations

3.1.1 Context and goals

Among the various homogenization procedures used to retrieve the equivalent medium parameters for composite structures, one of the most common in the field of MTMs consists in the determination of these parameters from reflection and transmission coefficients (scattering parameters, or Fresnel coefficients) of a slab under plane wave incidence . Several variants of this technique have been proposed, as reported in the state-of-the-art (Section 2.3.3). We refer to these techniques as "retrieval procedures from scattering parameters".

To our knowledge, this approach has only been developed for normal incidence, and thus only provides the equivalent medium parameters associated to this specific direction of propagation. In the present work, this technique has been extended to oblique incidences in order to investigate the properties of 2D or 3D MTMs for different propagation directions, in particular to evaluate their isotropy. For that purpose, an improved retrieval procedure which allows extracting dyadic permittivity and permeability from reflection and transmission coefficients obtained for various incidences (oblique and normal) has been developed and tested on some MTMs, such as wire media and arrays of magnetic resonators. Several aspects of this work have been presented by the author in [206, 207].

Let us note that an improved retrieval procedure which allows extracting equivalent medium parameters of bianisotropic MTMs (with some hypotheses on the constitutive relations) has been proposed and tested on planar SRRs in [139]. In this method, the structure is still characterized under normal incidence, but the orientation of the particle in the unit cell is changed, and the latter is periodically repeated in the plane perpendicular to the incidence direction, thereby forming a slab. This allows obtaining enough equations to deduce all the medium parameters. However, it is believed that changing the orientation of the particle in the unit cell for MTM slabs (typically with one layer of cells) does not result in the same structure, because of possible coupling that may exist between adjacent cells. In our retrieval procedure, the same MTM slab is considered under several different incidence directions.

The basic retrieval procedure from normal incidence is widely covered in the literature (see for instance [134–137]), which is why we directly start with the general formulation for arbitrary incidence, from which the well-known normal incidence extraction technique can be

deduced as a particular case.

The chapter is organized as follows: First, some general considerations and assumptions are provided in the rest of this section. Then, the problem of a slab under oblique plane wave incidence is described in Section 3.2 (direct problem), and the determination of the medium parameters from the calculated scattering parameters is detailed in Section 3.3 (inverse problem). We describe in Section 3.4 the technique used to compute the scattering parameters for a real composite MTM, and the retrieval procedure is tested on wires media and arrays of SRRs in Section 3.5. Conclusions on this type of retrieval procedures are provided in Section 3.6.

3.1.2 General strategy

The goal of the present type of retrieval procedures is to determine the medium parameters (permittivity, permeability,...) of a homogeneous slab exhibiting the same reflection and transmission coefficients as the real composite (often periodic) structure under study, for any incidence direction and polarization. This correspondence is illustrated in Figure 3.1. The general strategy for developing such a retrieval procedure can be summarized as follows:

1. Choice of a model of medium for the equivalent homogeneous slab (constitutive relations).
2. Development of the analytical expressions of the reflection and transmission coefficients for various incidence directions and polarizations, for the chosen model of medium.
3. Inversion of these analytical expressions to obtain the equivalent medium parameters in terms of the reflection and transmission coefficients.

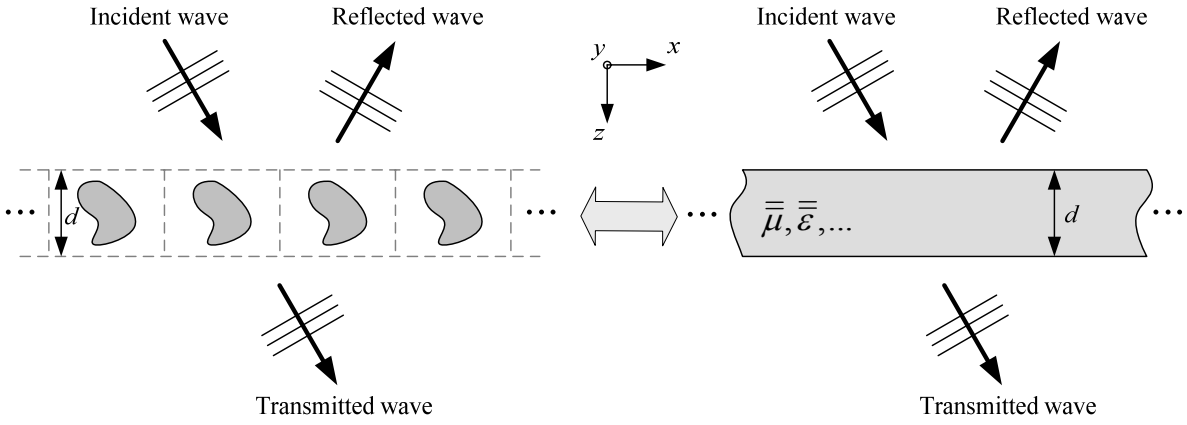

Figure 3.1: Correspondence between a 2D infinite periodic structure and a homogeneous slab in terms of reflection and transmission coefficients under plane wave incidence.

The reflection and transmission coefficients introduced in the resulting expressions are those calculated for the actual periodic structure, usually obtained by full wave simulations (see Section 3.4). It can be already pointed out that this retrieval procedure offers a redundancy of

information. Indeed, we can obtain an infinite number of equations by considering any incidence direction and polarization, whereas only a finite number of equivalent medium parameters need to be retrieved, which leads to an overdetermined system of equations. If the correspondence represented in Figure 3.1 is exact, we should always obtain the same medium parameters, independently of the chosen incidence directions. If this is not the case, this means that the chosen model for the equivalent homogeneous slab is not accurate, and that more parameters should be introduced in the model, or more complex constitutive relations should be considered.

3.1.3 Assumptions on the equivalent homogeneous material

Let us first recall the constitutive relations for a general linear bianisotropic medium (see Section 2.1.2):

$$\mathbf{D} = \bar{\bar{\varepsilon}} \cdot \mathbf{E} + \bar{\bar{\xi}} \cdot \mathbf{H} \tag{3.1a}$$

$$\mathbf{B} = \bar{\bar{\zeta}} \cdot \mathbf{E} + \bar{\bar{\mu}} \cdot \mathbf{H} \tag{3.1b}$$

Such a material is characterized by 36 parameters, which are not all independent from each other if reciprocity is assumed. Developing a retrieval procedure for all of these parameters from analytical expressions of reflection and transmission coefficients is by no means an easy task. Indeed, the only determination of the dispersion relation for a plane wave propagating in a general bianisotropic medium is a complex analytical problem [48]. To keep the problem within a reasonable level of complexity, the following assumptions on the material have been made:

- Magneto-electric coupling is not considered ($\bar{\bar{\xi}} = \bar{\bar{\zeta}} = 0$).
- The Cartesian coordinate system can be chosen such that $\bar{\bar{\varepsilon}}$ and $\bar{\bar{\mu}}$ is represented by diagonal matrices:

$$\bar{\bar{\varepsilon}} = \begin{bmatrix} \varepsilon_x & 0 & 0 \\ 0 & \varepsilon_y & 0 \\ 0 & 0 & \varepsilon_z \end{bmatrix} \quad , \quad \bar{\bar{\mu}} = \begin{bmatrix} \mu_x & 0 & 0 \\ 0 & \mu_y & 0 \\ 0 & 0 & \mu_z \end{bmatrix} \tag{3.2}$$

- The material does not exhibit spatial dispersion, which means that the medium parameters do not contain any spatial differential operators.

The chosen model is thus an electrically and magnetically anisotropic medium, hence six parameters to determine. The idea is to compute the reflection and transmission coefficients for a set of incidence directions and polarizations in order to obtain enough equations to determine these six medium parameters. The choice of material parameters considered here might appear somewhat limitative, in particular, neglecting the magneto-electric coupling, which can play an important role in MTMs [81]. However, the extent to which our retrieval procedure can be applied to a specific structure provides further insights on the electromagnetic coupling that occurs in that system. For example, a poor retrieval may indicate that not enough parameters have been taken into account in the model and to accurately describe the physical system under study. Hence, the key is not merely an exact retrieval procedure, but a procedure which exactitude can be evaluated.

3.1.4 Dispersion relation in anisotropic media

We consider plane wave propagation in an anisotropic medium described by (3.2). The corresponding fields can be expressed in a general way as

$$\begin{aligned} \mathbf{E}(\mathbf{r}) &= \mathbf{E}_0\, e^{-\boldsymbol{\gamma}\cdot\mathbf{r}} \qquad & \mathbf{D}(\mathbf{r}) &= \mathbf{D}_0\, e^{-\boldsymbol{\gamma}\cdot\mathbf{r}} \\ \mathbf{H}(\mathbf{r}) &= \mathbf{H}_0\, e^{-\boldsymbol{\gamma}\cdot\mathbf{r}} \qquad & \mathbf{B}(\mathbf{r}) &= \mathbf{B}_0\, e^{-\boldsymbol{\gamma}\cdot\mathbf{r}} \end{aligned} \tag{3.3}$$

where $\boldsymbol{\gamma} = \gamma_x\hat{\mathbf{x}} + \gamma_y\hat{\mathbf{y}} + \gamma_z\hat{\mathbf{z}}$ is the complex propagation vector. General properties of plane waves and definitions of associated parameters have been reported in Section 2.1.5.

The formalism presented in [48] allows obtaining the dispersion relation for an anisotropic medium. As the considered medium is both electrically and magnetically anisotropic, it leads to rather complex expressions which do not allow a simple analytical inversion as required here. For this reason, we rather consider two particular cases of propagation directions:

- The propagation vector lies in the xz plane ($\phi = 0$ plane), that is, $\gamma_y = 0$. In such a case, the dispersion relation writes

$$\left(\frac{\gamma_z^2}{\mu_x} + \frac{\gamma_x^2}{\mu_z} + \omega^2\varepsilon_y\right)\left(\frac{\gamma_z^2}{\varepsilon_x} + \frac{\gamma_x^2}{\varepsilon_z} + \omega^2\mu_y\right) = 0 \tag{3.4}$$

  Equation (3.4) can be satisfied in two ways:
  - If $\frac{\gamma_z^2}{\mu_x} + \frac{\gamma_x^2}{\mu_z} + \omega^2\varepsilon_y = 0$, the corresponding characteristic wave has its electric field along y, that is, $\mathbf{E}_0 = E_{0y}\hat{\mathbf{y}}$. This corresponds to a TE polarization.
  - If $\frac{\gamma_z^2}{\varepsilon_x} + \frac{\gamma_x^2}{\varepsilon_z} + \omega^2\mu_y = 0$, the corresponding characteristic wave has its magnetic field along y, that is, $\mathbf{H}_0 = H_{0y}\hat{\mathbf{y}}$. This corresponds to a TM polarization.
- The propagation vector lies in the yz plane ($\phi = 90°$ plane), that is, $\gamma_x = 0$. In such a case, the dispersion relation writes

$$\left(\frac{\gamma_z^2}{\mu_y} + \frac{\gamma_y^2}{\mu_z} + \omega^2\varepsilon_x\right)\left(\frac{\gamma_z^2}{\varepsilon_y} + \frac{\gamma_y^2}{\varepsilon_z} + \omega^2\mu_x\right) = 0 \tag{3.5}$$

  Equation (3.5) can be satisfied in two ways:
  - If $\frac{\gamma_z^2}{\mu_y} + \frac{\gamma_y^2}{\mu_z} + \omega^2\varepsilon_x = 0$, the corresponding characteristic wave has its electric field along x, that is, $\mathbf{E}_0 = E_{0x}\hat{\mathbf{x}}$. This corresponds to a TE polarization.
  - If $\frac{\gamma_z^2}{\varepsilon_y} + \frac{\gamma_y^2}{\varepsilon_z} + \omega^2\mu_x = 0$, the corresponding characteristic wave has its magnetic field along x, that is, $\mathbf{H}_0 = H_{0x}\hat{\mathbf{x}}$. This corresponds to a TM polarization.

These relations will be used in the developments of the retrieval procedure, as explained in the following sections.

3.2 Homogeneous slab under oblique plane wave incidence

This section presents the derivation of the reflection and transmission coefficients for a slab of anisotropic medium under oblique plane wave incidence.

3.2.1 Description of the slab problem

We consider a slab of homogeneous material described by (3.2) under oblique plane wave incidence, as illustrated in Figure 3.2. Zone 1 supports the incident (subscript '$1i$') and reflected (subscript '$1r$') waves. Zone 2 also supports two waves which are also referred to as incident (subscript '$2i$') and reflected (subscript '$2r$'). Zone 3 only supports the transmitted wave (subscript '3'). The electric and magnetic fields of each of these plane waves have the general form expressed in (3.3). Each propagation vector $\boldsymbol{\gamma}$ can be decomposed into its real and imaginary parts, or in its tangential and normal components (to the interface) as follows:

$$\boldsymbol{\gamma} = \boldsymbol{\alpha} + j\boldsymbol{\beta} = \boldsymbol{\gamma}_{\mathrm{t}} + \gamma_z \hat{\mathbf{z}} \tag{3.6}$$

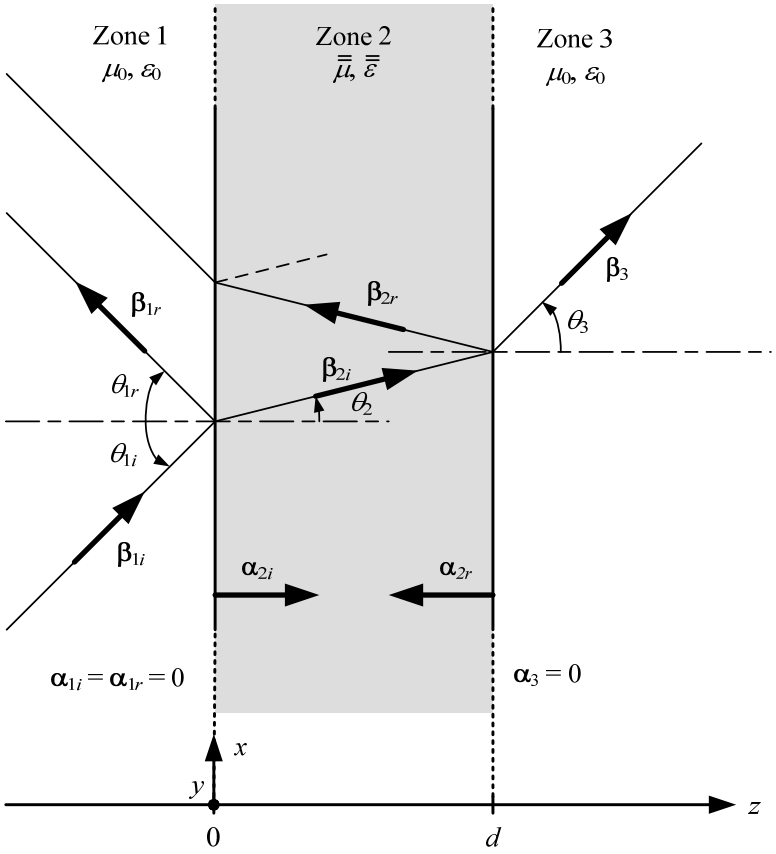

Figure 3.2: Oblique plane wave incidence on an anisotropic slab of thickness d. The incidence plane is here the xz plane (or $\phi = 0$ plane).

By continuity of the tangential fields at the two interfaces, all the propagation vectors lie in the same plane, which is referred to as the incidence plane. In general, the considered incidence plane will be characterized by the angle ϕ, as usually defined in a spherical coordinate system. It is worth emphasizing that the attenuation vector $\boldsymbol{\alpha}$ and the phase vector $\boldsymbol{\beta}$ are in general not collinear in the slab. In other words, the slab in general supports non-uniform plane waves. The following relations on the propagation vectors can be deduced from the continuity of the

tangential fields at the two interfaces:

$$\boldsymbol{\gamma}_{1i} = j\boldsymbol{\beta}_{1i} = j\left(\boldsymbol{\beta}_{1i,\mathrm{t}} + \beta_{1i,z}\hat{\mathbf{z}}\right) \tag{3.7a}$$
$$\boldsymbol{\gamma}_{1r} = j\boldsymbol{\beta}_{1r} = j\left(\boldsymbol{\beta}_{1r,\mathrm{t}} + \beta_{1r,z}\hat{\mathbf{z}}\right) \tag{3.7b}$$
$$\boldsymbol{\gamma}_{2i} = \boldsymbol{\alpha}_{2i} + j\boldsymbol{\beta}_{2i} = \alpha_{2i,z}\hat{\mathbf{z}} + j\left(\boldsymbol{\beta}_{2i,\mathrm{t}} + \beta_{2i,z}\hat{\mathbf{z}}\right) = j\boldsymbol{\beta}_{2i,\mathrm{t}} + \gamma_{2i,z}\hat{\mathbf{z}} \tag{3.7c}$$
$$\boldsymbol{\gamma}_{2r} = \boldsymbol{\alpha}_{2r} + j\boldsymbol{\beta}_{2r} = \alpha_{2r,z}\hat{\mathbf{z}} + j\left(\boldsymbol{\beta}_{2r,\mathrm{t}} + \beta_{2r,z}\hat{\mathbf{z}}\right) = j\boldsymbol{\beta}_{2r,\mathrm{t}} + \gamma_{2r,z}\hat{\mathbf{z}} \tag{3.7d}$$
$$\boldsymbol{\gamma}_{3} = j\boldsymbol{\beta}_{3} = j\left(\boldsymbol{\beta}_{3,\mathrm{t}} + \beta_{3,z}\hat{\mathbf{z}}\right) \tag{3.7e}$$

and

$$\boldsymbol{\beta}_3 = \boldsymbol{\beta}_{1i} \tag{3.8a}$$
$$\boldsymbol{\beta}_{1i,\mathrm{t}} = \boldsymbol{\beta}_{1r,\mathrm{t}} = \boldsymbol{\beta}_{2i,\mathrm{t}} = \boldsymbol{\beta}_{2r,\mathrm{t}} \tag{3.8b}$$
$$\beta_{1r,z} = -\beta_{1i,z} \tag{3.8c}$$
$$\gamma_{2r,z} = -\gamma_{2i,z} \tag{3.8d}$$
$$\theta_{1i} = \theta_{1r} = \theta_3 \equiv \theta \tag{3.8e}$$

with

$$|\boldsymbol{\beta}_{1i}| = |\boldsymbol{\beta}_{1r}| = k_0 = \frac{\omega}{c_0} \tag{3.9a}$$
$$\beta_{1i,z} = k_0 \cos\theta \tag{3.9b}$$
$$\left|\boldsymbol{\beta}_{1i,\mathrm{t}}\right| = k_0 \sin\theta \tag{3.9c}$$

3.2.2 Choice of incidence directions and polarizations

In general, for an arbitrary incidence direction and polarization:

- Birefringence (or dual refraction) may occur in the slab [208], which means that the incident wave splits into several plane waves when entering the medium. As a result, the fields inside the slab cannot be described by a single pair of plane waves (one incident and one reflected), as assumed in Section 3.2.1.
- The reflected and transmitted waves may contain any polarization, even if the incident wave is linearly TM or TE polarized. In this case, the slab problem is thus characterized by co-polar and cross-polar reflection and transmission coefficients.

To keep the problem within a reasonable level of complexity, we only consider here the two incidence planes characterized by $\phi = 0°$ and $\phi = 90°$, with TM or TE polarization. Indeed, in these cases, birefringence is not expected to occur, since the fields of the incident wave are consistent with the ones of the characteristic waves inside the slab. More precisely, a TM (or TE) polarized incident wave only excites the TM (or TE) polarized characteristic wave in the slab (see Section 3.1.4). As a result, the reflected and transmitted waves keep the same polarization as the incident wave, thereby avoiding cross-polarization effects.

3.2.3 Reflection and transmission coefficients

The (co-polar) reflection and transmission coefficients ρ and τ are defined in terms of ratios of the tangential electric fields, as expressed in (3.10), where the subscript 't' holds for 'x' or 'y', depending on the incidence direction and polarization.

$$\begin{cases} \rho = \dfrac{E_{1r,\mathrm{t}}\left(x,y,z=0\right)}{E_{1i,\mathrm{t}}\left(x,y,z=0\right)} = \dfrac{E_{01r,\mathrm{t}}}{E_{01i,\mathrm{t}}} \\ \tau = \dfrac{E_{3,\mathrm{t}}\left(x,y,z=d\right)}{E_{1i,\mathrm{t}}\left(x,y,z=0\right)} = \dfrac{E_{03,\mathrm{t}}}{E_{01i,\mathrm{t}}} e^{-j\beta_{1i,z}d} \end{cases} \tag{3.10}$$

For the considered incidence directions and polarizations, it can be shown that the reflection and transmission coefficients are given by

$$\begin{cases} \rho = \dfrac{\rho_0\left(1-u^2\right)}{1-u^2\rho_0^2} \\ \tau = \dfrac{u\left(1-\rho_0^2\right)}{1-u^2\rho_0^2} \end{cases} \quad \text{with} \quad \begin{cases} u = e^{-j\,\tilde{n}\,\beta_{1i,z}d} \\ \rho_0 = \dfrac{\tilde{z}-1}{\tilde{z}+1} \end{cases} \tag{3.11}$$

where $\tilde{n}$ is a modified refractive index defined by

$$\tilde{n} = \frac{\gamma_{2i,z}}{j\beta_{1i,z}} = \frac{\gamma_{2i,z}}{jk_0\cos\theta} \tag{3.12}$$

and $\tilde{z}$ is a modified normalized impedance whose expression depends on the considered incidence direction and polarization (see Table 3.1). The reflection and transmission coefficients can be

ϕ	Pol.	Dispersion relation	$\tilde{z}$
0°	TM	$\dfrac{\gamma_{2i,z}^2}{\varepsilon_x}+\dfrac{\gamma_{2i,x}^2}{\varepsilon_z}+\omega^2\mu_y=0 \Leftrightarrow \dfrac{\tilde{n}^2\cos^2\theta}{\varepsilon_{rx}}+\dfrac{\sin^2\theta}{\varepsilon_{rz}}-\mu_{ry}=0$	$\tilde{z}=\dfrac{\tilde{n}}{\varepsilon_{rx}}$
90°	TM	$\dfrac{\gamma_{2i,z}^2}{\varepsilon_y}+\dfrac{\gamma_{2i,y}^2}{\varepsilon_z}+\omega^2\mu_x=0 \Leftrightarrow \dfrac{\tilde{n}^2\cos^2\theta}{\varepsilon_{ry}}+\dfrac{\sin^2\theta}{\varepsilon_{rz}}-\mu_{rx}=0$	$\tilde{z}=\dfrac{\tilde{n}}{\varepsilon_{ry}}$
0°	TE	$\dfrac{\gamma_{2i,z}^2}{\mu_x}+\dfrac{\gamma_{2i,x}^2}{\mu_z}+\omega^2\varepsilon_y=0 \Leftrightarrow \dfrac{\tilde{n}^2\cos^2\theta}{\mu_{rx}}+\dfrac{\sin^2\theta}{\mu_{rz}}-\varepsilon_{ry}=0$	$\tilde{z}=\dfrac{\mu_{rx}}{\tilde{n}}$
90°	TE	$\dfrac{\gamma_{2i,z}^2}{\mu_y}+\dfrac{\gamma_{2i,y}^2}{\mu_z}+\omega^2\varepsilon_x=0 \Leftrightarrow \dfrac{\tilde{n}^2\cos^2\theta}{\mu_{ry}}+\dfrac{\sin^2\theta}{\mu_{rz}}-\varepsilon_{rx}=0$	$\tilde{z}=\dfrac{\mu_{ry}}{\tilde{n}}$

Table 3.1: Dispersion relation and definition of the modified normalized impedance $\tilde{z}$ for the four considered cases. The dispersion relations introduced in Section 3.1.4 have been rewritten using (3.12) and (3.7) to (3.9).

thus calculated with (3.11) and using the dispersion relation recalled in Table 3.1 to determine the two parameters $\tilde{n}$ and $\tilde{z}$, which will be referred to thereafter as the *modified wave parameters*.

Comments

- There are two possible values of $\tilde{n}$ (since we can only determine $\tilde{n}^2$). However, the choice of a particular solution for $\tilde{n}$ has no impact on ρ and τ. Indeed, if $\tilde{n}$ is replaced by $-\tilde{n}$, ρ_0 becomes $1/\rho_0$ and u becomes $1/u$, and thus ρ and τ remain unchanged.
- The general expressions for ρ and τ in (3.11) are the same as for normal incidence with isotropic media (see [137], for instance), except that the actual refractive index n and normalized characteristic impedance z are now replaced by the "modified" quantities $\tilde{n}$ and $\tilde{z}$.

3.3 Extraction of dyadic medium parameters

The extraction of the dyadic medium parameters is performed in two steps. First, the modified wave parameters $\tilde{n}$ and $\tilde{z}$ are derived from the scattering parameters ρ and τ. Second, the dyadic medium parameters are extracted from the modified wave parameters $\tilde{n}$ and $\tilde{z}$.

3.3.1 Extraction of the modified wave parameters $\tilde{n}$ and $\tilde{z}$ from ρ and τ

As a matter of fact, the modified wave parameters $\tilde{n}$ and $\tilde{z}$ have been defined in such a way that the expressions of ρ and τ given in (3.11) have the same form as for normal incidence with isotropic media, in which case the extraction of n and z from ρ and τ has been reported at several instances in the literature (see for instance [136, 137]). The resulting expressions are recalled in (3.13).

$$\tilde{z} = \frac{1+\rho_0}{1-\rho_0} = \pm\sqrt{\frac{(1+\rho)^2-\tau^2}{(1-\rho)^2-\tau^2}} \tag{3.13a}$$

$$u = \frac{\tau}{1-\rho_0\rho} = \frac{\tau}{1-\frac{\tilde{z}-1}{\tilde{z}+1}\rho} \tag{3.13b}$$

$$\begin{aligned}\gamma_{2i,z}d &= (\alpha_{2i,z} + j\beta_{2i,z})\, d = j\,\tilde{n}\,k_0 d\cos\theta \\ &= -\ln(u) + j2m\pi = -\ln|u| - j\left[\arg(u) - 2m\pi\right], \qquad m \in \mathbb{Z}\end{aligned} \tag{3.13c}$$

The calculation procedure is outlined below:

1. The extraction starts by calculating $\tilde{z}$ using (3.13a). The sign ambiguity is resolved by considering that the modulus of ρ_0, which corresponds to the reflection coefficient when the length of the slab is infinite, should not exceed unity. This leads to the following condition on the modified impedance:

$$|\rho_0| \leq 1 \qquad \Leftrightarrow \qquad \tilde{z}' = \mathrm{Re}\left[\tilde{z}\right] \geq 0 \tag{3.14}$$

2. The intermediate quantity u defined in (3.11) is subsequently calculated using (3.13b).
3. The modified refractive index $\tilde{n}$ (or equivalently $\gamma_{2i,z}$) is finally calculated using (3.13c). It can be seen that an ambiguity arises with the index m, which is often referred to as

the branch index. In the present work, the most appropriate value of m has been chosen according to the most expected results. It can be noted that, according to a recent paper [209], it seems that the branch index m can be determined without ambiguity by enforcing causality (Kramers-Kronig relations). This method has not been tested here.

3.3.2 Extraction of the medium parameters from $\tilde{n}$ and $\tilde{z}$

For an isotropic slab under normal incidence, the medium parameters can be straightforwardly determined from the wave parameters n and z using (2.39). In the present general case, information on the medium parameters can be deduced from $\tilde{n}$ and $\tilde{z}$ using the dispersion relation and the definition of $\tilde{z}$ reported in Table 3.1. It is found that for each of the four considered cases:

- Three of the six medium parameters are involved.
- One of the parameters can be directly determined from a single incidence direction (one value of θ).
- A relation between the two remaining parameters is obtained, which depends on θ.

The corresponding relations are reported in Table 3.2. As a result, it is possible to determine the two remaining parameters by considering two different incidence directions (two values of θ), and by solving a system of two equations and two unknowns. This makes sense only if the two involved parameters do not depend on θ, i.e. if these parameters are not subject to spatial dispersion. More specifically, if we consider two angles θ_a and θ_b with the corresponding values

ϕ	Pol.	1st parameter	Relation between 2nd and 3rd parameters
0°	TM	$\varepsilon_{rx} = \dfrac{\tilde{n}}{\tilde{z}}$	$\varepsilon_{rz}\left(\mu_{ry} - \tilde{n}\tilde{z}\cos^2\theta\right) = \sin^2\theta$
90°	TM	$\varepsilon_{ry} = \dfrac{\tilde{n}}{\tilde{z}}$	$\varepsilon_{rz}\left(\mu_{rx} - \tilde{n}\tilde{z}\cos^2\theta\right) = \sin^2\theta$
0°	TE	$\mu_{rx} = \tilde{n}\tilde{z}$	$\mu_{rz}\left(\varepsilon_{ry} - \dfrac{\tilde{n}}{\tilde{z}}\cos^2\theta\right) = \sin^2\theta$
90°	TE	$\mu_{ry} = \tilde{n}\tilde{z}$	$\mu_{rz}\left(\varepsilon_{rx} - \dfrac{\tilde{n}}{\tilde{z}}\cos^2\theta\right) = \sin^2\theta$

Table 3.2: Extraction of the dyadic permittivity and permeability from the modified wave parameters, for the four considered cases.

of the modified wave parameters ($\tilde{z}_a$, $\tilde{n}_a$) and ($\tilde{z}_b$, $\tilde{n}_b$), the two remaining parameters are given by the expressions shown in Table 3.3. If one of the two angles is 0 ($\theta_a = 0$, for instance), which

corresponds to normal incidence, the corresponding expressions reduce to the ones shown in Table 3.4.

ϕ	Pol.	Determination of the 2nd and 3rd parameters
0°	TM	μ_{rx} or $\mu_{ry} = \dfrac{\tilde{n}_a\tilde{z}_a A\,(1-B) - \tilde{n}_b\tilde{z}_b B\,(1-A)}{A-B}$
90°	TM	$\varepsilon_{rz} = \dfrac{A-B}{\tilde{n}_a\tilde{z}_a A - \tilde{n}_b\tilde{z}_b B}$
0°	TE	ε_{rx} or $\varepsilon_{ry} = \dfrac{\frac{\tilde{n}_a}{\tilde{z}_a} A\,(1-B) - \frac{\tilde{n}_b}{\tilde{z}_b} B\,(1-A)}{A-B}$
90°	TE	$\mu_{rz} = \dfrac{A-B}{\frac{\tilde{n}_a}{\tilde{z}_a} A - \frac{\tilde{n}_b}{\tilde{z}_b} B}$

Table 3.3: Determination of the two remaining parameters by considering two incidence directions θ_a and θ_b (in the same incidence plane, i.e. same value of ϕ). We have used the substitutions $A = \cos^2\theta_a$ and $B = \cos^2\theta_b$.

3.3.3 Strategy for the application of the retrieval procedure

At this stage, the question of the number of different incidence directions and polarizations that should be considered arises. By comparison with the retrieval procedure for normal incidence on isotropic slab, for which two equations with two unknowns are obtained [ρ, τ = function(ε,μ)], the present method offers a redundancy of information, as already mentioned in Section 3.1.2. Indeed, we can consider the four cases of Table 3.2 ($\phi = 0°$ or 90°, TM or TE), with different values of θ. In principle, we should always find the same parameters. If this is not the case, this means that the structure under study cannot be characterized by a homogeneous anisotropic medium described by (3.2), and that at least one of the assumptions made in Section 3.1.3 is not valid. A possible way of using this retrieval procedure to obtain the six parameters is described in Table 3.5. It can be noted that considering only the upper half or the lower half of Table 3.5 is enough to determine all the six parameters. If we consider all the cases of Table 3.5, we obtain three instances of ε_{rx}, ε_{ry}, μ_{rx} and μ_{ry}, and two instances of ε_{rz} and μ_{ry}. The degree to which the instances of the same parameters coincide provides an evaluation of the accuracy of the chosen model for the equivalent homogeneous medium.

In particular, if one of the two angles is 0 ($\theta_a = 0$), Table 3.5 reduces to Table 3.6. In this case, we obtain two instances of each of the six parameters.

ϕ	Pol.	Determination of the 2nd and 3rd parameters
0°	TM	μ_{rx} or $\mu_{ry} = \tilde{n}_a \tilde{z}_a$
90°	TM	$\varepsilon_{rz} = \dfrac{1-B}{\tilde{n}_a \tilde{z}_a - \tilde{n}_b \tilde{z}_b B}$
0°	TE	ε_{rx} or $\varepsilon_{ry} = \dfrac{\tilde{n}_a}{\tilde{z}_a}$
90°	TE	$\mu_{rz} = \dfrac{1-B}{\frac{\tilde{n}_a}{\tilde{z}_a} - \frac{\tilde{n}_b}{\tilde{z}_b} B}$

Table 3.4: Same as Table 3.3, but with $\theta_a = 0$.

Considered cases	Parameters or relations obtained	
TM, $\phi = 0°$, $\theta = \theta_a$	ε_{rx} + relation($\mu_{ry}, \varepsilon_{rz}$)	$\Rightarrow \varepsilon_{rx}$ (2x), μ_{ry}, ε_{rz}
TM, $\phi = 0°$, $\theta = \theta_b$	ε_{rx} + relation($\mu_{ry}, \varepsilon_{rz}$)	
TE, $\phi = 0°$, $\theta = \theta_a$	μ_{rx} + relation($\varepsilon_{ry}, \mu_{rz}$)	$\Rightarrow \mu_{rx}$ (2x), ε_{ry}, μ_{rz}
TE, $\phi = 0°$, $\theta = \theta_b$	μ_{rx} + relation($\varepsilon_{ry}, \mu_{rz}$)	
TM, $\phi = 90°$, $\theta = \theta_a$	ε_{ry} + relation($\mu_{rx}, \varepsilon_{rz}$)	$\Rightarrow \varepsilon_{ry}$ (2x), μ_{rx}, ε_{rz}
TM, $\phi = 90°$, $\theta = \theta_b$	ε_{ry} + relation($\mu_{rx}, \varepsilon_{rz}$)	
TE, $\phi = 90°$, $\theta = \theta_a$	μ_{ry} + relation($\varepsilon_{rx}, \mu_{rz}$)	$\Rightarrow \mu_{ry}$ (2x), ε_{rx}, μ_{rz}
TE, $\phi = 90°$, $\theta = \theta_b$	μ_{ry} + relation($\varepsilon_{rx}, \mu_{rz}$)	

Table 3.5: Possible strategy to obtain the six equivalent medium parameters (with redundancy).

Considered cases	Parameters or relations obtained	
TM, $\phi = 0°$, $\theta = 0°$ (TE, $\phi = 90°$, $\theta = 0$)	ε_{rx}, μ_{ry}	$\Rightarrow$ ε_{rx} (2x), μ_{ry} (2x), ε_{rz}, μ_{rz}
TM, $\phi = 0°$, $\theta = \theta_b$	ε_{rx} + relation($\mu_{ry}, \varepsilon_{rz}$)	
TE, $\phi = 90°$, $\theta = \theta_b$	μ_{ry} + relation($\varepsilon_{rx}, \mu_{rz}$)	
TE, $\phi = 0°$, $\theta = 0°$ (TM, $\phi = 90°$, $\theta = 0$)	μ_{rx}, ε_{ry}	$\Rightarrow$ ε_{ry} (2x), μ_{rx} (2x), ε_{rz}, μ_{rz}
TE, $\phi = 0°$, $\theta = \theta_b$	μ_{rx} + relation($\varepsilon_{ry}, \mu_{rz}$)	
TM, $\phi = 90°$, $\theta = \theta_b$	ε_{ry} + relation($\mu_{rx}, \varepsilon_{rz}$)	

Table 3.6: Similar to Table 3.5, but with $\theta_a = 0$.

3.4 Calculation of scattering parameters for real composite MTMs

The application of the developed retrieval procedure requires the reflection and transmission coefficients (scattering parameters, or Fresnel coefficients) for the slab of real composite MTM under plane wave incidence with several incidence directions and polarizations. These parameters are defined and calculated the same way as for frequency selective surfaces (FSSs) [210–215]. In the present case, these coefficients have been derived from the scattered fields numerically calculated with Ansoft HFSS from a single unit cell representation. This main points of this approach are outlined in this section.

3.4.1 Description

We consider here MTMs as periodic structures with infinite periodicity in two directions (x and y) and finite periodicity in the third direction (z), as illustrated in Figure 3.3. The structure shown in Figure 3.3 is made of only one cell in the z direction, but in general there can be any finite number of cells in that direction. The lattice is rectangular, with lattice constants a and b in the x and y directions, respectively. The excitation is a plane wave with arbitrary incidence direction given by the angles θ and ϕ.

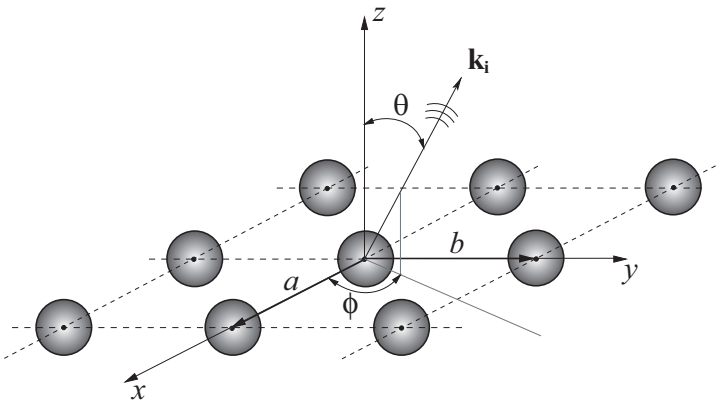

Figure 3.3: MTM slab as a 2D infinite periodic structure arranged in a rectangular lattice and excited by an incident plane wave (wave vector $\mathbf{k}_\mathrm{i}$).

The electromagnetic field above and below the structure must satisfy the periodicity requirements imposed by Floquet's theorem. As a consequence, these fields can be expanded in a set of $\mathrm{TM}_{\mathrm{mn}}$ and $\mathrm{TE}_{\mathrm{mn}}$ modes (with respect to z), which are referred to as Floquet modes[1] [210, 211, 215]. It can be shown that all these modes are plane waves with different wave vectors. An arbitrarily polarized incident plane wave can be expressed as a combination of the two fundamental Floquet modes, namely the TM_{00} and TE_{00} modes. If the periodicity is small enough [$\max(a, b) < \lambda/2$], higher order Floquet modes are evanescent (in the z

[1] The term Floquet harmonics is also sometimes used.

direction), and only the two fundamental modes propagate away from the structure. In other words, the reflected and transmitted scattered fields at a certain distance from the structure are essentially a combination of these two fundamental modes, and are thus plane waves with arbitrary polarization and wave vectors directed in a similar way as with an homogeneous slab (Figure 3.2). It can be noted that for normal incidence, the TM_{00} and TE_{00} modes become two TEM modes. This case can be considered as a limit case for oblique incidence where $\theta \to 0$.

3.4.2 Reflection and transmission coefficients

The performances of the MTM slab is characterized by reflection (ρ) and transmission (τ) coefficients associated with the two fundamental modes (TM_{00} and TE_{00}). Taking into account the interactions that may occur between these modes, the coefficients are defined by the following relations:

$$\begin{aligned} \begin{bmatrix} b_1^{\mathrm{TM}} \\ b_1^{\mathrm{TE}} \end{bmatrix} &= \begin{bmatrix} \rho_{\mathrm{co}}^{\mathrm{TM}} & \rho_{\mathrm{cx}}^{\mathrm{TE}} \\ \rho_{\mathrm{cx}}^{\mathrm{TM}} & \rho_{\mathrm{co}}^{\mathrm{TE}} \end{bmatrix} \begin{bmatrix} a_1^{\mathrm{TM}} \\ a_1^{\mathrm{TE}} \end{bmatrix} \\ \begin{bmatrix} b_2^{\mathrm{TM}} \\ b_2^{\mathrm{TE}} \end{bmatrix} &= \begin{bmatrix} \tau_{\mathrm{co}}^{\mathrm{TM}} & \tau_{\mathrm{cx}}^{\mathrm{TE}} \\ \tau_{\mathrm{cx}}^{\mathrm{TM}} & \tau_{\mathrm{co}}^{\mathrm{TE}} \end{bmatrix} \begin{bmatrix} a_1^{\mathrm{TM}} \\ a_1^{\mathrm{TE}} \end{bmatrix} \end{aligned} \tag{3.15}$$

where the a_1, b_1 and b_2 are the complex amplitudes of the incident, reflected and transmitted waves, respectively. We only consider here the excitation from one side of the structure (port 1), since only symmetrical structures will be considered for the equivalent medium extraction. The quantities $\rho_{\mathrm{co}}^{\mathrm{TM}}$, $\rho_{\mathrm{co}}^{\mathrm{TE}}$, $\tau_{\mathrm{co}}^{\mathrm{TM}}$ and $\tau_{\mathrm{co}}^{\mathrm{TE}}$ are the co-polar reflection and transmission coefficients, whereas $\rho_{\mathrm{cx}}^{\mathrm{TM}}$, $\rho_{\mathrm{cx}}^{\mathrm{TE}}$, $\tau_{\mathrm{cx}}^{\mathrm{TM}}$ and $\tau_{\mathrm{cx}}^{\mathrm{TE}}$ represent cross-polar coefficients. The mode denomination in superscript corresponds to that of the incident wave. As explained in Section 3.2.2, the developed retrieval procedure only applies to structures for which the cross-polar coefficients are zero. For structures which exhibit the required level of symmetry, the cross-polar coefficients are identically zero, and therefore do not need to be calculated. However, for structures which almost exhibit this level of symmetry, the cross-polar coefficients are expected to be small, but they should be calculated in order to determine to which extent the technique can be applied.

3.4.3 Implementation with Ansoft HFSS

The procedure to compute the reflection and transmission coefficients defined in (3.15) with Ansoft HFSS (v10) is summarized below and illustrated in Figure 3.4.

- The analysis of the 2D infinite periodic structure is reduced to the study of the unit cell with appropriate periodic boundary conditions (PBC), referred to as Master/Slave boundaries in HFSS. The phase shifts between the corresponding PBC are imposed by the direction of incidence.
- The structure is terminated in the $\pm z$ direction with absorbing boundary conditions, such as perfectly match layers (PML).
- The scattered field is calculated under plane wave incidence, which corresponds either to the TM_{00} or TE_{00} mode, with the chosen incidence direction.

- The reflection and transmission coefficients are calculated using the HFSS Fields Calculator by performing appropriate projections of the scattered electric field on the concerned mode function. These projections are made in transverse cross-sections (planes z = constant) at the termination planes of the cell.

All the required operations to define the simulation setup and to perform the calculation of the reflection and transmission coefficients have been implemented as Microsoft Visual Basic scripts (VBScripts), with the possibility to consider several incidence directions for one execution of the script.

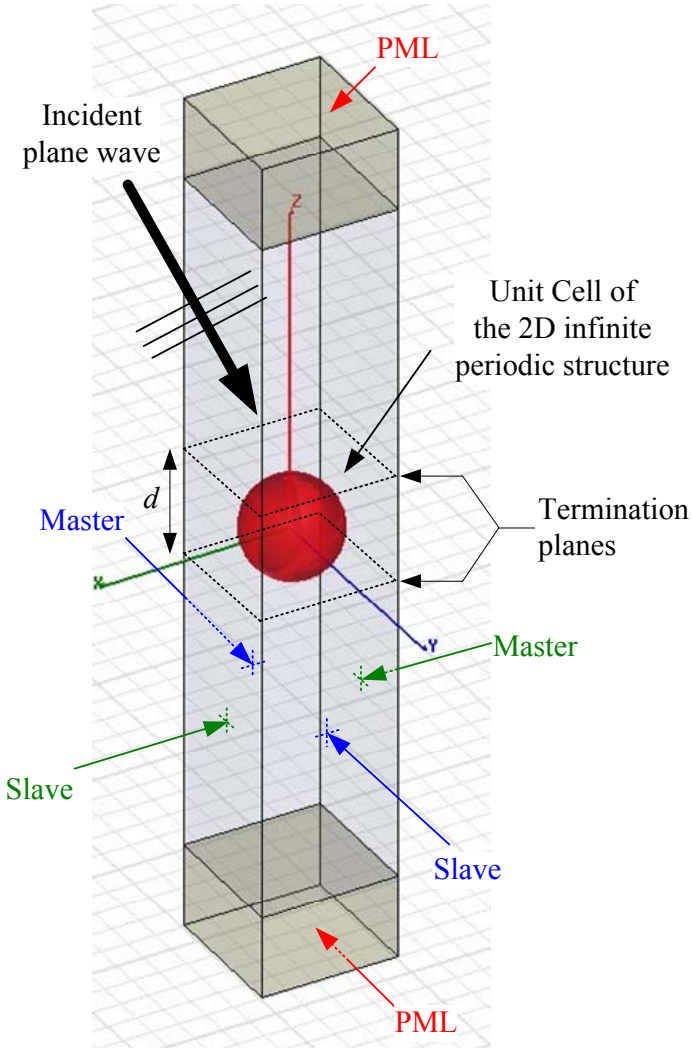

Figure 3.4: Simulation setup for the analysis of 2D periodic structures under plane wave incidence with HFSS (v10).

It can be mentioned that HFSS v10 is able to directly calculate reflection and transmission coefficients related to power densities, but these coefficients do not provide any information on phase and polarization. Finally, let us note that a more recent version of HFSS (v11) directly

provides the scattering parameters for this type of structures, using a waveguide-like approach and the concept of "Floquet ports". This version was however not available at the time when these investigations were carried out.

3.5 Application to specific MTM structures

3.5.1 General remarks

In this section, specific MTMs structures are investigated in terms of scattering parameters under arbitrary incidence, and where appropriate, using the developed retrieval procedure. We consider wire media and arrays of split-ring resonators (SRRs), which are the basis of inclusion-based LHM. The goal is essentially to evaluate the accuracy of the homogeneous anisotropic model described by (3.2) for the considered MTMs, and when possible to evaluate their degree of isotropy. Some common points on the considered application examples are outlined below:

- The numerical analysis of the real composite MTM is performed with only one layer of cells in the longitudinal z direction.
- The reflection and transmission coefficients are calculated with the technique outlined in Section 3.4.
- For the retrieval procedure, we apply the strategy described in Section 3.3.3, with $\theta_a = 0$ and $\theta_b = \theta$ (see Table 3.6). With this approach, we obtain two instances of each of the six medium parameters.
- Losses are not taken into account in the present analyzes in order to facilitate the interpretation of the results (dielectrics are lossless and metal is PEC).
- The thickness of the equivalent homogeneous slab is referred to as d and is specified for each structure.

3.5.2 Wire media

Wire media are MTM structures which exhibit plasma-like permittivity when the electric field is directed along the wires ; they have been introduced in Section 2.2.1.a.. Several variants of wire media have been considered.

a. 1D wire medium

The unit cell of the 1D wire medium is shown in Figure 3.5. The dyadic permittivity and permeability have been extracted with the developed technique with $\theta_a = 0$ and $\theta_b = 40°$. The results are shown in Figure 3.6, where we only show the real part of the parameters as their imaginary part is almost zero.

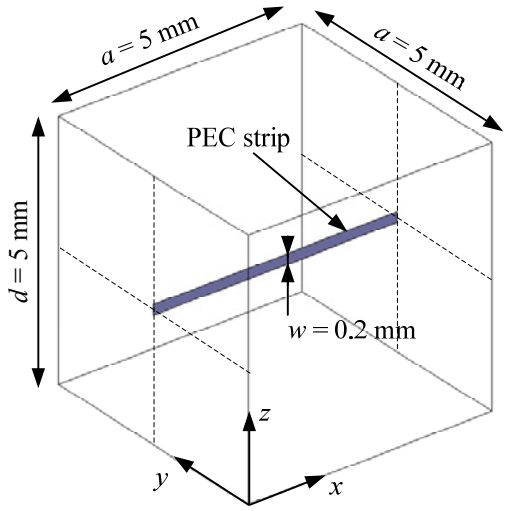

Figure 3.5: Unit cell of the 1D wire medium. The wires are infinitely thin metallic strips (PEC) of width $w = 0.2$ mm. The wires are infinite in the x direction.

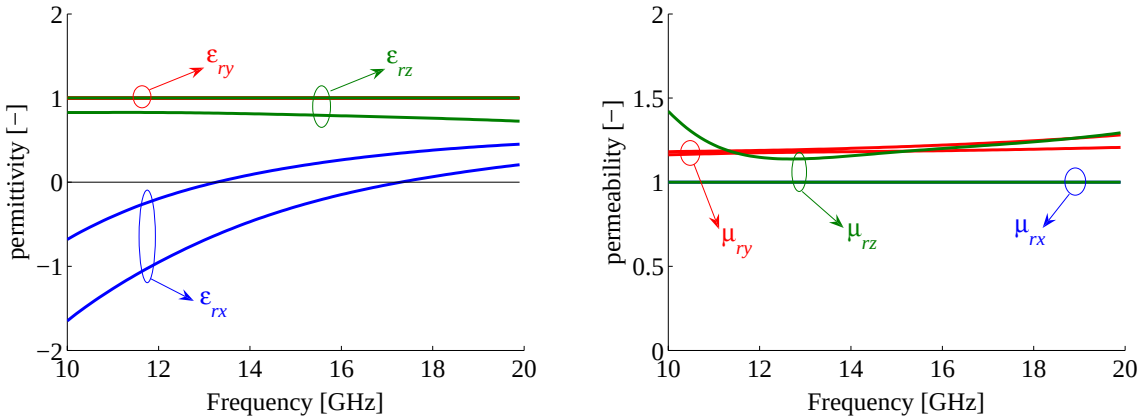

Figure 3.6: Equivalent dyadic permittivity and permeability for the 1D wire medium. Extraction from $\theta_a = 0$ and $\theta_b = 40°$. We obtain two instances of each parameter.

Comments

- As expected, ε_{rx} exhibits a plasma-like behaviour, whereas all the other parameters remain close to unity.
- The two instances of ε_{ry} and μ_{rx} are exactly the same (and equal to unity), whereas it is not the case for the other parameters.
- The fact that ε_{rx} is very different for $\theta = 0°$ and $40°$ (pol. TM, $\phi = 0°$) may be a manifestation of spatial dispersion [77], but no explanation is found concerning the differences for ε_{rz}, μ_{ry} are μ_{rz}.
- It can be noted that at the plasma frequency of 13.3 GHz (frequency where $\varepsilon_{rx} = 0$), the unit cell is not very small compared to the wavelength ($\lambda/a = 4.5$), which limits the validity domain of homogenization procedures.

Spatial dispersion

Although the retrieval procedure has been developed under the assumption that the medium does not exhibit spatial dispersion, we try here to compare the extracted ε_{rx} with analytical expressions which take spatial dispersion into account. To that purpose, we consider the case $\phi = 0°$ with TM polarization, as shown in Figure 3.7(a).

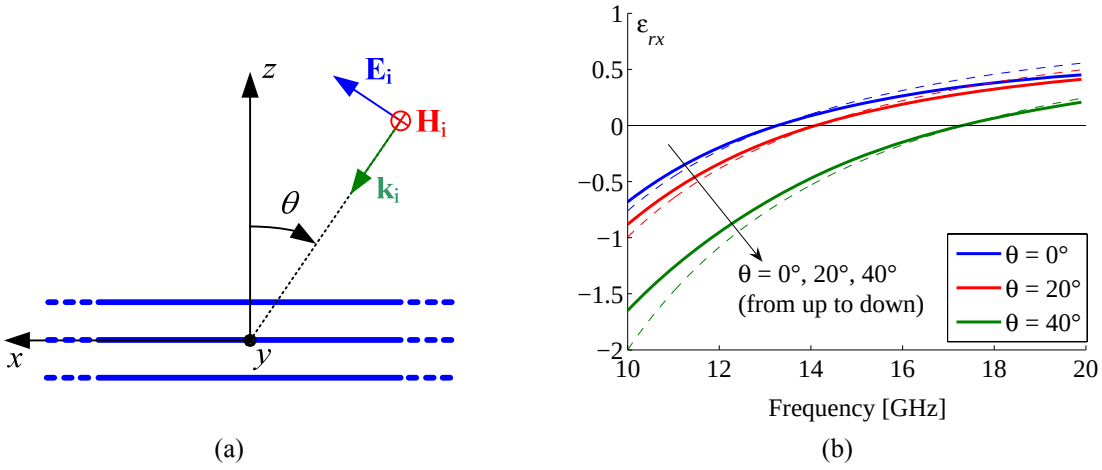

Figure 3.7: (a) 1D wire medium under TM oblique plane wave incidence. (b) ε_{rx} for different incidence angles θ. Continuous line: extracted with the developed retrieval procedure; dashed line: calculated with (3.16) with $f_\mathrm{p} = 13.3$ GHz.

According to Table 3.2, ε_{rx} can be directly determined from a single incidence direction (one value of θ), whereas we need at least two values of θ to obtain ε_{rz} and μ_{ry}. If the medium is spatially dispersive, some of the medium parameters may depend on the incidence angle θ. For instance, if ε_{rz} and μ_{ry} depend on θ because of spatial dispersion, it does not make sense to deduce them by solving a system of equations obtained by considering several values of θ. However, extracting ε_{rx} as a function of θ still makes sense since it can be directly calculated

from a single value of θ. Reference [77] provides an analytical model for the wire medium which takes spatial dispersion into account. The resulting non-local relative permittivity is given in (3.16).

$$\varepsilon_{rx} = 1 - \frac{k_\mathrm{p}^2}{k_0^2 - k_{ix}^2} = 1 - \left(\frac{k_\mathrm{p}}{k_0 \cos\theta}\right)^2 = 1 - \left(\frac{f_\mathrm{p}}{f \cos\theta}\right)^2 \tag{3.16}$$

where f_p is the plasma frequency for normal incidence (and $k_\mathrm{p} = 2\pi f_\mathrm{p}/c_0$). Figure 3.7(b) shows the extracted and calculated values for ε_{rx} for $\theta = 0°$, $20°$ and $40°$. A good agreement is observed, suggesting that the retrieval procedure can accurately represent this type of spatial dispersive effects.

b. Inductively loaded 1D wire medium

In order to lower the plasma frequency, and thus the size of the unit cell compared to the wavelength in the frequency range of interest, the wires are loaded with lumped inductances of 50 nH (one per unit cell). In the HFSS simulations, the inductance consists of a lumped impedance sheet (RLC boundary). The extracted parameters for the same cases as for the unloaded wire medium of Section 3.5.2.a. are shown in Figure 3.8.

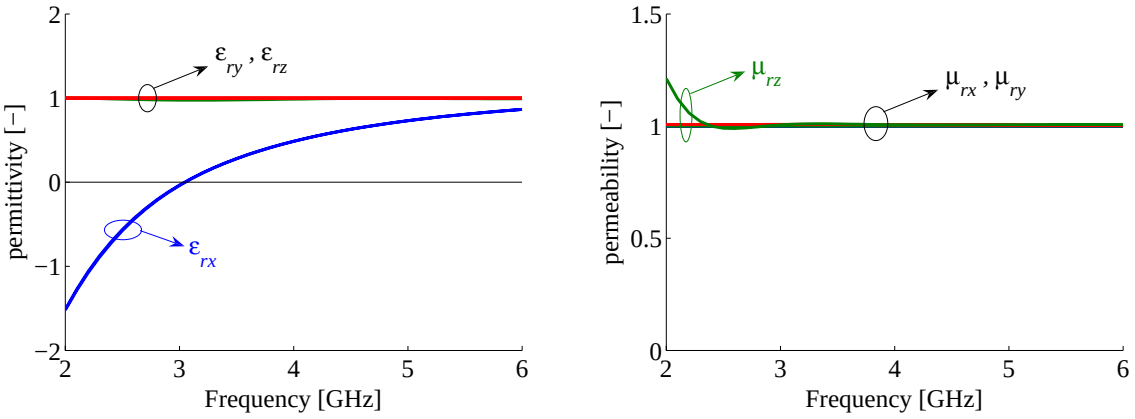

Figure 3.8: Equivalent dyadic permittivity and permeability for the inductively loaded 1D wire medium. Extraction from $\theta_a = 0$ and $\theta_b = 40°$. We obtain two instances of each parameter.

It can be seen that the different instances of the same parameters are almost identical (except for a small difference for μ_{rz} at low frequencies), which means that this structure can be accurately described by an equivalent anisotropic homogeneous medium. The fact that the two instances of ε_{rx} are almost the same suggests that this structure is not subject to spatial dispersion, as was the case for the unloaded wire medium. At the plasma frequency of 3 GHz, the unit cell of the loaded wire medium is quite small compared to the wavelength ($\lambda/a = 20$), which is favorable for homogenization.

To further assess the validity of the anisotropic homogeneous medium, it would be of inter-

est to compare the computed reflection and transmission coefficients with the ones calculated for the equivalent homogeneous slab, for very general incidence directions ($\phi \neq 0°$, $90°$ and $\theta \neq 0°$). To that purpose, the homogeneous slab problem should also be numerically analyzed by introducing the extracted frequency dependent parameters in the permittivity and permeability tensors in HFSS, since the corresponding analytical problem presents a rather high level of complexity.

c. 2D wire medium

The unit cell of the 2D wire medium is shown in Figure 3.9. We consider here the case in which the wires are connected at their crossing points. The dyadic permittivity and permeability have been extracted using the developed technique with $\theta_a = 0$ and $\theta_b = 40°$. Due to the symmetry of the structure, the cases with $\phi = 90°$ are the same as the ones with $\phi = 0°$, and thus $\varepsilon_{rx} = \varepsilon_{ry}$ and $\mu_{rx} = \mu_{ry}$. Furthermore, looking at Table 3.5 or Table 3.6 reveals that the two obtained instances of ε_{rz} and μ_{rz} will be the same. The extracted parameters are shown in Figure 3.10. They are very similar as for the 1D wire medium (see Figure 3.6), except that the dependence of ε_{rx} with θ is less pronounced for the 2D wire medium, which suggests that spatial dispersion is also less important for that structure.

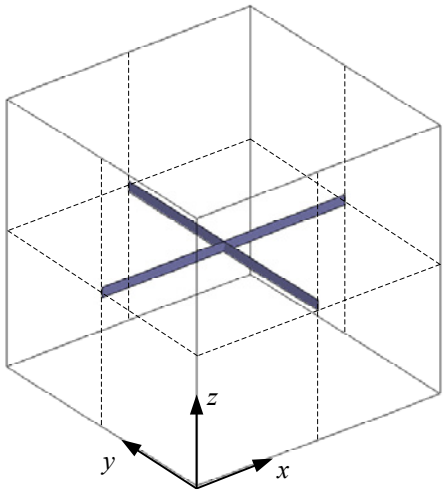

Figure 3.9: Unit cell of the 2D wire medium. The wires are infinite in the x and y directions. The dimensions are the same as in Figure 3.5.

d. Further possible work on wire media

Many variants of wire media can be analyzed with the developed retrieval procedure, like for instance:

- Discontinuous wires; this should lead to a resonant permittivity.
- 3D wire media (i.e. with wires along x, y and z), for higher level of isotropy [7, 8].

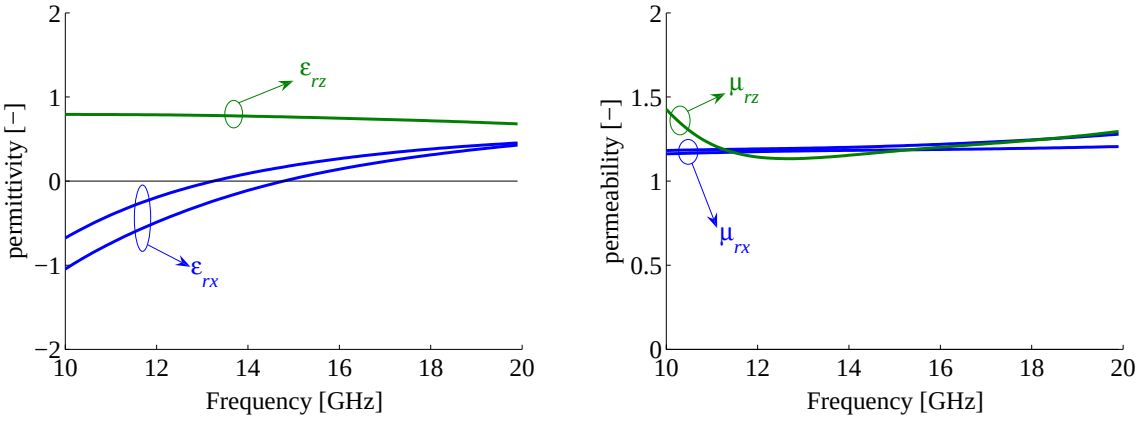

Figure 3.10: Equivalent dyadic permittivity and permeability for the 2D wire medium (real part only). Extraction from $\theta_a = 0$ and $\theta_b = 40°$. ε_{ry} and μ_{ry} are not shown since they are identical to ε_{rx} and μ_{rx}, respectively, by symmetry of the structure.

- Non-connected 2D or 3D wire media [216].
- Loaded wire media with various types of lumped loads (capacitive, resonant,...) [76,217].

3.5.3 Arrays of magnetic resonators

Arrays of magnetic resonators such as split-ring resonators (SRRs) may exhibit a resonant permeability when the magnetic field is directed along their axis, leading to negative values in a small frequency range just above the resonance frequency. These structures have been introduced in Section 2.2.1.a.. Here the goal is to investigate several variants of SRRs arrays in terms of scattering parameters, and where appropriate, to apply the developed retrieval procedure to determine the associated dyadic equivalent medium parameters.

a. 2D planar edge-coupled SRRs

The unit cell of a possible array of 2D planar edge-coupled[2] SRRs is shown in Figure 3.11. The reflection and transmission coefficients have been computed for nine incidence directions ($\phi = 0°$, $45°$, $90°$ with $\theta = 0°$, $30°$, $60°$), for both TM and TE polarizations. It appears that in almost all considered cases (except for $\phi = 45°$, $\theta = 0°$), the cross-polar coefficients are as large as the co-polar ones around the resonant frequency, as can be seen in Figure 3.12(a) for the particular case "TM, $\phi = 0°$, $\theta = 0°$", which corresponds to normal incidence with electric field along x.

Figure 3.12 shows the scattering parameters for three cases of normal incidence, from which the following comments can be formulated. First, the case "TM, $\phi = 0°$, $\theta = 0°$" approximately

[2]The term "edge-coupled" has been introduced in [84], by opposition to the "broadside-coupled" SRR.

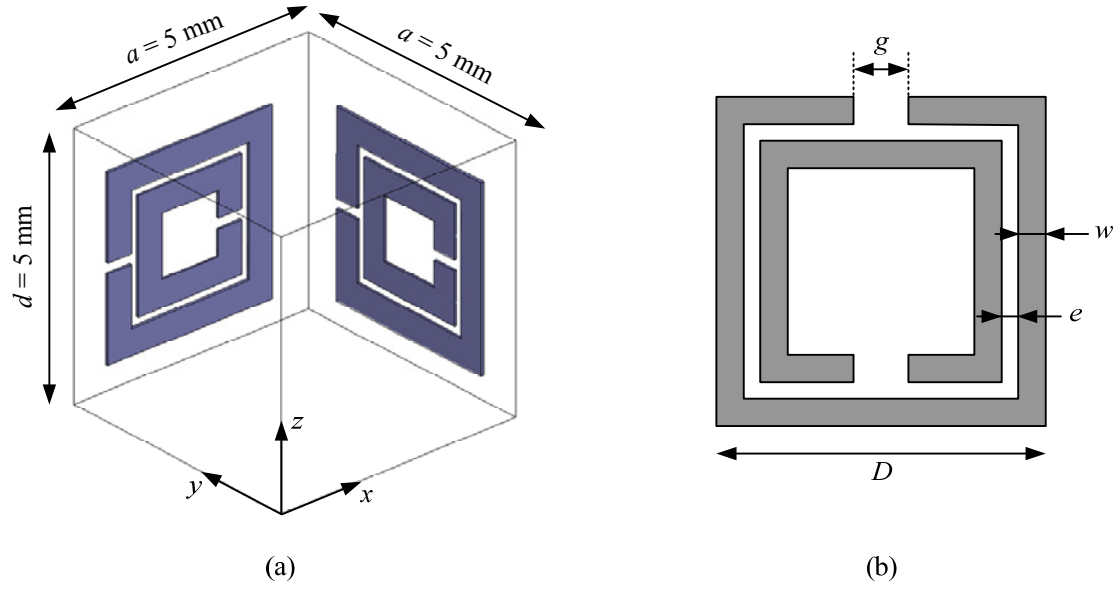

Figure 3.11: Array of 2D planar edge-coupled SRRs: (a) unit cell, (b) dimensions of the SRRs (D = 3.5 mm, w = 0.5 mm, g = 0.2 mm, e = 0.1 mm and the thickness of the metallization is t = 50 μm).

leads to the same coefficients as the case "TE, $\phi = 0°$, $\theta = 0°$" (not shown in the figure). If we make the assumption that they should be the same, that is, that the small differences are only a result of numerical imprecisions, we have

$$\begin{cases} \rho_{\text{co}}^{\text{TM}} = \rho_{\text{co}}^{\text{TE}} \\ \rho_{\text{cx}}^{\text{TM}} = \rho_{\text{cx}}^{\text{TE}} \end{cases} \quad \text{and} \quad \begin{cases} \tau_{\text{co}}^{\text{TM}} = \tau_{\text{co}}^{\text{TE}} \\ \tau_{\text{cx}}^{\text{TM}} = \tau_{\text{cx}}^{\text{TE}} \end{cases} \tag{3.17}$$

In (3.17), the coefficients are defined for $\phi = 0°$. It can be shown that the corresponding coefficients defined for any other angle $\tilde{\phi}$ can be deduced from the ones corresponding to $\phi = 0°$[3]. In particular, with $\tilde{\phi} = 45°$ and using the condition (3.17), the new coefficients are given by

$$\begin{cases} \tilde{\rho}_{\text{co}}^{\text{TM}} = \rho_{\text{co}}^{\text{TM}} - \rho_{\text{cx}}^{\text{TM}} \\ \tilde{\rho}_{\text{co}}^{\text{TE}} = \rho_{\text{co}}^{\text{TM}} + \rho_{\text{cx}}^{\text{TM}} \\ \tilde{\rho}_{\text{cx}}^{\text{TM}} = 0 \\ \tilde{\rho}_{\text{cx}}^{\text{TE}} = 0 \end{cases} \quad \text{and} \quad \begin{cases} \tilde{\tau}_{\text{co}}^{\text{TM}} = \tau_{\text{co}}^{\text{TM}} - \tau_{\text{cx}}^{\text{TM}} \\ \tilde{\tau}_{\text{co}}^{\text{TE}} = \tau_{\text{co}}^{\text{TM}} + \tau_{\text{cx}}^{\text{TM}} \\ \tilde{\tau}_{\text{cx}}^{\text{TM}} = 0 \\ \tilde{\tau}_{\text{cx}}^{\text{TE}} = 0 \end{cases} \tag{3.18}$$

which means that the cross-polar coefficients vanish for the new incidence plane $\tilde{\phi} = 45°$. As a matter of fact, the coefficients $\tilde{\rho}_{\text{co}}^{\text{TM}}$, $\tilde{\rho}_{\text{cx}}^{\text{TM}}$, $\tilde{\tau}_{\text{co}}^{\text{TM}}$ and $\tilde{\tau}_{\text{cx}}^{\text{TM}}$ are those shown in Figure 3.12(b), and $\tilde{\rho}_{\text{co}}^{\text{TE}}$, $\tilde{\rho}_{\text{cx}}^{\text{TE}}$, $\tilde{\tau}_{\text{co}}^{\text{TE}}$ and $\tilde{\tau}_{\text{cx}}^{\text{TE}}$ are those shown in Figure 3.12(c). It can be seen that:

- The computed cross-polar coefficients are very low [below -50 dB in Figure 3.12(b) and below -40 dB in Figure 3.12(c)], which is in good agreement with the predicted values [they should be zero according to (3.18)].

[3]These developments are not reported here; see Section 5.2.9 of the internal report [218].

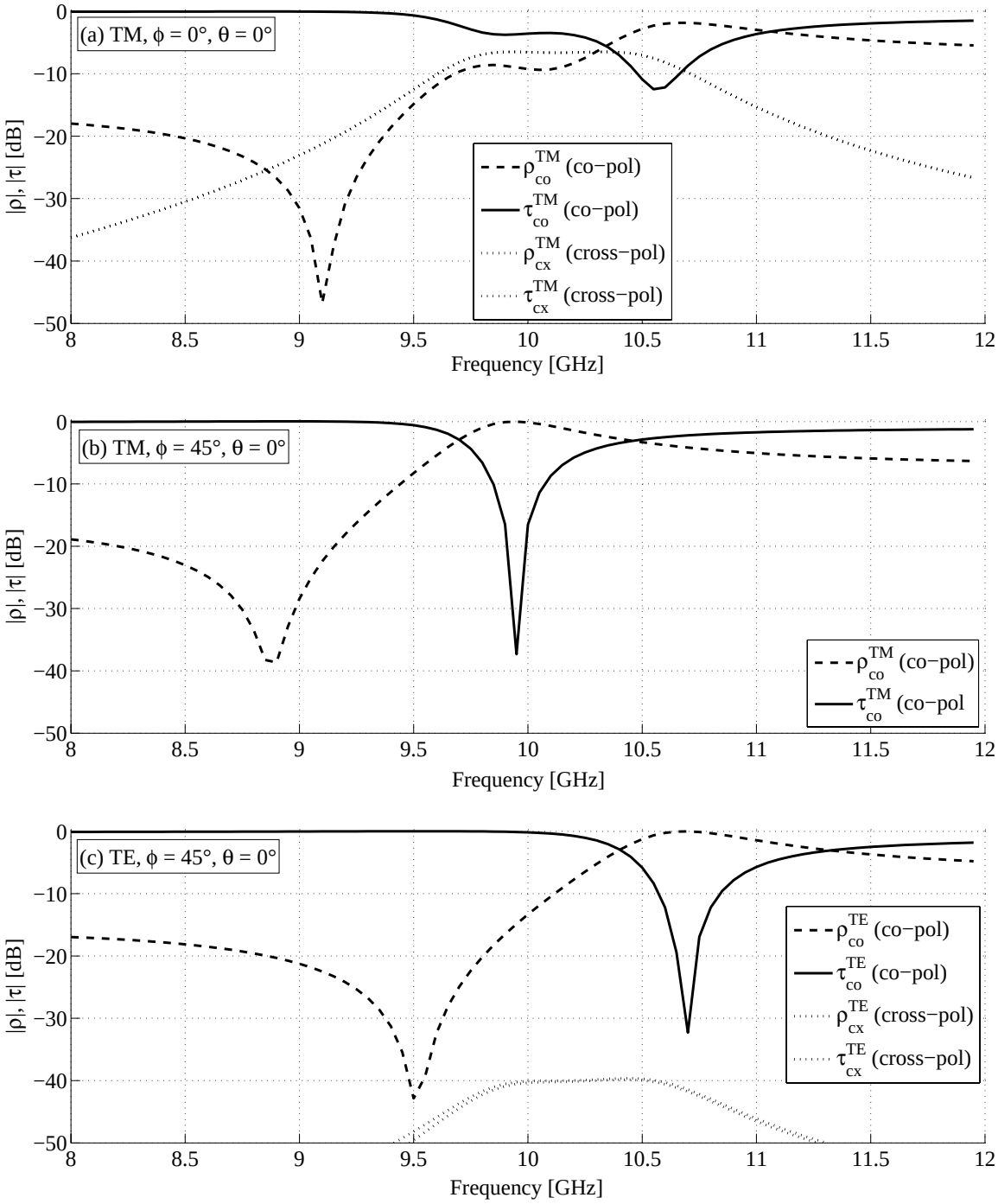

Figure 3.12: Reflection and transmission coefficients for the array of 2D SRRs whose unit cell is shown in Figure 3.11 for three chosen normal incidences. We recall that for normal incidence, TM and TE refer to the two orthogonal TEM modes whose properties can be obtained from oblique incidence when $\theta \to 0$. A resonance can be observed around 10 GHz. At this frequency, the unit cell is 6 times smaller than the wavelength.

- We indeed observe a clear difference between $\tilde{\rho}_{\text{co}}^{\text{TM}}$ and $\tilde{\rho}_{\text{co}}^{\text{TE}}$, as well as between $\tilde{\tau}_{\text{co}}^{\text{TM}}$ and $\tilde{\tau}_{\text{co}}^{\text{TE}}$. Equation (3.18) reveals that these differences are due to the non-zero cross-polar coefficients observed for $\phi = 0°$ [Figure 3.12(a)].

Physically, the cross-polarization observed for normal incidence seems to be related to the coupling between the two sets of orthogonal SRRs. Indeed, if we excite the SRRs perpendicular to y with an incident H field along y, the SRRs perpendicular to x will not be directly excited by the incident field. However, part of the magnetic flux induced in the first set of SRRs will also cross the other SRRs without canceling due to the lack of symmetry, thus exciting their resonance. This leads to a scattered field component with a polarization normal to that of the incident wave. However, it is believed that the cross-polarization observed for normal incidence can be explained by anisotropy, provided that the x and y axes of the equivalent anisotropic medium are rotated by 45° with respect to that of the actual periodic structure (i.e. at ϕ = 45° and 135°, where the cross-polar coefficients are zero). Under this condition, and if we look at normal incidence only, it would be possible to use the anisotropic model described in Section 3.1.3. However, looking at oblique incidence results, we still observe cross-polarization effects, which are not compatible with the chosen anisotropic model. In general, those cross-polarization effects are probably a manifestation of magneto-electric coupling. Indeed, the chosen array of 2D SRRs does not present enough degree of symmetry to avoid bianisotropy. In other words, this structure cannot be described by the simplified dyadic permittivity and permeability model expressed in (3.2), which means that the developed retrieval procedure cannot be applied to this structure. The only thing we can do is to extract the "transverse" permittivity and permeability from normal incidence scattering parameters with $\phi = 45°$, as shown in Figure 3.13.

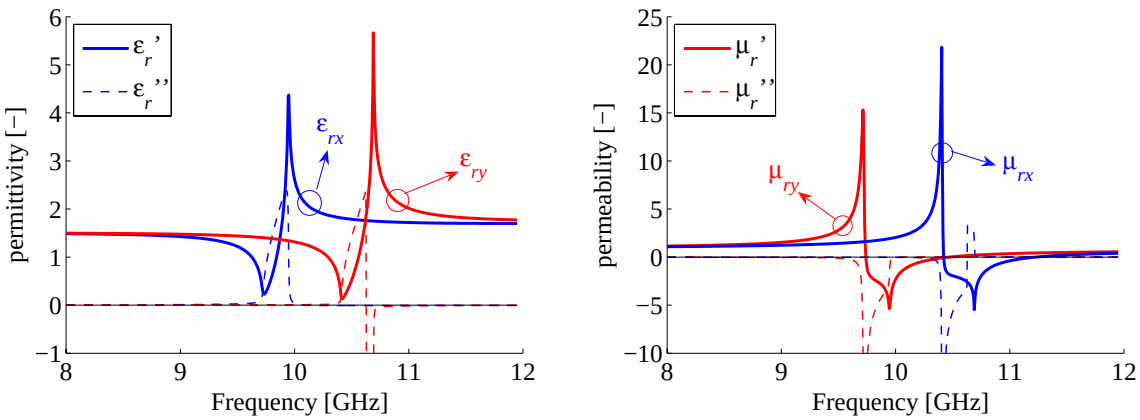

Figure 3.13: Equivalent "transverse" permittivity and permeability for the array of 2D SRRs whose unit cell is shown in Figure 3.11, obtained from normal incidence with $\phi = 45°$ (thus the axes of the anisotropic medium are rotated by 45° with respect to that of the actual periodic structure). The real and imaginary parts of the parameters are separated as follows: $\varepsilon_r = \varepsilon_r' - j\varepsilon_r''$ and $\mu_r = \mu_r' - j\mu_r''$.

The extracted parameters are very similar to the ones obtained for a single SRR under normal incidence, with the truncated resonance for μ and the anti-resonance for ε (see for instance [138]). These unusual behaviours are usually accompanied with a "wrong" sign of the imaginary part of at least one of the two parameters, which is in contradiction with the conventional requirement for a passive medium [see (2.11)]. This issue is further discussed in Section 3.6.2. Moreover, it can be noted that the extracted parameters do not satisfy the causality requirements expressed in (2.15), and not only around the resonance. Indeed, we have $\frac{d\varepsilon_r}{d\omega} < 0$ below and above the resonance band, for instance. These problems challenge the validity of parameters extracted from S parameters inversion, as discussed in the chapter conclusion (Section 3.6).

Beside these problems, the extracted parameters shown in Figure 3.13 reveal that the response for the two orthogonal polarizations is similar, but shifted in frequency of about 0.7 GHz. This structure is therefore not isotropic in terms of polarization for normal incidence, despite the first impression we can have by looking at the unit cell of Figure 3.11.

Further possible work

To compensate for the lack of symmetry which seems to be responsible for the cross-polarization and bianisotropic effects, it would be of interest to investigate some variants of the array of 2D planar edge-coupled SRRs shown in Figure 3.11. In particular, other SRR orientations in the unit cell should be tested, or the number of gaps per ring should be increased. It can however be noted that increasing the number of gaps has the disadvantage of increasing the resonant frequency of the SRRs, thus increasing their size compared to wavelength at resonance, which is not favorable for homogenization.

b. 2D crossed-SRRs (CSRRs)

Crossed-SRRs (CSRRs) are volumetric magnetic resonators which exhibit higher level of symmetry than conventional planar SRRs [79]. They are made of two or three intersecting SRRs; they have been briefly introduced in Section 2.2.1.a.. Figure 3.14 shows a possible unit cell for an array of 2D CSRRs (i.e CSRRs with 2 intersecting SRRs), with one gap per ring. The reflection and transmission coefficients have been first computed for normal incidence for several values of ϕ ($\phi = 0°$, $15°$, $30°$, $45°$) with TM polarization. The results are shown in Figure 3.15. A resonance can be observed around 0.87 GHz. At this frequency, the unit cell is 6.9 times smaller than the wavelength.

As the structure is invariant under a rotation of 90° around the z axis, the reflection and transmission coefficients should be independent of ϕ and the cross-polar coefficients should be zero, as demonstrated in Section 5.2.9 of [218]. Figure 3.15 reveals that those conditions are quite well satisfied. The fact they are not perfectly satisfied can only be related to numerical imprecision. Indeed, it is known that the response of the SRRs, and especially the location of the resonance frequency, is very sensitive to the mesh. Moreover, as we cannot force HFSS to use the same mesh for the two SRRs that form the CSRR, the condition of 90° invariance

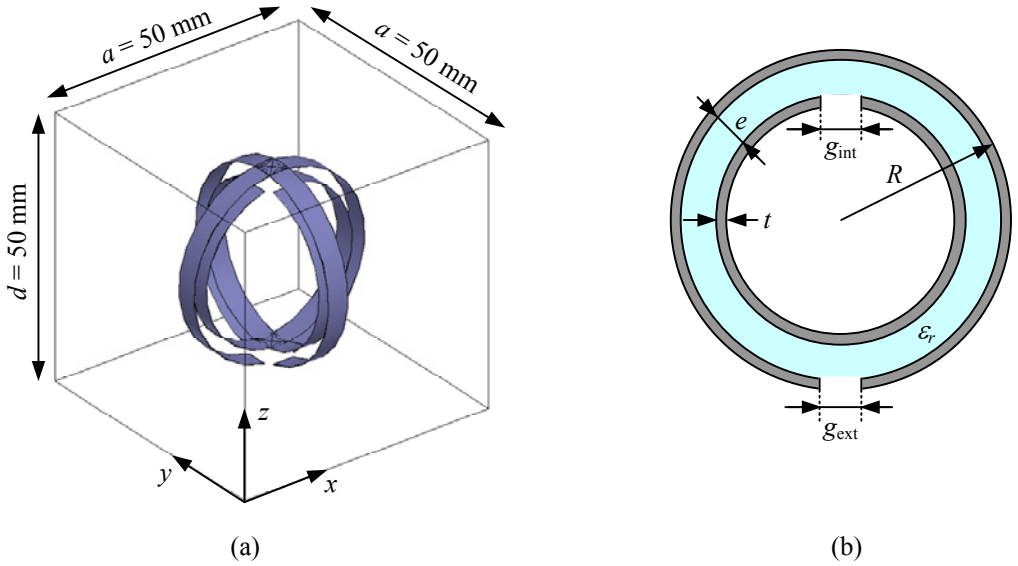

Figure 3.14: Array of 2D CSRRs: (a) unit cell, (b) dimensions of one SRR (R = 17.5 mm, t = 50 µm, $g_{\text{int}} = g_{\text{ext}}$ = 6 mm, e = 2.5 mm, the width of the metal strips is w = 4 mm and $\varepsilon_r = 1$).

mentioned above might not be well satisfied. To verify these statements, the same curves as shown in Figure 3.15 have been computed with a home made code based on integral equations and method of moments (MoM) [215]. With this code, we can force the mesh to be the same for the two SRRs. The results are shown in Figure 3.16.

Comments

- It can be seem that the cross-polar coefficients are negligible (below -46 dB) for all the considered values of ϕ.
- The variation of the co-polar coefficients with ϕ is negligible.
- In general, the two calculation methods give comparable results, except for a small frequency shift of 5 MHz ($< 1\%$).
- The phase difference observed for τ_{co} corresponds to $k_0 d$. This is due to a wrong definition of the reference planes for this parameter in the home made MoM code, but this has been corrected in a later version of the code.

It can be noted that despite the very good results obtained with the home made MoM code, it has not been used as the default tool since it cannot deal with dielectric inclusions. The reflection and transmission coefficients have also been computed for oblique incidences (ϕ = 0° and 45° with θ = 20° and 40°) and TM polarization (not shown here). It appears that the cross-polar coefficients remain negligible even under oblique incidence. However, this structure has not been investigated further with our retrieval procedure, since it is not symmetric with respect to the z axis and is thus not compatible with the model of an anisotropic homogeneous

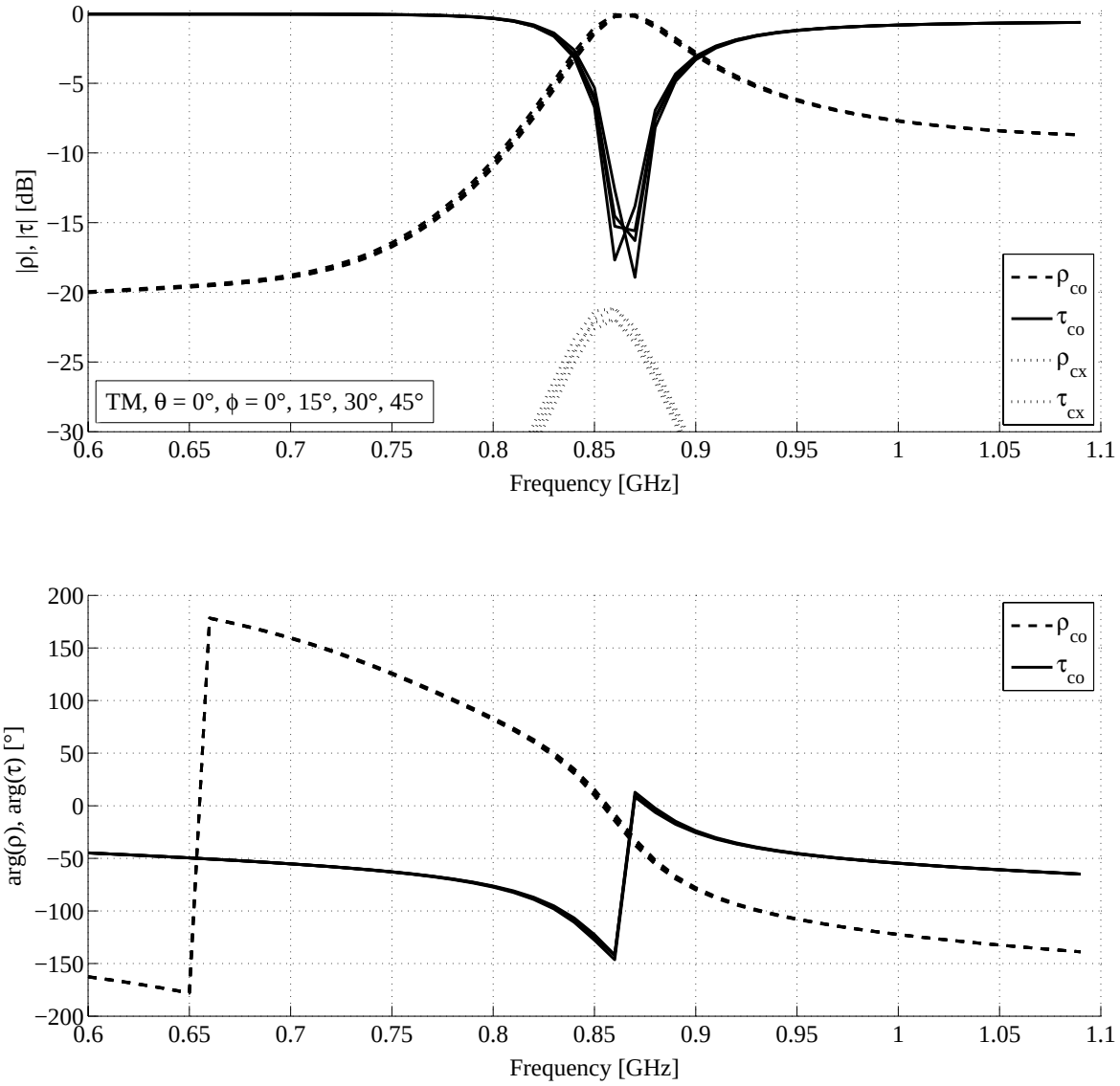

Figure 3.15: Reflection and transmission coefficients for the array of 2D CSRRs whose unit cell is shown in Figure 3.14, for normal incidence with $\phi = 0°$, 15°, 30° and 45°, pol. TM. The phase of the cross-polar coefficients is not shown for clarity, as their amplitude is quite low.

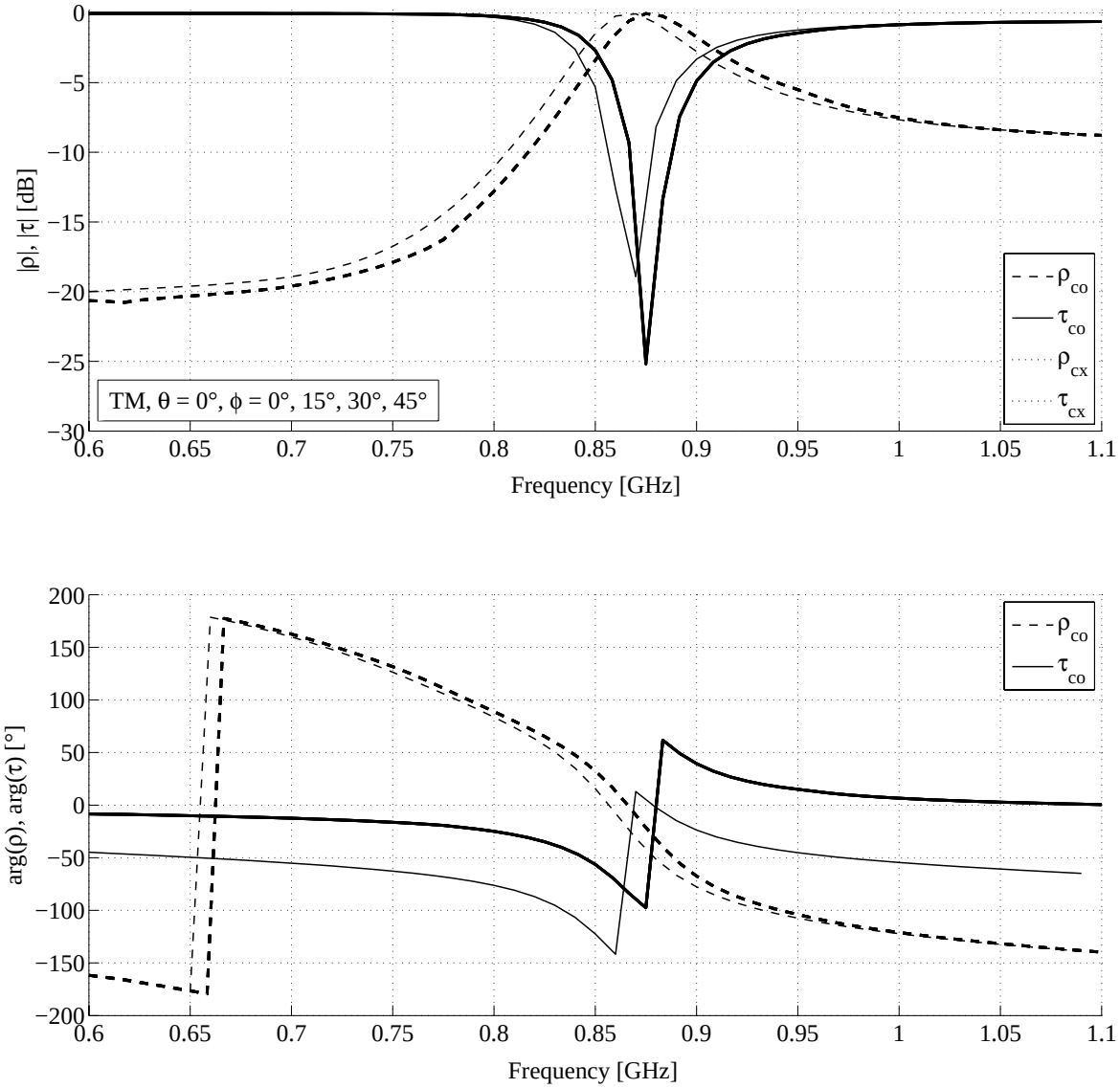

Figure 3.16: Thick lines: idem as in Figure 3.15, but calculated with a home made MoM code [215]. Thin line: the case "TM, $\phi = 0°$, $\theta = 0°$" calculated with HFSS (same as in Figure 3.15).

slab. To obtain a symmetrical structure with respect to the z axis, another orientation of the CSRR in the unit should be considered and more gaps per ring should be added. However, we will rather concentrate our efforts on the highly symmetrical CSRR presented in the next section.

c. 3D crossed-SRRs (CSRRs)

The highly symmetrical CSRR investigated here is made of three intersecting SRRs, with 2 gaps per ring, as shown in Figure 3.17. This type of 3D CSRR was initially proposed by the author in [219]. In order to decrease the resonant frequency, and thus the size of the unit cell compared to the wavelength at resonance, a small spacing between the rings of each SRR has been chosen ($e = 1$ mm), in conjunction with a high permittivity dielectric ($\varepsilon_r = 10$) placed between the rings. This has the effect of increasing the overall capacitance in the SRRs. According to [220, 221], this particle has all the required conditions of symmetry for isotropy and to avoid magneto-electric coupling. However, these considerations are based on the assumption that the response of the particle is of dipolar type, which in general requires that the unit cell is small enough compared to the wavelength. The application of the developed retrieval procedure will allow determining to which extend these properties are satisfied.

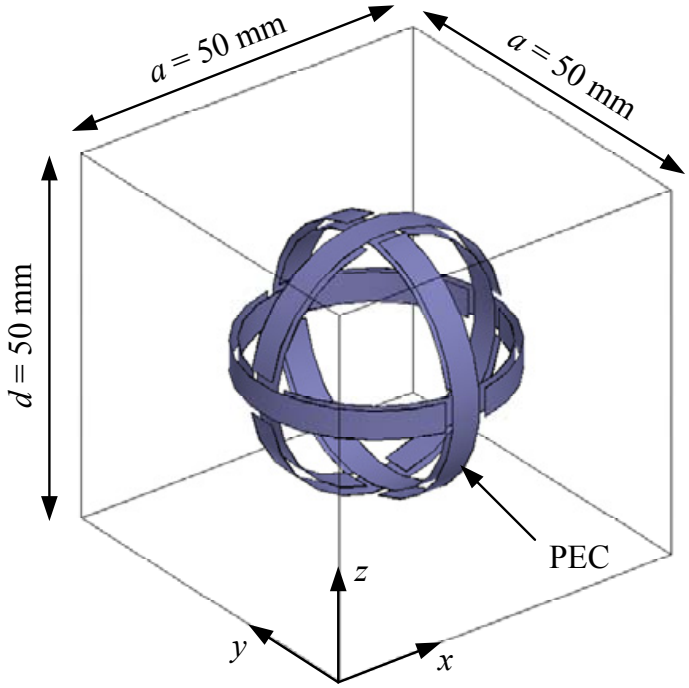

Figure 3.17: Unit cell of an array of 3D CSRRs. Each SRR has 2 gaps per ring. The dimensions of each SRR are the same as in Figure 3.14, except that $e = 1$ mm. A dielectric with $\varepsilon_r = 10$ has been placed between the rings of each SRR.

The reflection and transmission coefficients have been first computed for normal incidence for $\phi = 0°$ and $90°$ with TM polarization. The results are shown in Figure 3.18. A resonance can be observed around 0.45 GHz. At this frequency, the unit cell is 13.3 times smaller than the wavelength. First, it can be seen that the cross-polar coefficients are negligible (below -42 dB). Then, a small frequency shift of about 1% is observed between the two polarizations. This difference could be related to the sensitivity of the resonant frequency to the mesh, but the same observation has been made with the MoM home made code (for the same structure without the dielectric between the rings), for which we can impose the same mesh on the three SRRs. This means that this structure is not perfectly isotropic with respect to the polarization at normal incidence, which is indeed possible since the unit cell is not invariant under a rotation of $90°$ around the z axis. The reflection and transmission coefficients have been subsequently computed for oblique incidence with $\theta = 30°$ and $\phi = 0°$ and $90°$, for TM and TE polarizations. The results for two of these cases are shown in Figure 3.19.

Comments

- The cross-polar coefficients are negligible (below -40 dB) for all the considered cases, which means that the developed retrieval procedure can be (a priori) applied to this system.
- Under TM polarization, the considered oblique incidence is very similar to normal incidence, whereas it is rather different for TE polarization, for which an additional resonance around 0.48 GHz is observed. It can be noted that with TE polarization, the incident wave has a magnetic field component along z, which also excites the horizontal SRR, whereas this is not the case for TM polarization. In fact, this horizontal SRR is placed in a different context compared to the two vertical ones since it has no neighbors in the direction of its axis, as the slab is only made of one layer of cells in the z direction. This may be an indication that the coupling between adjacent cells plays an important role in that structure. This will be further investigated by looking at the extracted parameters.

The dyadic permittivity and permeability have been extracted with the developed retrieval procedure, with $\theta_a = 0°$ and $\theta_b = 30°$. The results are shown in Figure 3.20.

Comments

- As expected, the three components of the dyadic permeability exhibit a resonant behaviour.
- The two instances of each parameter are slightly different (frequency shift of about 1%). Strictly speaking, this means that the chosen model of homogeneous anisotropic medium does not apply to this structure. In other terms, this means that at least one of the assumption made in Section 3.1.3 is not satisfied. It is believed that the two first assumptions (no magneto-electric coupling and diagonal tensors for the permittivity and permeability) should be reasonably satisfied, whereas the main problem may come from

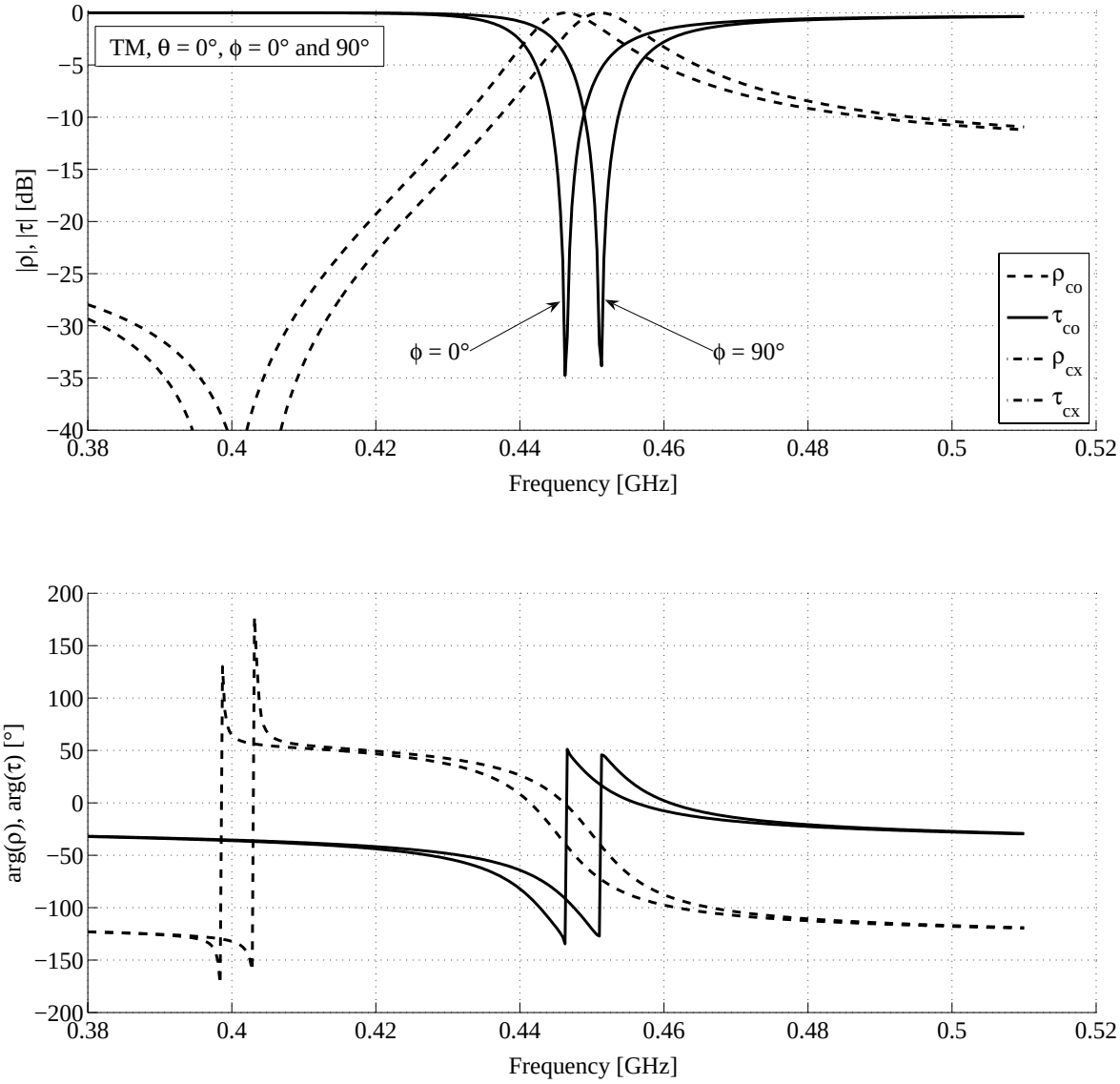

Figure 3.18: Reflection and transmission coefficients for the array of 3D CSRRs whose unit cell is shown in Figure 3.17, for normal incidence with $\phi = 0°$ and 90°, pol. TM. The phase of the cross-polar coefficients is not shown for clarity, as their amplitude is quite low.

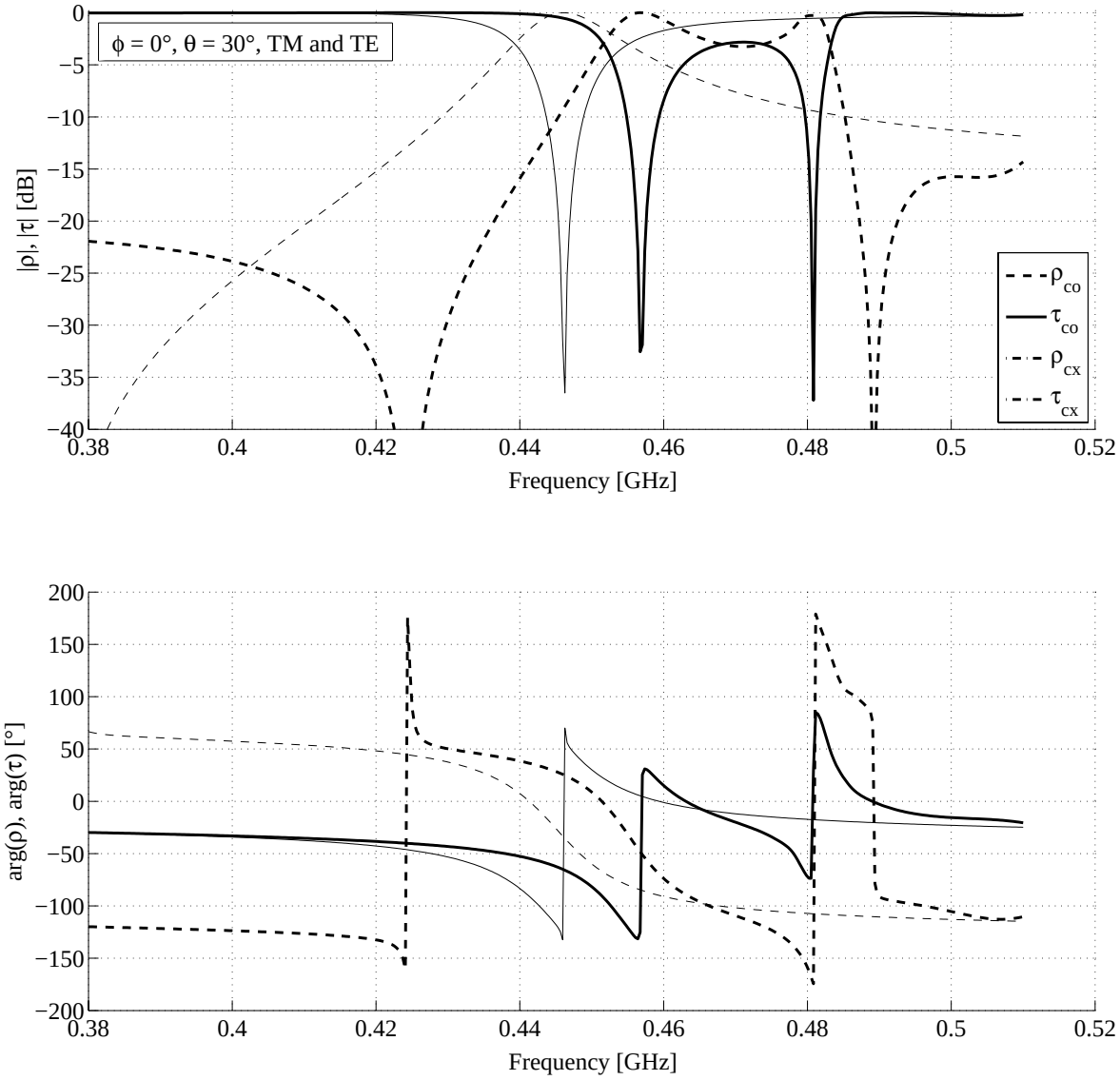

Figure 3.19: Reflection and transmission coefficients for the array of 3D CSRRs whose unit cell is shown in Figure 3.17, for oblique incidence with $\theta = 30°$, $\phi = 0°$. Thick line: TE, thin line: TM. The phase of the cross-polar coefficients is not shown for clarity, as their amplitude is quite low.

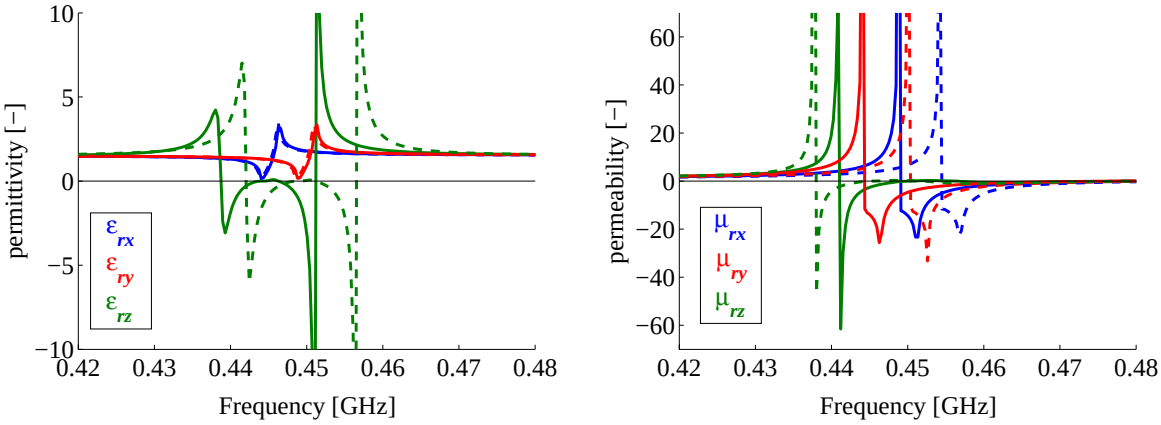

Figure 3.20: Equivalent dyadic permittivity and permeability for the array of 3D CSRRs whose unit cell is shown in Figure 3.17. Extraction from $\theta_a = 0$ and $\theta_b = 30°$. We obtain two instances of each parameter (one in continuous line, the other in dashed line). Only the real parts are shown here for clarity.

spatial dispersion, that is, the dependence of the parameters with the direction of the wave vector.

If we make abstraction of this small frequency shift between the two instances of each parameter, we can make the following comments (see Figure 3.21, where we show only one instance of each parameter):

- The x and y components of the two tensors are very similar to the ones obtained for SRRs under normal incidence, with the truncated resonance for μ and the anti-resonance for ε. This effect is well known for such homogenization procedures and seems to be due to the periodicity [138].
- The z component of the two tensors exhibits a rather different behaviour than their x and y counterparts. Indeed, the resonance for μ_{rz} is not truncated and ε_{rz} exhibits a rather unexpected and unexplained behaviour. It is believed that this phenomenon is related to the coupling between adjacent cells. Indeed, each unit cell has neighbors in the x and y directions but not in the z direction, as we have only considered one layer of cells in that direction.
- A small frequency shift of about 1% is observed between the x and y components of the tensors, which is related to the shift observed for the scattering parameters under normal incidence (see Figure 3.18).

In conclusion, it has been observed that even if the particle exhibits all the required conditions of symmetry for isotropy under dipolar response assumption [220, 221], a slab made of the repetition of this unit cell along the x and y directions does not correspond to a slab of homogeneous isotropic medium. It is believed that this phenomenon is related to the coupling between adjacent cells, as explained above.

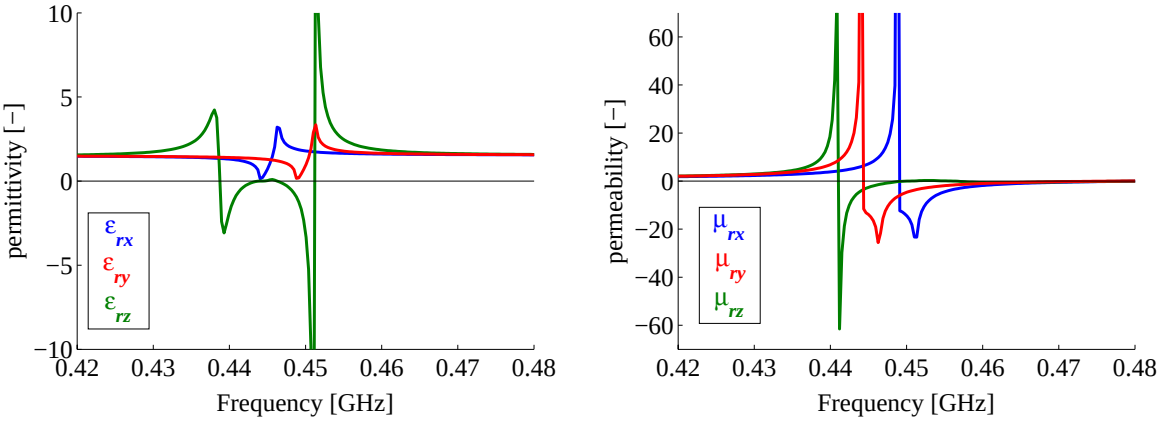

Figure 3.21: Same as in Figure 3.20, but with only one instance of each parameter.

d. Further possible work

To further assess the behaviour of such complex structures, it would be of interest to apply the same characterization method for:

- Various orientations of the CSRR in the unit cell.
- Several layers of cells along z, in order to asses the effect of the coupling between layers (see also the comments in Section 3.6.2). To be considered as physically acceptable, the extracted parameters should be independent of the thickness of the sample. To test this issue, it should be of interest to increase the number of layers of cells until the extracted parameters remain stable with the number of layers. Then, this would mean that the effect of the cells located at the boundaries of the slab, which do not see the same environment than the others, is limited in comparison to the overall effect of all the other cells which are inside the slab and which see neighbors in all the directions. Unfortunately, such investigations are very demanding in terms of computational resources and simulation time.
- Structures with smaller unit cells, in order to evaluate if the model of homogeneous anisotropic medium becomes more accurate.
- Left-handed media, such as combinations of magnetic resonators and wire media, or any other type of volumetric LHM with high level of isotropy reported in the literature.

3.6 Conclusions on retrieval procedures from S parameters

3.6.1 Summary of the main results obtained with the developed method

An enhanced retrieval procedure which allows extracting dyadic permittivity and permeability from reflection and transmission coefficients obtained for various incidences (oblique and nor-

mal) has been developed and implemented. This technique has been applied to basic MTM unit cells such as wire media and arrays of magnetic resonators. The developed retrieval procedure allowed evaluating the accuracy of the chosen model of anisotropic medium for specific MTMs by comparing the various instances obtained for each parameter. In particular, it has been observed that in most of the considered cases the chosen model is not valid because those instances are different. The only exception is the inductively loaded 1D wire medium investigated in Section 3.5.2.b., for which the model applies. For the later structure, the unit cell was quite small compared to the wavelength (20 times smaller), which is why it is believed that the retrieval procedure has more chance to apply for small unit cells, that is, for more effectively homogeneous structures. It can be noted that obtaining more compact 3D magnetic resonators similar to the one investigated in Section 3.5.3.c. is not evident. Indeed, the space between the rings should be further decreased and the permittivity of the dielectric increased. This has not been tested here since it results in an increase of the computation time, which is already prohibitive (highly inhomogeneous fields in the unit cell; difficulty to converge to a stable solution).

3.6.2 Discussion on the validity of the extracted parameters

Since their apparition in the field of MTMs [134,137], retrieval procedures based on the inversion of scattering parameters (or Fresnel-type reflection and transmission coefficients) have been subject to controversy, as discussed thereafter:

- **Sign of the imaginary parts of ε and μ:** Reference [138] has been criticized in [222, 223] (see also the reply in [224]) about the "wrong" sign obtained for the imaginary parts of the permittivity and permeability around resonance, such as observed for SRRs arrays in Section 3.5.3.a.. It has been claimed that such parameters are unphysical according to the second law of thermodynamics, as described in the book of Landau and Lifshitz [43]. Currently, this debate remains unsolved, as stated in [225], where it is explained that neither Poynting Theorem nor causality requires the imaginary parts of permittivity and permeability to be positive simultaneously. It is further explained in [226] that parameters with the "wrong" sign for the imaginary parts cannot satisfy the conditions for locality.
- **Dependence on the number of layers:** To be physically acceptable, medium parameters must be independent of the size and shape of the considered sample [222]. However, this is not the case for most of the considered MTM structures and we usually observe that the extracted parameters depend on the sample thickness, i.e. on the number of layers of cells in the MTM slab. This dependence with the number of layers can be explained by higher order inter-cell coupling phenomena, which cannot be accounted for by the simple dominant-mode S parameter analysis of a single cell. This has motivated the development of an improved technique for characterizing periodic structures with higher order inter-cell coupling phenomena, which is the subject of Chapter 6.
- **Spatial dispersion:** In reference [226] (see also [227]), it is explained that parameters extracted from Fresnel-type coefficients are non-local in nature, which means that they

depend on the direction of the wave vector and hence on the incidence angle θ. It is also explained that it is possible to extract local material parameters from Fresnel-type coefficients of MTM layers, at the expense of introducing transition layers at the slab interfaces (Drude layers).

The aforementioned limitations do not mean that negative refraction cannot occur from such MTMs, made of SRRs and wires for instance, but rather than the definition of equivalent medium parameters might be inaccurate or become a source of problems and misunderstanding. It is also sometimes considered that most of the practical implementations of MTMs reported in the literature do not rigorously satisfy an effective medium limit and are conceptually closer to photonic crystals. To that respect, it is possible to distinguish a MTM regime, as opposed to the effective medium or photonic crystal regimes, in which a refractive index can be rigorously established, but where the wave impedance can only be approximately defined [141]. However, according to many scientists and engineers in the field of MTMs, there is no fundamental difference between MTMs and conventional materials, since the engineered particles in MTMs play the role of the atoms and molecules in conventional materials. For the MTMs investigated so far, the main difference with conventional materials concerns the size of the unit cell compared to the wavelength. For that reason, the general feeling is that all the anomalous behaviours mentioned above should become less important if the size of the unit cell compared to the wavelength decreases.

3.6.3 Usefulness of the extracted parameters

In conclusion, the parameters extracted from inversion of Fresnel-type reflection and transmission coefficients do not describe the averaged induced polarizations and averaged fields, but only the scattering matrix for propagating components. As a result:

- they are not applicable to problems related to evanescent waves,
- it is not possible to use these parameters for a sample of other dimensions and shape or for a sample excited in another way.

For instance, these parameters can in principle not be used to accurately describe the behaviour of a source near a MTM sample (for example, they are not applicable to describe antenna substrates [226]). A usefulness for those parameters can still be found for the description of the scattering matrix (reflection and transmission coefficients under plane wave incidence). At this point, it is worth making a conceptual distinction between the usual retrieval procedure developed for normal incidence and the enhanced technique for oblique incidence presented in this work:

- For normal incidence only, it appears that the extracted parameters are only applicable to describe the problem from which they have been extracted, which means that they are of very little practical use. Nevertheless, it is noticeable that these parameters may be useful:
  - For the designer, since ε and μ represent another set of parameters representing

the same information as the initial reflection and transmission coefficients, but in another form. In particular, if the goal is to design a slab which acts as a phase shifter for plane waves with specific unusual properties (like negative or zero phase constant, with good matching), it might be useful to work on the extracted parameters, instead of on the reflection and transmission coefficients.

  - For the general understanding of the behaviour of MTMs. More precisely, the extracted parameters may help to identify whether a given effect observed on the scattering parameters is related to an electric or a magnetic resonance, for instance.

- For oblique incidence, it is noticeable that an additional usefulness of the extracted parameters can be identified, compared to the normal incidence case. Indeed, we have shown that the six medium parameters can be determined by performing a small number of S parameters full wave simulations. Thus, the extracted parameters can be further used to predict the reflection and transmission coefficients for any other incidence direction and polarization, without the need for performing additional full wave simulations. Of course, this is only valid if the MTM slab can be reasonably described by the chosen homogeneous anisotropic model, that is, if there is no magneto-electric coupling and if spatial dispersion is negligible for that structure, and for a given application.

3.6.4 Further possible work on retrieval procedures

In order to obtain more physically meaningful material parameters, but still from an extraction from scattering parameters, which can be easily obtained by full wave simulations and measurements, it should be of interest to implement and test the method suggested by Simovski and Tretyakov in [226]. In particular, it would be of primary interest to assess whether those parameters may describe the behaviour of a source placed in the vicinity of the MTM slab (antenna substrate or superstrate, for instance).

4 TL-based MTMs

4.1 Introduction

4.1.1 Context

In the context of the ESA project within which this part of the work was carried out, TL-based MTMs have been investigated as an alternative to lossy and narrow band inclusion-based MTMs. More specifically, one of the goals of this project was to explore the possibilities of realizing volumetric LHM based on the TL approach. These structures, which are described in Chapter 5, are essentially obtained by layering several planar TL-based MTMs implemented in coplanar stripline (CPS) technology. The investigation of these planar "building blocks" is the subject of this chapter. In a first step, isolated 1D planar TL-based MTMs implemented in a CPS host TL have been studied and characterized through S parameters measurements for validation purposes. As a matter of fact, it was decided to first validate the adopted modeling approach on the dual corresponding structures implemented in CPW, since the latter can be more conveniently experimentally characterized.

4.1.2 Content and organization of the chapter

This chapter presents all the material related to the analysis, design and realization of 1D planar MTMs based on the TL approach, such as the CPS structures (and their dual CPW counterparts) used as the building blocks for the volumetric TL structures described in Chapter 5. Although the initial focus concerned LHM, we have extended the investigations to the CRLH TL, which is a TL-based MTM exhibiting both useable LH and RH bands, with a possible seamless transition between them [3]. This structure has been introduced in Section 2.2.4 and its microwave applications discussed in Section 2.4. The CRLH TL has been investigated by many groups and is thus widely covered in the literature. Although based on these studies, this chapter brings significant new contributions to the various topics addressed (see Section 1.2.3), as well as new results for practical realizations of CRLH TLs.

This chapter is organized as follows. First, we present in detail the technique used to characterize periodic structures based on a circuital representation (Section 4.2). Then, the circuit theory of the CRLH TL is presented in Section 4.3. An original contribution here is the comparison between the various proposed models for the CRLH TL. Subsequently, some basic discontinuities in CPW and CPS are investigated and characterized with lumped element models, with special emphasis on series capacitors and shunt inductors, which are the

fundamental blocks of TL-based MTMs (Section 4.4). An original contribution here is the study of the duality principle between CPS and CPW discontinuities. Finally, Sections 4.5 and 4.6 presents some designs and realizations of CRLH TLs implemented in CPW and CPS, respectively, with special emphasis on the accuracy of the various proposed circuital models. It can be mentioned that many examples of CRLH TLs implemented in microstrip or CPW are available in the literature (see e.g. [3, 4]), whereas CPS implementations are less common. Some examples can however be found in [205, 228–230].

4.2 Bloch wave analysis based on circuital representation

We address in this section the characterization of 1D periodic structures represented by circuit models [40, 122–124]. More specifically, we further describe the *Bloch wave analysis* modeling technique already introduced in Section 2.3.1.a.. This technique is aimed at characterizing the propagation of Bloch waves in periodic structures by a set of equivalent parameters, referred to here as the *Bloch parameters*[1]. We explain in this section how to calculate these parameters from the knowledge of the unit cell. It is noticeable that the chosen formulation applies to the most general case of non-reciprocal and asymmetrical unit cells. In particular, this allows addressing some problems related to the "symmetrization" of some classes of periodic structures (see Section 4.2.8).

4.2.1 Description

We consider periodic structures whose unit cell of length d can be represented by a two-port network characterized by the transfer matrix (or $ABCD$ matrix) $\mathbf{T}_{\text{cell}}$, as shown in Figure 4.1(a). The constitutive equation for the unit cell writes

$$\begin{bmatrix} U(z) \\ I(z) \end{bmatrix} = \mathbf{T}_{\text{cell}} \begin{bmatrix} U(z+d) \\ I(z+d) \end{bmatrix} = \begin{bmatrix} A & B \\ C & D \end{bmatrix} \begin{bmatrix} U(z+d) \\ I(z+d) \end{bmatrix} \tag{4.1}$$

4.2.2 Floquet's Theorem and definition of the Bloch parameters

For a Bloch wave propagating in a periodic structure along $+z$, respectively $-z$, the voltages and currents at the terminal of successive cells are the same, except for a complex constant u^+, respectively u^-, as expressed in (4.2).

$$\begin{bmatrix} U^+(z) \\ I^+(z) \end{bmatrix} = u^+ \begin{bmatrix} U^+(z+d) \\ I^+(z+d) \end{bmatrix} \qquad \text{and} \qquad \begin{bmatrix} U^-(z) \\ I^-(z) \end{bmatrix} = u^- \begin{bmatrix} U^-(z+d) \\ I^-(z+d) \end{bmatrix} \tag{4.2}$$

These equations are a particular formulation of the Floquet's Theorem [40, 121], and also represent periodic boundary conditions (PBC). By analogy with the propagation along a uniform

[1] It can be noted that the *Bloch parameters* are similar to the *image parameters* introduced in filter theory [123, 231].

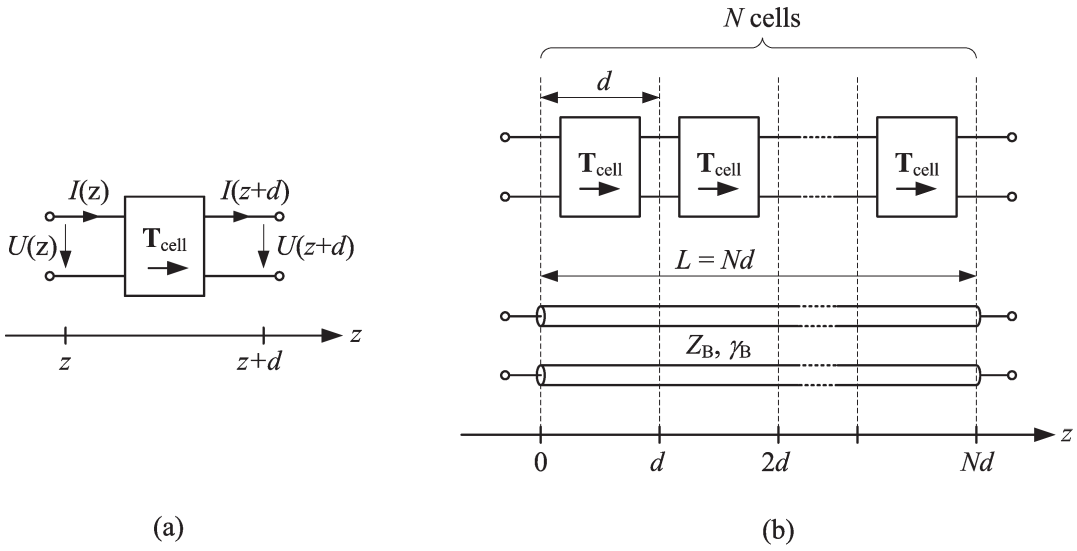

Figure 4.1: (a) General two-port network representation for the unit cell of a periodic structure of lattice constant d. (b) Equivalent TL model for a periodic structure, for reciprocal and symmetrical unit cells.

structure, the change of amplitude and phase over a spatial period may be represented as

$$u^+ = e^{+\gamma_B^+ d} \qquad \text{and} \qquad u^- = e^{-\gamma_B^- d} \tag{4.3}$$

where γ_B^+ and γ_B^- are complex quantities referred to as the *Bloch propagation constants*. Their real and imaginary parts as usually separated as follows: $\gamma_B^\pm = \alpha_B^\pm + j\beta_B^\pm$. The frequency dependence of the Bloch propagation constants is also called the *dispersion relation*, and its graphical representation the *dispersion diagram*. For a given $\beta_B^\pm d$, the quantities $\beta_B^\pm d + 2n\pi$ are also solutions of the problem, which is why the dispersion diagram is often restricted to the first Brillouin zone, that is, to values of $\beta_B^\pm d$ between $-\pi$ and $+\pi$.

By analogy with the propagation along a uniform TL, the ratio voltage/current for a wave propagating in the $+z$ *or* $-z$ direction corresponds to a characteristic impedance. In the context of periodic structures, we define the *Bloch impedances* Z_B^+ and Z_B^- associated to the two directions of propagation as

$$Z_B^+ = \frac{U^+(z+d)}{I^+(z+d)} = \frac{U^+(z)}{I^+(z)} \qquad \text{and} \qquad Z_B^- = -\frac{U^-(z+d)}{I^-(z+d)} = -\frac{U^-(z)}{I^-(z)} \tag{4.4}$$

The Bloch propagation constants γ_B^+ and γ_B^- and the Bloch impedances Z_B^+ and Z_B^- are referred to here as the *Bloch parameters*. The rest of this section determines the Bloch parameters from the knowledge of the transfer matrix $\mathbf{T}_{\text{cell}}$.

4.2.3 Eigenvalue problem

Observation of the equations (4.1) and (4.2) reveals that the parameters u^+ and u^- are the two eigenvalues of $\mathbf{T}_{\text{cell}}$. In other words, we have

$$\mathbf{T}_{\text{cell}} \begin{bmatrix} U^{\pm}(z+d) \\ I^{\pm}(z+d) \end{bmatrix} = u^{\pm} \begin{bmatrix} U^{\pm}(z+d) \\ I^{\pm}(z+d) \end{bmatrix} \quad \Rightarrow \quad \det\left(\mathbf{T}_{\text{cell}} - u^{\pm}\mathbf{E}\right) = 0 \tag{4.5}$$

where $\mathbf{E}$ is the 2×2 unit matrix. As a result, the Bloch parameters can be obtained by solving a classical matrix eigenvalue problem from $\mathbf{T}_{\text{cell}}$. Indeed, the Bloch propagation constants γ_{B}^+ and γ_{B}^- can be obtained from the eigenvalues of $\mathbf{T}_{\text{cell}}$ using (4.3), and the Bloch impedances Z_{B}^+ and Z_{B}^- can be deduced from the corresponding eigenvectors $[U^{\pm}(z+d), I^{\pm}(z+d)]^{\text{T}}$ using (4.4).

4.2.4 Bloch waves and equivalent TL

Using the definition of the Bloch parameters in Section 4.2.2, the propagation of Bloch waves in a periodic structure can be described by the incident (+) and reflected (−) voltage and current waves expressed in (4.6).

$$\begin{cases} U(z) = U^+(z) + U^-(z) = U_0^+ e^{-\gamma_{\text{B}}^+ z} + U_0^- e^{+\gamma_{\text{B}}^- z} \\ I(z) = I^+(z) + I^-(z) = I_0^+ e^{-\gamma_{\text{B}}^+ z} + I_0^- e^{+\gamma_{\text{B}}^- z} = \dfrac{U_0^+}{Z_{\text{B}}^+} e^{-\gamma_{\text{B}}^+ z} - \dfrac{U_0^-}{Z_{\text{B}}^-} e^{+\gamma_{\text{B}}^- z} \end{cases} \tag{4.6}$$

These expressions only apply to voltages and currents defined at the termination planes of the cells, i.e. at $z = z_0 + nd$, $(n \in \mathbb{Z})$. As a matter of fact, the expressions (4.6) describe the propagation along an equivalent TL which has different propagation constants and characteristic impedances for the two propagation directions. It is worth recalling that, at this stage, we have not made any assumption on the reciprocity or symmetry of the unit cell, and therefore the present developments apply to the general case. According to this equivalent TL model, the unit cell itself can be seen as a section of length d of this TL. As a result, a formulation of the transfer matrix $\mathbf{T}_{\text{cell}}$ in terms of the Bloch parameters can be found using (4.6). After some calculations, we find

$$\mathbf{T}_{\text{cell}} = \begin{bmatrix} A & B \\ C & D \end{bmatrix} = \frac{1}{Z_{\text{B}}^+ + Z_{\text{B}}^-} \begin{bmatrix} u^+ Z_{\text{B}}^+ + u^- Z_{\text{B}}^- & Z_{\text{B}}^+ Z_{\text{B}}^- \left(u^+ - u^-\right) \\ u^+ - u^- & u^+ Z_{\text{B}}^- + u^- Z_{\text{B}}^+ \end{bmatrix} \tag{4.7}$$

where u^+ and u^- are given by (4.3). It is worth mentioning here that, although introduced here for periodic structures, the four Bloch parameters γ_{B}^+, γ_{B}^-, Z_{B}^+ and Z_{B}^- can be used to characterize any two-port network. Indeed, they simply represent an alternative set of four complex parameters, in addition to the commonly used scattering, impedance or $ABCD$ parameters.

4.2.5 Bloch parameters in terms of the *ABCD* parameters

The four Bloch parameters can be expressed in terms of the $ABCD$ parameters by inverting (4.7), or by solving the eigenvalue problem described in Section 4.2.3. After some calculations, we find the solutions given in Table 4.1. For each parameter, we find two possible solutions, which correspond to the two possible signs for the parameter K defined in the table. However, it can be shown that choosing the sign for one of them determines the three others. As a result, there are in fact two sets of solutions for the Bloch parameters, as reported in Table 4.1. Nevertheless, these two mathematical solutions can be considered as equivalent, since one of them is obtained from the other by exchanging the role of the incident (+) and reflected (−) waves. Indeed, some observation of Table 4.1 reveals that

$$\begin{cases} u_1^+ = u_2^- \\ u_1^- = u_2^+ \end{cases} \Rightarrow \begin{cases} \gamma_{\mathrm{B1}}^+ = -\gamma_{\mathrm{B2}}^- \\ \gamma_{\mathrm{B1}}^- = -\gamma_{\mathrm{B2}}^+ \end{cases} \quad \text{and} \quad \begin{cases} Z_{\mathrm{B1}}^+ = -Z_{\mathrm{B2}}^- \\ Z_{\mathrm{B1}}^- = -Z_{\mathrm{B2}}^+ \end{cases} \tag{4.8}$$

Solution 1	Solution 2
$u^+ = \frac{1}{2}(A+D+K) = e^{+\gamma_{\mathrm{B}}^+ d}$	$u^+ = \frac{1}{2}(A+D-K) = e^{+\gamma_{\mathrm{B}}^+ d}$
$u^- = \frac{1}{2}(A+D-K) = e^{-\gamma_{\mathrm{B}}^- d}$	$u^- = \frac{1}{2}(A+D+K) = e^{-\gamma_{\mathrm{B}}^- d}$
$Z_{\mathrm{B}}^+ = \frac{A-D+K}{2C} = \frac{2B}{-A+D+K}$	$Z_{\mathrm{B}}^+ = \frac{A-D-K}{2C} = \frac{2B}{-A+D-K}$
$Z_{\mathrm{B}}^- = \frac{-A+D+K}{2C} = \frac{2B}{A-D+K}$	$Z_{\mathrm{B}}^- = \frac{-A+D-K}{2C} = \frac{2B}{A-D-K}$
with $K = \sqrt{(A-D)^2 + 4BC}$	

Table 4.1: The two sets of solutions for the Bloch parameters in terms of the $ABCD$ parameters.

a. Reciprocal case

A reciprocal unit cell is characterized by $AD - BC = 1$. In this case, it can be shown that $u^+u^- = 1$, hence $\gamma_{\mathrm{B}}^+ = \gamma_{\mathrm{B}}^- \equiv \gamma_{\mathrm{B}}$ (we also define $u = u^+ \Rightarrow u^- = 1/u$). As expected, the Bloch propagation constants in a reciprocal periodic structure are the same for the two propagation directions. The Bloch parameters are still given by the expressions in Table 4.1, but with $K = \sqrt{(A+D)^2 - 4}$. Moreover, the Bloch propagation constant can also be expressed as

$$\cosh(\gamma_{\mathrm{B}} d) = \frac{u + \frac{1}{u}}{2} = \frac{u^+ + u^-}{2} = \frac{A+D}{2} \quad \Rightarrow \quad \gamma_{\mathrm{B}} = \pm\frac{1}{d}\mathrm{arcosh}\left(\frac{A+D}{2}\right) \tag{4.9}$$

b. Reciprocal and symmetrical case

If in addition to be reciprocal, the unit cell is also symmetrical, we have $A = D$. In this case, it directly follows from Table 4.1 that $Z_{\mathrm{B}}^{+} = Z_{\mathrm{B}}^{-} \equiv Z_{\mathrm{B}}$. As expected, the Bloch impedances in a symmetrical periodic structure are the same for the two propagation directions. In such a case, a periodic structure with N cells of length d can be modeled in an exact way by an equivalent TL of length $L = Nd$ and parameters γ_{B} and Z_{B}, as illustrated in Figure 4.1(b). This equivalence applies for voltages and currents defined at the discrete locations $z = nd$ ($n \in \mathbb{Z}$). Using the symmetry condition, the expressions for the Bloch parameters can be simplified as shown in Table 4.2. Similarly to the general case, the two solutions can be considered as equivalent, since they correspond to the two possible choices for the incident and reflected propagation directions. Indeed, some observation of Table 4.2 reveals that

$$u_1 = 1/u_2 \;\Rightarrow\; \gamma_{\mathrm{B}1} = -\gamma_{\mathrm{B}2} \qquad \text{and} \qquad Z_{\mathrm{B}1} = -Z_{\mathrm{B}2} \tag{4.10}$$

As a result, if we want to model a finite size periodic structure with the equivalent TL model of parameters γ_{B} and Z_{B}, both solutions can be equally selected since they lead to the same transfer matrix for the whole structure. However, if we consider a periodic structure excited at one extremity, it is desirable to know which of the two solutions will correspond to the actual wave propagating away from the source. In such a case, the correct solution will be given by some additional passivity requirement. For instance, for a wave propagating along $+z$, passivity requires that the attenuation occurs along this direction. As a result, we have to choose the solution for which $\alpha_{\mathrm{B}} > 0$. If the structure is lossless ($\alpha_{\mathrm{B}} = 0$), we rather impose that the energy should propagate away from the source, that is, along $+z$. As a result we have to choose the solution for which $\mathrm{Re}[Z_{\mathrm{B}}] > 0$. It can be noted that for a passive structure, we always have $\mathrm{Re}[Z_{\mathrm{B}}] \cdot \alpha_{\mathrm{B}} \geq 0$, as demonstrated in Section 2.1.7 for the corresponding case of a plane wave propagating in a simple medium [see (2.44) with (2.29a) and (2.37)].

Solution 1	Solution 2
$u = A + K' = e^{+\gamma_{\mathrm{B}} d}$	$u = A - K' = e^{+\gamma_{\mathrm{B}} d}$
$Z_{\mathrm{B}} = \dfrac{K'}{C} = \dfrac{B}{K'}$	$Z_{\mathrm{B}} = -\dfrac{K'}{C} = -\dfrac{B}{K'}$
with $K' = K/2 = \sqrt{BC} = \sqrt{A^2 - 1}$	

Table 4.2: The two sets of solutions for the Bloch parameters in terms of the $ABCD$ parameters, for reciprocal and symmetrical unit cells.

The expressions of the Bloch parameters in Table 4.2 can also be rewritten in the more

common form

$$\begin{cases} \cosh\left(\gamma_{\mathrm{B}} d\right) = \dfrac{u + u^{-1}}{2} = A \quad \Rightarrow \quad \gamma_{\mathrm{B}} = \pm \dfrac{1}{d} \mathrm{arcosh} A \\ Z_{\mathrm{B}} = \pm \sqrt{\dfrac{B}{C}} \end{cases} \tag{4.11}$$

It can be noted that with this formulation, each Bloch parameter in (4.11) has a sign ambiguity ($\pm$). However, it should be kept in mind that, as already mentioned in the general case, the Bloch parameters are unambiguously linked in a such a way that choosing the sign for one of them determines the other. More specifically, for the present case of reciprocal and symmetrical unit cells, it can be shown that Z_{B} and γ_{B} are linked by the relation

$$\sinh\left(\gamma_{\mathrm{B}} d\right) = C Z_{\mathrm{B}} = \frac{B}{Z_{\mathrm{B}}} \tag{4.12}$$

As a result, if a choice has to be made between the two possible solutions, it is recommended to choose the sign for one of the parameters Z_{B} or γ_{B}, and to determine the other one using (4.12).

4.2.6 Influence of the reference planes position on the Bloch parameters

The reference planes define the beginning and the end of each unit cell. For a given physical infinite periodic structure, there is an infinity of possible reference planes positions, thus an infinite number of possible unit cells (each one of length d). The dependence of the Bloch parameters on the position of the reference planes is addressed in this section.

a. Bloch propagation constants

Let us suppose that the unit cell is separated at an arbitrary position along z into two networks of transfer matrices $\mathbf{T}_1$ and $\mathbf{T}_2$, such that $\mathbf{T}_{\mathrm{cell}} = \mathbf{T}_1 \mathbf{T}_2$. In a periodic structure made of the repetition of these cells, we redefine the reference planes such that the new unit cell is characterized by $\mathbf{T}'_{\mathrm{cell}} = \mathbf{T}_2 \mathbf{T}_1$. As known from linear algebra, the two matrices $\mathbf{T}_1 \mathbf{T}_2$ and $\mathbf{T}_2 \mathbf{T}_1$ have the same eigenvalues, which demonstrates that the Bloch propagation constants γ_{B}^{+} and γ_{B}^{-}, which are linked to the eigenvalues of the transfer matrix of the unit cell (see Section 4.2.3), do not depend on the position of the reference planes (since arbitrary in this reasoning).

b. Bloch impedances

Using a similar reasoning, it can be shown that the Bloch impedances Z_{B}^{+} and Z_{B}^{-} are dependent on the position of the reference planes. An interesting result can be found for the particular case of symmetrical periodic structures. More specifically, when the unit cell of a periodic structure is symmetrical, there always exists a second possible choice of reference planes which also leads to a symmetrical unit cell. This second unit cell is obtained by shifting the reference planes by a distance $d/2$, as suggested in Figure 4.2, where the two possible symmetrical unit cells are denoted by X and Y, while "half" denotes the two-port network corresponding to one half

of the unit cell. In such a configuration, the following relations between the Bloch impedances $Z_{\mathrm{B,X}}$ and $Z_{\mathrm{B,Y}}$ associated to these two possible symmetrical unit cells can be derived:

$$\begin{cases} Z_{\mathrm{B,X}} \cdot Z_{\mathrm{B,Y}} = \dfrac{B_{\mathrm{X}}}{C_{\mathrm{Y}}} = \dfrac{B_{\mathrm{Y}}}{C_{\mathrm{X}}} = \dfrac{B_{\mathrm{half}}}{C_{\mathrm{half}}} \\ \dfrac{Z_{\mathrm{B,X}}}{Z_{\mathrm{B,Y}}} = \dfrac{B_{\mathrm{X}}}{B_{\mathrm{Y}}} = \dfrac{C_{\mathrm{Y}}}{C_{\mathrm{X}}} = \dfrac{A_{\mathrm{half}}}{D_{\mathrm{half}}} \end{cases} \tag{4.13}$$

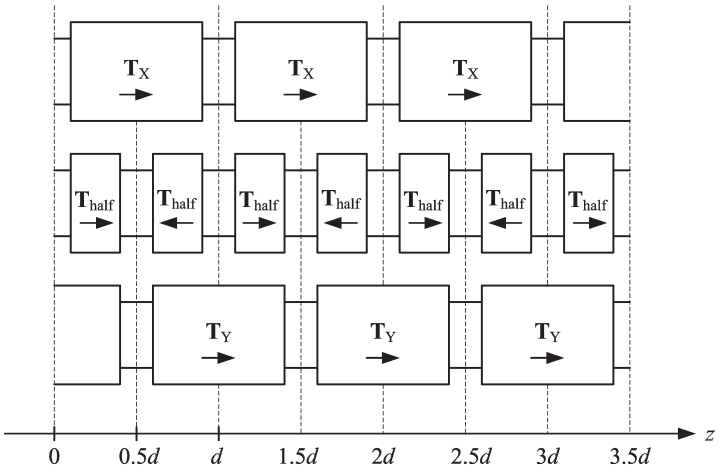

Figure 4.2: The two possible choices of reference planes for symmetrical unit cells: type X and Y.

4.2.7 Bloch parameters for lossless structures

For a lossless reciprocal periodic structure whose unit cell consists of a combination of series and shunt reactances, it can be shown that A and D are purely real and C and D are purely imaginary. In this case, we can distinguish pure pass-bands and pure stop-bands, in which the Bloch parameters exhibit the following properties:

- If $|A + D| > 2$, the structure exhibits a stop-band, which is characterized by $\gamma_{\mathrm{B}} = \alpha_{\mathrm{B}}$ or $\gamma_{\mathrm{B}} = \alpha_{\mathrm{B}} \pm j\pi/d$ [see (4.9)]. In such a band, the Bloch impedances Z_{B}^{+} and Z_{B}^{-} are purely imaginary (see Table 4.1).

- If $|A + D| < 2$, the structure exhibits a pass-band, which is characterized by $\gamma_{\mathrm{B}} = j\beta_{\mathrm{B}}$ [see (4.9)]. In such a band, the Bloch impedances Z_{B}^{+} and Z_{B}^{-} are complex conjugates, that is, $Z_{\mathrm{B}}^{+} = (Z_{\mathrm{B}}^{-})^{*}$ (see Table 4.1). Two cases can be further considered:

  - For symmetrical structures, we have $Z_{\mathrm{B}}^{+} = Z_{\mathrm{B}}^{-} = Z_{\mathrm{B}}$. As a result, Z_{B} is purely real.
  - For asymmetrical structures, we have $Z_{\mathrm{B}}^{+} \neq Z_{\mathrm{B}}^{-}$. As a result, Z_{B}^{+} and Z_{B}^{-} necessarily have a non zero imaginary part, which is a drawback for matching to real impedance.

4.2.8 Symmetrization

We introduce in this section the concept of *symmetrization* for a particular class of periodic structures. To the best of the author's knowledge, the following developments are reported for the first time in this thesis.

We consider reciprocal periodic structures which are obtained by cascading series and/or shunt impedances. More specifically, we consider the particular class of symmetrical periodic structures for which it is not possible to define a symmetrical unit cell without placing its boundaries across some of the shunt or series loading elements. This situation is illustrated in the two cases shown in Figure 4.3. When these models are used to represent real periodic structures, in which the loading elements represent physical capacitors or inductors, for instance, the symmetrical transfer matrix $\mathbf{T}_s$ cannot be directly obtained from full-wave simulations or measurements of a single cell, since the loading elements have to be either completely included in the unit cell or not included at all. As a result, only asymmetrical transfer matrices, such as $\mathbf{T}_a$ in Figure 4.3, can be obtained by full-wave simulation or measurement.

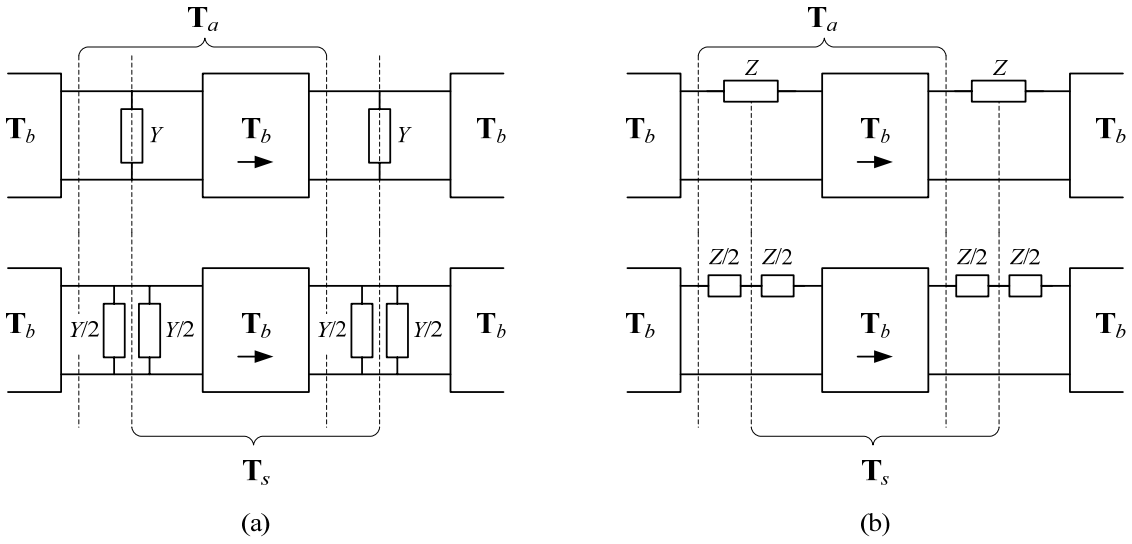

Figure 4.3: Symmetrical periodic structures for which the boundaries of the symmetrical unit cell $\mathbf{T}_s$ need to be placed across some loading elements. The network $\mathbf{T}_b$ is symmetrical. (a) With shunt loading elements, (b) with series loading elements.

The goal here is to determine the Bloch impedance Z_B associated to the symmetrical unit cell $\mathbf{T}_s$, from the knowledge of the Bloch impedances Z_B^+ and Z_B^- associated to the asymmetrical unit cell $\mathbf{T}_a$. This operation is referred to here as *symmetrization*. As we only consider here reciprocal structures, the Bloch propagation constant γ_B is not affected by the reference planes shift from $\mathbf{T}_a$ to $\mathbf{T}_s$ (see Section 4.2.6).

Here we briefly describe the adopted methodology to achieve this symmetrization for the case of the shunt loading elements of Figure 4.3(a). The corresponding results for the series

loading elements of Figure 4.3(b) are mentioned in parentheses.

1. We express $\mathbf{T}_a$ as a function of $\mathbf{T}_b$ and Y (Z).
2. Using the symmetry and reciprocity conditions for $\mathbf{T}_b$, we can determine $\mathbf{T}_b$ and Y (Z). We find $Y = \frac{D_a - A_a}{B_a}$ and $\mathbf{T}_b = [A_a, B_a; \frac{A_a^2-1}{B}, A_a]$ ($Z = \frac{A_a - D_a}{C_a}$ and $\mathbf{T}_b = [D_a, \frac{D_a^2-1}{C}; C_a, D_a]$)
3. We calculate $\mathbf{T}_s$ by distributing one half of Y (Z) on each side of $\mathbf{T}_b$.
4. We calculate the Bloch impedance Z_B associated to $\mathbf{T}_s$ using (4.11). We also calculate the Bloch impedances Z_B^+ and Z_B^- associated to $\mathbf{T}_a$ using Table 4.1.

Some calculations yield:

$$\text{For the shunt loading } Y \quad : \quad Y_\mathrm{B} = \frac{Y_\mathrm{B}^+ + Y_\mathrm{B}^-}{2} \tag{4.14a}$$

$$\text{For the series loading } Z \quad : \quad Z_\mathrm{B} = \frac{Z_\mathrm{B}^+ + Z_\mathrm{B}^-}{2} \tag{4.14b}$$

where $Y_\mathrm{B} = Z_\mathrm{B}^{-1}$ and similarly for Y_B^+ and Y_B^-. For lossless structures and in pass-bands (see Section 4.2.7), we simply have $Y_\mathrm{B} = \mathrm{Re}[Y_\mathrm{B}^+] = \mathrm{Re}[Y_\mathrm{B}^-]$ for the shunt loading and $Z_\mathrm{B} = \mathrm{Re}[Z_\mathrm{B}^+] = \mathrm{Re}[Z_\mathrm{B}^-]$ for the series loading. It is noticeable that Z or Y do not need to be explicitly calculated to determine Z_B or Y_B. However, inspecting the frequency dependence of Y or Z could help to assess the accuracy of the corresponding model (Figure 4.3).

4.2.9 Discussion: scope of the presented Bloch wave analysis

The Bloch wave analysis based on circuit models presented in this section has mainly been used for TL-based MTMs, for which a representation in terms of voltages and currents instead of fields is usually preferred. However, it can be applied to other types of MTMs as well, provided that equivalent models can be derived for these structures.

It can also be noted that the performances of TL-based MTMs are usually expressed in terms of the Bloch propagation constant γ_B and Bloch impedance Z_B, rather than in terms of equivalent medium parameters such as the permittivity ε and the permeability μ, as usually done for inclusion-based MTMs. Nevertheless, equivalent ε and μ can always be defined *in a formal way* from Z_B and γ_B, by analogy with the corresponding case of a plane wave propagating in a simple medium [see expressions (2.39), with (2.36) and (2.27)]. The ability of such formal parameters to represent polarizabilities in the "material" is not clearly demonstrated yet.

It is important to note that the Bloch wave analysis presented here is not fundamentally different from the retrieval procedure from scattering parameters described in section 2.3.3. Indeed, we obtain exactly the same expressions for the propagation constant and characteristic impedance. A difference is that the formalism presented here is more general in the sense that it can deal with non-reciprocal and non-symmetrical structures, which is not the case of the aforementioned retrieval procedure.

4.3 Theory of the CRLH TL

Composite right/left-handed transmission lines (CRLH TLs) are wideband TL-based MTMs which have recently led to numerous novel concepts and applications [3, 4]. This structure has already been introduced in Section 2.2.4 and its applications to guided-wave and antenna devices have been discussed in Sections 2.4.1 and 2.4.2, respectively. The CRLH TL is usually implemented as a periodic structure obtained by loading a host TL with series capacitances and shunt inductances. A typical dispersion diagram for such a structure is shown in Figure 4.4. The series capacitances and shunt inductances provide a left-handed (LH) behavior (phase and group velocities of opposite sign) at lower frequencies, whereas the host TL, sometimes modeled by lumped series inductances and shunt capacitances, provides a right-handed behavior (phase and group velocities of same sign) at higher frequencies. A seamless transition between the LH and RH bands can be achieved under the so-called *balanced condition* [3], which allows obtaining an almost constant Bloch impedance around the *transition frequency* f_0 between these two bands. The periodic implementations of the CRLH TL reported so far exhibit a band-pass behavior, with stop-bands below the LH band and above the RH band, as shown in Figure 4.4. As a consequence, the Bloch impedance progressively varies when the frequency moves away from f_0, until it reaches extreme values (0 or ∞) at the cutoff frequencies, as will be shown in some examples. In this section, we recall the three common models used to represent 1D lossless CRLH TLs, as well as their main properties in the balanced case.

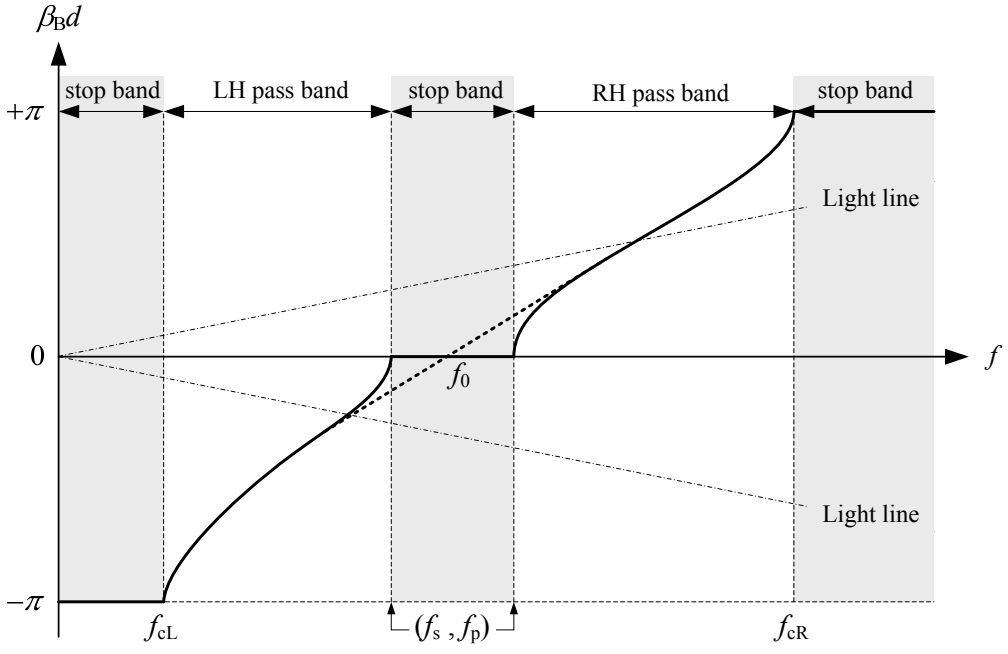

Figure 4.4: Typical dispersion diagram for unbalanced (continuous line) and balanced (dashed line) CRLH TLs.

4.3.1 Description and properties

a. Model 1: Ideal homogeneous CRLH TL

The *ideal homogeneous CRLH TL*, referred to here as "model 1", is a perfectly distributed TL whose infinitesimal section is represented in Figure 4.5. Conventional TL theory can be used to deduce the propagation constant and characteristic impedance of this structure, which has been extensively studied in section 3.1 of [3]. It is worth mentioning that a physical realization of the ideal homogeneous CRLH TL has not been reported yet. This concept is rather used as a simplified model for real periodic implementations, in which the series capacitances and shunt inductances are realized with lumped elements. It is noticeable that, in the balanced case, the ideal homogeneous CRLH TL allows propagation at all frequencies (no stop-bands) and exhibits a frequency independent characteristic impedance [3].

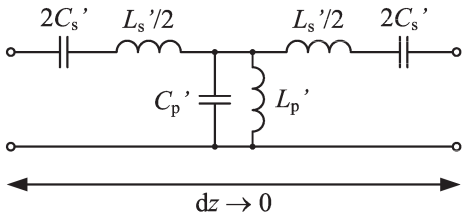

Figure 4.5: Infinitesimal section of the ideal homogeneous CRLH TL.

b. Model 2: LC network CRLH TL

The *LC network CRLH TL*, referred to here as "model 2", is a periodic structure implementation of the CRLH TL in which the RH contribution is accounted for by lumped series inductances and shunt capacitances, which is accurate if the size of the unit cell d is small compared to the guided wavelength in the host TL. The two possible symmetrical unit cells for this structure, referred to here as types Π and T, are shown in Figure 4.6. These two structures exhibit the same Bloch propagation constant γ_B, but their Bloch impedance ($Z_{B,\Pi}$ or $Z_{B,T}$) is different (see Section 4.2.6). The following additional quantities are usually introduced [3]:

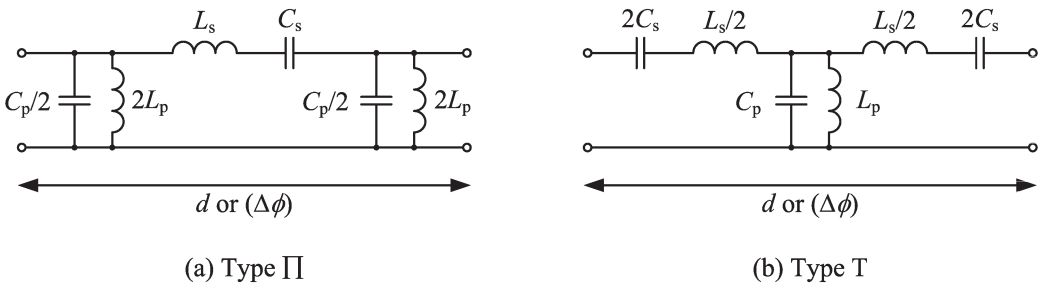

Figure 4.6: The two possible symmetrical unit cells of the LC network CRLH TL: types Π and T.

$$\begin{cases} \omega_{\mathrm{s}} = \dfrac{1}{\sqrt{L_{\mathrm{s}}C_{\mathrm{s}}}} \\ \omega_{\mathrm{p}} = \dfrac{1}{\sqrt{L_{\mathrm{p}}C_{\mathrm{p}}}} \end{cases} \qquad \begin{cases} \omega_{\mathrm{R}} = \dfrac{1}{\sqrt{L_{\mathrm{s}}C_{\mathrm{p}}}} \\ \omega_{\mathrm{L}} = \dfrac{1}{\sqrt{L_{\mathrm{p}}C_{\mathrm{s}}}} \end{cases} \qquad \begin{cases} Z_{\mathrm{R}} = \sqrt{\dfrac{L_{\mathrm{s}}}{C_{\mathrm{p}}}} \\ Z_{\mathrm{L}} = \sqrt{\dfrac{L_{\mathrm{p}}}{C_{\mathrm{s}}}} \end{cases} \tag{4.15}$$

The pulsations ω_{s} and ω_{p}[2] correspond to the resonances of the series and shunt branches, respectively. The Bloch wave analysis reported in Section 4.2 can be used to determine the Bloch parameters of this periodic structure, which has been studied in section 3.2 of [3]. The balanced condition for this structure writes

$$\omega_{\mathrm{s}} = \omega_{\mathrm{p}} \quad \Leftrightarrow \quad Z_{\mathrm{L}} = Z_{\mathrm{R}} \quad \Leftrightarrow \quad L_{\mathrm{s}}C_{\mathrm{s}} = L_{\mathrm{p}}C_{\mathrm{p}} \tag{4.16}$$

and the corresponding transition frequency between the LH and RH bands is given by

$$\omega_0 = \omega_{\mathrm{s}} = \omega_{\mathrm{p}} = \sqrt{\omega_{\mathrm{R}}\omega_{\mathrm{L}}} \tag{4.17}$$

In other words, the structure is balanced if the resonances of the series and shunt branches coincide. Under the balanced condition, the Bloch parameters are given by

$$\begin{cases} \cosh\left(\gamma_{\mathrm{B}}d\right) = 1 - \dfrac{\chi^2}{2} \\ Z_{\mathrm{B,\Pi}} = \dfrac{Z_{\mathrm{R}}}{\sqrt{1-\frac{\chi^2}{4}}} \\ Z_{\mathrm{B,T}} = Z_{\mathrm{R}}\sqrt{1-\dfrac{\chi^2}{4}} \end{cases} \quad \text{with} \quad \chi = \frac{\omega^2-\omega_0^2}{\omega\omega_{\mathrm{R}}} = \frac{\omega}{\omega_{\mathrm{R}}} - \frac{\omega_{\mathrm{L}}}{\omega} \tag{4.18}$$

It can be noted that the two Bloch impedances satisfy the following relations:

$$Z_{\mathrm{B,\Pi}} \cdot Z_{\mathrm{B,T}} = Z_{\mathrm{R}}^2 = Z_{\mathrm{L}}^2 \qquad \text{and} \qquad Z_{\mathrm{B,T}} \leq Z_{\mathrm{R}} = Z_{\mathrm{L}} \leq Z_{\mathrm{B,\Pi}} \tag{4.19}$$

At the transition frequency f_0, we have $\beta_{\mathrm{B0}} = 0$ and $Z_{\mathrm{B0,\Pi}} = Z_{\mathrm{B0,T}} = Z_{\mathrm{R}} = Z_{\mathrm{L}}$. The group velocity at f_0 is given by $v_{g0} = \omega_{\mathrm{R}}d/2$, which corresponds to one half of the velocity in the corresponding purely RH TL, i.e. a conventional TL of distributed elements $L'_{\mathrm{s}} = L_{\mathrm{s}}/d$ and $C'_{\mathrm{p}} = C_{\mathrm{p}}/d$. At the two extreme cutoff frequencies f_{cL} and f_{cR} (see Figure 4.4), the Bloch impedances take the particular values $Z_{\mathrm{B,\Pi}}(f_{\mathrm{cL}}) = Z_{\mathrm{B,\Pi}}(f_{\mathrm{cR}}) = \infty$ and $Z_{\mathrm{B,T}}(f_{\mathrm{cL}}) = Z_{\mathrm{B,T}}(f_{\mathrm{cR}}) = 0$. These performances will be illustrated with two examples in Section 4.3.3.

In the unbalanced case, the structure exhibits a similar behaviour, but with a gap (stop-band) between f_{s} and f_{p}, as shown in Figure 4.4. It can be noted that at these two frequencies, the Bloch impedance takes the particular values $Z_{\mathrm{B}}(f_{\mathrm{s}}) = 0$ and $Z_{\mathrm{B}}(f_{\mathrm{p}}) = \infty$, both for types Π and T. Finally, it can be mentioned that the two structures of Figure 4.6 tend to the ideal homogeneous CRLH TL of Figure 4.5 when the electrical size of the unit cell tends towards zero.

[2]For all pulsations ω, the corresponding frequency f is given by $f = \omega/(2\pi)$.

c. Model 3: LC loaded host TL CRLH TL

The *LC loaded host TL*, referred to here as "model 3", is a periodic structure implementation of the CRLH TL in which the RH contribution is accounted for by TL sections (host TL), instead of lumped series inductances and shunt capacitances. The two possible symmetrical unit cells for this structure, referred to here as types Π and T, are shown in Figure 4.7[3]. From

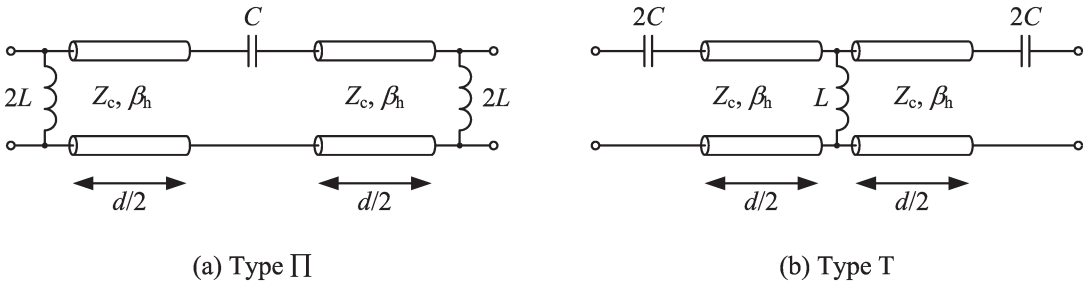

Figure 4.7: The two possible symmetrical unit cells of the LC loaded host TL CRLH TL: types Π and T.

the phase constant of the host TL β_h, we introduce the phase velocity in the host TL v_{ph}, the guided wavelength in the host TL λ_h, the electrical length $-\phi_\mathrm{h}$ and the time delay τ_h as

$$v_{ph} = \frac{\omega}{\beta_\mathrm{h}}, \qquad \lambda_\mathrm{h} = \frac{2\pi}{\beta_\mathrm{h}}, \qquad \phi_\mathrm{h} = -\beta_\mathrm{h} d, \qquad \tau_\mathrm{h} = \frac{d}{v_{ph}} = \frac{-\phi_\mathrm{h}}{\omega} \tag{4.20}$$

It can be noted that $-\phi_\mathrm{h}$ and τ_h correspond here to a host TL section of length d, and not $d/2$, as is sometimes the case in the literature. Moreover, ϕ_h corresponds to the phase shift along a host TL section of length d, which is negative for a conventional TL, which is why the electrical length is referred to as here $-\phi_\mathrm{h}$. For the mathematical expressions, the host TL can be conveniently characterized using only the time delay τ_h. Indeed, with the other parameters the lattice constant d and/or the frequency dependence has to be specified as well. For practical structures, the host TL is also often characterized by its effective relative permittivity $\varepsilon_{r,\mathrm{eff}}$, which is given by

$$\varepsilon_{r,\mathrm{eff}} = \left(\frac{c_0}{v_{ph}}\right)^2 \tag{4.21}$$

In addition, the following quantities are also introduced:

$$\begin{cases} Z_\mathrm{L} = \sqrt{\dfrac{L}{C}} \\ \tau_\mathrm{L} = \sqrt{LC} \end{cases} \quad \Leftrightarrow \quad \begin{cases} L = \tau_\mathrm{L} Z_\mathrm{L} \\ C = \dfrac{\tau_\mathrm{L}}{Z_\mathrm{L}} \end{cases} \tag{4.22}$$

The Bloch wave analysis reported in Section 4.2 can be used to determine the Bloch parameters of this periodic structure, which has been studied in [4, 27, 124–126]. The balanced condition for this structure writes

$$Z_\mathrm{c} = Z_\mathrm{L} = \sqrt{\frac{L}{C}} \tag{4.23}$$

[3]The circuits of Figure 4.7 are obviously not exactly Π or T networks, due to the presence of the TL sections. However, this terminology has been chosen by analogy with the structures of Figure 4.6.

and the corresponding transition frequency between the LH and RH bands, which cannot be obtained in closed form, is solution of the equation

$$2\omega_0\tau_{\mathrm{L}}\tan\left(\frac{1}{2}\omega_0\tau_{\mathrm{h}}\right)=1 \tag{4.24}$$

Under the balanced condition, the Bloch parameters are given by

$$\begin{cases} \cosh\left(\gamma_{\mathrm{B}}d\right)=1-\dfrac{\chi^2}{2} \\ Z_{\mathrm{B},\Pi}=Z_{\mathrm{c}}\dfrac{\cos\phi}{\sqrt{1-\frac{\chi^2}{4}}} \\ Z_{\mathrm{B,T}}=Z_{\mathrm{c}}\dfrac{\sqrt{1-\frac{\chi^2}{4}}}{\cos\phi} \end{cases} \quad \text{with} \quad \begin{cases} \chi=-\dfrac{\cos\phi}{\omega\tau_{\mathrm{L}}}-2\sin\phi \\ \phi=\dfrac{\phi_{\mathrm{h}}}{2}=-\dfrac{1}{2}\omega\tau_{\mathrm{h}} \end{cases} \tag{4.25}$$

It can be noted that the two Bloch impedances satisfy the following relation:

$$Z_{\mathrm{B},\Pi}\cdot Z_{\mathrm{B,T}}=Z_{\mathrm{c}}^2=Z_{\mathrm{L}}^2 \tag{4.26}$$

At the transition frequency f_0, we have $\beta_{\mathrm{B}0}=0$ and

$$\begin{cases} Z_{\mathrm{B}0,\Pi}=Z_{\mathrm{c}}\cos\phi_0 \\ Z_{\mathrm{B}0,\mathrm{T}}=\dfrac{Z_{\mathrm{c}}}{\cos\phi_0} \end{cases} \quad \text{with} \quad \phi_0=\phi(f_0)=-\frac{1}{2}\omega_0\tau_{\mathrm{h}} \tag{4.27}$$

As a result, the Bloch impedances at f_0 satisfy the inequality

$$Z_{\mathrm{B}0,\Pi}<Z_{\mathrm{c}}<Z_{\mathrm{B}0,\mathrm{T}} \tag{4.28}$$

The group velocity at f_0 is given by

$$v_{g0}=v_{p\mathrm{h}}\left|\frac{\cos\phi_0}{1+\frac{\sin(2\phi_0)}{2\phi_0}}\right| \tag{4.29}$$

which is always smaller than $v_{p\mathrm{h}}/2$. This is a limitation compared to conventional TLs since large group velocity corresponds to low phase variation with frequency, hence a wide-band behaviour. At the two extreme cutoff frequencies f_{cL} and f_{cR} (see Figure 4.4), the Bloch impedances take the particular values $Z_{\mathrm{B},\Pi}(f_{\mathrm{cL}})=Z_{\mathrm{B,T}}(f_{\mathrm{cR}})=\infty$ and $Z_{\mathrm{B,T}}(f_{\mathrm{cL}})=Z_{\mathrm{B},\Pi}(f_{\mathrm{cR}})=0$.

For unit cells whose length d is small compared to the guided wavelength in the host TL λ_{h}, the models of Figure 4.6 can be used to approximate those of Figure 4.7, whereas for larger unit cells the models of Figure 4.7 should be used [125, 126]. Such a correspondence will be illustrated with two examples in Section 4.3.3.

4.3.2 Homogeneity of the CRLH TL

For some applications such as leaky-wave antennas (see Section 2.4.2.a.), it is often desirable that the CRLH TL is effectively homogeneous, such that it effectively behaves as a uniform leaky-wave antenna radiating its dominant mode [3]. In this context, it is of particular interest to quantify the homogeneity of a given periodic structure. To that purpose, we introduce here the *homogeneity factor* r, which is defined as the size of the unit cell d in terms of the guided wavelength in the host TL λ_h, that is, $r = d/\lambda_\mathrm{h}$. A high level of homogeneity thus corresponds to a small value of r ($r < 0.1$ is often considered as a favorable value for applying effective medium concepts). By definition, this concept applies provided that a host TL is explicitly represented in the corresponding model. For the CRLH TL, it thus only applies to the LC loaded TL models of Figure 4.7 (i.e. model 3). For a balanced CRLH TL operated near its transition frequency f_0, the homogeneity factor can be evaluated at f_0 and we find

$$r_0 = r(f_0) = \frac{d}{\lambda_\mathrm{h}(f_0)} = f_0 \tau_\mathrm{h} = \frac{1}{\pi} \arctan\left(\frac{1}{2\omega_0 \tau_\mathrm{L}}\right) \tag{4.30}$$

As a result, a large value of the product $f_0\tau_\mathrm{L} = f_0\sqrt{LC}$ is needed to achieve a small value of r_0, hence a good level of homogeneity. On the one hand, this means that large series capacitances and shunt inductances must be implemented in small volumes in order to achieve a high level of homogeneity, for a given transition frequency f_0. As a matter of fact, this represents the main limitation for realizing highly homogeneous CRLH TLs [232]. On the other hand, working at higher frequencies allows using lower values of L and C, for a given homogeneity factor r_0. However, as the parasitic effects in real lumped elements increase with frequency, achieving high level of homogeneity for high transition frequencies f_0 is challenging as well [126].

An alternative way of evaluating the homogeneity of a periodic structure is to compare the unit cell size d to the Bloch wavelength in the periodic structure $\lambda_\mathrm{B} = 2\pi/|\beta_\mathrm{B}|$, instead of that in the host TL λ_h. This is equivalent to evaluate the homogeneity from the phase shift per unit cell $|\beta_\mathrm{B} d|$ (a small phase shift corresponds to a high level of homogeneity). In this context, the criterion $d/\lambda_\mathrm{B} < 1/4$, or equivalently $|\beta_\mathrm{B} d| < \pi/2$, has been proposed in [3] as a condition for *effective homogeneity*.

It is noticeable that none of the two aforementioned definitions of homogeneity provides entire satisfaction. Indeed, according to the second definition, a balanced CRLH TL will always be highly homogeneous around its transition frequency, where $\beta_\mathrm{B} = 0$ and $\lambda_\mathrm{B} = \infty$, even if the unit cell is not small in terms of the guided wavelength in the host TL, hence a contradiction with the first definition. On the other hand, a CRLH TL exhibiting good homogeneity according to the first definition will also be highly homogeneous in the low-frequency stop-band, which extends from 0 to f_cL (see Figure 4.4). However, this stop-band is an effect associated with the periodicity, which does not appear in the ideal homogeneous version of the CRLH TL presented in Section 4.3.1.a., and is therefore a manifestation of inhomogeneity. As a result, a more reliable definition of homogeneity should impose some restrictions on the size of the unit cell in terms of both the guided wavelength in the host TL λ_h and the wavelength in the periodic structure λ_B. From a practical point of view,

the importance of the homogeneity level, according to one definition or the other, should be discussed in function of the considered application.

4.3.3 Examples of CRLH TL responses: comparison of the models

We consider here two examples of CRLH TLs with different homogeneity factors. The aim is to compare the two periodic structure representations of Sections 4.3.1.b. and 4.3.1.c., that is, the LC network ("model 2") and the LC loaded TL ("model 3"). For each example, the parameters associated with model 3 are first chosen, and a correspondence is established with model 2 by considering that a small TL section of characteristic impedance Z_c and time delay τ_h can be approximated by a lumped series inductance L_s and a shunt capacitance C_p given by

$$L_s = Z_c \tau_h \qquad \text{and} \qquad C_p = \tau_h / Z_c \tag{4.31}$$

In other words, we approximate model 3 with model 2 using (4.31), and we evaluate the accuracy of such an approximation in function of the level of homogeneity of the structure. The two examples have been designed according to model 3 to exhibit the same transition frequency $f_0 = 5$ GHz, but with two different homogeneity factor r_0 (4.30). The first one exhibits a quite high level of homogeneity ($r_0 = 0.1$) and the second one a rather low level of homogeneity ($r_0 = 0.25$). For both examples, it has been chosen to impose the characteristic impedance of the host TL to $Z_c = 50\ \Omega$. The parameters of these two CRLH TL examples are reported in Table 4.3, and the corresponding Bloch parameters are shown in Figure 4.8, both for types Π and T unit cells[4]. It can be noted that there is no need here to specify the physical length of the unit cell d, since this information is implicitly contained in τ_h [see (4.20)].

	Homogeneity	L_p [nH]	C_s [pF]	Z_c [Ω]	τ_h [ps]	L_s [nH]	C_p [pF]
#1	$r_0 = 0.10$	2.449	0.980	50	20	1.0	0.4
#2	$r_0 = 0.25$	0.796	0.318	50	50	2.5	1.0

Table 4.3: Parameters of two CRLH TL examples with different homogeneity factors. The parameters L_p, C_s, Z_c and τ_h are used in model 3, and L_p, C_s, L_s and C_p in model 2. L_s and C_p are calculated from Z_c and τ_h using (4.31).

It can be observed in Figure 4.8 that model 2 can be used to approximate model 3 [using (4.31)], provided that the homogeneity factor is small enough, as is the case in the example #1. Indeed, it can be seen in Figure 4.8(a) that β_B is almost the same for the two models and that Z_B is comparable, except at high frequencies where a significant discrepancy between the two models is observed. In contrast, the two models do not match for structures with low level of homogeneity, as is the case in Figure 4.8(b).

The following comments can also be formulated on each model taken separately. For model 2, the Bloch impedance is always maximally flat around the transition frequency, where the

[4] When the main interest is on the pass-bands, in general we do not show $\alpha_B = \mathrm{Re}[\gamma_B]$ and $\mathrm{Im}[Z_B]$ in the stop-bands.

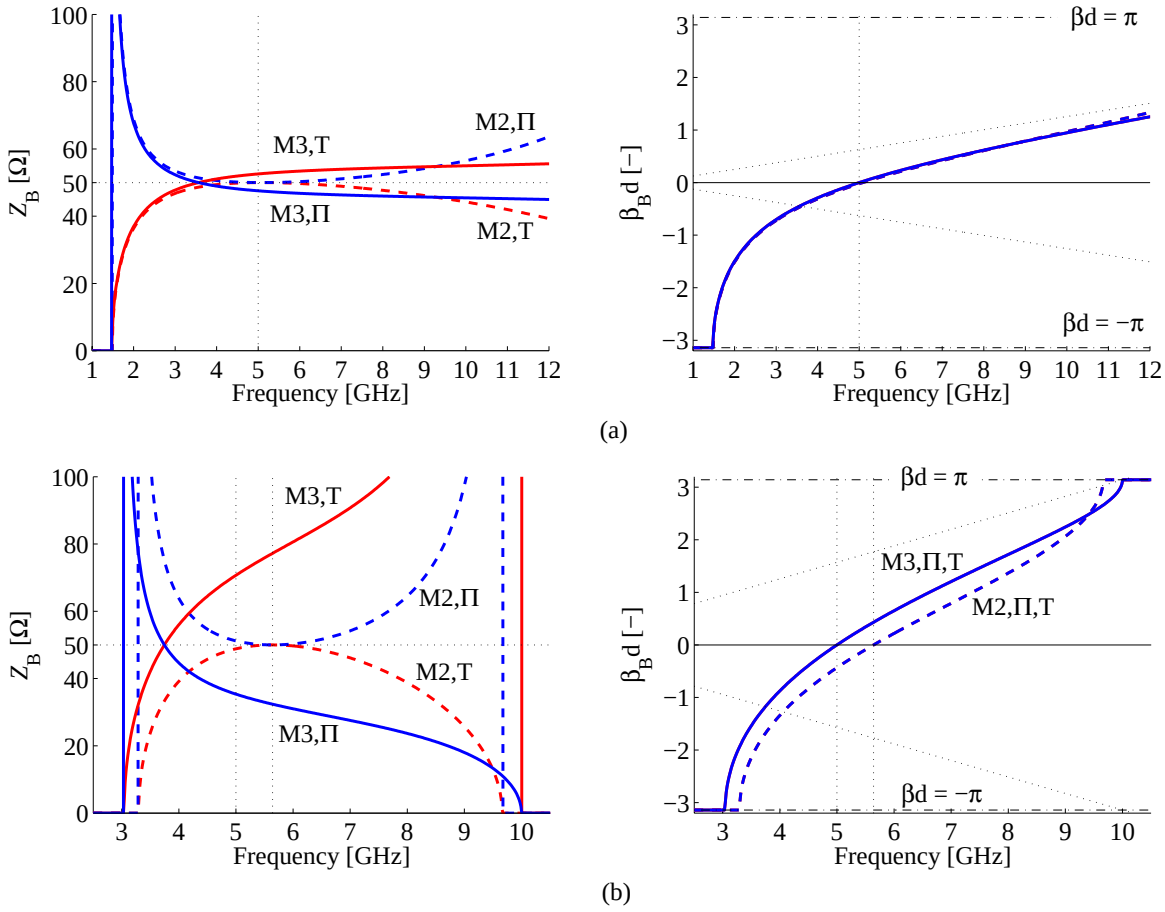

Figure 4.8: Bloch parameters for the two CRLH TL examples of Table 4.3. (a) Example #1, (b) example #2. Continuous line: model 3 (M3), dashed line: model 2 (M2); dark line: unit cell Π, light line: unit cell T). The dotted lines in the dispersion diagrams correspond to the dispersion in the host TL.

two unit cell types converge to the same value $Z_{\mathrm{R}} = Z_{\mathrm{L}}$ ($= Z_{\mathrm{c}} = 50\ \Omega$ in the present case). Moreover, it can be seen that the inequality (4.19) is satisfied at all frequencies. For model 3, the Bloch impedance at f_0 is not equal to that in the host TL Z_{c} [see (4.27)], and this difference increases with the homogeneity factor, as can be seen in Figure 4.8 by comparing cases (a) and (b). This particular feature of non-effectively homogeneous CRLH TLs (as example #2) can be used to achieve very high (type T) or low (type Π) impedance values at f_0, much beyond the range achievable with highly homogeneous CRLH TLs, for a given technology and fabrication tolerances [165].

Discussion: applicability of models 2 and 3

From the above comparison between models 2 and 3, we may conclude that model 3 is always better than model 2, since it accounts for the RH contribution in the most precise way, that is, using TL sections instead of lumped elements. However, there are some examples of CRLH TLs for which model 3 is not appropriate, or at least difficult to apply. An example of such structures is the CRLH TL shown in Figure 4.9(a), for which a host TL cannot be clearly identified since the lumped elements occupy all the space in the unit cell. This structure is therefore more conveniently analyzed using model 2, which is accurate provided that the lumped elements, in particular the series interdigital capacitor in Figure 4.9(a), are small enough to prevent propagation effects along them. In contrast, the CRLH TL shown in Figure 4.9(b) requires the use of model 3. Indeed, as its homogeneity factor r_0 is around 0.25 (poor homogeneity), it cannot be accurately represented by model 2. It can mentioned that this structure was designed to be balanced at $f_0 = 15$ GHz [165]. At such a high frequency, it is rather challenging to achieve high values of the loading L and C elements, as required for high level of homogeneity (Section 4.3.2), with an acceptable level of parasitics and losses. The type of model to use therefore depends on the topology of the considered CRLH TL, in particular on the space that the series capacitors and shunt inductors occupy in the unit cell.

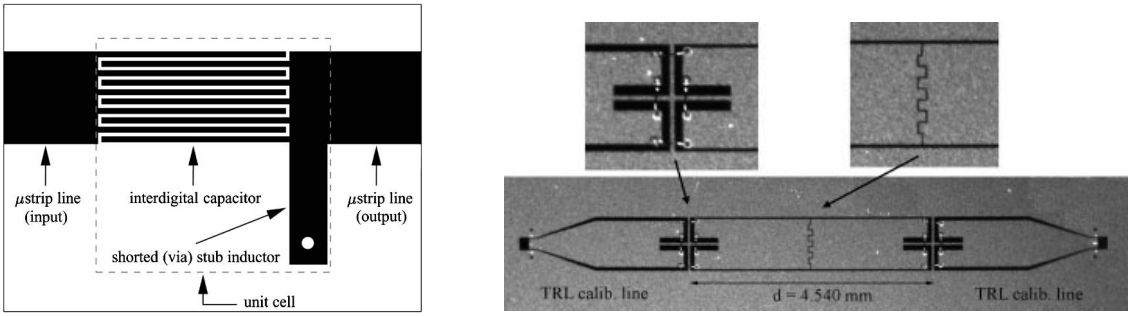

(a) **(b)**

Figure 4.9: Examples of CRLH TLs. (a) Unit cell in microstrip technology (taken from [107]), (b) Unit cell in micromachined CPW technology (taken from [165]).

4.3.4 Design considerations

The design of CRLH TLs consist in determining the four parameters of the considered model (model 2 or 3) in order to achieve a given phase shift per unit cell $\phi_{\text{cell}} = -\beta_{\text{B}} d$ and a given Bloch impedance Z_{B} at one or several frequencies. It should be noted that although the balanced condition is not needed if the CRLH TL is to be operated at a frequency $f_1 \neq f_0$, it is often imposed in order to reduce the general frequency variation of Z_{B}. Indeed, for an unbalanced CRLH TL, Z_{B} reaches extreme values (0 or ∞) at the two cutoff frequencies of the unbalance gap, which usually induces significant frequency dependence in the pass-bands surrounding this gap.

A common design goal consists in achieving given ϕ_{cell} and Z_{B} at a single frequency f_1. With the balanced condition, there are thus three equations involving the four parameters of the CRLH TL. As a result, one degree of freedom remains in the design, which can for instance be used to impose one of the parameters according to some restrictions linked with practical realization. A common approach consists in imposing the shunt inductance L_{p} because it is often the most critical element to implement, due to the difficulty to achieve high inductance values with reasonable level of parasitics and losses [126]. Once a parameter has been imposed, the three others can be calculated by inverting the expressions of the Bloch parameters. It can be noted that the degree of freedom can also be used to improve another performance of the CRLH TL, such as the bandwidth or the group velocity. The next paragraph discusses some aspects of balanced CRLH TL designs based on models 2 and 3.

a. Design based on model 2

We recall here that a CRLH TL represented by model 2 is characterized by the four parameters L_{s}, C_{p}, L_{p} and C_{s}. At a design stage, it is sometimes more convenient to consider the four parameters Z_{R}, Z_{L}, ω_{R} and ω_{L} given by (4.15). Under the balanced condition (4.16), there remains three parameters to determine: $Z_{\text{R}} = Z_{\text{L}}$, ω_{R} and ω_{L}.

Single frequency design Starting from the expressions of the Bloch parameters in (4.18), the following useful relations can be obtained (in pass-bands, where $\gamma_{\text{B}} = j\beta_{\text{B}}$ and $\phi_{\text{cell}} = -\beta_{\text{B}} d$):

$$\begin{cases} \chi = -2\sin\left(\dfrac{\phi_{\text{cell}}}{2}\right) = \dfrac{\omega}{\omega_{\text{R}}} - \dfrac{\omega_{\text{L}}}{\omega} \\ Z_{\text{B},\Pi} = Z_{\text{R}} / \cos\left(\dfrac{\phi_{\text{cell}}}{2}\right) \\ Z_{\text{B,T}} = Z_{\text{R}} \cos\left(\dfrac{\phi_{\text{cell}}}{2}\right) \end{cases} \tag{4.32}$$

As a result, imposing ϕ_{cell} and Z_{B} (i.e., $Z_{\text{B},\Pi}$ or $Z_{\text{B,T}}$, depending on the chosen unit cell type) at a given frequency f_1 provides $Z_{\text{R}} (= Z_{\text{L}})$ and a relation between ω_{L} and ω_{R}. Using the degree of freedom to impose one of the parameters allows determining all the others. Additional design guidelines based on model 2 can be found in [3].

Dual frequency design A particularly interesting property of the CRLH TL is the possibility to achieve the same functionality at two different arbitrary frequencies [3, 147]. In general, the goal of a dual frequency design is to achieve given ϕ_{cell} and Z_{B} at two different arbitrary frequencies f_1 and f_2. This results in four equations for the four CRLH TL parameters, which means that the balanced condition must be renounced to in order to carry out such a design. Here we focus on a common case where the matching requirement is the same at both frequencies, hence the same targeted Bloch impedance $Z_{\text{B}}(f_1) = Z_{\text{B}}(f_2) = Z_1$. In addition, the structure must provide the phase shifts $\phi_{\text{cell}}(f_1) = \phi_1$ and $\phi_{\text{cell}}(f_2) = \phi_2$. If we consider that we can approximate the real periodic CRLH TL by the ideal homogeneous model of Section 4.3.1.a., which exhibits a constant impedance in the balanced case, the aforementioned design is always possible and a solution is always found, as reported in [3]. However, for real periodic implementations of the balanced CRLH TL (i.e. according to model 2), the Bloch impedance is frequency dependent, which prevents such an arbitrary dual frequency design in the balanced case. Nevertheless, there is still a particular case of interest concerning specific dual frequency designs based on model 2. Indeed, equations (4.32) reveal that the CRLH TL exhibits the same Bloch impedance at two frequencies corresponding to opposite phase shifts $\pm\phi_{\text{cell}}$. This is of interest for applications which require a given phase shift in absolute value at two different frequencies f_1 and f_2, that is, $\phi_{\text{cell}}(f_1) = -\phi_{\text{cell}}(f_2) = \phi_1$, while being matched to the same reference impedance $Z_{\text{B}}(f_1) = Z_{\text{B}}(f_2) = Z_1$. The expressions for such a design are presented below. We consider that f_1 lies in the LH band, hence $f_2 > f_1$ lies in the RH band. Moreover, it can be shown that the two design frequencies are related by $\omega_1\omega_2 = \omega_{\text{L}}\omega_{\text{R}}$. Combining all these expressions, the four parameters of the CRLH TL can be expressed as

$$\begin{cases} Z_{\text{R}} = Z_{\text{L}} = \begin{cases} Z_1 \cos(\phi_1/2) & \text{for type } \Pi \\ Z_1 / \cos(\phi_1/2) & \text{for type T} \end{cases} \\ \omega_{\text{R}} = \dfrac{\omega_2 - \omega_1}{2\sin(\phi_1/2)} \\ \omega_{\text{L}} = \dfrac{\omega_1\omega_2}{\omega_2 - \omega_1} 2\sin(\phi_1/2) \end{cases} \tag{4.33}$$

The four circuit parameters L_{p}, L_{s}, C_{p} and C_{s} can be subsequently deduced using (4.15).

As an example, a design in which the specifications are $\phi_1 = 1$ rad, $Z_1 = 50\ \Omega$, $f_1 = 3$ GHz and $f_2 = 5$ GHz is considered. The resulting CRLH TL parameters calculated using (4.33) and (4.15) are given in Table 4.4, and the corresponding Bloch parameters are shown in Figure 4.10. It can be seen that the specifications are met with both types Π and T unit cells.

Type	L_{p} [nH]	C_{s} [pF]	L_{s} [nH]	C_{p} [pF]
Π	0.97	0.504	3.35	1.74
T	1.26	0.388	4.35	1.34

Table 4.4: Parameters of the CRLH TLs corresponding to the design example (see text).

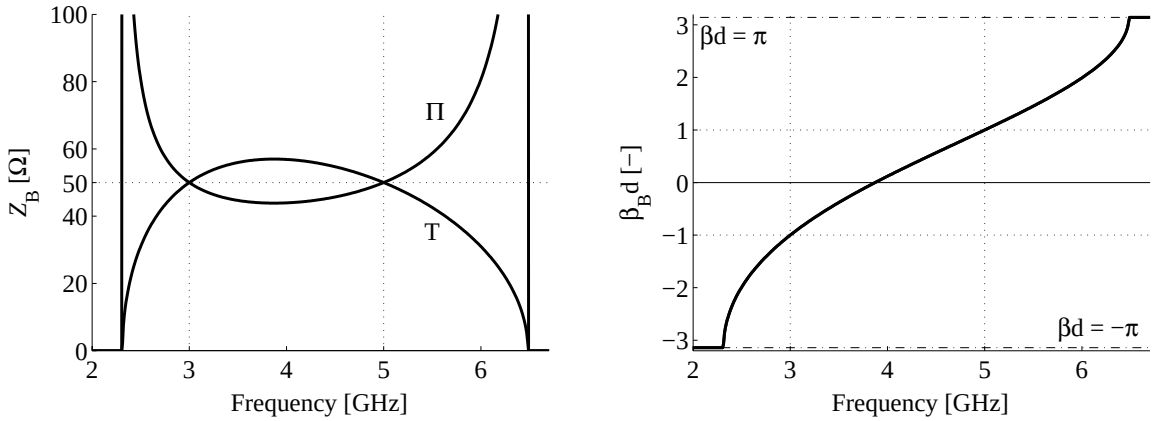

Figure 4.10: Bloch parameters corresponding to the two dual frequency designs of Table 4.4.

b. Design based on model 3

A CRLH TL represented by model 3 is characterized by the four parameters Z_c, τ_h (or ϕ_h), L and C. At a design stage, it is sometimes more convenient to consider the couple of parameters Z_L and τ_L given by (4.22) instead of L and C. Under the balanced condition, there remains three parameters to determine: $Z_c = Z_L$, τ_h and τ_L.

Single frequency design As for model 2, some useful relations can be obtained from the expressions of the Bloch parameters (4.25):

$$\begin{cases} \chi = -2\sin\left(\dfrac{\phi_{cell}}{2}\right) = -\dfrac{\cos(\phi_h/2)}{\omega\tau_L} - 2\sin(\phi_h/2) \\ \dfrac{Z_{B,\Pi}}{Z_c} = \dfrac{\cos\left(\frac{\phi_h}{2}\right)}{\cos\left(\frac{\phi_{cell}}{2}\right)} \\ \dfrac{Z_{B,T}}{Z_c} = \dfrac{\cos\left(\frac{\phi_{cell}}{2}\right)}{\cos\left(\frac{\phi_h}{2}\right)} \end{cases} \tag{4.34}$$

If ϕ_{cell} and Z_B are imposed at a given frequency f_1, (4.34) provides two relations between Z_c, ϕ_h and τ_L. Using the degree of freedom to impose one of the parameters allows determining all the others. It can be noted that the inversion of the design expressions (4.34) is mathematically more difficult than for model 2. Guidelines for single frequency designs at the transition frequency f_0 have been reported in [124, 125, 165, 171], and at an arbitrary frequency $f_1 \neq f_0$ in [124, 171]. It should be noted that closed-form expressions are not always found, which means that some transcendental equations must be solved numerically.

We further discuss here a particular case of design at a frequency $f_1 < f_0$ (LH band) for

which the resulting expressions become simple. Let us suppose that we want to use the same physical TL for the host TL of the CRLH TL and for the TLs connected to the structure, to which the latter must be matched. In such a case, the targeted Bloch impedance is $Z_{\mathrm{B}}(f_1) = Z_{\mathrm{c}}(= Z_{\mathrm{L}})$. In addition, we want the CRLH TL to provide the phase shift $\phi_{\mathrm{cell}}(f_1) = \phi_1 > 0$. For such specifications, it directly follows from (4.34) that $\phi_1 = \pm\phi_{\mathrm{h}}(f_1)$. We consider the case $\phi_1 = -\phi_{\mathrm{h}}(f_1)$ since f_1 is in the LH band. As a result, for the structure to provide a phase shift per unit cell $\phi_1 > 0$ at f_1, the host TL sections in the unit cell (of length d in total) must provide the opposite phase shift $\phi_{\mathrm{h}}(f_1) = -\phi_1$. This relation directly provides $\tau_{\mathrm{h}} = \phi_1/\omega_1$ [see (4.20)]. Moreover, using the first equation in (4.34), it can be shown that at the frequency f_1, the phase shift per unit cell can be separated into a RH contribution ϕ_{h}, which only depends on the host TL properties, and a LH contribution ϕ_{L}, which only depends on the LC loading elements:

$$\phi_{\mathrm{cell}}(f_1) = \phi_{\mathrm{h}}(f_1) + \phi_{\mathrm{L}}(f_1) \qquad \text{with} \quad \begin{cases} \phi_{\mathrm{h}}(f_1) = -\beta_{\mathrm{h}}(f_1)\, d = -\omega_1 \tau_{\mathrm{h}} < 0 \\ \phi_{\mathrm{L}}(f_1) = 4 \arctan\left(\dfrac{1}{4\omega_1 \tau_{\mathrm{L}}}\right) > 0 \end{cases} \tag{4.35}$$

Similar distinction can be made for the Bloch phase constant β_{B}. Concerning the design of interest, the L and C elements must therefore provide a phase shift $\phi_{\mathrm{L}}(f_1) = -2\phi_{\mathrm{h}}(f_1) = 2\phi_1$, which allows determining τ_{L} according to (4.35). The parameters L and C can be subsequently determined using (4.22). It is worth recalling that the above developments and the conceptual separation expressed in (4.35) are only valid at the frequency f_1 at which the RH (host TL) and LH (LC loadings) elements are matched, that is, when $Z_{\mathrm{B}}(f_1) = Z_{\mathrm{c}} = Z_{\mathrm{L}}$.

We consider here a design example in which the specifications are $\phi_1 = 1$ rad, $Z_1 = 50\ \Omega$ and $f_1 = 3$ GHz. The resulting CRLH TL parameters calculated using the aforementioned design procedure are given in Table 4.5 (they are the same for types Π and T), and the corresponding Bloch parameters are shown in Figure 4.11. It can be seen that the specifications are met with both types Π and T unit cells, and that the aforementioned condition $\phi_{\mathrm{cell}}(f_1) = -\phi_{\mathrm{h}}(f_1)$ is met.

L [nH]	C [pF]	Z_{c} [Ω]	τ_{h} [ps]
1.21	0.486	50	53.1

Table 4.5: Parameters of the CRLH TL corresponding to the design example (see text).

Dual frequency design Dual frequency designs with the same Bloch impedance at two chosen frequencies, as performed with model 2 in Section 4.3.4.a., are in general not possible for balanced CRLH TLs represented by model 3. Indeed, as can be observed in the examples in Figures 4.8 and 4.11, the Bloch impedance cannot take the same value at two different frequencies. As a result, the considered CRLH TL should be first approximated, whenever possible, by model 2 or even the ideal homogeneous model 1, which allow performing dual frequency designs. Subsequently, the performances of the designed structure should be verified based on model 3. Such an approach is not further discussed here.

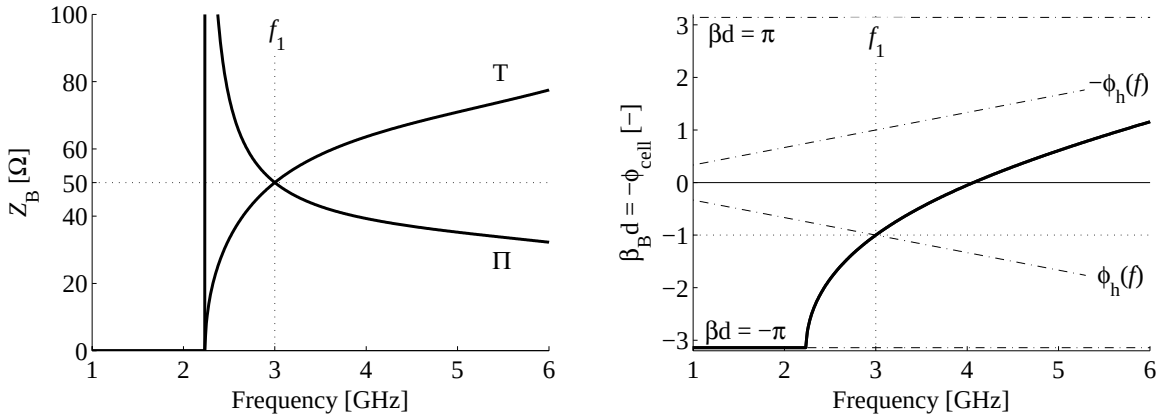

Figure 4.11: Bloch parameters corresponding to the design example of Table 4.5.

4.4 Layout elements in CPW and CPS

We describe here the physical implementation of the series capacitances and shunt inductances needed to realize CRLH TLs. These elements can be simply implemented by surface-mount technology (SMT) elements, but this approach is limited to rather low frequency, due to the high internal parasitics exhibited by these elements. Alternatively, the required series capacitances and shunt inductances can be directly implemented on the host TL by etching particular shapes, such as meander lines or gaps. These elements are referred to here as *layout elements*, and are the main concern of this section. It is noticeable that both SMT and layout elements represent *lumped* elements, since they share the same restriction that their size should be small enough to avoid propagation effects along them. This section describes the analysis and design of series capacitors and shunt inductors implemented in the two host TL considered in this work: the CPW and CPS.

4.4.1 Host TLs: CPW and CPS

The coplanar stripline (CPS), or coplanar strips, is the dual configuration of the coplanar waveguide (CPW). It consists of two parallel metallic strips on a dielectric substrate, as illustrated in Figure 4.12.

Analytical expressions for the relative effective permittivity $\varepsilon_{r,\text{eff}}$ and characteristic impedance Z_c based on quasi-static TEM conformal mapping techniques are presented in [233], Chapter 2 for the CPW and Chapter 6 for the CPS. These expressions are valid if the metallization is assumed to have perfect conductivity and zero thickness ($t = 0$). As the CPS is the dual of the CPW, their effective permittivity is the same and their characteristic impedance is

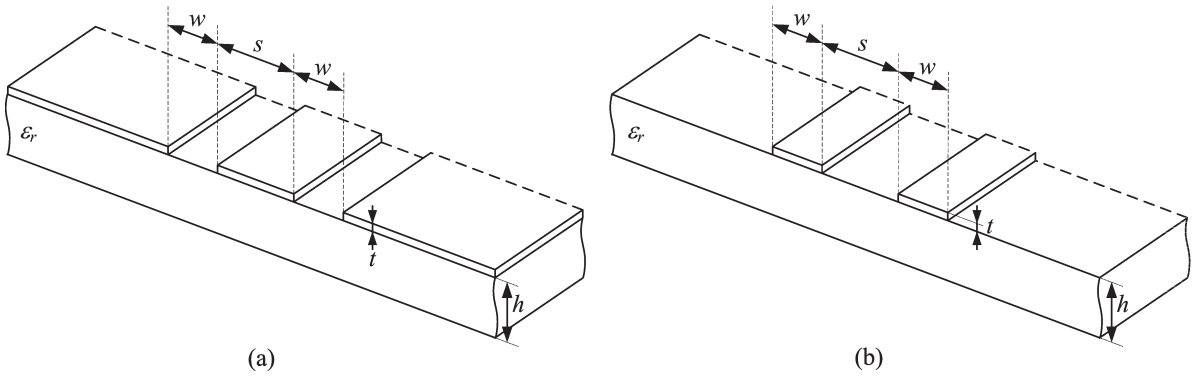

Figure 4.12: The two considered host TLs. (a) Coplanar waveguide (CPW), (b) coplanar stripline (CPS).

related by Booker's formula [233], that is

$$\begin{cases} \varepsilon_{r,\text{eff}}^{\text{CPS}} = \varepsilon_{r,\text{eff}}^{\text{CPW}} = \varepsilon_{r,\text{eff}} \\ Z_{\text{c}}^{\text{CPS}} Z_{\text{c}}^{\text{CPW}} = \dfrac{\eta^2}{4} \end{cases} \quad \text{with} \quad \eta = \frac{\eta_0}{\sqrt{\varepsilon_{r,\text{eff}}}} \quad \text{and} \quad \eta_0 = \sqrt{\frac{\mu_0}{\varepsilon_0}} \cong 377\ \Omega \tag{4.36}$$

This correspondence is strictly valid only under quasi-TEM approximation, in which it is assumed that the conductors are surrounded by a homogeneous medium of relative permittivity $\varepsilon_{r,\text{eff}}$. Figure (4.13) shows the evolution of Z_{c} for the CPS and CPW in function of the ratio s/w, for different values of $\varepsilon_{r,\text{eff}}$. It is worth mentioning that Z_{c} only depends on the substrate height h through the quantity $\varepsilon_{r,\text{eff}}$. It can be observed in Figure (4.13) that low values of Z_{c} (such as 50 Ω) are difficult to achieve in practice with CPS with low permittivity substrates, because of the very small required values of the ratio s/w.

4.4.2 Considerations on full-wave simulations and measurements

Most of the microwave circuits considered in this work cannot be designed nor analyzed using analytical formulas, but require full-wave simulations. Here, we briefly discuss some important issues concerning the type of simulations performed and the solvers used. We also comment on the measurement technique adopted for the characterization of the designed circuits.

a. Full-wave simulations

Most of the full-wave simulations have been performed with the commercial finite element method (FEM) solver Ansoft HFSS. The structure is excited with wave ports, and de-embedding is applied to place the reference planes at the boundaries of the considered discontinuity in the host TL. Moreover, the "port solver" of HFSS provides the effective permittivity and characteristic impedance of the host TL on which the port is applied. It can be noted that some simulation tests have also been performed with the commercial method of moment (MoM) solver Ansoft Designer (planar EM module). Although this solver is especially dedicated to

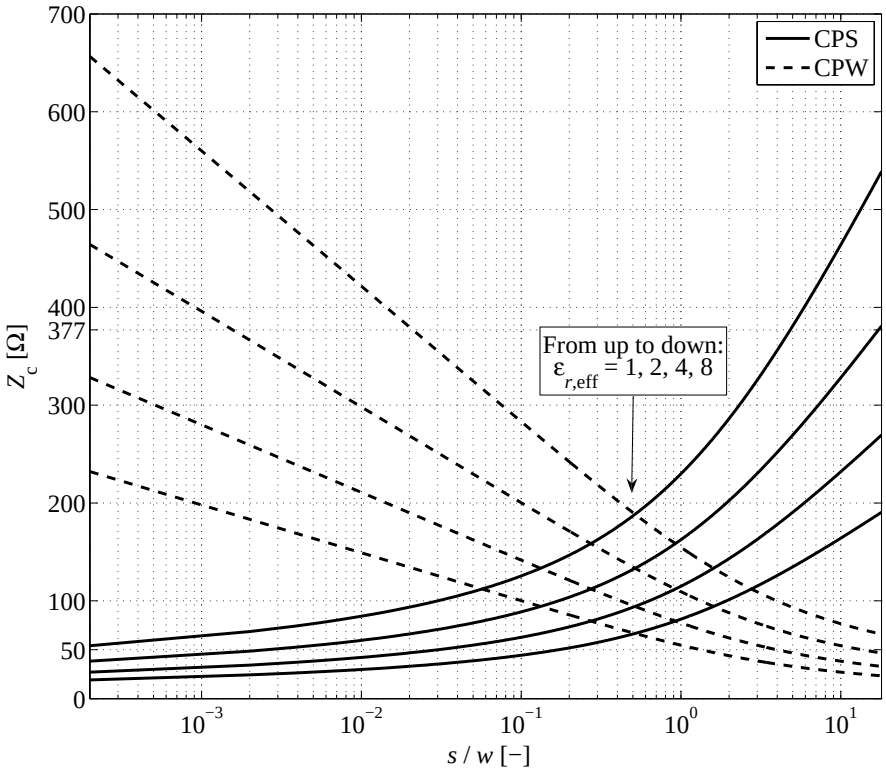

Figure 4.13: Evolution of Z_c for the CPS and CPW in function of the ratio s/w, for different values of $\varepsilon_{r,\mathrm{eff}}$ (quasi-TEM approximation).

planar multilayered structures, it was shown to be less appropriate for circuits implemented in CPS technology, since no well defined excitation (ports) exists for this type of TL. More specifically, such simulations are still possible, but the properties of the host CPS ($Z_c, \varepsilon_{r,\text{eff}}$) are not computed and automatic de-embedding is not possible. As a result, the properties of the host CPS must be determined in another way (HFSS, quasi-TEM) and the de-embedding must be performed manually.

b. Measurements

Measurements of the realized circuits have been performed with a network analyzer HP8510C. A TRL (Thru-Reflect-Line) calibration [234] has been used to obtain the S parameters at the desired reference planes, i.e., placed at the beginning and the end of the physical discontinuity, as in full wave simulations. It should be noted that the S parameters measured with this technique are referenced to the characteristic impedance of the host TL, which can be frequency dependent. As a result, an estimation of this impedance has to be performed in order to calculate the transfer (or impedance) matrix needed for lumped element model or Bloch parameters extractions. An important difficulty encountered with CPS-based circuits measurements, which does not occur with their CPW counterparts, is the necessity to use baluns to connect the CPS, which is a balanced TL, to the unbalanced ports of the network analyzer. This also implies that baluns are required in each standard of the TRL calibration kit.

4.4.3 Lumped element model extractions

In order to achieve the desired values of series capacitances and shunt inductances, an extraction tool is needed to evaluate the circuit model associated to a given layout element. We describe here in a synthetic manner the adopted method used to extract lumped element models for electrically short discontinuities in a host TL. The process is illustrated in Figure (4.14).

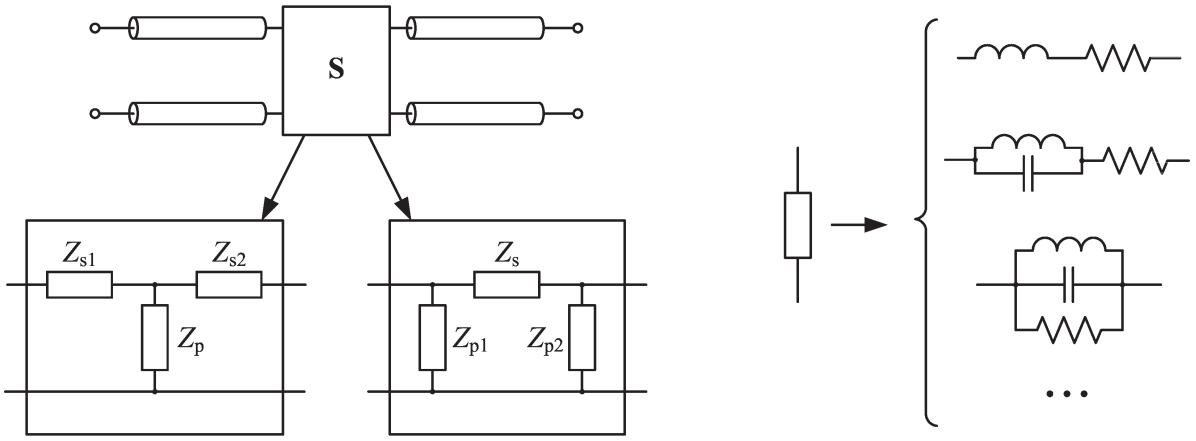

Figure 4.14: Extraction process for T and Π networks of *RLC* elements.

- The input of the method is the S parameters matrix of the discontinuity. It can be obtained from full-wave simulation or measurement, as explained in Section 4.4.2.
- The discontinuity is represented either by a T or Π network, as shown in Figure (4.14). The corresponding impedances can easily be deduced from the S parameters and the reference impedance [123].
- For each impedance, a model is chosen (such as RC series, RLC parallel,...), and the values of the corresponding R, L, C elements are extracted using one of the two following methods:

  Least mean square (LMS) extraction: The extracted R, L, C elements are those which fit the best, in a least mean square sense, the original impedance over the frequency range of interest. These regressions are applied separately on the real and imaginary parts of the impedance.

  Fixed frequency (FF) extraction: The extracted R, L, C elements are those which fit exactly the original impedance (real and imaginary parts) at a chosen frequency. If more than two elements are considered in the model (for instance an RLC combination), an additional equation is obtained by fitting the frequency derivative of the imaginary part of the immitance at the chosen frequency (see [3], Section 3.3.3 for an example of application of this method).
- The accuracy of the extracted model can be graphically evaluated by comparing, over the frequency range of interest and for each impedance, the extracted values with the initial data.
- In order to have a quantitative estimation of the accuracy of the whole extracted model, the S parameters of the T or Π network are calculated with the extracted impedances. In this reconstitution process, there is the possibility to neglect some elements which have been extracted but whose effect is expected to be small (parasitic elements). For instance, in a Π network representing a series gap capacitor, we may choose to neglect Z_{p1} and Z_{p2}, since the dominant effect is due to Z_{s}. Furthermore, we can also neglect an element in a given impedance, for instance the resistive part if it is very small. Finally, the reconstituted scattering parameters ($\tilde{S}$) are compared to the original ones (S) by means of two quantities which involve the four parameters at all the N frequency points of interest. These two quantities are the mean square error ΔS_{MSE} and the maximal error $\Delta S_{\max}$ defined as

$$\begin{cases} \Delta S_{\mathrm{MSE}} = \sqrt{\mathrm{mean}\left|\mathbf{S}-\tilde{\mathbf{S}}\right|^2} = \sqrt{\dfrac{1}{4}\displaystyle\sum_{i,j}\left[\dfrac{1}{N}\sum_{f}\left|S_{ij}-\tilde{S}_{ij}\right|^2\right]} = \sqrt{\dfrac{1}{4N}\displaystyle\sum_{i,j}\sum_{f}\left|S_{ij}-\tilde{S}_{ij}\right|^2} \\ \Delta S_{\max} = \max\left(\left|\mathbf{S}-\tilde{\mathbf{S}}\right|\right) = \displaystyle\max_{i,j}\left[\max_{f}\left(\left|S_{ij}-\tilde{S}_{ij}\right|\right)\right] = \max_{i,j,f}\left(\left|S_{ij}-\tilde{S}_{ij}\right|\right) \end{cases} \tag{4.37}$$

It is worth recalling here that the discontinuity should be small compared to the wavelength in order to be accurately described by simple lumped element models such as T or Π networks of R, L, C combinations.

It is also important to emphasize that the models chosen to represent given discontinuities are not chosen in the sole goal that a regression on this model fits the S parameters, but chosen prior to the regression based on a physical understanding of the discontinuity. Obviously, a good fit should be obtained if the physical representation is valid. However, it is important to have a relevant physical model to get a good understanding of the link between the layout geometry and the lumped elements values. Finally, let us mention that the model chosen should be a good tradeoff between precision and simplicity (namely, a small number of R, L and C), since it is preferable to have a compact model to develop efficient analytical or numerical circuit-based design methods.

4.4.4 Description of the considered layout elements

The most common fully planar geometries used to implement series capacitances and shunt inductances in CPW and CPS are the interdigital capacitor and the meander line inductor, as shown in Figure 4.15. They are dual structures, since an interdigital capacitor can be seen as a meander gap.

The lumped element models used to represent the considered layout elements are shown in Figure 4.16. These two models represent physical elements with non-zero length $L_{1\mathrm{C}}$ and $L_{1\mathrm{L}}$ (which correspond to L_1 in Figure 4.15), which means that the reference planes in the host TL are placed at the beginning and the end of the discontinuity. As a consequence, additional series inductance and shunt capacitance have to be included in the models to account for the propagation effects, which is accurate if the element is electrically small. Series capacitors are accurately modeled by a Π network comprising the capacitance C_{s} and an inductance L_{sC} in the series branch, and a capacitance C_{pC} shared between the two shunt branches, as shown in Figure 4.16(a). For the CPS implementation of Figure 4.16(b), C_{s} and L_{sC} account for the two capacitors (one in each strip), each of these being thus characterized by $2C_{\mathrm{s}}$ and $L_{\mathrm{sC}}/2$ (they appear in series in the equivalent model). Shunt inductors are accurately modeled by a T network comprising the inductance L_{p} and a capacitance C_{pL} in the shunt branch, and an inductance L_{sL} shared between the two series branches, as shown in Figure 4.16(b). For the CPW implementation of Figure 4.16(b), L_{p} and C_{pL} account for the two inductors (one in each slot), each of these being thus characterized by $2L_{\mathrm{p}}$ and $C_{\mathrm{pL}}/2$ (they appear in parallel in the equivalent model).

4.4.5 Duality between CPW and CPS circuits

We provide here some theoretical developments concerning the duality between CPW and CPS circuits involving layout elements. The motivation is to explore the possibilities of designing CPS circuits by considering their CPW dual counterparts, because the latter can be more

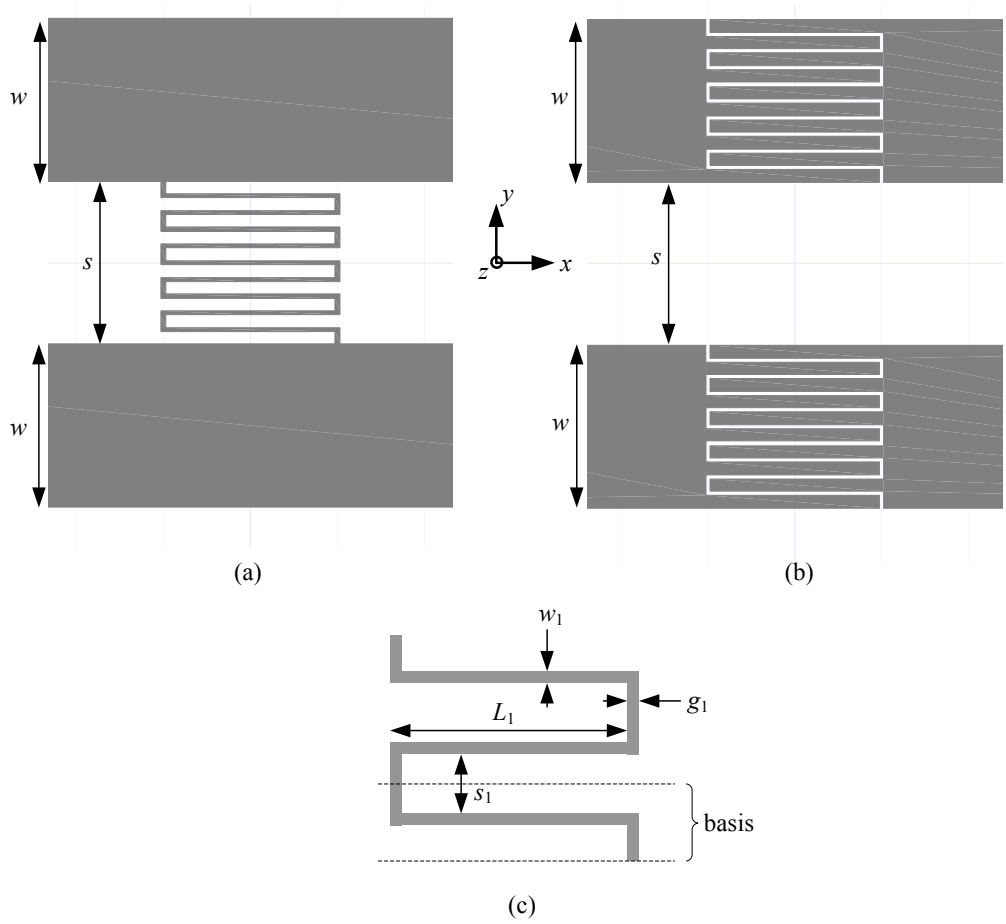

Figure 4.15: Basic layout elements in CPW and CPS. Metal is grey for CPS and white for CPW. The propagation direction is given by the x axis. (a) Series interdigital capacitor in CPW or shunt meander line inductor in CPS, (b) shunt meander line inductors in CPW or series interdigital capacitors in CPS, (c) geometrical detail of the meander line/gap. The number of meanders is characterized by the integer N, $2N-1$ being the number of horizontal segments [therefore $N = 5$ in (a) and (b)].

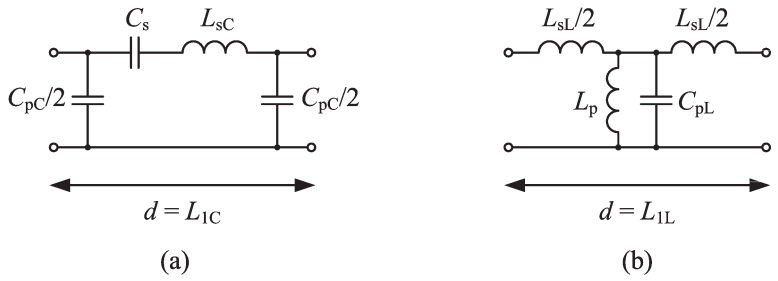

Figure 4.16: Lumped element models for the considered layout elements. (a) Series capacitor, (b) shunt inductor.

conveniently experimentally characterized, as explained in Section 4.4.2.b..

a. Theory

We assume that the CPS and CPW can be well described by the quasi-TEM approximation, with well defined voltages and currents. As the CPS and CPW are dual structures, the voltages and currents in these two systems are linked by the following relations, which are valid for thin (ideally 2D) metallization [235]:

$$\begin{cases} V^{\mathrm{CPS}} = \dfrac{\eta}{2} I^{\mathrm{CPW}} \\ I^{\mathrm{CPS}} = \dfrac{2}{\eta} V^{\mathrm{CPW}} \end{cases} \quad \Leftrightarrow \quad \begin{cases} V^{\mathrm{CPW}} = \dfrac{\eta}{2} I^{\mathrm{CPS}} \\ I^{\mathrm{CPW}} = \dfrac{2}{\eta} V^{\mathrm{CPS}} \end{cases} \tag{4.38}$$

where η is the characteristic impedance introduced in (4.36). It can be deduced from these relations that if a two-port network in one of the two configurations is characterized by a transfer (or ABCD) matrix $\mathbf{T}^a$, the corresponding transfer matrix $\mathbf{T}^b$ for the dual structure in the dual configuration is given by

$$\mathbf{T}^b = \mathbf{G} \cdot \mathbf{T}^a \cdot \mathbf{G} \quad \text{with} \quad \mathbf{G} = \begin{pmatrix} 0 & \eta/2 \\ 2/\eta & 0 \end{pmatrix}, \quad \text{or} \quad \begin{pmatrix} A^b & B^b \\ C^b & D^b \end{pmatrix} = \begin{pmatrix} D^a & \frac{\eta^2}{4} C^a \\ \frac{4}{\eta^2} B^a & A^a \end{pmatrix} \tag{4.39}$$

In terms of S parameters, this duality principle can be expressed as

$$\mathbf{S}^b = -\mathbf{H} \cdot \mathbf{S}^a \cdot \mathbf{H} \quad \text{with} \quad \mathbf{H} = \begin{pmatrix} 1 & 0 \\ 0 & -1 \end{pmatrix}, \quad \text{or} \quad \begin{pmatrix} S_{11}^b & S_{12}^b \\ S_{21}^b & S_{22}^b \end{pmatrix} = \begin{pmatrix} -S_{11}^a & S_{12}^a \\ S_{21}^a & -S_{22}^a \end{pmatrix} \tag{4.40}$$

provided that the corresponding reference impedances are related by Booker's formula [such as in (4.36)]. As a result, two reciprocal dual circuits have the same S parameters, except for a 180° phase shift on S_{11} and S_{22}. In particular, if one of the two-port networks contain only a series impedance Z^a, the dual two-port network will consist of a shunt impedance Z^b whose value is given by

$$Z^a Z^b = \frac{\eta^2}{4} \tag{4.41}$$

Similarly, a T network in one configuration becomes a Π network in the dual configuration, with the elements obtained with (4.41). If the two-port network represents the unit cell of a reciprocal and symmetrical periodic structure, it can be easily deduced from (4.39) that the Bloch propagation constants γ_{B} are the same for the two dual structures, and that the Bloch impedances Z_{B} are related by Booker's formula, as is the case for the uniform dual transmission lines [see (4.36)]:

$$\begin{cases} \gamma_{\mathrm{B}}^{\mathrm{CPS}} = \gamma_{\mathrm{B}}^{\mathrm{CPW}} \\ Z_{\mathrm{B}}^{\mathrm{CPS}} Z_{\mathrm{B}}^{\mathrm{CPW}} = \dfrac{\eta^2}{4} \end{cases} \tag{4.42}$$

b. Verification

The accuracy of the duality principle has been assessed on real structures. We consider the two layout elements of Figure 4.15(a) and (b) in both CPW and CPS configurations, with the geometrical parameters $s = w = 2$ mm, $g_1 = w_1 = 100$ µm, $s_1 = 110$ µm, $L_1 = 2$ mm and $N = 5$. These structures have been simulated with Ansoft HFSS and Ansoft Designer. The considered frequency range extends from 0.5 to 2.5 GHz. The method presented in Section 4.4.3 has been used to extract the parameters of the lumped element models shown in Figure 4.16. At the considered frequencies, the elements are very small compared to the wavelength ($\lambda/60$ at $f_{\max} = 2.5$ GHz), which means that the L_s and C_p elements accounting for the natural propagation along the length of the discontinuity can be neglected. More specifically, they have been extracted but they have not been considered for the evaluation of the accuracy of the model. As a result, the series capacitors are only represented by a series capacitance C_s and the shunt inductors by a shunt inductance L_p.

In a first step, we have considered the unrealistic case in which the duality is expected to be perfectly verified, that is, with zero thickness metallization ($t = 0$) and homogeneous surrounding medium ($\varepsilon_r = 1$). In a second step, simulations with $t = 17$ µm have also been performed with HFSS. The results are reported in Table 4.6. For each structure, the accuracy of the model is good [$\Delta S_\mathrm{MSE} < 0.031$ and $\Delta S_{\max} < 0.051$, see (4.37)]. According to the duality principle expressed in (4.41) for series/shunt impedances, the extracted element values for the two dual elements should satisfy

$$\frac{L_\mathrm{p}}{C_\mathrm{s}} = \frac{\eta^2}{4} \qquad \text{with} \quad \eta = \eta_0 \cong 377\ \Omega \tag{4.43}$$

In the fourth column of Table 4.6, we report the CPS element values calculated from its corresponding CPW dual (second column) using (4.43), while in the last column is reported the relative difference with the actual simulated value (third column).

Simulation	Element in CPW	Element in CPS	Element in CPS from duality (4.43)	Diff.
Designer, $t = 0$	$C_\mathrm{s} = 210$ fF	$L_\mathrm{p} = 7.72$ nH	$L_\mathrm{p} = 7.45$ nH	3%
HFSS, $t = 0$	$C_\mathrm{s} = 212$ fF	$L_\mathrm{p} = 6.11$ nH	$L_\mathrm{p} = 7.53$ nH	23%
HFSS, $t = 17$ µm	$C_\mathrm{s} = 248$ fF	$L_\mathrm{p} = 5.25$ nH	$L_\mathrm{p} = 8.80$ nH	68%
Designer, $t = 0$	$L_\mathrm{p} = 3.08$ nH	$C_\mathrm{s} = 83.3$ fF	$C_\mathrm{s} = 86.7$ fF	4%
HFSS, $t = 0$	$L_\mathrm{p} = 2.90$ nH	$C_\mathrm{s} = 111$ fF	$C_\mathrm{s} = 81.6$ fF	27%
HFSS, $t = 17$ µm	$L_\mathrm{p} = 2.50$ nH	$C_\mathrm{s} = 135$ fF	$C_\mathrm{s} = 70.4$ fF	48%

Table 4.6: Extracted parameters for the considered series capacitors and shunt inductors in the two dual CPW-CPS configurations.

Comments

- The duality principle is well verified for the results obtained with Designer, but not for those obtained with HFSS.
- The simulations with Designer and HFSS with $t = 0$ should give the same results. This is approximately the case for the CPW elements, for which a difference of 1% is observed for C_s and 6% for L_p. However, the correspondence is not good for the CPS elements, for which a difference of 29% is observed for C_s and 23% for L_p. According to Ansoft corporation, HFSS should be more reliable for CPS structures, but this is not confirmed by the duality principle (see first comment). These discrepancies remain unexplained at this time.
- For each element, the results with $t = 0$ and $t = 17$ µm are quite different, which means that the metallization thickness cannot be neglected for these structures. As a result, it cannot be expected that the duality principle expressed in its simple form in (4.43), which is based on a zero metallization thickness and the quasi-TEM approximation, is verified in such a case.
- Simulations of CPW with non-zero metallization thickness is not straightforward with Designer, which is why the corresponding cases with $t = 17$ µm have not been considered.

As a conclusion, the evaluation of the accuracy of the duality principle has been complicated by the observed discrepancies between HFSS and Designer results. Possible further work on this issue could consist in considering simpler layout elements, with lower level of details. Nevertheless, the presented results reveal that practical CPS circuits cannot be precisely characterized from their CPW dual counterparts, because of the non-zero metallization thickness which was shown to play an important role for the considered elements. Furthermore, the introduction of a substrate ($\varepsilon_r \neq 1$) is expected to further degrade the accuracy of the duality principle, which is based on the quasi-TEM approximation (ideally purely TEM). Finally, let us note that it has been decided on the basis of the results and discussion reported above to use Ansoft HFSS as the main simulation tool for the study of CPS and CPW TL-based MTMs.

4.4.6 Extracted parameters for typical layout elements

The layout elements studied here are the building blocks of the considered CRLH TLs. For these structures, the following substrate has been chosen: Rogers RT/Duroid 5870 ($\varepsilon_r = 2.33$, $\tan\delta = 0.0012$, $h = 0.51$ mm (20 mil) and $t = 17$ µm). The characteristics of the host TL are $s = w = 2$ mm, which results in the effective relative permittivity and characteristic impedance reported in Table 4.7. A good agreement is observed between the values obtained from quasi-static approximation and the actual values numerically calculated with HFSS. It is also noticeable that the TL parameters calculated with HFSS are in good agreement with the duality principle expressed in (4.36). Indeed, if we use the parameters of the CPW to calculate the impedance of the CPS using (4.36), we find $Z_\mathrm{c}^\mathrm{CPS} = 219\ \Omega$, which is very close to the actual value of 214 Ω.

	$\varepsilon_{r,\text{eff}}$ [-]	Z_c [Ω]
CPW	1.22 / 1.27	140 / 128
CPS	1.22 / 1.26	208 / 214

Table 4.7: Parameters of the CPW and CPS host TLs with the chosen substrate and dimensions ($\varepsilon_r = 2.33$, $h = 0.51$ mm, $s = w = 2$ mm). In each cell, the first number has been obtained from quasi-static approximation (see Section 4.4.1) and the second from the port solver of HFSS at 3 GHz.

We consider the two layout elements of Figure 4.15(a) and (b) in both CPW and CPS configurations, with the geometrical parameters $g_1 = w_1 = 100$ µm, $s_1 = 110$ µm, $N = 5$ and L_1 varies from 2 to 6 mm [see Figure 4.15(c)]. These structures have been simulated with Ansoft HFSS. The considered frequency range extends from 0.5 to 4.0 GHz. Losses have not been considered at this time (i.e., $\tan\delta = 0$ and the metallization is PEC in the simulations). The effect of losses will be investigated directly on the designed CRLH TLs, instead of on isolated lumped elements. The method presented in Section 4.4.3 has been used to extract the parameters of the lumped element models shown in Figure 4.16. Both the "least mean square" (LMS) and "fixed frequency" (FF) at 3 GHz extraction methods have been performed and compared. Figure 4.17 and 4.18 show the extracted lumped element values for the CPW and CPS elements, respectively, in function of the length of the discontinuity L_1 ($\equiv L_{1\text{C}}$ or $L_{1\text{L}}$). The discrete points in the figures (circles and stars) represent the extracted values, while the straight lines represent first order regression curves which approximately fit the extracted values (least mean square regressions). It can be noted that for the elements L_{sC}, C_{pC}, C_{pL} and L_{sL}, the regression curves have been forced to cross the point $(0, 0)$. Indeed, as these elements mainly account for the propagation of the wave along the physical length (L_1), they are supposed to be almost zero for $L_1 = 0$.

Comments

- For each structure, the accuracy of the model is reasonably good [$\Delta S_{\text{MSE}} < 0.037$ and $\Delta S_{\max} < 0.091$, see (4.37)]. Moreover, the accuracy of the models was comparable between the two extraction methods ("LMS" and "FF 3GHz"), which give comparable results.
- The dependence of the parameters with the physical length ($L_{1\text{C}}$ or $L_{1\text{L}}$) is in general quite well represented by first order regression curves, whose equations are given in the figures. These approximate relations will be used for the design of CRLH TLs in Section 4.5.

4.4.7 Description of some other layout elements

We briefly describe here some additional layout elements that have been used in the CPS CRLH TLs presented in Section 4.6.

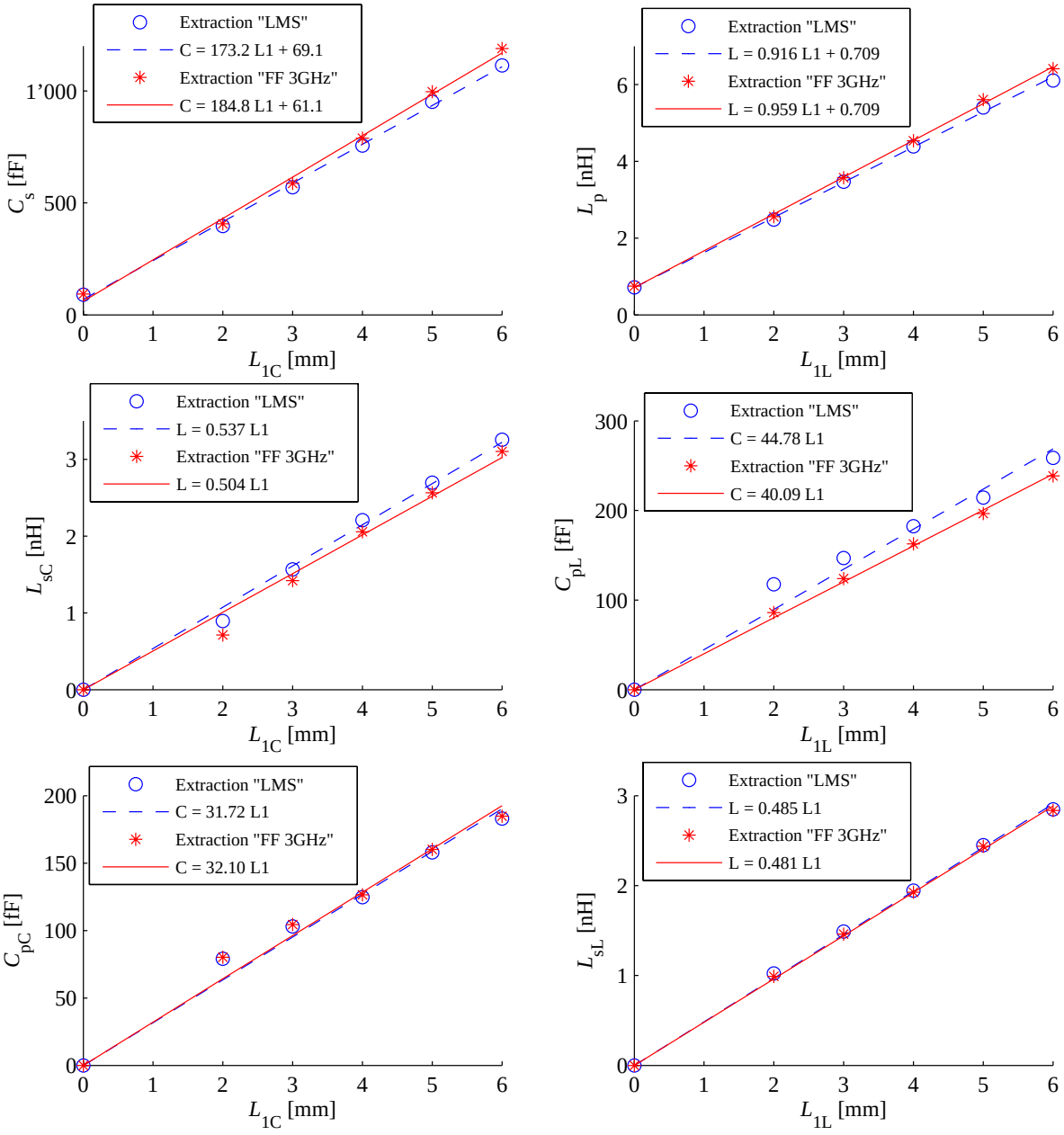

Figure 4.17: Extracted lumped elements for CPW layout elements, according to the model shown in Figure 4.16 and in function of the element length L_1 ($\equiv L_{1C}$ or L_{1L}). Left: series interdigital capacitors. Right: shunt meander inductors. For the expressions in the legends, L_1 is in [mm], L in [nH] and C in [fF].

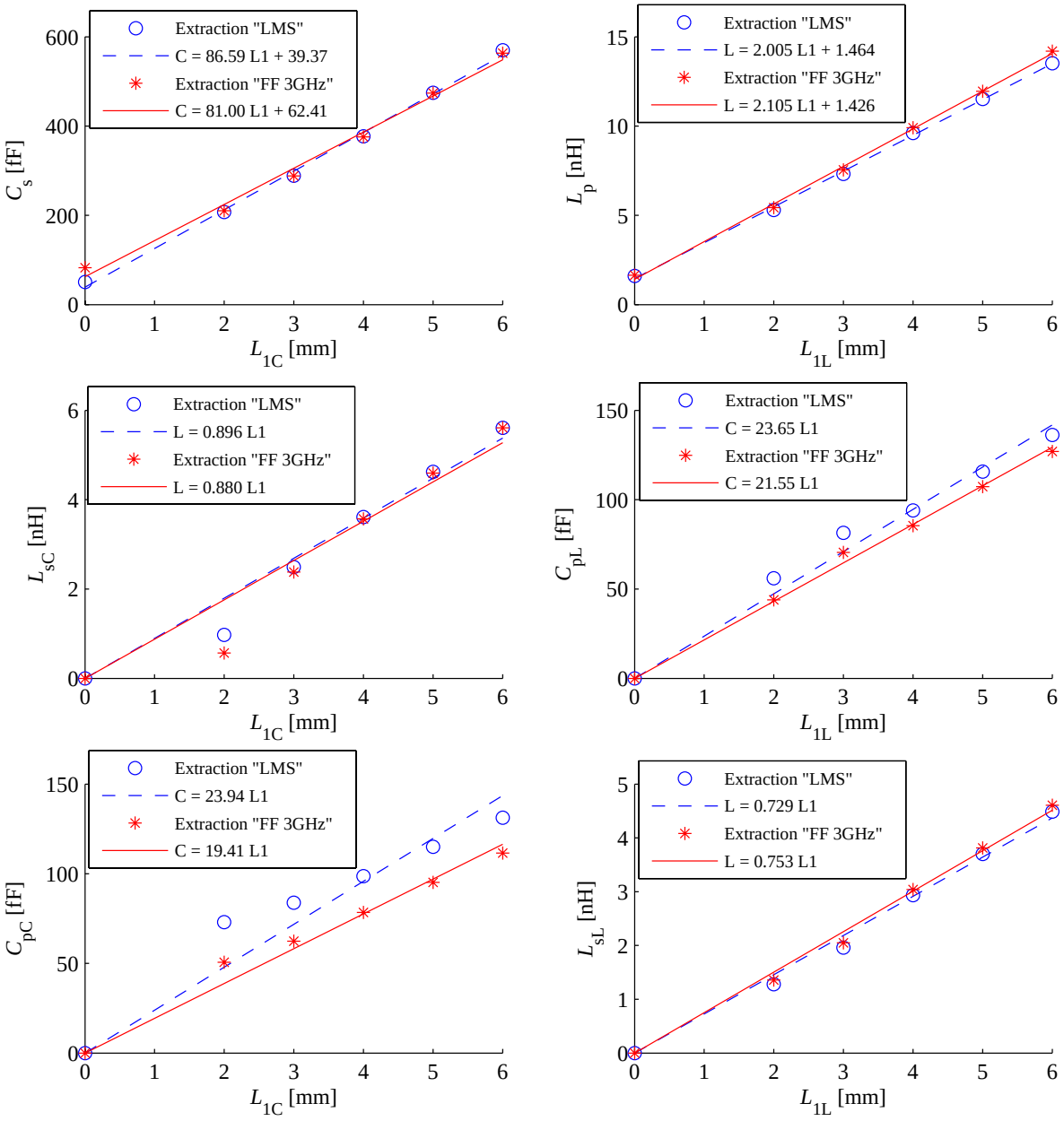

Figure 4.18: Extracted lumped elements for CPS layout elements, according to the model shown in Figure 4.16 and in function of the element length L_1 ($\equiv L_{1C}$ or L_{1L}). Left: series interdigital capacitors. Right: shunt meander inductors. For the expressions in the legends, L_1 is in [mm], L in [nH] and C in [fF].

a. Geometrically symmetrical elements

The layout elements investigated so far are symmetrical in terms of S parameters (electrically symmetrical), but their geometry was asymmetrical with respect to the propagation axis (geometrically asymmetrical). Figure 4.19 presents two geometrically symmetrical layout elements, also based on meander lines or slots. The topology of Figure 4.19(b) consists in locally enlarging the slot/strip of the host CPS/CPW in order to achieve a larger inductance/capacitance value.

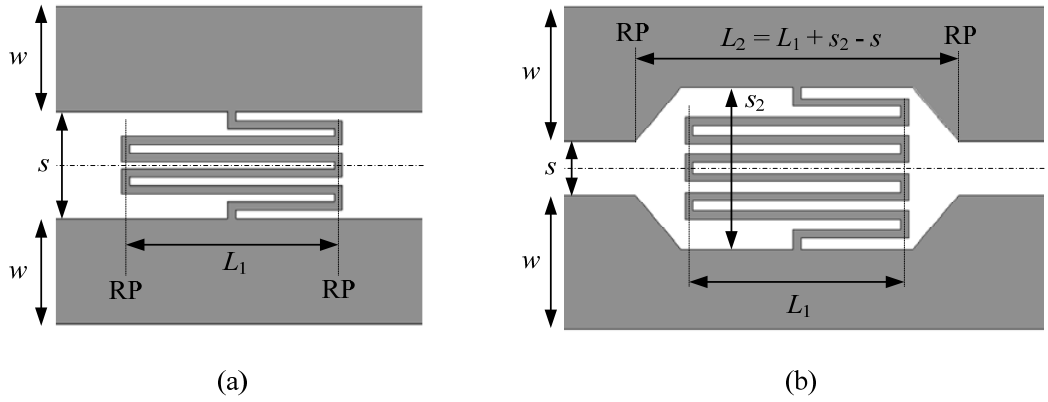

Figure 4.19: Geometrically symmetrical layout elements. Shunt inductors in CPS or series capacitors in CPW. 'RP' denotes the position of the reference planes. The characteristic dimensions of the meander line are labeled as in Figure 4.15(c). The number of meanders is characterized by the integer N, $2N$ being the number of horizontal segments [therefore $N = 3$ in (a) and $N = 4$ in (b)].

Due to the geometrical symmetry, it is expected that these elements are less sensitive to problems of radiation and excitation of parasitic even CPW or CPS modes, compared to the corresponding asymmetrical structures. Moreover, the computation time can be significantly reduced by using symmetry walls available in solvers such as HFSS. The drawback resides in the fact that these elements are not perfectly electrically symmetrical, that is, in terms of S parameters. However, it has been observed that for the considered elements, this small asymmetry can be neglected in the lumped element models.

b. Metal-insulator-metal (MIM) capacitors

The CPS host TL is particularly appropriate for the implementation of metal-insulator-metal (MIM) capacitors, simply by using the other face of the substrate. Figure 4.20 shows the different topologies of series MIM capacitors considered in this work.

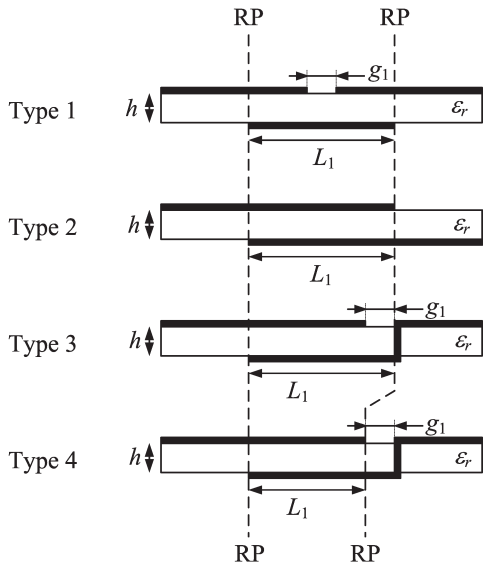

Figure 4.20: Four different topologies of series MIM capacitors in CPS (cross section view). 'RP' denotes the position of the reference planes.

Comments on the considered MIM topologies

- Type 1 provides lower values of the series capacitance C_s compared to the other types (for a given length L_1), because it approximately consists of two MIM capacitors of length $L_1/2$ connected in series.
- Type 2 is particular because the circuit continues on the other side of the substrate. When implemented in periodic structures, this topology leads to pseudo-periodic structures (one period over two is located on the other side of the substrate).
- Types 3 and 4 require a vertical connection (vias, metal plates,...) between the two sides of the substrate.
- Types 3 and 4 are basically the same, except for the position of the reference planes. When the total size of the element has to be accounted for in the model, type 3 should be used. However, the choice of reference planes in type 4 allows better comparison with type 2, in situations where type 4 is used to approximate type 2 to transpose a pseudo-periodic structure into a real periodic structure.
- Although it is not exactly the case for each type of MIM capacitors, we can make the approximation that these structures are electrically symmetrical.

As an example, a pair of MIM capacitors (one in each strip) of type 2 and length $L_1 = 3$ mm implemented with the same substrate and host TL as in Section 4.4.6, except that the substrate thickness is twice smaller ($h = 0.254$ mm), was shown to exhibit a series capacitance $C_s = 321$ fF, which is comparable with the interdigital capacitor of the same length reported in Figure 4.18.

An advantage of MIM capacitors over interdigital capacitors is the absence of small details in the geometry, which makes them less sensitive to fabrication tolerances (under etching). However, a disadvantage of the considered MIM capacitors is the rather strong dependence on the precision of the substrate thickness and permittivity. For instance, with a RT/Duroid 5870 substrate of thickness $h = 0.254$ mm, the manufacturer provides a tolerance of 7% on h, which approximately corresponds to the tolerance on the series capacitance C_s (this has been verified by simulation for the MIM capacitor of type 2 with $L_1 = 3$mm).

Finally, it is noticeable that all the elements considered in this section (except MIM capacitors of types 3 and 4) can be realized as fully planar elements, i.e. without resorting to more elaborated technical realizations, such as vertical connections (via holes) or wire bonds, as is sometimes required for other elements such as loop inductors or shorted stub inductors.

4.5 CRLH TLs in CPW

4.5.1 Motivation and objectives

As explained in the chapter introduction, the CPW host TL has been chosen for our first investigations on CRLH TLs. The objective is (i) to evaluate the accuracy of the different CRLH TL models (see Section 4.3) for CPW structures based on the layout lumped elements investigated in Section 4.4, (ii) to achieve the balanced condition, and (iii) to evaluate the correspondence between simulations and measurements for this type of structures. A certain number of parameters have been imposed in order to provide a framework for these investigations:

- Although not necessary for all applications, the balanced condition has been imposed in the designs. Such a condition may be required for leaky-wave antennas designed to radiate at broadside, for instance.
- The transition frequency f_0 has been set to 3 GHz.
- At this stage, no particular specifications is set on the Bloch impedance of the CRLH TL.
- The chosen substrate is the same as in Section 4.4.6, that is, the Rogers RT/Duroid 5870 with $\varepsilon_r = 2.33$, $\tan\delta = 0.0012$, $h = 0.51$ mm (20 mil) and $t = 17$ µm.
- The characteristics of the CPW host TL are the same as in Section 4.4.6, that is, $s = w = 2$ mm, which corresponds to a characteristic impedance $Z_\mathrm{c} = 128\ \Omega$ and an effective relative permittivity $\varepsilon_{r,\mathrm{eff}} = 1.27$.

4.5.2 Models for the considered CRLH TLs

Three different models for the CRLH TL have been presented in Section 4.3.1, which were referred to as models 1, 2 and 3. As explained in Section 4.3.3, the accuracy of each model is strongly dependent on the topology of the considered CRLH TLs. The goal of this section is

thus to determine which of the models is the most appropriate for the structures considered here.

a. Layout of a typical CPW CRLH TL considered in this work

Figure 4.21(a) shows a typical example of a one-cell CRLH TL in CPW as considered in this work (unit cell type T). Determining the most appropriate model for such a structure is not as obvious as for the two extreme topologies shown in Figure 4.9. Indeed, structures with large layout elements (compared to the total size of the unit cell) and short (even zero) interconnecting TLs between them, like in Figure 4.9(a), are in general well represented by model 2. By contrast, structures with small layout elements connected with long TL sections, like in Figure 4.9(b), are better represented by model 3. Based on this criterion, the considered structure appears as an intermediate case between models 2 and 3. Guidelines for the modeling and design of this particular type of topologies are provided in this section. Although these considerations are presented here for the one-cell CPW type T CRLH TL shown in Figure 4.21(a), a similar approach can be used for type Π and CPS CRLH TLs as well.

b. Detailed model: model 4

Using the models shown in Figure 4.16 for the layout elements, the structure shown in Figure 4.21(a) can be modeled as shown in Figure 4.21(b). This model, referred to here as "model 4", is more complete and realistic than the previously introduced models 1 to 3, which are mainly used for preliminary designs. Such a model can be used provided that the layout elements do not "overlap" along the propagation direction, that is, provided that $d_1 > 0$, or equivalently, $L_{1C} + L_{1L} < d$. As we want the model of Figure 4.21(b) to represent the unit cell of length d, a host TL section of length $-L_{1C}/2$ must be added at each extremity of the model. This has the effect of shifting the reference planes from the edges of the series capacitors to their center. As the structure consists of a single cell of type T, the two series capacitors should implement a capacitance value of $2C_s$, according to the terminology chosen so far. Although model 4 is expected to be very accurate, it cannot be used as such for simple CRLH TL designs due to its high level of complexity. This complexity mainly comes from the elements representing the RH contribution, since the LH contribution is only accounted for by the elements L_p and $2C_s$. To that respect, we discuss in the following sections two possibilities of reducing this complexity, either by representing the RH contribution only with TL sections (model 3) or only with lumped elements (model 2).

c. Reduction to model 3

A possible approximation consists in replacing the elements L_{sC}, C_{pC}, C_{pL} and L_{sL} in model 4, which account for the propagation of the wave along the non-zero length of the capacitors and inductors, by host TL sections of length L_{1C} and L_{1L}, respectively. In other words, we assume that the natural RH propagation along the length of the layout elements can be represented

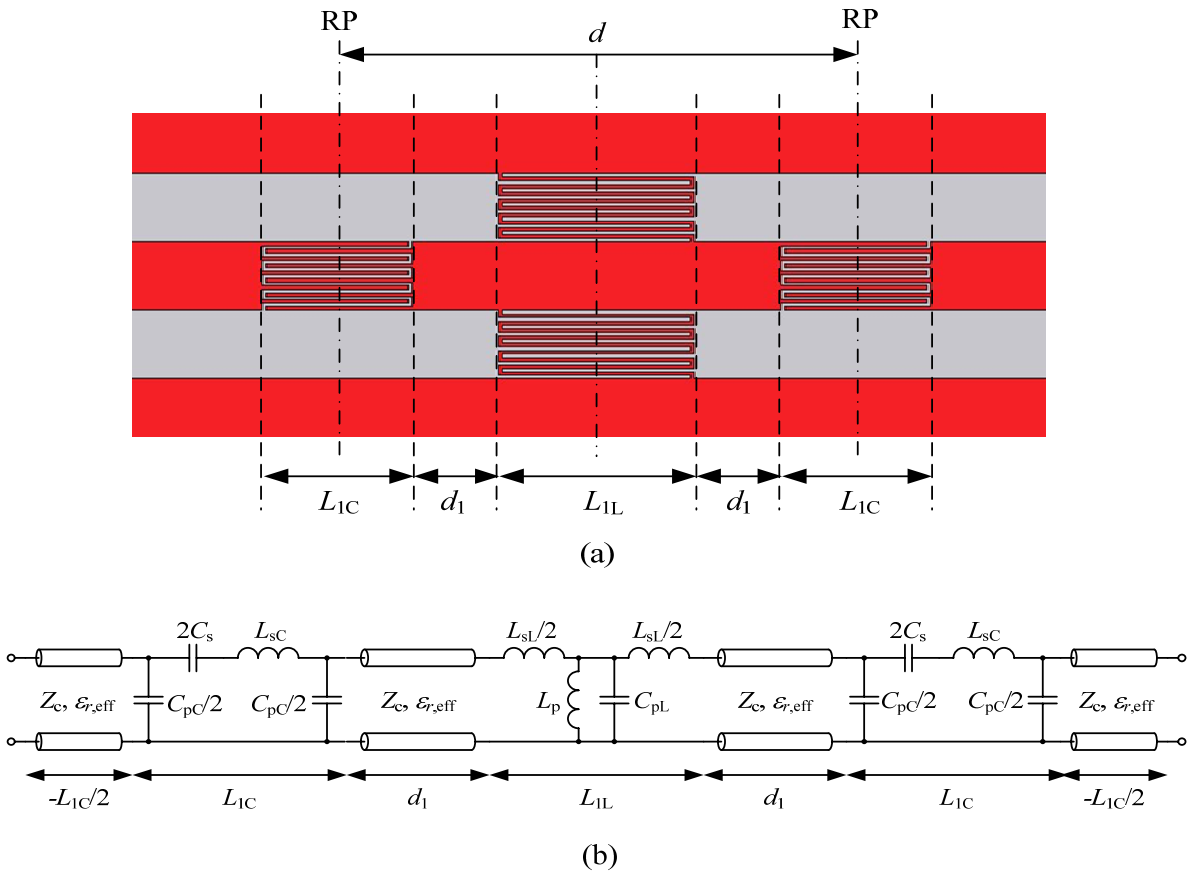

Figure 4.21: (a) Typical layout of a one-cell CRLH TL of type T in CPW as considered in this work. 'RP' denotes the position of the reference planes, which are located in the center of the series capacitors. (b) Detailed model ("model 4").

by the same parameters as the propagation in the host TL. This is also equivalent to consider that the layout elements have a zero length. Applying this approximation on model 4 results in model 3, which is recalled in Figure 4.22(a). The accuracy of this approximation is expected to increase when the length of the layout elements L_{1C} and L_{1L} decreases compared to the length d_1 of the interconnecting host TL sections.

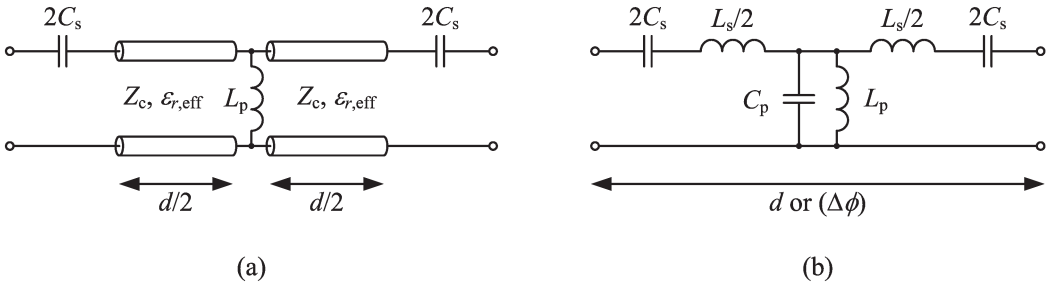

Figure 4.22: (a) Model 3 and (b) model 2 for a one-cell CRLH TL of type T.

d. Reduction to model 2

When the interconnecting host TL sections of length d_1 are small compared to the guided wavelength, they can be approximated by lumped element models, as shown in Figure 4.23 with the parameters given in (4.44).

$$\begin{cases} L_{\mathrm{TL}} = Z_{\mathrm{c}}\tau_1 \\ C_{\mathrm{TL}} = \tau_1/Z_{\mathrm{c}} \end{cases} \qquad \text{with} \qquad \tau_1 = \frac{d_1}{c_0}\sqrt{\varepsilon_{r,\mathrm{eff}}} \tag{4.44}$$

This approximation is also applied on the two extreme TL sections of negative length. We further make the approximation consisting in regrouping all the series impedances and all the shunt admittances together, according to the topology of model 2 shown in Figure 4.22(b). The parameters of this model are simply obtained by adding all the series/shunt contributions, which leads to

$$\begin{cases} L_{\mathrm{s}} = L_{\mathrm{sL}} + 2L_{\mathrm{sC}} + Z_{\mathrm{c}}\dfrac{\sqrt{\varepsilon_{r,\mathrm{eff}}}}{c_0}(d - 2L_{1\mathrm{C}} - L_{1\mathrm{L}}) \\ C_{\mathrm{p}} = C_{\mathrm{pL}} + 2C_{\mathrm{pC}} + \dfrac{1}{Z_{\mathrm{c}}}\dfrac{\sqrt{\varepsilon_{r,\mathrm{eff}}}}{c_0}(d - 2L_{1\mathrm{C}} - L_{1\mathrm{L}}) \end{cases} \tag{4.45}$$

and L_{p} and C_{s} are the same as in model 4.

e. Accuracy of the considered models

Here we evaluate the accuracy of the different proposed models on a CRLH TL example which has been designed to be balanced with $f_0 = 3$ GHz. Such a design can be carried out using model 3 and the procedure summarized below:

- We first recall that the properties of the host TL (Z_{c} and $\varepsilon_{r,\mathrm{eff}}$) are known since its characteristics have been imposed from the beginning.

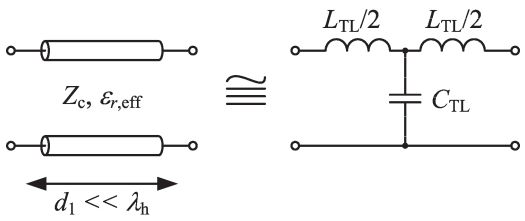

Figure 4.23: Lumped element model for small TL sections, with the parameters given in (4.44).

- The shunt inductance L_p has been imposed. Based on the prior investigations on isolated layout elements presented in Section 4.4.6, a large but realistic value has been chosen to achieve a good homogeneity for the unit cell (see Section 4.3.2).
- The value of the series capacitance has been determined to satisfy the balanced condition (4.23). A capacitor implementing this capacitance value has been designed (again based on the results of Section 4.4.6).
- The length of the host TL sections have been determined using (4.24), first in terms of the time delay τ_h, and then converted into a physical length d using (4.20) and (4.21).

The resulting structure is the one shown in Figure 4.21(a) with $L_{1C} = 4$ mm, $L_{1L} = 6$ mm and $d = 13.56$ mm ($\Rightarrow d_1 = 1.78$ mm). All the transverse dimensions of the layout elements are the same as in Section 4.4.6. For the elements C_s, L_{sC}, C_{pC}, L_p, C_{pL} and L_{sL} in model 4, we use the values extracted with the method "FF 3GHz" (stars in Figure 4.17), which is expected to provide more precise results around the transition frequency $f_0 = 3$ GHz than the "LMS" method. All the parameters associated with the three considered models are gathered in Table 4.8. As desired, the designed structure is (almost) balanced according to model 3. Indeed, we have

$$\sqrt{L_p/C_s} = 127.5\ \Omega \cong Z_c \tag{4.46}$$

The Bloch parameters calculated from the three models are shown in Figure 4.24, along with the values extracted from a full-wave (HFSS) simulation of the whole unit cell. The following comments can be formulated on the results observed in Figure 4.24:

- The full-wave results reveal a band gap from about 2.8 to 3.0 GHz, which means that this CRLH TL is not well balanced. This unbalance gap results in a frequency dependence of the Bloch impedance around this gap.
- It can be seen that model 4 almost exactly fits the full-wave results, and is thus very accurate.
- According to model 3, this CRLH TL is almost balanced, as imposed in the design. As a matter of fact, model 3 appears to be the less accurate for the considered structure.
- Model 2 provides quite good results at low frequencies and around the transition frequency (despite a frequency shift of about 0.08 GHz). However, its accuracy degrades at higher frequencies.

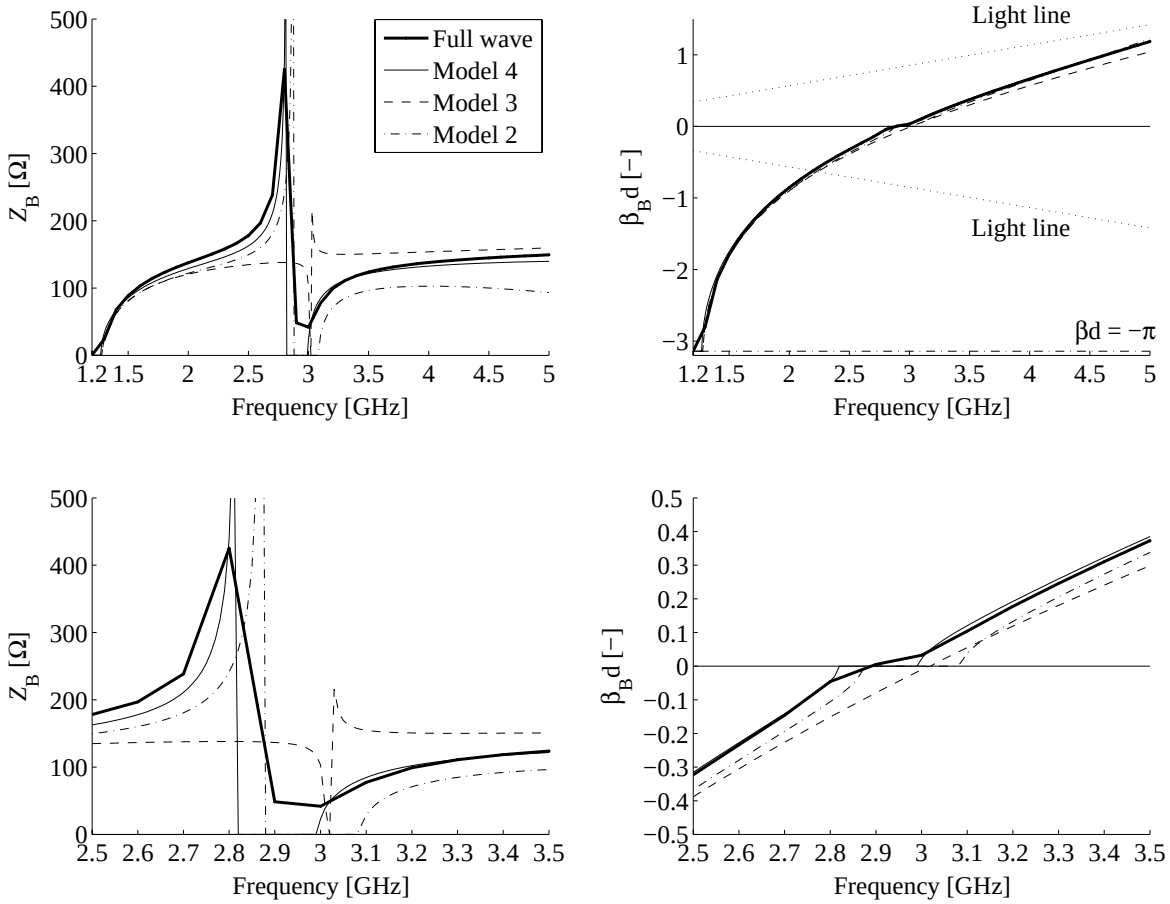

Figure 4.24: Bloch parameters according to different models for the CRLH TL whose parameters are reported in Table 4.8. Top: whole frequency range, bottom: zoom around the LH-RH transition.

Model 4	Model 3	Model 2
$C_s = 394.5$ fF		
$L_p = 6.415$ nH		
$Z_c = 128\ \Omega$		$C_p = 478.8$ fF
$\varepsilon_{r,\text{eff}} = 1.27$		$L_s = 6.738$ nH
$d = 13.56$ mm		
$L_{1C} = 4$ mm	$\tau_h = 50.94$ ps	
$L_{1L} = 6$ mm		
$d_1 = 1.78$ mm		
$L_{sC} = 2.057$ nH		
$C_{pC} = 126.6$ fF		
$L_{sL} = 2.836$ nH		
$C_{pL} = 238.5$ fF		

Table 4.8: Parameters of models 2, 3 and 4 for the considered example of one-cell CRLH TL of type T in CPW. Some parameters are used in several models.

Finally, let us mention that the homogeneity factor at $f_0 = 3$ GHz for this CRLH TL is $r_0 = d/\lambda_h = 0.15$, i.e, d is 6.5 times smaller than λ_h (see Section 4.3.2). Such a value cannot be considered as highly homogeneous, but is typical for this type of structures. In any case, the structure was shown to be homogeneous enough for applying lumped elements models such as model 2 with a reasonable level of accuracy.

In conclusion, for the considered structure model 3 only allowed approaching the targeted performances. As a result, it can be used in a preliminary design, but is clearly not sufficient for the design of a well balanced CRLH TL. On the other hand, model 2 was shown to exhibit the best compromise between accuracy and complexity, and should therefore be used in a second step of the design. A particular design technique based on this model is presented in Section 4.5.3. If needed, model 4 can be used to further improve the design using a circuit simulator, such as the one included in Ansoft Designer, for instance.

4.5.3 Design procedure based on model 2

We propose here a design procedure based on model 2 whose goal is to determine the geometrical parameters associated with the chosen topology of layout elements, in order to achieve the balanced condition with a given transition frequency f_0. In this technique, we fix the transverse dimensions of the meander lines/gaps in the layout elements (i.e. w_1 (= g_1), s_1 and N in Figure 4.15) according to the level of precision achievable with the considered fabrication technique. The values of the lumped elements are thus only changed by tuning their longitudinal dimension (L_{1C} or L_{1L}). As a result, the design consists in determining the three lengths L_{1C}, L_{1L} and d for which the specifications are met. In this context, the approximate relations for the elements C_s, L_{sC} and C_{pC} in function of L_{1C} and L_p, C_{pL} and L_{sL} in function of L_{1L} derived in Section

4.4.6 will be exploited in the design. More specifically, using the analytical expressions for the balanced condition (4.16) and the transition frequency (4.17), the expressions for L_{p} and C_{s} in (4.45), and the approximate expressions reported in Figure 4.17 for the lumped elements in function of their physical length, it is possible to determine analytically the combinations of the parameters $L_{1\mathrm{C}}$, $L_{1\mathrm{L}}$ and d which meet the desired specifications. As a matter of fact, we obtain two equations for three parameters, hence one degree of freedom in the design. For instance, Figure 4.25 shows the corresponding design curves obtained with this technique for the one-cell CPW CRLH TL of type T with $f_0 = 3$ GHz, where $L_{1\mathrm{C}}$ has been chosen as the free parameter. Similar design curves can also be derived for type Π and CPS CRLH TLs.

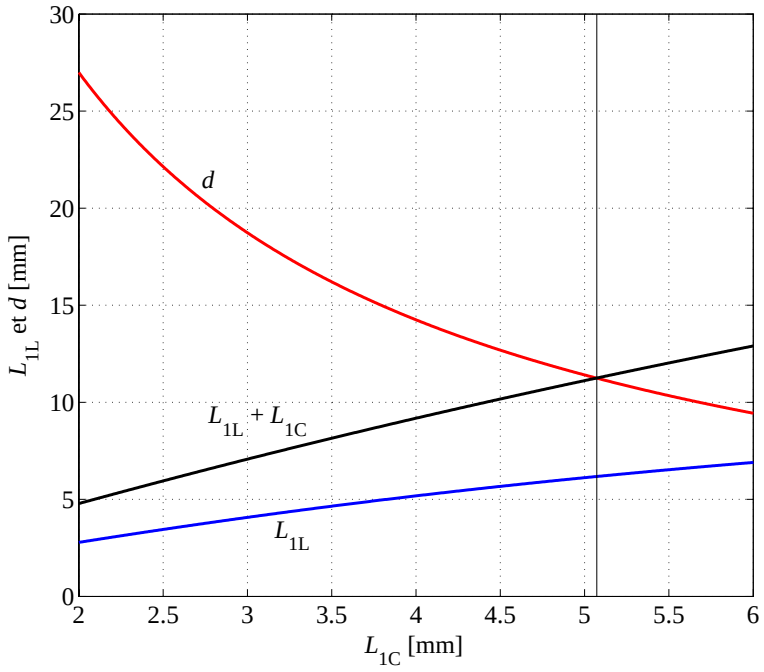

Figure 4.25: Combinations of the three parameters $L_{1\mathrm{C}}$, $L_{1\mathrm{L}}$ and d for which the desired specifications are met (balanced condition with $f_0 = 3$ GHz) for a one-cell CPW CRLH TL of type T with the elements of Figure 4.17 (extraction "FF 3GHz").

It can be noted that this design method is applicable only if $L_{1\mathrm{C}} + L_{1\mathrm{L}} > d$ (the limit case is represented by the vertical line in Figure 4.25). Otherwise, there is some "overlapping" between the series capacitors and the shunt inductors (i.e., $d_1 < 0$ in Figure 4.21).

4.5.4 Designs, realizations and performances

a. Designs

Two CPW one-cell balanced CRLH TLs of type T with $f_0 = 3$ GHz have been designed using the design curves shown in Figure 4.25. The general topology is the one shown in Figure

4.21(a) with the transverse dimensions of the layout elements the same as in Section 4.4.6, that is, $g_1 = w_1 = 100$ µm, $s_1 = 110$ µm and $N = 5$ [see Figure 4.15(c)]. Two values of L_{1C} have been chosen, and the corresponding values of L_{1L} and d have been deduced from the design curves. The resulting values are reported in Table 4.9. The second design corresponds to a

Name of the structure	L_{1C} [mm]	L_{1L} [mm]	d_1 [mm]	d [mm]
CPW CRLH TL T v1 (1 cell)	4	5.24	2.46	14.16
CPW CRLH TL T v2 (1 cell)	5	6.21	0.045	11.30

Table 4.9: Longitudinal dimensions for two designs of CPW one-cell CRLH TL of type T [Figure 4.21].

case where the length d_1 of the interconnecting TL sections is almost zero, hence a maximum homogeneity with the chosen layout elements. The homogeneity of these CRLH TLs can be evaluated as explained in Section 4.3.2. We have:

- For "CPW CRLH TL T v1 (1 cell)" at 3 GHz: $d/\lambda_h = 0.16$ and $d/\lambda_0 = 0.14$.
- For "CPW CRLH TL T v2 (1 cell)" at 3 GHz: $d/\lambda_h = 0.13$ and $d/\lambda_0 = 0.11$.

where λ_0 is the free space wavelength. Both structures have been analyzed, built and experimentally characterized. As both structures exhibit very similar behaviour, we only report here the results for the second design ("CPW CRLH TL T v2 (1 cell)"), which is referred to thereafter as "the designed CRLH TL". For this structure, all the parameters associated with the three considered models are gathered in Table 4.10. As imposed in the design, this CRLH TL is (almost) balanced according to model 2. Indeed, we have

$$f_s = \frac{1}{2\pi\sqrt{L_s C_s}} = 3 \text{ GHz} \cong f_p = \frac{1}{2\pi\sqrt{L_p C_p}} \tag{4.47}$$

b. Physical realization

The designed structures have been realized using a conventional PCB etching process (see Figure 4.26). Special attention had to be paid on the modification of the dimensions due to under etching. Several tests have been performed in order to determine the different parameters of the process (duration of UV insulation, duration of etching in acid) which allow minimizing the under etching and especially making it reproducible. With the current process, each metal/slot transition is shifted of about 5 µm due to under etching. In other words, a strip of width 100 µm on the mask will have an actual width of 90 µm). For the considered structures, the under etching has been corrected on the masks, in such a way that the realized structures exhibit the desired dimensions with very good accuracy.

The structures are connected to the measurement setup with SMA connectors for 50 Ω coaxial cables. This results in a mismatch with the CPW host TL of 128 Ω, but the effect of these transitions is removed by means of a TRL calibration.

Model 4	Model 3	Model 2
$C_s = 492.6$ fF		
$L_p = 6.664$ nH		
$Z_c = 128\ \Omega$		$C_p = 425.9$ fF
$\varepsilon_{r,\text{eff}} = 1.27$		$L_s = 5.696$ nH
$d = 11.30$ mm		
$L_{1C} = 5$ mm	$\tau_h = 42.45$ ps	
$L_{1L} = 6.21$ mm		
$d_1 = 0.045$ mm		
$L_{sC} = 2.520$ nH		
$C_{pC} = 160.5$ fF		
$L_{sL} = 2.987$ nH		
$C_{pL} = 249.0$ fF		

Table 4.10: Parameters of models 2, 3 and 4 for the designed CRLH TL. Some parameters are used in several models.

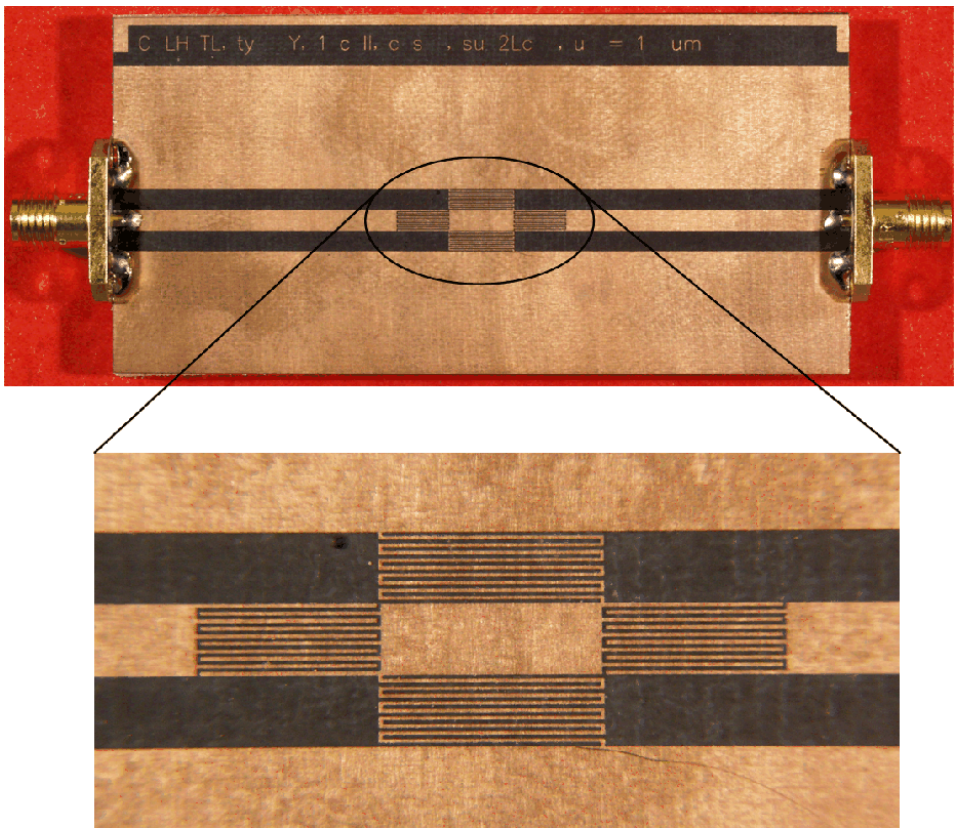

Figure 4.26: Picture of the designed one-cell CRLH TL.

c. Measurement results

The S parameters referred to the impedance of the host TL have been measured from 0.9 to 7.2 GHz with a HP8510C network analyzer by means of a TRL calibration. As illustrated in Figure 4.21(a), the reference planes are located in the middle of the series capacitors. The structures have been simulated with Ansoft HFSS and Ansoft Designer, for comparison. It is worth mentioning that with Designer, the metallization is considered as lossless and infinitely thin (considering non-zero metallization thickness and finite conductivity for CPW structures rather complicates the definition of the model in Designer). The measured and simulated S parameters are shown in Figure 4.27 and the extracted Bloch parameters in Figure 4.28.

Comments

- Significant discrepancies can be observed between HFSS and measurement results, especially for S_{11} and Z_{B}. However, the agreement for β_{B} is globally good.
- Surprisingly, Ansoft Designer results in a better agreement with measurements than HFSS results, despite the fact that metallization losses and thickness have not been taken into account.
- According to HFSS results, the designed structure exhibits the desired properties: it is almost perfectly balanced with $f_0 = 2.97$ GHz, which validates the proposed design method. The Bloch impedance around the transition frequency is slightly above $Z_{\mathrm{c}} = 128\ \Omega$, as can be expected from a CRLH TL with type T unit cell [see (4.28)].
- The measurement results reveal a band gap from $f_{\mathrm{p}} = 2.75$ GHz to $f_{\mathrm{s}} = 3.20$ GHz (0.45 GHz), which can be clearly observed on the Bloch parameters but is hardly detectable on the S parameters. It is noticeable that this band gap has an important effect on the frequency dependence of the Bloch impedance.
- The cutoff frequency of the LH band is $f_{\mathrm{cL}} = 1.16$ GHz, hence a LH bandwidth of 1.59 GHz, which corresponds to a bandwidth of 81% relative to the central frequency of the LH band.

Concerning the differences between HFSS and measurement results, some possible causes have been investigated. The resulting conclusions are summarized below:

- The effect of the tolerance on the metallization thickness t has been investigated. The designed structure has been simulated with $t = 12$ µm instead of 17 µm. This only resulted in a slight modification of the results, which was insufficient to explain the differences between simulations and measurements.
- The effect of an imprecision of the relative permittivity of the substrate has been investigated. The manufacturer provides the following value: $\varepsilon_r = 2.33 \pm 0.02$. The designed structure has been simulated with $\varepsilon_r = 2.2$, which is even beyond the tolerance range. This resulted in moderate modifications in the results, but insufficient to explain the differences between simulations and measurements.

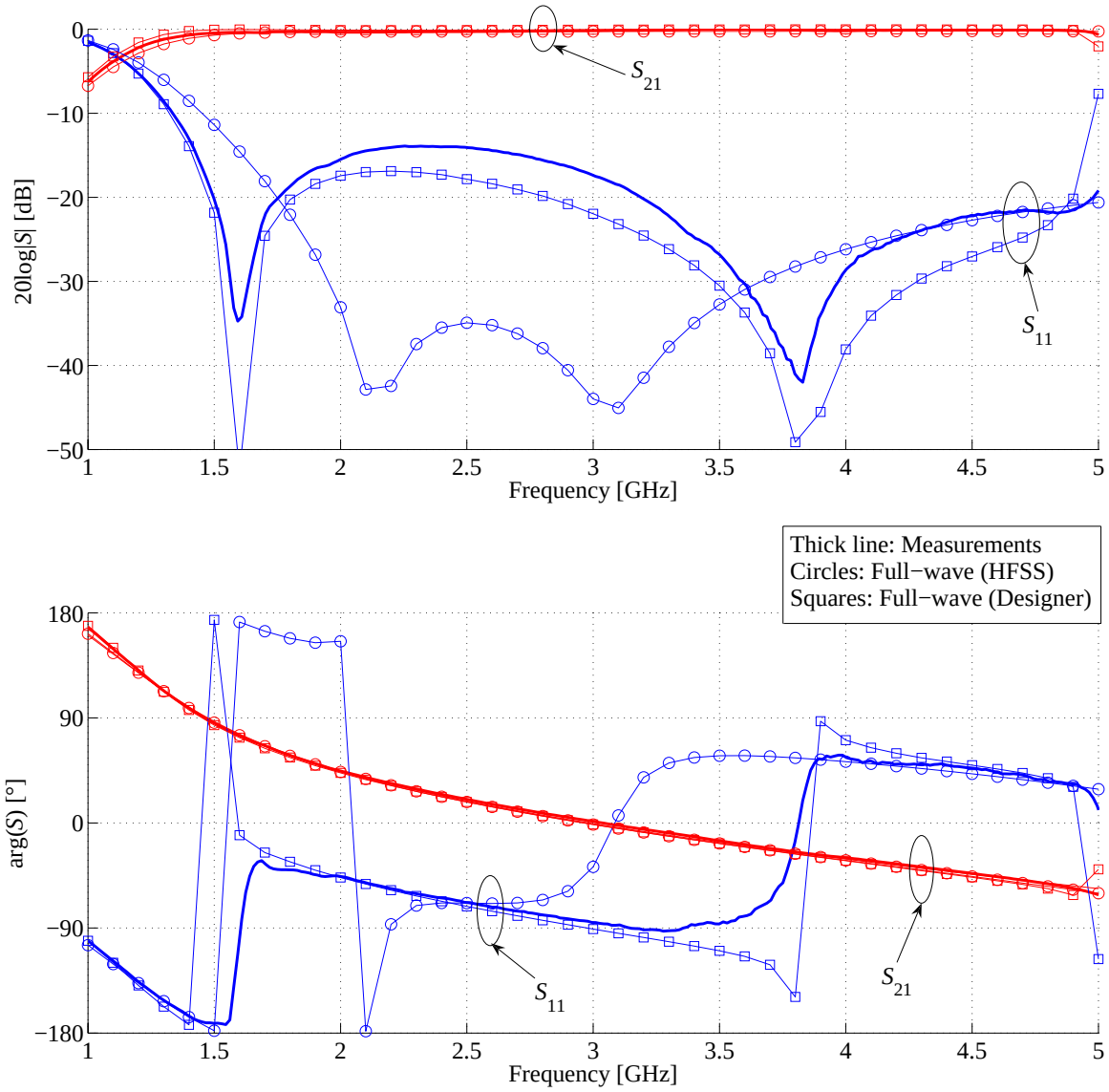

Figure 4.27: Measured and simulated S parameters for the designed CRLH TL. The reference impedance is the characteristic impedance of the host TL (about 128 Ω).

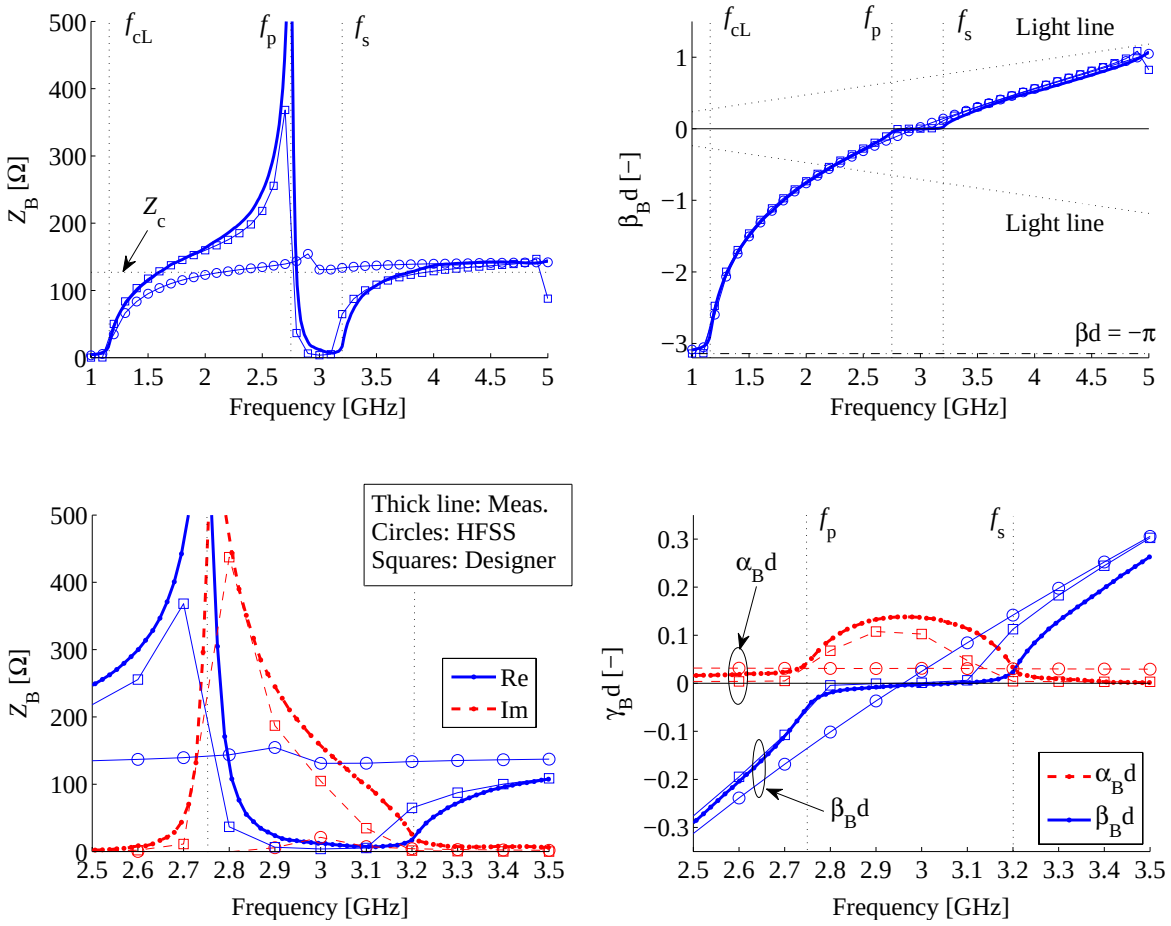

Figure 4.28: Bloch parameters extracted from full-wave simulation and measurement for the designed CRLH TL. Top: whole frequency range, Re[Z_B] and $\beta_B d$ only. Bottom: zoom around the transition frequency $f_0 = 3$ GHz, real and imaginary parts.

- The effect of an additional under etching of 10 µm has been investigated (all the strips are reduced by 20 µm and all the slots are enlarged by the same amount). It appeared that the corresponding simulation results are quite close to the measurements, although these new dimensions do not correspond to the actual dimensions of the realized structure. As a result, the question of the validity of HFSS simulations for structures with such small details should be further investigated.
- The strong mismatch between the 50 Ω coaxial cables and the 128 Ω host CPW could also be problematic. Indeed, such a mismatch is not favorable from the point of view of the excitation of higher order modes at these transitions. For a reliable TRL calibration, these higher order modes must have decayed to negligible values before reaching the structure under test. To that purpose, a distance λ_h is sometimes recommended between the SMA connectors and the device under test [234], a condition which is often not respected in practice due to the prohibitive size of the resulting devices. For the designed structure, this length was only $\lambda_h/3$ at 3 GHz, a value which may not be sufficient.
- The geometrical asymmetry of the considered layout elements possibly causes a problem of excitation of the parasitic even CPW mode, a phenomenon which does not manifest the same way in simulations and measurements. This may partially explain the differences between simulations and measurements.

In order to assess in more detail these problems of accuracy of HFSS, mismatch in the TRL calibration and elements asymmetry (the three last points above), some isolated layout elements (series capacitors and shunt inductors) with various geometrical parameters have been simulated and measured. The main conclusion is that the correspondence between measurement and simulation results worsens when the level of details increases, which can be related to the accuracy of the numerical solver for structures with small details (meander lines/gaps of 100 µm, for instance). As a result, it is desirable to keep the level of details above 150 µm, for which the correspondence between simulations and measurements is quite good. In any case, the results obtained here for the isolated elements have clearly demonstrated that the 50 Ω to 128 Ω mismatch does not prevent from a reliable TRL calibration. Finally, comparison of geometrically symmetrical and asymmetrical elements revealed that the geometrical asymmetry is not likely to be the cause of the discrepancies between simulations and measurements, as suggested above.

d. Multi-cell CRLH TLs

The two designed CRLH TLs have also been realized with 2 and 8 unit cells. The length L_1 of the series capacitors C_s inside the periodic structure (i.e., not the two extreme ones) have been determined using the approximate curves shown in Figure 4.17, in order to obtain a capacitance value twice as low as the two series capacitances $2C_s$ located at the two extremities, as it is required for CRLH TLs of type T. The resulting capacitance length L_1 is 2.33 mm for the designed structure. All the other dimensions are the same as for the corresponding one-cell CRLH TL. A picture of the resulting 2-cell CRLH TL is shown in Figure 4.29.

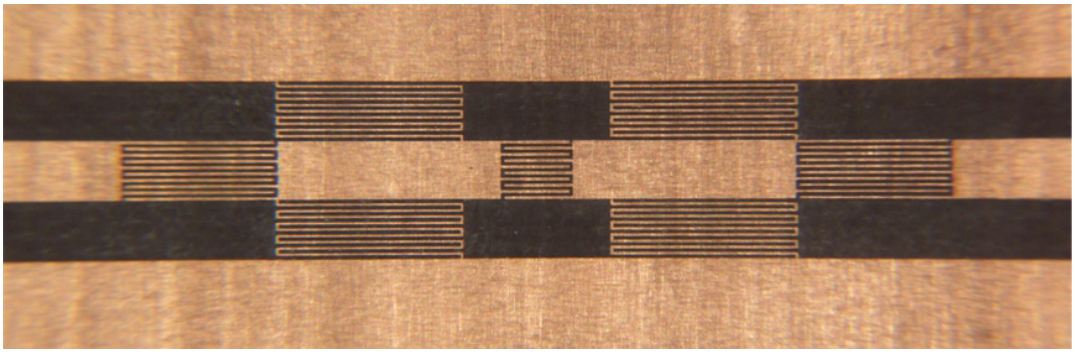

Figure 4.29: Layout of the designed CRLH TL with two cells. The reference planes are located in the center of the first and last series capacitors.

The S parameters referred to the impedance of the host TL have been measured from 0.9 to 7.2 GHz with a HP8510C network analyzer by means of a TRL calibration. For these measurements, a test fixture has been used for the connections with the network analyzer, thereby avoiding the need for soldering connectors on the devices, as was done for the measurements of the one-cell CRLH TLs previously presented. The measured and simulated S parameters are shown in Figures 4.30 and 4.31. The HFSS simulation has been performed only for the 2-cell structure, the 8-cell structure being too demanding for available computational resources.

Comments

- We observe the same kind of differences between HFSS and measurement results as for the one-cell CRLH TL: the correspondence for S_{21} is quite good, but not for S_{11}. Nevertheless, the correspondence for the phase of S_{21} is always very good (this phase is approximately zero at the transition frequency $f_0 = 3$ GHz).
- As for the one-cell CRLH TL, Ansoft Designer results agree better with measurements than HFSS results, despite the fact that metallization losses and thickness have not been taken into account.
- The presence of the unwanted unbalance gap can hardly be observed on the S parameters for the 2-cell CRLH TL, but it can be clearly seen for the 8-cell structure.

4.5.5 Conclusions on CPW CRLH TLs

We have presented here our first investigations on practical implementations of CRLH TLs. The CPW host TL was chosen as a preliminary test case before the investigation of CRLH TLs in CPS, which are more problematic regarding experimental characterizations due to the need for baluns in the measurement setup. The main conclusions of these investigations are summarized below:

- The accuracy of the various circuit models for CRLH TLs strongly depends on the topology of the layout elements used in the structure. For the considered CRLH TLs, it has

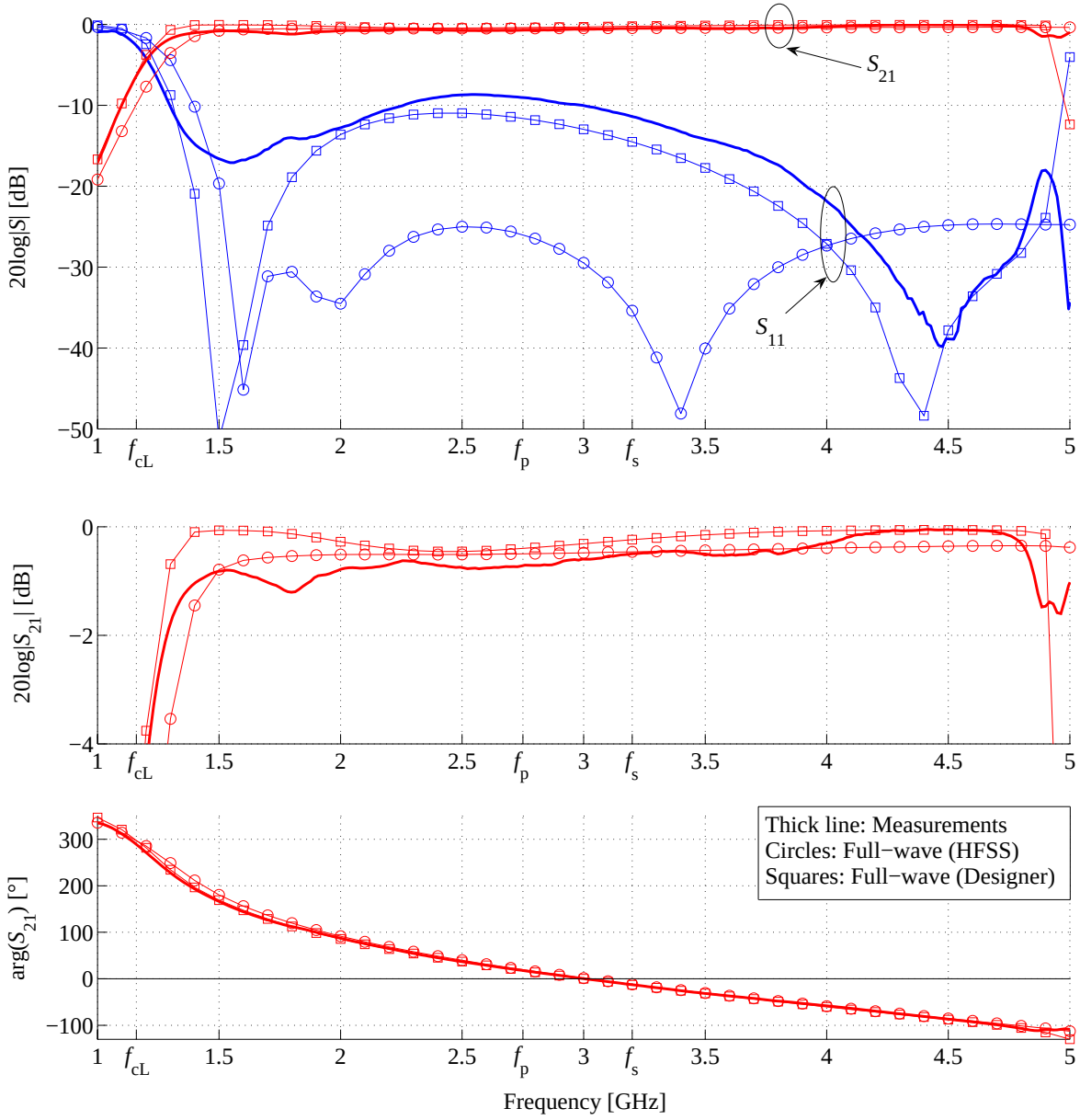

Figure 4.30: Measured and simulated S parameters for the designed CRLH TL with 2 cells. A vertical zoom on S_{21} is also provided. Only the phase of S_{21} is shown for clarity. The reference impedance is the characteristic impedance of the host TL (about 128 Ω).

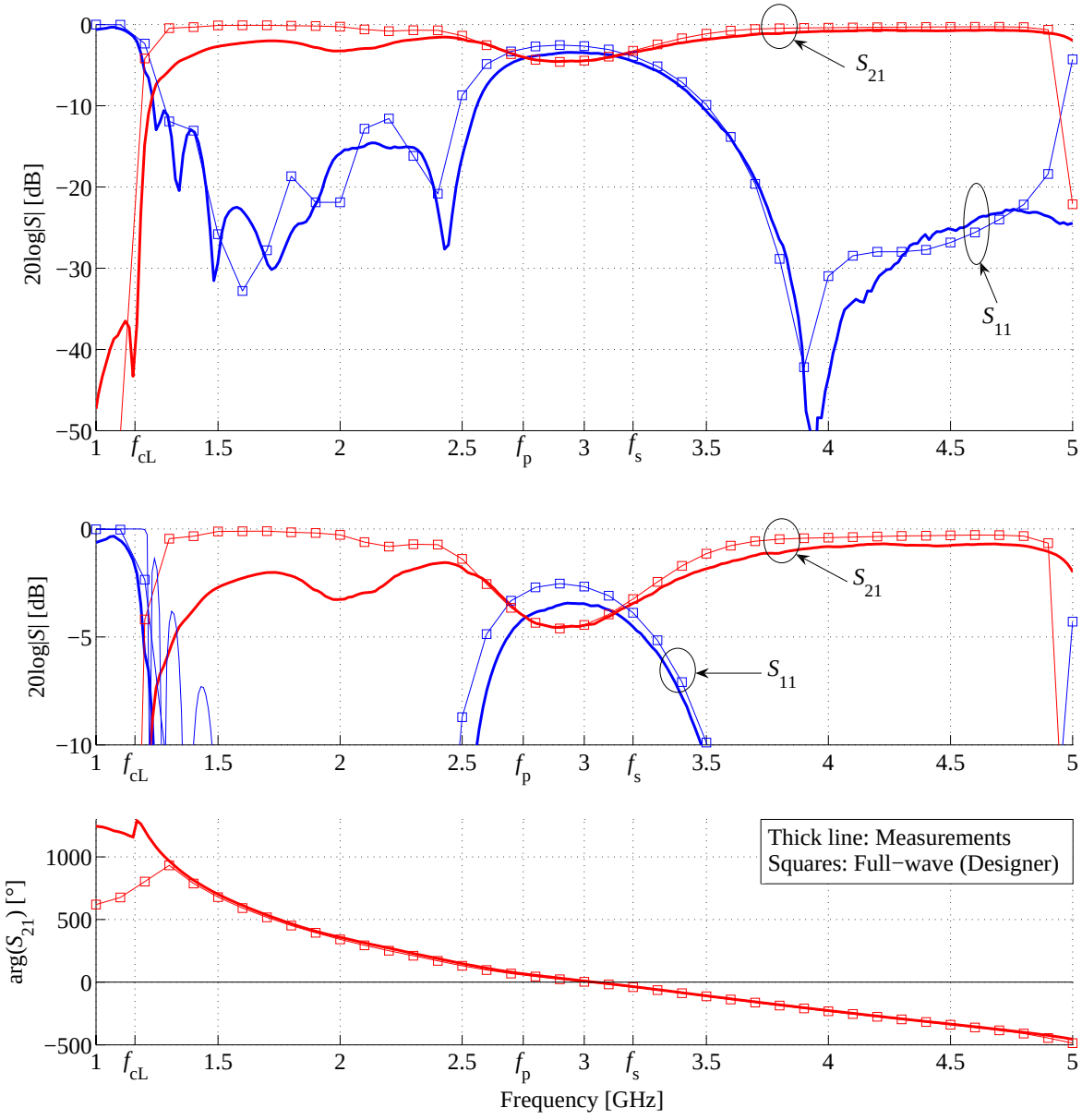

Figure 4.31: Measured and simulated S parameters for the designed CRLH TL with 8 cells. A vertical zoom on the S parameters is also provided. Only the phase of S_{21} is shown for clarity. The reference impedance is the characteristic impedance of the host TL (about 128 Ω).

been observed that the model 2 of Figure 4.22(b) offers the best compromise between accuracy and complexity (see Section 4.5.2).

- Achieving the balanced condition with a desired transition frequency is a difficult task because the layout elements loading the host TL are more complex that just a series capacitance or a shunt inductance. To that respect, an elaborated design technique has been developed and successfully tested. This technique allows designing balanced CRLH TLs with a given transition frequency, for a given topology of layout elements (see Section 4.5.3).
- Significant discrepancies have been observed between Ansoft HFSS and measurement results. As a consequence, CRLH TLs which are perfectly balanced according to HFSS results appear strongly unbalanced according to measurement results. These discrepancies were shown to increase with the level of details of the structure. We have come to the conclusion that the dimensions of the small details (meander lines/gaps) should be kept above 150 µm to guaranty a reasonable level of accuracy between HFSS and measurements. Surprisingly, Ansoft Designer has provided better results than HFSS, despite the fact that metallization losses and thickness have not been taken into account. Nevertheless, Designer is less appropriate for CPS circuits, which is why we keep on using HFSS for further investigations on CPS CRLH TLs.

The accuracy of the CRLH TL models and numerical solvers should be further investigated in the context of real applications. In particular, the impact of a given degree of unbalance on the performances of a device should be first assessed, before putting more effort toward the achievement of a perfect correspondence between simulations and measurements around the transition frequency.

4.6 CRLH TLs in CPS

4.6.1 Motivation and objectives

The objective of this section is to investigate CRLH TLs implemented in CPS, which are the building blocks of the volumetric layered TL-based MTM studied in Chapter 5. No particular specifications are imposed at this stage, except that these structures are aimed at being operated in the LH band with a high level of homogeneity, for the reasons explained in Chapter 5. Several results presented in this section can be found in [236].

4.6.2 Description of the considered CRLH TL

a. Design goals

The design method developed in Section 4.5.3 can also be used for the design of balanced CPS CRLH TLs. However, it has been observed that it is difficult to obtain compact unit cells in terms of wavelength, as wanted here, while keeping the balanced condition, because this

requires high values of both the series capacitance C_s and the shunt inductance L_p. In many practical designs, the main difficulty is to obtain high shunt inductances (L_p) values. On the contrary, high values of series capacitances are easier to obtain, for instance by using high permittivity substrates or different topologies such as metal-insulator-metal (MIM) capacitors. For this reason, it has been decided to renounce to the balanced condition, and thus to consider unbalanced CRLH TLs. For the designed structures, we will be in the case $f_s < f_p$. By contrast with the CPW CRLH TLs presented in Section 4.5, the designs will be performed here on asymmetrical unit cells, thereby avoiding the need for twice as large lumped elements at the two extremities of the periodic structure.

b. Host TL

The following choices have been made for the host TL [see Figure 4.12(b)]:

- Substrate: Rogers RT/Duroid 5870 ($\varepsilon_r = 2.33$, $\tan\delta = 0.0012$, $h = 0.254$ mm (10 mil) and $t = 17$ µm).
- Dimensions of the host TL: $s = 1$ mm and $w = 2.5$ mm.

With these parameters, the effective relative permittivity $\varepsilon_{r,\text{eff}}$ and characteristic impedance Z_c of the CPS are given in Table 4.11. The chosen dimensions allows decreasing Z_c compared to the initial case $s = w = 2$ mm adopted for the study of the layout elements in Section 4.4.6. Indeed, it is expected that a lower mismatch with the 50 Ω coaxial cables will be beneficial for S parameters measurements.

	$\varepsilon_{r,\text{eff}}$ [-]	Z_c [Ω]
$s = 1$ mm, $w = 2.5$ mm	1.13 / 1.20	165 / 166
$s = 2$ mm, $w = 2$ mm	1.12 / 1.17	217 / 218

Table 4.11: Parameters of the CPS host TL with the chosen substrate and dimensions. In each cell, the first number has been obtained from quasi-static approximation (see Section 4.4.1) and the second from the port solver of HFSS at 3 GHz.

c. Shunt inductors

The geometrically symmetrical meander line inductor shown in Figure 4.19(b) has been chosen to implement the shunt inductances, with the dimensions $s_2 = 3$ mm, $g_1 = w_1 = 150$ µm, $s_1 = 200$ µm, $L_1 = 4$ mm ($\Rightarrow L_2 = 6$ mm) and $N = 4$. This layout element has been simulated with HFSS from 1 to 5 GHz and the corresponding lumped element model has been extracted with the "fixed frequency" (FF) at 3 GHz extraction method described in Section 4.4.3. The extracted parameters are [see Figure 4.16(b)]: $L_p = 8.89$ nH, $C_{pL} = 116$ fF and $L_{sL} = 5.69$ nH. The accuracy of the model is good [$\Delta S_{\text{MSE}} < 0.020$ and $\Delta S_{\text{max}} < 0.040$, see (4.37)].

d. Series capacitors

The MIM capacitor of type 2 shown in Figure 4.20 has been chosen to implement the series capacitances, with $L_1 = 3$ mm. In the same conditions as for the shunt inductor, a lumped element model has been extracted from full wave simulations. We obtain [see Figure 4.16(a)]: $C_\mathrm{s} = 386$ fF, $L_\mathrm{sC} = 1.46$ nH and $C_\mathrm{pC} = 88.0$ fF. The accuracy of the model is good [$\Delta S_\mathrm{MSE} < 0.024$ and $\Delta S_\mathrm{max} < 0.054$, see (4.37)].

e. CRLH TLs

The considered CRLH TL is obtained by cascading the shunt inductor with the series capacitor, without adding interconnecting TL sections. The resulting structure is shown in Figure 4.32 (with two cells), along with the circuit model (model 2) corresponding to this asymmetrical unit cell. It can be observed that because of the chosen topology of capacitors, one cell over two is located on the other side of the substrate, which means that the lattice constant is $2d$ instead of d. However, this small difference between two consecutive cells does not significantly affect the overall performances of the structure, which therefore will be still considered as a d-periodic structure.

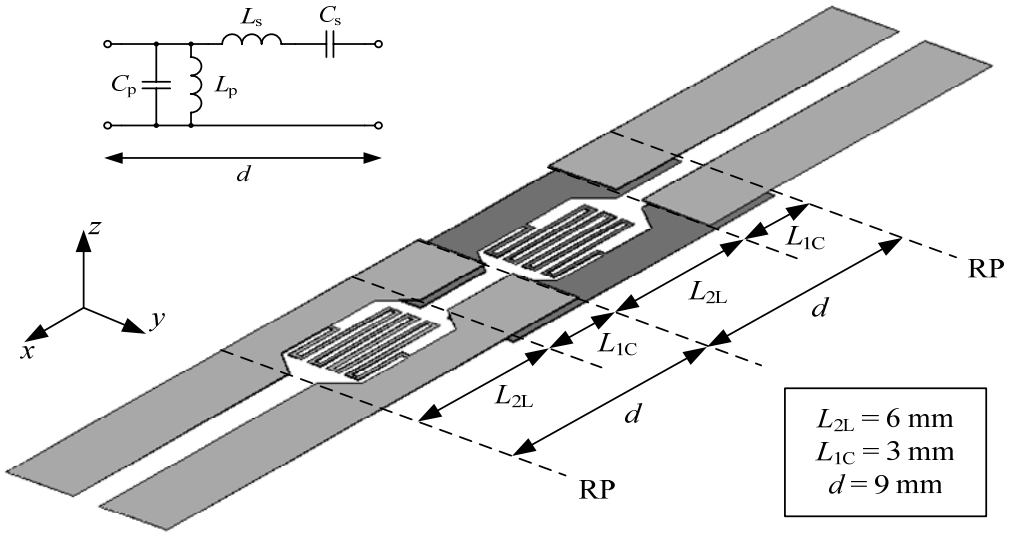

Figure 4.32: Layout of the considered CPS CRLH TL with two unit cells. One cell over two (in dark) is located on the other side of the substrate (which is not shown for clarity). 'RP' denotes the position of the reference planes.

Using the models shown in Figure 4.16 for the layout elements, the considered (pseudo) unit cell can be modeled as shown in Figure 4.33(a). This model has been referred to here as "model 4", by analogy with the terminology chosen in Section 4.5 for CPW structures. This model being relatively complex for analytical manipulations, it can be further approximated by the "model 2" shown in Figure 4.33(b), with C_s and L_p identical as in model 4, and L_s and

C_p given by

$$\begin{cases} L_\mathrm{s} = L_\mathrm{sL} + L_\mathrm{sC} = 7.15 \text{ nH} \\ C_\mathrm{p} = C_\mathrm{pL} + C_\mathrm{pC} = 204 \text{ fF} \end{cases} \tag{4.48}$$

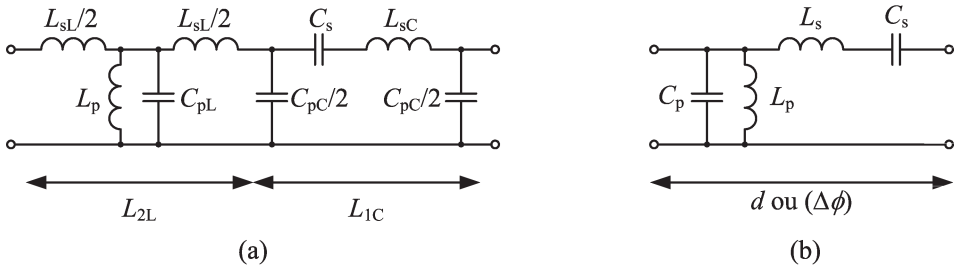

Figure 4.33: Circuit model for the considered asymmetrical CRLH TL unit cell. (a) Model 4, (b) model 2.

4.6.3 Performances: Full-wave and circuit models

A single (pseudo) unit cell of this structure has been simulated with HFSS from 1 to 5 GHz, and the Bloch parameters have been extracted from the resulting S parameters assuming a d-periodic structure. The results are shown in Figures 4.34 and 4.35. First, it can be observed on the dispersion diagram of Figure 4.35 that the structure exhibits a LH bandwidth of 1.79 GHz, from $f_\mathrm{cL} = 1.21$ GHz to $f_\mathrm{s} = 3$ GHz, and an unbalance gap from f_s to $f_\mathrm{p} = 3.78$ GHz. The homogeneity of this CRLH TL can be evaluated as explained in Section 4.3.2, except that we take f_s as the reference instead of f_0. We find $d/\lambda_\mathrm{h} = 0.099$, thus the unit cell is ten times smaller that the guided wavelength at the highest frequency of the LH band, which can be considered as a good level of homogeneity for structures based on layout elements (higher level of homogeneity can be achieved with SMT loading elements, but these structures appear as rather limited in frequency).

Some precisions are needed here concerning the Bloch impedances shown in Figures 4.34 and 4.35. As the considered unit cell is asymmetrical, it has different Bloch impedances for the two propagation directions. Figure 4.34 shows these two Bloch impedances Z_B^+ and Z_B^- extracted from full-wave results. It can be seen that these two impedances have important imaginary parts at all frequencies, and that they approximately satisfy the relation $Z_\mathrm{B}^+ = (Z_\mathrm{B}^-)^*$ in the pass-bands, which was shown in Section 4.2.7 to be a property of lossless asymmetrical periodic structures. These complex impedances do not allow for matching to real impedances, which is why symmetrical structures are usually preferred in practical applications of the CRLH TL. As a result, in an application using a given number of cells of the designed CRLH TL, the first and last cells should be modified in such a way that the structure is terminated with lumped elements of value $2C_\mathrm{s}$ or $2L_\mathrm{p}$, according to the symmetrical type T or Π unit cells, respectively. Here, we do not implement these termination elements, but we rather apply the symmetrization process described in Section 4.2.8. This technique allows determining the Bloch impedance of the symmetrical (type T or Π) periodic structure corresponding to the actual

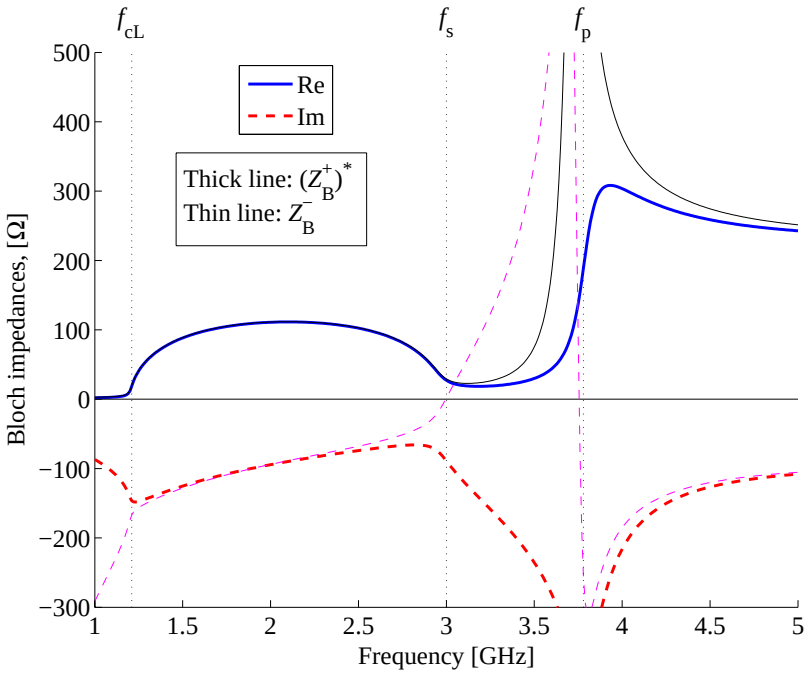

Figure 4.34: Bloch impedances for the considered asymmetrical CPS CRLH TL, extracted from full-wave simulation.

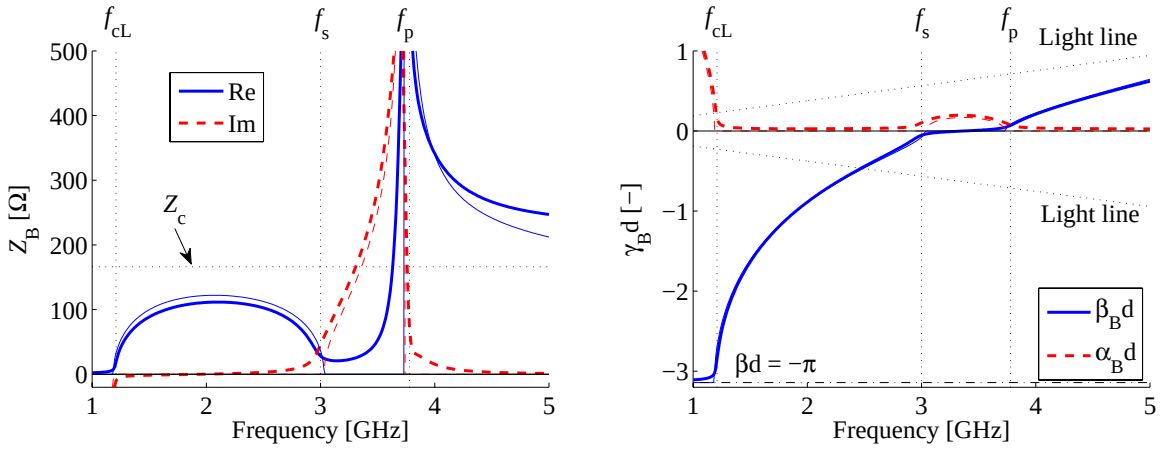

Figure 4.35: Bloch parameters for the considered CPS CRLH TL, extracted from full-wave simulation (thick line) and circuit model 2 (thin line). The Bloch impedance is that of the symmetrical type T unit cell corresponding to the actual asymmetrical unit cell (see text).

asymmetrical one, by assuming that this symmetrization with the termination elements can be done in an exact way.

Let us first consider the circuit model 2 shown in Figure 4.33(b), on which we apply the symmetrization process described in Figure 4.3(b). It simply consists in redistributing the series branch on both sides of the unit cell, which thus leads to the type T unit cell. For such a transformation, the new symmetrical Bloch impedance was shown to be the average of the two Bloch impedances of the initial asymmetrical structure, or

$$Z_{\mathrm{B}} = \frac{Z_{\mathrm{B}}^{+} + Z_{\mathrm{B}}^{-}}{2} \tag{4.49}$$

Considering that the physical unit cell can be represented by model 2 with a reasonable level of accuracy, which is the case here, the operation expressed in (4.49) can also be applied on the full-wave results, which leads to the Bloch impedance shown in Figure 4.35. This quantity is thus the Bloch impedance of the symmetrical type T unit cell corresponding to the periodic structure under study. In Figure 4.35, the results obtained with model 2 are also shown. A very good agreement is observed with the full-wave results.

4.6.4 Balanced-unbalanced transitions: Baluns

For the experimental characterization, baluns are required for the transitions between the balanced host CPS and the unbalanced coaxial cables of the measurement setup. Such baluns also need to be implemented in each standard of the TRL calibration kit. The chosen baluns, referred to as double-Y baluns, make the transition between CPS and CPW with finite width ground planes (FWCPW). A description and design rules for this kind of baluns can be found in [233, 237–239]. This topology of balun was chosen because it can provide very wide band balanced-unbalanced transitions compared to other types of baluns. The complete transition between a 115 Ω FWCPW and the 166 Ω host CPS is shown in Figure 4.36. The FWCPW and CPS lines in the baluns have a characteristic impedance of 121 Ω and 125 Ω, respectively. These two impedances must be (approximately) the same for proper operation of the balun. It can be noted that the two ground planes of each of the three FWCPW in the balun have to be connected, by air bridges or wire-bonds, for instance. In the present case, these connections have been realized by soldering copper wires of 130 µm of diameter.

4.6.5 Realizations and measurement results

Two prototypes of the designed CRLH TL with 2 and 6 cells have been realized using the same PCB etching process already discussed in Section 4.5.4.b.. An even number of cells had to be considered due to the pseudo periodicity of the structure, such that the two extremities of the circuit are on the same side of the substrate. A picture of the 6-cells CRLH TL is shown in Figure 4.37. The S parameters referred to the impedance of the host TL have been measured from 0.9 to 7.2 GHz with a HP8510C network analyzer by means of a TRL calibration. The measured and simulated S parameters for the two CRLH TLs are shown in Figures 4.38 and

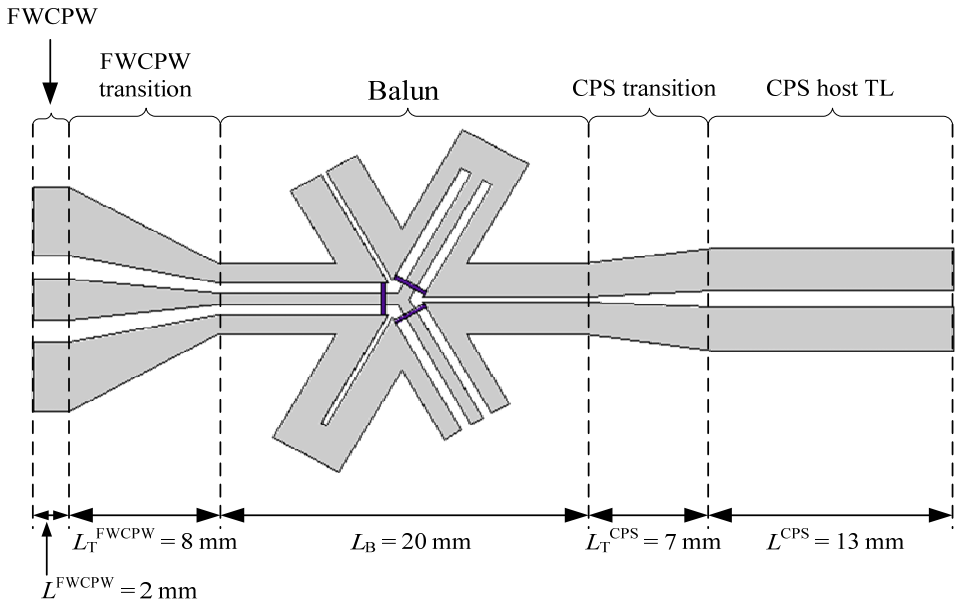

Figure 4.36: Complete transition between a FWCPW and the CPS host TL including a double-Y balun. The total length of the transition is 50 mm. Note the presence of three air bridges (in dark) in the center of the balun.

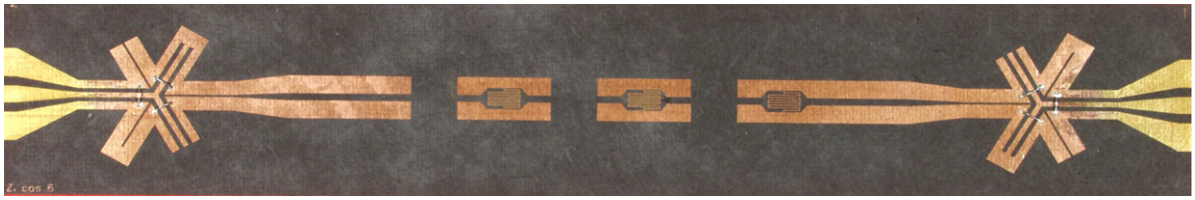

Figure 4.37: Picture of the designed CPS CRLH TL with 6 unit cells and the two baluns. One cell out of two is on the other side of the substrate.

4.39. The results obtained with model 2 are also shown for comparison. As these structures are asymmetrical, we have $S_{11} \neq S_{22}$, but here we only show S_{11} for clarity.

Comments

- The agreement between simulation and measurement results is quite good, excpet around 2.6 GHz and 1.5 GHz, where unphysical behaviors have been observed ($|S| > 0$ dB). The corresponding bands on the graphs have been removed. As this phenomenon appears for each structure at the same frequency[5], it is believed that it is related to parasitic effects occurring in the baluns. Indeed, reference [237] explains that resonances of the even FWCPW and common CPS modes can affect the performances of the baluns. This phenomenon may significantly affect the accuracy of the TRL calibration, since the latter

[5]This is also the case for a third structure based on another design, which is not commented here.

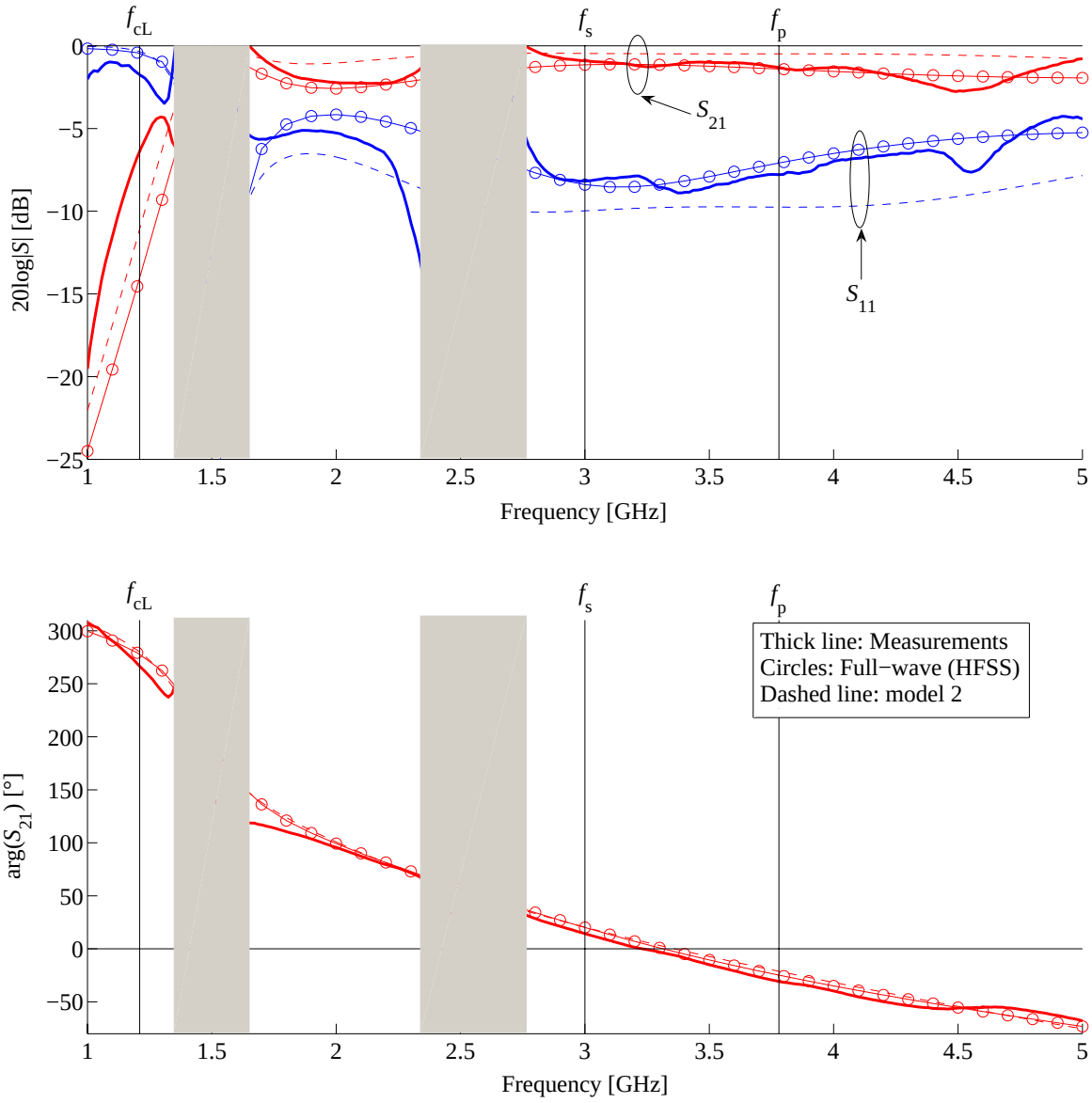

Figure 4.38: S parameters for the 2-cell CPS CRLH TL. The reference impedance is the characteristic impedance of the host TL (about 166 Ω). S_{22} and arg(S_{11}) are not shown for clarity.

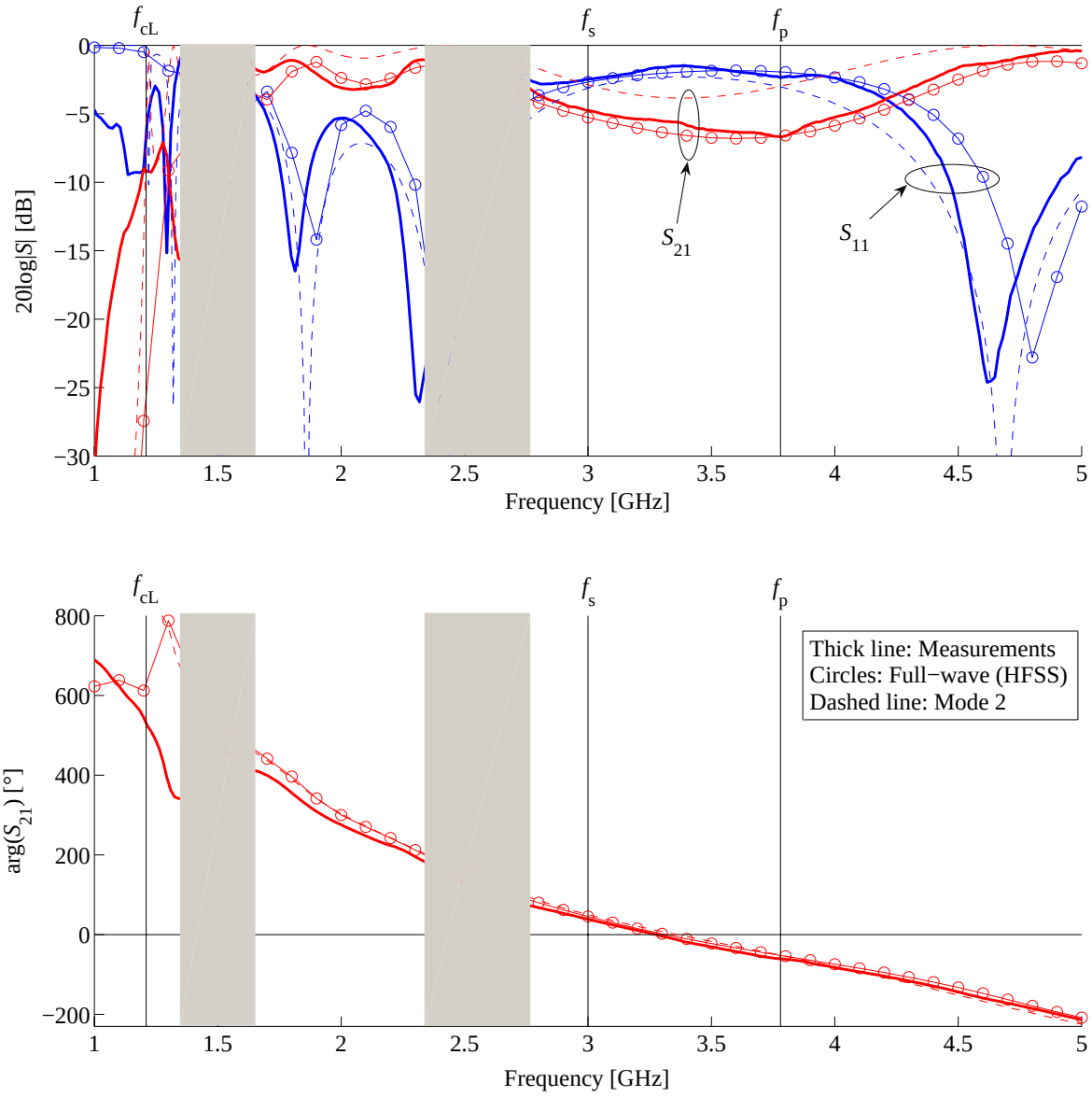

Figure 4.39: S parameters for the 6-cell CPS CRLH TL. The reference impedance is the characteristic impedance of the host TL (about 166 Ω). S_{22} and arg(S_{11}) are not shown for clarity.

is based on the assumption that only one mode can propagate in the structure and calibration standards.

- The model 2 provides results of reasonable accuracy. It can be noted that the accuracy of this model is always good for the phase of S_{21}.
- In the pass-bands, the structure is not well matched, mainly because of the asymmetry of the chosen unit cell topology.
- The unbalance gap revealed by the Bloch wave analysis of a single unit cell (from f_s to f_p, see Figure 4.35) cannot be clearly observed in the S parameters for the 2-cell CRLH TL. However, for the 6-cells CRLH TL, the presence of this band gap can be seen in the modulus of the S parameters, although its limits cannot be clearly seen.
- As expected, the phase of S_{21} is zero at some frequency in the band gap between f_s and f_p.

4.6.6 Conclusions on CPS CRLH TLs

We have presented the investigations performed on a practical implementation of CRLH TL implemented in CPS. The main conclusions of these investigations are summarized below:

- We have realized and characterized a CPS CRLH TL based on layout elements for which the unit cell is more than ten times smaller than the wavelength in all the whole LH band, hence a fairly high level of homogeneity. This structure employs meander line inductors and MIM capacitors using both sides of the substrate.
- The measurement of CPS circuits by means of a TRL calibration was shown to be problematic, probably because of parasitic effects occurring in the baluns, or between the two baluns (excitation of parasitic modes). However, these unwanted effects seem to appear only in some specific frequency bands, where unphysical behaviours have been observed.
- Outside these bands, a good agreement between simulations and measurements has been observed, thereby validating the analytical and numerical analyzes.

It can be noted that a second prototype based on another design has been built and measured. Very similar conclusions have been reached with this variant. These results will be used for the realization of the volumetric TL-based MTM presented in Chapter 5.

5 Volumetric layered TL-based MTMs

5.1 Introduction and motivations

5.1.1 Context and investigated structures

The main goal of the ESA project within which this part of the work was carried out consisted in the investigation of novel antenna concepts using LHM slabs to enhance the radiation performances. It is important to note here that it has been decided from the very beginning of the project to concentrate the efforts on volumetric (or 3D) LHM that can be considered as material filling, and thus to go beyond the well demonstrated antenna applications of planar 1D and 2D LHM, which essentially consist of guiding or radiating structures. However, most of the volumetric LHM reported at that time consisted of arrays of metallic and/or dielectric resonant inclusions suffering from a very narrow band of operation (see Section 2.2), which is why other solutions have been sought after.

The retained solution is based on a recently proposed topology of volumetric MTM based on the TL approach [117]. These structures are obtained by layering several planar TL-based MTMs on top of each other. The idea is to take benefit of the non-resonant nature of planar TL-based MTMs to realize volumetric structures which are expected to act as materials, in the common sense of the word. These structures will be referred to in this work as "volumetric layered TL-based MTMs". A possible implementation of such a structure is shown in Figure 5.1. It consists of a stacking of 1D CRLH TLs implemented in a coplanar stripline (CPS) host TL, as those investigated in Section 4.6. The main goal of the investigations carried out in the context of the project was to assess the ability of such a structure to act as a volumetric LHM (or more generally a MTM with a CRLH response) when it is embedded in a radiating system such as the patch antenna shown in Figure 5.1. Potential antenna enhancements that can be expected from such a MTM-based antenna are basically the same as for the CRLH TL antenna applications reported in Section 2.4.2.b., that is, miniaturized or enlarged half-wavelength resonant antennas, zero-order resonant antennas or multi band antennas obtained by combining several of these principles. When used as a grounded slab, such a MTM can also lead to potential interesting leaky-wave antenna concepts. A selection of results on volumetric layered TL-based MTMs reported is this chapter have been presented by the author in [236].

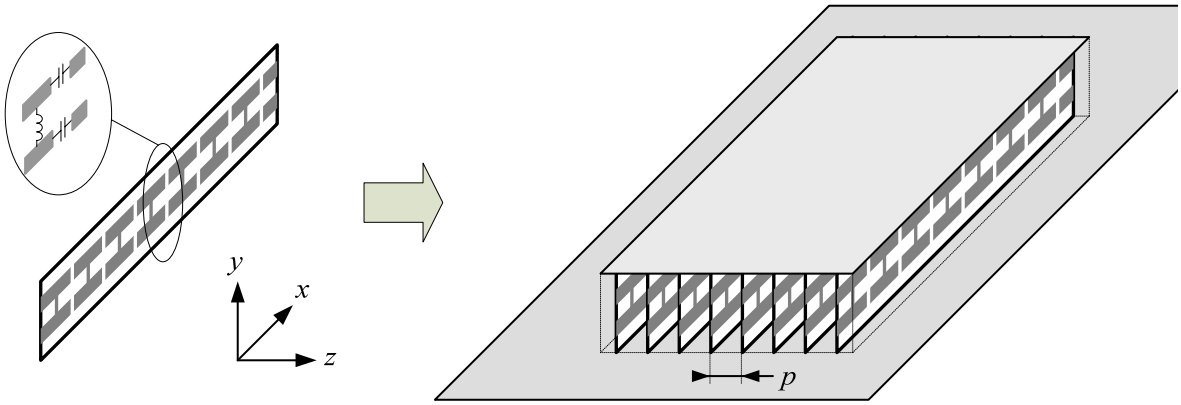

Figure 5.1: Volumetric layered TL-based MTM obtained by stacking 1D planar CRLH TLs implemented in CPS technology. The structure can be used as a substrate for microstrip patch antennas.

5.1.2 Content and organization of the chapter

This chapter presents a detailed selection of the most relevant investigations performed on volumetric layered TL-based MTMs and their planar antenna applications. The chapter is organized as follows. First, the effect of stacking CPS CRLH TLs in the vertical direction is investigated in Section 5.2. Then, the realized prototype of volumetric layered TL-based MTM is presented in Section 5.3, and its properties when it is placed in a microstrip configuration are numerically investigated in Section 5.4. A simple experimental test in which the realized structure is used as a substrate for a microstrip line is subsequently reported in Section 5.5. Finally, the investigations performed on microstrip patch antennas using the realized MTM slab as a substrate are reported in Section 5.6. Conclusions on the type of structures can be found in Section 5.7.

5.1.3 Preliminary remark

As the main goal is to assess the overall behaviour of this type of structures, we do not have at this stage precise specifications on the Bloch propagation constant and Bloch impedance of the structure. As a result, some parameters have been imposed in order to provide a framework for these investigations:

- The chosen substrate for the layers is the same as in Section 4.6, that is, the Rogers RT/Duroid 5870 with $\varepsilon_r = 2.33$, $\tan\delta = 0.0012$, $h = 0.254$ mm (10 mil) and $t = 17$ µm.
- The characteristics of the CPS host TL of a single layer are the same as in Section 4.4.6, that is, $s = w = 2$ mm, which corresponds to a characteristic impedance $Z_c = 218\ \Omega$ and an effective relative permittivity $\varepsilon_{r,\text{eff}} = 1.17$.

5.2 Effect of stacking CPS circuits

The effect of stacking CPS circuits in the vertical direction is investigated in this section, first on the host TL, then on the shunt inductors and series capacitors, and finally on the CRLH TLs.

5.2.1 Effect of stacking on the properties of the host TL

First of all, the effect of the separation distance between layers on the properties of the host TL is investigated. It is clear that the host TL is now a multiconductor TL with an infinite number of conductors, but we only consider here the mode of operation illustrated in Figure 5.2(a), in which each CPS in the stacking supports a "CPS-like" mode with propagation along x, as illustrated by the field lines in the figure. As a consequence, the unit cell along the vertical direction consists of a single CPS between periodic boundary conditions, as shown in Figure 5.2(b). The port solver of HFSS has been used to compute the effective relative permittivity $\varepsilon_{r,\text{eff}}$ and characteristic impedance Z_c for the configuration shown in Figure 5.2(b). Although the structure is not perfectly symmetrical along the vertical direction (because of the presence of the substrate), the PBC have been approximated with PMC. This approximation will be adopted for all the simulations performed in Section 5.2. Figure 5.3 shows the evolution of $\varepsilon_{r,\text{eff}}$ and Z_c with the separation distance p, for the chosen CPS line in the stacked configuration. It can be observed that Z_c dramatically increases when p decreases.

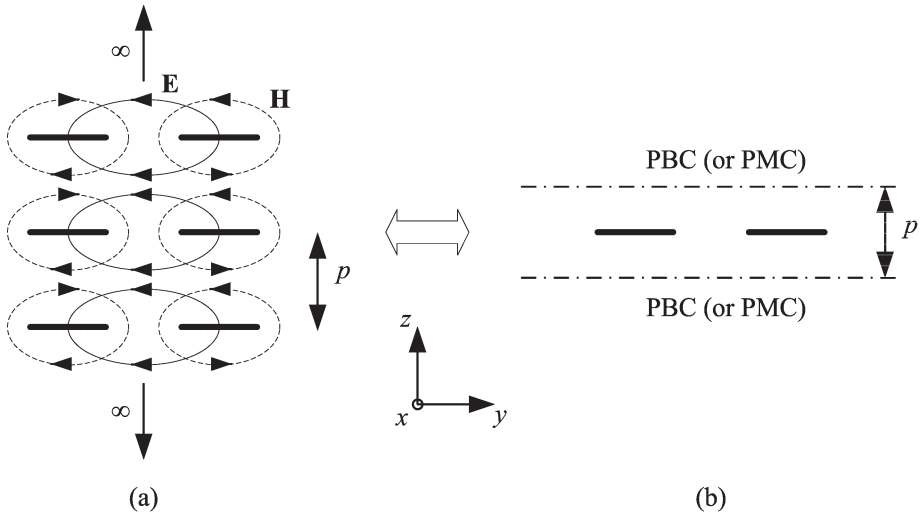

Figure 5.2: (a) CPS stacked in the vertical z direction (cross-section view). The substrates are not shown here. (b) Equivalent structure for the considered mode of operation. Periodic boundary conditions (PBC) can be replaced (approximated) by perfect magnetic conductors (PMC) if the unit cell is (almost) symmetrical along the vertical direction.

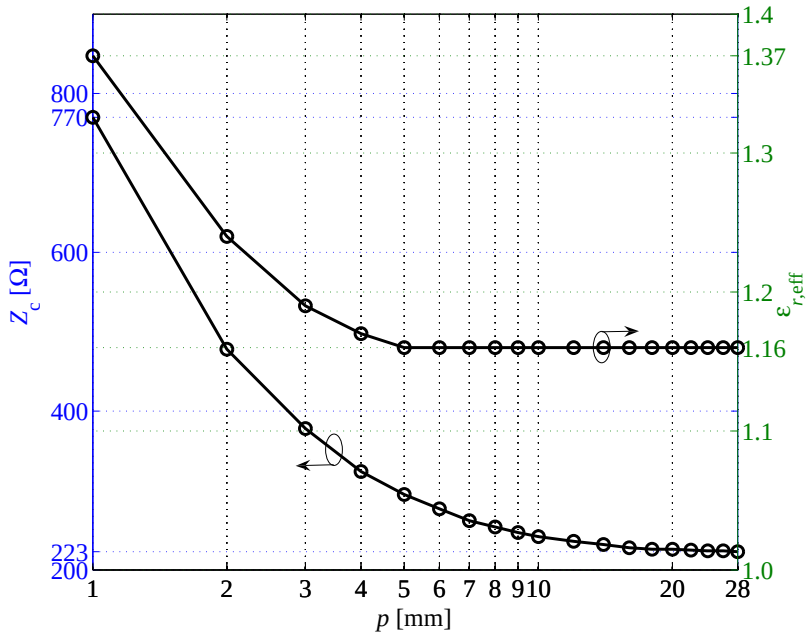

Figure 5.3: Evolution of $\varepsilon_{r,\mathrm{eff}}$ and Z_c for the chosen CPS in the stacked configuration in function of the separation distance p.

5.2.2 Effect of stacking on layout elements

The goal is to evaluate how the properties of layout elements such as shunt inductors and series capacitors are affected when the same structure is stacked in the vertical direction. It can be noted that in principle, a circuit element is used to represent a localized effect, and its value is therefore not expected to change with the surrounding environment. Moreover, if the objects placed in the vicinity of a primary circuit influence the properties of the latter, these effects should be accounted for by coupling elements such as mutual inductances and coupling capacitances. Such a representation would be the most representative of the physical mechanism involved in the system. However, a different and more straightforward approach has been adopted here. Indeed, instead of determining the aforementioned coupling elements, we have rather directly determined the *effective* inductances and capacitances seen by the host CPS in its stacked configuration. The resulting quantities, which thus implicitly contains the information on the coupling mechanism, have been simply deduced from circuit model extraction performed on the corresponding discontinuity loading the host TL of Figure 5.2(b).

a. Shunt inductors

We consider the geometrically symmetrical shunt meander line inductors shown in Figure 4.19(a) with the geometrical parameters $g_1 = w_1 = 150$ µm, $s_1 = 157$ µm, $N = 3$ and L_1 takes two different values: $L_1 = 2$ and 4 mm. The effect of stacking is evaluated by

comparing two cases: a single open CPS and a stacked CPS with a quite small inter-layer spacing $p = 2$ mm. These structures have been simulated with HFSS from 1 to 5 GHz and the corresponding lumped element models have been extracted with the "fixed frequency" (FF) at 3 GHz extraction method described in Section 4.4.3. The results are reported in Table 5.1. For each structure, the accuracy of the model is good [$\Delta S_{\mathrm{MSE}} < 0.05$ and $\Delta S_{\max} < 0.08$, see (4.37)]. It can be observed that the stacking results in

- a decrease of the shunt inductance L_{p} ($\sim 20\%$), and
- an important decrease of the shunt capacitance C_{pL} and an important increase of the series inductance L_{sL}.

	L_1 [mm]	L_{p} [nH]	C_{pL} [fF]	L_{sL} [nH]
Open	2	3.55	48.3	1.67
	4	6.01	92.5	3.11
Stacked	2	2.65	16.16	3.29
$p = 2$ mm	4	4.87	58.3	6.45

Table 5.1: Extracted lumped elements for two shunt meander line inductors in CPS in two different situations: open CPS and stacked CPS with $p = 2$ mm (see Figure 4.16(b) for the equivalent circuit).

b. Series capacitors

We consider the metal-insulator-metal (MIM) capacitors of type 3 shown in Figure 4.20 (one in each conductor of the CPS) with the dimensions $g_1 = 0.5$ mm and L_1 takes two different values: $L_1 = 1.5$ and 3.5 mm. The effect of stacking is evaluated by comparing two cases: a single open CPS and a stacked CPS with $p = 2$ mm. These structures have been simulated with HFSS from 1 to 5 GHz and the corresponding lumped element models have been extracted with the "fixed frequency" (FF) at 3 GHz extraction method described in Section 4.4.3. The results are reported in Table 5.2. For each structure, the accuracy of the model is good [$\Delta S_{\mathrm{MSE}} < 0.04$ and $\Delta S_{\max} < 0.12$, see (4.37)]. It can be observed that the stacking results in

- very small modification of the series capacitance C_{s}.
- an important decrease of the shunt capacitance C_{pL} and an important increase of the series inductance L_{sL}. This is the same tendency as observed for the shunt inductors.

The fact that series inductances increase and shunt capacitances decrease with the stacking is consistent with the increase of the characteristic impedance of the host TL observed in Section 5.2.1.

	L_1 [mm]	C_s [fF]	L_{sC} [nH]	C_{pC} [fF]
Open	1.5	133	0.17	40.2
	3.5	318	2.44	69.4
Stacked	1.5	140	2.12	18.0
$p = 2$ mm	3.5	325	5.74	32.5

Table 5.2: Extracted lumped elements for two series MIM capacitors in CPS in two different situations: open CPS and stacked CPS with $p = 2$ mm (see Figure 4.16(a) for the equivalent circuit).

c. Intermediate conclusion

At this stage, we can make the observation that it becomes harder to satisfy the balanced condition recalled in (5.1) when the CPS are stacked, compared to the open configuration.

$$Z_c = \sqrt{\frac{L_p}{C_s}} \tag{5.1}$$

Indeed, the stacking of CPS leads to an increase of Z_c and a decrease of L_p, whereas C_s is only slightly affected. The problem is that higher values of L_p with a reasonable level of parasitics and losses are difficult to achieve with the chosen topology. Moreover, decreasing C_s is not desirable because it results in a lower level of homogeneity, as explained in Section 4.3.2. For this reason, it has been decided to renounce to the balanced condition for the developed prototype of volumetric layered TL-based MTM. This is not a fundamental limitation since the main concern is on the LH band of the structure.

5.2.3 Effect of stacking on CRLH TLs

The goal is to evaluate how the performances (Bloch parameters) of a CRLH TL in CPS are affected when the same structure is stacked in the vertical direction. In the present example, we consider a CRLH TL with asymmetrical unit cells (in terms of S parameters) made of the elements investigated in Section 5.2.2:

- Shunt inductors: as in Section 5.2.2.a. with $L_1 = 4$ mm.
- Series capacitors: as in Section 5.2.2.b. with $L_1 = 1.5$ mm.

The chosen lattice constant for this structure is $d = 8$ mm. The resulting unit cell is shown in Figure 5.4. The effect of stacking is evaluated by comparing several cases: stacked CPS with $p = 30$ mm (almost open) and $p = 8$, 4, 3, 2, 1 mm. These structures have been simulated with HFSS from 1 to 5 GHz, and the Bloch parameters have been extracted with the formalism described in Section 4.2. Figure 5.5 shows the Bloch phase constant for the considered cases. It can be observed that the lower limit of the LH band f_{cL} is almost not affected by the stacking. By contrast, the upper limit of the LH band, which corresponds here to the series resonance of the CRLH TL f_s, considerably decreases with p, especially when the layers are close to each

other ($p < 4$ mm). Although not shown here, the upper limit of the unbalance gap, which corresponds here to the parallel resonance of the CRLH TL f_{p}, increases when p decreases, thereby confirming that the balanced condition is difficult to achieve for such a stacking of CRLH TLs. As a consequence, a trade-off has to be made for the selection of the vertical periodicity p: it has to be small enough in order to obtain a bulk structure which has more chances to behave as an equivalent medium, but it should not be too small in order to keep a reasonably large LH band that can be further exploited. A value around $p = 4$ mm has been chosen for the further investigations.

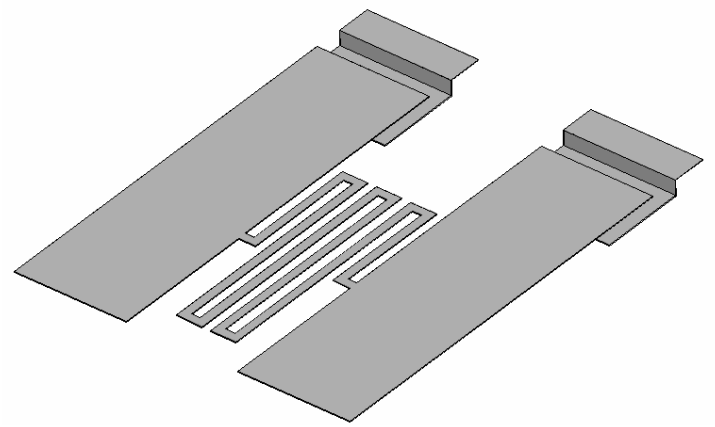

Figure 5.4: Unit cell of length $d = 8$ mm of the considered CPS CRLH TL (the substrate is not shown for clarity).

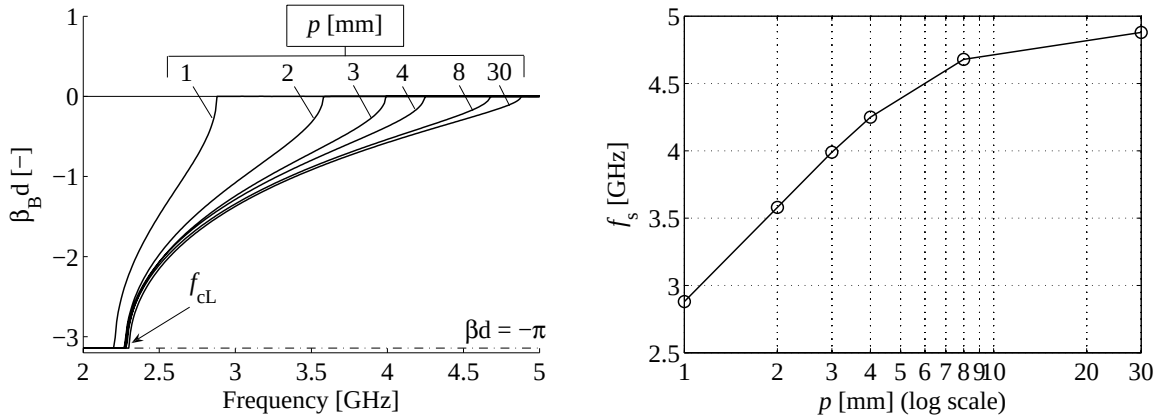

Figure 5.5: Left: Bloch phase constant for the chosen CPS CRLH TL in the stacked configuration ($p = 1$ to 30 mm). Right: Variation of the upper limit of the LH band f_{s} with the vertical periodicity p.

5.3 Description of the realized layered TL-based MTM

Based on the considerations of Section 5.2, a volumetric layered TL-based MTM has been designed. It is described in this section and is further analyzed in the rest of the chapter.

5.3.1 Description

The chosen CRLH topology is similar to the one considered in Section 5.2.3, except that we use MIM capacitors of type 2 instead of type 3 (see Figure 4.20), in order to avoid the need for vertical connections between the two sides of the substrate. This results in a pseudo periodic structure, as already discussed in Section 4.6.2.e.. The main characteristics of the considered prototype are reported below:

- Substrate: Rogers RT/Duroid 5870: $\varepsilon_r = 2.33$, $\tan\delta = 0.0012$, $h = 0.254$ mm (10 mil) and $t = 17$ µm.
- Dimensions of the CPS host TLs: $s = w = 2$ mm.
- Shunt inductors: same geometrical parameters as in Section 5.2.2.a. with $L_1 = 4$ mm.
- Series capacitors: MIM type 2 with $L_1 = 1.5$ mm.
- Longitudinal periodicity: $d = 6.5$ mm.
- Vertical periodicity: $p = 4$ mm + $h = 4.254$ mm.
- The structure is embedded in Foam (Rohacell, $\varepsilon_r = 1.07$).

A single layer of this structure is shown in Figure 5.6.

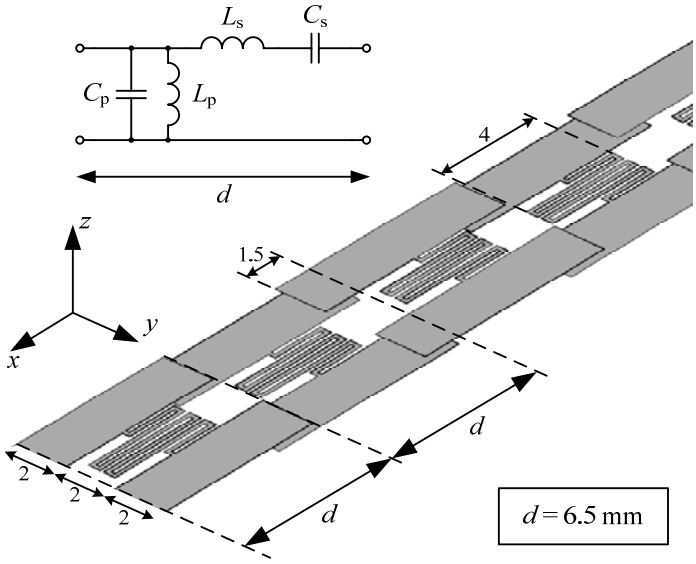

Figure 5.6: 1D CPS CRLH TL to be used for the stacking. The vertical periodicity (along z) is $p = 4.254$ mm. The substrate is not shown for clarity.

5.3.2 Bloch parameters from scattering parameters

A single (pseudo) unit cell of this structure in its stacked environment has been simulated with HFSS from 1 to 5 GHz. The Bloch parameters have been deduced from the resulting S parameters as explained in Section 4.2. The lossless case has been considered here. The results are shown in Figure 5.7. The structure exhibits a LH band of 2.13 GHz from $f_{cL} = 2.08$ GHz to $f_s = 4.21$ GHz, with a quite good level of homogeneity. Indeed, the unit cell is about ten times smaller than the guided wavelength in the host TL ($d/\lambda_h = 0.099$) and the free-space wavelength ($d/\lambda_0 = 0.091$) at the upper frequency of the LH band f_s. Along the vertical direction, the unit cell is about 17 times smaller than the free-space wavelength at f_s ($p/\lambda_0 = 0.06$). The Bloch impedance diagram is typical for this kind of asymmetrical unit cells, with two different Bloch impedances for the two propagation directions. In the present case, we exactly observe $Z_B^+ = (Z_B^-)^*$ in the pass-bands, which was shown in Section 4.2.7 to be a property of lossless asymmetrical periodic structures.

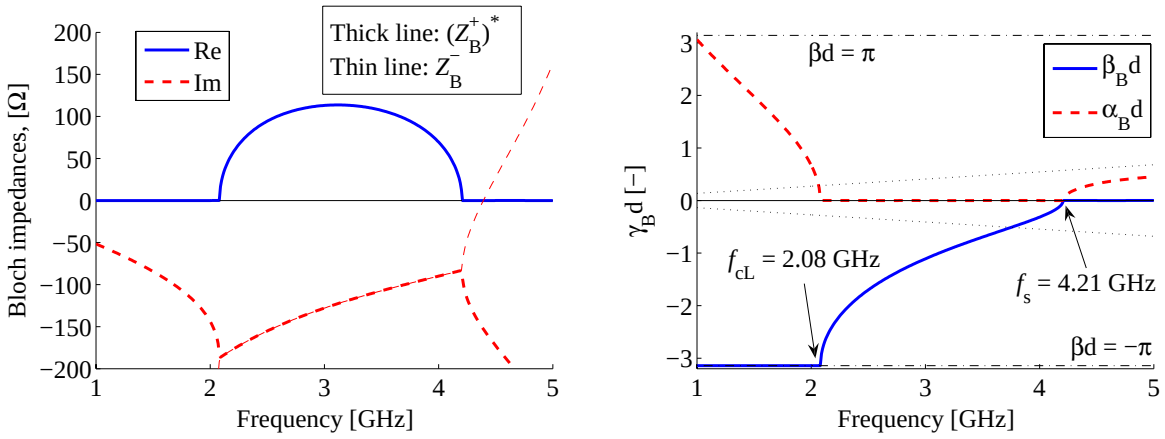

Figure 5.7: Bloch parameters for the considered CPS CRLH TL in its stacked environment, extracted from full-wave S parameter simulation.

5.3.3 Approximation of the pseudo-periodicity with a true periodicity

For the further numerical analyzes, the actual pseudo-periodic structure has been approximated by a true periodic structure. This is done by replacing the MIM capacitors of type 2 with MIM capacitors of type 4, with the same value of L_1, and with $g_1 = 0.3$ mm (see Figure 4.20). This modification of the unit cell is illustrated in Figure 5.8. Full wave simulations (S parameters) revealed that this approximation results in negligible differences. As a result, the true periodic structure shown in Figure 5.8(b) will be used to approximate the actual structure of Figure 5.8(a).

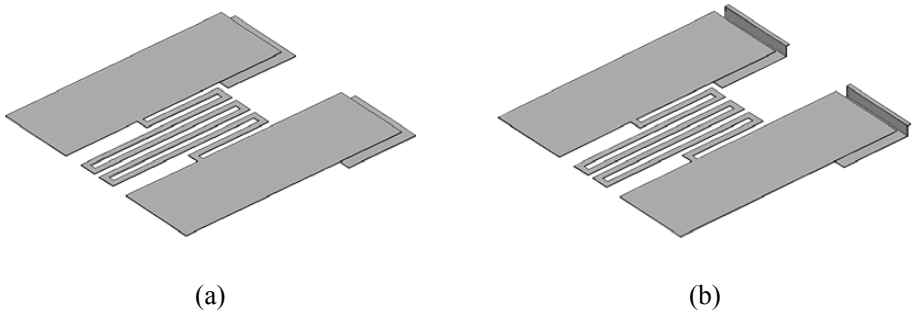

Figure 5.8: (a) Unit cell of the actual pseudo periodic structure with the MIM capacitors of type 2, and (b) its true periodic approximation with the MIM capacitors of type 4. The substrate is not shown for clarity.

5.3.4 Realization

The realized volumetric layered TL-based MTM slab is shown in Figure 5.9. From now on, this structure will be referred to here as the "meta-slab". The main points concerning the realization of this structure are outlined below:

- The overall width of each plate containing a CPS CRLH TL is $q = 10$ mm.
- The realized meta-slab comprises 27 of these plates, each one containing 19 unit cells. As a result, the overall dimensions of the slab are approximately 115 x 125 x 10 mm.
- Layers of foam (Rohacell) of thickness 4 mm have been placed between the plates. All these elements have been stuck together. The thickness and electromagnetic effects of the glue was shown in other realizations to have negligible effects.

5.4 Meta-slab in microstrip configurations

5.4.1 Studied configurations

As explained in the chapter introduction, the realized meta-slab is intended to be used as a substrate in a microstrip configuration like a patch antenna. It appears that the presence of metal plates (patch and/or ground plane) at proximity of the structure strongly affects its dispersion diagram, as explained in this section. The two configurations analyzed here are illustrated in Figure 5.10 (left-hand side). The right-hand side of Figure 5.10 shows the corresponding equivalent structures for the numerical analysis, where PBC or PMC are used to account for the transverse periodicity. All the simulations reported in this section have been performed in the lossless case, in order to facilitate the interpretation of the results.

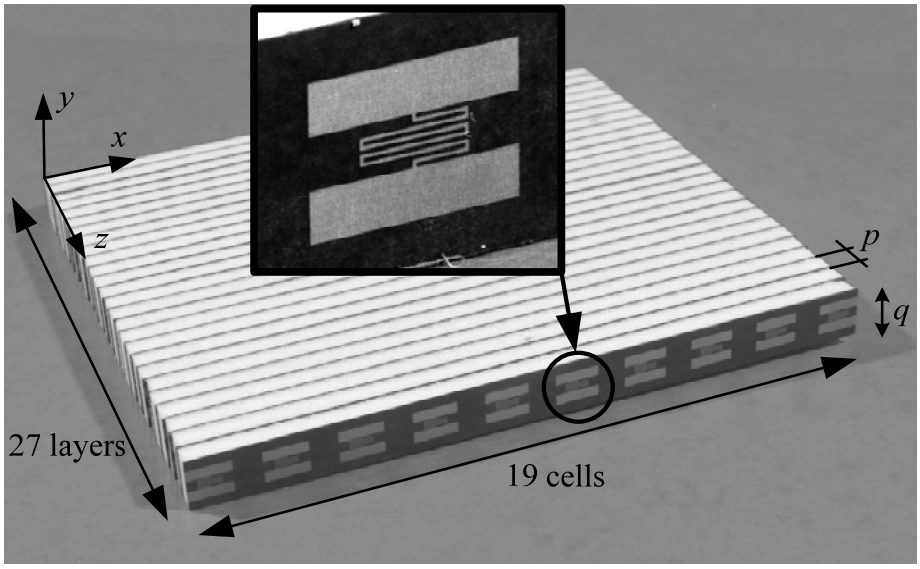

Figure 5.9: Picture of the realized volumetric layered TL-based MTM, referred to here as the "meta-slab".

5.4.2 Analysis methods

In both configurations of Figure 5.10 (right-hand side), the host TL is now a multiconductor TL (MTL) with N+1 conductors, with $N = 3$ in (a) and $N = 2$ in (b). As a result, N independent quasi-TEM modes can propagate without cut-off along the host MTL, which is why a simple extraction of Bloch parameters from dominant-mode S parameters is not possible anymore. Two other methods have been used to determine the dispersion diagram.

a. Eigenmode analysis

The numerical software used (Ansoft HFSS) provides an eigenmode solver which directly calculates the dispersion diagram of a periodic structure from its unit cell, rather than extracting it from S parameters. With this method, periodic boundary conditions (PBC) can be used to represent the periodicity in the transverse direction (along z). It can be noted that this method only provides the Bloch phase constant β_{B}, but not the Bloch attenuation constant α_{B}.

b. Extraction from multimode scattering parameters

This method is described in detail in Chapter 6. It consists of an extension of the dominant-mode Bloch wave analysis to cases in which the unit cell is represented in terms of several modes of the host guiding structure. This method allows obtaining the Bloch phase constant β_{B} as well as the attenuation constant α_{B}. It can be noted that this approach may be less accurate than the eigenmode analysis, since only the N propagating modes of the host MTL

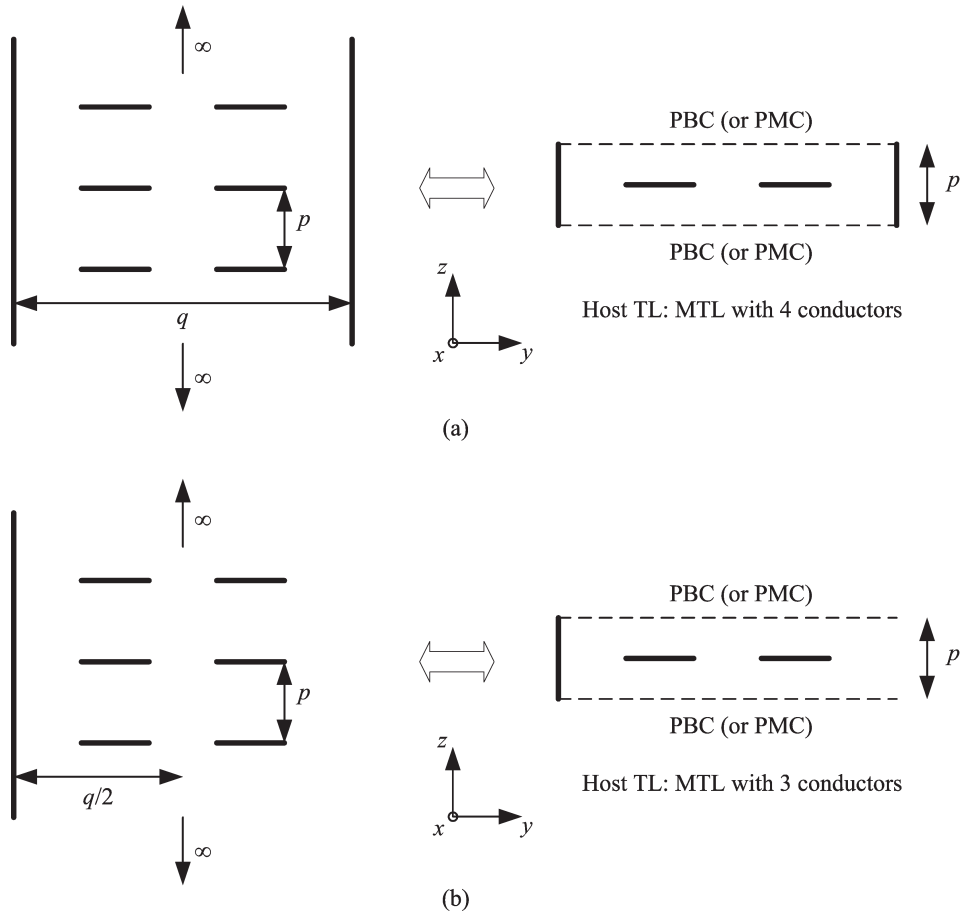

Figure 5.10: Stacked CPS CRLH TLs at proximity of metal plates and equivalent structures for the analysis (cross-section view). (a) Between a ground plane and a patch, which locally forms a parallel plate waveguide (PPWG), (b) near a ground plane (GP). For the chosen structure, we have $p = 4.254$ mm and $q = 10$ mm. The substrates are not shown here.

are considered in the representation of the unit cell, whereas possible inter-cell coupling due to higher order evanescent modes is not taken into account. By contrast, the eigenmode analysis is exact in that sense, since it is not based on a representation of the unit cell truncated to a finite number of modes. The present method may also include the effect of a finite number of evanescent modes, but this alternative will not be implemented here. With this method, PMC are used to represent the periodicity in the transverse direction (along z) since PBC cannot be used with wave ports in such a configuration with HFSS.

5.4.3 Meta-slab in a parallel plate waveguide (PPWG)

We consider here the configuration of Figure 5.10(a), in which the meta-slab is placed between a ground plane and a patch, which locally corresponds to a parallel plate waveguide (PPWG). The corresponding unit cell is shown in Figure 5.11. The dispersion diagram for propagation along x has been calculated with the two methods described in Section 5.4.2. Figure 5.12 shows the comparison between the two methods and Figure 5.16 the comparison with the open configuration, i.e., the case without the metal plates.

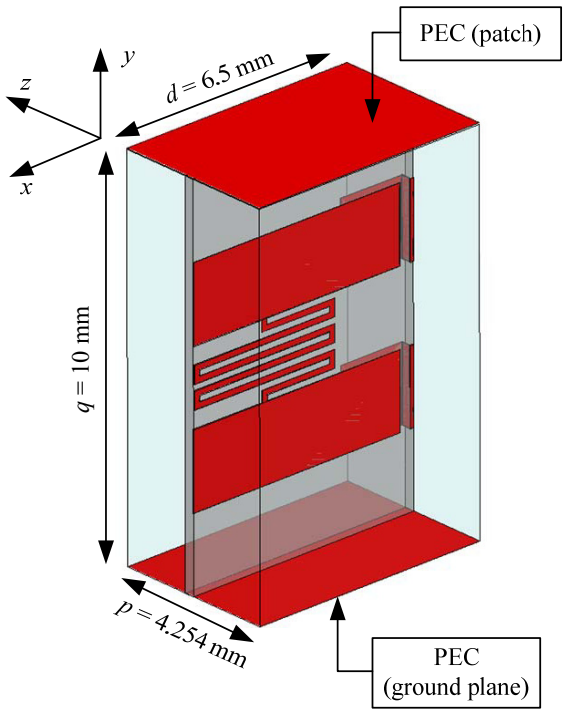

Figure 5.11: Unit cell of the meta-slab in a PPWG. For the eigenmode analysis, PBC (without phase-shift) are used in the z direction to account for the transverse periodicity and PBC with variable phase-shift are used in the x direction to obtain the dispersion relation for propagation along x. For the multimode analysis, PMC are used in the z direction and wave ports with multiple modes are placed in the x direction.

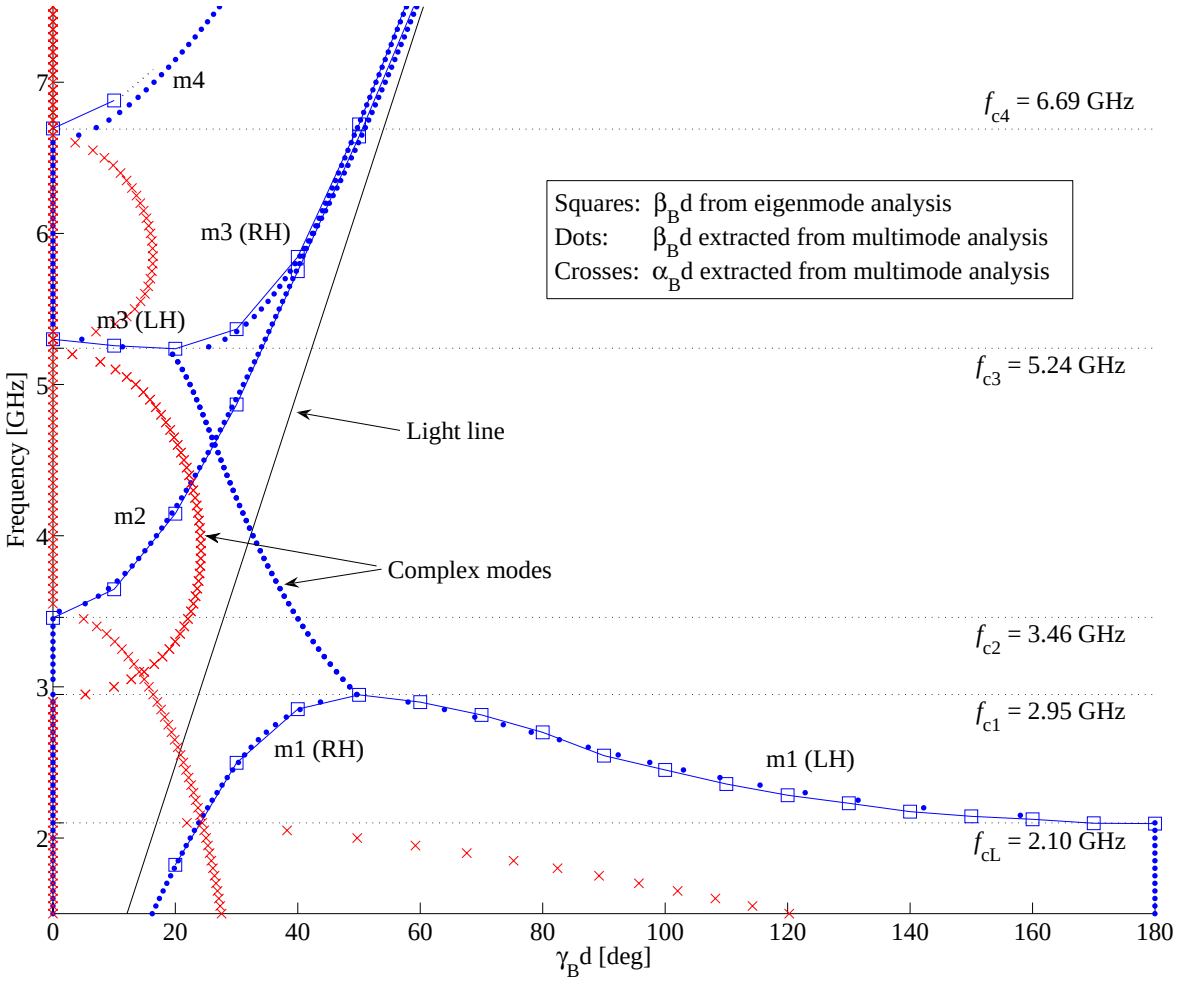

Figure 5.12: Dispersion diagram for the meta-slab in a PPWG obtained with the two proposed methods. For the eigenmode analysis, only the three first eigenmodes have been calculated. The modes have been labeled from "m1" to "m4", some of them being separated in a LH and a RH contribution. The quantity $\alpha_{\mathrm{B}}d$ is plotted with the same units as $\beta_{\mathrm{B}}d$, which is degree here.

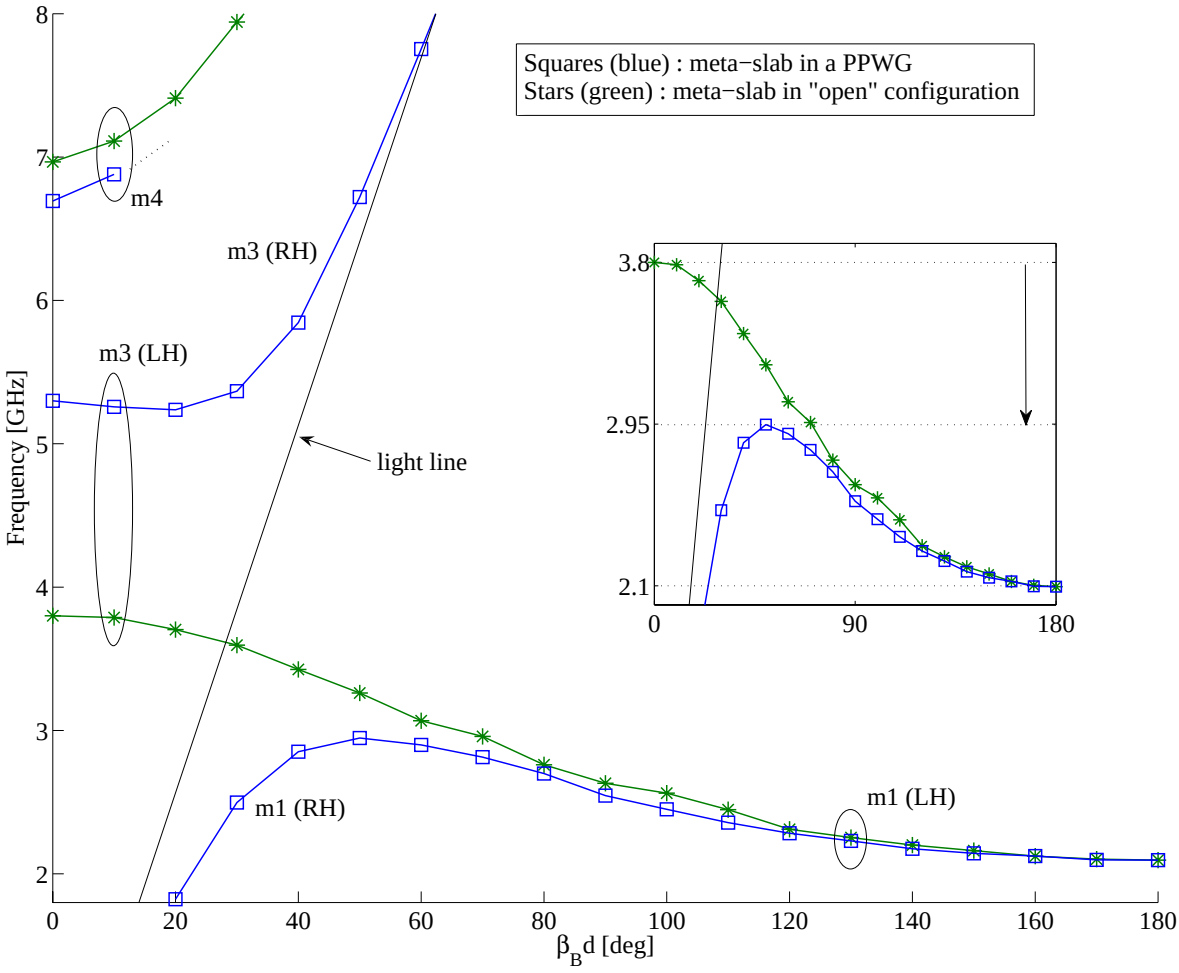

Figure 5.13: Comparison between the dispersion diagrams (obtained by eigenmode analysis) for the meta-slab in a PPWG (the mode "m2" is not shown) and the meta-slab in "open" configuration. The ellipses suggest how the modes should correspond between the two configurations. The inset is a frequency zoom on the first LH band.

Comments

- A very good agreement can be observed between the two methods (see Figure 5.12), with the main difference being the revelation of a complex mode band between f_{c1} and f_{c3} (both $\alpha, \beta \neq 0$) by the extraction from multimode analysis, which is not obtained by the eigenmode analysis. With the latter method we obtain a stop band, which is more visible in Figure 5.13. It can be noted that the multimode analysis required about 9 minutes of full wave simulation against 5 hours for the eigenmode analysis.
- In comparison with the open configuration, the PPWG configuration exhibits an additional complex mode band (two coupled modes with complex-conjugate propagation constants), which results from contra-directional coupling between the LH CPS mode and the RH PPWG mode. The consequence of this phenomenon is twofold:
  - The useable LH bandwidth is reduced compared to the open configuration: from 1.7 GHz to 0.85 GHz, hence a reduction of 50% (see the inset in Figure 5.13).
  - Instead of purely LH bands, we observe bands with mixed RH/LH behaviour. Indeed, at a given frequency in the LH band, both the "m1 (LH)" and the "m1 (RH)" modes can propagate (or the "m3 (LH)" and "m3 (RH)" modes at higher frequencies).

  It can be noted that very similar phenomena have already been observed and discussed for the shielded mushroom structure [240]. The way these modes are excited for a given excitation (slot in the ground plane, coaxial cable, microstrip line...) is of fundamental interest.
- The eigenmode analysis allows observing the eigen fields at some specific points in the dispersion diagram, thereby allowing to identify the nature of each Floquet mode:
  - The modes "m1 (LH)", "m3 (LH)" and "m4" resemble CPS modes. The two external conductors seem to be at the same potential.
  - The modes "m1 (RH)" and "m3 (RH)" resemble PPWG modes. The two conductors of the CPS seem to be at the same potential.
  - The mode "m2" resembles an even CPS mode. The two conductors of the CPS seem to be at the same potential, as well as the two external conductors. As a result, this configuration is similar to that of a stripline loaded with series capacitances in the central strip (the shunt inductances have almost not influence on this mode), which is consistent with the dispersion observed for this mode.
- When the structure is simulated with a PEC symmetry wall parallel to the xz plane (in the middle of the structure), the same dispersion diagram is obtained, but without the mode "m2", which satisfies a PMC symmetry condition.
- A balanced structure would be obtained if there is a continuous transition between the "m3 (LH)" and "m4" modes. Although all the configurations considered here are strongly unbalanced, we can nevertheless conclude that a meta-slab which is designed to be balanced in the open configuration will probably become unbalanced when placed in a PPWG.
- Let us finally note that the dispersion diagram calculated here with the eigenmode analysis for the open configuration should correspond to the one extracted from S parameters

shown in Figure 5.7. A good agreement is observed, especially at low frequencies (f_{cL} is almost the same). A slight difference is however observed in the higher part of the LH band. Indeed, the upper limit of this band is $f_{\mathrm{s}} = 4.21$ GHz in Figure 5.7 and 3.8 GHz in Figure 5.13. This difference may be explained by some non negligible inter-cell coupling related to higher order evanescent modes of the host guiding structure, which are not accounted for with the extraction from dominant-mode S parameters.

5.4.4 Meta-slab above a ground plane (GP)

We consider here the configuration of Figure 5.10(b), in which the meta-slab is placed above a ground plane (GP). The corresponding unit cell is shown in Figure 5.14. A PMC wall has been placed on the top of the cell to simulate an open structure in that direction. This PMC imposes conditions, and thus modes (referred to here as "waveguide-like" modes), which are not present in the real open structure. A rather small distance of $L_{\mathrm{air}} = 4$ mm between the structure and the PMC cover has been chosen so as to push the appearance of waveguide-like modes at higher frequencies. It has been observed that increasing L_{air} does not significantly affect the low frequency LH band of the dispersion diagram, which is of primary interest here. The dispersion diagram for propagation along x has been calculated with the two methods described in Section 5.4.2. Figure 5.15 shows the comparison between the two methods and Figure 5.16 the comparison with the open configuration, i.e., without the metal plates.

Comments

- In general, a good correspondence can be observed between the two methods (see Figure 5.15), except:
  - for the complex mode band, as already observed for the meta-slab in a PPWG, and
  - for the mode "m2", which does not appear with the multimode analysis (see comment below).
- Similarly to the meta-slab in a PPWG, the meta-slab above a GP exhibits an additional complex mode band, which this time results from contra-directional coupling between the LH CPS mode and the RH mode that has cutoff around 2 GHz. As a result, this structure also exhibits mixed RH/LH mode behaviour in the lower LH pass-band.
- The eigenmode analysis allows observing the eigen fields at some specific points in the dispersion diagram, thereby allowing to identify the nature of each Floquet mode:
  - The modes "m1 (LH)", "m3 (LH)" and "m4" resemble CPS modes.
  - The modes "m1 (RH)" and "m3 (RH)" are harder to identify. They should be similar to the mode "m2" of the meta-slab in a PPWG, i.e., modes for which the structure mainly consists of a TL loaded with series capacitances, and where the shunt inductances have negligible effect due to the fact that the two CPS conductors have similar potential with respect to ground. This explains the cutoff of the mode "m1 (RH)" (around 2 GHz).

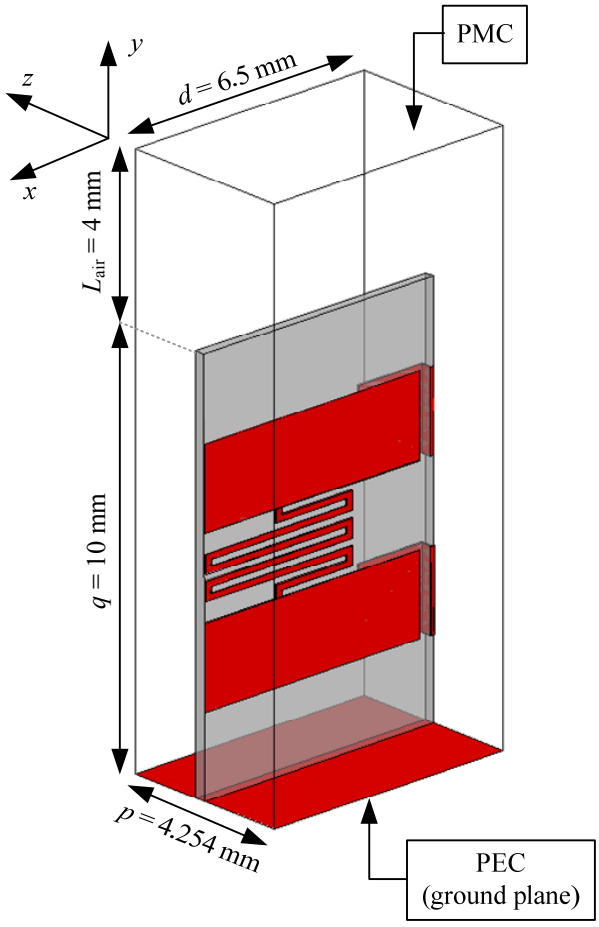

Figure 5.14: Unit cell of the meta-slab above a GP. For the eigenmode analysis, PBC (without phase-shift) are used in the z direction to account for the transverse periodicity and PBC with variable phase-shift are used in the x direction to obtain the dispersion relation for propagation along x. For the multimode analysis, PMC are used in the z direction and wave ports with multiple modes are placed in the x direction.

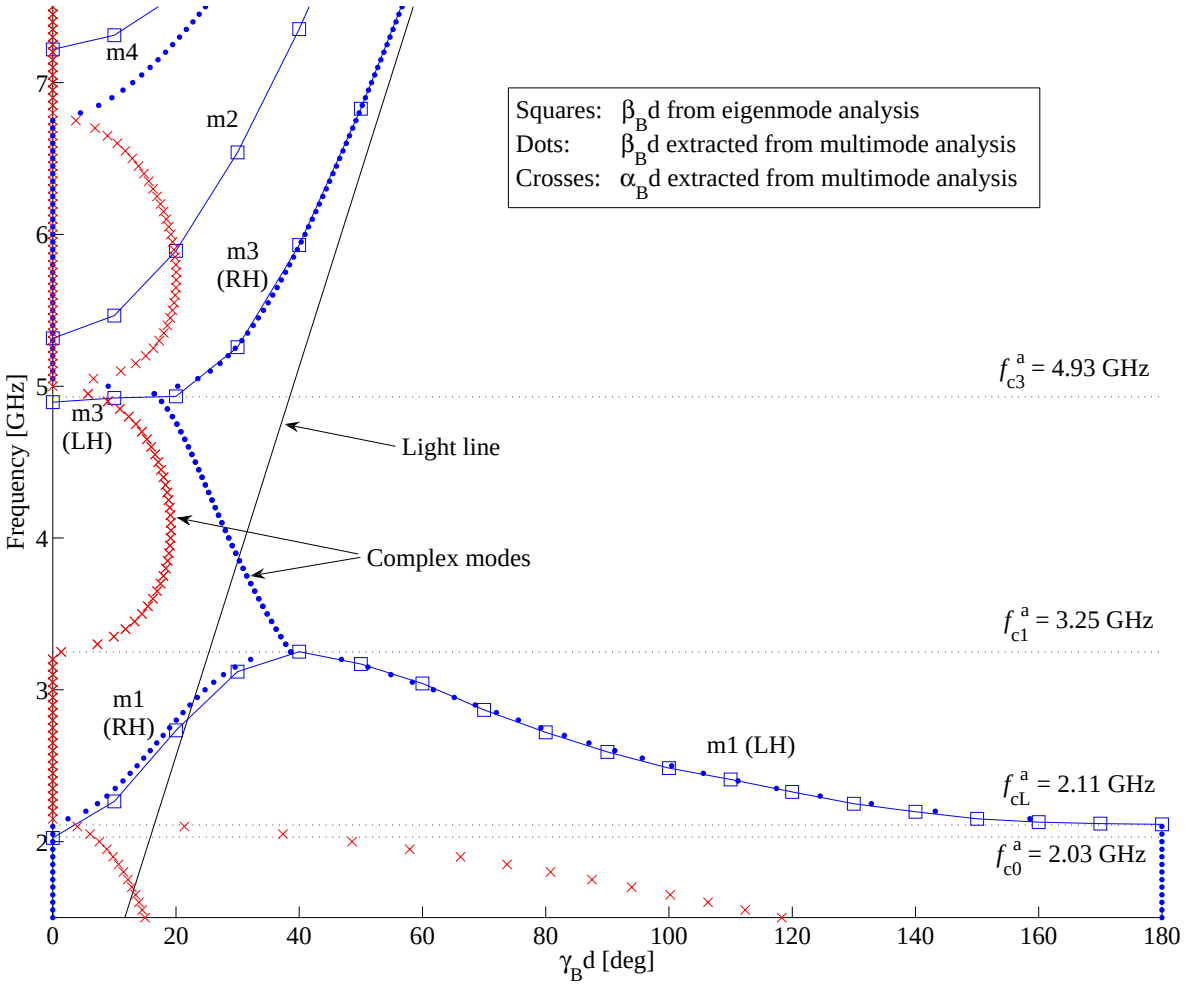

Figure 5.15: Dispersion diagram for the meta-slab above a GP obtained with the two proposed methods. For the eigenmode analysis, only the four first eigenmodes have been calculated. The modes have been labeled from "m1" to "m4", some of them being separated in a LH and a RH contribution. The quantity $\alpha_{\mathrm{B}}d$ is plotted with the same units as $\beta_{\mathrm{B}}d$, which is degree here.

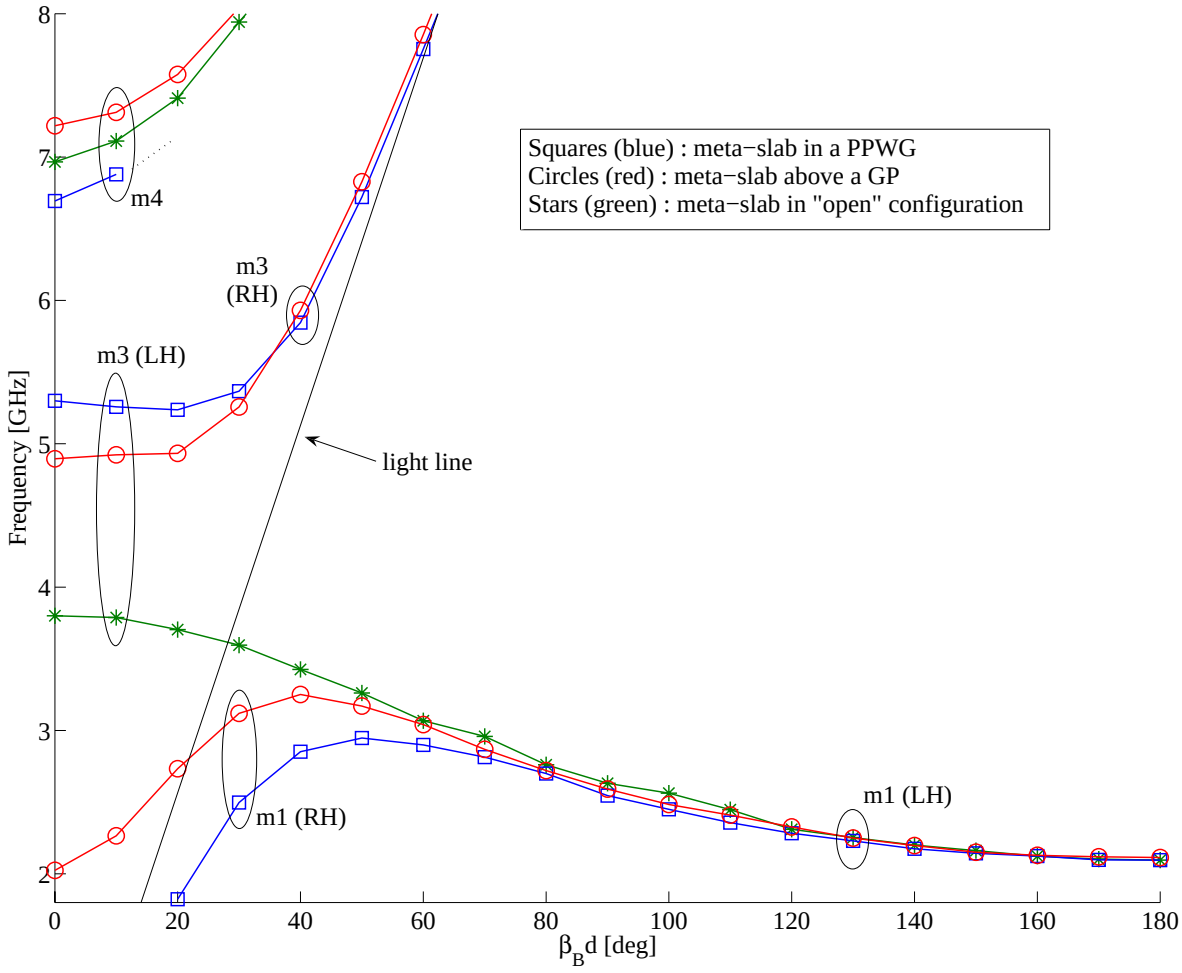

Figure 5.16: Comparison between the dispersion diagrams (obtained by eigenmode analysis) for the meta-slab above a GP (the mode "m2" is not shown) and the meta-slab in "open" configuration. The PPWG configuration is also recalled here. The ellipses suggest how the modes should correspond between the three studied configurations.

– The mode "m2" is a "waveguide-like" mode that should not exist in the real open structure. It is imposed by the PMC used to cover the structure. The electric field is mainly directed along z and the magnetic field has x and y components. This mode is equivalent to the TE_{10} mode of a rectangular waveguide with twice the length in the y direction (the PMC acts as a symmetry plane). This model gives a cutoff frequency of 5.36 GHz, which is close to the observed value of 5.32 GHz. It is normal that this mode does not appear with the multimode analysis, since with this method PMC are used in the z direction to account for the transverse periodicity, instead of PBC.

5.4.5 Summary

In this section, we have assessed the alteration of the dispersion relation of the meta-slab when the latter is used in a microstrip configuration, that is, above a ground plane and between a ground plane and a patch (PPWG configuration). The most important observed effect is the contra-directional coupling occurring between LH and RH modes, which results in:

- a complex mode band, i.e. a band with two coupled modes with complex conjugate propagation constants,
- a limitation of the usable LH band compared to the initial "open" configuration, and
- mixed RH/LH mode bands, instead of purely LH band as in the "open" configuration.

All these considerations represent the basic description of the meta-slab in various configurations that can be used for the investigations of possible antenna applications of the meta-slab, such as microstrip patch antennas or leaky wave antennas.

5.5 Meta-slab as a substrate for a microstrip line

5.5.1 Principle

In order to perform a first experimental assessment of the properties of the realized meta-slab, we have chosen the simple configuration in which the latter is used as a substrate for a microstrip (MS) line. Concretely, the S parameters of this "meta-MS line" have been measured with a network analyzer by means of a TRL calibration. This measurement has been chosen because it is the most straightforward to perform on the meta-slab.

5.5.2 Description

An illustration of the considered meta-MS line is shown in Figure 5.17. The strip is parallel to the CRLH TLs forming the meta-slab. We have chosen a quite large strip width $w = 17$ mm $\cong 4p$, where p is the distance between two consecutive plates in the meta-slab. This choice results from a compromise: the strip should be wide enough in order to obtain a sufficient coupling with the meta-slab, but it should not be too wide to avoid significant transverse currents flowing

on the strip. With the chosen width, we can consider that the structure is locally similar to the PPWG configuration studied in Section 5.4.3. We will therefore try to determine if a correspondence between the measured S parameters and the dispersion diagram of Figure 5.12 can be established.

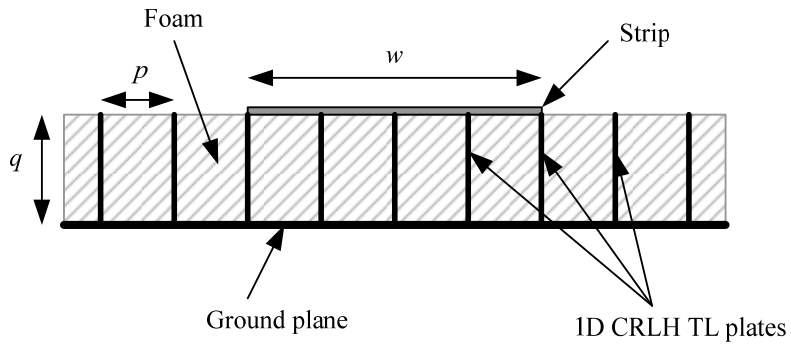

Figure 5.17: Illustration of the considered meta-MS line (cross-section view): the meta-slab is used as a substrate for a MS line ($w = 17$ mm $\cong 4p$). We recall that $p = 4.254$ mm and $q = 10$ mm.

5.5.3 Practical implementation

Some practical details concerning the realization and measurement setup are reported below:

- A section of MS line with a foam substrate (Rohacell, $\varepsilon_r = 1.07$) of length $a = 50$ mm has been added on both sides of the meta-MS line in order to perform a TRL calibration referenced to these lines, as shown in Figure 5.18. The characteristic impedance of these lines is 95 Ω, and their effective relative permittivity is 1.05. It can be noted that for these lines the strip width w corresponds to $\sim \lambda/6$ and the height of the MS line q to $\sim \lambda/10$ at the frequency of 3 GHz. These values are rather large for MS lines, which is not favorable in terms of unwanted radiation effects at discontinuities. According to [241], the main frequency limitations for MS lines are given by the following criteria (with application to the present case):
  - Cutoff of the first higher order mode: $f_c = 6.9$ GHz.
  - The coupling between the lowest order TM surface wave mode and the quasi-TEM mode becomes significant at 20.9 GHz.

  The measurement can thus be in principle performed until 6.9 GHz without being affected by the aforementioned problems.
- The actual length of the slab is $L_{\text{slab}} = 124.8$ mm. The width of the meta-slab was 113.6 mm, but it has been completed with foam layers at both sides to make it square, hence $W_{\text{slab}} = L_{\text{slab}}$.
- The measurements have been performed with a test fixture, thereby avoiding the need of soldering connectors. The various elements that form the measured device, i.e. the

meta-slab, the foam layers, the strip and the ground plane (see Figure 5.18) have not been stuck together, in order to allow the re-use of these elements in various configurations. The resulting drawback resides in a rather bad repeatability of the connections, which is crucial with TRL calibrations.

- The ground plane is made of brass of thickness 2 mm.
- The strips are made of beryllium bronze of thickness 0.2 mm. The strips have been obtained by chemical etching.

A pictures of the prototype in its measurement setup is shown in Figure 5.19.

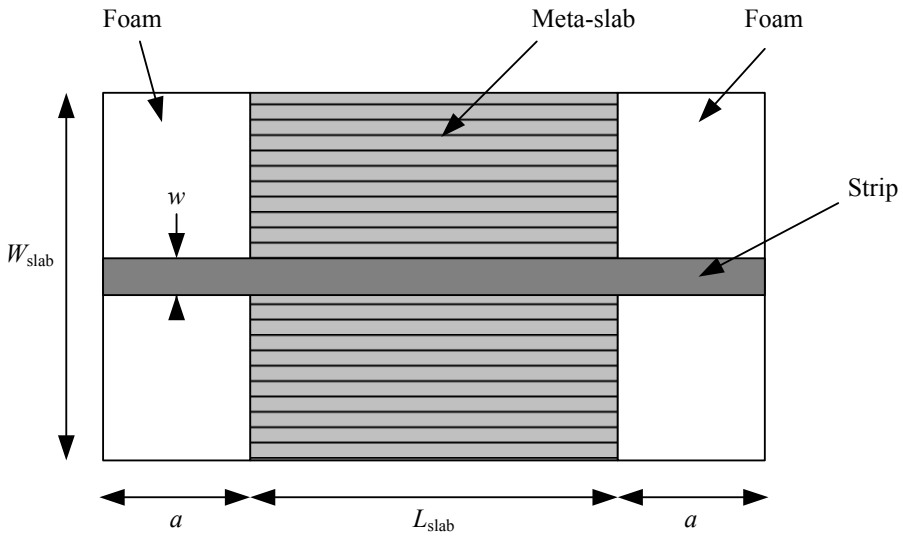

Figure 5.18: Top view of the meta-MS line between two conventional MS lines over foam substrate.

5.5.4 Measured S parameters

The S parameters of the meta-MS line have been measured with a HP8510C network analyzer by means of a TRL calibration. The reference planes are located at the edges of the meta-slab. The results are shown in Figure 5.20.

It can be observed that the full stop band (or complex mode band) predicted in the dispersion diagram of Figure 5.12 (between f_{c1} and f_{c2}) can be clearly seen on the measured S parameters, especially its low frequency limit f_{c1}, at which a sharp transition can be observed. The band from f_{c2} to f_{c3} has mainly a stop band behaviour, which may indicate that the mode "m2" is only slightly excited. Between f_{cL} and f_{c1}, the structure may support the propagation of both the LH and RH modes. However, a simple inspection of the S parameters does not allow to evaluate to which extend the LH mode is excited.

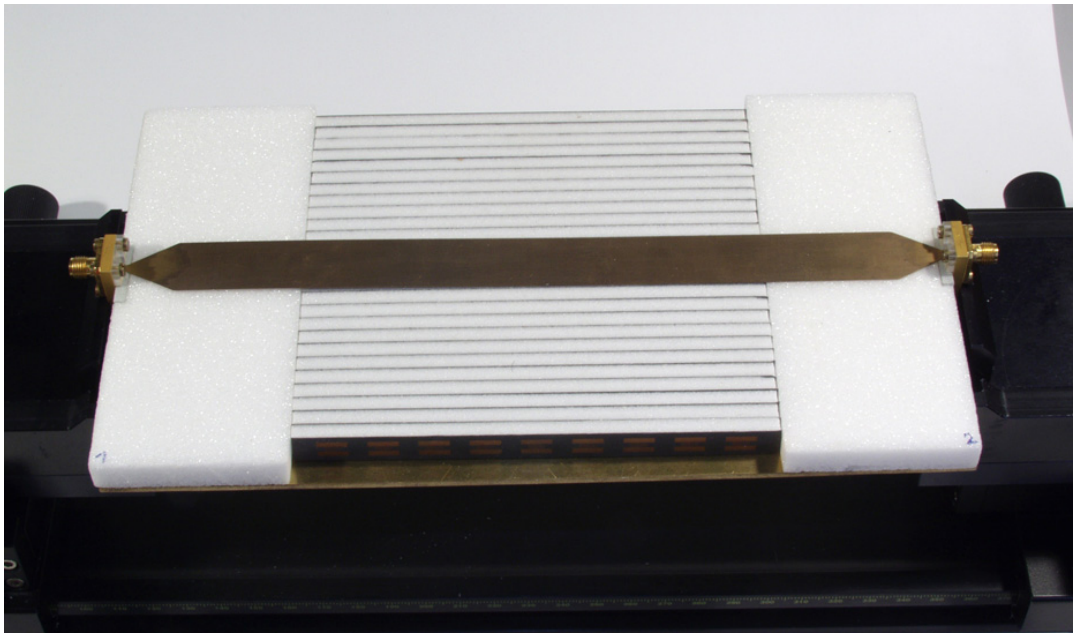

Figure 5.19: Picture of the meta-MS line in its measurement setup.

5.5.5 Conclusion

The measured S parameters did not allow a clear assessment of the ability of a MS line to excite the LH mode of the meta-slab. This is due to the mixed RH/LH mode behaviour of the structure at these frequencies, the RH mode being more compatible with the natural fields of the MS line which excites the meta-slab. As a result, we do not have at the moment a clear idea on the ability of a patch to excite the LH mode of the meta-slab. It can be anticipated that the way of exciting such a structure plays an important role. The results shown here reveal that bringing the power through a MS line may not be an efficient way of coupling power to the LH mode, but this coupling could be rather different if the power is coupled through a slot in the ground plane, for instance. As the main focus is on antenna applications of this class of MTMs, the meta-slab will be further tested directly embedded in a radiating system, which is the subject of the next section.

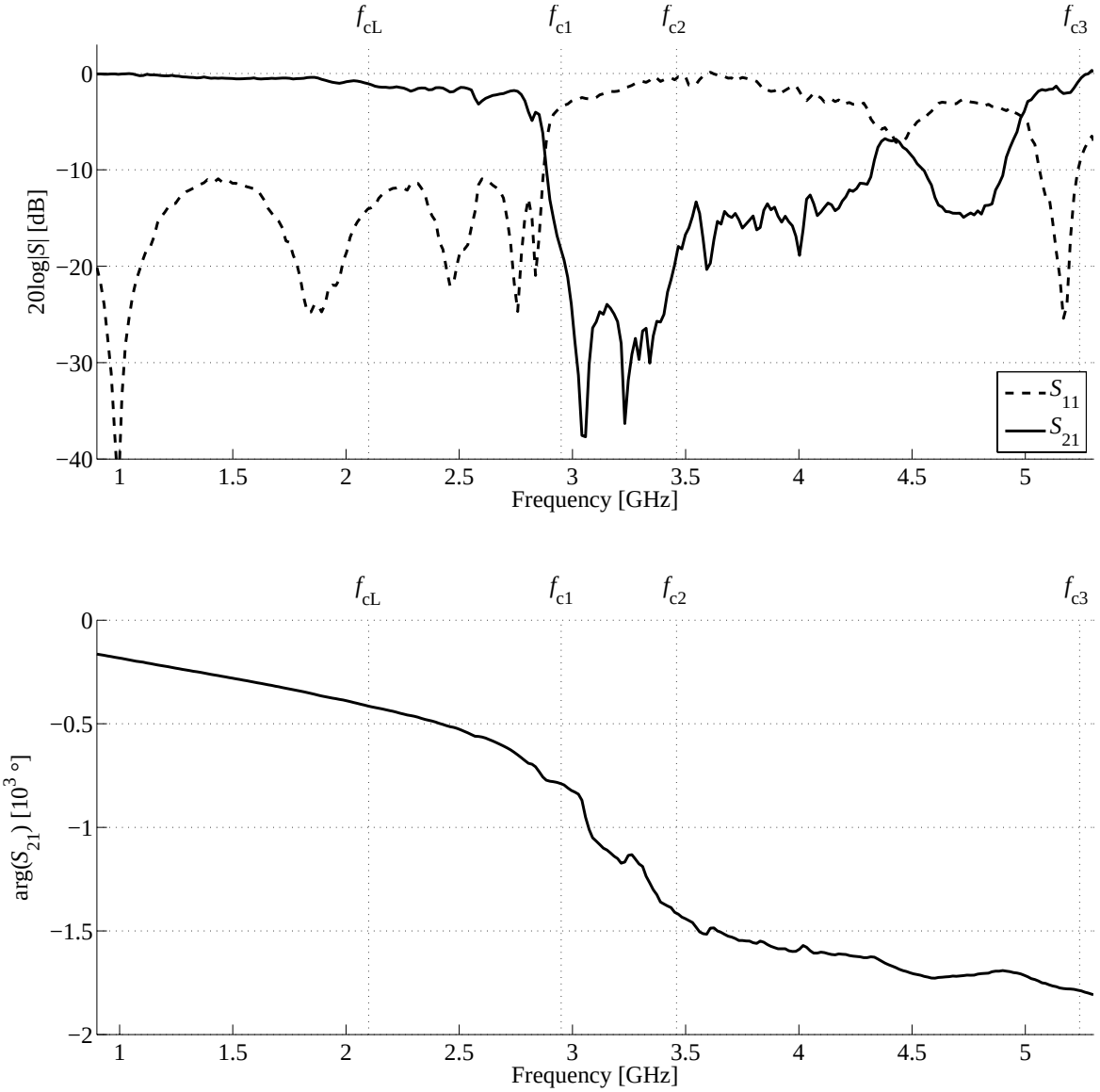

Figure 5.20: Measured S parameters for the considered meta-MS line. The reference impedance is the characteristic impedance of the connecting TL (95 Ω). The frequencies highlighted in the dispersion diagram of Figure 5.12 are also shown in the figure. The phase of S_{11} is not shown for clarity.

5.6 Meta-slab as a substrate for microstrip antennas

5.6.1 Motivations and description

The goal is to investigate potential applications of the designed meta-slab for microstrip (MS) patch antennas in which the meta-slab is used as a substrate. Such a configuration is illustrated in Figure 5.21. This kind of structures will be referred to here as "meta-patch antennas", or simply "meta-patches". To derive potential interesting features of this kind of structures, and by similarity with the cavity model used for conventional MS patch antennas [242], we make the assumption that the meta-slab is limited to the size of the patch, as suggested in Figure 5.21. This is obviously not the case in the actual measured structures since the realized meta-slab is much larger than the patch. The accuracy of this approximation will be discussed with the measurement results. Locally, the meta-patch behaves like the "meta-slab in a PPWG", for which the dispersion diagram is shown in Figure 5.12.

As for conventional patch antennas, the space below the patch can be seen as a mean of providing the required phase shift between the two radiating apertures. For modes with broadside radiation, the electric field in the apertures should be out of phase, as illustrated in Figure 5.21. The richness of the dispersion diagram of this structure provides many possibilities of achieving this condition, thereby offering interesting multi-frequency capabilities.

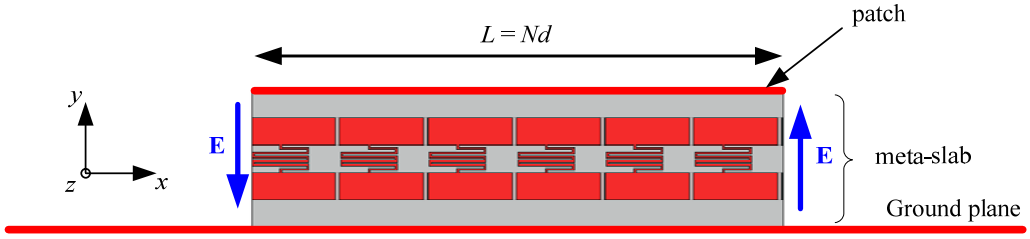

Figure 5.21: "Meta-patch" antenna of N cells ($N = 6$ in the figure). We consider here that the meta-slab is limited to the size of the patch. The excitation is not shown.

5.6.2 Resonances of the meta-patch

a. TL model

For the derivation of its resonant frequencies, a MS patch of length L can be modeled as a TL section of length L open at both ends [242]. With this model, the resonances of the patch are given by the following relation:

$$\beta L = n\pi, \quad n \in \mathbb{Z} \tag{5.2}$$

where β is the phase constant of the equivalent TL representing the MS patch. For odd values of n (odd modes) the electric fields at the two radiating edges of the patch are out of phase, leading then to constructive interferences at broadside. For even values of n (even modes) the

electric fields at the two radiating edges of the patch are in phase, leading then to destructive interferences at broadside, hence a null of radiation in that direction. If the patch itself is a periodic structure made of N cells of lattice constant d ($L = Nd$), Equation (5.2) becomes

$$\beta_{\mathrm{B}} d = \frac{n\pi}{N}, \quad n \in \mathbb{Z} \tag{5.3}$$

where β_{B} is the Bloch phase constant of the periodic structure. For the meta-patch, the resonant frequencies satisfying (5.3) can be deduced from the corresponding dispersion diagram, which is recalled in Figure 5.22. For instance, in the case $N = 6$, we observe six quite close resonances in the first mixed RH/LH mode. We report in Table 5.3 all the resonant frequencies f_{r} occurring in the first mixed RH/LH mode (between $f_{\mathrm{cL}} = 2.10$ GHz and $f_{\mathrm{c1}} = 2.95$ GHz) for different values of N. We also show in the table the corresponding values of the phase shift per unit cell ($\beta_{\mathrm{B}} d$), the size of the unit cell in terms of free space wavelength (λ_{r0}/d), the size of the patch in terms of free space wavelength (L/λ_{r0}) and the relative effective permittivity ($\varepsilon_{r,\mathrm{eff}}$) of a conventional MS patch operated in its fundamental mode which leads to the same patch length (for odd modes only). It is worth noting that the effect of fringing fields at the edges of the patch (increase of its effective length) has not been considered for the deduction of the resonant frequencies, since this effect cannot be evaluated as easily as for homogeneous substrates [241].

Comments

- At all the reported resonant frequencies, the size of the unit cell is small compared to the free-space wavelength, namely, between 16 and 22 times smaller, hence a good level of homogeneity.
- Meta-patches with low values of N ($N \leq 4$) exhibit resonant frequencies at which the patch is quite small in terms of the free-space wavelength (in the range $\sim 0.10 - 0.25\lambda_0$), which could be of interest for miniaturization. A similar operating mode has already been exploited with patches made of mushroom like structures, as reported in the state-of-the art (Section 2.4.2.b.).
- Meta-patches with a higher number of cells ($N > 4$) are less interesting in terms of miniaturization, but they offer interesting multi-frequency capabilities. More precisely, we can obtain several close resonant frequencies corresponding to odd modes (odd values of n), in comparison with conventional patches where those frequencies are harmonically related. Some antennas based on this principle have been reported in the literature and discussed at the end of Section 2.4.2.b..

b. Cavity model

A MS patch antenna can also be modeled as a cavity closed by PMC on its four vertical walls [242]. This model provides the same resonant frequencies as the TL model, but it provides more information on the fields topology at the resonances. As a verification, the eigenmode solver of HFSS has been used to directly determine the resonant frequencies of a meta-patch of N cells

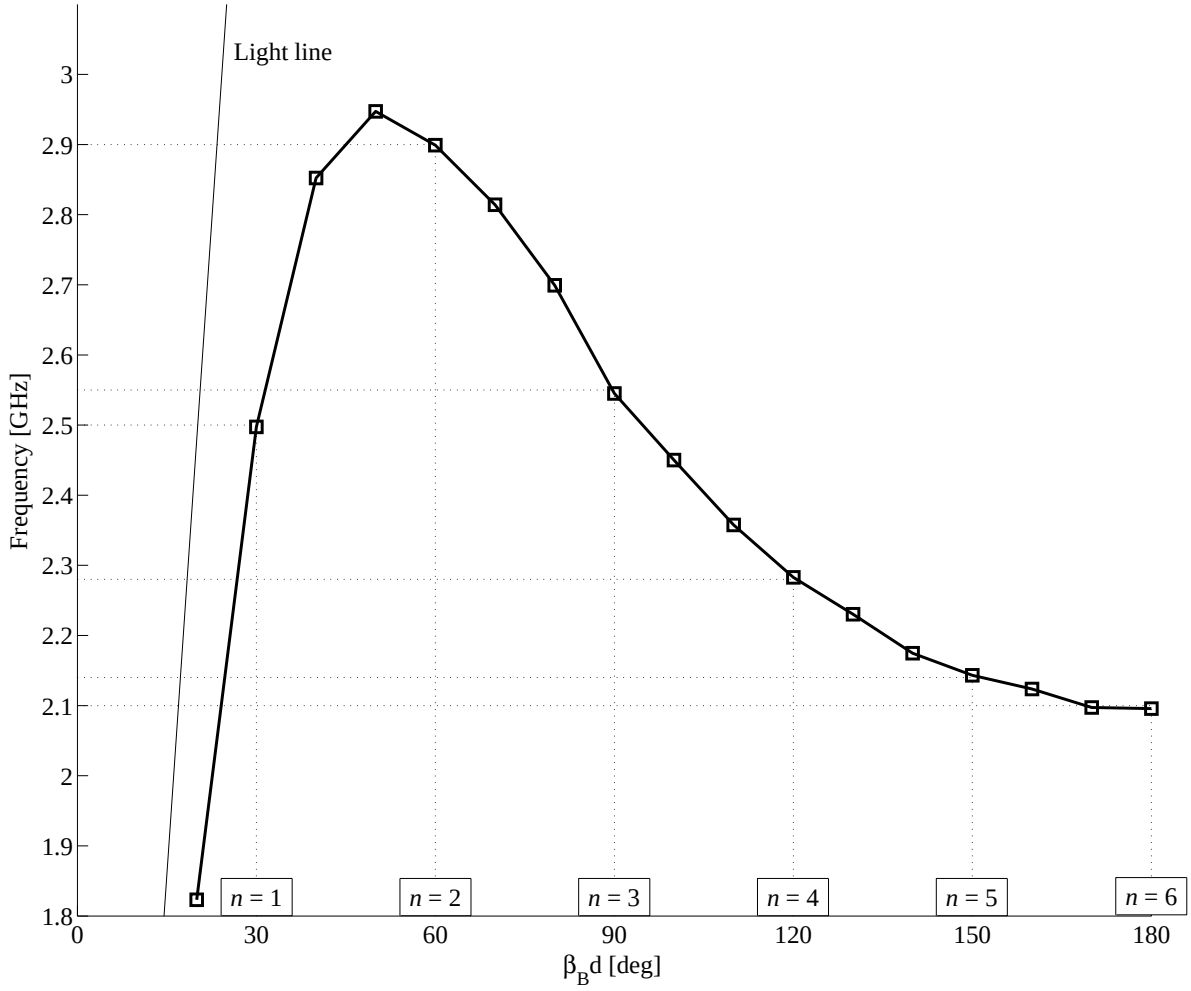

Figure 5.22: Dispersion diagram for the meta-patch configuration, obtained from eigenmode analysis (same as in Figure 5.12). The focus is on the fist mixed RH/LH mode band. The dotted lines correspond to the resonant frequencies of a meta-patch with $N = 6$ cells in the longitudinal direction.

N	n	$\beta_{\mathrm{B}}d$ [°]	f_{r} [GHz]	λ_{r0}/d	L/λ_{r0}	$\varepsilon_{r,\mathrm{eff}}$
1	1	180 (LH)	2.10	22	0.05	
2	1	90 (LH)	2.55	18	0.11	20.5
	2	180 (LH)	2.10	22	0.09	
3	1	60 (LH)	2.90	16	0.19	7.04
	2	120 (LH)	2.28	20	0.15	
	3	180 (LH)	2.10	22	0.14	
4	1	45 (RH)	2.90	16	0.25	3.96
	2	90 (LH)	2.55	18	0.22	
	3	135 (LH)	2.20	21	0.19	6.88
	4	180 (LH)	2.10	22	0.18	
5	1	36 (RH)	2.71	17	0.29	2.90
	2	72 (LH)	2.79	17	0.30	
	3	108 (LH)	2.38	19	0.26	3.76
	4	144 (LH)	2.16	21	0.23	
	5	180 (LH)	2.10	22	0.23	
6	1	30 (RH)	2.50	19	0.33	2.37
	2	60 (LH)	2.90	16	0.38	
	3	90 (LH)	2.55	18	0.33	2.28
	4	120 (LH)	2.28	20	0.30	
	5	150 (LH)	2.14	22	0.28	3.23
	6	180 (LH)	2.10	22	0.27	

Table 5.3: Resonant frequencies f_{r} occurring in the first mixed RH/LH mode band and related quantities for meta-patches with different numbers of cells N.

represented by its equivalent cavity shown in Figure 5.23. The computed eigenfrequencies are reported in Table 5.4 and compared with the values of Table 5.3, which were deduced from the dispersion diagram.

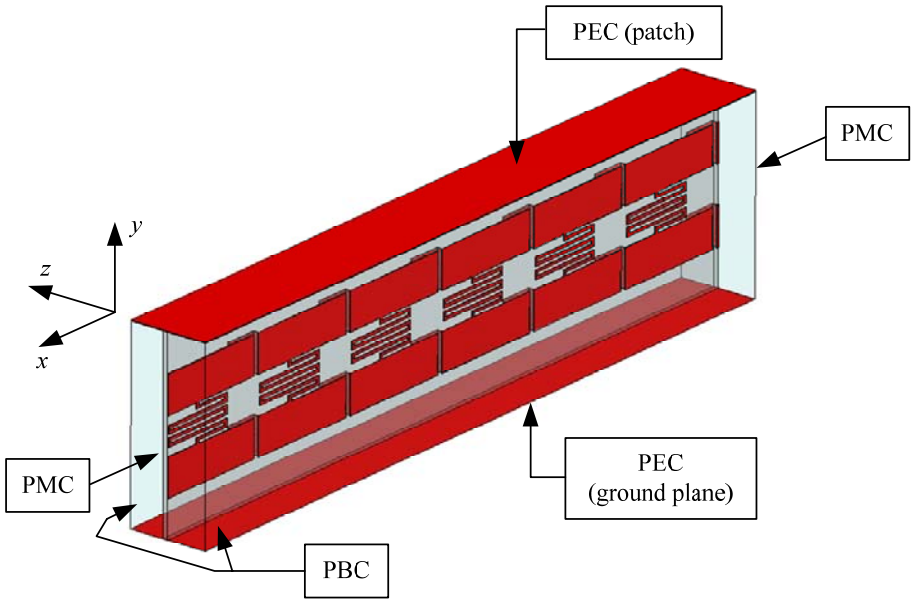

Figure 5.23: Equivalent cavity for a meta-patch of N cells ($N = 6$ in the figure). As we are only interested in modes with fields variation along x, a single row of cells is considered and periodic boundary conditions (PBC) are applied in the z direction to account for the transverse periodicity, which therefore becomes infinite.

Comments

- A very good correspondence is observed between the two approaches (differences less than 3%).
- An inspection of the fields inside the system at different resonances allowed identifying the corresponding value of n.
- The resonant frequency for the modes corresponding to $\beta_B d = 180°$ are never found by the eigenmode solver of HFSS for the cavity model. This point of the dispersion diagram is the lower limit of the LH pass-band.

Based on the results provided by the cavity model, the radiated fields of a patch antenna can be estimated from the electric field distribution in the two radiating edges, through the definition of equivalent magnetic current densities [242]. For a conventional patch, this electric field is vertically directed and almost constant over the apertures. For the meta-patches investigated here, the situation may be rather different. Indeed, Figure 5.24 shows the electric field distribution in the radiating apertures (faces with PMC in Figure 5.23) for two selected resonances.

	$n = 1$	$n = 2$	$n = 3$	$n = 4$	$n = 5$	$n = 6$
$N = 1$	2.10 / —					
$N = 2$	2.55 / 2.57	2.10 / —				
$N = 3$	2.90 / 2.89	2.28 / 2.31	2.10 / —			
$N = 4$	2.90 / 2.93	2.55 / 2.58	2.20 / 2.25	2.10 / —		
$N = 5$	2.71 / 2.70	2.79 / 2.80	2.38 / 2.40	2.16 / 2.18	2.10 / —	
$N = 6$	2.50 / 2.49	2.90 / 2.91	2.55 / 2.60	2.28 / 2.34	2.14 / 2.19	2.10 / —

Table 5.4: Resonant frequencies of a meta-patch of N cells. Comparison between the values deduced from the dispersion diagram (first value in each cell; same as in Table 5.3) and the values directly calculated with the eigenmode solver of HFSS (second value in each cell).

In case (a), the resonance occurs in the LH branch of the first mixed RH-LH mode. This mode has been identified as a LH CPS mode, which is confirmed by the observed electric field distribution. If an equivalent magnetic current density is defined from this electric field, it appears that the effects of these currents will partially cancel each other, since these currents are close to each other and directed in opposite directions. This configuration is therefore less favorable for radiation compared to the case of a conventional patch. However, it is impossible at this stage to determine if this issue will prevent the structure from efficiently radiating at this resonance. In case (b), the resonance occurs in the RH branch of the first mixed RH-LH mode. This mode has been identified as a RH PPWG mode, which is confirmed by the observed electric field distribution. This situation is less critical according to the criterion mentioned above, since the electric field distribution resembles the one of a PPWG mode, although affected by the presence of the two strips of the CPS.

5.6.3 Choice of the excitation

The main question now concerns the choice of the feeding system that will allow exciting the predicted meta-patch resonances. These resonances will essentially be identified from the input impedance of the antenna. It appears that this type of problems, i.e. a whole meta-patch antenna with its excitation, is out of scope for numerical or analytical modeling, due to the high level of complexity and high number of subwavelength unit cells. Therefore, an experimental approach has been adopted. As many experimental tests are being planed, the chosen feeding system should offer a certain level of modularity to allow the re-use of the elements in various configurations. Possible candidates for the feeding system are [242]:

- Microstrip line feed.
- Aperture-coupled feed (slot in the ground plane).
- Probe feed (or coaxial feed).

The advantages and drawbacks of each solution in the present context are summarized in Table 5.5. From an electromagnetic point of view, the most favorable excitation is probably

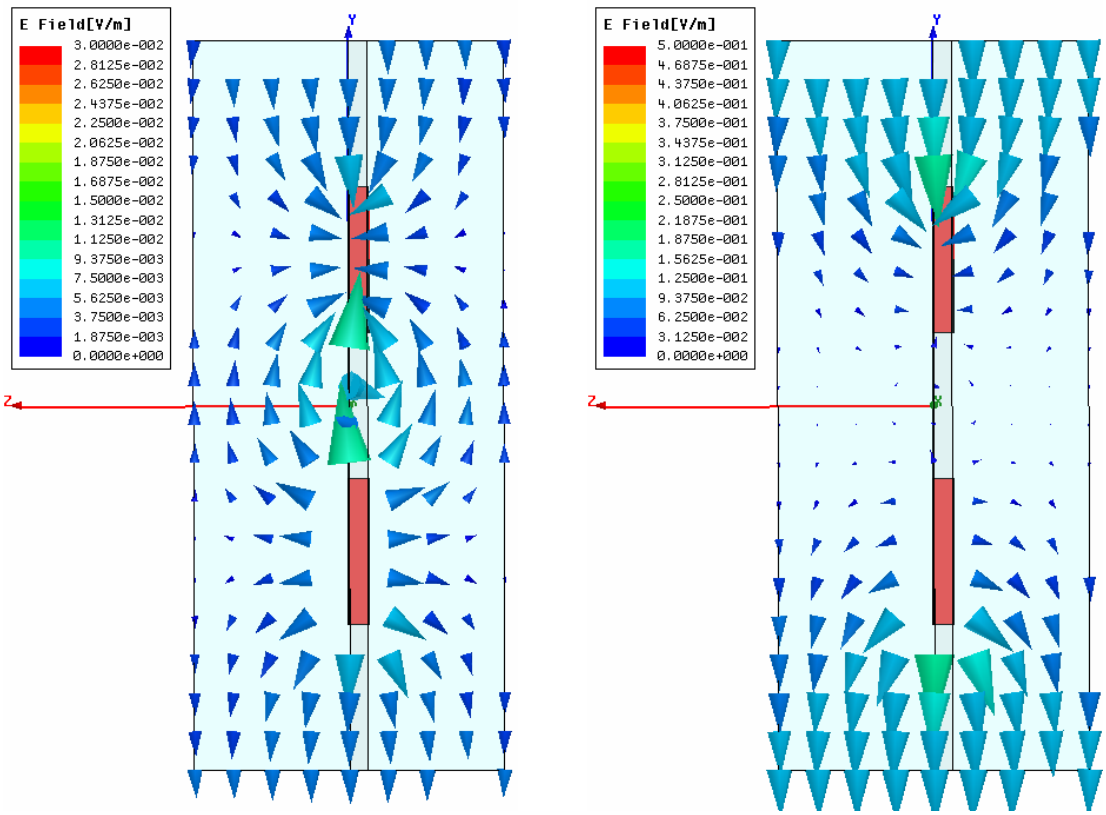

(a) $n = 5$, $\beta_B d = 150°$.

(b) $n = 1$, $\beta_B d = 30°$.

Figure 5.24: Electric field distribution in the radiating apertures of the meta-patch with $N = 6$ obtained with the cavity model (eigenmode solver of HFSS).

the coaxial probe, for the advantages mentioned in the table. However, it has not been chosen since not appropriate for the adopted modular approach. Preliminary tests have been carried out with MS line feeds, but they did not allow a clear assessment on the modes actually being excited in the structure. As a result, most of the further tests have been performed with an aperture-coupled feed.

	Advantages	Drawbacks
MS line	High level of coupling to the patch over a quite large bandwidth.	Thick substrate (10 mm): - Need for a large strip for a 50 Ω line. - Wide MS lines over thick substrates are subject to radiation.
Aperture	- The feeding part can be designed independently of the radiating part. - The radiation of the meta-patch is almost not affected by the feeding part.	- Low level of coupling to the patch far from the slot resonance. - The patch resonances are affected by the slot resonance if too close to it.
Probe	- High level of coupling to the patch over a reasonable bandwidth. - The radiation of the meta-patch is almost not affected by the feeding part.	Not appropriate for the re-use of the elements for various tests (the meta-slabs must be drilled and the probe must be soldered to the patch).

Table 5.5: Advantages and drawbacks of the three considered feeding system.

5.6.4 Aperture coupled meta-patch antennas

a. Goals and adopted approach

The goal is here to excite the meta-patch through a slot in the ground plane in order to highlight the existence of the resonances predicted in Section 5.6.2, and thereby validate the concept. As this type of complex problems could not be solved with simple analytical models nor with numerical simulations, an experimental approach has essentially been adopted. A schematic illustration of the considered aperture coupled MS patch antennas is shown in Figure 5.25.

The goal of the measurements is to detect the occurrence of meta-patch resonances from the input impedance of the antenna. A TRL calibration has been used to place the reference plane at the position of the slot, in order to remove the effect of the feeding line. Among the different possible ways of defining a resonant frequency for an antenna, we have considered here that resonant frequencies correspond to maxima of the real part of the input impedance (at the position of the slot), referred to here as Z_{a}. In some cases, the radiation pattern has also been measured in order to further identify the nature of the observed resonances.

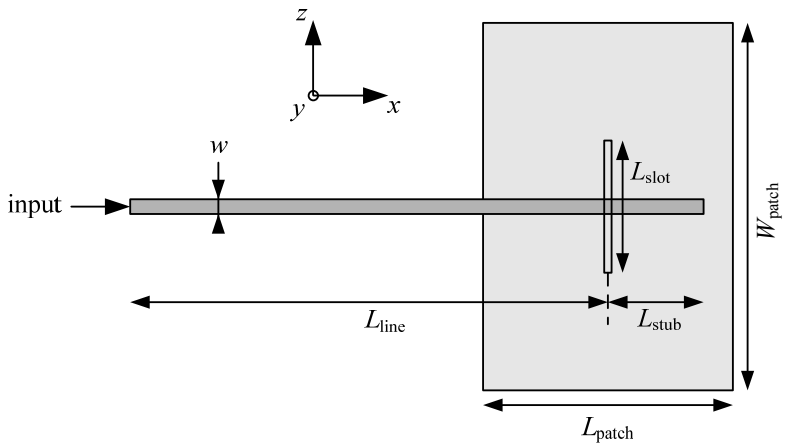

Figure 5.25: Top view of an aperture coupled patch antenna, with definition of the relevant dimensions. The strip is located on the other side of the ground plane. The slot is centered below the patch. The width of the slot is W_{slot}.

b. Studied cases

A full measurement campaign has been carried out on various configurations of aperture coupled meta-patch antennas. In particular, we have considered:

- Four different rectangular patches of length L_{patch} corresponding to $N = 3$, 4, 5 and 6 unit cells (of size $d = 6.5$ mm). The case without patch has also been considered for comparison.
- The two possible orientations of the meta-slab with respect to the slot.
- Two different feeding parts (with different slot dimensions).
- Reference cases where the meta-slab has been replaced by foam (Rohacell, $\varepsilon_r = 1.07$) of same thickness ($q = 10$ mm).

We have further performed tests with reduced meta-slabs with the same dimensions of the considered patch. A plethora of measurement results has thus been obtained. Very complex behaviours have been observed, thereby complicating the interpretation of the results in the light of the goal mentioned above. Describing and comparing all these results is out of scope of the present report. We rather focus here on some of the most relevant results[1].

c. Design of the feeding part

Problematic of the slot resonance

For many practical designs of aperture coupled patch antennas, the slot is close to its first resonance at the operating frequency of the antenna, such that the coupling between the line and the patch is maximized. Moreover, the resonance of the slot can be advantageously

[1] All the results have been reported in a Technical Note in the context of the related ESA project [243].

coupled with the patch resonance to widen the bandwidth of the antenna. However, for the configurations of interest here, the goal is to identify the resonances of the meta-patch from the input impedance, which is why the resonance of the slot is not a desirable effect because it may partially hide the meta-patch resonances, thereby complicating the interpretation of the results. As a result, rather than being a resonant element, the slot is used as a way of coupling power to the meta-patch in order to evaluate how the predicted resonances can be excited. A compromise must therefore be made for the design of the coupling slot. On the one hand, setting the slot resonance far above the band of the expected meta-patch resonances allows a clear separation of the slot and patch resonances, but the coupled power will be small. On the other hand, setting the slot resonance close or into the band of the meta-patch resonances results in a strong power coupling but the slot and patch resonances will be combined.

Details of the feed designs

A first feed with slot dimensions corresponding to the first case mentioned above has been designed to resonate at 3.9 GHz, which is significantly above the LH band of interest ($\sim 2-3$ GHz). After some tests, a second slot has been subsequently designed to resonate around 3 GHz, in order to enhance the power coupled to the patch.

For both feeding systems, the feed line is printed on a FR4 substrate ($\varepsilon_r = 4.4$, $\tan\delta = 0.02$) of thickness $h = 1.6$ mm. A strip width of $w = 3.04$ mm has been chosen for a characteristic impedance $Z_c = 50\ \Omega$. The effective permittivity of this MS line is $\varepsilon_{r,\text{eff}} = 3.37$. For a maximum coupling through the slot, the effective length L_{stub} of the open ended stub (including the effect of the fringing fields) should be a quarter wavelength at the frequency of interest, such that the current is maximum below the slot. The characteristic dimensions for the two considered feeding parts, referred to here as feeds "F1" and "F2", are reported in Table 5.6.

	L_{slot}	W_{slot}	$f_{\text{res,slot}}$	L_{stub}	$L_{\text{stub}} = \lambda_g/4$ at
Feed "F1"	25 mm	0.5 mm	3.9 GHz	15.72 mm	2.5 GHz
Feed "F2"	35 mm	1.0 mm	2.9 GHz	13.45 mm	2.9 GHz

Table 5.6: Characteristic dimensions of the two considered feeding parts (see Figure 5.25).

The measured and simulated input impedance for these two feeding parts (without meta-slab and patch) are shown in Figure 5.26. A good agreement between simulation and measurement is observed. Two resonances can be observed in the considered frequency band. The first one is the first resonance of the slot. The second one is a dipole-like half wavelength resonance of the stub. In the frequency range of interest (2 - 3 GHz), the input impedance of the feed "F1" is mainly inductive and smoothly varying, whereas it experiences more variation for the feed "F2".

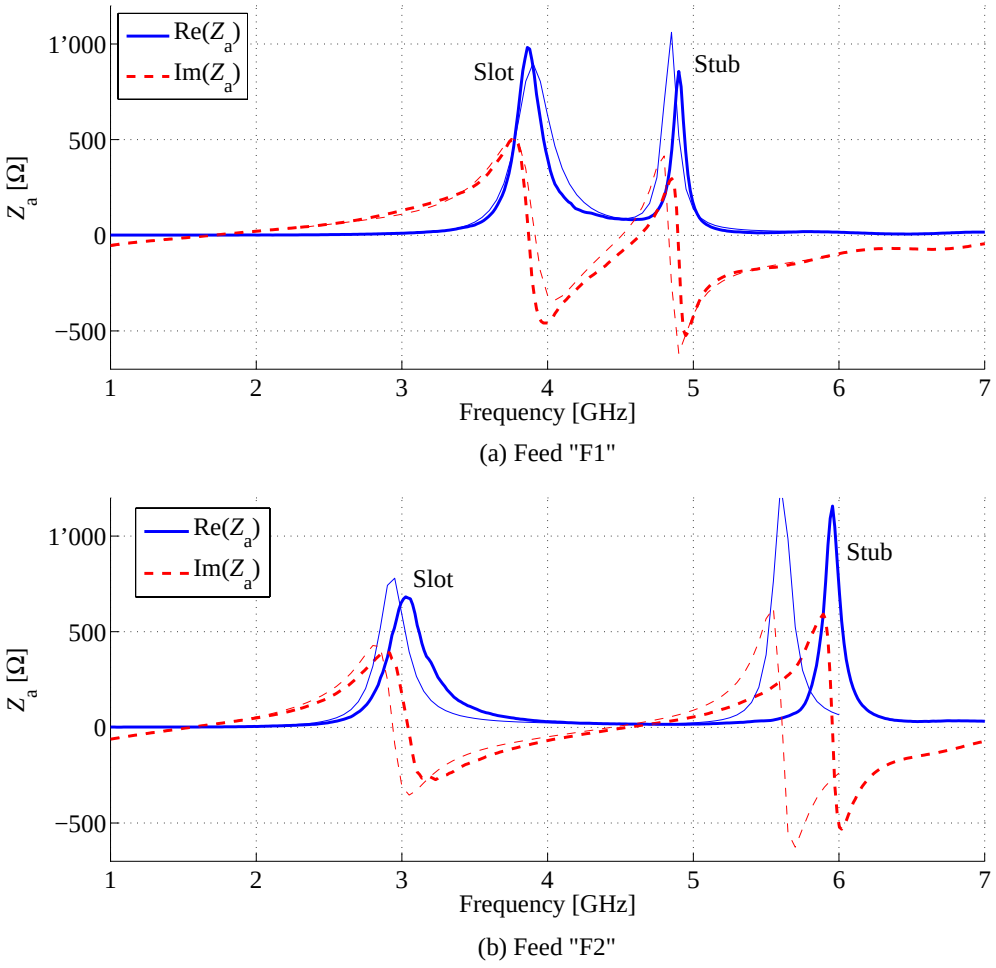

Figure 5.26: Input impedance of the two considered feeding parts without patch and meta-slab. Thick line: measurement, thin line: HFSS.

d. Practical realization

Two pictures of the realized system are shown in Figure 5.27. All the elements of the system (feed, meta-slab, patch) have not been stuck together in order to allow their re-use in various configurations. Alternatively, we have used a special fixation system to maintain all the elements together and to perform the alignment. The patches are made of beryllium bronze with a thickness of 0.2 mm. They have been obtained by chemical etching.

e. Measurement results for a first representative configuration

We consider here the case of the aperture coupled meta-patch with $L_{\text{patch}} = 6N = 39$ mm and $W_{\text{patch}} = 50.7$ mm, with the feed "F1". The measured input impedance is shown in Figure 5.28, where the same information is presented in different manners, for comparison with other cases and interpretation. In particular, we compare with the same structure using a foam substrate in place of the meta-slab, and with the same structure in which the patch has been removed (i.e., the meta-slab above the slot).

It can be noted here that a strict correspondence between the predicted resonances and the observed peaks is hard to establish. Indeed, the prediction have been done without taking fringing fields effect into account, which was shown to be rather important for the considered patch antennas over foam substrates. The results reveal several peaks that can be attributed to resonances, and are discussed point by point below:

- The stub resonance can still be found around 4.9 GHz. We can see an additional resonance just before the stub resonance.
- Above the stub resonance (between 5 and 7 GHz), the patch has only little effect [see comparison with the case "without patch" in (d)].
- Instead of a distinct slot resonance initially around 3.9 GHz, we can see three peaks between 2.9 and 3.9 GHz [see (a) and (c)]. These peaks, which appear in the complex mode band of the dispersion diagram, seem to also exist when the patch is removed, although they are less pronounced in the latter case [see (c)]. The presence of these peaks remains unexplained.
- For the reference patch antenna over foam substrate, the patch resonance can only be seen on the vertical zooms (b) and (d) (peak surrounded with a circle at 2.73 GHz), since it is partially hidden by the slot resonance occurring near 3.9 GHz.
- For the meta-patch, we essentially observe a single resonance in the frequency range of interest (mixed RH/LH band), which is only visible on the vertical zooms (b) and (d) (peak surrounded with a circle at 1.85 GHz). This peak probably corresponds to the resonance occurring in the RH branch of the first mixed RH/LH mode (resonance with $n = 1$ in Figure 5.22), since it is the more likely to be excited in such a configuration. It can be noted that this resonance is lower than that of the same patch over foam, which can be explained by the fact that the meta-slab acts here as a conventional loading dielectrics. The fact that this RH resonance appears lower in frequency than expected

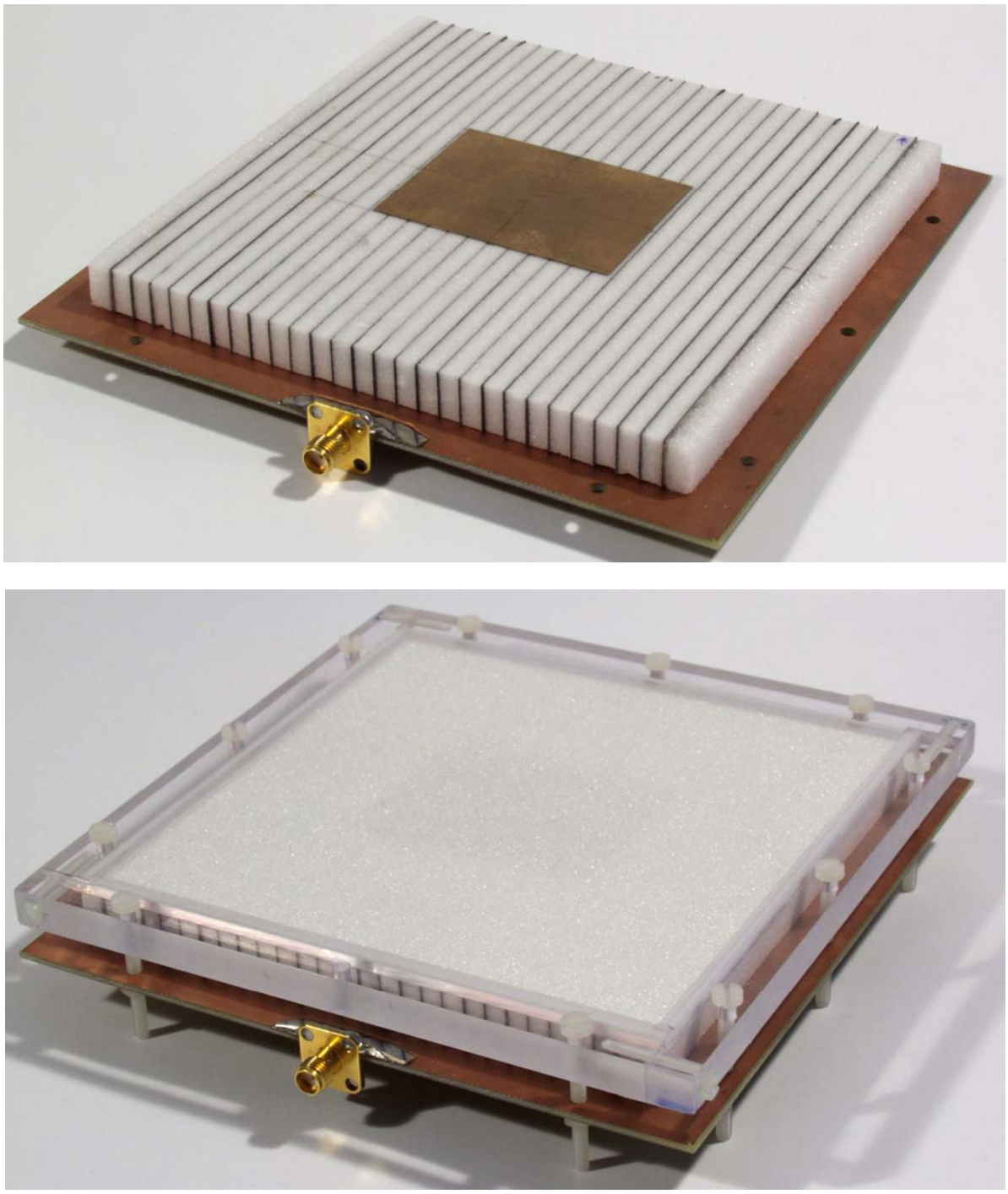

Figure 5.27: Pictures of the realized aperture coupled meta-patch antenna. Bottom: same as top, but with a polycarbonate (Makrolon) frame and a foam layer (thickness 3 mm) to maintain all the elements together. The frame is fixed at the ground plane by means of 11 nylon screws.

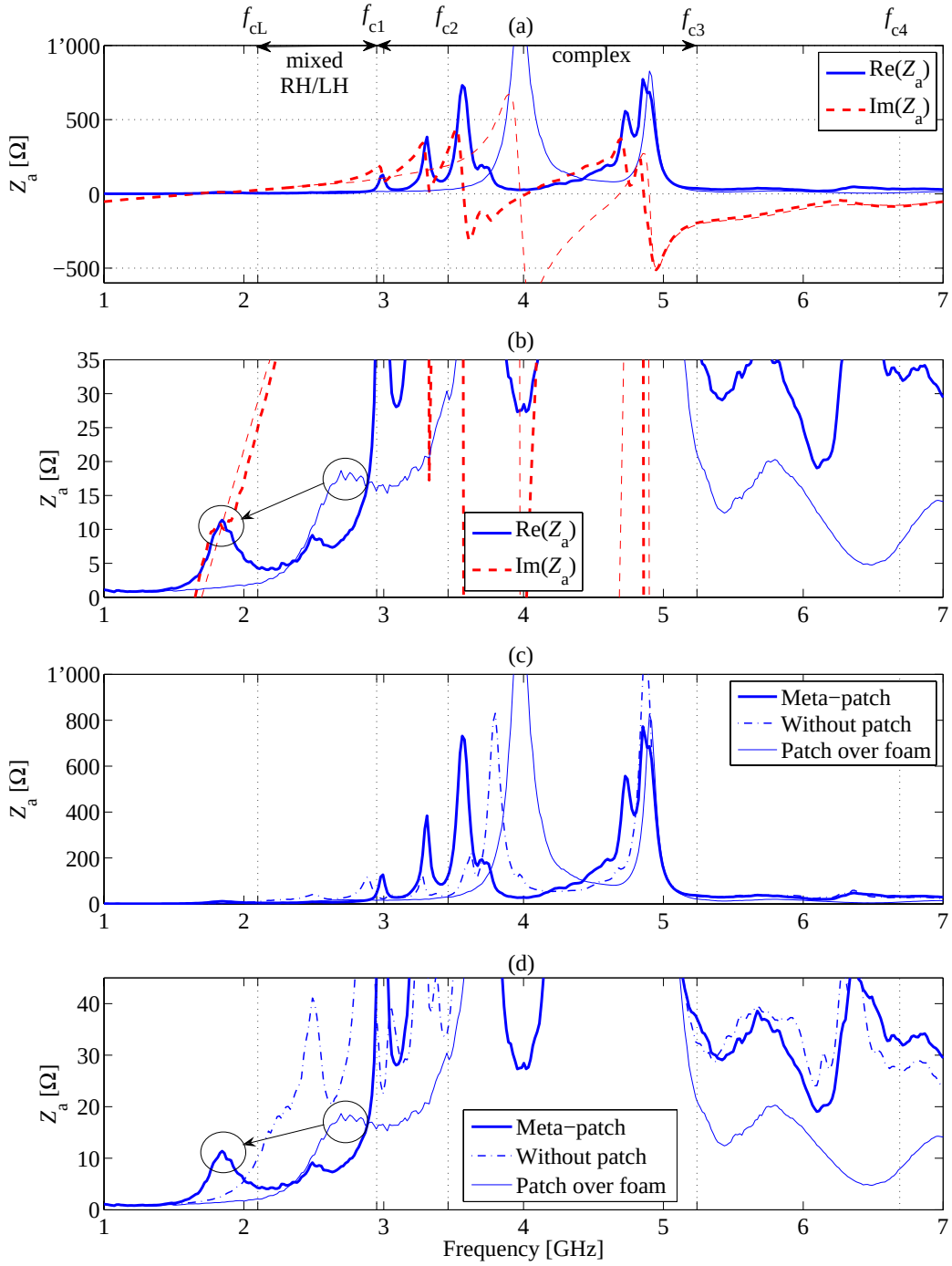

Figure 5.28: Measured input impedance of the considered aperture coupled meta-patch (in thick continuous line in all the plots). (a) Real and imaginary parts, with comparison with the same antenna over a foam substrate (thin line). (b) Vertical zoom of (a). (c) Real part only, with comparison with the same antenna over a foam substrate and the same antenna without the patch. (d) Vertical zoom of (c).

may be related to fringing fields effect at the edges of the patch, which was shown to be rather important for such thick patch antennas.

- A small peak around 2.5 GHz can be observed. However, this peak is also present for the case without patch, and therefore it cannot be attributed to the meta-patch.

As a conclusion, we did not observe most of the patch resonances predicted in Table 5.3 and illustrated in Figure 5.22. This can be related to the following issues:

- The real meta-slab is not limited to the size of the patch, as assumed in Section 5.6.1 for the derivation of the resonant frequencies. As a result, some modes may continue to propagate after the patch, which therefore does not impose a clear limit for the appearance of resonant modes in the equivalent cavity below it.
- The feeding system used may not be accurate for identifying resonances in that frequency range (2 - 3 GHz), since the coupled power is too low.

To that respect, a second feed system (feed "F2") was designed and tested, and a smaller meta-slab which has exactly the same size as the patch has been realized. The corresponding results are reported in the next section.

f. Measurement results for a second representative configuration

We consider here a meta-patch antenna with a reduced meta-slab, as shown in Figure 5.29. The patch dimensions are the same as in the previous example. The two designed feeds have been tested. The most interesting results have been obtained with the feed "F2". The corresponding measured input impedance is shown in Figure 5.30.

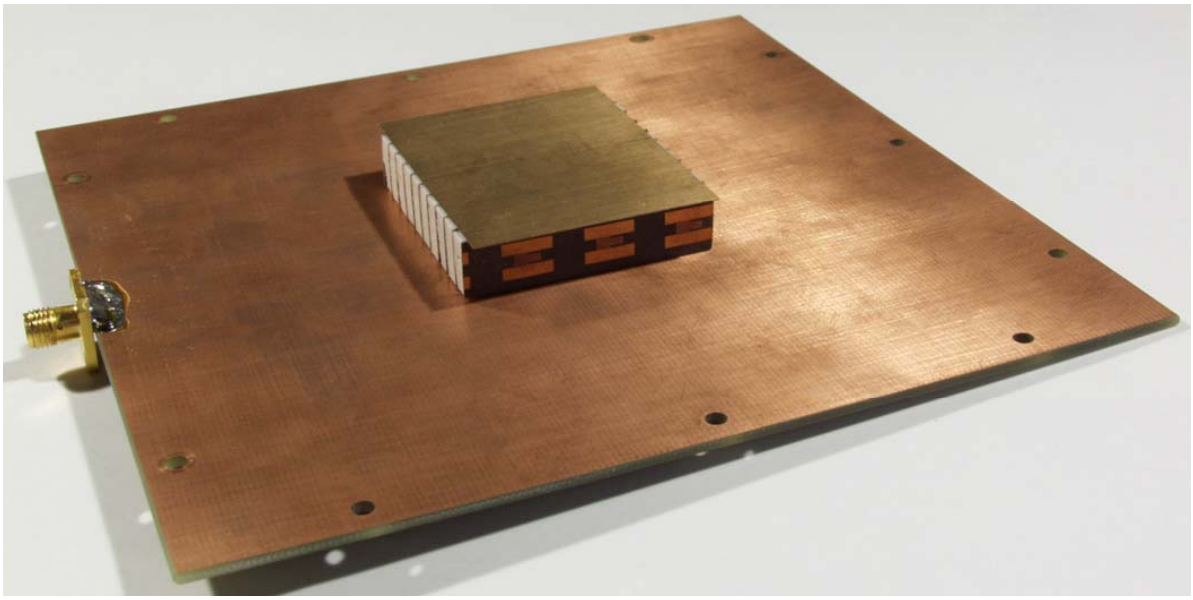

Figure 5.29: Aperture coupled meta-patch antenna using a reduced meta-slab.

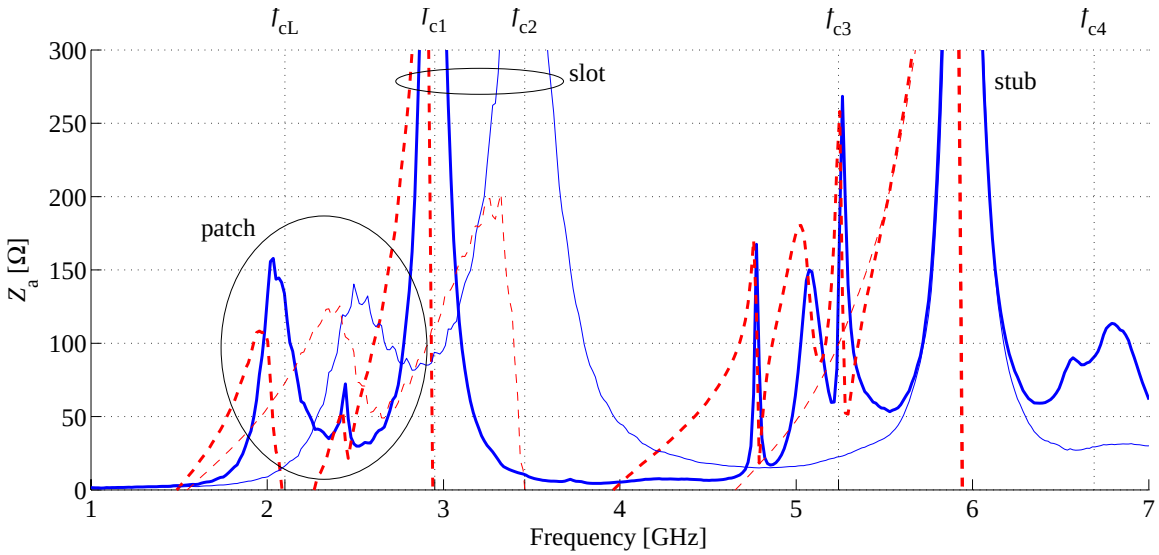

Figure 5.30: Measured input impedance of the antenna shown in Figure 5.29. Thin line: same antenna with a foam substrate in place of the meta-slab. Continuous line: real part; dashed line: imaginary part.

The observed resonances are commented below:

- We observe an interesting phenomenon: two resonances can be seen in the mixed RH/LH band of interest (from f_{cL} to f_{c1}), at 2.03 GHz and 2.44 GHz. The most important resonance (at 2.03 GHz) is probably the RH resonance of the patch, i.e. the resonance $n = 1$ occurring in the RH range of the mixed RH/LH band. The fact that it does not appear at the expected frequency may be related to fringing field effects. The second resonance (at 2.44 GHz) can be one of the higher order $n > 1$ resonances occurring in the LH branch of the mixed RH/LH mode.
- The third peak corresponds to the slot resonance. It appears around 3 GHz, as for the feeding part alone [see Figure 5.26(b)].
- Three close resonances appear at 4.77 GHz, 5.07 GHz and 5.26 GHz. They may be associated with higher order Floquet modes of the meta-slab (modes "m2", "m3" or "m4" in the dispersion diagram of Figure 5.12).
- The last peak occurring around 6 GHz should correspond to the second resonance of the slot, or the resonance of the stub, or a combination of both.

The nature of some these resonances has been further assessed by inspecting the corresponding radiation patterns. We show in Figure 5.31 the measured radiation patterns for the two resonances of primary interest. It can be observed that these two resonances exhibit a patch-like radiation pattern. As the maximum is directed toward broadside, they may correspond to the odd modes of the meta-patch, i.e. the modes with $n = 1$, 3 or 5 listed in Table 5.3. However, as the predicted resonant frequencies in Table 5.3 are based on an approximate model of the actual structure, it is rather difficult to determine which resonance is actually excited in the

meta-patch. Let us finally mention that the nature of the other observed resonances have also been assessed through their measured radiation pattern. However, no clear cut information was obtained from these investigations.

5.7 Conclusions on meta-slabs and meta-patch antennas

5.7.1 Summary and conclusions on meta-patch antennas

First, analytical investigations based on the cavity model and dispersion diagrams revealed that meta-patches may offer interesting multi-frequency capabilities (Section 5.6.2). More precisely, several rather close resonant frequencies may occur in the mixed RH/LH band of the dispersion diagram of the meta-patch. However, the ability of a given excitation to excite these resonances could not be assessed by simple analytical models or numerical investigations, which is why an experimental approach has been adopted for the investigations of the whole antennas. A full measurement campaign has been carried out on aperture coupled meta-patch antennas, as the aperture coupling seemed the most appropriate to highlight the existence of the predicted resonances in order to validate the concept. For that purpose, input impedances and radiation patterns have been measured in various configurations.

In general, rather complex behaviours have been observed, suggesting that the meta-slab, the patch and the feeding part interact in a subtle way, thereby leading to complex phenomena which were not able to be fully explained by the simple cavity model used to predict the resonant frequencies. In summary, we observed that:

- The developed system did not allow highlighting the existence of all the predicted resonances in the mixed RH/LH band (Table 5.3). In most cases, the only patch resonance that can be seen from the input impedance in this frequency region seems to be the resonance occurring in the RH branch of the first mixed RH/LH mode. Probably, the chosen excitation is not able to efficiently excite the other resonances occurring in the LH branch, which essentially exhibits a CPS-like field distribution.
- Several other resonances have been observed in other frequency bands, like in the complex mode band for instance, but their origin was not able to be identified and explained.

The identification of the nature of the resonant frequencies observed from the input impedance by using the numerically calculated dispersion diagram appeared to be a rather difficult task. In particular, it is believed that the interpretation of the results was complicated by the following issues:

- The resonant frequencies of the meta-patches may be significantly affected by the presence of fringing fields effect at the edges of the patch, which, with such a thick substrate (10 mm), may lead to a wrong estimation of the resonant frequencies with the cavity model. For antennas over conventional homogeneous substrates, this phenomenon can simply be taken into account by increasing the effective length of the patch, but no such simple models are available for the application of such a correction to meta-patches.

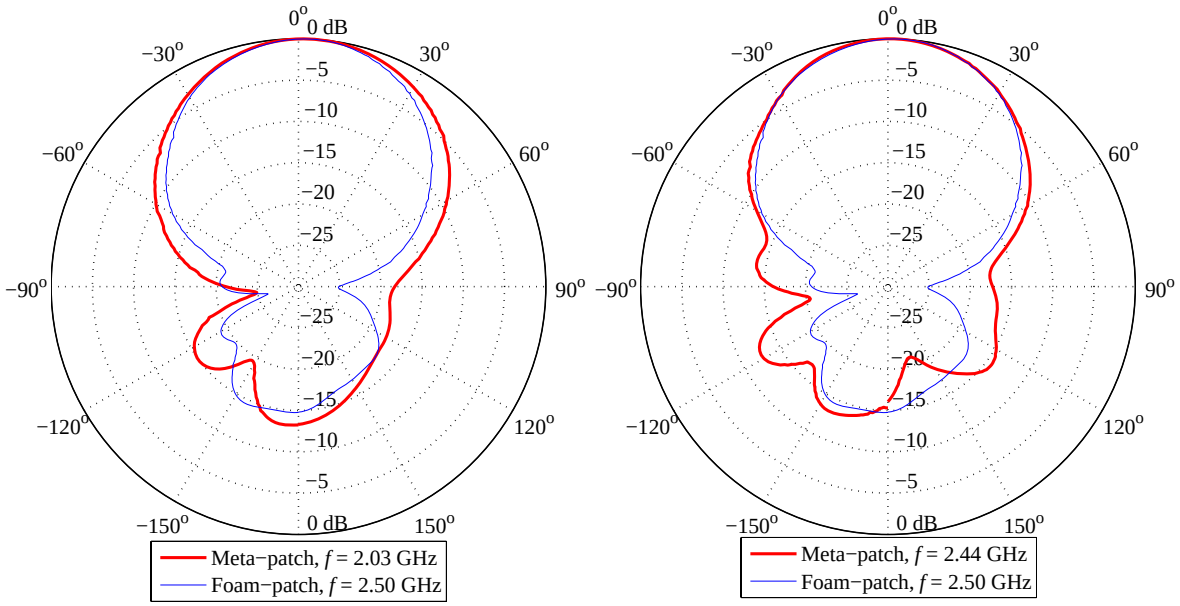

(a) E plane

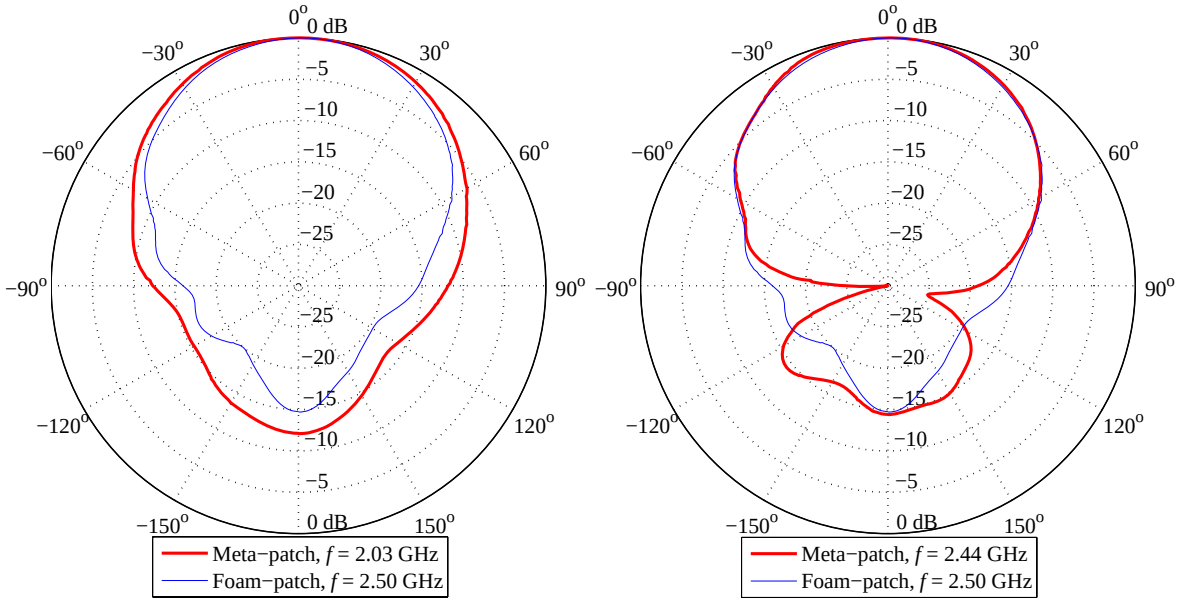

(b) H plane

Figure 5.31: Radiation patterns for the aperture coupled meta-patch antenna with the reduced meta-slab, at the two resonances which are attributed to the patch. In each plot, the reference case of the same patch antenna with a foam substrate at its own resonant frequency is also shown. Only the co-polarization is shown, in the E and H planes (defined as for a conventional aperture coupled patch antenna).

- Although the aperture coupled feed appeared to be an appropriate solution for a good separation between the feed and the radiating part, the excitation of the meta-patch through the slot is subject to the following problems:
  - If the resonances of the meta-patch are too far away from the slot resonance, the coupling through the slot is very poor.
  - If the resonances of the meta-patch are too close to the slot resonance, the latter affects the patch resonances, which results in a frequency shift compared to the expected values.

The meta-patches with reduced meta-slabs (limited to the size of the patch) appeared to exhibit less complex behaviours than the corresponding structures using the full size meta-patch. In particular, two resonances exhibiting patch-like radiation patterns have been observed in the frequency range of interest (mixed RH/LH band). These resonances may be related to the odd modes of the meta-patches predicted by the cavity model and dispersion diagram (Section 5.6.2), but the exact nature of each mode could not be determined by a simple inspection of the corresponding radiation patterns.

Possible recommendations for further activities on meta-patch antennas could be the evaluation of the nature of each resonance through near field measurements, or the investigation of meta-patch antennas using a coaxial probe feed. This feeding mechanism is a priori not subject to the aforementioned limitations of the aperture coupled feed.

5.7.2 Discussion on volumetric layered TL-based MTMs

We provide here a general discussion on volumetric layered TL-based MTMs based on the results obtained in this work and other related studies.

From a dispersion point of view, we have shown that such volumetric structures based on the TL approach may support LH mode propagation. The main problem however comes from the excitation of these modes by an external field, which can be the natural field of a patch antenna as considered here, or an incident plane wave from free-space, rather than an embedded source. The main reason is that the fields associated with the LH modes essentially exhibit the distribution of the host TL in which the structure is implemented (CPS in our case), and are thereby partially incompatible with the external excitation fields, hence a rather poor coupling. This problem seems inherent to any type of volumetric MTMs based on loaded TL networks, as discussed in the following comparison with other related studies.

Several investigations on various topologies of volumetric MTMs based on the TL approach have been reported (see the state-of-the-art, Section 2.2.4), but only few of them consider the problem of the excitation from an external source. First, let us consider again the pioneer work on volumetric layered TL-based MTMs initially reported in [117], and further investigated in [244–246]. In these studies, the planar structures which are stacked consist of 2D CRLH TL networks with the topology shown in Figure 5.32. The two-dimensionality of the stacked circuits was required for the targeted focusing applications. By contrast, our investigations were only concerned with 1D CRLH TLs for the stacking, since the targeted antenna application

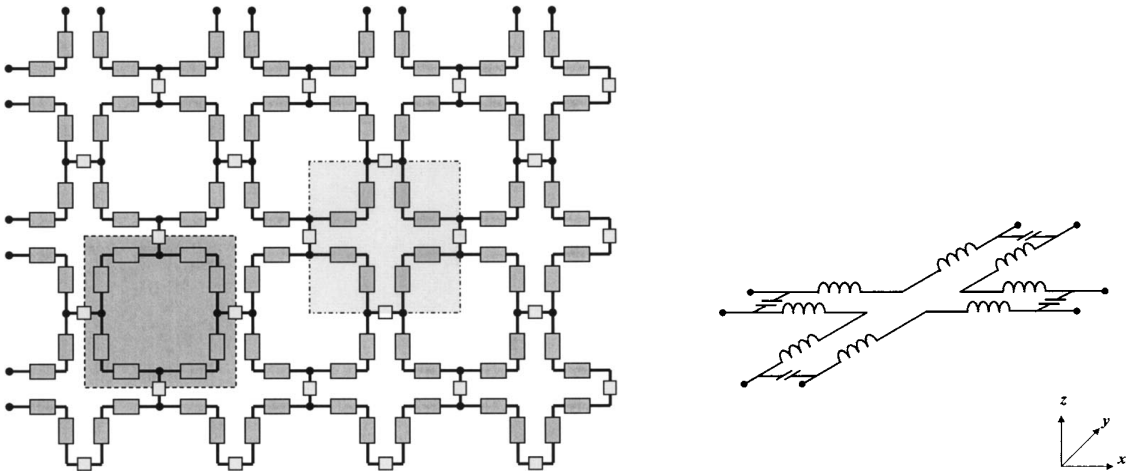

(a) (b)

Figure 5.32: (a) 2D TL network with generalized lumped loading to be used for the stacking. (b) Equivalent circuit for the unit cell shown in light grey in (a), for a purely RH medium (for a LHM, the positions of the L and C elements are interchanged). (Taken from [117]).

only required a LH effect in a specific direction of propagation. This difference, which might simply appear as a simplification from a 2D to a 1D configuration, eventually appears to have an important effect on the coupling capabilities of the resulting volumetric structures. Indeed, an efficient coupling from free-space was achieved with the 2D stacked structures [245], whereas their 1D counterparts investigated in this work were unable to be efficiently excited from an external field. A possible explanation of this phenomenon relies on the fact that a 2D TL network such as the one shown in Figure 5.32 can also be seen as a 2D array of capacitively loaded rings interconnected by shunt inductances, as suggested by the unit cell shown in dark grey in Figure 5.32. The resulting loops seem to enable a better coupling from the magnetic field of the incoming wave (directed along the loops axis), compared to the case of the 1D stacked circuits. From this point of view, the structure of Figure 5.32 shares many similarities with an array of SRRs.

It also results from these considerations that this stacking of 2D MTMs, which was initially intended to be a non-resonant structure since based on the TL approach, eventually exhibits a resonant behaviour due to the formation of SRR-like loops. It can be noted that this structure was indeed analyzed in [117] as a WG loaded with resonant capacitively loaded loops. Therefore the question arises, whether a volumetric MTM based on the TL approach can be simultaneously non-resonant and efficiently coupled from free-space. To our understanding, the main difficulty relies on the implementation of the series capacitances required in non-resonant TL-based MTMs. Indeed, the latter require a host TL in which a discontinuity is introduced to enable a capacitive effect, but cannot be directly implemented in free-space. By contrast, implementing the shunt inductances is less problematic since metallic wires in free space basically provide the desired response, similarly to inductive connections between the two conductors of

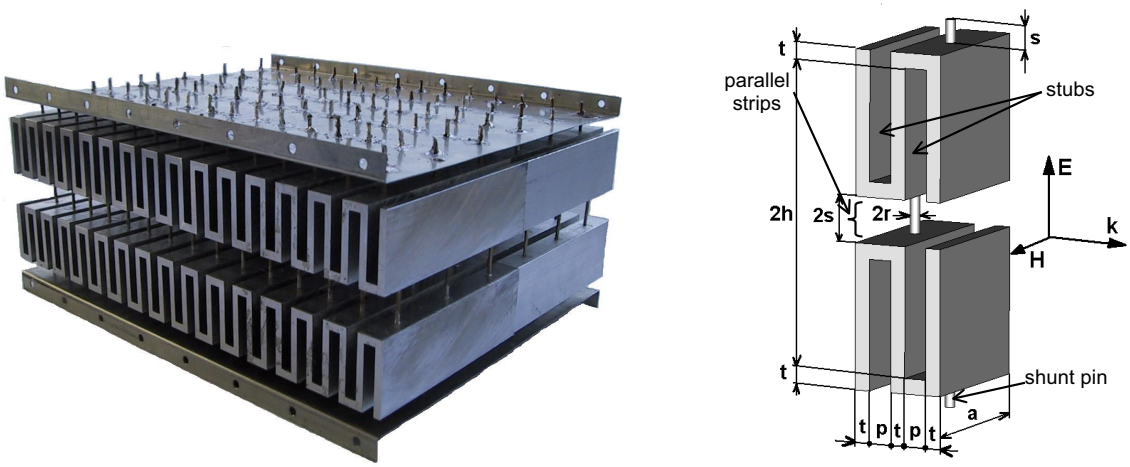

(a) (b)

Figure 5.33: (a) Volumetric TL-based MTM with 1D LH propagation and efficient coupling from free-space. More layers can be added in the vertical direction if needed. (b) Unit cell. (Taken from [248]).

a TL.

Another example supporting this argumentation is the volumetric MTM presented in [247,248] and shown in Figure 5.33. This structure can be seen as a PPWG periodically loaded in a LH fashion. The conducting vertical pins implement the shunt inductances, and the series capacitances are realized by short circuited parallel strip stubs operated above their first "quarter wavelength frequency". Although this TL-based structure was shown to be efficiently coupled from free-space, it cannot be considered as a non-resonant MTM since the series capacitances are implemented by shorted stubs, which are resonant elements by essence.

As a conclusion, the series capacitances in volumetric TL-based MTMs for which an excitation from free-space is possible always seem to appear through resonant elements, such as the SRR-like loops in the stacked MTM of Figure 5.32, or the shorted stubs in the volumetric MTM shown in Figure 5.33. This means that the conceptual distinction between TL-based MTMs and MTMs made of arrays of resonant inclusions, which appeared evident for 1D or 2D structures, seems to loose its very meaning for volumetric MTMs that can be effectively coupled from free-space. In other words, a volumetric MTM with free-space coupling capabilities would always rely on resonances, whatever it is implemented as an array of inclusions or a loaded TL network. It can be noted that these considerations emanate from a personal appreciation of the MTM field in general, but they have not been further demonstrated in this work. A careful inspection of all the reported volumetric LHM would be required to confirm or invalidate these statements, which is out of scope of the present research work.

Let us finally note that a possible way of coupling power into a volumetric TL-based MTM consists in using transition layers similar to electrically short horn antennas, as reported in [118]. Although this technique allows an efficient coupling from free-space, it requires an

additional layer (transition layer) between the MTM and free-space, which may prevent the occurrence of interesting interface effects such as the ones involved in subwavelength focusing. This alternative has not been considered in the above discussion, since it results in conceptually different structures due to the addition of transition layers.

6 Enhanced periodic structure analysis based on a multiconductor transmission line model

6.1 Introduction

6.1.1 Motivation

The motivation for developing the periodic structure analysis technique presented in this chapter arose from different aspects of the works carried out in this thesis.

- First, retrieval procedures from scattering parameters, such as the technique investigated in Chapter 3, were shown to suffer from a dependence of the extracted parameters with the size of the considered MTM sample (see discussion in Section 3.6.2), which is a result of complex coupling phenomena occurring between cells. This can be seen as an effect of inter-cell couplings occurring through the higher order evanescent modes of the host guiding structure, which are not captured by the simple dominant-mode analysis of the unit cell. To that respect, a description of the unit cell involving more modes of the host guiding structure is required.
- Second, it was of particular interest to extend the Bloch wave analysis presented in Section 4.2, which essentially applies to two-conductor periodic structures, to more complex structures consisting of periodically loaded multiconductor transmission lines (MTLs). These structures cannot be analyzed with the dominant-mode Bloch wave analysis of Section 4.2 since several modes of the host guiding structure are propagating. An example of such a structure is the volumetric layered TL-based MTM investigated in Chapter 5 (the "meta-slab").

Although the two aforementioned classes of problems seem rather different, a common formulation has been found thanks to the technique presented here, which can in principle apply to any periodic structure which is based on a multimodal or multiconductor representation of its unit cell. Most of the material presented in this chapter can be found in [249].

6.1.2 Context and related works

Propagation of waves in periodic structures is a classical subject which has recently benefited from a renewed interest in the context of the analysis of electromagnetic bandgap (EBG)

structures and metamaterials (MTMs). Analysis of periodic structures mainly consists in describing the propagation of so-called Floquet modes (or Bloch waves) through the definition of Bloch propagation constants and Bloch impedances. Determining these parameters from the description of the unit cell of the periodic structure has been referred to in this work as the *Bloch wave analysis*.

The most common and simplest implementation of Bloch wave analysis consists in determining the Bloch parameters by solving a classical matrix eigenvalue problem from the transfer matrix of the unit cell expressed in terms of the fundamental mode of the host guiding structure, as detailed in Section 4.2. This simple approach assumes that the coupling between adjacent cells is accurately described by a single mode of the host TL. Here we consider two classes of periodic structures for which such a representation based on dominant-mode interaction between cells is not sufficient, and which thus require more elaborated techniques such as the one presented in this chapter.

- The first class of periodic structures concerns periodically loaded MTLs. Examples of such structures are TL-based MTMs such as the shielded mushroom and related structures [240, 250], and novel types of coupled-line couplers [162, 163]. For these structures, the dispersion relation is conveniently obtained from the resolution of a classical eigenvalue problem involving the generalized transfer matrix of the unit cell associated to the conductor voltages and currents of the host MTL, as reported in [240, 250].

- The second class concerns periodically loaded waveguides (WGs) operated in their monomode region, but where non-negligible higher order evanescent mode coupling occurs between adjacent cells. Examples of such structures are found in corrugated WGs and WGs periodically loaded with irises and other metallic or dielectric loadings [40, 251–259]. The corresponding results reported in the literature focus on the determination of the dispersion relation from an eigenvalue problem involving a generalized (or multimodal) representation of the unit cell in terms of the modes of the host WG. To this aim, two approaches have been considered, the first of which consists in deducing the dispersion relation from the eigenvalues of the generalized transfer matrix of the unit cell [251–254] (i.e. by solving a classical eigenvalue problem), whereas the second one consists in solving a generalized eigenvalue problem involving the generalized scattering matrix of the unit cell [252, 255–258]. Although the approach with the transfer matrix benefits from a very simple formulation and fast implementation, it suffers from potential numerical instabilities from exponentially growing terms if evanescent modes of the host WG are included in the multimodal representation of the unit cell. On the other hand, the approach with the scattering matrix ensures that these instabilities are prevented, and is thus unconditionally stable [252]. In the framework of numerical techniques aimed at computing the dispersion relation for periodic structures, a similar approach based on the resolution of a generalized eigenvalue problem was reported in [259]. This technique was preferred to the alternative approach involving a nonlinear determinant equation, which is generally more computational time consuming and does not easily provide information on complex modes [259].

Except for some specific works mentioned below, the aforementioned techniques for periodically loaded WGs and MTLs are restricted to the determination of the dispersion relation, through the calculation of eigenvalues. However, they do not exploit the corresponding eigenvectors, which contain information on the composition of the Floquet modes in terms of the host WG modes as well as the impedance properties of the periodic structure. These parameters are of interest for modeling the terminations (excitation and matching) of a finite length periodic structure. These issues have only been partially considered in some studies, in which the eigenvectors were used (i) to evaluate the field repartition between the conductors of a periodically loaded MTL for a given Floquet mode [260], and (ii) to reconstruct the total fields in an EBG WG, from which a Bloch impedance was defined [256].

In this work, we propose to model any type of periodic structures by an equivalent MTL. This technique provides the dispersion relation, as well as all the parameters needed to model in a systematic way the excitation and matching. This approach can be seen as an extension of the Bloch wave analysis based on dominant-mode interaction, which consists in modeling a periodic structure with an equivalent TL whose parameters are the Bloch propagation constant and Bloch impedance (Section 4.2). This extended technique was initially proposed by the authors in [261] but only applied to periodically loaded MTLs. An important aspect of this method is that its formulation is the same for periodically loaded WGs and MTLs, thereby providing a general and systematic framework applicable to both classes of periodic structures. Moreover, we will show that this technique is especially interesting for periodically loaded WGs supporting a single propagating Floquet mode, for which simplified efficient two-port models can be derived from the initial MTL model.

The proposed technique can be applied to a wide range of problems involving periodic structures. Here, it is applied to one example of each of the two main classes mentioned above. Both examples are negative-refractive-index (NRI) MTMs. The first one is a loaded MTL known as the shielded mushroom structure [240, 260]. This structure supports two propagating Floquet modes of opposite nature (positive/negative refractive index) at the same frequency. In this case, it is of particular interest to quantify the ability of a given excitation to couple power to each Floquet mode, a problem that can be solved using the presented approach. The second example consists of a periodic array of split-ring resonators (SRRs) and wires (SRR-wire medium, see Section 2.2.1.a.). For these structures, the importance of higher order mode interaction, as highlighted in [262, 263], results in the inaccuracy of an analysis based on dominant-mode interaction. In contrast, the proposed technique allows precisely modeling the dispersion and matching for these structures.

6.1.3 Content and organization of the chapter

The chapter is organized as follows: first, the general theoretical formulation of the developed technique is provided in Section 6.2. Then, its application to periodically loaded MTLs is described in Section 6.3 using the example of the shielded mushroom structure, and its application to periodically loaded WGs with higher order mode interaction is considered in Section 6.4 using the example of a SRR-wire medium. Conclusions on the developed technique are

reported in Section 6.5.

6.2 Theoretical formulation

6.2.1 Description and principle

We consider the propagation in periodically loaded WGs. A typical unit cell consists of a WG region containing obstacles, connected to two uniform WG sections. Note that here the term "WG" is used with its very general meaning of a one-dimensional guiding structure, i.e. it can designate a WG with any type of boundaries, a TL, or even a MTL. We focus on situations where N modes of the host WG, either propagating or evanescent, are needed to accurately represent the electromagnetic field at the termination planes of the cells. These modes will be referred to thereafter as the host WG modes, to clearly distinguish them from the Floquet modes associated to the periodic structure. Considering that the propagation of each host WG mode can be represented by equivalent voltage and current, a circuit representation as shown in Figure 6.1 can be adopted [122, 264, 265]. Due to the host WG modes orthogonality, each empty WG section is represented by N uncoupled TLs, each TL corresponding to a WG mode [265]. The obstacle region is represented by a 2N-port network which couples the various TLs together.

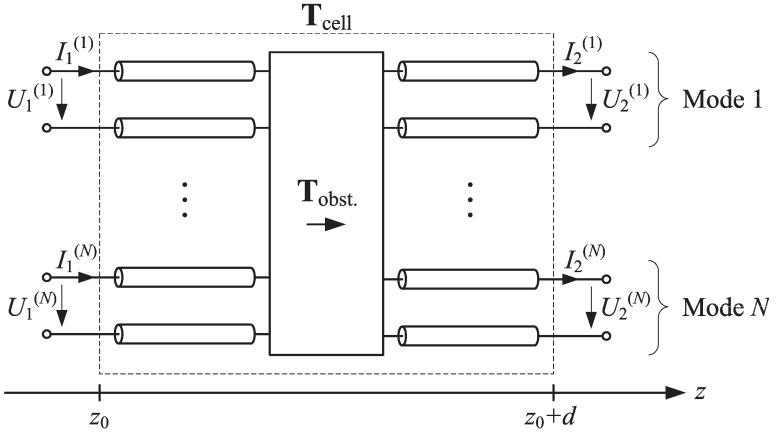

Figure 6.1: Circuit model of the unit cell: obstacles in a WG section for which N modes are considered. Each pair of ports corresponds to a mode.

The whole unit cell can also be represented by a generic 2N-port network characterized by its generalized transfer matrix $\mathbf{T}_{\text{cell}}$, as shown in Figure 6.2(a). Using the column vector notation for the voltages and currents

$$\mathbf{U}_i = \begin{bmatrix} U_i^{(1)} \\ \vdots \\ U_i^{(N)} \end{bmatrix}, \qquad \mathbf{I}_i = \begin{bmatrix} I_i^{(1)} \\ \vdots \\ I_i^{(N)} \end{bmatrix}, \qquad i = 1, 2 \tag{6.1}$$

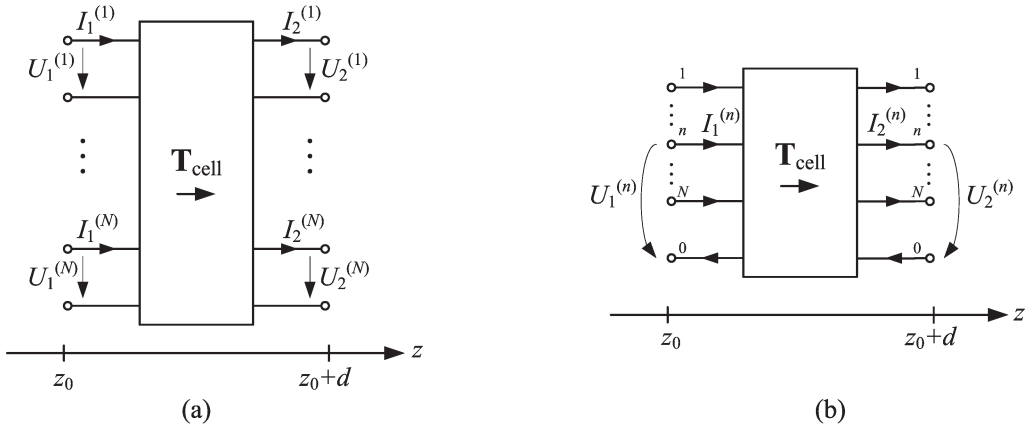

Figure 6.2: Network representations of the unit cell. The U and I are associated to the host WG modes. (a) 2N-port network, (b) 2(N+1)-terminal network.

the constitutive equation for the unit cell writes, in matrix form,

$$\begin{bmatrix} \mathbf{U}_1 \\ \mathbf{I}_1 \end{bmatrix} = \mathbf{T}_{\text{cell}} \begin{bmatrix} \mathbf{U}_2 \\ \mathbf{I}_2 \end{bmatrix} = \begin{bmatrix} \mathbf{A} & \mathbf{B} \\ \mathbf{C} & \mathbf{D} \end{bmatrix} \begin{bmatrix} \mathbf{U}_2 \\ \mathbf{I}_2 \end{bmatrix} \tag{6.2}$$

where $\mathbf{T}_{\text{cell}}$ is a $2N \times 2N$ matrix, which is partitioned here into the four sub-matrices $\mathbf{A}$, $\mathbf{B}$, $\mathbf{C}$, and $\mathbf{D}$. An alternative terminal-based representation, as usually used for multiconductor structures [266, 267], is also considered and shown in Figure 6.2(b). In this representation, a single reference terminal (number 0) is used for the return path of all the modal currents $I_i^{(N)}$, whereas the modal voltages $U_i^{(N)}$ are represented as differences of potential between the terminals and the reference. It should be noted that although the two circuits of Figure 6.2 differ in their graphical representation, they represent the same constitutive equations (6.2). It is worth emphasizing that the voltages and currents shown in Figure 6.2(b) are the host WG modal quantities, and therefore they are not associated to any physical conductor in the structure.

The obstacles in the periodic structure introduce some coupling between the host WG modes, and therefore an analogy with the coupling occurring between the conductors of a MTL can be drawn. Indeed, in a physical MTL, exciting one conductor will in general induce voltages and currents on the other conductors. Similarly, exciting a periodic structure with the fundamental host WG mode produces field contributions associated to the higher order host WG modes. Therefore, the aim of the technique presented in this paper consists in modeling a periodic structure of M cells of length d with a MTL section of length $L = Md$, as suggested in Figure 6.3, where the terminal-based graphical representation of the unit cell of Figure 6.2(b) has been chosen for the periodic structure. Such an analogy is valid at the termination planes of the cells, i.e. at the discrete locations $z = z_0 + md$ $(m \in \mathbb{Z})$. As a matter of fact, the presented method consists in an extension of the well-known equivalent TL modeling for dominant-mode periodic structures investigated in Section 4.2. The rest of this section is dedicated to the determination of the parameters of the equivalent MTL model. This demonstrates that the proposed equivalence is rigorous from a theoretical point of view.

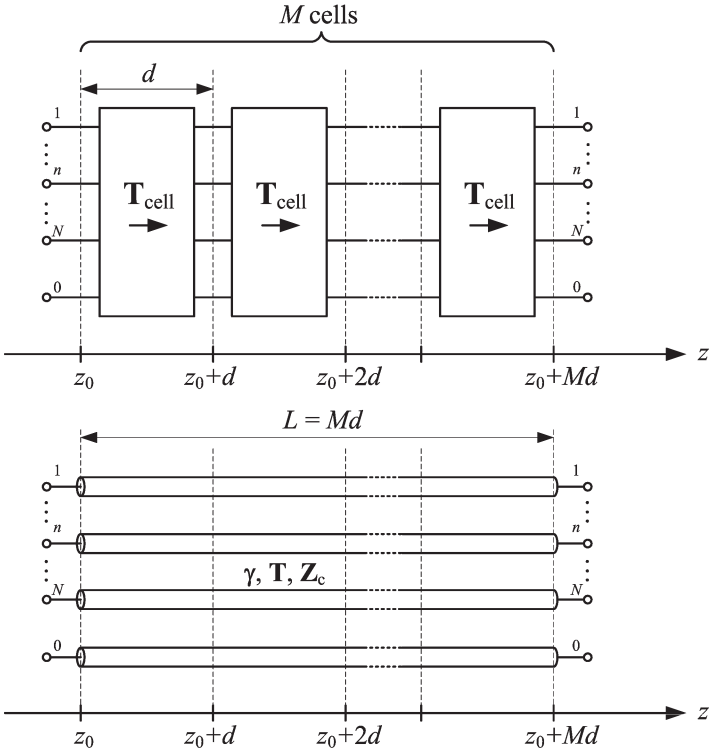

Figure 6.3: Equivalent MTL model for a periodic structure.

6.2.2 Basics of MTL theory

For the sake of clarity, aspects of MTL theory pertinent to the modeling technique presented in this chapter are recalled here. Further information on the topic can be found in [266, 267].

The propagation along a physical MTL is usually described by two sets of quantities (voltages, currents, impedances...), usually referred to as *natural* and *modal* [266]. The so-called *natural* quantities are associated with the actual voltages between the physical conductors of the MTL and currents flowing through these conductors. They are also called the *conductor* or *line* voltages and currents [267]. On the other hand, the *modal* quantities are associated with the quasi-TEM modes that can propagate along the MTL.

In a physical MTL with $N+1$ conductors, N quasi-TEM modes propagate, each of them being characterized by a propagation constant γ and a modal characteristic impedance $\hat{Z}_\mathrm{c}$. The propagation of a wave along the MTL can be represented as a superposition of these modes in terms of the corresponding modal voltages and currents $(\hat{U}, \hat{I})$, as expressed in column vector form in 6.3 and 6.4, where a distinction is made between the incident $(+)$ and reflected $(-)$ waves:

$$\hat{\mathbf{U}}(z) = \hat{\mathbf{U}}^+(z) + \hat{\mathbf{U}}^-(z) = e^{-\boldsymbol{\gamma} z}\hat{\mathbf{U}}_0^+ + e^{+\boldsymbol{\gamma} z}\hat{\mathbf{U}}_0^- \tag{6.3a}$$

$$\hat{\mathbf{I}}(z) = \hat{\mathbf{I}}^+(z) + \hat{\mathbf{I}}^-(z) = e^{-\boldsymbol{\gamma} z}\hat{\mathbf{I}}_0^+ + e^{+\boldsymbol{\gamma} z}\hat{\mathbf{I}}_0^- \tag{6.3b}$$

with

$$\hat{\mathbf{U}}^{+}(z) = +\hat{\mathbf{Z}}_{\mathrm{c}}\hat{\mathbf{I}}^{+}(z) \tag{6.4a}$$
$$\hat{\mathbf{U}}^{-}(z) = -\hat{\mathbf{Z}}_{\mathrm{c}}\hat{\mathbf{I}}^{-}(z) \tag{6.4b}$$

and

$$\boldsymbol{\gamma} = \mathrm{diag}\left\{\gamma_1, \ldots, \gamma_N\right\} \tag{6.5a}$$
$$\hat{\mathbf{Z}}_{\mathrm{c}} = \mathrm{diag}\left\{\hat{Z}_{\mathrm{c}1}, \ldots, \hat{Z}_{\mathrm{c}N}\right\} \tag{6.5b}$$

The diagonal matrices $\boldsymbol{\gamma}$ and $\hat{\mathbf{Z}}_{\mathrm{c}}$ gather the propagation constants and modal characteristic impedances for all modes, respectively. Following the notation used in [266], the circumflex "ˆ" is used for modal quantities ($\hat{U}$, $\hat{I}$), to distinguish these from the natural ones (U, I).

In a MTL, the modal and natural quantities are linked by the $N \times N$ transformation matrices $\mathbf{T}$ and $\mathbf{W}$, as expressed in (6.6). The columns of $\mathbf{T}$ and $\mathbf{W}$ represent the natural voltages and currents repartition on the conductors when only the corresponding mode is present.

$$\mathbf{U}(z) = \mathbf{T}\hat{\mathbf{U}}(z) \tag{6.6a}$$
$$\mathbf{I}(z) = \mathbf{W}\hat{\mathbf{I}}(z) \tag{6.6b}$$

A characteristic impedance matrix in natural coordinates $\mathbf{Z}_{\mathrm{c}}$ is defined to link the natural voltages and currents, as expressed in (6.7):

$$\mathbf{U}^{+}(z) = +\mathbf{Z}_{\mathrm{c}}\mathbf{I}^{+}(z) \tag{6.7a}$$
$$\mathbf{U}^{-}(z) = -\mathbf{Z}_{\mathrm{c}}\mathbf{I}^{-}(z) \tag{6.7b}$$

with

$$\mathbf{U}^{\pm}(z) = \mathbf{T}\hat{\mathbf{U}}^{\pm}(z) \tag{6.8a}$$
$$\mathbf{I}^{\pm}(z) = \mathbf{W}\hat{\mathbf{I}}^{\pm}(z) \tag{6.8b}$$

It can be noted that $\mathbf{Z}_{\mathrm{c}}$ is in general non-diagonal and symmetrical.

Using (6.4), (6.7) and (6.8), it can be shown that the modal and natural characteristic impedance matrices are linked by (6.9).

$$\mathbf{Z}_{\mathrm{c}} = \mathbf{T}\hat{\mathbf{Z}}_{\mathrm{c}}\mathbf{W}^{-1} \tag{6.9}$$

The matrices $\hat{\mathbf{Z}}_{\mathrm{c}}$, $\mathbf{T}$ and $\mathbf{W}$ are not uniquely defined, but the following normalization can be used [266, 267]:

$$\mathbf{W}^{\mathrm{T}} = \mathbf{T}^{-1} \tag{6.10}$$

The matrix $\mathbf{Z}_{\mathrm{c}}$, however, is uniquely defined. In summary, a MTL is fully characterized by the three following $N \times N$ matrices: $\boldsymbol{\gamma}$, $\mathbf{Z}_{\mathrm{c}}$ and $\mathbf{T}$.

6.2.3 Correspondence between a periodic structure and its MTL model

As mentioned previously, we use here the MTL model as a representation of a periodic structure. As a result, the aforementioned modal and natural quantities represent physical quantities different from the case of the physical MTL. We make here a distinction between the two classes of periodic structures studied in this work.

a. General case: periodically loaded WGs

This is the general case considered so far, for which the transfer matrix $\mathbf{T}_{\text{cell}}$ is expressed in terms of the modes of the host WG. In this case:

1. The natural quantities of the MTL modeling the periodic structure correspond to the host WG modal quantities.
2. The modal quantities of the MTL modeling the periodic structure correspond to the Floquet modal quantities of the periodic structure.

This correspondence is summarized in the two first lines of Table 6.1.

b. Particular case: periodically loaded MTLs

For periodically loaded MTLs, the "host WG" is a physical MTL which supports several quasi-TEM modes and an infinity of higher order modes. In the case where the higher order modes are all evanescent and play a negligible role in the periodic structure, the latter can be analyzed in a convenient way from a terminal-based representation of the unit cell, i.e. a representation which links the natural quantities of the host MTL at the two termination planes of the cell. The resulting correspondence is summarized in the third line of Table 6.1.

A fundamental feature of the presented modeling technique is that its formulation is the same in the two aforementioned cases. The only difference lies in the nature of the transfer matrix $\mathbf{T}_{\text{cell}}$, either associated to the host WG modes, as in the general case ("modal $\mathbf{T}_{\text{cell}}$"; second line of Table 6.1), or to the physical conductors, as in the particular case of periodically loaded MTLs ("terminal $\mathbf{T}_{\text{cell}}$"; third line of Table 6.1). In both cases, $\mathbf{T}_{\text{cell}}$ can be obtained from full-wave simulation, as discussed in Section 6.2.5.

6.2.4 Parameters of the equivalent MTL

We consider here the determination of the parameters of the MTL ($\boldsymbol{\gamma}_{\text{B}}$, $\mathbf{Z}_{\text{B}}$ and $\mathbf{T}_{\text{B}}$) from the knowledge of the transfer matrix of the unit cell $\mathbf{T}_{\text{cell}}$, so that the model is exactly equivalent to the periodic structure under study. Note that here the subscript 'B', for Bloch, is used to emphasize that these MTL parameters are associated to the MTL model of the periodic structure (i.e. $\boldsymbol{\gamma}_{\text{B}}$, $\mathbf{Z}_{\text{B}}$ and $\mathbf{T}_{\text{B}}$ correspond to $\boldsymbol{\gamma}$, $\mathbf{Z}_{\text{c}}$ and $\mathbf{T}$ in Section 6.2.2). We restrict the present analysis to reciprocal and symmetrical unit cells.

Utilization of the MTL model		Natural quantities ($\mathbf{U}$, $\mathbf{I}$, $\mathbf{Z}_\mathrm{c}$), associated to:	Modal quantities ($\hat{\mathbf{U}}$, $\hat{\mathbf{I}}$, $\hat{\mathbf{Z}}_\mathrm{c}$, $\boldsymbol{\gamma}$), associated to:
Physical MTL		physical conductors	quasi-TEM modes
MTL modeling a periodic structure	modal $\mathbf{T}_\mathrm{cell}$	host WG modes	Floquet modes
	terminal $\mathbf{T}_\mathrm{cell}$	physical conductors	

Table 6.1: Correspondence for the natural and modal quantities in various utilizations of the MTL model.

A common approach for determining the Bloch propagation constants $\boldsymbol{\gamma}_\mathrm{B}$ consists in applying periodic boundary conditions (PBCs) on the total fields at the terminal planes of the unit cell, in conjunction with Floquet's theorem [40, 121, 122]. Due to the orthogonality of the host WG modes, the PBCs apply to each of these modes separately. As a result, the Bloch propagation constants $\boldsymbol{\gamma}_\mathrm{B}$ are linked to the eigenvalues of $\mathbf{T}_\mathrm{cell}$, as expressed in (6.11) [240].

$$\mathbf{T}_\mathrm{cell} \begin{bmatrix} \mathbf{U}_2 \\ \mathbf{I}_2 \end{bmatrix} = e^{+\boldsymbol{\gamma}_\mathrm{B} d} \begin{bmatrix} \mathbf{U}_2 \\ \mathbf{I}_2 \end{bmatrix} \tag{6.11}$$

This technique is now extended to obtain the other parameters of the equivalent MTL ($\mathbf{Z}_\mathrm{B}$ and $\mathbf{T}_\mathrm{B}$) from the eigenvectors of $\mathbf{T}_\mathrm{cell}$. This is achieved by considering that $\mathbf{T}_\mathrm{cell}$ is the transfer matrix of a MTL, and by applying concepts of MTL theory recalled in Section 6.2.2. These developments have already been reported for physical MTLs in [266] (Section 1.4.1), and are revisited here in the light of the present MTL modeling technique for periodic structures. First, we consider the transfer matrix of the unit cell expressed in terms of the modes of the equivalent MTL, which are here the Floquet modes of the periodic structure (see Table 6.1). This matrix writes $\hat{\mathbf{T}}_\mathrm{cell}$ and links the Floquet modal quantities at both sides of the unit cell, as expressed in (6.12).

$$\begin{bmatrix} \hat{\mathbf{U}}_1 \\ \hat{\mathbf{I}}_1 \end{bmatrix} = \hat{\mathbf{T}}_\mathrm{cell} \begin{bmatrix} \hat{\mathbf{U}}_2 \\ \hat{\mathbf{I}}_2 \end{bmatrix} = \begin{bmatrix} \hat{\mathbf{A}} & \hat{\mathbf{B}} \\ \hat{\mathbf{C}} & \hat{\mathbf{D}} \end{bmatrix} \begin{bmatrix} \hat{\mathbf{U}}_2 \\ \hat{\mathbf{I}}_2 \end{bmatrix} \tag{6.12}$$

The four sub-matrices $\hat{\mathbf{A}}$, $\hat{\mathbf{B}}$, $\hat{\mathbf{C}}$, and $\hat{\mathbf{D}}$ are diagonal, since they are associated to the (uncoupled) modal quantities of the equivalent MTL. As in the case of ordinary two-conductor TLs, the elements of the transfer matrix can be written as a function of the propagation constant and characteristic impedance [122, 123]:

$$\hat{\mathbf{T}}_\mathrm{cell} = \begin{bmatrix} \hat{\mathbf{A}} & \hat{\mathbf{B}} \\ \hat{\mathbf{C}} & \hat{\mathbf{D}} \end{bmatrix} = \begin{bmatrix} \cosh(\boldsymbol{\gamma}_\mathrm{B} d) & \sinh(\boldsymbol{\gamma}_\mathrm{B} d)\, \hat{\mathbf{Z}}_\mathrm{B} \\ \hat{\mathbf{Y}}_\mathrm{B} \sinh(\boldsymbol{\gamma}_\mathrm{B} d) & \cosh(\boldsymbol{\gamma}_\mathrm{B} d) \end{bmatrix} \tag{6.13}$$

where $\hat{\mathbf{Z}}_\mathrm{B} = \hat{\mathbf{Y}}_\mathrm{B}^{-1}$ is the modal Bloch impedance matrix [corresponding to $\hat{\mathbf{Z}}_\mathrm{c}$ in (6.4)]. The diagonalization of $\hat{\mathbf{T}}_\mathrm{cell}$ yields

$$\hat{\mathbf{T}}_\mathrm{cell} \begin{bmatrix} \mathbf{E} & -\hat{\mathbf{Z}}_\mathrm{B} \\ \hat{\mathbf{Y}}_\mathrm{B} & \mathbf{E} \end{bmatrix} = \begin{bmatrix} \mathbf{E} & -\hat{\mathbf{Z}}_\mathrm{B} \\ \hat{\mathbf{Y}}_\mathrm{B} & \mathbf{E} \end{bmatrix} \begin{bmatrix} e^{+\boldsymbol{\gamma}_\mathrm{B} d} & \mathbf{0} \\ \mathbf{0} & e^{-\boldsymbol{\gamma}_\mathrm{B} d} \end{bmatrix} \tag{6.14}$$

where $\mathbf{E}$ is the $N \times N$ identity matrix. Using the modal to natural transformation (6.6), we have

$$\mathbf{T}_{\text{cell}} = \mathbf{T}_{\text{c}} \hat{\mathbf{T}}_{\text{cell}} \mathbf{T}_{\text{c}}^{-1} \quad \text{with} \quad \mathbf{T}_{\text{c}} = \begin{bmatrix} \mathbf{T}_{\text{B}} & \mathbf{0} \\ \mathbf{0} & \mathbf{W}_{\text{B}} \end{bmatrix} \tag{6.15}$$

Finally, introducing (6.14) in (6.15), and using relation (6.9) between natural and modal impedance matrices yields

$$\underbrace{\begin{bmatrix} \mathbf{A} & \mathbf{B} \\ \mathbf{C} & \mathbf{D} \end{bmatrix}}_{\mathbf{T}_{\text{cell}}} \underbrace{\begin{bmatrix} \mathbf{T}_{\text{B}} & -\mathbf{Z}_{\text{B}}\mathbf{W}_{\text{B}} \\ \mathbf{Y}_{\text{B}}\mathbf{T}_{\text{B}} & \mathbf{W}_{\text{B}} \end{bmatrix}}_{\mathbf{M}} = \underbrace{\begin{bmatrix} \mathbf{T}_{\text{B}} & -\mathbf{Z}_{\text{B}}\mathbf{W}_{\text{B}} \\ \mathbf{Y}_{\text{B}}\mathbf{T}_{\text{B}} & \mathbf{W}_{\text{B}} \end{bmatrix}}_{\mathbf{M}} \underbrace{\begin{bmatrix} e^{+\boldsymbol{\gamma}_{\text{B}} d} & \mathbf{0} \\ \mathbf{0} & e^{-\boldsymbol{\gamma}_{\text{B}} d} \end{bmatrix}}_{\mathbf{G}} \tag{6.16}$$

where $\mathbf{Y}_{\text{B}} = \mathbf{Z}_{\text{B}}^{-1}$. As a result, all the parameters of the equivalent MTL can be deduced from the transfer matrix $\mathbf{T}_{\text{cell}}$ by solving the eigenvalue problem (6.16):

1. The eigenvalues of $\mathbf{T}_{\text{cell}}$ are the positive and negative exponentials of $\boldsymbol{\gamma}_{\text{B}} d$, and are gathered in the diagonal matrix $\mathbf{G}$.
2. The corresponding eigenvectors are gathered in the matrix $\mathbf{M}$, from which the information on the natural Bloch impedances ($\mathbf{Z}_{\text{B}}$) and modal-natural transformations ($\mathbf{T}_{\text{B}}$ and $\mathbf{W}_{\text{B}}$) can be deduced. As in the case of physical MTLs, the normalization constraint $\mathbf{W}_{\text{B}}^{\text{T}} = \mathbf{T}_{\text{B}}^{-1}$ can be used.

A more compact form of (6.16) can be obtained if the symmetry condition of the unit cell is taken into account in the developments. This formulation is reported in Appendix A. If the structure consists of a single mode or two-conductor periodic structure ($N = 1$), the corresponding expressions reduce to the well known expressions derived in Section 4.2.5.b.

$$\cosh(\gamma_{\text{B}} d) = A \quad \text{and} \quad Z_{\text{B}} = \sqrt{B/C} \tag{6.17}$$

It should be emphasized that the only approximation involved in the presented modeling technique is the truncation of the unit cell representation to a finite number of host WG modes. However, based on the truncated circuital representation, the proposed approach is exact for finite or infinite structures, for quantities defined at the termination planes of the cells, since no other approximation has been made in the developments. As a result, the general MTL formalism can be used to describe any finite length periodic structure with particular sources and terminations, the precision being only limited by the number of modes considered to represent the unit cell.

6.2.5 Determination of the transfer matrix

Applying the proposed modeling technique requires the knowledge of the transfer matrix of the unit cell $\mathbf{T}_{\text{cell}}$. In the following examples, $\mathbf{T}_{\text{cell}}$ has been obtained from full-wave simulation of a single unit cell using Ansoft HFSS. This solver provides the generalized scattering and impedance matrices, from which the generalized transfer matrix can be easily obtained using conversion formulas. The eigenvalue problem (6.16) is subsequently solved using Matlab.

For periodically loaded WGs with higher order evanescent mode interaction, the resolution of the classical eigenvalue problem (6.16) may suffer from numerical instabilities from exponentially growing terms associated to the evanescent modes of the host WG [252]. If this problem occurs, a formulation equivalent to (6.16), but expressed in terms of the generalized scattering matrix, may be preferred since unconditionally stable. However, this problem has not been encountered in the considered examples, since we have limited the modal expansion to accessible modes (typically between 2 and 10), whereas localized modes have not been considered [254, 256].

For periodically loaded MTLs, we use the "driven terminal" solution type of HFSS, which provides the generalized impedance matrix of the unit cell in terms of the conductor voltages and currents of the host MTL, rather than in terms of its quasi-TEM modes. The corresponding transfer matrix is subsequently obtained using conversion formulas.

6.3 Application to periodically loaded MTLs

6.3.1 Introduction

This section illustrates the application of the modeling technique presented in Section 6.2 to the first class of periodic structures mentioned in the introduction, namely, periodically loaded MTLs. Here we consider periodically loaded MTLs which can be characterized from a terminal-based representation of their unit cell (Section 6.2.3.b.). When possible, this approach is preferred to the general one, in which the unit cell is expressed in terms of the quasi-TEM modes of the host MTL (Section 6.2.3.a.), since it allows a straightforward modeling of the connections of the structure to other TLs or MTLs, as will be shown below. In this context, the equivalent MTL modeling technique described in Section 6.2 can be used to analyze and design specific matching and excitation circuits. Some of these possibilities are illustrated here using the particular example of the shielded mushroom structure.

6.3.2 Description of the structure

The mushroom structure can be seen as a microstrip implementation of the 2D CRLH TL. In this example, a shielded version of this structure is considered, as depicted in Figure 6.4(a). The structure has a 2D square periodicity in the xy plane. Here, we consider propagation along the x direction and the periodicity in the y direction is accounted for by perfect magnetic conductors (PMC). The structure can thus be seen as a MTL with $N + 1 = 3$ conductors periodically loaded with series capacitive gaps and shunt inductive vias, as represented in the circuit model of Figure 6.4(b). This structure supports $N = 2$ Floquet modes.

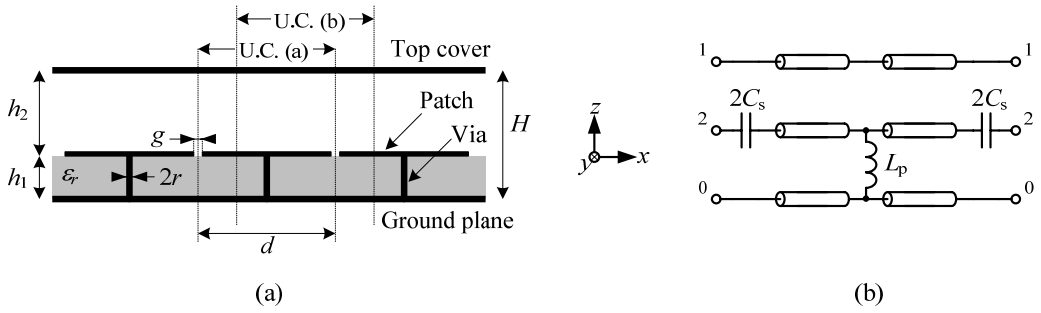

Figure 6.4: (a) Lateral view of the shielded mushroom structure with two possible definitions for the unit cell (U.C.) ($d = 10$ mm, $r = 0.2$ mm, $g = 0.2$ mm, $H = 15$ mm, $h_1 = 3.17$ mm and $\varepsilon_r = 2.33$). (b) Loaded MTL model for the symmetrical unit cell "U.C. (a)" ($L_\mathrm{p} = 1.32$ nH, $C_\mathrm{s} = 350$ fF, and the parameters of the host MTL calculated as in [240, 268]).

6.3.3 Full-wave analysis

An important point concerning the definition of the unit cell is discussed here. The structure shown in Figure 6.4(a) does not allow the definition of a symmetrical unit cell, such as "U.C. (a)", without placing its boundaries across some of the loading elements (the vias or the gaps). However, for the terminal-based simulation with HFSS, an asymmetrical unit cell, such as "U.C. (b)", had to be considered because the MTL ports need to be placed somewhere on the host MTL where no discontinuity is present. A post-processing operation on the resulting transfer matrix has been subsequently performed in order to obtain the corresponding transfer matrix for the symmetrical unit cell "U.C. (a)". It can be noted that this operation, which is similar to the one presented in Section 4.2.8 for two-conductor structures, is based on an a-priori knowledge of the unit cell based on the model of Figure 6.4(b) and is therefore an approximation. Nevertheless, this approximation is linked with the determination of $\mathbf{T}_\mathrm{cell}$ in this particular example and not with the modeling technique itself.

6.3.4 Results: dispersion diagram

The Bloch MTL parameters $\boldsymbol{\gamma}_\mathrm{B}$, $\mathbf{Z}_\mathrm{B}$ and $\mathbf{T}_\mathrm{B}$ have been calculated from the full-wave simulated transfer matrix $\mathbf{T}_\mathrm{cell}$ using the MTL modeling technique presented in Section 6.2. The dispersion diagram $f(\boldsymbol{\gamma}_\mathrm{B})$ is shown in Figure 6.5 (the parameters $\mathbf{Z}_\mathrm{B}$ and $\mathbf{T}_\mathrm{B}$ are not shown here but will be used in Section 6.3.5).

A Typical dispersion for this type of structures is observed [240, 268]. This dispersion diagram also shares many similarities with the one obtained for the volumetric layered TL-based MTM investigated in Chapter 5, when it is placed in a parallel plate WG (Section 5.4.3). Also shown in Figure 6.5 are the dispersion relation directly calculated with the eigenmode solver of HFSS, and the one obtained from the circuit model of Figure 6.4(b). A very good agreement is observed between the three methods, although the eigenmode solver does not provide

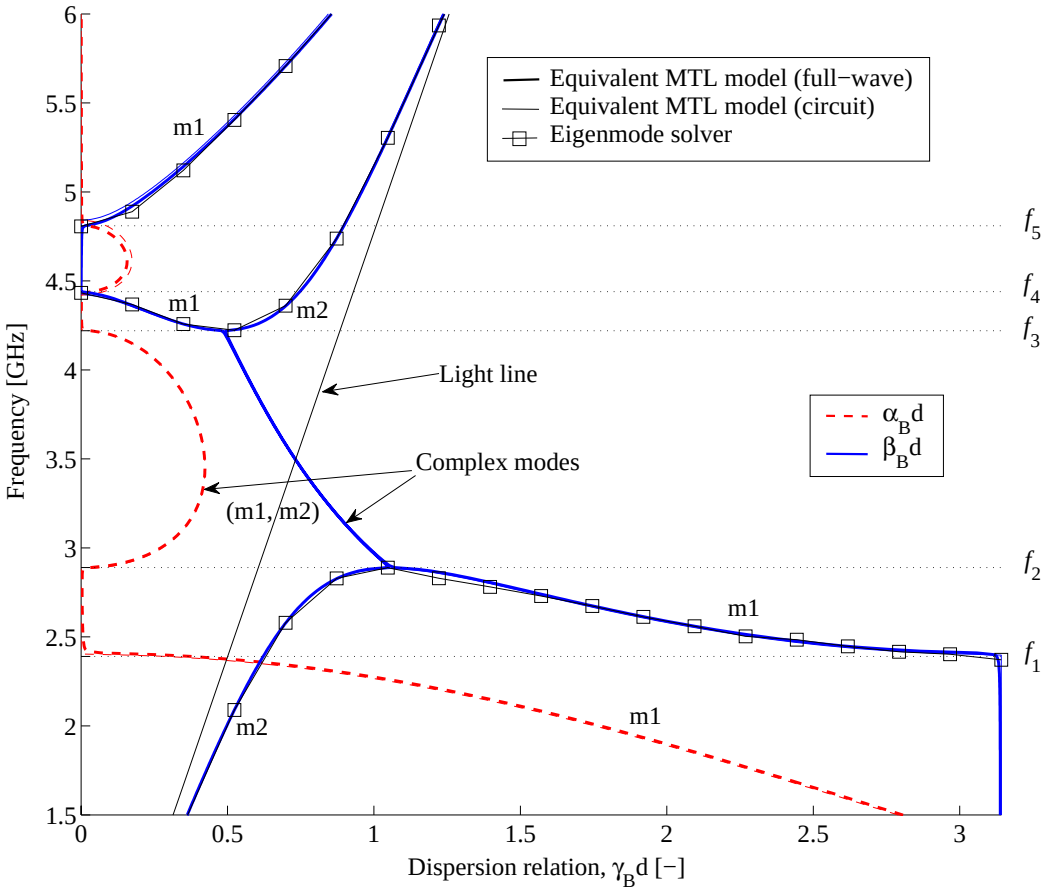

Figure 6.5: Dispersion diagram for the shielded mushroom structure shown in Figure 6.4(a). The two Floquet modes are numbered "m1" and "m2".

information on the complex mode band (from f_2 to f_3), where the propagation constants exist by pair of complex conjugates. An important characteristic of these structures is that the left-handed (LH) mode, characterized by anti-parallel phase and group velocities, couples to the right-handed (RH) parallel plate WG mode, which results in a complex mode band (from f_2 to f_3) and two mixed RH/LH mode bands (from f_1 to f_2 and from f_3 to f_4). This coupling between modes is considered as a drawback if the structure is to be used as a LHM. In such a case, it is of particular interest to quantify the ability of a given excitation to couple power to the LH mode. This fundamental issue cannot be assessed with existing techniques, but can be solved using the presented MTL modeling technique.

6.3.5 The Excitation Problem

We consider here the excitation of the shielded mushroom structure by a parallel plate WG consisting of the extension of the top cover and ground plane, as shown in Figure 6.6(a). The corresponding model is shown in Figure 6.6(b), where the periodic structure is modeled by its equivalent MTL of parameters $\boldsymbol{\gamma}_\mathrm{B}$, $\mathbf{Z}_\mathrm{B}$ and $\mathbf{T}_\mathrm{B}$. The parameters $\beta_\mathrm{e} = k_0$ and $Z_\mathrm{ce} = \eta_0 H/d = 565.5\ \Omega$ are the phase constant and characteristic impedance of the parallel plate WG, where k_0 and η_0 are the free-space wave number and characteristic impedance, respectively. The adopted representation in terms of the terminal-based voltages and currents (third line of Table 6.1) allows directly connecting the MTL model of the periodic structure with the TL model of the parallel plate WG. The conductor 2 of the MTL model is simply left open.

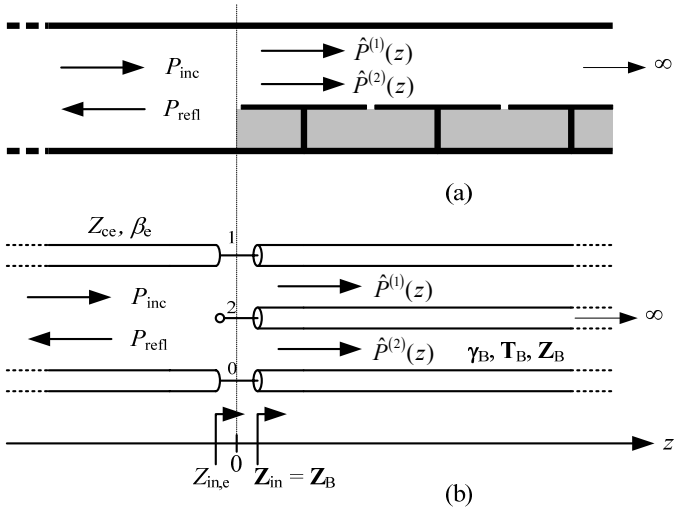

Figure 6.6: Semi-infinite mushroom structure excited with a parallel plate WG. (a) Illustration. (b) Equivalent circuit involving the equivalent MTL model for the periodic structure.

Let P_inc be the incident power, P_refl the reflected power, and $\hat{P}^{(m)}$ the power transmitted to the m^th Floquet mode in the periodic structure. The powers $\hat{P}^{(m)}$ can be calculated from

the corresponding modal voltage and current using (6.18).

$$\hat{P}^{(m)}(z) = \mathrm{Re}\left\{\left[\hat{U}^{(m)}(z)\right]\left[\hat{I}^{(m)}(z)\right]^{*}\right\} \tag{6.18}$$

We define N power transmission coefficients Π at the interface ($z = 0$) and a power reflection coefficient Γ as follows:

$$\Pi_m = \hat{P}^{(m)}(0) \Big/ P_{\mathrm{inc}} \quad ; \quad \Gamma = P_{\mathrm{refl}}/P_{\mathrm{inc}} = |\rho|^2 \tag{6.19}$$

The coefficients Π_m and Γ can be further expressed in terms of the parameters of the circuit shown in Figure 6.6(b). Using a generalized Norton equivalent for the excitation [267], the fact that the input impedance matrix of the semi-infinite periodic structure is $\mathbf{Z}_{\mathrm{in}} = \mathbf{Z}_{\mathrm{B}}$, and the natural/modal transformation in (6.6), we find

$$\Pi_m = \frac{4Z_{\mathrm{ce}}\,\mathrm{Re}\left[\hat{Z}_{\mathrm{B}m}\right]}{\left|Z_{\mathrm{ce}} + Z_{\mathrm{in,e}}\right|^2}\left|\mathbf{T}_{\mathrm{B}}(1,m)\right|^2 \tag{6.20a}$$

$$\rho = \frac{Z_{\mathrm{in,e}} - Z_{\mathrm{ce}}}{Z_{\mathrm{in,e}} + Z_{\mathrm{ce}}} \quad \text{with} \quad Z_{\mathrm{in,e}} \equiv \frac{U^{(1)}(0)}{I^{(1)}(0)} = \mathbf{Z}_{\mathrm{B}}(1,1) \tag{6.20b}$$

where $\hat{Z}_{\mathrm{B}m}$ is the modal Bloch impedance of the m^{th} Floquet mode, which is given by the m^{th} element of the diagonal matrix $\hat{\mathbf{Z}}_{\mathrm{B}} = \mathbf{T}_{\mathrm{B}}^{-1}\mathbf{Z}_{\mathrm{B}}\mathbf{T}_{\mathrm{B}}^{-1\mathrm{T}}$ [see (6.9) and 6.10]. Figure 6.7 shows the power reflection and transmission coefficients calculated from (6.20) for the structure of Figure 6.6. It can be verified that the energy conservation condition $\Gamma + \Pi_1 + \Pi_2 = 1$ is satisfied at all frequencies.

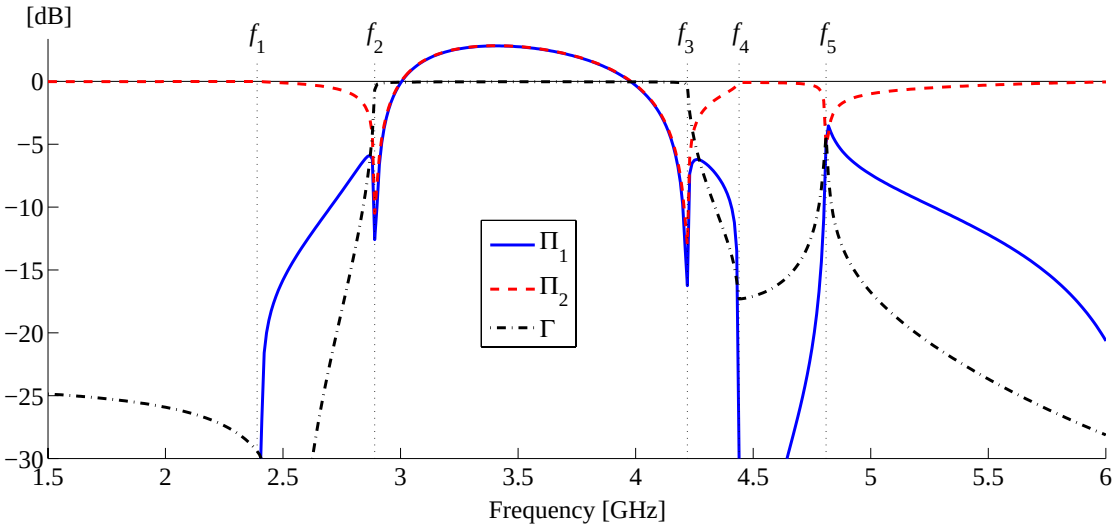

Figure 6.7: Power reflection (Γ) and transmission (Π) coefficients for the semi-infinite shielded mushroom structure excited by a parallel plate WG. The numbering for the Π corresponds to the numbering of the modes in Figure 6.5.

As could be anticipated from the nature of each Floquet mode, most of the power incident from the parallel plate WG is coupled to the RH mode "m2". Nevertheless, In the mixed

RH/LH bands (from f_1 to f_2 and from f_3 to f_4) the LH mode "m1" is also excited and the present technique allows, for the first time, to quantify the relative excitation of each mode. A rather counterintuitive behavior of the transmission coefficients in the complex mode band (from f_2 to f_3) is observed, since Π_1 and Π_2 are larger than 1 (0 dB). However, as these two modes are complex and exchange power between each other, they should rather be considered as a pair of modes for which a single transmission coefficient $\Pi_c = \Pi_1 + \Pi_2$ can be defined. Although not visible in this dB plot, for such a backward coupling [162] we have $\Pi_2 = -\Pi_1$ in this band, and thus $\Pi_c = 0$. This means that the total power transmitted into the periodic structure is zero and all the power is reflected ($\Gamma = 0$ dB). This kind of complex mode bands have been advantageously used for the development of improved MTM-based coupled-line couplers [162, 163], for which the present modeling technique might also be beneficial for efficient analysis and design involving matching considerations.

Finally, it can be pointed out that we have illustrated here the application of the MTL modeling technique to the "excitation problem", but similar developments can also be carried out to describe the "matching problem", that is, the reverse problem of that shown in Figure 6.6. In general, the technique allows to model any type of finite length periodically loaded MTL with any type of excitation and load, using the general formalism for physical MTL [266, 267].

6.3.6 Further Possible Applications on periodically loaded MTLs

The developed technique can also be advantageously used to investigate various configurations involving other types of MTMs similar to the shielded mushroom structure. Some of these configurations are discussed below [261].

a. Shielded mushroom structure with additional inductive loadings

A possible way of avoiding the unwanted coupling of the LH mode with the RH parallel plate WG mode in the shielded mushroom structure consists in placing additional inductive loadings between the patches and the top cover [3, 109], as suggested in Figure 6.8(a) and (b). This approach has also been used in [250, 269] for a volumetric MTM consisting of a stacking of 2D dual TLs similar to the shielded mushroom structure, in order to increase the coupling from an incident plane wave to the LH mode. The additional inductive loadings have the effect of eliminating the parasitic parallel plate WG mode, and thus only a single LH Floquet mode propagates in the frequency range of interest.

The main challenge with this new structure consists in determining the parameters which lead to the desired dispersion diagram, while maximizing the transmitted power into the structure (or equivalently, minimizing the reflection coefficient, as there is only one propagating Floquet mode). It can be noted that two reference planes definitions for a symmetrical unit cell can be considered, as shown in Figure 6.8(a) and (b), with possibly different coupling characteristics from an incident wave.

Designs with good matching to free space based on periodically loaded MTL models have

been reported in [250, 269]. However, no detail was given on the design procedure used. It is clear that the whole M-cell structure can be analyzed as a whole and its parameters tuned until the desired dispersion with a good matching is achieved. On the other hand, the proposed modeling technique provides more physical insight that can help for the design. Indeed, a single interface can be investigated separately as performed in Section 6.3.5. In this context, preliminary investigations on the structure of Figure 6.8(a) revealed that the input impedance seen from the excitation parallel plate WG seems to always exhibit a non-zero imaginary part. This means that a perfect matching is probably impossible, and that the design should be oriented toward the decrease of this imaginary part, while adjusting the real part to the impedance of the excitation parallel plate WG. The modeling technique presented in this work appears to be a useful tool to achieve this goal.

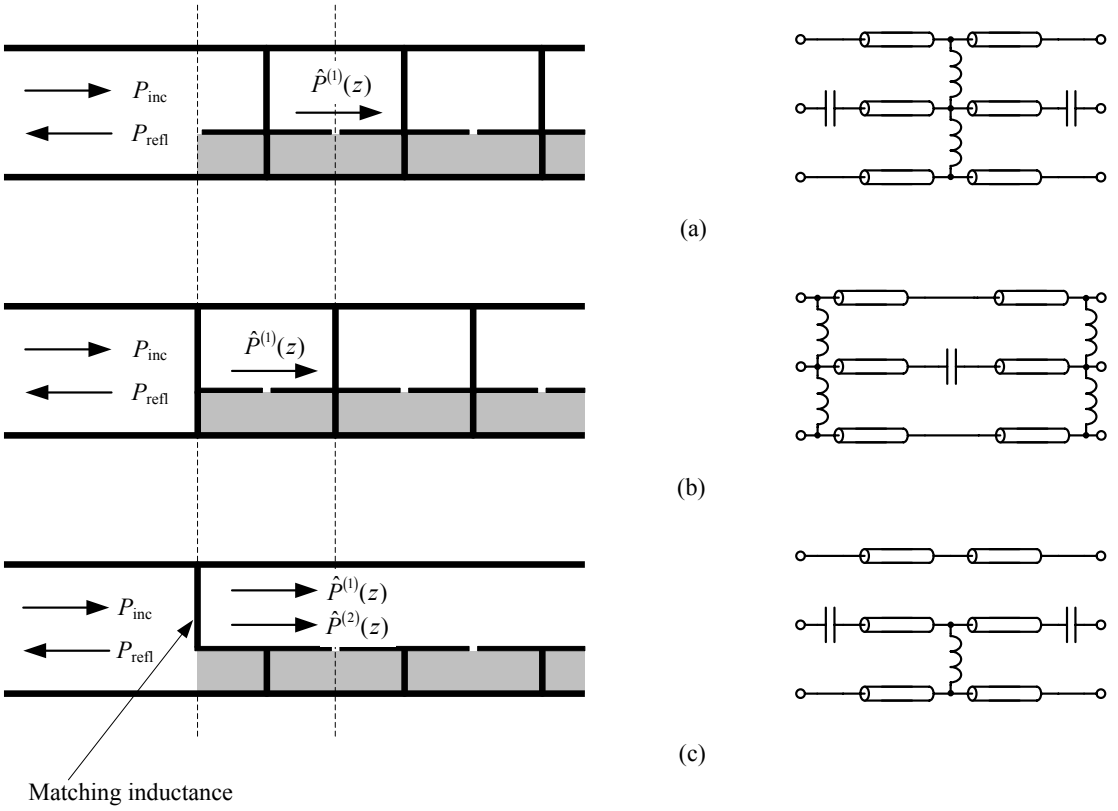

Figure 6.8: Variants of the shielded mushroom structure excited with a parallel plate WG, and circuit models for the unit cell. (a) and (b) Shielded mushroom structure with additional inductive loadings (two possible definitions for the reference planes of the unit cell) [250, 269]. (c) Shielded mushroom structure with a matching inductance at the extremity [270].

b. Shielded mushroom structure with matching inductances

In the problematic of maximizing the power transmitted to the LH mode for the shielded mushroom and related structures, it has been proposed in [270] to introduce additional inductive vias between the patches and the top cover only at the extremities of the periodic structure, thereby acting as matching circuits. This configuration is illustrated in Figure 6.8(c). This structure still supports mixed RH/LH propagation, but the matching inductance allows increasing the power coupled to the LH mode. Compared to the structures discussed in Section 6.3.6.a., this approach uses less inductive elements, thereby simplifying the fabrication process. A design with good matching to free space based on periodically loaded MTL models has been reported in [270], but no detail was given on the design procedure used.

The configuration of Figure 6.8(c) is a typical problem that can be addressed with the proposed method. Indeed, in the model of Figure 6.6(b), the matching inductor can be modeled as a shunt inductance between conductors 1 and 2 at the interface, and the relative excitation of the LH and RH modes can be assessed by calculating the corresponding modal powers, as performed in Section 6.3.5. In general, the proposed technique allows investigating in a systematic way any type of problems involving the excitation of specific Floquet modes in the periodic structure using particular matching circuits at the interfaces.

c. Others

In general, it is believed that the developed technique based on equivalent MTL models for periodic structures can be advantageously used for many types of periodically loaded MTLs. In the field of MTMs, this may open the door to the study of generalized TL-based MTMs obtained by periodically loading a host MTL with series capacitances and shunt inductances in various fashions.

6.4 Application to periodically loaded WGs with higher order mode interaction

6.4.1 Introduction

We consider here periodically loaded WGs with higher order evanescent mode interaction between cells. We focus on the case where the periodic structure supports only a single propagating Floquet mode, as is commonly the case when the host WG itself is operated in its monomode region. The approximation usually employed consists in neglecting the effect of the higher order host WG modes, in which case the structure can be modeled by an equivalent TL whose parameters are the Bloch propagation constant γ_{B0} and Bloch impedance Z_{B0} obtained from the dominant-mode transfer matrix of the unit cell using $\cosh(\gamma_{B0}d) = A$ and $Z_{B0} = \sqrt{B/C}$. This is the dominant-mode (or "monomode") Bloch wave analysis already described in Section 4.2. In contrast, the technique presented in section 6.2 allows to achieve a given desired level

of accuracy, provided that enough host WG modes are taken into account in the representation of the unit cell. The drawback is that the resulting MTL model contains an important number of parameters (the $N \times N$ matrices $\boldsymbol{\gamma}_\mathrm{B}$, $\mathbf{Z}_\mathrm{B}$ and $\mathbf{T}_\mathrm{B}$), and is therefore not convenient to perform particular designs of finite length periodic structures with given phase shift and matching requirements. Consequently, we propose a simplified and approximate model with a reduced set of parameters derived from the complete MTL model. In terms of complexity, this approach is comparable with the simple TL model obtained from the dominant-mode analysis, while providing an accurate description of the periodic structure by taking into account the higher order mode interaction phenomena.

6.4.2 Reduction of the MTL Model: Principle

We consider a finite M-cell periodic structure described by its equivalent MTL, as shown in Figure 6.9. It is assumed that the host WG extends after both termination planes of the periodic structure, from a sufficient distance for the evanescent host WG modes excited at the boundaries to decay to negligible values. As a result, each of these modes is terminated on its wave impedance $Z_{\mathrm{m}n}$, as shown in Figure 6.9. The parameters γ_1 and $Z_{\mathrm{m}1}$ are the propagation constant and wave impedance of the fundamental mode of the host WG.

It can be seen that the terminated periodic structure of Figure 6.9 reduces to a two-port network. The reduction to a simplified model only requires a single assumption, which is that the evanescent Floquet modes excited at one interface of the periodic structure do not reach the other interface (i.e. they are *localized* modes [254]), which is a common assumption in TL-based models in general. Under this assumption, the interface of the periodic structure can be represented as in Figure 6.10(a).

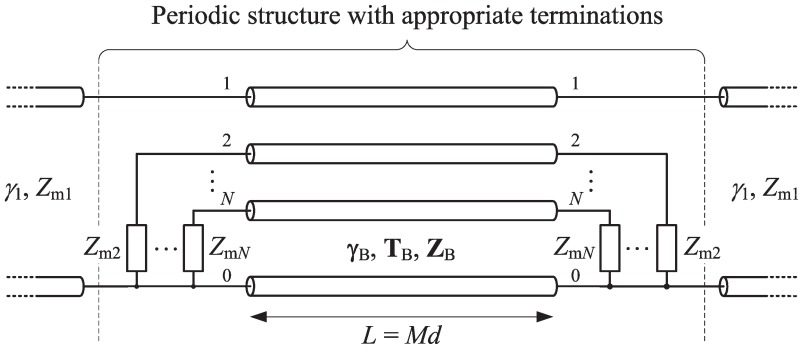

Figure 6.9: MTL model for a finite length periodic structure in a monomode host WG. The host WG extends after both termination planes.

We refer to the models of Figure 6.10 as hybrid because they involve both natural and modal quantities. It is worth recalling that here, the natural quantities are associated to the host WG modes, and the modal ones to the Floquet modes (see second line of Table 6.1). Therefore, the network of transfer matrix $\mathbf{T}_\mathrm{c}$ at the interface implements the natural/modal transformation given by (6.6) [see also (6.15)]. The hybrid representation allows accounting

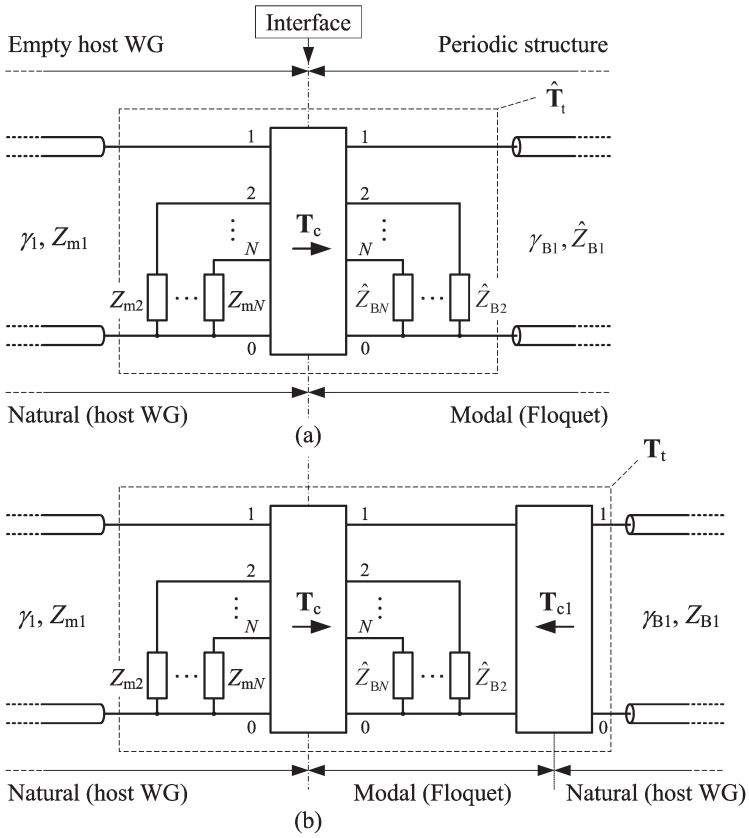

Figure 6.10: Two possible hybrid natural/modal circuit models for the interface between a periodic structure in a monomode host WG and the surrounding empty WG.

in the same manner for the localized effect of the higher order modes on both sides of the interface. Indeed, the evanescent host WG modes are terminated on their wave impedance $Z_{\mathrm{m}n}$ and the evanescent Floquet modes on their modal Bloch impedance $\hat{Z}_{\mathrm{B}n}$. These localized effects can be gathered in a single two-port network of transfer matrix $\hat{\mathbf{T}}_{\mathrm{t}}$, which is depicted in dashed line in Figure 6.10(a). In the periodic structure, at a sufficient distance from the interface, only the first Floquet mode is present. Thus, it is represented in Figure 6.10(a) by a TL of Bloch parameters γ_{B1} and $\hat{Z}_{\mathrm{B1}}$, which are the first elements of the diagonal matrices $\boldsymbol{\gamma}_{\mathrm{B}} = \mathrm{diag}\left\{\gamma_{\mathrm{B1}}, \ldots, \gamma_{\mathrm{B}N}\right\}$ and $\hat{\mathbf{Z}}_{\mathrm{B}} = \mathrm{diag}\left\{\hat{Z}_{\mathrm{B1}}, \ldots, \hat{Z}_{\mathrm{B}N}\right\}$ associated to the MTL model.

The hybrid natural/modal model of Figure 6.10(a) provides a simple representation of the interface, but it suffers from the disadvantage that the parameters $\hat{\mathbf{T}}_{\mathrm{t}}$ and $\hat{Z}_{\mathrm{B1}}$ are not uniquely defined. Indeed, quantities associated to the modes of the MTL, such as $\hat{\mathbf{Z}}_{\mathrm{B}}$, $\mathbf{T}_{\mathrm{B}}$ or $\mathbf{W}_{\mathrm{B}}$ are subject to some arbitrariness (Section 6.2.2). To overcome this limitation, it is of interest to obtain a model involving only natural quantities. To that purpose, the modified interface model of Figure 6.10(b) is proposed, where the network of transfer matrix $\mathbf{T}_{\mathrm{c1}}$ has been introduced. This network implements the reverse modal/natural transformation, but only between the first Floquet mode and the first host WG mode. In this new representation, the first Floquet mode is thus only described through its projection on the first host WG mode, and is represented by the TL of parameters γ_{B1} and Z_{B1}. The parameter Z_{B1} can be seen as the Bloch impedance of the first Floquet mode projected on the first host WG mode.

The model of Figure 6.10(b) is incomplete in the sense that it does not explicitly represent the projections of the first Floquet mode on other host WG modes than the fundamental. Nevertheless, this information can be recovered if needed, since the composition of the first Floquet mode in terms of the host WG modes is given by the first column of $\mathbf{T}_{\mathrm{B}}$ and $\mathbf{W}_{\mathrm{B}}$ for the voltages and currents, respectively. Using the interface model of Figure 6.10(b), the finite size periodic structure of Figure 6.9 can be now represented by the approximate *reduced model* of Figure 6.11. The only approximation made when modeling the structure of Figure 6.9 by the reduced model of Figure 6.11 is the assumption that the higher order Floquet modes excited at one extremity of the periodic structure do not reach the other one.

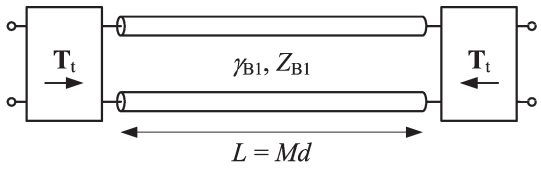

Figure 6.11: Reduced model for a periodic structure in a monomode host WG and for which only a single Floquet mode is propagating.

Finally, It is noticeable that the reduced model of Figure 6.11 only involves natural quantities associated to the first host WG mode. As a result, it can be shown that its parameters γ_{B1}, Z_{B1} and $\mathbf{T}_{\mathrm{t}}$ are uniquely defined.

6.4.3 Parameters of the Reduced Model

This section details the calculation of the parameters $Z_{\mathrm{B}1}$ and $\mathbf{T}_{\mathrm{t}}$ of the model of Figure 6.11. The notation shown in (6.21) is used to partition any $N \times N$ matrix $\mathbf{X}$, so as to make a distinction between the first line and column and the rest of the matrix.

$$\mathbf{X} = \left[\begin{array}{c|ccc} X_{11} & X_{12} & \cdots & X_{1N} \\ \hline X_{21} & X_{22} & \cdots & X_{2N} \\ \vdots & \vdots & \ddots & \vdots \\ X_{N1} & X_{N2} & \cdots & X_{NN} \end{array}\right] = \left[\begin{array}{c|c} X^{11} & \mathbf{X}^{1n} \\ \hline \mathbf{X}^{n1} & \mathbf{X}^{nn} \end{array}\right] \tag{6.21}$$

We first recall that the modal Bloch impedance matrix $\hat{\mathbf{Z}}_{\mathrm{B}}$ can be calculated from the parameters of the equivalent MTL using [see (6.9) and (6.10)]

$$\hat{\mathbf{Z}}_{\mathrm{B}} = \mathrm{diag}\left\{\hat{Z}_{\mathrm{B}1}, \ldots, \hat{Z}_{\mathrm{B}N}\right\} = \mathbf{T}_{\mathrm{B}}^{-1}\mathbf{Z}_{\mathrm{B}}\mathbf{W}_{\mathrm{B}} \tag{6.22}$$

with $\mathbf{W}_{\mathrm{B}} = \mathbf{T}_{\mathrm{B}}^{-1\mathrm{T}}$. The transfer matrices of the natural/modal conversion networks shown in Figure 6.10(b) are given by

$$\mathbf{T}_{\mathrm{c}} = \left[\begin{array}{cc} \mathbf{T}_{\mathrm{B}} & \mathbf{0} \\ \mathbf{0} & \mathbf{W}_{\mathrm{B}} \end{array}\right] \quad ; \quad \mathbf{T}_{\mathrm{c}1} = \left[\begin{array}{cc} T_{\mathrm{B}}^{11} & 0 \\ 0 & W_{\mathrm{B}}^{11} \end{array}\right] \tag{6.23}$$

As can be seen in (6.23), the network $\mathbf{T}_{\mathrm{c}1}$ simply scales the voltage and current by T_{B}^{11} and W_{B}^{11}, respectively. As a result, the impedance $Z_{\mathrm{B}1}$ of the TL representing the first Floquet mode in Figure 6.10(b) is given by

$$Z_{\mathrm{B}1} = \hat{Z}_{\mathrm{B}1}\frac{T_{\mathrm{B}}^{11}}{W_{\mathrm{B}}^{11}} \tag{6.24}$$

so that the two models of Figure 6.10 are equivalent in terms of the input impedance seen from the empty host WG. Finally, the four elements of the transfer matrix $\mathbf{T}_{\mathrm{t}}$ are obtained from the graphical representation of Figure 6.10(b), by applying port reduction to $\mathbf{T}_{\mathrm{c}}$ and by multiplying by $\mathbf{T}_{\mathrm{c}1}^{-1}$. We find

$$\mathbf{T}_{\mathrm{t}} = \left[\begin{array}{cc} 1 - \frac{1}{T_{\mathrm{B}}^{11}}\mathbf{T}_{\mathrm{B}}^{1n}\hat{\mathbf{Z}}_{\mathrm{B}}^{nn}\mathbf{Q}\mathbf{T}_{\mathrm{B}}^{n1} & -\frac{1}{W_{\mathrm{B}}^{11}}\mathbf{T}_{\mathrm{B}}^{1n}\hat{\mathbf{Z}}_{\mathrm{B}}^{nn}\mathbf{Q}\mathbf{Z}_{\mathrm{m}}^{nn}\mathbf{W}_{\mathrm{B}}^{n1} \\ -\frac{1}{T_{\mathrm{B}}^{11}}\mathbf{W}_{\mathrm{B}}^{1n}\mathbf{Q}\mathbf{T}_{\mathrm{B}}^{n1} & 1 - \frac{1}{W_{\mathrm{B}}^{11}}\mathbf{W}_{\mathrm{B}}^{1n}\mathbf{Q}\mathbf{Z}_{\mathrm{m}}^{nn}\mathbf{W}_{\mathrm{B}}^{n1} \end{array}\right] \tag{6.25}$$

where $\mathbf{Q} = \left(\mathbf{T}_{\mathrm{B}}^{nn}\hat{\mathbf{Z}}_{\mathrm{B}}^{nn} + \mathbf{Z}_{\mathrm{m}}^{nn}\mathbf{W}_{\mathrm{B}}^{nn}\right)^{-1}$ and $\mathbf{Z}_{\mathrm{m}} = \mathrm{diag}\left\{Z_{\mathrm{m}1}, \ldots, Z_{\mathrm{m}N}\right\}$ is the diagonal matrix gathering all the host WG wave impedances.

It can be noted that the two-port network $\mathbf{T}_{\mathrm{t}}$ is in general non-reciprocal and does not satisfies passivity requirements. This could be expected from the fact that one of its ports (on the periodic structure side) only accounts for a partial representation of the total fields, which is projected on the fundamental host WG mode only. However, the reduced model of the whole finite periodic structure shown in Figure 6.11 is reciprocal and satisfies passivity requirements.

6.4.4 Application Example: SRR-wire Medium

a. Description of the Structure

We apply here the developed modeling technique to a SRR-wire metamaterial (Section 2.2.1.a.) whose unit cell is shown in Figure 6.12. A three-dimensional array of these cells exhibits a negative refractive index (or left-handed behavior) for propagation along x and when excited by an electric field $\mathbf{E}$ along z and a magnetic field $\mathbf{H}$ along y, as shown in Figure 6.12. The symmetries of the structure allows to model the transverse periodicity by applying perfect electric conductor (PEC) on the faces perpendicular to z and perfect magnetic conductor (PMC) on the faces perpendicular to y. The periodic structure is thus reduced to a periodically loaded "TEM WG".

The SRR consists of a single metallic ring loaded with two capacitors of value $2C_{\mathrm{L}}$, such that the total capacitance in the ring is C_{L}. The wires are infinitely long metallic strips loaded with inductors. Each cell of the 3-D array comprises a single wire, which is located in the center between two adjacent SRRs (along y). To preserve the symmetry of the unit cell along y, the boundaries of the cells coincide with the positions of the wires, which is why each cell comprises two half-wires. Each half-wire is loaded with an inductance $2L_{\mathrm{w}}$, such that the total inductance per unit cell in a wire is L_{w}. Without entering into the details of the physical behavior of this structure, it has been shown that the coupling between consecutive SRRs requires a multimodal representation of the unit cell, hence a case study for our method [262, 263].

b. Full-wave Analysis

In the full-wave simulations (HFSS), the metallic patterns are modeled as 2D sheets of PEC and the lumped elements are modeled as surface impedance boundaries. Due to the symmetries with respect to the xy and xz planes, the full-wave model can be reduced to only one fourth of the actual structure. We have considered $N = 7$ host WG modes (i.e. the modes of the quarter host WG) in the representation of the unit cell. This choice will be justified below.

c. Results: Bloch Parameters

The Bloch propagation constant and Bloch impedance have been calculated from both the *multimode* representation (γ_{B1} and Z_{B1} of the reduced model of Figure 6.11) and from the *monomode* representation (γ_{B0} and Z_{B0} from dominant-mode analysis). The results are shown in Figure 6.13. Typical dispersion and impedance for this type of structures is observed. The frequency band of interest corresponds to the negative refractive index (or left-handed) band, which extends from $f_{\mathrm{c}} = 5.25$ GHz to $f_{\mathrm{s}} = 6.70$ GHz and is characterized by anti-parallel phase and group velocities. Significant differences between the two considered approaches are observed, both in terms of dispersion and impedance. Also shown in Figure 6.13(a) is the dispersion relation directly calculated with the eigenmode solver of HFSS, which can be considered as the "exact" solution for the dispersion, since it is not based on a unit cell representation trun-

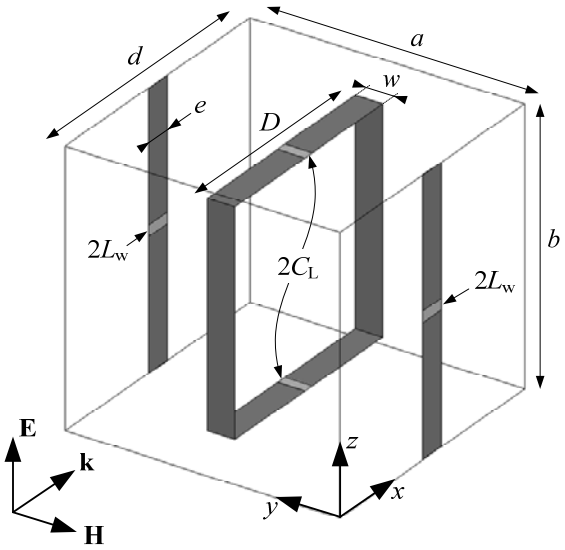

Figure 6.12: Unit cell of the considered SRR-wire medium. Dark gray and light gray represent metal and lumped elements, respectively. The faces perpendicular to z, resp. y, are perfect electric conductors (PEC), resp. perfect magnetic conductors (PMC). The SRR is square and centered in the unit cell and the wires are connected to the upper and lower PEC walls ($d = 5$ mm, $a = 5$ mm, $b = 4.9$ mm, $e = w = 0.5$ mm, $D = 4$ mm, $C_L = 83$ fF and $L_w = 2.5$ nH).

cated to a finite number of host WG modes. An excellent agreement between the γ obtained from the eigenmode analysis and the one obtained with the proposed method (γ_{B1}) is observed, which confirms that enough host WG modes have been considered in the representation of the unit cell. The Bloch parameters are further discussed in the next section in the light of design considerations.

d. Results: S Parameters and Design Considerations

The advantages of the proposed technique from a design point of view are further discussed by considering a 10-cell periodic structure made of the repetition along x of the cell of Figure 6.12. Figure 6.14 shows the corresponding S parameters obtained from the reduced model of Figure 6.11 [using (6.24) and (6.25) for Z_{B1} and $\mathbf{T}_t$, and (6.16) for γ_{B1}] and from the simple monomode TL model (TL of parameters γ_{B0} and Z_{B0}). These are to be compared with the real S parameters of the 10-cell structure, also obtained with HFSS. It can be observed that the reduced model provides very accurate results in comparison with the monomode TL model. Better accuracy can be achieved by increasing the number of host WG modes in the representation of the unit cell, but the convergence is rather slow.

It should be noted that cascading 10 times the unit cell from its multimode representation results in almost the same S parameters as the reduced model. This means that the assumption done in the derivation of this model (Section 6.4.2) is fully satisfied in this case. On the other hand, cascading 10 times the unit cell from its monomode representation results in exactly the same S parameters as the monomode TL model, by definition of this model.

Now we use these results to illustrate two possible design scenarios. It should be mentioned that, instead of designing two different structures, we use for the present discussion the results already calculated for the selected example at two different frequencies f_1 and f_2.

In the first case, we consider that the 10-cell structure has been designed using the monomode Bloch wave analysis to be matched to the host WG at the frequency $f_1 = 5.91$ GHz with a phase response $\arg(S_{21}) = 271°$ (4.74 rad). Thus, the unit cell must be designed to exhibit $Z_{B0} = Z_{m1}$ for matching and $\gamma_{B0}d = 4.74/10$ rad $= 0.474$ rad at f_1 (as is the case in Figure 6.13). Figure 6.14 confirms that the 10-cell structure is indeed matched at f_1 with the desired phase shift, according to the monomode TL model. However, the actual return loss at f_1 is only -12.4 dB, hence a rather poor matching, and the phase response is 322°, hence a difference of 51° with the targeted value. Moreover, Figure 6.13 reveals that the multimode Bloch impedance Z_{B1} at f_1 is 470 Ω, hence a difference of 27% compared to the targeted value of $Z_{m1} = 369$ Ω, and the phase shift per unit cell $\gamma_{B1}d$ is 0.574 rad instead of 0.474 rad.

In the second case, we consider that the 10-cell structure has been designed using the proposed multimode Bloch wave analysis (reduced model) to be matched to the host WG at the frequency $f_2 = 6.19$ GHz with a phase response $\arg(S_{21}) = 186°$ (3.25 rad). For a first design, we propose to neglect the effect of the termination networks $\mathbf{T}_t$. In such a case, the unit cell has to be designed to exhibit $Z_{B1} = Z_{m1}$ for matching and $\gamma_{B1}d = 3.25/10$ rad $= 0.325$ rad at f_2 (as is the case in Figure 6.13). Figure 6.14 shows that a good matching is achieved at f_2

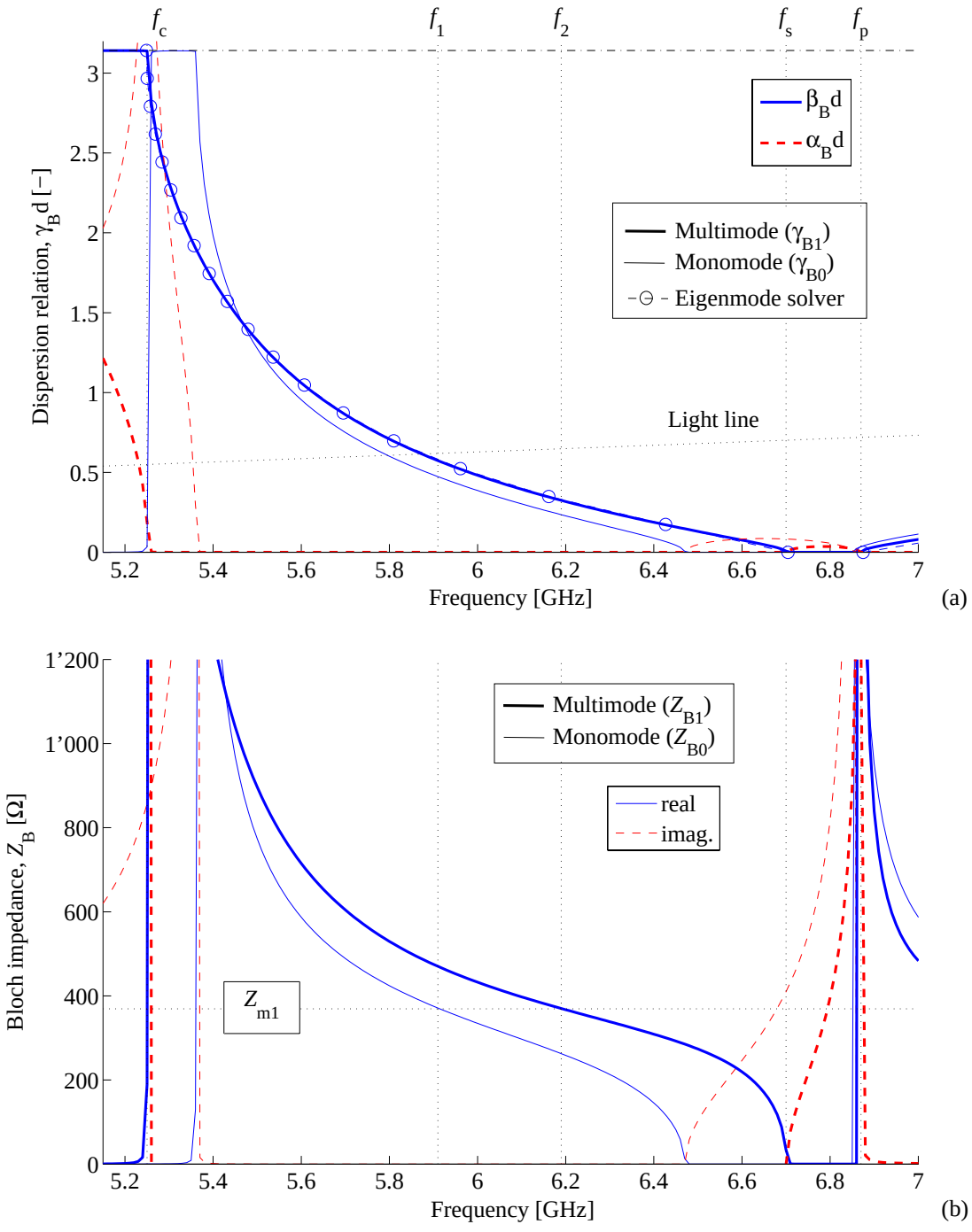

Figure 6.13: Bloch parameters of the SRR-wire medium whose unit cell is shown in Figure 6.12, from multimode and monomode Bloch wave analysis. (a) Bloch propagation constants $\gamma_\mathrm{B} = \alpha_\mathrm{B} + j\beta_\mathrm{B}$ (dispersion relation), (b) Bloch impedances. $Z_\mathrm{m1} = 369\ \Omega$ is the wave impedance of the first mode of the host WG.

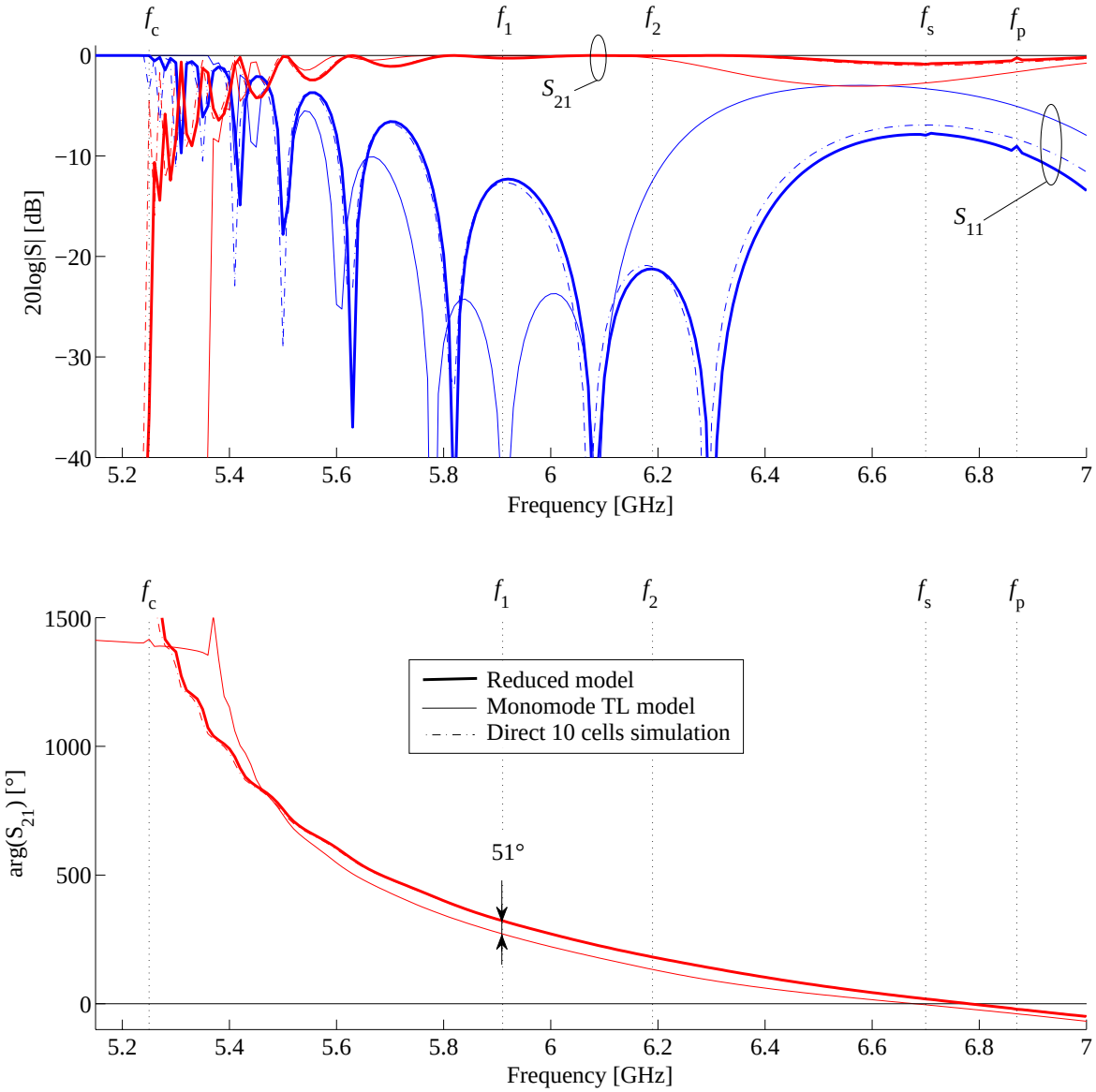

Figure 6.14: S parameters for a 10-cell SRR-wire medium whose unit cell is shown in Figure 6.12. The phase of S_{11} is not shown for clarity. Wherever the dash-dotted line is not visible, it is hidden behind the thick line.

($S_{11} = -21.0$ dB), while the phase response is 181°, hence a difference of 5° with the targeted value. This example demonstrates the superiority of the proposed multimode approach over the dominant-mode analysis. Indeed, a reasonably good design can be made even by neglecting the termination networks $\mathbf{T}_\mathrm{t}$.

6.4.5 Further possible work for improved matching

The example considered in Section 6.4.4 showed that the reduced model of Figure 6.11 very accurately describes the actual finite size periodic structure, and that a reasonably good design can be achieved by neglecting the termination networks $\mathbf{T}_\mathrm{t}$. If a better matching is required, the effect of these networks should be somehow accounted for in the design.

A first possibility consists in adding matching elements before and after the periodic structure in order to cancel, or at least reduce, the termination effects represented by $\mathbf{T}_\mathrm{t}$. Although not shown here, for the chosen example, $\mathbf{T}_\mathrm{t}$ can be modeled with very good accuracy by a simple series impedance. This can be used as a starting point for the design of a specific matching circuit. In many cases, this approach however suffers from the following disadvantages:

- Adding a matching element, such as an iris for instance, at the termination planes of the periodic structure will affect the termination condition on the evanescent host WG modes, which were assumed in Figure 6.9 to be terminated on their wave impedance Z_{mn}. To avoid this, the matching elements should be placed at some distance from the interfaces, to allow for the evanescent host WG modes to sufficiently decay as assumed in the derivation of the reduced model. Otherwise, the matching elements must also be represented as 2N-port networks and included as such in the models of Figures 6.9 and 6.10.
- Adding a matching element allows improving the matching but also affects the phase response of the overall structure. As a result, the requirement on the phase shift per unit cell should be changed in order to account for this modification, which considerably complicates the design.

A second and very powerful approach to avoid the aforementioned limitations is discussed here. Compensation of the interface effects accounted for in $\mathbf{T}_\mathrm{t}$ can be achieved by modifying the two extreme cells of the periodic structure. This technique however requires the derivation of a slightly different reduced model which includes the last cells in the termination networks, as shown in Figure 6.15(a). The transfer matrix of the new termination network can be calculated in a very similar way as performed in Section 6.4.3 (the resulting expressions are not reported here). Neglecting the small non-reciprocity and asymmetry in $\mathbf{T}_\mathrm{t}$, the latter can represented by a TL section of length d, as shown in Figure 6.15(b), with the Bloch parameters $\tilde{\gamma}_{\mathrm{B1}}$ and $\tilde{Z}_{\mathrm{B1}}$ calculated using the simple Bloch wave analysis described in Section 4.2. The design thus consists in designing a unit cell different from the others, so that when placed at the last position in the periodic structure, exhibits the same Bloch parameters as the cells inside the periodic structure, that is, $\tilde{\gamma}_{\mathrm{B1}} = \gamma_{\mathrm{B1}}$ and $\tilde{Z}_{\mathrm{B1}} = Z_{\mathrm{B1}}$. Preliminary tests on the chosen SRR-wire example revealed that the matching at the desired frequency could be improved simply

by tuning the ring capacitance C_{L}, while keeping the desired phase response. This alternative approach has not been further investigated in this work.

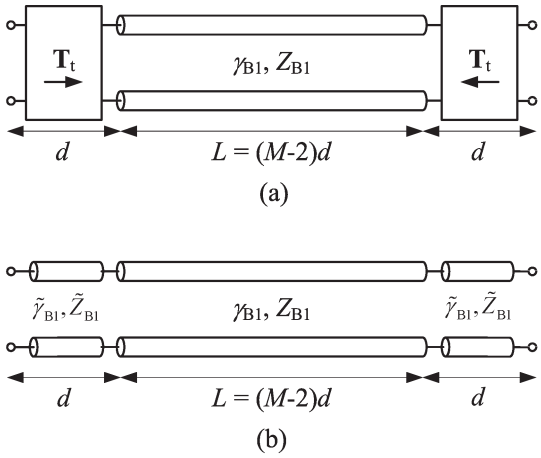

Figure 6.15: (a) Modified reduced model for a periodic structure in a monomode host WG and for which only a single Floquet mode is propagating (to be compared with the model of Figure 6.11). The termination networks $\mathbf{T}_{\mathrm{t}}$ include the termination effects *and* the last cell. (b) Equivalent model if $\mathbf{T}_{\mathrm{t}}$ is reciprocal and symmetrical.

6.5 Chapter Conclusion

A general analysis technique for periodic structures requiring a multimodal representation of their unit cell has been proposed, and consists in representing the periodic structure by an equivalent MTL. Whereas existing periodic structure analyses are restricted to the determination of the dispersion diagram, the proposed technique provides all the parameters needed for an accurate modeling of both the dispersion and the terminations of finite size periodic structures. The formulation applies to a wide range of periodic structures, such as periodically loaded MTLs and periodically loaded WGs with higher order evanescent mode interaction between cells. The only difference lies in the representation of the unit cell, respectively either in terms of conductor voltages and currents, or in terms of host WG modal quantities.

We have demonstrated that such an equivalence between a periodic structure and its MTL model is exact, from a theoretical point of view. Subsequently, the pertinence of modeling a periodic structure with an equivalent MTL has been assessed on two selected examples of negative-refractive-index MTMs. The first example is the shielded mushroom structure, a periodically loaded MTL supporting at the same frequencies two propagating Floquet modes of opposite nature. For this structure, the proposed technique allowed for the first time to quantitatively assess the amount of power coupled to each Floquet mode from a given excitation. For periodically loaded WGs with evanescent mode interaction supporting a single propagating Floquet mode, a simplified model representing the propagation along this mode has been proposed. The accuracy of this model has been demonstrated on the second example, which

is a SRR-wire MTM exhibiting significant coupling between cells. For such a structure, the proposed method allows a much more efficient designs than the commonly used dominant-mode periodic structure analysis, both in terms of dispersion and matching.

These two examples have demonstrated the usefulness of the proposed technique for modeling accurately the dispersion and terminations in a wide range of problems involving periodic structures, thereby providing the designer with an efficient tool to synthesize efficient excitation and matching circuits.

7 CRLH TLs based on a lattice network unit cell

7.1 Introduction

7.1.1 Outline

This chapter presents a novel unit cell topology for the composite right/left-handed transmission line (CRLH TL). Conventional periodic implementations of CRLH TLs reported so far consist of ladder-type structures, such as the type Π and T unit cells investigated in Section 4.3. In this chapter, we show that a unit cell under the form of a lattice network, i.e. a circuit with crossed diagonal arms [231], exhibits many interesting properties. In particular, this novel CRLH TL exhibits an overall reduced frequency dispersion of its Bloch parameters, thereby extending the bandwidth of operation for the related applications. More specifically, this chapter will demonstrate the following advantages over its conventional counterpart (in the balanced case):

- All-pass behaviour (no stop-bands below the LH band and above the RH band). As a result, the LH band extends down to DC.
- Frequency-independent Bloch impedance.
- Larger group velocity, hence a reduced frequency variation of the phase response.

The fundamental properties of this structure are theoretically investigated in Section 7.2 and the aforementioned performances are confirmed by full-wave and measurement results on some selected practical implementations in Section 7.3. The advantages offered by the novel proposed CRLH TL may lead to significant improvements for the well-known CRLH TL applications. In Section 7.4, potential applications to leaky-wave antennas and series-fed arrays are discussed. This new CRLH TL topology was first proposed by the author in [271], and subsequently investigated in [272–274].

7.1.2 Basic idea

The novel proposed CRLH TL topology is based on the following observation. It is known that a uniform TL can be approximated by a periodic structure made of the repetition of the unit cell shown in Figure 7.1(a), if the period d is small compared to the guided wavelength. This structure exhibits a low-pass behaviour with cutoff frequency $\omega_c = 2/\sqrt{L_s C_p}$. Another possible approximation consists of the lattice unit cell shown in Figure 7.1(b) [275]. This

structure is known to exhibit an all-pass behaviour, which results in a frequency-independent equivalent characteristic impedance. The fundamental idea of this work is thus to apply the lattice topology of Figure 7.1(b) to the implementation of all-pass CRLH TLs. The resulting structure has been referred to in this work as the "type X CRLH TL", which completes the type Π and T "conventional" unit cells already investigated in Section 4.3.

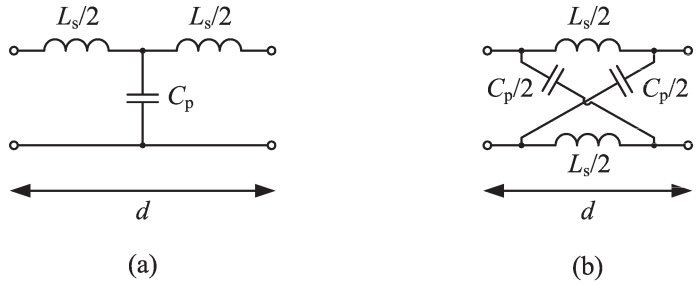

Figure 7.1: Unit cell of periodic structures approximating a uniform TL. (a) Low-pass LC model. (b) All-pass LC model.

7.1.3 Discretization of the TL equations

Before investigating the fundamental properties of the type X CRLH TL, it is of particular interest to further clarify the role of the lattice network in the context of the spatial discretization scheme used to approximate the TL equations. Let us first consider the well known telegraphist's equations expressed in (7.1)

$$\begin{aligned} \frac{\partial V}{\partial z} &= -Z'I \\ \frac{\partial I}{\partial z} &= -Y'V \end{aligned} \tag{7.1}$$

where Z' and Y' are the per-unit length series impedance and shunt admittance of the TL, respectively. Several spatial discretization schemes for (7.1) are considered:

1. First, discretizing V and I in z results in

$$\begin{aligned} \frac{V(z+\Delta z)-V(z)}{\Delta z} &= -Z'I(z) \\ \frac{I(z+\Delta z)-I(z)}{\Delta z} &= -Y'V(z) \end{aligned} \tag{7.2}$$

   It can be shown that the two-port network implementing these equations is non-reciprocal, which is why an equivalent circuit for the incremental TL section cannot be drawn.

2. Second, discretizing V in $z+\Delta z$ and I in z results in

$$\begin{aligned} \frac{V(z+\Delta z)-V(z)}{\Delta z} &= -Z'I(z) \\ \frac{I(z+\Delta z)-I(z)}{\Delta z} &= -Y'V(z+\Delta z) \end{aligned} \tag{7.3}$$

The corresponding equivalent circuit for an incremental TL section is shown Figure 7.2(a). It corresponds to an asymmetrical L-network.

3. Now, if both V and I are discretized in $z + \Delta z/2$ (i.e. we take the average between the values in z and $z + \Delta z$), the corresponding equations become

$$\begin{aligned} \frac{V(z+\Delta z) - V(z)}{\Delta z} &= -Z' \frac{I(z+\Delta z) + I(z)}{\Delta z} \\ \frac{I(z+\Delta z) - I(z)}{\Delta z} &= -Y' \frac{V(z+\Delta z) + V(z)}{\Delta z} \end{aligned} \tag{7.4}$$

The two-port network implementing these equations is the lattice network shown in Figure 7.2(b) [275].

The highly symmetrical discretization scheme of point 3. above provides a better approximation than the ladder type one, since the resulting lattice network for the incremental TL section is an *all-pass circuit* [275].

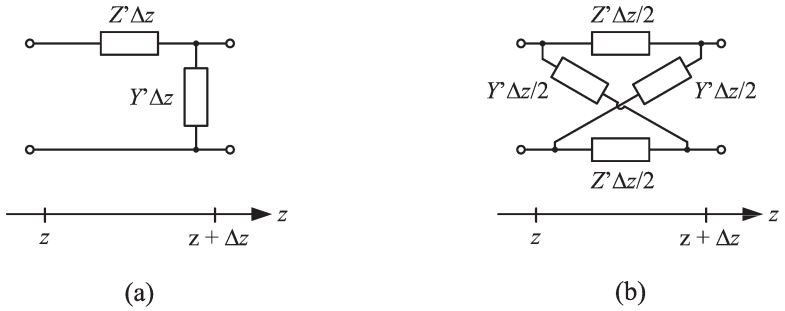

Figure 7.2: Equivalent circuit for an incremental TL section of length Δz according to different spatial discretization schemes. (a) Asymmetrical ladder (or L-) network. (b) Symmetrical all-pass lattice (or X-) network.

7.2 Theoretical Analysis

The fundamental properties of the novel type X CRLH TL are theoretically assessed by calculating the Bloch parameters using the formalism reported in Section 4.2. As for the conventional CRLH TL investigated in Section 4.3, we consider the two possible ways of representing the RH contribution, either with lumped elements (referred to as "model 2"), or with distributed elements (referred to as "model 3").

7.2.1 Model with lumped RH contribution (model 2)

a. Description

First, we recall in Figure 7.3 the two possible types Π and T symmetrical unit cells that can be periodically cascaded in order to realize the conventional CRLH TL. In these models, the

RH contribution is accounted for by lumped series inductances and shunt capacitances, which is accurate if the size of the unit cell d is small compared to the guided wavelength in the host TL. The corresponding type X CRLH TL unit cell is shown in Figure 7.4.

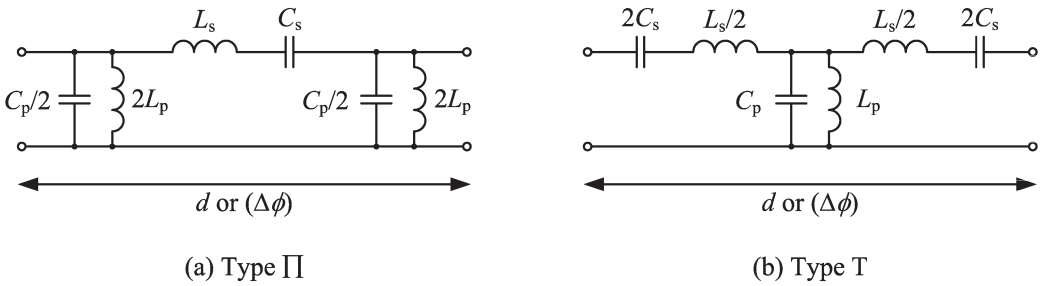

Figure 7.3: The two possible symmetrical unit cells of the CRLH TL with lumped RH elements: types Π and T.

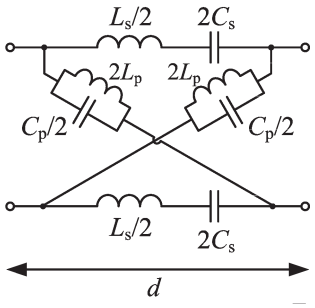

Figure 7.4: Unit cell of the novel all-pass type X CRLH TL based on the lattice topology.

b. Properties

It can be shown that the novel (type X) and the conventional (types Π and T) CRLH TLs can be made balanced (closure of the stop band between the LH and RH bands) under the same balanced condition, which writes $Z_{\mathrm{R}} = Z_{\mathrm{L}}$, with $Z_{\mathrm{R}} = \sqrt{L_{\mathrm{s}}/C_{\mathrm{p}}}$ and $Z_{\mathrm{L}} = \sqrt{L_{\mathrm{p}}/C_{\mathrm{s}}}$. The transition frequency f_0 between the LH and RH bands is the same in all cases and writes $\omega_0 = 1/\sqrt{L_{\mathrm{s}}C_{\mathrm{s}}} = 1/\sqrt{L_{\mathrm{p}}C_{\mathrm{p}}}$ ($\omega_0 = 2\pi f_0$). The Bloch parameters for the type X CRLH TL in the balanced case are given by

$$\begin{cases} \tanh\left(\dfrac{\gamma_{\mathrm{B}}d}{2}\right) = j\dfrac{\chi}{2} \\ Z_{\mathrm{B}} = Z_{\mathrm{R}} = Z_{\mathrm{L}} \end{cases} \qquad \text{with} \qquad \chi = \frac{\omega^2 - \omega_0^2}{\omega\omega_{\mathrm{R}}} = \frac{\omega}{\omega_{\mathrm{R}}} - \frac{\omega_{\mathrm{L}}}{\omega} \tag{7.5}$$

with all the variables defined as in (4.15). These expressions are to be compared with the ones obtained for the conventional CRLH TL in (4.18).

The expressions in (7.5) confirm that the novel type X CRLH TL exhibits an all-pass behaviour in the balanced case. Indeed, as $\tanh(\gamma_{\mathrm{B}}d/2)$ is always purely imaginary, γ_{B} is also

imaginary at all frequencies ($\gamma_B = j\beta_B$). This also results in a frequency-independent Bloch impedance ($Z_B = Z_R$), which may be of interest for wideband matching purposes. Moreover, when the frequency tends to zero the unit cell becomes a simple swap of the two conductors, as can be seen by inspecting the circuit of Figure 7.4. This is further confirmed by the fact that the quantity $\beta_B d$ reaches $-\pi$ at zero frequency, while keeping the same constant Bloch impedance.

At the transition frequency f_0, we have $Z_B = Z_R$ for all types of CRLH TLs. Moreover, it can be shown that the group velocity at f_0 is also the same in all cases and equal to $v_{g0} = \omega_R d/2$, which corresponds to one half of the phase velocity in the host TL given by $v_{ph} = \omega_R d = 1/\sqrt{L'_s C'_p}$, where $L'_s = L_s/d$ and $C'_p = C_p/d$.

c. Example

As an example, we consider balanced CRLH TLs of types Π, T and X with the same following parameters: $L_s = 1.67$ nH, $C_p = 667$ fF, $L_p = 1.38$ nH and $C_s = 551$ fF. These structures have been designed to obtain a transition frequency $f_0 = 5.25$ GHz and a Bloch impedance of 50 Ω at f_0. The corresponding Bloch parameters are shown in Figure 7.5.

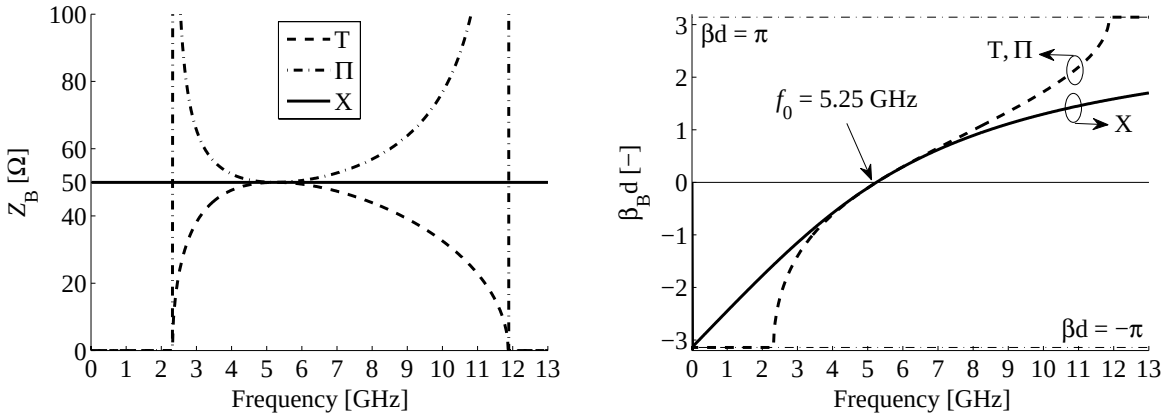

Figure 7.5: Bloch parameters for balanced CRLH TLs of type Π, T and X with the same parameters (see text).

The all-pass behavior and frequency-independent Bloch impedance of the novel type X CRLH TL is confirmed by the calculated Bloch parameters. The group velocity for type X is always larger than for types Π and T, except at f_0 where it is the same, as already analytically observed in Section 7.2.1.b.. In summary, the main advantage of the novel structure over its conventional counterpart is a more wideband behavior, both in terms of impedance and phase. Finally, it can be noted that the group velocity of the type X structure approaches infinity when the frequency increases. However, for any practical implementation, the model of Figure 7.4 is not expected to be accurate at very high frequencies since the unit cell becomes large compared to the wavelength, and thus the simple L_s-C_p model for the RH contribution may

not be accurate anymore. In the next section, a more general model of CRLH TLs is used to investigate the issue of group velocity.

7.2.2 Model with distributed RH contribution (model 3)

a. Description

We consider here a more general model for the CRLH TL, in which the RH contribution is accounted for by TL sections (host TL) instead of lumped series inductances and shunt capacitances, as was the case for the structures considered in Section 7.2.1. With this approach, the models of Figure 7.3 become those shown in Figure 7.6. For small unit cells compared to the guided wavelength in the host TL ($\beta_\mathrm{h} d \ll 1$), the models of Figure 7.3 can be used to approximate those of Figure 7.6, whereas for larger unit cells the models of Figure 7.6 should be used. The novel corresponding type X topology investigated here is shown in Figure 7.7. In this structure, the lattice topology is applied to the LH elements only (L and C), which are gathered in the center of the unit cell.

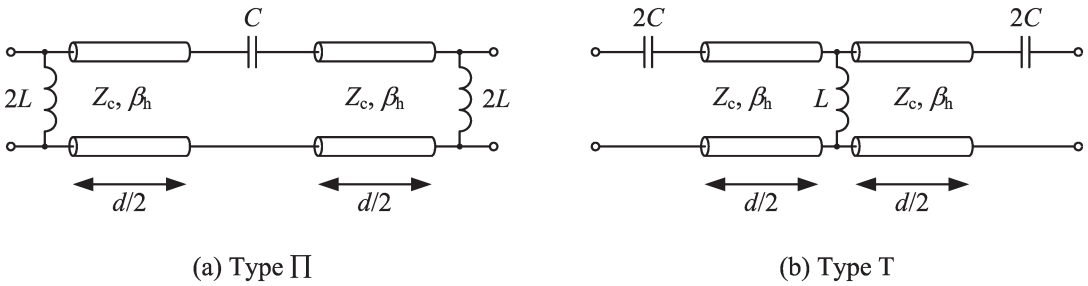

Figure 7.6: The two possible symmetrical unit cells of the CRLH TL with distributed RH elements: types Π and T.

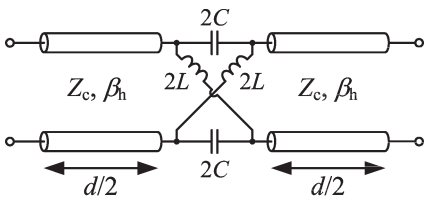

Figure 7.7: Unit cell of the novel type X CRLH TL with distributed RH elements.

b. Properties

First, it can be shown that the novel (type X) and the conventional (types Π and T) CRLH TLs with distributed RH elements can be made balanced under the same condition, which writes $Z_\mathrm{c} = \sqrt{L/C}$. The Bloch parameters for the type X CRLH TL in the balanced case are

given by

$$\begin{cases} \tanh\left(\dfrac{\gamma_{\mathrm{B}} d}{2}\right) = j\dfrac{\chi}{2} \\ Z_{\mathrm{B}} = Z_{\mathrm{c}} = Z_{\mathrm{L}} \end{cases} \quad \text{with} \quad \begin{cases} \chi = 2\dfrac{1 + 2\omega\tau_{\mathrm{L}} \tan\phi}{2\omega\tau_{\mathrm{L}} - \tan\phi} \\ \phi = \dfrac{\phi_{\mathrm{h}}}{2} = -\dfrac{1}{2}\omega\tau_{\mathrm{h}} \end{cases} \tag{7.6}$$

with all the variables defined as in (4.20) and (4.22). The transition frequency f_0 between the LH and RH bands is the same in all cases and is solution of the equation $2\omega_0\tau_{\mathrm{L}} \tan(\omega_0\tau_{\mathrm{h}}/2) = 1$, where τ_{h} is the time delay through a host TL section of length d and $\omega_0 = 2\pi f_0$. The type X CRLH TL exhibits an all-pass behavior and a frequency-independent Bloch impedance, as was the case for the type X structure with lumped RH elements studied in Section 7.2.1. The expressions in (7.6) are to be compared with the ones obtained for the conventional CRLH TL in (4.25).

c. Group velocity

The group velocity v_{g0} at f_0 for the conventional and the novel CRLH TLs with distributed RH elements is expressed in (7.7), where v_{ph} represents the phase velocity in the host TL and r_0 is the size of the unit cell d compared to the guided wavelength in the host TL at the transition frequency f_0, as defined in Section 4.3.2. Typical values of this "homogeneity factor" r range from 1/4 to 1/20, 1/4 being sometimes considered as the limit value for considering the resulting periodic structure as effectively homogeneous, as discussed in Section 4.3.2. It can be mentioned that (7.7) is only valid for $r_0 < 1/2$, but structures with higher values of r_0 do not present any interest in the present context.

$$v_{g0}^{\text{types T,}\Pi} = v_{ph}\left|\frac{\cos(\pi r_0)}{1 + \frac{\sin(2\pi r_0)}{2\pi r_0}}\right| \quad \text{and} \quad v_{g0}^{\text{type X}} = v_{ph}\frac{1}{\left|1 + \frac{\sin(2\pi r_0)}{2\pi r_0}\right|} \tag{7.7}$$

It follows from (7.7) that the group velocity at f_0 is always larger with type X than with types Π and T. Indeed, we have

$$\frac{v_{g0}^{\text{type X}}}{v_{g0}^{\text{types T,}\Pi}} = \frac{1}{|\cos(\pi r_0)|} = \frac{1}{\left|\cos\left(\frac{1}{2}\omega_0\tau_{\mathrm{h}}\right)\right|} \geq 1 \tag{7.8}$$

The quantities in (7.7) and (7.8) are plotted in Figure 7.8. It can be seen that for the conventional CRLH TL, v_{g0} is always smaller than one half of the velocity in the host TL v_{ph}, whereas this is the opposite for the novel CRLH TL. Furthermore, it is observed that this increase in group velocity becomes less significant for highly effectively homogeneous structures (i.e. structures with $r_0 \ll 1$). For instance, with $r_0 = 0.2$ this increase is 24%, whereas it is only 5% for $r_0 = 0.1$. Let us finally note that the group velocity for a given type X structure remains bounded ($v_g < v_{ph}$) at all frequencies, and that its value at $f = 0$ (DC) is given by

$$v_{g,\mathrm{DC}} = \frac{v_{ph}}{1 + 4\frac{\tau_{\mathrm{L}}}{\tau_{\mathrm{h}}}} \tag{7.9}$$

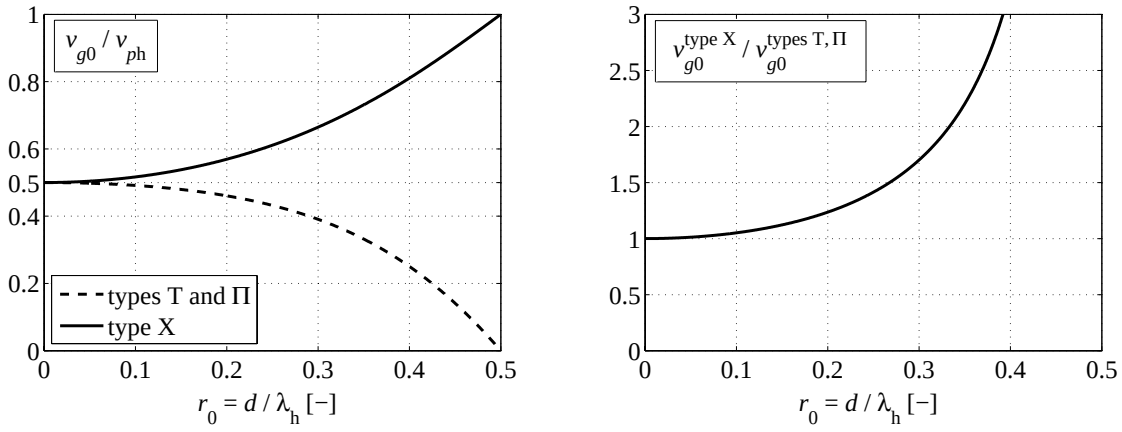

Figure 7.8: Group velocity at the transition frequency v_{g0} for balanced CRLH TLs of types Π, T and X with distributed RH elements, in function of the homogeneity factor r_0.

d. Design considerations

Design equations for balanced type X CRLH TLs can be easily obtained. It should be first observed that the unit cell of Figure 7.7 consists of the cascade of three networks: two TL sections and the X network itself. An all-pass behaviour can be obtained only if these three parts are matched together. As the equivalent (or Bloch) impedance of the X network itself is $Z_\mathrm{L} = \sqrt{L/C}$, an all-pass behaviour is achieved if $Z_\mathrm{c} = Z_\mathrm{L}$, that is, in the balanced case. It can be noted here that the all-pass nature of this periodic structure can be understood from the fact that interference phenomena between the periodic obstacles, which are typical to EBG structures, do not occur here since all the elements are matched at all frequencies, thereby preventing the appearance of stop-bands related to these interference phenomena (Bragg frequencies).

As a result of the matching between the cascaded networks, the corresponding phase shifts can be added to obtain the total phase shift per unit cell. In other words, we can expand the phase shift per unit cell $\phi_\mathrm{B} = -\beta_\mathrm{B} d$ into a RH (ϕ_h) and a LH (ϕ_L) contribution as follows:

$$\phi_\mathrm{B} = \phi_\mathrm{h} + \phi_\mathrm{L} \qquad \text{with} \quad \begin{cases} \phi_\mathrm{h} = -\beta_\mathrm{h} d = -\omega\tau_\mathrm{h} < 0 \\ \phi_\mathrm{L} = 2\arctan\left(\dfrac{1}{2\omega\tau_\mathrm{L}}\right) > 0 \end{cases} \tag{7.10}$$

The same distinction applies to the phase constant β_B, which yields

$$\beta_\mathrm{B} = \beta_\mathrm{h} - \frac{2}{d}\arctan\left(\frac{1}{2\omega\tau_\mathrm{L}}\right) \tag{7.11}$$

which is a simplified expression equivalent to (7.6).

We consider here a design which consists in imposing the transition frequency f_0, the Bloch impedance $Z_\mathrm{B}(f_0) = Z_0$ and the homogeneity factor $r(f_0) = r_0$. Imposing the homogeneity factor r_0, which is equivalent to impose the electrical length of the unit cell, might appear

unusual for conventional CRLH TLs. However, it makes sense for the type X structure since the latter is advantageous only for specific values of r_0, as will be shown in the examples below. For the aforementioned design requirements, the four parameters of the CRLH TL are given by

$$\begin{cases} \tau_{\mathrm{h}} = \dfrac{r_0}{f_0} \\ \tau_{\mathrm{L}} = \dfrac{1}{2\omega_0 \tan(\pi r_0)} \end{cases} \quad \text{and} \quad \begin{cases} Z_{\mathrm{c}} = Z_{\mathrm{L}} = Z_0 & \text{for type X} \\ Z_{\mathrm{c}} = Z_{\mathrm{L}} = Z_0 \cos(\pi r_0) & \text{for type T} \\ Z_{\mathrm{c}} = Z_{\mathrm{L}} = Z_0 / \cos(\pi r_0) & \text{for type } \Pi \end{cases} \tag{7.12}$$

The corresponding design expressions for types Π and T are also shown in (7.12); only the expression for Z_{c} differs. The parameters L and C can be subsequently deduced from Z_{L} and τ_{L} using (4.22). Design expressions for a required phase shift and impedance at $f_1 \neq f_0$ can also be deduced within a reasonable level of complexity (not shown here).

e. Examples

The performances of balanced CRLH TLs of standard types Π and T are now compared with those of the new type X for the same circuit element values and for two different values of the homogeneity factor r_0. All the structures are designed to exhibit a transition frequency $f_0 =$ 5 GHz. For the first example, we have $L = 1.12$ nH, $C = 226$ fF, $Z_{\mathrm{c}} = 70.4\ \Omega$ and $\tau_{\mathrm{h}} = 50$ ps, which corresponds to an homogeneity factor of $r_0 = 1/4$. For the second example, $L = 3.45$ nH, $C = 696$ fF, $Z_{\mathrm{c}} = 70.4\ \Omega$ and $\tau_{\mathrm{h}} = 20$ ps, which corresponds to an homogeneity factor of $r_0 =$ 1/10. The Bloch parameters for these two cases are shown in Figure 7.9. It can be observed in Figure 7.9(a) that for highly effectively homogeneous structures ($r_0 = 0.1$), the novel and the conventional CRLH TLs exhibit a very similar behavior around the transition frequency f_0 and at higher frequencies, and the increase in v_{g0} achieved by type X is only 5%. Nevertheless, the use of the type X structure is still advantageous at lower frequencies (wider LH band, constant Z_{B}). For structures with electrically larger unit cells like in the case $r_0 = 1/4$ of Figure 7.9(a), the novel type X CRLH TL clearly exhibits advantages over its conventional counterpart over the whole frequency band. Indeed, while Z_{B} experiences significant variation with frequency for types Π and T, it remains constant for type X. Furthermore, the increase in v_{g0} is 41% in this case.

As a result, for applications where the CRLH TL is operated near the transition frequency, the type X structure offers significant advantages over its conventional counterpart, provided that the homogeneity factor r_0 is not too small. Recommended values of r_0 for the use of the type X structure range from 1/8 to 1/4, where we can really take benefit from its advantages while keeping the unit cell reasonably small compared to the guided wavelength in the host TL ($r_0 < 1/4$).

7.2.3 Discussion on the applicability of the two type X models

It has been shown above that the novel type X structure is especially interesting when the unit cell is not too small compared to the wavelength. For such structures, it is clear that the model

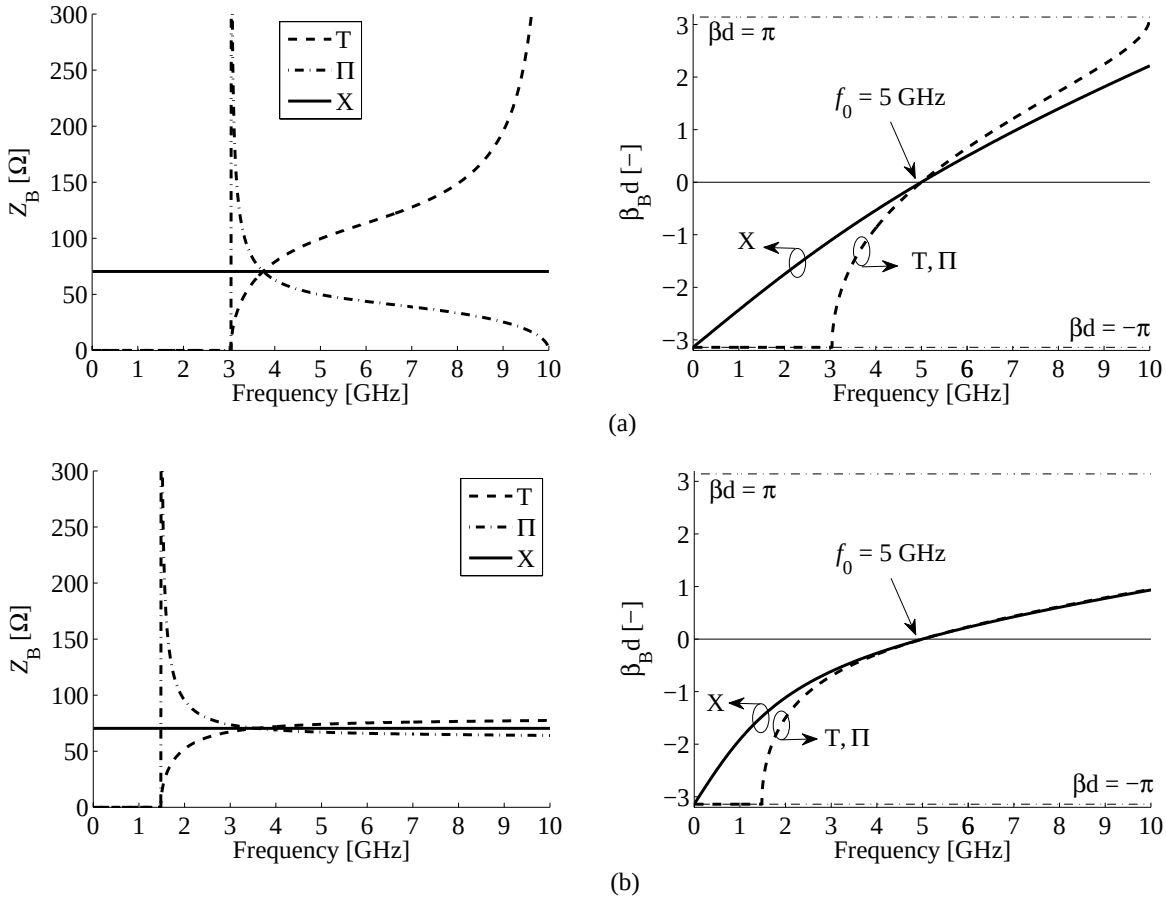

Figure 7.9: Bloch parameters for balanced CRLH TLs of types Π, T and X with distributed RH elements with the same parameters (see text). (a) Design with $r_0 = 1/4$. (b) Design with $r_0 = 1/10$.

with distributed RH elements of Figure 7.7 will be more accurate than the one with lumped RH elements of Figure 7.4. It is still not clear whether a circuit implementing the model of Figure 7.4 can be realized, whereas implementations of the one shown in Figure 7.7 is quite straightforward, as will be shown in the next section.

7.3 Implementations

We investigate here various practical implementations of the novel type X CRLH TL, thereby demonstrating its superior performances with full-wave and measurement results. The reported structures implement the circuit of Figure 7.7, i.e. the one with the distributed RH contribution. It is clear that the novel X topology requires the implementation of series capacitances in both conductors of the TL. For this reason, it will be more conveniently implemented in balanced TLs, such as coplanar stripline (CPS) or parallel stripline. However, implementations in microstrip or coplanar waveguide (CPW) with finite width ground planes can also be considered.

7.3.1 First implementation in parallel stripline: numerical results

A possible implementation of the novel type X unit cell of Figure 7.7 in parallel stripline technology is shown in Figure 7.10. This structure corresponds to the first example of section 7.2.2.e., i.e. the one with $r_0 = 1/4$. The series capacitances are realized with MIM capacitors, whereas narrow strips with vias provide the shunt inductances. The Bloch parameters extracted from full-wave simulation of the unit cell and those calculated from the circuit model are shown in Figure 7.11, with comparison to the corresponding type Π structure. A very good agreement between circuit model and full-wave results is observed, except for a spike at f_0 for the simulated Z_{B} resulting from the fact that the implemented structures are not perfectly balanced. This example confirms the advantages of the novel unit cell type X over its conventional type Π counterpart: The LH band extends down to DC, the Bloch impedance is almost frequency independent and the group velocity at f_0 is 41% larger. This first implementation example has been presented in [272].

7.3.2 Second implementation in parallel stripline: practical realization

a. Description

Figure 7.12 shows a more realistic implementation of the type X CRLH TL in parallel stripline technology similar to the one investigated in Section 7.3.1. The structure consists of a 3-layer printed circuit, as shown in the inset of Figure 7.12. The main circuit is printed on a RT/Duroid 5870 substrate ($\varepsilon_r = 2.33$, $\tan\delta = 0.0012$) of thickness $h = 1.57$ mm, and two additional layers of RT/Duroid 6006 ($\varepsilon_r = 6$, $\tan\delta = 0.0019$) of thickness $h_2 = 0.254$ mm support the plates of the MIM capacitors. The structure has been designed to be balanced

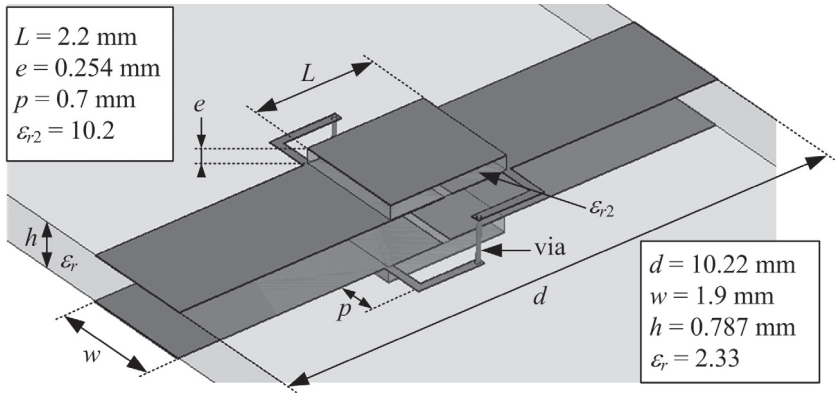

Figure 7.10: Unit cell of the implemented CRLH TL type X. The width of the strips forming the shunt inductors and the gap in the capacitors are 0.15 mm.

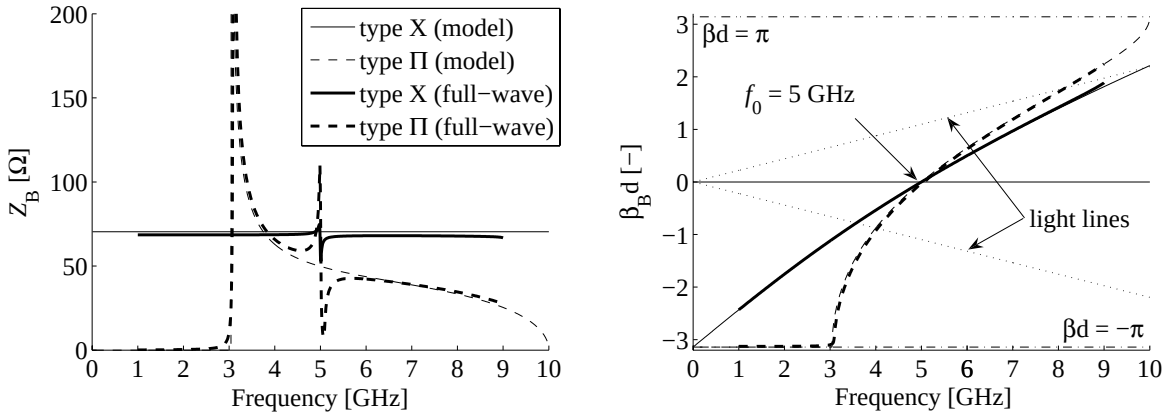

Figure 7.11: Bloch parameters extracted from full-wave simulation results (HFSS) and circuit models for the implemented CRLH TLs of type X (Figure 7.10) and Π.

with a transition frequency $f_0 = 6$ GHz and a Bloch impedance of 50 Ω. The length of the unit cell is $d = 6$ mm, which corresponds to a homogeneity factor $r_0 = 0.183$. The circuit model parameters corresponding to this design are (see Figure 7.7) $L = 1.02$ nH, $C = 408$ fF, $Z_c = 50$ Ω and $\beta_h/k_0 = 1.53$. For comparison, the corresponding type Π CRLH TL, which has the same values for the circuit parameters, has also been designed and simulated. It is similar to the structure shown in Figure 7.12, but with the shunt inductors located in the center between two consecutive series capacitors.

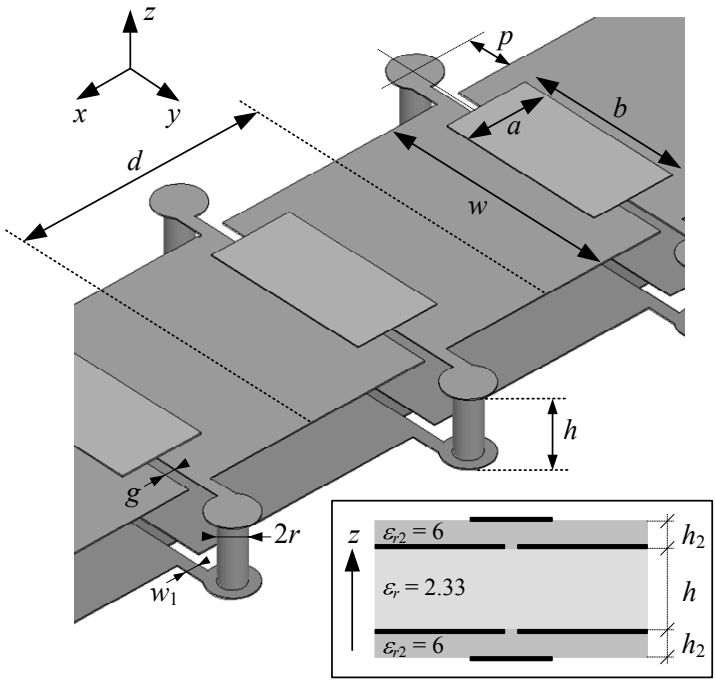

Figure 7.12: Proposed type X CRLH TL in parallel stripline technology ($d = 6$ mm, $h = 1.57$ mm, $h_2 = 0.254$ mm, $w = 5.75$ mm, $a = 2$ mm, $b = 4$ mm, $g = 0.25$ mm, $p = 1.05$ mm, $w_1 = 0.3$ mm, $2r = 0.6$ mm).

b. Simulation and Circuit Model Results

The Bloch parameters extracted from full-wave simulation results (Ansoft HFSS) of a single unit cell and those calculated from the circuit model using the aforementioned parameters are shown in Figure 7.13, for both X and Π structures. A very good agreement between circuit model and full-wave results is observed, except for a spike at $f_0 = 6$ GHz for the simulated Bloch impedance Z_B resulting from the fact that the implemented structures are not perfectly balanced. This example confirms the analytically demonstrated advantages of the novel type X unit cell over its conventional type Π counterpart: 1) the LH band extends down to DC for the type X CRLH TL (with $\beta_B d = -\pi$ at $f = 0$), whereas the Π structure exhibits a stop-band below 2.9 GHz; 2) the Bloch impedance for type X is almost frequency independent, whereas it experiences significant frequency variation for the Π structure, especially in the LH band, as

a consequence of the presence of the low frequency stop-band; and 3) the group velocity at f_0 is 15% larger for type X than for type Π (ideally 19% according to (7.8) with $r_0 = 0.183$).

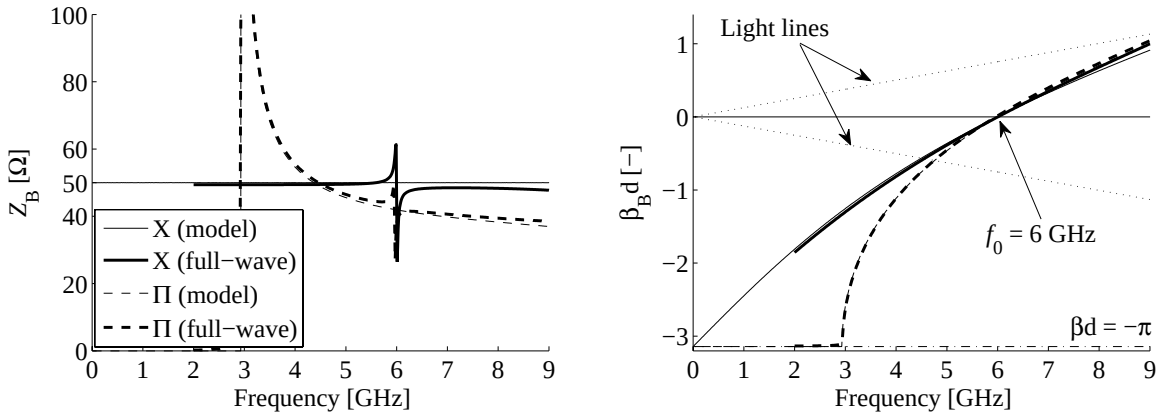

Figure 7.13: Bloch parameters extracted from full-wave simulation results (HFSS) and circuit models for the implemented CRLH TLs of types X and Π.

c. Realization and Measurement Results

A single unit cell of the type X CRLH TL shown in Figure 7.12 has been realized using conventional printed circuit techniques. Simple microstrip to parallel stripline transitions have been used to connect the unit cell to the unbalanced ports of the network analyzer. The S parameters of the unit cell have been measured by means of a TRL calibration, thereby allowing to place the reference planes at the boundaries of the cell. The measured S parameters are shown in Figure 7.14, together with the corresponding full-wave simulation results. The realized unit cell exhibits the desired performances, which are an all-pass behavior with a 0° phase shift at $f_0 = 6$ GHz. Nevertheless, the return loss, although better than -15 dB on the whole bandwidth, is not as low as expected from simulation results, which is attributed to the use of the microstrip to parallel stripline transitions in the TRL calibration. Similar problems have already been encountered with the measurement of CPS circuits (Section 4.6.5). In contrast, the accuracy on the transition frequency f_0 is excellent ($< 0.1\%$) and the insertion loss is better than 1 dB on the whole 2-9 GHz bandwidth. Figure 7.15 shows the Bloch parameters extracted from the measurement results, together with the corresponding full-wave simulation results. As could be anticipated, the disagreement on the return loss S_{11} results in a disagreement on the Bloch impedance Z_B, and an excellent agreement for the phase constant β_B can be observed, as was the case for the phase of S_{21}. This first practical implementation of type X CRLH TL has been reported in [274].

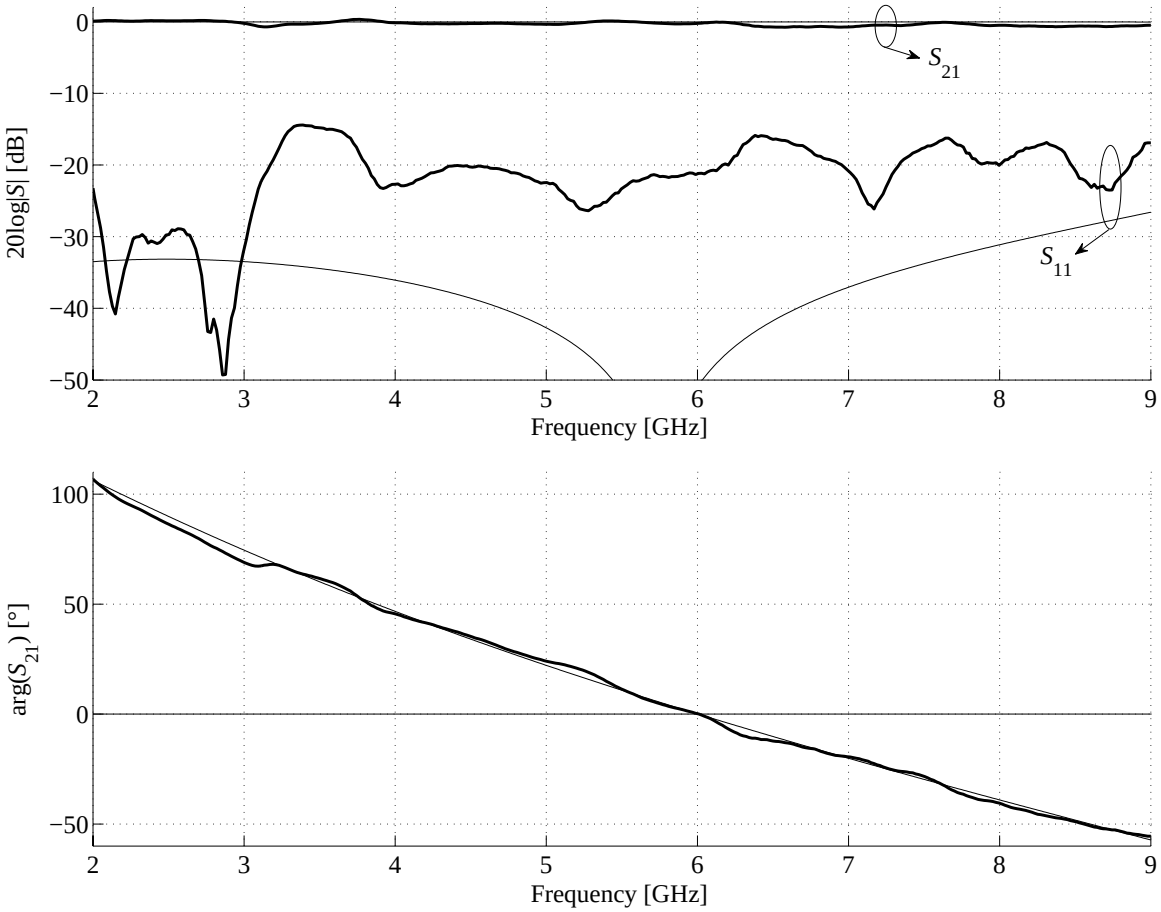

Figure 7.14: Measured (thick line) and simulated (thin line) S parameters of a single unit cell of the type X CRLH TL shown in Figure 7.12 (the phase of S_{11} is not shown for clarity).

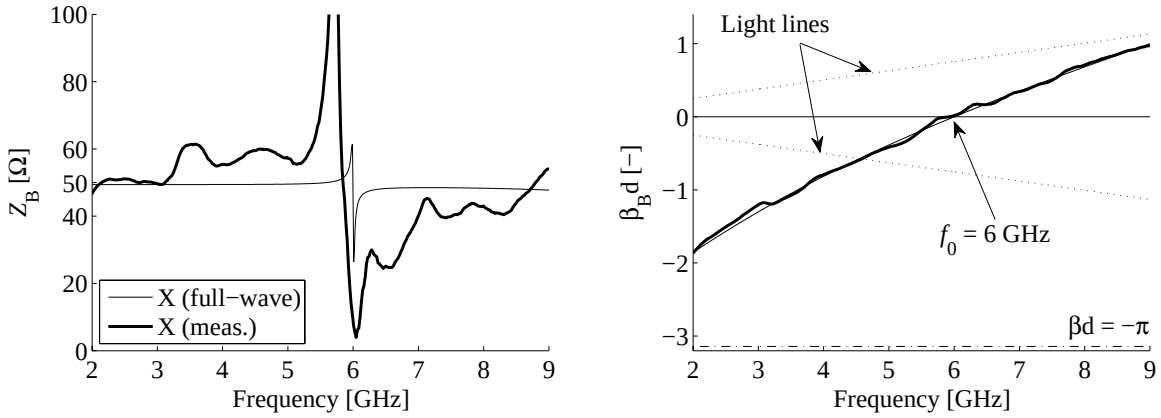

Figure 7.15: Same as in Figure 7.13, but comparison between measurement and full-wave results for the type X unit cell.

7.3.3 Implementation in CPW-like technology

We consider here an alternative implementation of the type X CRLH TL in a CPW-like host TL with finite width ground planes (GP), as shown in Figure 7.16. The series capacitances are realized by MIM capacitors using the other side of the substrate, as for the CPS structures proposed in Section 4.6. This results in a pseudo d-periodic structure, due to the alternation of the strip and GPs positions with respect to the substrate. This topology has been chosen since it presents the following advantages:

- No vertical connections are needed for the shunt inductors.
- No multilayered topology is required for the series capacitors.
- The chosen host TL is asymmetrical and thus does not require any balun.

The circuit is printed on a RT/Duroid 5870 substrate ($\varepsilon_r = 2.33$, $\tan\delta = 0.0012$) of thickness $h = 0.254$ mm. The structure has been designed to be balanced with a transition frequency f_0 = 6 GHz, a Bloch impedance of 50 Ω and a homogeneity factor $r_0 = 0.25$. The circuit model parameters corresponding to this design are (see Figure 7.7) $L = 0.66$ nH, $C = 265$ fF, $Z_c = 50$ Ω, $\beta_h/k_0 = 1.21$ and $d = 10.33$ mm. The Bloch parameters extracted from full-wave simulation results (Ansoft HFSS) of a single unit cell are shown in Figure 7.17. It can be seen that the targeted performances are achieved, except for the small unbalance spike usually observed at f_0.

A 10-cell structure has been realized using conventional printed circuit techniques. A picture of the realized structure can be seen in Figure 7.18. No particular transitions are required for the connection to the measurement setup. The measured S parameters are shown in Figure 7.19, together with the corresponding full-wave simulation results. An all-pass behaviour is globally observed, with approximately the required phase response (transition frequency f_0 around 6 GHz). A reasonably good correspondence is observed between measurements and

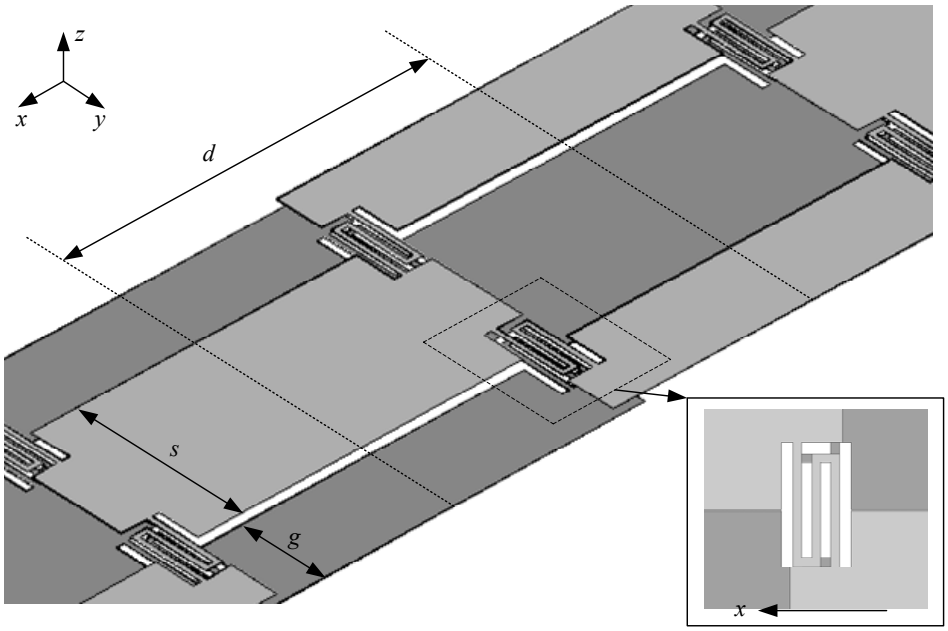

Figure 7.16: Proposed type X CRLH TL in CPW-like technology. The two different colors correspond to the two sides of the substrate, which is not shown for clarity. The inset shows a top view of the meander line shunt inductors (d = 10.33 mm, s = 5 mm, g = 2.5 mm, and the width of the meander lines in the shunt inductors is 0.15 mm).

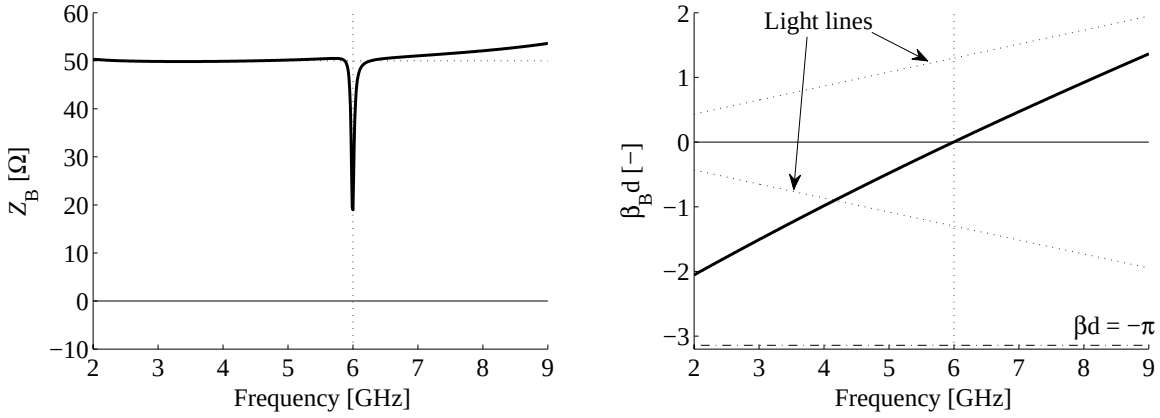

Figure 7.17: Bloch parameters extracted from full-wave simulation results (HFSS) for the type X CRLH TL of Figure 7.16.

simulations, although the measured return loss is worse in the LH band (< 6 GHz). The transition frequency f_0 is 6.02 GHz for the simulation results and 5.91 GHz for the measurements. Alternatively, the measured phase of S_{21} at the targeted $f_0 = 6$ GHz is -25°, hence a difference of -2.5° per unit cell with the expected 0° value, which is quite low.

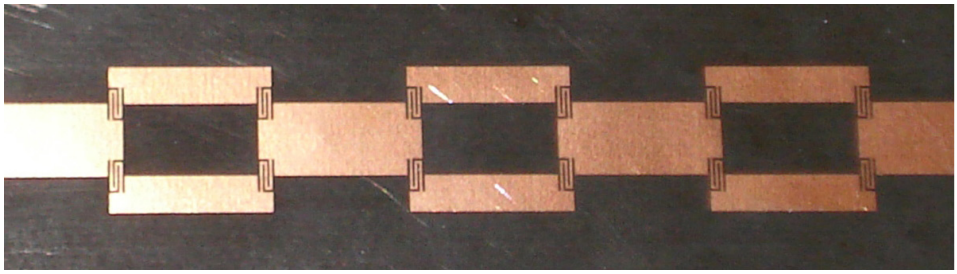

Figure 7.18: Picture of the realized type X CRLH TL in CPW-like technology.

Let us finally note a reduction of S_{21} and an increase of S_{11} around 4 GHz, which corresponds to the lower limit of the fast wave region (see γ_B in Figure 7.17). According to the dispersion diagram, leaky-wave radiation may occur from about 4 GHz to > 9 GHz. The overall losses occurring in the structure can be assessed through the calculation of the "efficiency" $\eta = |S_{11}|^2 + |S_{21}|^2$, which is shown in Figure 7.20 for the considered structure. The relative part of radiation and ohmic losses cannot be simply assessed by inspecting the plot of η, but the rather abrupt variation of the losses at the lower limit of the fast wave band suggests that leaky-wave radiation plays a significant role in this structure. This phenomenon should be further investigated in the light of leaky-wave antenna applications of the structure.

7.3.4 Silicon-based micromachined implementation in CPW

We briefly report here another considered implementation of the type X CRLH TL in a silicon-based micromachined CPW with finite width ground planes, whose unit cell is shown in Figure 7.21. This structure has been initially presented in [273]. As we use a single shunt inductance in each slot of the CPW, bridges are needed to connect the two ground planes in order to minimize the excitation of the parasitic odd CPW mode. The structure has been designed to be balanced with a transition frequency $f_0 = 17.5$ GHz and a Bloch impedance of 50 Ω. The length of the unit cell is $d = 2.23$ mm, which corresponds to an homogeneity factor $r_0 = 0.32$. The circuit model parameters (see Figure 7.7) are around $L \cong 100$ pH and $C \cong 40$ fF. The Bloch parameters extracted from full-wave simulation results (Ansoft HFSS) of a single unit cell are shown in Figure 7.22, which shows that the targeted performances are almost achieved. It can be mentioned that parasitic resonances have been observed at higher frequencies (> 22 GHz), which have been attributed to the unwanted excitation of the parasitic odd CPW mode resulting from the geometrical asymmetry of the structure. This issue can be assessed with a more detailed multiconductor TL circuit model, as the one shown in Figure 7.21.

The possible reconfiguration of this structure using MicroElectroMechanical Systems (MEMS) technology has been considered [276], aiming at improving the performances of the

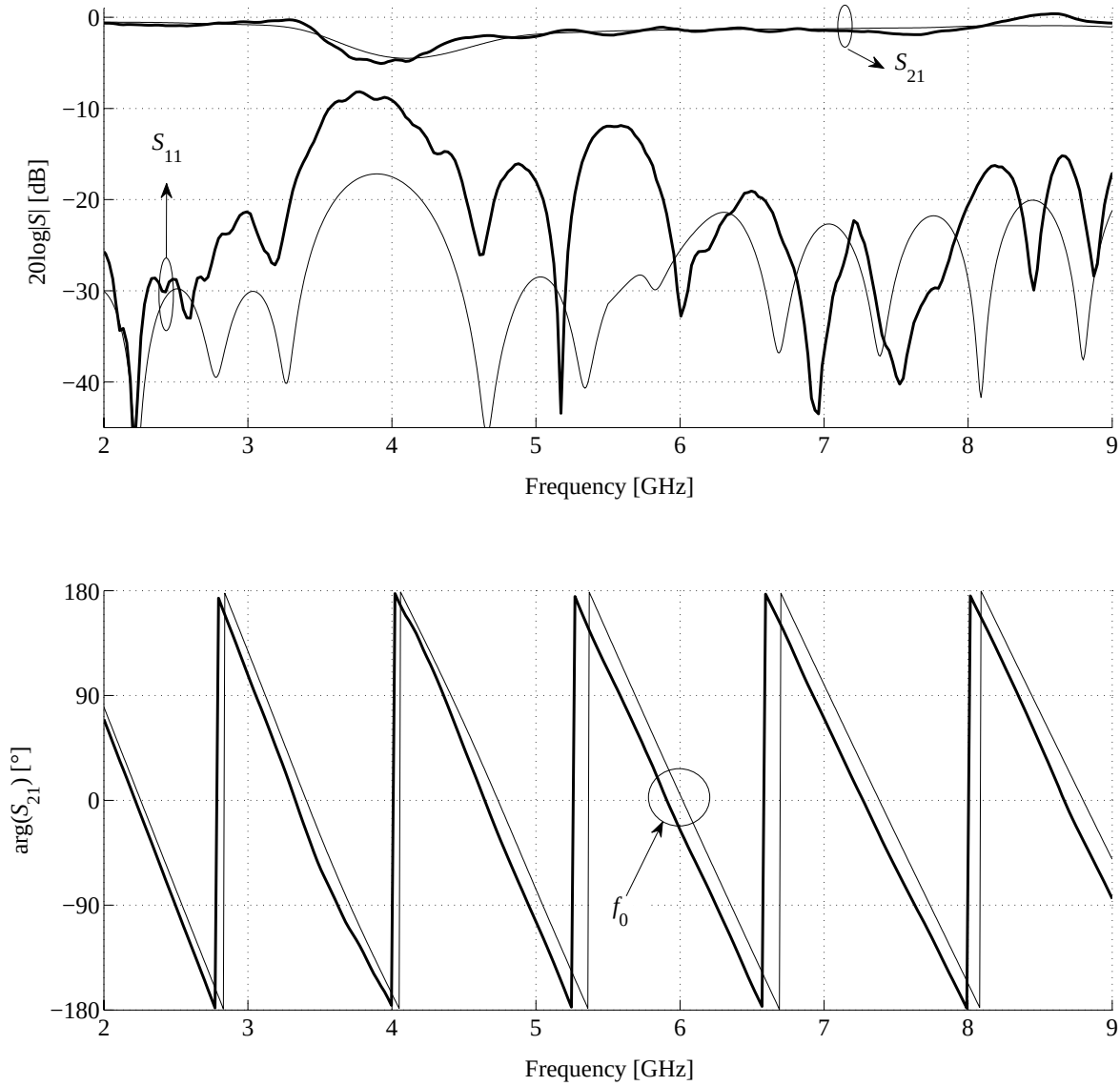

Figure 7.19: Measured (thick line) and simulated (thin line) S parameters of a 10-cell type X CRLH TL as shown in Figure 7.16 (the phase of S_{11} is not shown for clarity).

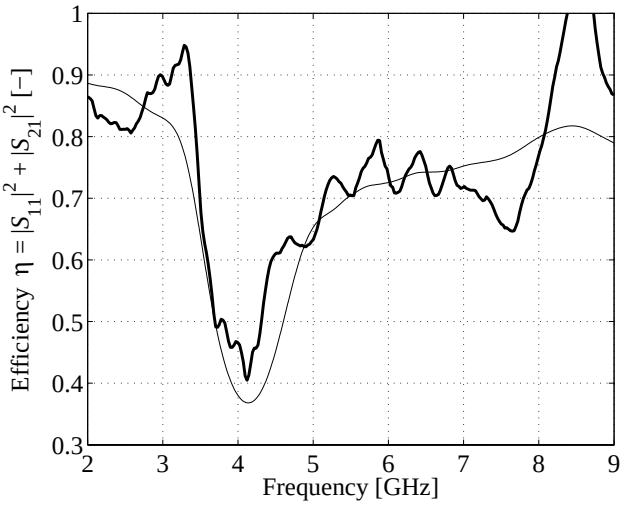

Figure 7.20: Measured (thick line) and simulated (thin line) efficiency η for the considered 10-cell type X CRLH TL.

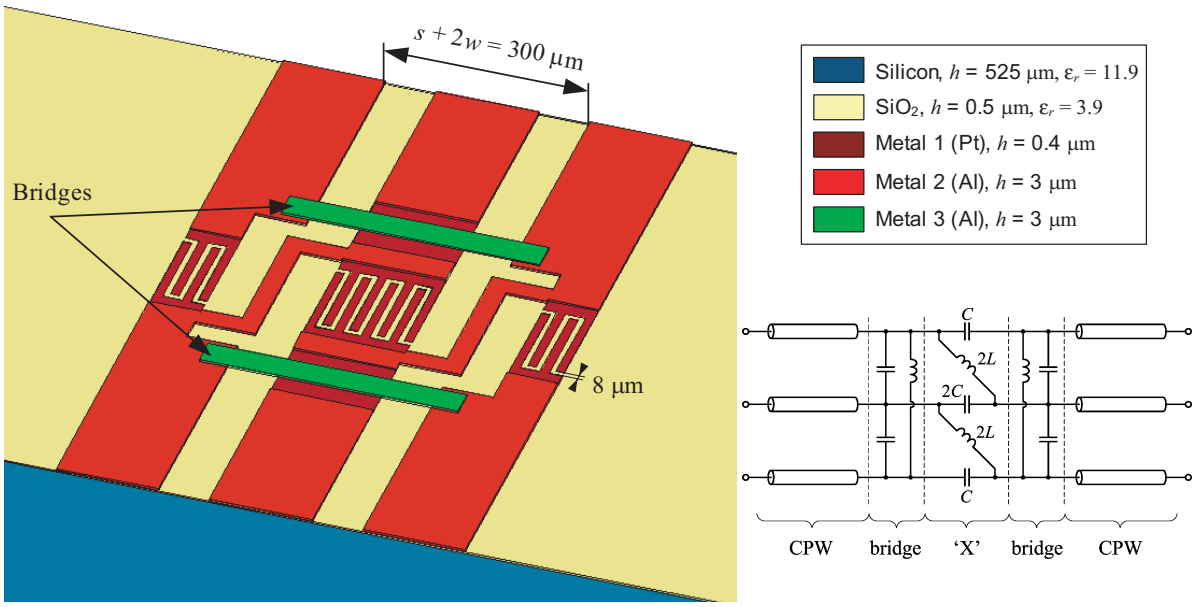

Figure 7.21: Unit cell of the proposed type X CRLH TL in micromachined CPW with finite width ground planes, along with the detailed multiconductor circuit model.

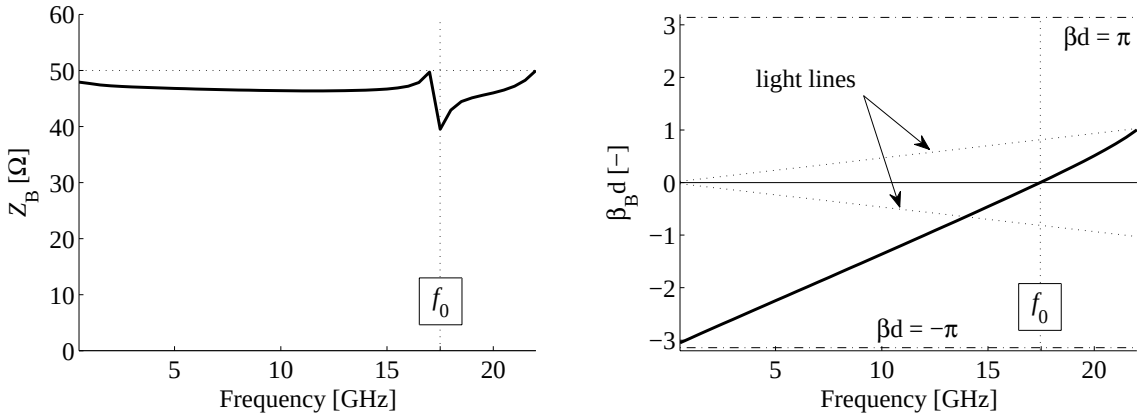

Figure 7.22: Bloch parameters extracted from full-wave simulation results (HFSS) for the type X CRLH TL of Figure 7.21.

MEMS-reconfigurable CRLH TL of the conventional type previously presented in [170]. To that respect, designs with MEMS-based tunable shunt capacitors placed in the host TL sections have been carried out, and the resulting structures are under fabrication. These unit cells are aimed at being used in CRLH TL based phase-shifters [110, 126] or series power dividers [153, 154].

7.4 Applications

The novel type X unit cell can be potentially used to improve the performances of most of the reported CRLH TL applications, provided that it is possible to implement the required series capacitances in both conductors of the host TL used. In this section, we discuss potential improvements of two well-demonstrated CRLH TL antenna systems —the leaky-wave antenna and the series-fed array— achieved by using the novel type X unit cell [272]. An interesting application of the lattice topology to another class of structures (i.e. not to CRLH TLs) is also discussed at the end of this section.

7.4.1 Leaky-wave antennas with reduced beam squinting

CRLH TLs can be used in their fast wave region as leaky-wave antennas (LWA) capable of backfire to endfire scanning, with the unique feature of broadside radiation at the transition frequency f_0 (in the balanced case) (Section 2.4.2.a.). It is known that the direction of the main beam $\theta_{\max}$ (defined from the normal to the antenna, as in Figure 2.7) approximately varies with frequency according to (7.13), where k_0 is the free space wave number.

$$\sin\theta_{\max} = \beta_B / k_0 \tag{7.13}$$

This beam squinting with frequency is often considered as a drawback, which is why it is of interest to minimize the frequency dependence of β_B [228]. As an example, according to

(7.13) a LWA made of the balanced type X unit cell shown in Figure 7.10 will exhibit a beam squint at broadside of 28°/GHz, compared to 40°/GHz for the LWA made of the corresponding conventional type X unit cell, hence a reduction of about 30%. The corresponding values of $\theta_{\max}$ calculated using (7.13) for the two structures are shown in Figure 7.23, from which we can graphically assess the beam squinting reduction, as well as the increase of the fast wave (radiation) bandwidth.

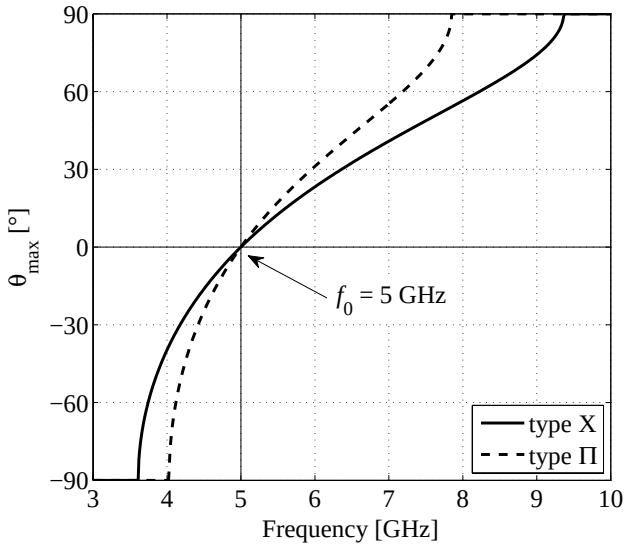

Figure 7.23: Predicted main beam direction [using (7.13)] for two CRLH TL LWAs with the same parameters.

7.4.2 Phase shifter for series-fed arrays

CRLH TLs operated in the slow wave region of the LH band can be combined with conventional TLs to provide non-radiating phase shifters with 0° phase shift [110] that can be used in series-fed arrays to feed the elements in phase [149, 205]. Figure 7.24 shows the conceptual model for such a phase shifter and the principle of the series-fed array. As the phase incurred by such phase shifters is frequency dependent, the direction of the main beam also changes with frequency, which is generally an undesirable phenomenon.

The actual topology of the considered phase shifter is shown in Figure 7.25. Here we compare two of these devices including a one-cell CRLH TL of type X or Π. Both phase shifters are designed to exhibit a 0° phase shift at $f_1 = 5$ GHz, and the CRLH TL is matched to the conventional TLs at that frequency, i.e. $Z_{\mathrm{B}}(f_1) = Z_{\mathrm{c}}$. In both cases, we have $L_2 = 3$ mm (1 cell only), $L_1 = 12$ mm, $Z_{\mathrm{c}} = 170\ \Omega$ and $\varepsilon_{r,\mathrm{eff}} = 1.31$ (for the host TL). For type X, we have $L = 2.56$ nH and $C = 135$ fF (those values are close to the ones provided in [205]), and for type X we have $L = 2.15$ nH and $C = 74.5$ fF. The calculated Bloch parameters for these two CRLH TLs are shown in Figure 7.26. It can be observed that they are both matched to

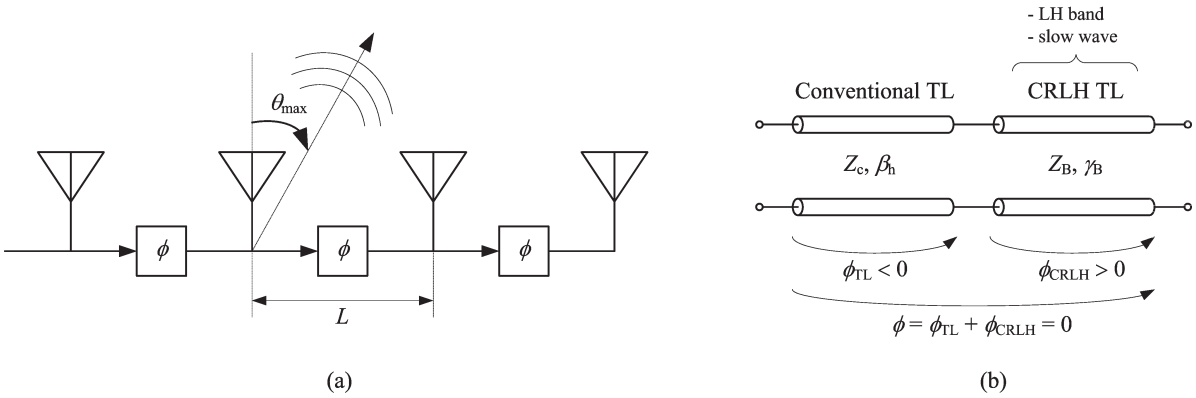

Figure 7.24: (a) Schematic representation of a series-fed array. (b) Principle of a 0° non radiating phase shifter made of the combination of a conventional TL section and a CRLH TL operated in the slow wave part of the LH band [149].

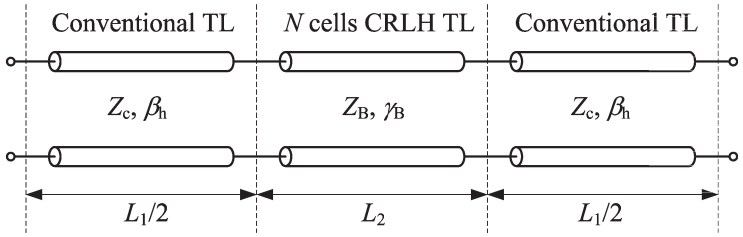

Figure 7.25: Considered phase shifter based on phase compensation between conventional and CRLH TLs.

170 Ω with the same required phase shift per cell at 5 GHz.

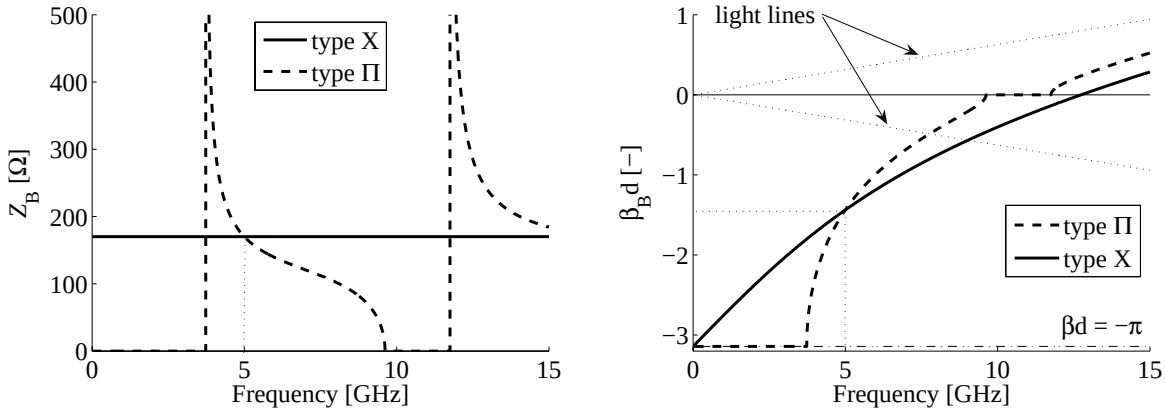

Figure 7.26: Bloch parameters for the two considered CRLH TLs of type X and Π to be used in a phase shifter for a series-fed array.

Figure 7.27 shows the calculated S parameters for the two designed phase shifters based on the topology shown in Figure 7.25. It can be seen that the type X structure provides a better matching and a lower group delay than the conventional type Π structure, as could be anticipated from the Bloch parameters shown in Figure 7.26. As a result, this improved phase shifter will lead to a reduced beam squinting when used in a series-fed array, as performed in [149, 205] with conventional CRLH TLs.

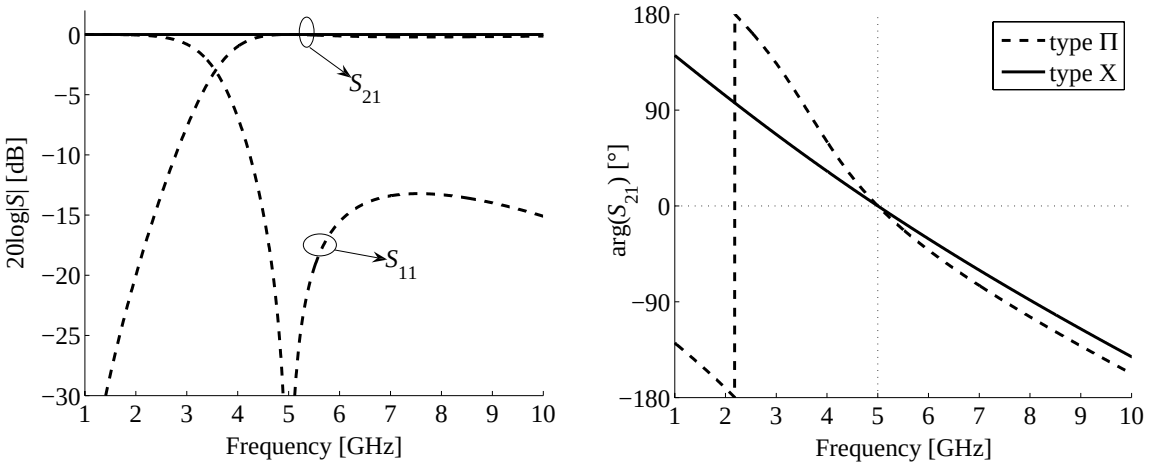

Figure 7.27: Calculated S parameters for two phase shifters using a one-cell CRLH TL of type X or Π (see text). For the type X structure, we identically have S_{11} = 0 and S_{21} = 1, due to the perfect matching.

7.4.3 Other applications of the lattice topology: 2D TL networks

Although the main focus of this chapter is the utilization of the lattice network in the development of CRLH TLs, this configuration can also be advantageously used in other closely related topics. In particular, we discuss here some ideas for applying the lattice network to unloaded TL networks, i.e. networks only made of interconnected TLs and supporting RH propagation. In the MTM field, these networks are used as artificial materials to interface with LHM lenses based on the TL approach [3, 4], in novel TL-based cloaking systems [277, 278], or in artificial lens antennas [279, 280], for instance. They are also used as the host medium for multidimensional TL-based MTMs (see for instance [116, 118, 281]).

Here we concentrate on 2D unloaded TL networks. Their conventional implementation using the shunt node or series node configurations (see for instance [250]) suffer from additional dispersion compared to the corresponding 1D TL, which results from the connection of the two orthogonal sets of TLs. Indeed, for propagation along one set of TLs in the network, the other set of orthogonal TLs appears as a periodical loading, which results in a pass-band/stop-band behaviour similar to the one obtained in EBG structures. Although the TL network is usually operated much below the first stop-band, where it can be considered as effectively homogeneous, its Bloch impedance already experiences non-negligible frequency variation, which is a drawback for wideband matching [277, 279]. To overcome these limitations, we propose here a 2D TL network based on the lattice network which exhibits dispersion-free propagation (constant impedance and linear phase constant) for axial propagation. The circuit model of such a network is shown in Figure 7.28(b), and its conventional shunt-node counterpart in Figure 7.28(a). The main idea is to connect the orthogonal sets of TLs according to a X-node configuration, and to add shorted stubs in series in the connection using the same TL sections as in the xy plane. For axial propagation (along x or y), the node appears as a lattice network with shorted stubs in the series branches and open stubs in the crossed diagonal branches. It can easily be shown from these considerations that the Bloch parameters of this network are (for axial propagation) $Z_{\mathrm{B}} = Z_{\mathrm{c}}$ and $\beta_{\mathrm{B}} = 2\beta_{\mathrm{h}}$, which confirms the dispersion-free behaviour. The corresponding expressions for the shunt node network of Figure 7.28(a) are more complex since the network exhibits dispersion. They can be found in [4, 277, 279], for instance. It can be mentioned that at low frequencies, where the shunt node network is effectively homogeneous and isotropic, its Bloch parameters are approximately given by $Z_{\mathrm{B}} = Z_{\mathrm{c}}/\sqrt{2}$ and $\beta_{\mathrm{B}} = \sqrt{2}\beta_{\mathrm{h}}$.

We show in Figure 7.29 two possible realizations of the X-node configuration of Figure 7.28(b). Preliminary numerical analyzes revealed superior performances for the novel X-node network compared to its conventional shunt node counterpart. The key challenge for this type of structures is the design and implementation of series shorted stubs exhibiting the required properties. Interestingly, simulation results also revealed that approximating the series shorted stubs by lumped inductances already results in significant improvements compared to the shunt node configuration, although a stop-band still exists at high frequencies. An important work remains to be done towards the experimental validation of the novel proposed X-node network in practical systems such as the ones mentioned at the beginning of this section, but these investigations are out of the scope of the present thesis.

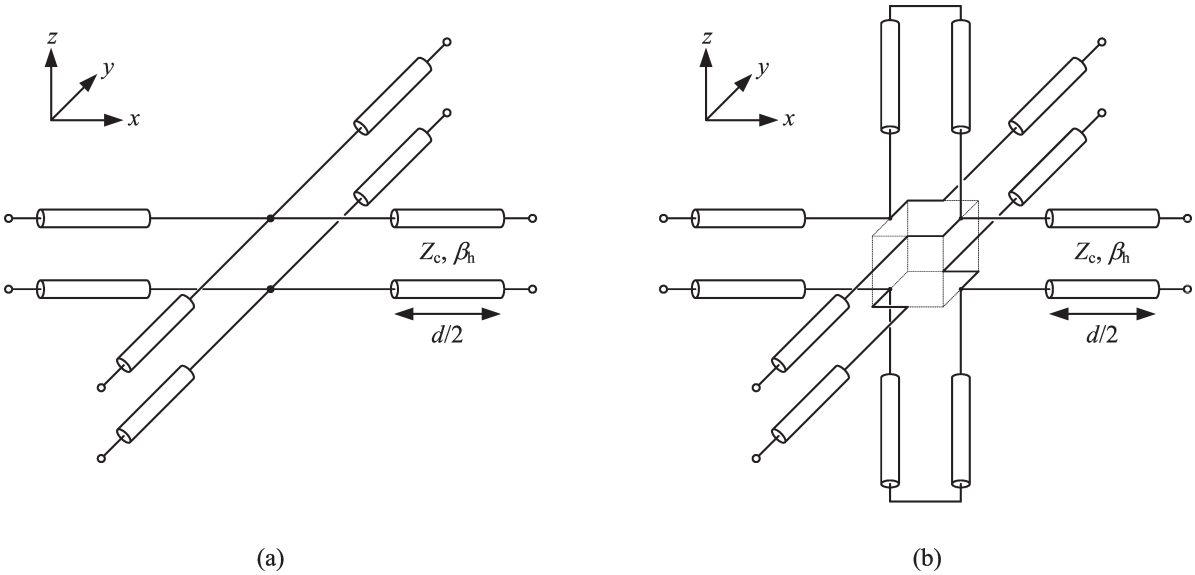

Figure 7.28: Unit cell of 2D TL networks. (a) Shunt node configuration. (b) X-node configuration. All the TL sections have the same length and properties.

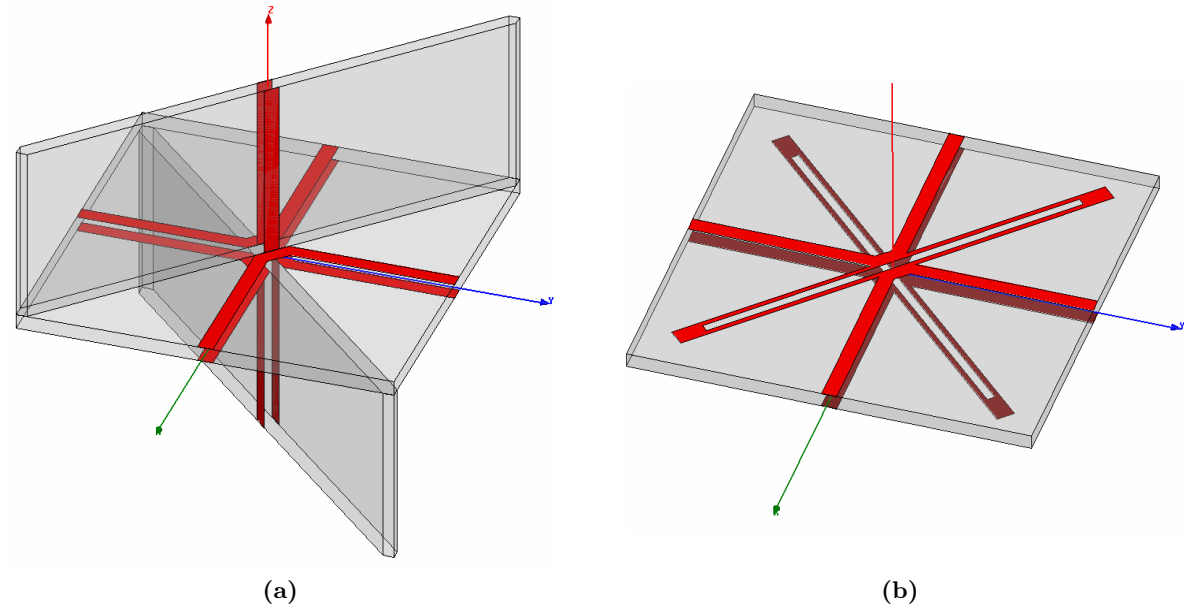

Figure 7.29: Possible realizations of the 2D X-node TL network shown in Figure 7.28(b). (a) With the series shorted stubs along the vertical direction (the shortcuts at the end of these stubs are not explicitly shown since the structure is terminated in $z = \pm d/2$ by horizontal PEC planes). (b) Fully planar implementation. The series shorted stubs are in the same plane as the TL network. Each stub is split into two stubs appearing in parallel in the circuit in order to keep a high level of symmetry.

7.5 Summary and perspectives

A novel topology of CRLH TL unit cell based on the lattice (X-crossed) network has been proposed and analyzed. Compared to its conventional counterpart, this structure has the advantage of exhibiting an all-pass behaviour, a frequency-independent Bloch impedance and a larger group velocity, thereby allowing for wider bandwidth operation. These performances have been confirmed by full-wave and experimental results on various practical implementations, in parallel stripline and CPW technology. The aforementioned performances may result in improved bandwidth for most of the well-known CRLH TL applications. In particular, we have shown using simple idealized models that the larger group velocity of the proposed structure may lead to a reduction of the beam squinting when used in leaky-wave antennas or in phase shifters for series-fed arrays. Other applications of the lattice topology to 2D unloaded TL networks have also been highlighted.

Further work should be dedicated to the experimental verification of the potential applications highlighted in Section 7.4. One of the key challenges concerns the control of the radiation characteristics of a leaky-wave antenna using the type X unit cell, such as its attenuation constant α_B or the polarization of its radiated field. Other interesting applications may also be found in the recently proposed UWB applications of the CRLH TL, which require large bandwidth for pulse manipulations [146, 156, 157].

8 Conclusions and perspectives

8.1 Summary of the main findings and discussion

This thesis deals with electromagnetic metamaterials (MTMs) from an engineering point of view. After a comprehensive survey of the state-of-the-art (both at modeling and technological levels), several techniques for the characterization of practical MTMs of various types have been developed or revisited in the light of microwave applications. Globally, the achievements of this thesis can be separated into four main original contributions:

i) Development of a procedure for retrieving dyadic medium parameters from scattering parameters (Chapter 3).
ii) Investigation of volumetric layered TL-based MTMs and assessment of potential antenna applications (Chapter 5).
iii) Development of an enhanced Bloch wave analysis for periodic structures based on multi-conductor transmission line modeling (Chapter 6).
iv) Development of a novel composite right/left-handed (CRLH) TL based on a lattice network unit cell (Chapter 7).

The main assessments associated with each part are summarized below and discussed in the general context of this thesis.

i) *Dyadic medium parameters retrieval procedure*

In the first part of the work, we developed, implemented, and tested an improved retrieval procedure which allows extracting dyadic medium parameters from scattering parameters obtained under various incidences, thereby extending current techniques which only deal with normal incidence (Chapter 3). This technique was applied to inclusion-based MTMs such as wire media and arrays of magnetic resonators, which are the building blocks of the first reported LHM implementations. Although the initial goal was to assess the isotropy of the selected structures, the main achievement obtained with this technique is the ability to evaluate to which extent a given MTM slab can be considered as an equivalent homogeneous medium obeying some specific constitutive relations. Globally, it was observed that the accuracy of such a model increases with the degree of homogeneity, or equivalently, when the electrical size of the unit cell decreases. The applicability, limitations, and usefulness of this class of retrieval procedures have been widely discussed in the conclusions of the corresponding chapter (Section 3.6).

The most interesting results were obtained with a highly isotropic magnetic resonator proposed in this thesis: the 3D crossed split-ring resonator (CSRR) (Section 3.5.3.c.). For this

structure, the developed technique revealed a resonant behaviour for the three components of the permeability tensor, with negative values above the resonant frequency. This example allowed highlighting the importance of coupling effects occurring between adjacent cells in this type of MTMs. Indeed, as a one-layer MTM sample was considered for the extraction, each cell had neighbors in the transverse directions but not in the longitudinal one, a difference that could be directly observed on the respective components of the permeability and permittivity tensors. This also results in a dependence of the extracted parameters with the sample shape and size, as discussed in Section 3.6.2.

ii) *Volumetric layered TL-based MTMs and antenna applications*

The second main contribution consists in the extensive analysis of a volumetric left-handed medium (LHM) based on the TL approach, obtained by layering several planar artificial TLs of the CRLH type (Chapter 5). The goal was to obtain a volumetric LHM that could be considered as a material filling in planar antenna systems. A prototype of such volumetric layered TL-based LHM was designed and built. Dispersion analyzes revealed that this volumetric structure supports LH propagation in a given direction over a quite large bandwidth, compared to other resonant LHM such as SRR-wire media.

This structure was subsequently tested as a substrate for a classical patch antenna in the light of improving its radiation performances. In such a configuration, the overall structure including the ground plane and the patch results in a complex multiconductor TL system which exhibits several propagating Floquet modes. In particular, mixed RH/LH mode behaviour was observed in the frequency range of interest, instead of a purely LH mode as desired. Nevertheless, according to its dispersion diagram this "meta-patch" antenna potentially offers interesting multi-frequency capabilities due to the appearance of closely spaced resonances in the mixed RH/LH band.

An extensive measurement campaign on various configurations of meta-patch antennas was carried out. It was observed that the realized LHM strongly affects the radiation properties of the patch antenna, thereby leading to complex phenomena which were not able to be fully explained by simple analytical and numerical models. Moreover, most of the predicted resonances could not be highlighted in that system, which was attributed to the inability of the chosen excitation to effectively couple power to the LH mode. In this context, an important contribution consisted in the assessment of the ability of such a volumetric TL-based structure to behave as material filling in this type of configurations. Globally, it appeared that the main problem comes from the excitation of the predicted LH Floquet modes from an external field, since these modes mainly exhibit the field distribution of the host TL used, which is in general incompatible with the external excitation fields. An interesting discussion with comparison to other related studies has been provided in the conclusion of the corresponding chapter (Section 5.7.2).

iii) *Enhanced Bloch wave analysis based on multiconductor transmission line modeling*

In the third main contribution, we developed an enhanced Bloch wave analysis for periodic structures requiring a multimodal representation of their unit cell. This contribution was

motivated by the observation under i) of a strong dependence of extracted parameters with the sample size. This new technique was successfully demonstrated on resonant-type MTMs which exhibit higher order coupling phenomena between adjacent cells, such as SRR-wire media, as well as to elaborated MTM structures consisting of periodically loaded multiconductor TLs (MTLs), such as the shielded mushroom structure or the volumetric TL LHM studied under ii). The main idea of this technique is to model any type of periodic structure with an equivalent MTL, a model which provides al the parameters needed to describe the phase response (dispersion) and the terminations (excitation and matching) of finite size periodic structures.

This technique represents an important contribution in the context of periodic structure modeling, since it consists in an extension and unification of several previously reported incomplete methods, which only dealt with monomode representations or only provided the dispersion relation. Moreover, it provides a general common framework for two rather different classes of periodic structures: periodic waveguides with higher order mode interaction and periodically loaded MTLs.

iv) *Novel composite right/left-handed (CRLH) TL based on a lattice network unit cell*

The last main contribution was the intoduction and development of a novel unit cell topology for the CRLH TL, which employs a lattice network in place of the more conventional ladder-type topology (Chapter 7). This new CRLH TL was shown to exhibit a more wideband behaviour than its conventional counterpart, both in terms of impedance and phase. More specifically, it exhibits an all-pass behaviour, a frequency independent Bloch impedance and an increased group velocity. These performances have been numerically and experimentally demonstrated on several practical implementations in parallel stripline or CPW technology. Possibilities of using this unit cell to reduce the beam squinting in leaky-wave antennas and in series-fed arrays have been highlighted. It is foreseen that this new CRLH TL can be potentially used to improve the performances of many well-known applications of the CRLH TL.

Miscellaneous contributions

Beside the four main contributions discussed above, this thesis report also comprises additional detailed information on the two following related topics. First, the state-of-the-art of Chapter 2 provides a comprehensive and classified survey on LHM fundamental theory, practical implementations, characterization techniques and microwave applications (i.e. not only limited to the topics considered in this work). Second, a detailed report on technical issues pertinent to the analysis, design and realization of CRLH TLs is provided in Chapter 4. Several small but interesting contributions have been brought to the topic, as listed in Section 1.2.3. This material was used at several instances in the subsequent chapters. It is noticeable that these two chapters have been written in a comprehensive way in order to give to this document a textbook value for possible future work performed at LEMA-EPFL on MTMs.

8.2 Salient points in metamaterials'research and Perspectives

In this thesis, several aspects of the wide MTM field have been addressed, which allowed identifying some salient points and key challenges in the topic.

Homogenization

One of the main challenge in the MTM field is homogenization. Indeed, several homogenization techniques and retrieval procedures have been reported (Section 2.3), but they often lead to different parameters for the same MTM structure, especially around resonances. This does not mean that interesting effects such as negative refraction cannot be observed from these MTMs, but rather than the definition of equivalent medium parameters might be inaccurate or become a source of problems and misunderstanding. As a matter of fact, most of the reported practical implementations of LHM are operated in an intermediate regime between the effective medium and photonic crystal regimes, in which refraction phenomena still dominate over diffraction phenomena, but where an unambiguous definition of material parameters is complicated by complex effects like spatial dispersion. To that respect, the main challenge to minimize these unwanted effects consists in the achievement of highly homogeneous MTMs, i.e. structures with unit cells much smaller than the wavelength. This is physically possible, but requires embedding higher capacitances and inductances in smaller volumes, which may be very challenging technologically.

In this work, we have mainly considered characterization techniques consisting of retrieval procedures, rather than homogenization techniques. Indeed, both the dyadic parameters extraction of Chapter 3 and the Bloch wave analysis of Section 4.2 — or its multimodal extension of Chapter 6 — are aimed at determining a set of equivalent parameters through a formal correspondence with a given problem. The physical meaning and the ability of medium parameters extracted from these techniques to represent the polarizabilities in the material are highly questionable (Section 3.6). However, the main outcome of these techniques is a set of dispersion/impedance parameters, which keep their full meaning and are often more relevant for practical microwave applications for which the requirements are expressed in terms of phase shift and matching.

"Free-space coupled" metamaterials

A second key challenge concerns the realization of wideband volumetric LHM that can be effectively coupled from external sources. Indeed, nowadays most of these "free-space coupled" MTMs are of the resonant type (arrays of resonant metallic and/or dielectric particles), and are thus rather narrow band by essence. On the other hand, the reported wideband MTMs are of the TL type, and thus essentially consist of planar 1D or 2D guiding and radiating structures. Some realizations of volumetric LHM based on the TL approach have also been reported, such as the structure of Chapter 5 and other examples, but they suffer from a poor excitation from free-space (see discussion in Section 5.7.2). This problematic is thus related to the question already formulated in the thesis introduction, whether TL-based MTMs can be considered as materials in the common sense of the word, with well defined medium parameters such as ε and μ, or if they only emulate the propagation of waves in real materials. To that respect, it is

believed that the link between inclusion-based MTMs and TL-based MTMs should be further clarified.

The general feeling of the author is that inclusion-based MTMs can be conceptually considered as materials, since the engineered particles in these MTMs play the role of the atoms and molecules in conventional materials, but at a different length scale. On the other hand, TL-based MTMs seem to be conceptually different from materials since they rely on host TLs, and thereby mimic the propagation of waves in a material from a dispersion and impedance point of view, but fail to represent polarization effects in materials.

Nevertheless, it is also noticeable that the coupling between free-space and volumetric TL-based LHM can be improved by using some transition layers or some types of matching circuits, as discussed in Section 6.3.6. In this context, the periodic structure modeling presented in Chapter 6 represent an efficient design tool towards this goal.

Metamaterial applications

Independently of the aforementioned problematic on homogenization and conceptual distinction between classes of MTMs, perspectives still exist for improving existing or developing novel microwave applications advantageously using MTMs. On the basis of the work accomplished in this thesis, some recommendations can be formulated, especially for the antenna field.

It appears that most of the well demonstrated antenna applications of MTMs use the TL approach (CRLH TLs), in which the MTM itself *is* the antenna, and not a scatterer (material filling) modifying the radiation of a primary antenna. Moreover, the performances of such antennas are usually not dependent from the ability of the chosen MTM to behave as a material filling, since this problematic is irrelevant in this case. As a result, whenever possible the system should be directly investigated in terms of dispersion and impedance, which are often the most relevant parameters for the behaviour of the antenna, instead of in terms of ambiguous equivalent medium parameters that fail to accurately describe complex problems such as a source near a MTM slab, for instance.

Finally, let us note that although the LH behaviour (negative refractive index) was initially the main concern in MTM applications, the most interesting applications have been obtained, to the author's point, by combining LH and RH effects to achieve phase compensation effects or multi-frequency capabilities, and by using the zero refractive index point (or $\beta = 0$ point) that can be achieved with such structures.

A Appendix: Bloch MTL parameters for symmetrical unit cells

A more compact form of the eigenvalue problem (6.16) can be obtained if the symmetry condition of the unit cell is taken into account in the developments. This formulation is reported here.

We first consider the sum and difference of the eigenvalue problem (6.16) with its inverse, that is

$$\left(\mathbf{T}_{\text{cell}} \pm \mathbf{T}_{\text{cell}}^{-1}\right)\mathbf{M} = \mathbf{M}\left(\mathbf{G} \pm \mathbf{G}^{-1}\right) \tag{A.1}$$

For a reciprocal and symmetrical unit cell, we have [254]

$$\mathbf{T}_{\text{cell}}^{-1} = \begin{bmatrix} \mathbf{A} & -\mathbf{B} \\ -\mathbf{C} & \mathbf{A}^{\text{T}} \end{bmatrix} \tag{A.2}$$

As a result,

$$\mathbf{T}_{\text{cell}} + \mathbf{T}_{\text{cell}}^{-1} = 2\begin{bmatrix} \mathbf{A} & \mathbf{0} \\ \mathbf{0} & \mathbf{A}^{\text{T}} \end{bmatrix} \quad \text{and} \quad \mathbf{T}_{\text{cell}} - \mathbf{T}_{\text{cell}}^{-1} = 2\begin{bmatrix} \mathbf{0} & \mathbf{B} \\ \mathbf{C} & \mathbf{0} \end{bmatrix} \tag{A.3}$$

Inserting (A.3) into (A.1) with the + sign and using the definitions of $\mathbf{M}$ and $\mathbf{G}$ in (6.16) yields the following eigenvalue problem [254]

$$\mathbf{A}\mathbf{T}_{\text{B}} = \mathbf{T}_{\text{B}}\cosh\left(\boldsymbol{\gamma}_{\text{B}} d\right) \tag{A.4}$$

As a result, the two Bloch parameter matrices $\mathbf{T}_{\text{B}}$ and $\boldsymbol{\gamma}_{\text{B}}$ can be obtained by solving the classical eigenvalue problem (A.4) involving only the sub-matrix $\mathbf{A}$ of the unit cell. Indeed, the eigenvalues of $\mathbf{A}$ are the hyperbolic cosines of $\boldsymbol{\gamma}_{\text{B}} d$, and the corresponding eigenvectors are the columns of $\mathbf{T}_{\text{B}}$. As expected from reciprocity, the Bloch propagation constants $\boldsymbol{\gamma}_{\text{B}} d$ only exist by pairs of opposite values (the cosh is an even function). The remaining Bloch parameter matrix $\mathbf{Z}_{\text{B}}$ is obtained by inserting (A.3) into (A.1) with the − sign, which yields

$$\mathbf{Z}_{\text{B}} = \mathbf{T}_{\text{B}}\left[\sinh\left(\boldsymbol{\gamma}_{\text{B}} d\right)\right]^{-1}\mathbf{T}_{\text{B}}^{-1}\mathbf{B} \tag{A.5}$$

or equivalently

$$\mathbf{Y}_{\text{B}} = \mathbf{C}\mathbf{T}_{\text{B}}\left[\sinh\left(\boldsymbol{\gamma}_{\text{B}} d\right)\right]^{-1}\mathbf{T}_{\text{B}}^{-1} \tag{A.6}$$

with $\mathbf{Y}_{\text{B}} = \mathbf{Z}_{\text{B}}^{-1}$ and $\sinh\left(\boldsymbol{\gamma}_{\text{B}}\right) = \pm\left[\cosh^2\left(\boldsymbol{\gamma}_{\text{B}} d\right) - 1\right]^{1/2}$. The ± sign in the expression of $\sinh\left(\boldsymbol{\gamma}_{\text{B}} d\right)$ is associated with the two possible opposite values of $\boldsymbol{\gamma}_{\text{B}}$. Practically, this means that we have to determine the sign of each $\boldsymbol{\gamma}_{\text{B}}$ such that it represents an incident wave, before calculating $\mathbf{Z}_{\text{B}}$ or $\mathbf{Y}_{\text{B}}$.

List of Acronyms

AMC artificial magnetic conductor

BC-SRR broadside-coupled split-ring resonator

BW backward wave

BWM backward wave medium

CPS coplanar stripline

CPW coplanar waveguide

CRLH composite right/left-handed

CRLH TL composite right/left-handed transmission line

CSRR crossed split-ring resonator

DNG double negative

DNM double negative medium

DPM double positive medium

DPS double positive

EBG electromagnetic bandgap

EC-SRR edge-coupled split-ring resonator

EM electromagnetic

ENG epsilon negative

FEM finite element method

FF fixed frequency

FSS frequency selective surface

FW forward wave

FWCPW finite width coplanar waveguide

FWM forward wave medium

GP ground plane

HIS high impedance surface

LH left-handed

LHM left-handed medium

LMS least mean square

LW leaky-wave

LWA leaky-wave antenna

MEMS MicroElectroMechanical Systems

MIM metal-insulator-metal

MNG mu negative

MoM method of moments

MS microstrip

MTL multiconductor transmission line

MTM metamaterial

NIM negative index medium

NPV negative phase velocity

NRI negative refractive index

PBC periodic boundary condition

PBG photonic bandgap

PCB printed circuit board

PEC perfect electric conductor

PIM positive index medium

PMC perfect magnetic conductor

PPV positive phase velocity

PPWG parallel plate waveguide

PRI positive refractive index

RH right-handed

RHM right-handed medium

SMT surface-mount technology

SNG single negative

SRR split-ring resonator

TE transverse electric

TEM transverse electromagnetic

TL transmission line

TM transverse magnetic

TRL thru-reflect-line

UWB ultra wideband

WG waveguide

Bibliography

[1] A. Sihvola, "Electromagnetic emergence in metamaterials," in *NATO Advanced Workshop on Bianisotropics 2002 - 9th International Conference on Electromagnetics of Complex Media*, ser. Series II: Mathematics, Physics and Chemistry - Vol 89, S. Zouhdi, A. Sihvola, and M. Arsalane, Eds. Marrakesh, Morocco: Kluwer Academic Publishers, 2002, pp. 3–17.

[2] M. Lapine and S. A. Tretyakov, "Contemporary notes on metamaterials," *IET Microw. Antennas Propag.*, vol. 1, no. 1, pp. 3–11, February 2007.

[3] C. Caloz and T. Itoh, *Electromagnetic Metamaterials: Transmission Line Theory and Microwave Applications*. Wiley-Interscience and IEEE press, 2006.

[4] G. V. Eleftheriades and K. G. Balmain, *Negative-Refraction Metamaterials: Fundamental Principles and Applications*. Wiley-Interscience and IEEE press, 2005.

[5] N. Engheta and R. W. Ziolkowski, *Metamaterials: Physics and Engineering Explorations*. Wiley-Interscience and IEEE press, 2006.

[6] V. G. Veselago, "The electrodynamics of substances with simultaneously negative values of epsilon and mu." *Soviet Physics Uspekhi*, vol. 10, no. 4, pp. 509–514, 1968.

[7] J. B. Pendry, A. J. Holden, W. J. Stewart, and I. Youngs, "Extremely low frequency plasmons in metallic mesostructures," *Physical Review Letters*, vol. 76, no. 25, pp. 4773–4776, 1996.

[8] J. B. Pendry, A. J. Holden, D. J. Robbins, and W. J. Stewart, "Low frequency plasmons in thin-wire structures," *J. Phys.: Condens. Matter*, vol. 10, pp. 4785–4809, 1998.

[9] ——, "Magnetism from conductors and enhanced nonlinear phenomena," *IEEE Transactions on Microwave Theory and Techniques*, vol. 47, no. 11, pp. 2075–2084, 1999.

[10] D. R. Smith, W. J. Padilla, D. C. Vier, S. C. Nemat-Nasser, and S. Schultz, "Composite medium with simultaneously negative permeability and permittivity," *Physical Review Letters*, vol. 84, no. 18, pp. 4184–4187, 2000.

[11] R. A. Shelby, D. R. Smith, S. C. Nemat-Nasser, and S. Schultz, "Microwave transmission through a two-dimensional, isotropic, left-handed metamaterial," *Applied Physics Letters*, vol. 78, no. 4, pp. 489–491, 2001.

[12] J. B. Pendry, "Negative refraction makes a perfect lens," *Physical Review Letters*, vol. 85, no. 18, pp. 3966–3969, 2000.

[13] R. A. Shelby, D. R. Smith, and S. Schultz, "Experimental verification of a negative index of refraction," *Science*, vol. 292, pp. 77–79, 2001.

[14] P. M. Valanju, R. M. Walser, and A. P. Valanju, "Wave refraction in negative-index media: Always positive and very inhomogeneous," *Physical Review Letters*, vol. 88, no. 18, p. 187401, 2002.

[15] J. B. Pendry and D. R. Smith, "Comment on "wave refraction in negative-index media: Always positive and very inhomogeneous"," *Physical Review Letters*, vol. 90, no. 2, p. 029703, 2003.

[16] P. M. Valanju, R. M. Walser, and A. P. Valanju, "Valanju, walser and valanju reply," *Physical Review Letters*, vol. 90, no. 2, p. 029704, 2003.

[17] D. R. Smith, D. Schurig, and J. B. Pendry, "Negative refraction of modulated electromagnetic waves," *Applied Physics Letters*, vol. 81, no. 15, pp. 2713–2715, 2002.

[18] J. Pacheco, T. M. Grzegorczyk, B.-I. Wu, Y. Zhang, and J. A. Kong, "Power propagation in homogeneous isotropic frequency-dispersive left-handed media," *Physical Review Letters*, vol. 89, no. 25, p. 257401, 2002.

[19] N. Garcia and M. Nieto-Vesperinas, "Left-handed materials do not make a perfect lens," *Physical Review Letters*, vol. 88, no. 20, p. 207403, 2002.

[20] ——, "Erratum : Left-handed materials do not make a perfect lens," *Physical Review Letters*, vol. 90, no. 22, p. 229903, 2003.

[21] J. B. Pendry, "Comment on "left-handed materials do not make a perfect lens"," *Physical Review Letters*, vol. 91, no. 9, p. 099701, 2003.

[22] N. Garcia and M. Nieto-Vesperinas, "Nieto-vesperinas and garcia reply," *Physical Review Letters*, vol. 91, no. 9, p. 099702, 2003.

[23] ——, "Is there an experimental verification of a negative index of refraction yet?" *Optics Letters*, vol. 27, no. 11, pp. 885–887, 2002.

[24] C. Caloz and T. Itoh, "Application of the transmission line theory of left-handed (LH) materials to the realization of a microstrip "LH line"," in *IEEE Antennas and Propagation Int. Symp. (AP-S) and USNC/URSI Meeting*, vol. 2. San Antonio, TX: IEEE, June 2002, pp. 412–415.

[25] A. K. Iyer and G. V. Eleftheriades, "Negative refractive index metamaterials supporting 2-D waves," in *IEEE MTT-S Int. Microwave Symp. Dig.*, Seattle, WA, June 2002, pp. 1067–1070.

[26] A. A. Oliner, "A periodic-structure negative-refractive-index medium without resonant elements," in *IEEE Antennas and Propagation Int. Symp. (AP-S) and USNC/URSI Meeting*, San Antonio, TX, June 2002, p. 41.

[27] G. V. Eleftheriades, A. K. Iyer, and P. C. Kremer, "Planar negative refractive index media using periodically L-C loaded transmission lines," *IEEE Transactions on Microwave Theory and Techniques*, vol. 50, no. 12, pp. 2702–2712, 2002.

[28] C. G. Parazzoli, R. B. Greegor, K. Li, B. E. C. Koltenbah, and M. Tanielian, "Experimental verification and simulation of negative index of refraction using snell's law," *Physical Review Letters*, vol. 90, no. 10, p. 107401, 2003.

[29] A. A. Houck, J. B. Brock, and I. L. Chuang, "Experimental observations of a left-handed material that obeys snell's law," *Physical Review Letters*, vol. 90, no. 13, p. 137401, 2003.

[30] A. Grbic and G. V. Eleftheriades, "Growing evanescent waves in negative-refractive-index transmission-line media," *Applied Physics Letters*, vol. 82, no. 12, pp. 1815–1817, 2003.

[31] ——, "Overcoming the diffraction limit with a planar left-handed transmission-line lens," *Physical Review Letters*, vol. 92, no. 11, p. 117403, 2004.

[32] J. B. Pendry, D. Schurig, and D. R. Smith, "Controlling electromagnetic fields," *Science*, vol. 312, pp. 1780–1782, June 2006.

[33] D. Schurig, J. J. Mock, B. J. Justice, S. A. Cummer, J. B. Pendry, A. F. Starr, and D. R. Smith, "Metamaterial electromagnetic cloak at microwave frequencies," *Science*, vol. 314, pp. 977–980, November 2006.

[34] B. E. Spielman, S. Amari, C. Caloz, G. V. Eleftheriades, T. Itoh, D. R. Jackson, R. Levy, J. D. Rhodes, and R. V. Snyder, "Metamaterials face-off. metamaterials: A rich opportunity for discovery or an overhyped gravy train [speaker's corner]," *IEEE Microwave Magazine*, vol. 10, no. 3, pp. 8–42, May 2009.

[35] S. A. Tretyakov, "Research on negative refraction and backward-wave media: A historical perspective," in *EPFL Latsis Symposium 2005*, Lausanne, Switzerland, February 2005, pp. 30–35.

[36] R. Marqués, F. Martin, and M. Sorolla, *Metamaterials with Negative Parameters: Theory, Design, and Microwave Applications*, ser. Wiley Series in Microwave and Optical Engineering, T. A. U. Kai Chang, Ed. Hoboken, NJ: Wiley-Interscience, 2008.

[37] W. S. Weiglhofer, "Constitutive characterization of simple and complex mediums," in *Introduction to Complex Mediums for Optics and Electromagnetics*, W. S. Weiglhofer and A. Lakhtakia, Eds. Bellingham: SPIE - The International Society for Optical Engineering, 2003, pp. 27–61.

[38] C. M. Krowne, "Electromagnetic theorems for complex anisotropic media," *IEEE Transactions on Antennas and Propagation*, vol. AP-32, no. 11, pp. 1224–1230, 1984.

[39] A. Lakhtakia and W. S. Weiglhofer, "Constraint on linear, homogeneous, constitutive relations," *Physical Review E*, vol. 50, no. 6, pp. 5017–5019, 1994.

[40] R. E. Collin, *Field Theory of Guided Waves*, 2nd ed. New York: IEEE Press, 1991.

[41] C. A. Balanis, *Advanced Engineering Electromagnetics*. John Wiley & Sons, 1989.

[42] J. D. Jackson, *Classical Electrodynamics*, 3rd ed. New-York: John Wiley & Sons, 1999.

[43] L. Landau and E. Lifchitz, *Electrodynamique des milieux continus*, ser. Physique theorique. Moscou: Editions MIR, 1969.

[44] S. A. Tretyakov, "Electromganetic field energy density in artificial microwave materials with strong dispersion and loss," *physics Letters A*, vol. 343, no. 1-3, pp. 231–237, 2005.

[45] A. Tonning, "Energy density in continuous electromagnetic media," *IRE Transactions on Antennas and Propagation*, vol. 8, no. 4, pp. 428–434, 1960.

[46] T. J. Cui and J. A. Kong, "Time-domain electromagnetic energy in a frequency-dispersive left-handed medium," *Physical Review B*, vol. 70, p. 205103, 2004.

[47] A. D. Boardman and K. Marinov, "Electromagnetic energy in a dispersive metamaterial," *physical Review B*, vol. 73, p. 165110, 2006.

[48] R. D. Graglia, P. L. E. Uslenghi, and R. E. Zich, "Dispersion relation for bianisotropic materials and its symmetry properties," *IEEE Transactions on Antennas and Propagation*, vol. 39, no. 1, pp. 83–90, 1991.

[49] M. Born and E. Wolf, *Principles of Optics*. UK: Pergamon Press, 1980.

[50] R. W. Ziolkowski and E. Heyman, "Wave propagation in media having negative permittivity and permeability," *Physical Review E*, vol. 64, p. 056625, 2001.

[51] D. R. Smith and N. Kroll, "Negative refractive index in left-handed materials," *Physical Review Letters*, vol. 85, no. 14, pp. 2933–2936, 2000.

[52] I. V. Lindell, S. A. Tretyakov, K. I. Nikoskinen, and S. Ilvonen, "BW media - media with negative parameters, capable of supporting backward waves," *Microwave and Optical Technology Letters*, vol. 31, no. 2, pp. 129–133, 2001.

[53] R. A. Depine and A. Lakhtakia, "A new condition to identify isotropic dielectric-magnetic materials displaying negative phase velocity," *Microwave and Optical Technology Letters*, vol. 41, no. 4, pp. 315–316, 2004.

[54] M. W. McCall, A. Lakhtakia, and W. S. Weiglhofer, "The negative index of refraction demystified," *European Journal of Physics*, vol. 23, pp. 353–359, 2002.

[55] P. Kinsler and M. W. McCall, "Criteria for negative refraction in active and passive media," *Microwave and Optical Technology Letters*, vol. 50, no. 7, pp. 1804–1807, July 2008.

[56] A. Lakhtakia, M. W. McCall, W. S. Weiglhofer, J. Gerardin, and J. Wang, "On mediums with negative phase velocity: a brief overview," *arXiv:physics/0205027*, 2002.

[57] S. Ramo, J. R. Whinnery, and T. Van Duzer, *Fields and Waves in Communication Electronics*, 2nd ed. John Wiley & Sons, 1984.

[58] L. B. Felsen and N. Marcuwitz, *Radiation and Scattering of Waves*, ser. The IEEE Series on Electromagnetic Wave Theory. Hoboken: Wiley-Interscience and IEEE Press, 2003.

[59] D. R. Smith and D. Schurig, "Electromganetic wave propagation in media with indefinite permittivity and permeability tensors," *physical Review Letters*, vol. 90, no. 7, p. 077405, February 2003.

[60] T. M. Grzegorczyk, M. Nikku, X. Chen, B.-I. Wu, and J. A. Kong, "Refraction laws for anisotropic media and their application to left-handed metamaterials," *IEEE Transactions on Microwave Theory and Techniques*, vol. 53, no. 4, pp. 1443–1450, April 2005.

[61] J. B. Pendry, "A chiral route to negative refraction," *Science*, vol. 306, pp. 1353–1355, 2004.

[62] M. Notomi, "Theory of light propagation in strongly modulated photonic crystals: Refractionlike behavior in the vicinity of the photonic band gap," *Physical Review B*, vol. 62, no. 16, pp. 10 696–10 705, October 2000.

[63] C. Luo, S. G. Johnson, J. D. Joannopoulos, and J. B. Pendry, "All-angle negative refraction without negative refractive index," *Physical Review B*, vol. 65, p. 201104, May 2002.

[64] W. T. Lu, J. B. Sokoloff, and S. Sridhar, "Refraction of electromagnetic energy for wave packets incident on a negative-index medium is always negative," *Physical Review E*, vol. 69, p. 026604, 2004.

[65] R. W. Ziolkowski, "Pulsed and CW gaussian beam interactions with double negative metamaterial slabs," *Optics Express*, vol. 11, no. 7, pp. 662–681, April 2003.

[66] J. Lu, T. M. Grzegorczyk, Y. Zhang, J. Pacheco Jr, B.-I. Wu, and J. A. Kong, "Cherenkov radiation in materials with negative permittivity and permeability," *Optics Express*, vol. 11, no. 7, pp. 723–734, 2003.

[67] S. A. Ramakrishna, "Physics of negative refractive index materials," *Reports on Progress in Physics*, vol. 68, pp. 449–521, 2005.

[68] D. R. Smith, D. Schurig, M. Rosenbluth, S. Schultz, S. A. Ramakrishna, and J. B. Pendry, "Limitations on subdiffraction imaging with a negative refractive index slab," *Applied Physics Letters*, vol. 82, no. 10, pp. 1506–1508, 2003.

[69] M. Mojahedi, K. J. Malloy, G. V. Eleftheriades, J. Woodley, and R. Y. Chiao, "Abnormal wave propagation in passive media," *IEEE Journal of Selected Topics in Quantum Electronics*, vol. 9, no. 1, pp. 30–39, 2003.

[70] A. Alu and N. Engheta, "Guided modes in a waveguide filled with a pair of single-negative (SNG), double-negative (DNG), and/or double-positive (DPS) layers," *IEEE Transactions on Microwave Theory and Techniques*, vol. 52, no. 1, pp. 199–210, 2004.

[71] ——, "Pairing an epsilon-negative slab with a mu-negative slab: Resonance, tunneling and transparency," *IEEE Transactions on Antennas and Propagation*, vol. 51, no. 10, pp. 2558–2571, 2003.

[72] R. W. Ziolkowski, "Propagation in and scattering from a matched metamaterial having a zero index of refraction," *Physical Review E*, vol. 70, p. 046608, 2004.

[73] T. J. Cui and J. A. Kong, "Causality in the propagation of transient electromagnetic waves in a left-handed medium," *Physical Review B*, vol. 70, p. 165113, 2004.

[74] R. W. Ziolkowski and A. D. Kipple, "Causality and double-negative metamaterials," *Physical Review E*, vol. 68, p. 026615, August 2003.

[75] S. I. Maslovski, S. A. Tretyakov, and P. A. Belov, "Wire media with negative effective permittivity: a quasi-static model," *Microwave and Optical Technology Letters*, vol. 35, no. 1, pp. 47–51, 2002.

[76] S. A. Tretyakov, S. I. Maslovski, and P. A. Belov, "An analytical model of metamaterials based on loaded wire dipoles," *IEEE Transactions on Antennas and Propagation*, vol. 41, no. 10, pp. 2652–2658, 2003.

[77] P. A. Belov, R. Marqués, S. I. Maslovski, I. S. Nefedov, M. Silveirinha, C. R. Simovski, and S. A. Tretyakov, "Strong spatial dispersion in wire media in the very large wavelength limit," *Physical Review B*, vol. 67, p. 113103, 2003.

[78] R. Marqués, J. Martel, F. Mesa, and F. Medina, "Left-handed-media simulation and transmission of EM waves in subwavelength split-ring-resonator-loaded metallic waveguides," *Physical Review Letters*, vol. 89, no. 18, p. 183901, 2002.

[79] P. Gay-Balmaz and O. J. F. Martin, "Efficient isotropic magnetic resonators," *Applied Physics Letters*, vol. 81, no. 5, pp. 939–941, 2002.

[80] ——, "Electromagnetic resonances in individual and coupled split-ring resonators," *Journal of Applied Physics*, vol. 92, no. 5, pp. 2929–2936, 2002.

[81] R. Marqués, F. Medina, and R. Rafii-El-Idrissi, "Role of bianisotropy in negative permeability and left-handed metamaterials," *Physical Review B*, vol. 65, p. 144440, 2001.

[82] N. Katsarakis, T. Koschny, M. Kafesaki, E. N. Economou, and C. M. Soukoulis, "Electric coupling to the magnetic resonance of split ring resonators," *Applied Physics Letters*, vol. 84, no. 15, pp. 2943–2945, 2004.

[83] J. D. Baena, R. Marqués, F. Medina, and J. Martel, "Artificial magnetic metamaterial design by using spiral resonators," *Physical Review B*, vol. 69, p. 014402, 2004.

[84] R. Marqués, F. Mesa, J. Martel, and F. Medina, "Comparative analysis of edge- and broadside-coupled split ring resonators for metamaterial design - theory and experiments," *IEEE Transactions on Antennas and Propagation*, vol. 51, no. 10, pp. 2572–2581, 2003.

[85] T. Koschny, M. Kafesaki, E. N. Economou, and C. M. Soukoulis, "Effective medium theory of left-handed materials," *Physical Review Letters*, vol. 93, no. 10, p. 107402, 2004.

[86] K. Aydin, K. Guven, M. Kafesaki, L. Zhang, C. M. Soukoulis, and E. Ozbay, "Experimental observation of true left-handed transmission peaks in metamaterials," *Optics Letters*, vol. 29, no. 22, pp. 2623–2625, 2004.

[87] C. R. Simovski, P. A. Belov, and S. He, "Backward wave region and negative material parameters of a structure formed by lattices of wires and split-ring resonators," *IEEE Transactions on Antennas and Propagation*, vol. 51, no. 10, pp. 2582–2591, 2003.

[88] T. Koschny, L. Zhang, and C. M. Soukoulis, "Isotropic three-dimensional left-handed metamaterials," *Physical Review B*, vol. 71, p. 121103, 2005.

[89] C. R. Simovski and S. He, "Frequency range and explicit expressions for negative permittivity and permeability for an isotropic medium formed by a lattice of perfectly conducting omega particles," *Physics Letters A*, vol. 311, pp. 254–263, 2003.

[90] J. Huangfu, L. Ran, H. Chen, X. Zhang, K. Chen, T. M. Grzegorczyk, and J. A. Kong, "Experimental confirmation of negative refractive index of a metamaterial composed of omega-like metallic patterns," *Applied Physics Letters*, vol. 84, no. 9, pp. 1537–1539, 2004.

[91] L. Ran, J. Huangfu, H. Chen, Y. Li, X. Zhang, K. Chen, and J. A. Kong, "Microwave solid-state left-handed material with a broad bandwidth and an ultralow loss," *Physical Review B*, vol. 70, p. 073102, 2004.

[92] H. Chen, L. Ran, J. Huangfu, X. Zhang, K. Chen, T. M. Grzegorczyk, and J. A. Kong, "Left-handed materials composed of only S-shaped resonators," *Physical Review E*, vol. 70, p. 057605, 2004.

[93] H. S. Chen, L. X. Ran, J. T. Huangfu, X. M. Zhang, K. S. Chen, T. M. Grzegorczyk, and J. A. Kong, "Magnetic properties of S-shaped split-ring resonators," *progress In Electromagnetics Research, PIER*, vol. 51, pp. 231–247, 2005.

[94] J. Zhou, L. Zhang, G. Tuttle, T. Koschny, and C. M. Soukoulis, "Negative index materials using simple short wire pairs," *Physical Review B*, vol. 73, p. 041101, January 2006.

[95] M. Kafesaki, I. Tsiapa, N. Katsarakis, T. Koschny, C. M. Soukoulis, and E. N. Economou, "Left-handed metamaterials: The fishnet structure and its variations," *Physical Review B*, vol. 75, p. 235114, June 2007.

[96] O. G. Vendik and M. S. Gashinova, "Artificial double negative (DNG) media composed by two different dielectric sphere lattices embedded in a dielectric matrix," in *European Microwave Conference (EuMC)*, Amsterdam, 2004, pp. 1209–1212.

[97] C. L. Holloway, E. F. Kuester, J. Baker-Jarvis, and P. Kabos, "A double negative (DNG) composite medium composed of magnetodielectric spherical particles embedded in a matrix," *IEEE Transactions on Antennas and Propagation*, vol. 51, no. 10, pp. 2596–2603, October 2003.

[98] A. Rennings, C. Caloz, and I. Wolff, "A novel clustered dielectric cubes metamaterial (CDC-MTM)," in *IEEE Antennas and Propagation Int. Symp. (AP-S) and USNC/URSI Meeting*, Albuquerque, NM, July 2006, pp. 483–486.

[99] R. Marqués, J. Martel, F. Mesa, and F. Medina, "A new 2D isotropic left-handed metamaterial design: theory and experiment," *Microwave and Optical Technology Letters*, vol. 35, no. 5, pp. 405–408, 2002.

[100] S. Hrabar, J. Bartolic, and Z. Sipus, "Waveguide miniaturization using uniaxial negative permeability metamaterial," *IEEE Transactions on Antennas and Propagation*, vol. 53, no. 1, pp. 110–119, January 2005.

[101] J. Esteban, C. Camacho-Penalosa, J. E. Page, T. M. Martin-Guerrero, and E. Marques-Segura, "Simulation of negative permittivity and negative permeability by means of evanescent waveguide modes - theory and experiment," *IEEE Transactions on Microwave Theory and Techniques*, vol. 53, no. 4, pp. 1506–1514, April 2005.

[102] S. Hrabar and G. Jankovic, "Experimental investigation of waveguide filled with uniaxial thin-wire-based ENG metamaterial," in *IEEE Antennas and Propagation Int. Symp. (AP-S) and USNC/URSI Meeting*, Albuquerque, NM, July 2006, pp. 475–478.

[103] T. Ueda, A. Lai, and T. Itoh, "Demonstration of negative refraction in a cutoff parallel-plate waveguide loaded with 2-D square lattice of dielectric resonators," *IEEE Transactions on Microwave Theory and Techniques*, vol. 55, no. 6, pp. 1280–1287, June 2007.

[104] A. Lai, C. Caloz, and T. Itoh, "Composite right/left-handed transmission line metamaterials," *IEEE Microwave Magazine*, pp. 34–50, September 2004.

[105] G. V. Eleftheriades, O. Siddiqui, and A. K. Iyer, "Transmission line models for negative refractive index media and associated implementations without excess resonators," *IEEE Microwave and Wireless Components Letters*, vol. 13, no. 2, pp. 51–53, 2003.

[106] A. Sanada, C. Caloz, and T. Itoh, "Characteristics of the composite right/left-handed transmission lines," *IEEE Microwave and Wireless Components Letters*, vol. 14, no. 2, pp. 68–70, 2004.

[107] C. Caloz and T. Itoh, "Transmission line approach of left-handed (LH) materials and microstrip implementation of an artificial LH transmission line," *IEEE Transactions on Antennas and Propagation*, vol. 52, no. 5, pp. 1159–1166, 2004.

[108] D. Sievenpiper, L. Zhang, R. F. Jimenez Broas, N. G. Alexopolous, and E. Yablonovitch, "High-impedance electromagnetic surfaces with a forbidden frequency band," *IEEE Transactions on Microwave Theory and Techniques*, vol. 47, no. 11, pp. 2059–2074, November 1999.

[109] A. Sanada, C. Caloz, and T. Itoh, "Planar distributed structures with negative refractive index," *IEEE Transactions on Microwave Theory and Techniques*, vol. 52, no. 4, pp. 1252–1263, 2004.

[110] M. A. Antoniades and G. V. Eleftheriades, "Compact linear lead/lag metamaterial phase shifters for broadband applications," *IEEE Antennas and Wireless Propagation Letters*, vol. 2, pp. 103–106, 2003.

[111] A. Grbic and G. V. Eleftheriades, "An isotropic three-dimensional negative-refractive-index transmission-line metamaterial," *Journal of Applied Physics*, vol. 98, p. 043106, August 2005.

[112] W. J. R. Hoefer, P. P. M. So, D. Thompson, and M. M. Tentzeris, "Topology and design of wide-band 3D metamaterials made of periodically loaded transmission line arrays," in *IEEE MTT-S Int. Microwave Symp. Dig.*, Long Beach , CA, June 2005, pp. 313–316.

[113] P. Alitalo, S. Maslovski, and S. A. Tretyakov, "Three-dimensional isotropic perfect lens based on LC-loaded transmission lines," *Journal of Applied Physics*, vol. 99, p. 064912, March 2006.

[114] M. Zedler and P. Russer, "Investigation on the dispersion relation of a 3D LC-based metamaterial with an omnidirectional left-handed frequency band," in *IEEE MTT-S Int. Microwave Symp. Dig.*, San Francisco , CA, June 2006, pp. 1477–1479.

[115] M. Zedler, C. Caloz, and P. Russer, "A 3-D isotropic left-handed metamaterial based on the rotated transmission-line matrix (TLM) scheme," *IEEE Transactions on Microwave Theory and Techniques*, vol. 55, no. 12, pp. 2930–2941, December 2007.

[116] P. Alitalo, S. Maslovski, and S. A. Tretyakov, "Experimental verification of the key properties of a three-dimensional isotropic transmission-line superlens," *Journal of Applied Physics*, vol. 99, p. 124910, June 2006.

[117] A. K. Iyer and G. V. Eleftheriades, "Volumetric layered transmission-line metamaterial exhibiting a negative refractive index," *Journal of the Optical Society of America B*, vol. 23, no. 3, pp. 553–570, 2006.

[118] P. Alitalo, O. Luukkonen, and S. A. Tretyakov, "A three-dimensional backward-wave network matched with free space," *Physics Letters A*, vol. 372, pp. 2720–2723, 2008.

[119] F. Martin, J. Bonache, F. Falcone, M. Sorolla, and R. Marqués, "Split ring resonator-based left-handed coplanar waveguide," *Applied Physics Letters*, vol. 83, no. 22, pp. 4652–4654, 2003.

[120] J. D. Baena, J. Bonache, F. Martin, R. Marqués Sillero, F. Falcone, T. Lopetegi, M. A. G. Laso, J. Garcia-Garcia, I. Gil, M. F. Portillo, and M. Sorolla, "Equivalent-circuit models for split-ring resonators and complementary split-ring resonators coupled to planar transmission lines," *IEEE Transactions on Microwave Theory and Techniques*, vol. 53, no. 4, pp. 1451–1461, April 2005.

[121] D. A. Watkins, *Topics in Electromagnetic Theory.* John Wiley & Sons, 1958.

[122] R. E. Collin, *Foundations for Microwave Engineering*, ser. McGraw-Hill Series in Electrical Engineering. McGraw-Hill, Inc., 1992.

[123] D. M. Pozar, *Microwave Engineering.* Addison-Wesley Publishing Company, Inc., 1990.

[124] J. Perruisseau-Carrier, "Microwave periodic structures based on microelectromechanical systems (MEMS) and micromachining techniques," Ph.D. dissertation, Ecole Polytechnique Fédérale de Lausanne (EPFL), Lausanne, November 2007.

[125] J. Perruisseau-Carrier and A. K. Skrivervik, "Bloch wave approach to the design of optimally matched non-effective medium composite right/left handed transmission lines," *IET Microw. Antennas Propag.*, vol. 1, no. 1, pp. 50–55, 2007.

[126] ——, "Composite right/left-handed transmission line metamaterial phase shifters (MPS) in MMIC technology," *IEEE Transactions on Microwave Theory and Techniques*, vol. 54, no. 4, pp. 1582–1589, 2006.

[127] A. Grbic and G. V. Eleftheriades, "Periodic analysis of a 2-D negative refractive index transmission line structure," *IEEE Transactions on Antennas and Propagation*, vol. 51, no. 10, pp. 2604–2611, 2003.

[128] D. R. Smith, D. C. Vier, N. Kroll, and S. Schultz, "Direct calculation of permeability and permittivity for a left-handed metamaterial," *Applied Physics Letters*, vol. 77, no. 14, pp. 2246–2248, October 2000.

[129] D. R. Smith and J. B. Pendry, "Homogenization of metamaterials by field averaging (invited paper)," *Journal of the Optical Society of America B*, vol. 23, no. 3, pp. 391–403, 2006.

[130] A. Sihvola, *Electromagnetic mixing formulas and applications*, ser. IEE Electromagnetic Waves Series. London: The Institution of Electrical Engineers, 1999, vol. 47.

[131] J.-M. Lerat, N. Malléjac, and O. Acher, "Determination of the effective parameters of a metamaterial by field summation method," *Journal of Applied Physics*, vol. 100, p. 084908, 2006.

[132] O. Acher, J.-M. Lerat, and N. Malléjac, "Evaluation and illustration of the properties of metamaterials using field summation," *Optics Express*, vol. 15, no. 3, pp. 1096–1106, February 2007.

[133] C. Croënne, J.-M. Lerat, N. Malléjac, O. Acher, and D. Lippens, "Retrieval technique by field summation: application to double negative media," in *Metamaterials' 2007: First International Congress on Advanced Electromagnetic Materials in Microwave and Optics*, Rome, Italy, 22-24 October 2007, pp. 706–709.

[134] D. R. Smith, S. Schultz, P. Markos, and C. M. Soukoulis, "Determination of effective permittivity and permeability of metamaterials from reflection and transmission coefficients," *Physical Review B*, vol. 65, p. 195104, 2002.

[135] P. Markos and C. M. Soukoulis, "Transmission properties and effective electromagnetic parameters of double negative metamaterials," *Optics Express*, vol. 11, no. 7, pp. 649–661, 2003.

[136] R. W. Ziolkowski, "Design, fabrication, and testing of double negative metamaterials," *IEEE Transactions on Antennas and Propagation*, vol. 51, no. 7, pp. 1516–1529, 2003.

[137] X. Chen, T. M. Grzegorczyk, B.-I. Wu, J. Pacheco Jr, and J. A. Kong, "Robust method to retrieve the constitutive effective parameters of metamaterials," *Physical Review E*, vol. 70, p. 016608, 2004.

[138] T. Koschny, P. Markos, D. R. Smith, and C. M. Soukoulis, "Resonant and antiresonant frequency dependence of the effective parameters of metamaterials," *Physical Review E*, vol. 68, p. 065602, 2003.

[139] X. Chen, B.-I. Wu, J. A. Kong, and T. M. Grzegorczyk, "Retrieval of the effective constitutive parameters of bianisotropic metamaterials," *Physical Review E*, vol. 71, p. 046610, 2005.

[140] T. Koschny, P. Markos, E. N. Economou, D. R. Smith, D. C. Vier, and C. M. Soukoulis, "Impact of inherent periodic structure on effective medium description of left-handed and related metamaterials," *Physical Review B*, vol. 71, p. 245105, 2005.

[141] D. R. Smith, D. C. Vier, T. Koschny, and C. M. Soukoulis, "Electromagnetic parameter retrieval from inhomogeneous metamaterials," *Physical Review E*, vol. 71, p. 036617, 2005.

[142] S. A. Tretyakov, *Analytical Modeling in Applied Electromagnetics*, ser. Artech House electromagnetic analysis series. Norwood: Artech House, 2003.

[143] A. Ishimaru, S. W. Lee, Y. Kuga, and V. Jandhyala, "Generalized constitutive relations for metamaterials based on the quasi-static lorentz theory," *IEEE Transactions on Antennas and Propagation*, vol. 51, no. 10, pp. 2550–2557, 2003.

[144] H.-Y. Yao, L.-W. Li, Q. Wu, and J. A. Kong, "Macroscopic performance analysis of metamaterials synthesized from microscopic 2-D isotropic cross split-ring resonator array," *Progress In Electromagnetics Research, PIER*, vol. 51, pp. 197–217, 2005.

[145] R. Marqués, F. Medina, F. Mesa, and J. Martel, "On the electromagnetic modelling of left-handed metamaterials," in *NATO Advanced Workshop on Bianisotropics 2002 - 9th International Conference on Electromagnetics of Complex Media*, ser. Series II: Mathematics, Physics and Chemistry - Vol 89, S. Zouhdi, A. Sihvola, and M. Arsalane, Eds. Marrakesh, Morocco: Kluwer Academic Publishers, 2002, pp. 132–140.

[146] C. Caloz and S. Gupta, "Dispersion and nonlinearity engineered metamaterial devices," in *Metamaterials' 2007: First International Congress on Advanced Electromagnetic Materials in Microwave and Optics*, Rome, Italy, 22-24 October 2007, pp. 627–630.

[147] I. H. Lin, M. DeVincentis, C. Caloz, and T. Itoh, "Arbitrary dual-band components using composite right/left-handed transmission lines," *IEEE Transactions on Microwave Theory and Techniques*, vol. 52, no. 4, pp. 1142–1149, April 2004.

[148] D. Kholodnyak, E. Serebryakova, I. Vendik, and O. Vendik, "Broadband digital phase shifter based on switchable right- and left-handed transmission line sections," *IEEE Microwave and Wireless Components Letters*, vol. 16, no. 5, pp. 258–260, May 2006.

[149] G. V. Eleftheriades, M. A. Antoniades, and F. Qureshi, "Antenna applications of negative-refractive-index transmission-line structures," *IET Microw. Antennas Propag.*, vol. 1, no. 1, pp. 12–22, 2007.

[150] M. A. Antoniades and G. V. Eleftheriades, "A broadband wilkinson balun using microstrip metamaterial lines," *IEEE Antennas and Wireless Propagation Letters*, vol. 4, pp. 209–212, 2005.

[151] R. Islam and G. V. Eleftheriades, "Phase-agile branch-line couplers using metamaterial lines," *IEEE Microwave and Wireless Components Letters*, vol. 14, no. 7, pp. 340–342, 2004.

[152] H. Okabe, C. Caloz, and T. Itoh, "A compact enhanced-bandwidth hybrid ring using an artificial lumped-element left-handed transmission-line section," *IEEE Transactions on Microwave Theory and Techniques*, vol. 52, no. 3, pp. 798–804, 2004.

[153] M. A. Antoniades and G. V. Eleftheriades, "A broadband series power divider using zero-degree metamaterial phase-shifting lines," *IEEE Microwave and Wireless Components Letters*, vol. 15, no. 11, pp. 808–810, November 2005.

[154] A. Lai, K. M. K. H. Leong, and T. Itoh, "A novel N-port series divider using infinite wavelength phenomena," in *IEEE MTT-S Int. Microwave Symp. Dig.*, Long Beach , CA, 12-17 June 2005, pp. 1001–1004.

[155] C. Camacho-Penalosa, J. Mata-Contreras, and T. M. Martin-Guerrero, "Composite right/left-handed transmission lines in distributed amplification and mixing," in *NATO Advanced Research Workshop: Metamaterials for Secure Information and Communication Technologies*, Marrakech, Morocco, 7-10 May 2008, pp. 291–301.

[156] S. Abielmona, S. Gupta, and C. Caloz, "Experimental demonstration and characterization of a tunable CRLH delay line system for impulse/continuous wave," *IEEE Microwave and Wireless Components Letters*, vol. 17, no. 12, pp. 864–866, December 2007.

[157] H. V. Nguyen and C. Caloz, "CRLH delay line pulse position and modulation transmitter," *IEEE Microwave and Wireless Components Letters*, vol. 18, no. 8, pp. 527–529, August 2008.

[158] R. Islam and G. V. Eleftheriades, "A planar metamaterial co-directional coupler that couples power backwards," in *IEEE MTT-S Int. Microwave Symp. Dig.*, Philadelphia , PA, 8-13 June 2003, pp. 321–324.

[159] L. Liu, C. Caloz, C. C. Chang, and T. Itoh, "Forward coupling phenomena between artificial left-handed transmission lines," *Journal of Applied Physics*, vol. 92, no. 9, pp. 5560–5565, 2002.

[160] C. Caloz and T. Itoh, "A novel mixed conventional microstrip and composite right/left-handed backward-wave directional coupler with broadband and tight coupling characteristics," *IEEE Microwave and Wireless Components Letters*, vol. 14, no. 1, pp. 31–33, 2004.

[161] C. Caloz, A. Sanada, and T. Itoh, "A novel composite right-/left-handed coupled-line directional coupler with arbitrary coupling level and broad bandwidth," *IEEE Transactions on Microwave Theory and Techniques*, vol. 52, no. 3, pp. 980–992, 2004.

[162] R. Islam, F. Elek, and G. V. Eleftheriades, "Coupled-line metamaterial coupler having co-directional phase but contra-directional power flow," *Electronics Letters*, vol. 40, no. 5, 2004.

[163] H. V. Nguyen and C. Caloz, "Generalized coupled-mode approach of metamaterial coupled-line couplers: Coupling theory, phenomenological explanation, and experimental demonstration," *IEEE Transactions on Microwave Theory and Techniques*, vol. 55, no. 5, pp. 1029–1039, May 2007.

[164] N. Engheta, "An idea for thin subwavelength cavity resonators using metamaterials with negative permittivity and permeability," *IEEE Antennas and Wireless Propagation Letters*, vol. 1, pp. 10–13, 2002.

[165] J. Perruisseau-Carrier and A. K. Skrivervik, "Design of wideband high and low impedance metatransmission lines," *Microwave and Optical Technology Letters*, vol. 49, no. 8, pp. 1926–1329, August 2007.

[166] M. Gil, I. Gil, J. Bonache, J. Garcia-Garcia, and F. Martin, "Metamaterial transmission lines with extreme impedance values," *Microwave and Optical Technology Letters*, vol. 48, no. 12, pp. 2499–2505, December 2006.

[167] A. Diaz-Bolado, F. Bongard, J. Perruisseau-Carrier, and J. R. Mosig, "Application of composite right/left handed transmission lines to antenna matching," in *European Conference on Antennas and Propagation (EuCAP)*, Nice, France, 6-10 November 2006.

[168] C. Damm, J. Freese, M. Schüssler, and R. Jakoby, "Electrically controllable artificial transmission line transformer for matching purposes," *IEEE Transactions on Microwave Theory and Techniques*, vol. 55, no. 6, pp. 1348–1354, June 2007.

[169] W. Tong, Z. Hu, H. S. Chua, P. D. Curtis, A. A. P. Gibson, and M. Missous, "Left-handed metamaterial coplanar waveguide components and circuits in GaAs MMIC technology," *IEEE Transactions on Microwave Theory and Techniques*, vol. 55, no. 8, pp. 1794–1800, August 2007.

[170] J. Perruisseau-Carrier, T. Lisec, and A. K. Skrivervik, "Circuit model and design of silicon-integarted CRLH TLs analogically controlled by MEMS," *Microwave and Optical Technology Letters*, vol. 48, no. 12, pp. 2496–2499, 2006.

[171] J. Perruisseau-Carrier, A. K. Skrivervik, and J. R. Mosig, "Micromachined and MEMS-reconfigurable ku-band TL-based metamaterials," in *NATO Advanced Research Workshop: Metamaterials for Secure Information and Communication Technologies*, Marrakech, Morocco, 7-10 May 2008, pp. 418–427.

[172] F. Bilotti and L. Vegni, "Resonant microwave absorbers without a metallic backing based on metamaterials," in *NATO Advanced Research Workshop: Metamaterials for Secure Information and Communication Technologies*, Marrakech, Morocco, 7-10 May 2008, pp. 32–36.

[173] L. Liu, C. Caloz, and T. Itoh, "Dominant mode leaky-wave antenna with backfire-to-endfire scanning capability," *Electronics Letters*, vol. 38, no. 23, pp. 1414–1416, 2002.

[174] A. Grbic and G. V. Eleftheriades, "Experimental verification of backward-wave radiation from a negative refractive index metamaterial," *Journal of Applied Physics*, vol. 92, no. 10, pp. 5930–5935, 2002.

[175] S. Lim, C. Caloz, and T. Itoh, "Electronically scanned composite right/left handed microstrip leaky-wave antenna," *IEEE Microwave and Wireless Components Letters*, vol. 14, no. 6, pp. 277–279, 2004.

[176] ——, "Metamaterials-based electronically controlled transmission-line structure as a novel leaky-wave antenna with tunable radiation angle and beamwidth," *IEEE Transactions on Microwave Theory and Techniques*, vol. 52, no. 12, pp. 2678–2690, 2004.

[177] F. P. Casares-Miranda, C. Camacho-Penalosa, and C. Caloz, "High-gain active composite right/left-handed leaky-wave antenna," *IEEE Transactions on Antennas and Propagation*, vol. 54, no. 8, pp. 2292–2300, August 2006.

[178] C. Caloz and T. Itoh, "1D and 2D leaky-wave antennas based on metamaterials concepts," in *27th ESA Antenna Workshop on Innovative Periodic Antennas*, Santiago de Compestela, Spain, 2004, pp. 167–174.

[179] C. Allen, C. Caloz, and T. Itoh, "Leaky-waves in a metamaterial-based two-dimensional structure for a conical beam antenna application," in *IEEE MTT-S Int. Microwave Symp. Dig.*, vol. 1, Fort Worth , TX, 2004, pp. 305–308.

[180] C. Allen, K. M. K. H. Leong, C. Caloz, and T. Itoh, "A two-dimensional edge excited metamaterial-based leaky wave antenna," in *IEEE Antennas and Propagation Int. Symp. (AP-S) and USNC/URSI Meeting*, vol. 2B, Washington, DC, 2005, pp. 320–323.

[181] A. Lai, K. M. K. H. Leong, and T. Itoh, "Leaky-wave steering in a two-dimensional metamaterial structure using wave interaction excitation," in *IEEE MTT-S Int. Microwave Symp. Dig.*, San Francisco , CA, 11-16 June 2006, pp. 1643–1646.

[182] S. Hrabar and G. Jankovic, "Scanning leaky-wave antenna based on a waveguide filled with plasma-like ENG metamaterial," in *IEEE Melecon 2006*, Malaga, Spain, 16-19 May 2006, pp. 280–283.

[183] M. Schüssler, J. Freese, and R. Jakoby, "Design of compact planar antennas using LH-transmission lines," in *IEEE MTT-S Int. Microwave Symp. Dig.*, vol. 1, Fort Worth , TX, 2004, pp. 209–212.

[184] C. J. Lee, K. M. K. H. Leong, and T. Itoh, "Design of resonant small antenna using composite right/left-handed transmission line," in *IEEE Antennas and Propagation Int. Symp. (AP-S) and USNC/URSI Meeting*, Washington, DC, 2005.

[185] ——, "Composite right/left-handed transmission line based compact resonant antennas for rf module integration," *IEEE Transactions on Antennas and Propagation*, vol. 54, no. 8, pp. 2283–2291, 2006.

[186] H. Iizuka and P. S. Hall, "Left-handed dipole antennas and their implementations," *IEEE Transactions on Antennas and Propagation*, vol. 55, no. 5, pp. 1246–1253, 2007.

[187] S. Otto, A. Rennings, C. Caloz, P. Waldow, and T. Itoh, "Composite right/left-handed lamda-resonator ring antenna for dual-frequency operation," in *IEEE Antennas and Propagation Int. Symp. (AP-S) and USNC/URSI Meeting*, vol. 1A, Washington, DC, 2005, pp. 684–687.

[188] A. Rennings, S. Otto, C. Caloz, and P. Waldow, "Enlarged half-wavelength resonator antenna with enhanced gain," in *IEEE Antennas and Propagation Int. Symp. (AP-S) and USNC/URSI Meeting*, vol. 3A, Washington, DC, 2005, pp. 683–686.

[189] F. Qureshi, M. A. Antoniades, and G. V. Eleftheriades, "A compact and low-profile metamaterial ring antenna with vertical polarization," *IEEE Antennas and Wireless Propagation Letters*, vol. 4, pp. 333–336, 2005.

[190] A. Lai, K. M. K. H. Leong, and T. Itoh, "Dual-mode compact microstrip antenna based on fundamental backward wave," in *Asia-Pacific Microwave Conference (APMC)*, vol. 4, 2005.

[191] S. F. Mahmoud, "A new miniaturized annular ring patch resonator partially loaded by a metamaterial ring with negative permeability and permittivity," *IEEE Antennas and Wireless Propagation Letters*, vol. 3, pp. 19–22, 2004.

[192] S. A. Tretyakov and M. E. Ermutlu, "Modeling of patch antennas partially loaded with dispersive backward-wave materials," *IEEE Antennas and Wireless Propagation Letters*, vol. 4, pp. 266–269, 2005.

[193] A. Alu, F. Bilotti, N. Engheta, and L. Vegni, "Subwavelength, compact, resonant patch antennas loaded with metamaterials," *IEEE Transactions on Antennas and Propagation*, vol. 55, no. 1, pp. 13–25, 2007.

[194] F. Bilotti, A. Alu, and L. Vegni, "Design of miniaturized metamaterial patch antennas with mu-negative loading," *IEEE Transactions on Antennas and Propagation*, vol. 56, no. 6, pp. 1640–1647, June 2008.

[195] S. Enoch, G. Tayeb, P. Sabouroux, N. Guérin, and P. Vincent, "A metamaterial for directive emission," *Physical Review Letters*, vol. 89, no. 21, p. 213902, 2002.

[196] G. Lovat, P. Burghignoli, F. Capolino, D. R. Jackson, and D. R. Wilton, "Analysis of directive radiation from a line source and in a metamaterial slab with low permittivity," *IEEE Transactions on Antennas and Propagation*, vol. 54, no. 3, pp. 1017–1030, March 2006.

[197] R. W. Ziolkowski and A. D. Kipple, "Application of double negative materials to increase the power radiated by electrically small antennas," *IEEE Transactions on Antennas and Propagation*, vol. 51, no. 10, pp. 2626–2640, 2003.

[198] R. W. Ziolkowski and A. Erentok, "Metamaterial-based efficient electrically small antennas," *IEEE Transactions on Antennas and Propagation*, vol. 54, no. 7, pp. 2113–2130, July 2006.

[199] D. A. Tonn and R. Bansal, "Practical considerations for increasing radiated power from an electrically small antenna by application of a double negative metamaterial," in *IEEE Antennas and Propagation Int. Symp. (AP-S) and USNC/URSI Meeting*, vol. 2A, Washington, DC, 2005, pp. 602–605.

[200] P. M. T. Ikonen, S. I. Maslovski, C. R. Simovski, and S. A. Tretyakov, "On artificial magnetodielectric loading for improving the impedance bandwidth properties of microstrip antennas," *IEEE Transactions on Antennas and Propagation*, vol. 54, no. 6, pp. 1654–1662, June 2006.

[201] H. Mosallaei and K. Sarabandi, "Design and modeling of patch antenna printed on magneto-dielectric embedded-circuit metasubstrate," *IEEE Transactions on Antennas and Propagation*, vol. 55, no. 1, pp. 45–52, January 2007.

[202] P. Ikonen and S. Tretyakov, "Comments on "design and modeling of patch antenna printed on magnetodielectric embedded-circuit metasubstrate"," *IEEE Transactions on Antennas and Propagation*, vol. 55, no. 10, pp. 2935–2936, October 2007.

[203] H. Mosallaei and K. Sarabandi, "Reply to "comments on 'design and modeling of patch antenna printed on magneto-dielectric embedded-circuit metasubstrate'"," *IEEE Transactions on Antennas and Propagation*, vol. 55, no. 10, pp. 2936–2937, October 2007.

[204] A. Alu, F. Bilotti, N. Engheta, and L. Vegni, "Subwavelength planar leaky-wave components with metamaterial bilayers," *IEEE Transactions on Antennas and Propagation*, vol. 55, no. 3, pp. 882–891, March 2007.

[205] M. A. Antoniades and G. V. Eleftheriades, "A metamaterial series-fed linear dipole array with reduced beam squinting," in *IEEE Antennas and Propagation Int. Symp. (AP-S) and USNC/URSI Meeting*, Albuquerque, NM, 2006, pp. 4125–4128.

[206] F. Bongard, I. Stevanovic, O. J. F. Martin, and J. R. Mosig, "Characterization of metamaterial slabs in terms of scattering parameters under oblique plane wave incidence," in *European Conference on Antennas and Propagation (EuCAP)*, Nice, France, 2006.

[207] F. Bongard, J. Perruisseau-Carrier, A. K. Skrivervik, and J. R. Mosig, "A review on metamaterial activities at LEMA-EPFL," in *Metamaterials' 2007: First International Congress on Advanced Electromagnetic Materials in Microwave and Optics*, Rome, Italy, 2007, pp. 938–941.

[208] J. A. Kong, *Theory of Electromagnetic Waves*. Wiley-Interscience, 1975.

[209] V. V. Varadan and R. Ro, "Unique retrieval of complex permittivity and permeability of dispersive materials from reflection and transmitted fields by enforcing causality," *IEEE Transactions on Microwave Theory and Techniques*, vol. 55, no. 10, pp. 2224–2230, 2007.

[210] M. Bozzi and L. Perregrini, "Analysis of multilayered printed frequency selective surfaces by the MoM/BI-RME method," *IEEE Transactions on Antennas and Propagation*, vol. 51, no. 10, pp. 2830–2836, 2003.

[211] M. Bozzi, L. Perregrini, J. Weinzierl, and C. Winnewisser, "Efficient analysis of quasi-optical filters by a hybrid MoM/BI-RME method," *IEEE Transactions on Antennas and Propagation*, vol. 49, no. 7, pp. 1054–1064, 2001.

[212] C.-C. Chen, "Diffraction of electromagnetic waves by a conducting screen perforated periodically with circular holes," *IEEE Transactions on Microwave Theory and Techniques*, vol. MTT-19, no. 5, pp. 475–481, 1971.

[213] ——, "Scattering by a two-dimensional periodic array of conducting plates," *IEEE Transactions on Antennas and Propagation*, vol. AP-18, no. 5, pp. 660–665, 1970.

[214] ——, "Transmission through a conducting screen perforated periodically with apertures," *IEEE Transactions on Microwave Theory and Techniques*, vol. MTT-18, no. 9, pp. 627–632, 1970.

[215] I. Stevanovic, P. Crespo-Valero, K. Blagovic, F. Bongard, and J. R. Mosig, "Integral-equation analysis of 3-D metallic objects arranged in 2-D lattices using the ewald transformation," *IEEE Transactions on Microwave Theory and Techniques*, vol. 54, no. 10, pp. 3688–3697, 2006.

[216] M. Silveirinha and C. A. Fernandes, "Homogenization of 3-D-connected and nonconnected wire metamaterials," *IEEE Transactions on Microwave Theory and Techniques*, vol. 53, no. 4, pp. 1418–1430, 2005.

[217] P. A. Belov, C. R. Simovski, and S. A. Tretyakov, "Two-dimensional electromagnetic crystals formed by reactively loaded wires," *Physical Review E*, vol. 66, p. 036610, 2002.

[218] F. Bongard, "Technical note TNWP200: LHM design and analysis," EPFL-LEMA, Tech. Rep., 30 October 2007.

[219] F. Bongard, P. Morel, J. R. Mosig, and O. J. F. Martin, "Perfectly isotropic magnetic resonator," in *Workshop on Metamaterials for Microwave and Optical Technologies*, San Sebastian, Spain, 18-20 July 2005.

[220] J. D. Baena, L. Jelinek, R. Marqués, and J. Zehentner, "Electrically small isotropic three-dimensional magnetic resonators for metamaterial design," *Applied Physics Letters*, vol. 88, p. 134108, 2006.

[221] ——, "Analysis of 2D- and 3D-isotropic split ring resonators," in *18th International Conference on Applied Electromagnetics and Communications (ICECom 2005).*, Dubrovnik, Croatia, 12-14 Oct. 2005.

[222] R. A. Depine and A. Lakhtakia, "Comment i on "resonant and antiresonant frequency dependence of the effective parameters of metamaterials"," *Physical Review E*, vol. 70, p. 048601, 2004.

[223] A. L. Efros, "Comment ii on "resonant and antiresonant frequency dependence of the effective parameters of metamaterials"," *Physical Review E*, vol. 70, p. 048602, 2004.

[224] T. Koschny, P. Markos, D. R. Smith, and C. M. Soukoulis, "Reply to comments on "resonant and antiresonant frequency dependence of the effective parameters of metamaterials"," *Physical Review E*, vol. 70, p. 048603, 2004.

[225] V. V. Varadan and R. Ro, "Analyticity, causality, energy conservation and the sign of the imaginary part of the permittivity and permeability," in *IEEE Antennas and Propagation Int. Symp. (AP-S) and USNC/URSI Meeting*, Albuquerque, NM, 2006, pp. 499–502.

[226] C. R. Simovski and S. A. Tretyakov, "Local constitutive parameters of metamaterials from an effective-medium perspective," *Physical Review B*, vol. 75, p. 195111, 2007.

[227] ——, "On effective material parameters of metamaterials," in *23rd Annual Review of Progress in Applied Computational Electromagnetics (ACES)*, Verona, Italy, 2007, pp. 150–155.

[228] M. A. Antoniades and G. V. Eleftheriades, "A CPS leaky-wave antenna with reduced beam squinting using NRI-TL metamaterials," *IEEE Transactions on Antennas and Propagation*, vol. 56, no. 3, pp. 708–721, March 2008.

[229] R. Goto, H. Deguchi, and M. Tsuji, "Composite right/left-handed transmission lines based on conductor-backed coplanar strips," *IEICE Trans. Electron.*, vol. E89-C, no. 9, pp. 1306–1311, 2006.

[230] ——, "Composite right/left-handed transmission lines based on conductor-backed coplanar strips for antenna application," in *European Microwave Conference (EuMC)*, Manchester, UK, September 2006, pp. 1040–1043.

[231] E. A. Guillemin, *Synthesis of Passive Networks.* John Wiley & Sons, 1964.

[232] C. Caloz, A. Lai, and T. Itoh, "The challenge of homogenization in metamaterials," *New Journal of Physics*, vol. 7, p. 167, August 2005.

[233] R. N. Simons, *Coplanar Waveguide Circuits, Components and Systems*, ser. Wiley Series in Microwave and Optical Engineering. Wiley-Interscience, 2001.

[234] Agilent-Technologies, "Product note 8510-8A: Agilent network analysis applying the 8510 TRL calibration for non-coaxial measurements."

[235] W. J. Getsinger, "Circuits duals on planar transmission media," in *IEEE MTT-S Int. Microwave Symp. Dig.*, vol. 83, 1983, pp. 154–156.

[236] F. Bongard, J. R. Mosig, and M. Van der Vorst, "Investigations on volumetric layered transmission line metamaterials for antenna applications," in *European Conference on Antennas and Propagation (EuCAP)*, Edinburgh, UK, 2007.

[237] V. Trifunovic and B. Jokanovic, "Balance measurements in double-Y baluns," in *IEE Proc.-Microw. Antennas Propag.*, vol. 149, 2002, pp. 257–260.

[238] ——, "Review of printed marchand and double Y baluns: Characteristics and application," *IEEE Transactions on Microwave Theory and Techniques*, vol. 42, no. 8, pp. 1454–1462, 1994.

[239] ——, "Four decade bandwidth uniplanar balun," *Electronics Letters*, vol. 28, no. 6, pp. 534–535, 1992.

[240] F. Elek and G. V. Eleftheriades, "Dispersion analysis of the shielded sievenpiper structure using multiconductor transmission-line theory," *IEEE Microwave and Wireless Components Letters*, vol. 14, no. 9, pp. 434–436, 2004.

[241] F. Gardiol, *Microstrip Circuits*, ser. Wiley Series in Microwave and Optical Engineering. John Wiley & Sons, 1994.

[242] C. A. Balanis, *Antenna Theory, Analysis and Design*. John Wiley & Sons, 1997.

[243] F. Bongard, "Technical note TNWP400: LHM-based antenna demonstration model," EPFL-LEMA, Tech. Rep., 13 December 2007.

[244] A. K. Iyer and G. V. Eleftheriades, "Characterization of a volumetric negative-refractive-index transmission-line (NRI-TL) metamaterial for incident waves from free-space," in *European Conference on Antennas and Propagation (EuCAP)*, Nice, France, 2006.

[245] ——, "A multilayer negative-refractive-index transmission-line (NRI-TL) metamaterial free-space lens at X-band," *IEEE Transactions on Antennas and Propagation*, vol. 55, no. 10, pp. 2746–2753, October 2007.

[246] ——, "Mechanisms of subdiffraction free-space imaging using a transmission-line metamaterial superlens: An experimental verification," *Applied Physics Letters*, vol. 92, p. 131105, March 2008.

[247] J. Machac, P. Buchar, J. Zehentner, and A. S. Omar, "1D volume metamaterial derived from LH parallel strips," *Proceedings of the European Microwave Association*, vol. 2, no. 1, pp. 83–88, March 2006.

[248] ——, "New bulk metamaterial," in *European Microwave Conference (EuMC)*, Paris, France, October 2005.

[249] F. Bongard, J. Perruisseau-Carrier, and J. R. Mosig, "Equivalent multiconductor transmission line model for periodic structures and application to metamaterials," *Submitted to IEEE Transactions on Microwave Theory and Techniques*, 2009.

[250] M. Stickel, F. Elek, J. Zhu, and G. V. Eleftheriades, "Volumetric negative-refractive-index metamaterials based upon the shunt-node transmission-line configuration," *Journal of Applied Physics*, vol. 102, p. 094903, 2007.

[251] H. K. Liu and T. L. Dong, "Propagation characteristics for periodic waveguide based on generalized conservation of complex power technique," *IEEE Transactions on Microwave Theory and Techniques*, vol. 54, no. 9, pp. 3479–3485, September 2006.

[252] W. S. Best, R. J. Riegert, and L. C. Goodrich, "Dispersion analysis of the linear vane-type waveguide using the generalized scattering matrix," *IEEE Transactions on Microwave Theory and Techniques*, vol. 43, no. 9, pp. 2101–2108, September 1995.

[253] Tsuji, S. M. Matsumoto, H. Shigesawa, and K. Takiyama, "Guided-wave experiments with dielectric waveguides having finite periodic corrugation," *IEEE Transactions on Microwave Theory and Techniques*, vol. MTT-31, no. 4, pp. 337–344, April 1983.

[254] M. S. Navarro, T. E. Rozzi, and Y. T. Lo, "Propagation in a rectangular waveguide periodically loaded with resonant irises," *IEEE Transactions on Microwave Theory and Techniques*, vol. 28, no. 8, pp. 857–865, 1980.

[255] S. Simsek and E. Topuz, "Some properties of generalized scattering matrix representations for metallic waveguides with periodic dielectric loading," *IEEE Transactions on Microwave Theory and Techniques*, vol. 55, no. 11, pp. 2336–2344, 2007.

[256] G. Goussetis, A. P. Feresidis, and P. Kosmas, "Efficient analysis, design, and filter applications of EBG waveguide with periodic resonant loads," *IEEE Transactions on Microwave Theory and Techniques*, vol. 54, no. 11, pp. 3885–3892, November 2006.

[257] R. Lech and J. Mazur, "Propagation in rectangular waveguides periodically loaded with cylindrical posts," *IEEE Microwave and Wireless Components Letters*, vol. 14, no. 4, pp. 177–179, April 2004.

[258] W. S. Best, R. J. Riegert, and L. C. Goodrich, "Analytical dispersion analysis of loaded periodic circuits using the generalized scattering matrix," *IEEE Transactions on Microwave Theory and Techniques*, vol. 44, no. 12, pp. 2152–2158, December 1996.

[259] S. Amari, R. Vahldieck, J. Bornemann, and P. Leuchtmann, "Spectrum of corrugated and periodically loaded waveguides from classical matrix eigenvalues," *IEEE Transactions on Microwave Theory and Techniques*, vol. 48, no. 3, pp. 453–460, 2000.

[260] F. Elek and G. V. Eleftheriades, "On the slow wave behaviour of the shielded mushroom structure," in *IEEE MTT-S Int. Microwave Symp. Dig.*, Atlanta, GA, 15-20 June 2008, pp. 1333–1336.

[261] F. Bongard, J. Perruisseau-Carrier, and J. R. Mosig, "Bloch wave analysis for multi-mode periodic structures: Applications to transmission line metamaterials," in *NATO Advanced Research Workshop: Metamaterials for Secure Information and Communication Technologies*, Marrakech, Morocco, 7-10 May 2008, pp. 264–273.

[262] D. Seetharamdoo, R. Sauleau, K. Mahdjoubi, and A.-C. Tarot, "Effective parameters of resonant negative refractive index metamaterials: Interpretation and validity," *Journal of Applied Physics*, vol. 98, p. 063505, 2005.

[263] B. Bandlow and R. Schuhmann, "Analysis of higher order modes in the design of metamaterials by the use of periodic unit cells," in *Metamaterials' 2007: First International Congress on Advanced Electromagnetic Materials in Microwave and Optics*, Rome, Italy, 2007, pp. 736–739.

[264] N. Marcuwitz, *Waveguide Handbook*. Mc-Graw-Hill Book Company, 1951.

[265] G. Conciauro, M. Guglielmi, and R. Sorrentino, *Advanced Modal Analysis*. John Wiley & Sons, 2000.

[266] J. A. B. Faria, *Multiconductor Transmission-Line Structures*, ser. Wiley Series in Microwave and Optical Engineering. Wiley-Interscience, 1993.

[267] C. R. Paul, *Analysis of Multiconductor Transmission Lines*, ser. Wiley Series in Microwave and Optical Engineering. Wiley-Interscience, 1994.

[268] F. Elek and G. V. Eleftheriades, "Simple analytical dispersion equations for the shielded sievenpiper structure," in *IEEE MTT-S Int. Microwave Symp. Dig.*, San Francisco, CA, 2006, pp. 1651–1654.

[269] J. Zhu, M. Stickel, and G. V. Eleftheriades, "A broadband negative-refractive-index transmission-line (NRI-TL) stacked metamaterial for incident plane waves," in *IEEE Antennas and Propagation Int. Symp. (AP-S)*, Honolulu, HI, June 2007, pp. 2357–2360.

[270] J. Zhu and G. V. Eleftheriades, "Fully printed volumetric negative-refractive-index transmission-line slabs using a stacked shunt-node topology," in *IEEE MTT-S Int. Microwave Symp. Dig.*, Atlanta, GA, 15-20 June 2008, pp. 173–176.

[271] F. Bongard and J. R. Mosig, "A novel composite right/left-handed unit cell and potential antenna applications," in *2nd Young Scientist Meeting on Metamaterials (YSMM'08)*, Barcelona, Spain, 7-8 February 2008.

[272] ——, "A novel composite right/left-handed unit cell and potential antenna applications," in *IEEE Antennas and Propagation Int. Symp. (AP-S) and USNC/URSI Meeting*, San-Diego, CA, 2008, pp. 1–4.

[273] F. Bongard, J. Perruisseau-Carrier, and J. R. Mosig, "A novel composite right/left-handed unit cell based on a lattice topology: theory and applications," in *Metamaterials' 2008: Second International Congress on Advanced Electromagnetic Materials in Microwave and Optics*, Pamplona, Spain, 21-26 September 2008.

[274] ——, "Enhanced CRLH transmission line performances using a lattice network unit cell," *Accepted for publication in IEEE Microwave and Wireless Components Letters*, 2009.

[275] P. Russer, *Electromagnetics, Microwave Circuit and Antenna Design for Communications Engineering*, 2nd ed. Norwood: Artech House, Inc, 2006.

[276] J. Perruisseau-Carrier, F. Bongard, M. Fernández-Bolaños, and J. R. Mosig, "Silicon-integrated fixed and reconfigurable CRLH unit cells based on the lattice topology," in *IEEE Antennas and Propagation Int. Symp. (AP-S) and USNC/URSI Meeting*, Charleston, SC, 1-5 June 2009.

[277] P. Alitalo, O. Luukkonen, L. Jylhä, J. Venermo, and S. A. Tretyakov, "Transmission-line networks cloaking objects from electromagnetic fields," *IEEE Transactions on Antennas and Propagation*, vol. 56, no. 2, pp. 416–424, February 2008.

[278] P. Alitalo, F. Bongard, J.-F. Zürcher, J. Mosig, and S. Tretyakov, "Experimental verification of broadband cloaking using a volumetric cloak composed of periodically stacked cylindrical transmission-line networks," *Applied Physics Letters*, vol. 94, p. 014103, January 2009.

[279] P. Alitalo, O. Luukkonen, J. Vehmas, and S. A. Tretyakov, "Impedance-matched microwave lens," *IEEE Antennas and Wireless Propagation Letters*, vol. 7, pp. 187–191, 2008.

[280] P. Alitalo, F. Bongard, J. Mosig, and S. Tretyakov, "Transmission-line lens antenna with embedded source," in *European Conference on Antennas and Propagation (EuCAP)*, Berlin, Germany, 23-27 March 2009.

[281] ——, "Backward-wave slab with electrically tunable index of refraction," in *European Conference on Antennas and Propagation (EuCAP)*, Berlin, Germany, 23-27 March 2009.

CV

Frédéric Bongard was born in Yverdon, Switzerland, in 1978. He received the B.Sc. and M.Sc. degrees in electrical engineering from the Ecole Polytechnique Fédérale de Lausanne (EPFL), Lausanne, Switzerland, in 2003.

From 2003 to 2004, he was an Assistant with the Acoustics part of the Laboratory of Electromagnetics and Acoustics (LEMA), EPFL, where his main task was to realize and test a microphone array designed during the Master Project. This system is aimed at enhancing the hearing comfort for classical music concerts in the Cathedral of Lausanne.

Since October 2004, he has been with the Electromagnetics part of the LEMA, where he is currently a Research and Teaching Assistant. His research interests include periodic structures modeling, the characterization of metamaterials, and the investigation of potential applications of metamaterials to the antenna field. As a Research Assistant, he has been involved in two main EU projects:

- European Space Agency (ESA-ESTEC) Project: Metamaterials for antenna (sub)systems.
- METAMORPHOSE: FP6 European Network of Excellence on Metamaterials.

As a teaching assistant, he has been involved in the supervision of Bachelor and Master projects, and in assistantship for the exercises of Electromagnetics and Antenna courses.

List of publications

Referred Journal Papers

1st author

1. F. Bongard, J. Perruisseau-Carrier, and J. R. Mosig, "Enhanced CRLH Transmission Line Performances Using a Lattice Unit Cell," Accepted for publication in *IEEE Microwave and Wireless Components Letters*, 2009.
2. F. Bongard, J. Perruisseau-Carrier, and J. R. Mosig, "Enhanced Periodic Structure Analysis Based on a Multiconductor Transmission Line Model and Application to Metamaterials," Submitted to *IEEE Transactions on Microwave Theory and Techniques*, 2009.

Others

3. P. Alitalo, F. Bongard, J.-F. Zürcher, J. Mosig, and S. Tretyakov, "Experimental verification of broadband cloaking using a volumetric cloak composed of periodically stacked cylindrical transmission-line networks," *Applied Physics Letters*, vol. 94, p. 014103, January 2009.
4. I. Stevanovic, P. Crespo-Valero, K. Blagovic, F. Bongard, and J. R. Mosig, "Integral-Equation Analysis of 3-D Metallic Objects Arranged in 2-D Lattices Using the Ewald Transformation," *IEEE Transactions on Microwave Theory and Techniques*, vol. 54, pp. 3688-3697, October 2006.

Referred Conference Papers

1st author

1. F. Bongard, J. Perruisseau-Carrier, and J. R. Mosig, "A novel composite right/left-handed unit cell based on a lattice topology: theory and applications," in *Metamaterials' 2008: Second International Congress on Advanced Electromagnetic Materials in Microwave and Optics*, Pamplona, Spain, 2008.
2. F. Bongard and J. R. Mosig, "A novel composite right/left-handed unit cell and potential antenna applications," in *IEEE Antennas and Propagation Int. Symp. (AP-S) and USNC/URSI Meeting*, San-Diego, CA, 2008, pp. 1-4.
3. F. Bongard, J. Perruisseau-Carrier, and J. R. Mosig, "Bloch Wave Analysis for Multimode Periodic Structures: Applications to Transmission Line Metamaterials," in *NATO Ad-*

vanced Research Workshop: Metamaterials for Secure Information and Communication Technologies, Marrakech, Morocco, 2008.

4. F. Bongard, J. R. Mosig, and M. Van der Vorst, "Investigations on volumetric layered transmission line metamaterials for antenna applications," in *European Conference on Antennas and Propagation (EuCAP)*, Edinburgh, UK, 2007.
5. F. Bongard, J. Perruisseau-Carrier, A. K. Skrivervik, and J. R. Mosig, "A Review on metamaterial activities at LEMA-EPFL," in *Metamaterials' 2007: First International Congress on Advanced Electromagnetic Materials in Microwave and Optics*, Rome, Italy, 2007, pp. 938-941.
6. F. Bongard, I. Stevanovic, O. J. F. Martin, and J. R. Mosig, "Characterization of metamaterial slabs in terms of scattering parameters under oblique plane wave incidence," in *European Conference on Antennas and Propagation (EuCAP)*, Nice, France, 2006.

Others

7. J. Perruisseau-Carrier, F. Bongard, M. Fernández-Bolaños, and J. R. Mosig, "Silicon-Integrated Fixed and Reconfigurable CRLH Unit Cells Based on the Lattice Topology," Accepted for presentation in *IEEE Antennas and Propagation Int. Symp. (AP-S) and USNC/URSI Meeting*, Charleston, SC, 2009.
8. P. Alitalo, F. Bongard, J. Mosig, and S. Tretyakov, "Transmission-line lens antenna with embedded source," Accepted for presentation in *European Conference on Antennas and Propagation (EuCAP)*, Berlin, Germany, 2009.
9. P. Alitalo, F. Bongard, J. Mosig, and S. Tretyakov, "Backward-wave slab with electrically tunable index of refraction," Accepted for presentation in *European Conference on Antennas and Propagation (EuCAP)*, Berlin, Germany, 2009.
10. A. Diaz-Bolado, F. Bongard, J. Perruisseau-Carrier, and J. R. Mosig, "Application of Composite Right/Left Handed Transmission Lines to Antenna Matching," in *European Conference on Antennas and Propagation (EuCAP)*, Nice, France, 2006.

Referred Workshop and Seminar Presentations

1. F. Bongard and J. R. Mosig, "A novel composite right/left-handed unit cell and potential antenna applications," in *2nd Young Scientist Meeting on Metamaterials (YSMM'08)*, Barcelona, Spain, 2008.
2. F. Bongard, P. Morel, J. R. Mosig, and O. J. F. Martin, "Perfectly Isotropic Magnetic Resonator," in *Workshop on Metamaterials for Microwave and Optical Technologies*, San Sebastian, Spain, 2005.

Others

1st author

1. F. Bongard, L. Golestanirad, and J. R. Mosig, "Bloch Wave Analysis of Periodically Loaded Multiconductor Transmission Lines: Application to Metamaterial Structures," in *Ansoft Workshop: First-Pass System Success*, Paris, France, 2008.
2. F. Bongard, O. J. F. Martin, J. R. Mosig, and M. van der Vorst, "The Effect of a Metamaterial Torus on the Radiation of a Dipole," in *Microwave Technology and Techniques Workshop Enabling Future Space Systems*, Estec, Noordwijk, The Netherlands, 2006.

Others

3. J. Perruisseau-Carrier, F. Bongard, A. K. Skrivervik, and J. R. Mosig, "Efficient Modeling and Design of Reconfigurable Reflecting Cells and Application to a MEMS-based Digital Implementation," Submitted to *IEEE Transactions on Microwave Theory and Techniques*, 2009.
4. P. Alitalo, O. Luukkonen, F. Bongard, J.-F. Zürcher, J. R. Mosig, and S. A. Tretyakov, "Broadband cloaking of selected objects in the microwave regime with a volumetric cloak comprising layered networks of transmission lines," Accepted for presentation in *IEEE Antennas and Propagation Int. Symp. (AP-S) and USNC/URSI Meeting*, Charleston, SC, 2009.
5. J. Perruisseau-Carrier, F. Bongard, and A. K. Skrivervik, "Wideband Digitally MEMS-Controlled Reflectarray Cells," in EMTS 2007, *International Symposium on Electromagnetic Theory*, Ottawa, Canada, 2007.